

# CFD Platforms: an Introduction to Onera's Softwares



**Jean Jacques Thibert**  
Scientific Director  
of the Fluid Mechanics  
and Energetics Branch

This second issue of Aerospace Lab is dedicated to Computational Fluid Dynamics (CFD). The objective is to develop platforms for our industrial partners, as well as for our own research. This activity started at Onera in the late sixties, when the first computers became available. A dramatic progress in CFD has been achieved since the beginning, due to both a continuous increase in computer power and the development of advanced algorithms. Thus, CFD has become an essential tool for industry, both for performance prediction and for design purposes, and one of Onera's missions is to provide industry with the most advanced platforms. CFD is a multidisciplinary activity, since skills in physics, applied mathematics, informatics and aeronautical engineering are needed. This will be detailed in this issue, where the "elsA" and "CEDRE" platforms, dedicated respectively to aerodynamics and propulsion, are presented in detail.

### Review of the physics underlying the numerical methods

Fluid motion is fully described by the Navier-Stokes equations, which express the conservation of mass, momentum, energy and, if necessary, chemical species. Although these equations are well known, their solution in practical applications is beyond the scope of present and foreseeable computers. Models are thus required to account for different physical phenomena. For non-reactive flows, the transition to turbulence, as well as at least part of the turbulent motion are to be modeled [1].

When dealing with reactive flows, models are also required for the source terms, which arise from the chemical reactions appearing in the species mass balance equations. For laminar flows, Arrhenius laws are simply used, whereas for turbulent flows, different models have been developed in order to treat diffusion flames, premixed flames, or intermediate situations [2]. For these flows, thermodynamic properties also have to be accurately computed [3].

In propulsion systems, different phase flows are present. The different models for the special case of gas-particle flows, which are of major importance in the aerospace context, are described in [4].

Radiative flux and power must be calculated in many applications using CFD, such as predictions of pollutant emissions and service life of aeroengine combustors, the design of thermal protection systems and the ignition of solid propellant rocket motors, the design of spacecraft heat shields for atmospheric (re-)entries, etc. In such

configurations, media are composed of gases (combustion products or plasma) and particles (soot, alumina, water droplets). Since the use of a line-by-line approach is not possible for industrial configurations, radiative properties are computed by means of approximate band models, which are presented in [5].

### Mathematical aspects

The Navier-Stokes equations associated with the different turbulence models must be discretized on meshes to be solved. Onera CFD platforms are based on a finite volume approach. Structured or unstructured meshes can be used, depending on the type of application. Three types of discretization techniques are presented in [6].

After space discretization, a system of ordinary differential equations is obtained. A very large number of iterative methods are available in the literature. A presentation of the two main methods implemented in elsA (LU Relaxation) or CEDRE (GMRES resolution) is made in [7]. The convergence acceleration techniques based on multigrid methods for block-structured grids, which have been used at Onera for many years, are also presented. A dual time-stepping approach, in which a steady state with respect to the dual time is approximately reached at each physical time-step, is described for unsteady flow calculations.

Many design problems of industrial interest can be formulated mathematically as finite-dimensional optimizations, through discretization

and parameterization of the shape of the object of interest. Hence, a good knowledge of global and local optimization algorithms is important to aerodynamic design engineers. The classical algorithms that are currently used at Onera for aerodynamic shape optimization are presented. In addition, many local optimization algorithms require the gradient of the functions of interest with respect to the design parameters. The different ways to compute those derivatives - often called "sensitivities" - are also described in [8].

Most real configurations involve different physics. This is the case, for example, of aeroelasticity. Different coupling techniques are presented in [9].

## Softwares architecture

The development of the elsA platform for complex external and internal flow aerodynamics and multidisciplinary applications was initiated at Onera in 1997. The multi-purpose feature of elsA allows the sharing of many common CFD features for a wide range of aerospace applications: aircraft, helicopters, turbo machinery, missiles, launchers, etc. The elsA software is based on an Object-Oriented design method and on an Object-Oriented implementation, based on three programming languages: C++, Fortran and Python. The strategy for interoperability is based on a component approach, which relies on standard interfaces for the CFD simulation components [10].

CEDRE® is a multi-physics platform for general unstructured grids, for both research and industrial applications, in the fields of energetics and propulsion. The software architecture follows a multi-domain, multi-solver approach. Different solvers are considered for

each physical system: gas phase, dispersed phase, thermal fields in solids and radiation. These solvers share the CEDRE architecture and libraries, and can be either coupled to perform a multi-physics computation, or operated alone [11].

## Various applications that can be computed using Onera's platforms

The different applications presented in [12] underline the capabilities of the elsA software to compute the flow around different aircraft, such as airplanes, helicopters and missiles. The aerodynamics of propellers, compressors and turbines is also addressed. Examples include performance prediction and shape optimization. Examples including aeroelasticity and thermal effects are also described.

A selection of recent CEDRE applications in the aerospace field are presented in [13] to illustrate various functionalities of the platform. These applications have been selected to cover a wide range of applications in the field of aerothermodynamics and combustion. Many of them are "multi-physics", in the sense that they are based on the coupling of independent solvers for, respectively, gas flow, condensed phase transport, solid conduction, radiation, etc. Some of them include an external coupling to other codes.

Even though impressive results have already been achieved with CFD, we are still far from computing an aircraft or an engine in their entire utilization domain accurately and at an affordable cost. To achieve this goal, further advances are needed in the topics listed above. Therefore, for at least several decades, experiments will still be needed to complement CFD. The "numerical wind tunnel" is not for tomorrow... ■

## References

- [1] B. AUPOIX, D. ARNAL, H. BÉZARD, B. CHAOUAT, F. CHEDEVERGNE, S. DECK, V.GLEIZE, P. GRECARD and E. LAROCHE - *Transition and Turbulence Modeling*. Aerospace Lab Issue 2 March 2011.
- [2] F. DUPOIRIEUX and N. BERTIER - *The Models of Turbulent Combustion in the CHARME Solver of CEDRE*. Aerospace Lab Issue 2 March 2011.
- [3] D. DUTOYA - *Thermodynamics in CEDRE*. Aerospace Lab Issue 2 March 2011.
- [4] A. MURRONE and P. VILLEDIEU - *Numerical Modeling of Dispersed Two-Phase Flows*. Aerospace Lab Issue 2 March 2011.
- [5] L. Tessé and J.-M. Lamet - *Radiative Transfer Modeling Developed at Onera for Numerical Simulations of Reactive Flows*. Aerospace Lab Issue 2 March 2011.
- [6] B. COURBET, C. BENOIT, V. COUAILLIER, F. HAIDER, M.-C. LE PAPE and S. PÉRON - *Space Discretization Methods*. Aerospace Lab Issue 2 March 2011.
- [7] C. MARMIGNON, V. COUAILLIER and B. COURBET - *Solution Strategies for Integration of Semi-Discretized Flow Equations in elsA and CEDRE*. Aerospace Lab Issue 2 March 2011.
- [8] J. PETER, G. CARRIER, D. BAILLY, P. KLOTZ, M. MARCELET and F. RENAC - *Local and Global Search Methods for Design in Aeronautics*. Aerospace Lab Issue 2 March 2011.
- [9] M. ERRERA, A. DUGEAI, PH. GIRODROUX-LAVIGNE, J-D GARAU, M. POINOT, S. CERQUEIRA and G. CHAINERAY - *Multi-Physics Coupling Approaches for Aerospace Numerical Simulations*. Aerospace Lab Issue 2 March 2011.
- [10] L. CAMBIER, M. GAZAIX, S. HEIB, S. PLOT, M. POINOT, J.-P. VEUILLLOT, J.-F. BOUSSUGE and M. MONTAGNAC - *An Overview of Multi-Purpose elsA Flow Solver*. Aerospace Lab Issue 2 March 2011.
- [11] A. REFLOCH, B. COURBET, A. MURRONE, P. VILLEDIEU, C. LAURENT, P. GILBANK, J. TROYES, L. TESSÉ, G. CHAINERAY, J.B. DARGAUD, E. QUÉMERAIS and F. VUILLOT, - *CEDRE Software*. Aerospace Lab Issue 2 March 2011.
- [12] J. RENEUX, P. BEAUMIER and P. GIRODROUX-LAVIGNE - *Advanced Aerodynamic Applications with the elsA Software*. Aerospace Lab Issue 2 March 2011.
- [13] D. SCHERRER, F. CHEDEVERGNE, P. GRECARD, J. TROYES, A. MURRONE, E. MONTREUIL, F. VUILLOT, N. LUPOGLAZOFF, M. HUET, B. SAINTE-ROSE, P. THORIGNY, N. BERTIER, J.M. LAMET, T. LE PICHON, E. RADENAC, A. NICOLE, L. MATUSZEWSKI and M. ERRERA - *Recent CEDRE Applications*. Aerospace Lab Issue 2 March 2011.

B. Aupoix, D. Arnal  
 H. Bézard, B. Chaouat,  
 F. Chedeveigne, S. Deck,  
 V. Gleize, P. Grenard, E. Laroche  
 (Onera)

E-mail: bertrand.aupoix@onera.fr

# Transition and Turbulence Modeling

Although the basic equations of fluid motions have been well known for long, their complete solution in practical applications is beyond the scope of present and foreseeable computers. Models are thus required to account for the transition to turbulence mechanisms as well as to represent at least a part of the turbulent motion. This paper aims at giving an overview of the present modeling practices and the models developed or imported by Onera and implemented in the CEDRE and/or *e/sA* solvers.

## Introduction

Fluid motions are fully described by the Navier-Stokes equations which express the conservation of mass, momentum and, if needed, energy and/or chemical species. From a theoretical point of view, solving these equations remains a challenge beyond the present capabilities of mathematicians and is one of the Millennium Problems proposed by the Clay Mathematics Institute. From an engineering point of view, practical flows in aerospace applications are mostly turbulent. As turbulence is characterized by a large variety of scales (see e.g. [40]), all these scales must be captured in the flow computation. This is the Direct Numerical Simulation approach (DNS) which is far beyond the capabilities of present and foreseeable computers. Extrapolating the progress in computer power and computer sciences, it is expected that the DNS computation of the flow around an airliner in cruise conditions or around a car on a (US) highway could be feasible circa 2080 [77]. Therefore, only a simplified vision of the flow can be computed and models are required to represent the part of the physics which cannot be resolved. This holds both for the prediction of the flow instabilities which lead to the transition from the laminar to the turbulent regime and for the fully turbulent regime. Transition and turbulence modeling aspects are detailed below.

## Transition modeling

Since the classical experiments performed by Reynolds [65], constant interest has been shown in the instability of laminar flows and the transition to turbulence for solving fluid mechanics problems. This interest results from the fact that transition controls important hydrodynamic quantities such as drag or heat transfer. For instance, the heating rates generated by a turbulent boundary layer may be several times higher than those for a laminar boundary layer; therefore transition prediction is of great importance for hypersonic re-entry vehicles. In the case of commercial transport aircraft at high subsonic speed, the achievement of laminar flow can significantly reduce the drag on the wings and hence the fuel consumption of the aircraft.

When a laminar flow develops along a given body, it is strongly affected by various types of disturbances generated by the model itself (roughness, vibrations...) or existing in the free-stream (turbulence, noise...). These disturbances are the sources of complex

mechanisms which ultimately lead to turbulence. There are in fact two main paths to turbulence:

- If the laminar boundary layer develops on a “perfectly smooth” wall, in a low free-stream disturbance environment (for instance in flight conditions), transition results from the amplification of unstable waves: this process is called “natural transition”.
- In the presence of strong disturbances (high free-stream turbulence, large roughness elements), these waves are no longer observed. In this case, streamwise streaks appear and play a major role in the transition process; this mechanism has been named “bypass” by Morkovin [54].

Both aspects will be analyzed successively in the following paragraphs.

## Natural transition

### General description

To describe the laminar-turbulent transition process in two-dimensional (2D) or three-dimensional (3D) boundary layers, it is helpful to distinguish three successive steps, as illustrated in Figure 1. The first step, which takes place close to the leading edge, is the *receptivity*. Receptivity describes the means by which forced disturbances such as free-stream noise or free-stream turbulence enter the laminar boundary layer and excite its eigenmodes. In the second phase, these eigenmodes take the form of periodic waves, the energy of which is convected in the streamwise direction. Some of them are amplified and will be responsible for transition. Their evolution is well described by the linear *stability* theory. When the wave amplitude becomes finite, nonlinear interactions occur and lead rapidly to turbulence.

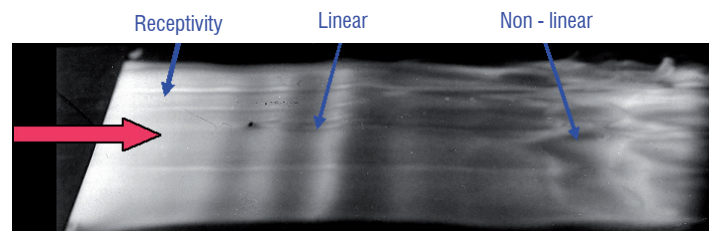


Figure 1 - “Natural” transition on a 2D flat plate, visualization in water channel (Werlé, Onera).

In 2D flows, the linearly growing waves are referred to as Tollmien-Schlichting (TS) waves. In 3D boundary layer flows, for instance on a swept wing, the mean velocity profile has two components: a streamwise component  $u$  in the external streamline direction, and a cross-flow component  $w$  in the direction normal to the previous one. The streamwise velocity profile is unstable in regions of zero or positive pressure gradient (decelerated flows). It generates waves similar to the 2D TS waves, with a wave number direction close to the free-stream direction. The cross-flow velocity profile is highly unstable in negative pressure gradients (accelerated flows). It generates cross-flow (CF) waves with a wave number vector making an angle of 85 to 89° with respect to the free-stream direction.

As it will be explained later, the receptivity process and the nonlinear interactions are different for TS and CF disturbances. In the linear phase, however, the same stability theories are applicable for both types of waves.

### Natural transition modeling

In the framework of the classical linear stability theory, the disturbances are written as:

$$r' = \hat{r}(y) \exp[i(\alpha x + \beta z - \omega t)] \quad (1)$$

$r'$  is a velocity, pressure or density fluctuation;  $\hat{r}$  is an amplitude function;  $x$  and  $z$  are the directions normal and parallel to the leading edge,  $y$  is the direction normal to the wall. When considering the spatial theory (which is the most relevant for a wide range of boundary layer problems),  $\alpha = \alpha_r + i\alpha_i$  is the (complex) wave number in the  $x$  direction.  $\beta$  and  $\omega$  are real and represent the wave number component in the  $z$  direction and the frequency. The angle  $\psi$  defined as:

$$\tan \psi = \beta / \alpha_r \quad (2)$$

represents the wave number direction, i.e. the direction normal to the wave crests.

Introducing expression (1) into the linearized Navier-Stokes equations and assuming that the mean flow is parallel, leads to a system of ordinary differential equations for the amplitude functions (eigenvalue problem). For the simplest case of a 2D, low speed flow with  $\beta = 0$ , the stability equations can be combined to obtain the well-known Orr-Sommerfeld equation. Depending on the value of  $\psi$ , the solutions of the linear stability equations represent either TS or CF waves.

Non linear PSE (Parabolized Stability Equations) can be used in order to model the *non linear interactions* between waves just before the breakdown to turbulence, see [37]. The disturbances are now expressed as a double series of  $(n, m)$  modes of the form:

$$r' = \sum_{n=-\infty}^{n=+\infty} \sum_{m=-\infty}^{m=+\infty} \hat{r}_{nm}(x, y) \exp\left[i\left(\int \alpha_{nm}(\xi) d\xi + m\beta z - n\omega t\right)\right]. \quad (3)$$

As for the linear theory,  $\alpha_{nm}$  is complex;  $\beta$  and  $\omega$  are real numbers. Each mode is denoted as  $(n, m)$ ; the integers  $n$  and  $m$  characterize the frequency and the spanwise wave number, respectively. When these disturbances are introduced into the Navier-Stokes equations, a system of coupled partial differential equations is obtained; this (nearly) parabolic system is solved by a marching procedure in the

$x$ -direction. Any non-linear PSE computation requires a choice of the “most interesting” interaction scenario between particular modes (“major modes”) and imposition of initial amplitudes  $A_m$  for these modes. The numerical results show that the non linear behaviors are different depending on the nature of the dominant instability at transition: in the case of TS waves, resonances between 2D ( $\beta = 0$ ) and oblique modes lead to a sudden increase of the mode amplitudes; in the case of CF waves, a saturation is observed before the breakdown to turbulence.

As far as the receptivity process is concerned, a distinction must be made between TS and CF instabilities:

- TS instability is very sensitive to the free-stream disturbances (noise or the free-stream turbulence), which are usually quantified by the non-dimensional parameter  $Tu$ .

- The CF waves cover a wide frequency range. In particular, zero frequency waves are highly amplified by the cross-flow mean velocity component  $w$ . They take the form of stationary vortices nearly aligned with the external streamlines. At low  $Tu$ , these vortices play the major role in the transition process by creating a steady inflection point on the streamwise velocity profile. It is now recognized that the source of the CF vortices lies in the micron-sized roughness elements (i.e. the surface polishing) at the location where the vortices start to be amplified [61], typically between 1 and 5% chord on a swept wing. It follows that improving the surface polishing of the leading edge decreases the initial amplitude of the vortices and delays transition.

### Natural transition prediction

The most popular method for predicting transition is the  $e^N$  criterion, developed more than 50 years ago by Smith and Gamberoni [74] and by van Ingen [84], see review in [4]. The so-called  $N$  factor is the total growth rate of the most unstable disturbances. For the simplest case of 2D, incompressible flows, it is computed by integrating  $-\alpha_i$  in the  $x$  direction. The procedure becomes more complicated for compressible and/or 3D flows, but the principle remains the same. Transition is assumed to occur for some specified value  $N_T$  of  $N$ ; for instance,  $N_T$  lies in the range 8-10 on 2D airfoils in low turbulence wind tunnels. The  $e^N$  method is based on the linear theory only and does not take the receptivity and the non linear mechanisms into account explicitly.

As the use of the  $e^N$  method is often time consuming, the development of simplified methods is of unquestionable practical interest. The simplest solution is to apply analytical criteria expressing relationships between boundary layer integral parameters at the transition point, see for instance [53], [35], [3]. The latter criteria have been implemented in the *e/sA* code. Another possibility is to use simplified stability methods (the so-called “database methods”), the complexity of which is intermediate between analytical criteria and exact stability computations [59].

The above methods, however, are not well adapted to massively parallel RANS computations because they use non-local quantities such as momentum thickness or shape factor. To avoid these difficulties, Menter [52] proposed a purely local transition model which consists of two transport equations for the intermittency function and for a pseudo-momentum thickness Reynolds number, coupled with a SST  $-k\omega$  turbulence model. At Onera, this model has been implemented in the *e/sA* code. Once calibrated by comparison with experimental

data or stability results, it gives satisfactory results for 2D flows, see [23]. It does not include the cross-flow instability.

At first sight, the non linear PSE could be considered as the most rigorous tool for transition prediction, because they describe both the linear and the non linear developments of the unstable waves. However, it is important to keep in mind that the abscissa corresponding to the resonance (for TS waves) or to the mode saturation (for CF waves) depends on the initial amplitude  $A_m$  imposed on the major modes. Increasing  $A_m$  leads to an upstream movement of this abscissa and of the numerical breakdown location. In other words, the choice of the  $N$  factor, which constitutes the major difficulty of the linear  $e^N$  method, is now replaced by the choice of  $A_m$ . Therefore the non linear PSEs cannot yet be considered as mature enough for practical transition prediction. A measure of the receptivity is needed.

## Bypass Transition

### General description

In many practical situations, laminar-turbulent transition occurs at lower Reynolds numbers than those predicted by the classical linear stability theory. This suggests that another transition mechanism may exist. This process, called “transient growth”, results from the non-normality of the eigenfunctions (solutions of the linear stability equations): if two eigenfunctions are not orthogonal, the perturbation energy of their sum can increase even if both of them are damped. The physics of the transient growth is the following. A longitudinal vortex superimposed to the boundary layer shear stress pushes up low speed particles from the wall to the top of the shear layer, and pulls down high speed particles toward the wall, leading to a spanwise alternation of low and high speed streamwise structures called streaks. This phenomenon was called “lift-up” by Landahl [43]. In other words, as soon as longitudinal vortices are present in a laminar boundary layer, streaks are likely to appear rapidly downstream. An early laminar-turbulent transition can be triggered if the energy of the streaks grows significantly; this is the “bypass” transition process, meaning that the classical process driven by the TS or CF waves has been short-circuited.

Bypass transition can be observed when the laminar boundary layer is subjected to a large free-stream turbulence level  $Tu$  (typically larger than 1%). The longitudinal vortices which initiate the transient growth process are generated by the large structures of the free-stream turbulence. In this case, the streaks are called “Klebanoff modes”. An example of smoke visualization for a flat plate boundary layer with  $Tu = 6\%$  is shown in the left hand part of Figure 2 [49]. The streamwise streaks are clearly visible. Note that transition is out of the figure.

Recent studies have demonstrated that streamwise streaks also play a significant role in the transition process downstream of an isolated roughness element. An excellent review of the recent experimental investigations on this subject has been given by Ergin and White [32]. The flow about an isolated 3D element consists of a steady horseshoe vortex wrapped around the upstream side of the obstacle, with two steady counter-rotating legs trailing downstream. These steady disturbances evolve rapidly downstream into low- and high-speed streaks aligned with the flow direction. Transition is defined as the

location where a turbulent wedge starts to develop with a half-angle around  $10^\circ$ , see right hand part of Figure 2. At sufficiently high Reynolds numbers, *unsteady disturbances* (often associated with hairpin vortices) originate from the separated region just aft of the roughness element and can contribute to the transition process.

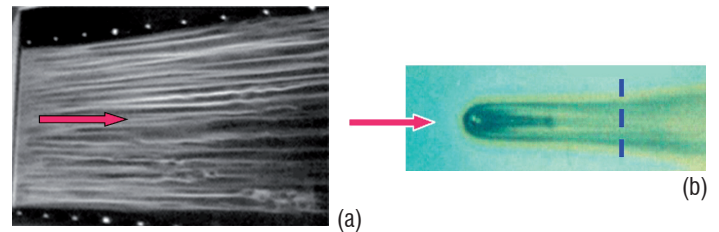


Figure 2 - Examples of bypass transitions.  
(a) Transition induced by a high free-stream turbulence level.  
(b) Transition induced by an isolated roughness element.

### Bypass transition modeling

The linear development of the streamwise structures responsible for bypass transition can be described by an optimal growth theory, in which the disturbances are written as:

$$r' = \hat{r}(x, y) \exp[i(\beta z - \omega t)]. \quad (4)$$

Again  $r'$  is a velocity, pressure or density fluctuation;  $\hat{r}$  is an amplitude function;  $\omega$  is the frequency and  $\beta = 2\pi / \lambda_z$  the spanwise wave number ( $\lambda_z$  is the spanwise wavelength).

By contrast with the classical linear theory, the length scales are different in the  $x, y$  and  $z$  directions. The streamwise coordinate  $x$  is made dimensionless with a characteristic length  $L$  (for instance the length of a flat plate or the chord of an airfoil) and the corresponding velocity  $u'$  is scaled with the free-stream velocity  $U_e$ . The  $y$  and  $z$  coordinates, on the other hand, are made dimensionless with the usual boundary layer scale  $l = \sqrt{\nu L / U_e}$  and the corresponding velocities  $v'$  and  $\omega'$  are scaled by  $U_e / Re_l$ , with  $Re_l = U_e l / \nu$ .

These boundary layer-type approximations lead to a parabolic system which can be solved by a marching procedure in  $x$  with initial conditions imposed at the starting location  $x_0$ . The objective is to maximize the growth  $G$  of the disturbance energy between  $x_0$  and some downstream position  $x_1$ . This can be done by solving the direct system (from  $x_0$  to  $x_1$ ) and the adjoint system (from  $x_1$  to  $x_0$ ) iteratively, see details in [45][14][85] for instance. The numerical results show that the maximum growth is obtained with streamwise vortices as initial disturbances ( $u' \ll v'$  and  $\omega'$ ) and streamwise streaks at the final station ( $u' \gg v'$  and  $\omega'$ ). In addition the frequency with the highest amplitude is  $\omega = 0$ , i.e. the disturbances are steady. These results are in qualitative agreement with the experimental observations.

As stated before, the optimal growth (or transient growth) theory is linear. A complete picture of the bypass transition phenomena also includes a modeling of the receptivity process and of the non linear phenomena leading to the breakdown to turbulence. It is not yet clear today if the receptivity mechanisms generating the streaks are linear or not. Concerning the non linear final stage, it seems that streaks of sufficiently large amplitude become unsteady and that the breakdown to turbulence results from a sudden Kelvin-Helmholtz instability.

## Bypass transition prediction

Many empirical criteria have been developed for many years in order to predict the occurrence of bypass transitions. For instance, the effect of high free-stream turbulence levels is taken into account by the well-known correlation proposed by Abu Ghannam and Shaw [1]. Concerning the problem of boundary layer tripping by large, isolated 3D roughness elements of height  $k$ , a relevant parameter is a characteristic Reynolds number  $Rk$  defined as:

$$Rk = \frac{U_k k}{\nu_k} \quad (5)$$

$U_k$  and  $\nu_k$  denote the mean velocity and the kinematic viscosity at the altitude  $y = k$ . These values are computed in the undisturbed flow. Von Doenhoff and Braslow [87] developed an empirical correlation between the critical value of  $Rk$  (denoted as  $Rk_{crit}$ ) which triggers transition and the ratio  $d/k$ , where  $d$  is a measure of the spanwise or chordwise extent of the protuberance (for circular cylinders normal to the wall,  $d$  is the diameter).  $Rk_{crit}$  is of the order of 500-600 for  $d/k = 1$  and 200-250 for  $d/k = 10$ . Systematic applications of this criterion showed that it remains valid for a wide range of applications, in 2D and 3D flows, from subsonic to supersonic flows.

The transition model proposed by Menter et al. [52] can also predict transition in the presence of large values of  $Tu$ . Examples of applications for turbo-machinery problems using the RANS code elsA can be found in [11].

Quite recently, attempts have been made to use the transient growth theory in order to quantify or to predict the effects of roughness on transition. Following the work of Luchini [45], Vermeersch [85][86] developed a system of parabolic, linear transport equations for the streamwise velocity and temperature fluctuations of the streamwise streaks. To close the system, the vertical velocity fluctuation  $v'$  is modeled by an analytical relationship. Transition is assumed to occur when the ratio between the shear stress generated by the streaks to the viscous stress reaches some predefined critical value. This model was successfully applied to bypass transition problems, both in the case of large free-stream turbulence levels and in the case of boundary layer tripping by large roughness elements. In the latter case, it was possible to determine a theoretical curve for  $Rk_{crit}$  as a function of  $d/k$ . This curve was in good agreement with the von Doenhoff and Braslow criterion mentioned above. This confirms that the transient growth theory contains (at least a part of) the physics of the boundary layer tripping mechanisms.

## Outlooks

After more than fifty years, the  $e^N$  method remains the most widely used method to estimate the "natural" transition location, although its deficiencies are well identified: the receptivity mechanisms are not accounted for explicitly and the nonlinear phase is replaced by a continuous linear amplification up to the onset of transition. The nonlinear PSE equations, on the other hand, are now a classical research tool. Although they cannot be used for systematic practical applications, they are a help in understanding the basic phenomena leading to transition. As much information has been collected during the last ten or fifteen years on receptivity, a rather complete but partly empirical modeling of "natural" transition is now available.

The state-of-the-art for the modeling of bypass transition is not so advanced. Most of the practical prediction methods used today are based on simple criteria, which ignore the complicated physics of the phenomena. Recent investigations have shown that the linear transient growth theory appears to be an efficient tool for the understanding and the modeling of these phenomena. The validity of this approach needs to be validated in complex situations, in particular for 3D and/or compressible flows. In addition, the picture of the receptivity and non linear mechanisms has to be completed.

## Turbulence modeling

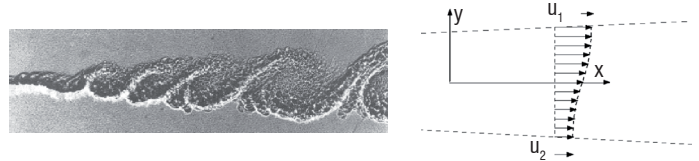


Figure 3 - Instantaneous (left, from [16]) and averaged (right) visions of the mixing layer between two parallel flows of different velocities.

Reynolds [66] proposed decomposing the flow into a mean motion, defined as an ensemble-average (and in most cases, a time average), and turbulent fluctuations. This leads to the Reynolds Averaged Navier-Stokes (RANS) equations. This mean motion was at that time what was measured by most sensors such as pressure probes which naturally time average. However, this average motion has no real existence and cannot really be seen, except using averaging sensors. Figure 3 points out the difference between the real flow and the time-averaged flow in the simple case of a mixing layer. Big, highly corrugated, rollers are visible in one case, completely smeared out in the other one in which a nearly parallel flow is obtained. However, this mean motion is often all that has to be known: no one is interested in the subtle details of the high frequency, small fluctuations of the drag of an airplane, only in the average drag.

On the other hand, extreme values can be important, e.g. the peak thermal loads to be sure the material can withstand them. Similarly, people are interested in the weather forecast in order to find out about tomorrow's weather, but do not care about the average weather. These requirements led to the development of the Large Eddy Simulation (LES) technique, in which a filter is applied to the equations to separate the large enough motions, which can be resolved, from the too small ones, which have to be modeled, in order to solve the most important and energy bearing turbulent motions and get a good idea of the turbulent motion. These techniques are more expensive because a fine grid is required to capture the energy bearing structures and, moreover, the time evolution of these structures has to be computed, while the RANS approach often reduces to a steady problem. Application of the LES technique to an airliner or a car is not foreseen before the middle of the century [77]. Hybrid methods that reduce the computing load by restricting the use of LES techniques to the regions of the flow where they bring significant improvements are presently blooming.

By averaging or filtering the Navier-Stokes equations, a part of the fluid motion is resolved and a part is not. The turbulent, unresolved part appears in the averaged or filtered Navier-Stokes equations as extra terms which represent the mixing of the resolved fluid motion by the unresolved part. The unresolved motion carries momentum,

energy or chemical species within the resolved part. The averaging or filtering thus introduces turbulent stresses and heat or species fluxes which have to be modeled. There are six independent components for the turbulent stress tensor and three for the heat or species flux vectors. The system of equations is now unclosed; as there are more unknowns than equations, models are required.

## RANS approach

### Present status

As pointed out above, turbulent, or Reynolds, stresses and turbulent heat or species fluxes appear in the Reynolds Averaged Navier-Stokes equations. Transport equations for these quantities can be derived from the Navier-Stokes equations. However, the information lost in the averaging process cannot be retrieved, so that these transport equations involve new terms, for which transport equations could be derived, and so on ad infinitum... Modeling is thus required.

In the RANS approach, the modeling of the turbulent stresses and heat or species fluxes heavily relies upon the assumption that the turbulent motion is close to an equilibrium state. Although there is a large range of turbulent scales, with this assumption, the turbulent motion can be characterized by the knowledge of the large, energy bearing scales, the energy distribution in the smaller scales being imposed from the large scales. Therefore, most models only characterize turbulence by two quantities: a turbulent velocity scale and a turbulent length (or equivalently time) scale. The turbulent velocity scale is often deduced from the turbulent kinetic energy, usually labeled  $k$ , the transport equation of which is easily derived from the Navier-Stokes equations and the modeling of which is relatively simple.

RANS turbulence models can be sorted into three main groups:

In the first group, Eddy Viscosity Models (EVM) assume an analogy between the mixing of the averaged flow by the turbulent motion and the transport by the Brownian motion of particles within gases to express the turbulent stresses and heat or species fluxes in a way similar to the viscous stresses and heat or species fluxes. They thus introduce an eddy viscosity, thermal conductivity or diffusivity which, unlike its laminar counterpart, is not a property of the fluid but of the flow motion. From dimensional analysis, they are proportional to the product of the turbulent velocity and length scales. This approach is not fully justified: there is no scale separation between the mean and turbulent motions as there is a scale separation between the gas motion and the Brownian motion. Nevertheless, such models are widely used in the industry as they can give fair predictions of simple, sheared flows, such as boundary layers, wakes, mixing layers... which are of large practical importance. The most popular eddy viscosity models were  $k-\varepsilon$  models (e.g. [44]) where  $\varepsilon$  is the turbulent kinetic dissipation rate, i.e. the rate at which turbulent kinetic energy is transformed into heat, and gives a turbulence length scale (see, e.g. [40]). These  $k-\varepsilon$  models usually fail to predict boundary layer separation and hence, e.g., overestimate the maximum airfoil lift or the compressor performances. They are superseded by the Spalart and Allmaras model [75] and by  $k-\omega$  models, mainly the Shear Stress Transport (SST) model [50], which give improved predictions and are now aeronautic industry workhorses. Again mimicking fluid properties, the thermal conductivity and diffusivity are generally deduced from the eddy viscosity by respectively assuming constant turbulent Prandtl and Schmidt numbers. Although this is nearly the only approach used, it is not fully justified. The standard value for the

turbulent Prandtl number (0.9) holds in the main part of the boundary layer, but not very close to the wall, nor in free shear flows.

The second group solves the crudeness of the eddy viscosity assumption which cannot represent correctly all of the components of the turbulent stress tensor and of the heat or species flux vectors. More complex relationships, similar to the ones used in rheology, or derived from tensor representation theorems, can be used to express the turbulent stresses and heat or species fluxes in terms of the turbulence length and velocity scales and of the mean flow gradients. These models are named Non-Linear Eddy Viscosity Models (NLEVM) or Explicit Algebraic Reynolds Stress Models (EARSM) according to the way they are derived. Non-linear representations can also be used to model the heat or species flux vector. These non-linear models provide fair representations of all of the components of the turbulent stress tensor and of the heat or species flux vector and hence better predictions of more complex flows than simple sheared flows, e.g. they can capture some rotation and curvature effects, as shown in Figure 4.

All the above models link the turbulent stresses and heat or species flux to local velocity, temperature and species gradients. However, turbulence does not adjust instantaneously to the mean flow. This leads to the third group of models, solving the transport equations for the turbulent stresses (and for the turbulent heat or species flux) to capture the turbulence memory and non-equilibrium effects. This requires a larger effort as there are six independent components to the turbulent stress tensor and moreover information about the turbulent length scale is still required. The use of Reynolds stress transport equations is an old practice at the academic level (see, e.g. [55]), mainly in pressure-based codes for incompressible flows. Those models seem particularly appropriate to describe flows characterized by separation, rotation and strong curvature effects such as encountered in turbo-machinery [38]. Their introduction in industrial codes, solving averaged Navier-Stokes equations for compressible flows, is a breakthrough of the European research project FLOMANIA [36]. When the thermal problem is considered, three transport equations for the heat flux vector components are to be added, and generally two more transport equations for characteristic scales for the turbulent thermal field, which leads to twelve transport equations. Transport models for the turbulent heat or species fluxes are thus still at the research level.

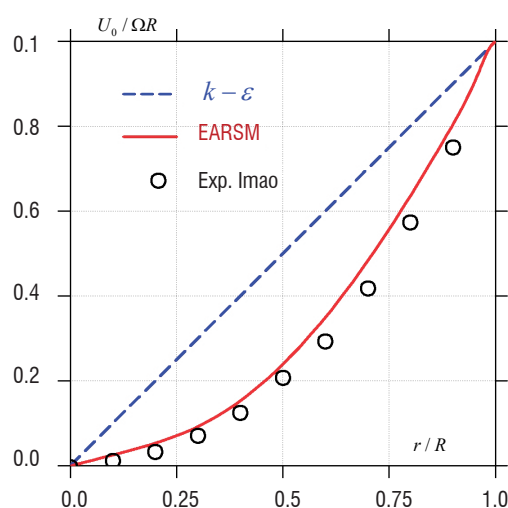


Figure 4 - Mean azimuthal velocity profiles in a rotating pipe: the  $k-\varepsilon$  eddy viscosity model cannot capture the rotation effect upon the turbulent motion and predicts a solid body rotation while the EARSM does and gives fair predictions.

## Some Onera achievements

As pointed out by the Reno workshop organized by NASA to define the needs in turbulence modeling [67], the prediction of boundary layer separation, which e.g. governs the maximum lift or compressor performance predictions, has been a big challenge for a long time. The idea of imposing mathematical constraints to turbulence models was proposed by Cousteix et al. [24] and extended by Catris and Aupoix [18] to correctly capture the physics of boundary layers close to separation. This finally led to the derivation of the  $k-kL$  model by Bézard and Daris [13]. This model has been derived in an eddy viscosity form and in an EARSM form and is one of the models currently used by Dassault Aviation.

Extra transport equations for the thermal scales can be added to get rid of the constant turbulent Prandtl number hypothesis. The above mentioned  $k-kL$  model has been complemented with its thermal counterpart as a four equations  $k-kL-k_\theta-k_\theta L_\theta$  model. This set of scale equations can be coupled with a simple eddy viscosity/thermal conductivity formulation, thus producing physical variations of the turbulent Prandtl number while keeping the simplicity and robustness of classical two-equation models [12], or with more complex explicit algebraic expressions for improving the Reynolds stress tensor and the heat flux vector representation [31].

Another important problem of turbulent flows comes from the effect of strong deviations from equilibrium caused, for instance, by rapid variations in the mean flow. This aspect is mirrored through the well-known weaknesses of the usual modeled dissipation rate equation. Such complex situations rule out the underlying hypothesis of spectral equilibrium that is implicitly assumed in classical RANS models. For dealing with non-equilibrium situations, new models using several length scales and called multiscale models have been introduced [71] and further developed by split spectrum schemes devised to mimic in an approximate way the change of the spectrum shape. The multiscale concept takes into account some spectral information while staying within the useful framework of the RANS modeling. From a practical point of view, many levels of closure can be considered, but in practice, two spectral slices will be sufficient to describe the effects of non equilibrium distributions. In this context, four-equation multiscale turbulence models based on a split spectrum energy-flux scheme and energy frequency scheme [Masson, 1996] were developed and successfully applied on several basic and more complex 2D and 3D non-equilibrium flows such as shock-boundary layer interaction, transonic channels and an airfoil in stall conditions.

Compressibility can strongly affect the turbulence dynamics. In most aeronautic applications, the turbulent motion remains nearly incompressible, so that the key effect is linked to the mean density variations. Turbulence models are developed for incompressible flows and usually straightforwardly applied to compressible flows. The analysis of scalings in a compressible boundary layer gave the hint that the current practice is not correct and led to the derivation of a general rule to extend any turbulence model to correctly account for density gradients within a boundary layer flow [17].

High speed mixing layers, which are encountered e.g. in scramjets, are among the rare examples of aeronautic flows where the turbulent motion can exhibit a compressible character. The sonic eddy concept [15] states that any turbulent structure must be such that information can circulate within it, i.e. the velocity difference between two points

must always be smaller than the speed of sound. This yields a limit on the turbulence length scale, which was first validated and then used to extend in a general way any turbulence model to capture this compressibility effect [6].

As the refraction index is linked to the density, density fluctuations within the flow affect the optical properties of the flow. This has led to the development of aero-optical models for deducing the image blurring from a RANS computation. This requires modeling of both the density fluctuation variance and the way density fluctuations are correlated along the optical path. Models have been derived for boundary layer and mixing layer flows, and validated with respect to LES simulations [83], [7].

Onera has developed a large expertise in flows over rough surfaces, for a wide range of applications such as turbo-machinery or solid propellant rocket nozzles. The standard way to account for wall roughness in industrial codes is the “equivalent sand grain” approach, in which the turbulence model is altered in the wall region to reproduce the drag and heat transfer increases. A general technique to extend any turbulence model to account for wall roughness has been developed and applied to several turbulence models [5], [8]. This technique has also been adapted to account for riblets, small grooves on the wall surfaces like on shark skin, which can equally well lead to a reduction or increase in drag [10].

Of course, most of these models or model improvements are implemented in CEDRE and *e/sA*.

## Some outlooks

The prediction of the separation point is now fairly well understood. However, the model behavior in the separated region, especially close to the separation and reattachment points, is still an issue as models usually underestimate turbulence in this region. This is one of the topics addressed by the European ATAAC project (<http://cfm.mace.manchester.ac.uk/twiki/bin/view/ATAAC/WebHome>) in which Onera is involved.

The present industrial trend is to move from eddy viscosity models towards non-linear models and models with transport equations for the Reynolds stresses. A first Reynolds stress model is implemented in *e/sA*, others will soon be, and the improvement of the Reynolds stress transport models is one of the present activities of Onera.

It has been shown that classical Reynolds stress transport models, which only use information about the Reynolds stress and the turbulence length scale, are unable to reproduce some flow cases. This is blamed upon the lack of information about the underlying turbulence spatial structures. Cooperation with the University of Cyprus has started on models which account for turbulence structures [9].

For thermal applications, there is a trend to get rid of the constant turbulent Prandtl number assumption, and to move to non-linear representations of the turbulent heat flux vector through explicit algebraic expressions. Onera plans to develop, implement and test improved thermal models, with particular attention to hot exhaust jet applications. The next step of directly transporting the heat flux components is promising but needs further developments before being used industrially.

### Direct Numerical Simulations

New industrial needs in aerodynamics include transient dynamics of separated flows as well as the control of noise so the simulation of unsteady turbulent flows is now required. Consequently, a steady RANS solution would not be what the engineer needs in these kinds of applications. But, remembering that one of the salient features of turbulent flows is their multiscale character, Direct Numerical Simulation can explicitly simulate all of the active scales present in a turbulent flow, since the governing equations are discretized directly and solved numerically. The total number of nodes of such a "modeling free" simulation may scale as  $O(\text{Re}_L^3)$  where  $\text{Re}_L$  denotes the Reynolds number based on the integral length scale. If solid walls are present, the near wall structures need to be resolved leading to an even stronger dependence on the Reynolds number. Practical turbulent flows encountered in aeronautics exhibit such a wide range of excited length and time scales (shock waves, boundary and free shear layers,...) at high Reynolds number ( $\approx 10^5 - 10^8$ ) that DNS becomes inappropriate due to prohibitive cost. In other words, DNS remains an efficient research tool which gives significant insights into turbulence physics but will not be used as a predictive tool for design purposes for at least several decades. This is one of the reason why modeling is necessary prior to solving the Navier Stokes equations.

### Large Eddy Simulations

The Large Eddy Simulation approach relies on a decomposition of the field between the large and the small scales of the flow. This approach seeks to directly calculate the largest ones (responsible for turbulence production) while modeling the effects of the smaller-scale eddies. The primary obstacle to practical use of LES on industrial flows which involve wall boundary layers at high Reynolds number remains computing power resources. Indeed, the scales of motion responsible for turbulence production impose severe demands on the grid. In [77], it is proposed that LES of wall turbulence should be considered as a quasi-DNS (QDNS) since the requested resolution for capturing the near wall layer is roughly ten times less expensive than for DNS. The accuracy of DNS/LES for wall-bounded flows has been recently assessed at Onera in various applications including transitional flows [46], [63] and flow control applications [25], [57].

### Hybrid methods

Hybrid RANS/LES was invented to alleviate the LES resolution constraints in the near-wall regions. Basically, the objective is to combine the fine-tuned RANS modeling in the attached boundary layers with the accuracy of LES in the separated regions. Hybrid methods can be categorized into two major classes corresponding respectively to "global" and "zonal" hybrid methods (or "weak" and "strong" RANS/LES coupling methods, see Figure 5). We should point out to the reader that some flow situations are characterized by a scale separation between the unsteadiness of the mean field and turbulence. This situation arises when the boundary condition imposes flow unsteadiness (like the flow around a helicopter blade). Subsequently, unsteady statistical approaches like URANS (Unsteady Reynolds Averaged Navier Stokes) might be used. However, many cases such as a landing gear do not have this scale separation.

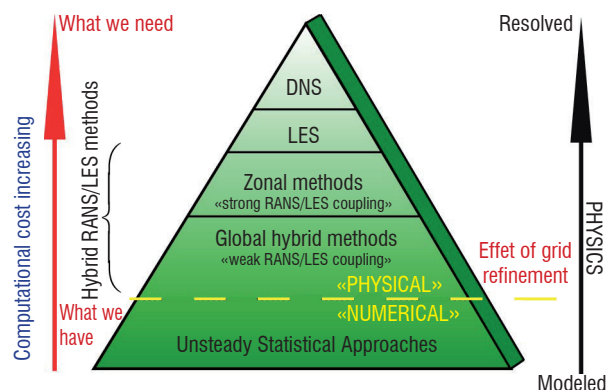


Figure 5 - Classification of unsteady approaches according to levels of modeling and readiness (adapted from Sagaut, Deck and Terracol [68]).

Among hybrid RANS/LES methods, the approach that has probably drawn most attention in the recent time frame is the Detached Eddy Simulation (DES97) which was proposed by Spalart et al. [76] (see also [79]). The idea is to simulate the attached boundary layer in RANS mode whereas the separated flow should be ideally simulated in LES mode. The methods in which the attached boundary layer is modeled in RANS mode can be considered as weak RANS/LES coupling methods since there is no mechanism to transfer the modeled turbulence energy into resolved turbulence energy. These methods introduce a "grey-area" in which the solution is neither pure RANS nor pure LES since the switch from RANS to LES does not imply an instantaneous change in the resolution level. In practice, the eddy viscosity remains continuous across the RANS/LES interface but the rapid decrease of the level of RANS eddy viscosity enables the development of strong instabilities. This family of techniques is well adapted for simulating massively separated flows characterized by a large scale unsteadiness dominating the time-averaged solution (see [68] for further discussion). Two weaknesses in the use of hybrid methods for technical flows have been identified traditionally. The first one concerns a possible delay in the formation of instabilities in mixing layers due to the advection of the upstream RANS eddy viscosity. The second one deals with the treatment of the "grey-area", where the model switches from RANS to LES, and where the velocity fluctuations, the "LES-content", are expected not to be sufficiently developed to compensate for the loss of modeled turbulent stresses ("Model-Stress Depletion" (MSD)). This can lead to unphysical outcomes, like an underestimation of the skin friction which, at worst, can lead to artificial separation denoted as "Grid Induced Separation" (GIS). In order to get rid of this latter drawback, Spalart et al. [78] proposed a modification of the model length scale presented as a Delayed Detached Eddy Simulation (DDES) to delay the switch into the LES mode and to prevent "Model-Stress Depletion". This method, implemented in both CEDRE and elsA solvers has been successfully used to simulate the buzz in a supersonic inlet [82], side-loads in an over-expanded nozzle flow [30] as well as the reactive flow over a backward facing step [70].

In a different spirit, Deck [26], [27] proposed a Zonal Detached Eddy Simulation (ZDES) approach, in which RANS and DES domains are selected individually. The motivation is to be fully safe from MSD and GIS and to clarify the role of each region. An example of application of this method on a high-lift device is provided in Figure 6. Besides this case, ZDES has been thoroughly validated with experimental data

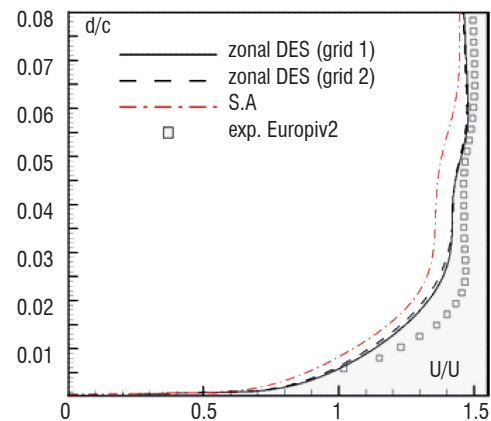
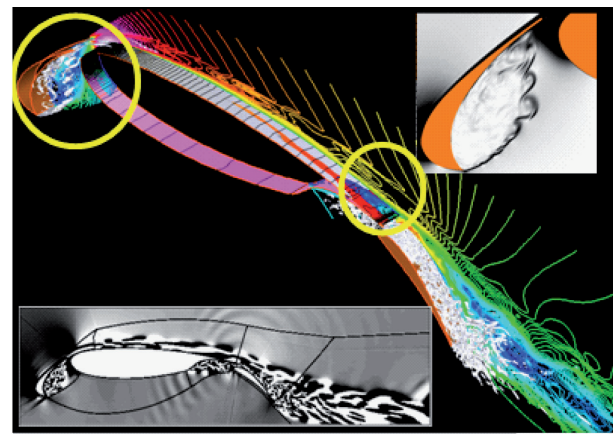
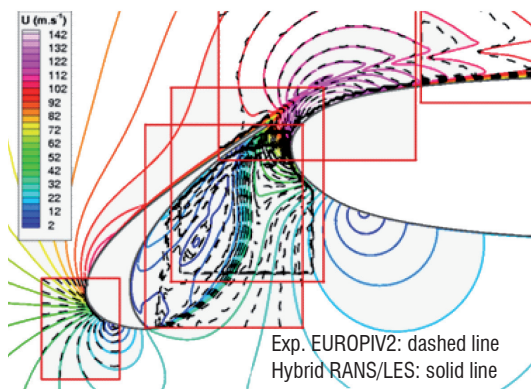
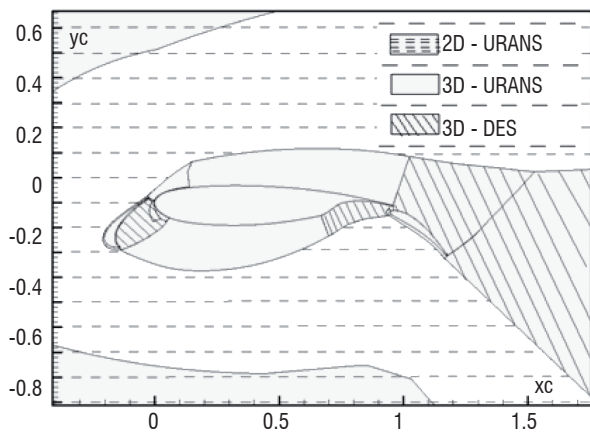


Figure 6 - ZDES of the flow around a three-element airfoil. Instantaneous flow field and comparison of Reynolds averaged data with PIV experimental data (from [27]).

including spectral and second order analysis on a wide range of applications covering both subsonic [28][88] and supersonic [73] base flows and jets [22]. Some other applications in the frame of applications with the *e/sA* solver can be found in [62].

Further improvements of this class of hybrid methods, like the Scale Adaptive Simulation (SAS) proposed by Menter et al. [51], are currently being investigated at Onera. Recently, the Partially Integrated Transport Modeling (PITM) method viewed as a continuous approach for hybrid RANS/LES modeling allowing seamless coupling between the RANS and LES regions has been developed in the framework of eddy viscosity models [72] and second moment closures [19], [20], [21], especially for simulating unsteady flows on relatively coarse grids, providing a saving of computing time. From a theoretical point of view, the PITM method finds its basic foundation in the spectral space by considering the Fourier transform of the two-point fluctuating velocity correlation equations in homogeneous turbulence [20]. The extension to non-homogeneous turbulence is developed easily within the approximate framework of the tangent homogeneous space. As a result of the modeling, it is found that the sub-filter stress model relies on transport equations that look formally like the corresponding Reynolds stress transport equations but the coefficients used in the model are no longer constants. They are now some functions of a dimensionless parameter involving the cutoff wave number and of the turbulent length scale built using the total turbulent kinetic energy and the total dissipation rate. The sub-filter stress model has been used for simulating unsteady flows of complex physics encountered in engineering applications such as for instance the injection induced flow viewed in Figure 7. The flow which develops in the channel is subjected to a fluid injection from the lower wall and is bounded by the upper rigid wall. This figure clearly illustrates the three dimension-

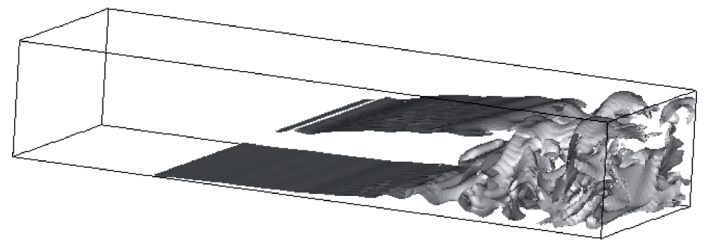


Figure 7 - Isosurface of instantaneous filtered vorticity in the spanwise direction.

al nature of the flow. These structures are squeezed upwards in the normal direction to the axial flow as previously observed by Apte [2].

Within "weak" RANS/LES coupling methods, boundary layers are treated in RANS mode which can appear to be a limitation in specific cases which are quite sensitive to the Lagrangian history of the upstream or free-stream turbulence. A generic example is provided by a shallow separation bubble on a smooth surface induced by a moderate adverse pressure gradient. The use of predefined "pure" RANS and "pure" LES zones may alleviate this "grey-area" issue. The main problem that arises when dealing with zonal RANS/LES approach originates from the very different spectral content of the solution between these two resolution levels. One of the first attempts to derive a consistent discontinuous coupling between RANS and LES was suggested in [60]. This latter approach is based on the definition of the exchange of information at the RANS/LES interface, which relies on the definition of some interface variables to construct a transfer operator at the interface. In the case where the RANS zone is located downstream a LES domain, Nolin et al. [47], [56] proposed a filtering process to reconstruct an eddy viscosity from the LES field.

The zonal RANS/LES coupling method has been successfully used to simulate the transitional and separated flow around an airfoil near stall [64] (Figure 8). In addition, we should also mention the NLDE (Non-Linear Disturbance Equations) approach extended to the case of a RANS/LES decomposition [42]. Within this perturbation approach, the LES field is broken down as the sum of a mean field (RANS) and a turbulent fluctuation which is computed using modified filtered Navier-Stokes equations (see [80] for a successful application of this method in aeroacoustics).

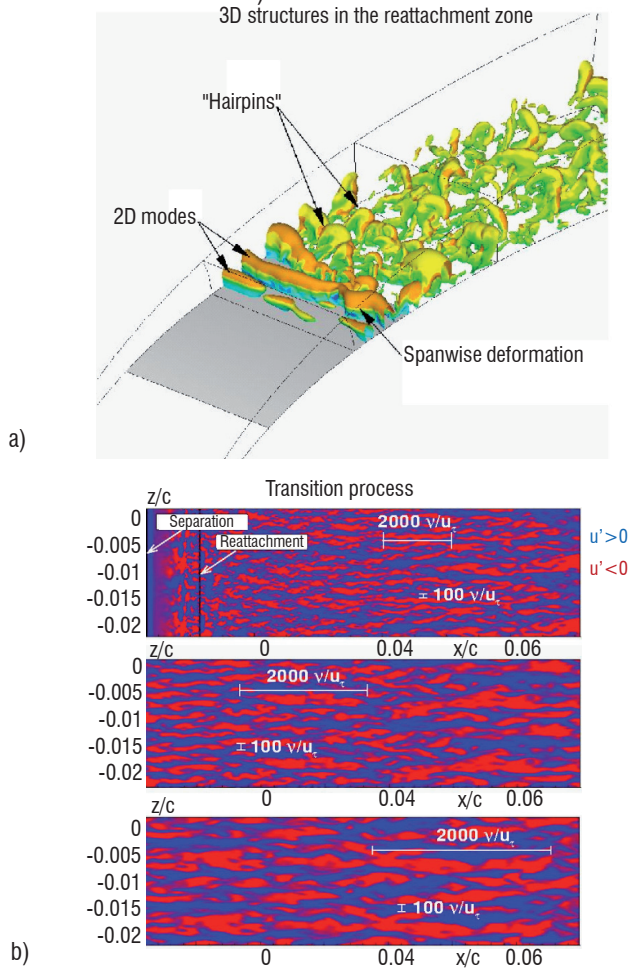


Figure 8 - Transitional and separated flow around an OA209 airfoil near stall.  
a) Pressure fluctuation contours  $p' = -2, 1 \cdot 10^{-3} Pa$   
b) Streamwise velocity fluctuations  $u'$

The case where the LES domain is located downstream from a RANS domain is probably the more difficult to deal with since appropriate inflow conditions need to be specified. The generation of inlet condi-

tions for spatially developing turbulent flows remains one of the challenges that must be addressed prior to the application of LES and hybrid RANS/LES to industrial flows [69]. Several techniques including mapping/recycling methods or synthetic turbulence methods have been developed (see [41] for a review). Some recent applications at Onera on synthetic methods can be found in [81], [58], [29], [33] in the frame respectively of NLDE, LES and ZDES.

### Some outlooks

In the frame of hybrid RANS/LES methods, it can be concluded that current approaches can handle accurately massively separated flows at high Reynolds numbers for which the location of separation is more or less triggered by the geometry. Conversely, as discussed by Sagaut and Deck [69], one of the next foreseen challenges will be firstly to simulate accurately shallow separation and more generally pressure-gradient-driven separation issues. Such simulations imply the ability to capture accurately the boundary layer dynamics at high Reynolds number and eventually transition. So far, most LES (in a wall-turbulence resolved sense) have concerned low Reynolds number and two-dimensional configurations (the span being considered as a homogeneous direction). The next foreseeable challenge will then concern the ability to handle accurately geometrically complex configurations with validated numerical tools at relevant Reynolds numbers.

### Conclusion

This article has given an overview of the variety of modeling approaches presently investigated and developed at Onera, ranging from the solution of averaged equations ( $e^N$  approach for transition and RANS approach for turbulent flows) to the model-free solution of the Navier-Stokes equations, through LES and hybrid approaches. Each class of approach has its strengths and deficiencies, in terms of ability to reproduce the physics as well as of computing cost, the more accurate approaches being the more expensive, or even unaffordable. Short and medium term outlooks have been discussed for each type of models. Although industry can currently only deal with averaged approaches for everyday design, developing expertise on each modeling level ensures that Onera is able to respond to all of today's and tomorrow's industrial demands and to improve each modeling level from the knowledge gained from other levels. The large majority of models presented here are available in the CEDRE and/or *elsA* solvers.

Author names appear in alphabetic order.

### References

- [1] B. ABU-GHANNAM and R. SHAW - *Natural Transition of Boundary Layers - The Effects of Turbulence, Pressure Gradient and Flow History*. Journal of Mechanical Engineering Sciences, 22(5): 213-228 (1980).
- [2] S.A. APTE and V. YANG - *A Large Eddy-Simulation Study of Transition and Flow Instability in a Porous-Walled Chamber with Mass Injection*. Journal of Fluid Mechanics, vol. 477, pp. 215-225 (2003).
- [3] D. ARNAL, M. HABIBALLAH and C. COUSTOLS - *Laminar Instability Theory and Transition Criteria in Two- and Three-Dimensional Flows*. La Recherche Aérospatiale 1984-2 (1984).
- [4] D. ARNAL - *Practical Transition Prediction Methods: Subsonic and Transonic Flows*. VKI Lectures Series Advances in Laminar-Turbulent Transition Modeling (2008).
- [5] B. AUPOIX and P.R. SPALART - *Extensions of the Spalart - Allmaras Turbulence Model to Account for Wall Roughness*. International Journal of Heat and Fluid Flows, Vol. 24, pp.454-462 (2003).

- [6] B. AUPOIX - *Modelling of Compressibility Effects in Mixing Layers*. Journal of Turbulence, Vol. 5, February 2004.
- [7] B. AUPOIX, E. LAMBALLAIS and M. SCHVALLINGER - *Modelling Density Fluctuations in Mixing Layers*. Advances in Turbulence X, H.I. Anderson and P.-Å. Krogstad editors, pp. 365-368, CIMNE, Barcelona (2004).
- [8] B. AUPOIX. *A General Strategy to Extend Turbulence Models to Rough Surfaces. Application to Smith's k-L model*. Journal of Fluid Engineering, Vol. 129, N° 10, pp. 1245-1254, October 2007.
- [9] B. AUPOIX, S.C. KASSINOS and C.A. LANGER - *ASBM-BSL: An Easy Access to the Structure Based Model Technology*. 6<sup>th</sup> International Symposium on Turbulent Shear Flow Phenomena TSFP-6, N. Kasagi, J.K. Eaton, J.A.C. Humphrey, A.V. Johansson and H.J. Sung editors, pp. 367-372, Seoul, Korea, June 22-24 (2009).
- [10] B. AUPOIX, G. PAILHAS and R. HOUEVILLE - *Modelling Riblet Effects*. 8<sup>th</sup> International Symposium on Engineering Turbulence Modelling and Measurements, ERCOFTAC, Marseille, France, 9-11 June, 2010.
- [11] A. BENYAHIA and R. HOUEVILLE - *Transition Prediction in Transonic Turbine Configurations Using a Correlation-Based Transport Equation Model*. 45<sup>th</sup> Applied Aerodynamics Symposium, Marseille, 22-24 March 2010.
- [12] H. BÉZARD and T. DARIS - *A New  $k_\rho - k_\rho L_\rho$  Turbulence Model for Heat Flux Predictions*. 3<sup>rd</sup> International Symposium on Turbulence and Shear Flow Phenomena, June 25-27, Sendai, Japan (2003).
- [13] H. BÉZARD and T. DARIS - *Calibrating the Length Scale Equation with an Explicit Algebraic Reynolds Stress Constitutive Relation*. 6<sup>th</sup> International Symposium on Engineering Turbulence Modelling and Measurements, W. Rodi and M. Mulas editors, pp. 77-86, Elsevier, Sardinia, May 23-25 (2005).
- [14] D. BIAU - *Etude des structures longitudinales dans la couche limite laminaire et de leur lien avec la transition*. Ph D Thesis, ISAE, Toulouse (2006).
- [15] R.E. BREIDENTHAL and S. EDDY - *A Model for Compressible Turbulence*. AIAA Journal, Vol. 30, N° 1, pp. 101-104, January 1992.
- [16] G.L. BROWN and A. ROSHKO - *On density Effects and Large Structure in Turbulent Mixing Layers*. Journal of Fluid Mechanics, Vol. 64, N° 4, pp. 775-816, July 1974.
- [17] S. CATRIS and B. AUPOIX - *Density Corrections for Turbulence Models*. Aerospace Sciences and Technology, Vol. 4, N° 1, pp. 1-11, January 2000.
- [18] S. CATRIS and B. AUPOIX - *Towards a Calibration of the Length-Scale Equation*. International Journal of Heat and Fluid Flows, Vol. 21, N° 5, pp. 606-613, October 2000.
- [19] B. CHAOUAT and R. SCHIESTEL - *A New Partially Integrated Transport Model for Subgrid-Scale Stresses and Dissipation Rate for Turbulent Developing Flows*. Physics of Fluids, vol. 17, No. 1, pp 1-19 (2005).
- [20] B. CHAOUAT and R. SCHIESTEL - *From Single-Scale Turbulence Models to Multiple-Scale and Subgrid-Scale Models by Fourier Transform*. Theoretical and Computational Fluids Dynamics, vol 21, No. 3, pp 201-229 (2007).
- [21] B. CHAOUAT and R. SCHIESTEL - *Progress in Subgrid-Scale Transport Modeling for Continuous Hybrid Non-Zonal Rans/Les Simulations*. International Journal of Heat and Fluid Flow, vol. 30, pp 602-616 (2009).
- [22] N. CHAUVET and S. DECK, L. JACQUIN - *Zonal-Detached Eddy Simulation of a Controlled Propulsive Jet*. AIAA Journal, vol 45, No. 10, pp 2458-2473, 2007.
- [23] C. CONTENT and R. HOUEVILLE - *Local Correlation-Based Transition Model*. 8<sup>th</sup> International ERCOFTAC Symposium on Engineering Turbulence and Modelling, Marseille, 9-11 June 2010
- [24] J. COUSTEIX, V. SAINT-MARTIN, R. MESSING, H. BÉZARD and B. AUPOIX - *Development of the  $k - \varphi$  Turbulence Model*. 11<sup>th</sup> Symposium on Turbulent Shear Flows. Institut National Polytechnique, Université Joseph Fourier, Grenoble, France, September 8-11 (1997).
- [25] J. DANDOIS, E. GARNIER and P. SAGAUT - *Numerical Simulation of active separation control by a synthetic jet*. Journal of Fluid Mechanics, vol 574, pp 25-58 (2007).
- [26] S. DECK - *Numerical Simulation of Transonic Buffet Over a Supercritical Airfoil*. AIAA Journal, vol. 43, No. 7, pp 1556-1566, 2005.
- [27] S. DECK - *Zonal-Detached Eddy Simulation of the Flow around a High-Lift Configuration*. AIAA Journal, vol. 43, No. 11, pp 2372-2384, 2005.
- [28] S. DECK and P. THORIGNY - *Unsteadiness of an Axisymmetric Separating-Reattaching Flow: Numerical Investigation*. Physics of fluids, 19, 065103 (2007).
- [29] S. DECK, P.E. WEISS, M. PAMIÈS and E. GARNIER - *On the use of Stimulated Detached Eddy Simulation for Spatially Developing Boundary Layers*. Advances in Hybrid RANS-LES modelling. NMF97, pp 67-76, edited by S-H Peng and W. Haase, Springer-Verlag, Berlin Heidelberg.
- [30] S. DECK - *Delayed Detached Eddy Simulation of the End-Effect Regime and Side-Loads in an Overexpanded Nozzle Flow*. Shock Waves, 19, 239-249, 2009.
- [31] L. DUPLAND and H. BÉZARD - *A New Explicit Algebraic Model for Turbulent Heat Flux Predictions*. HEFAT 2005, Cairo, Egypt (2005).
- [32] F.G. ERGIN and E.B. WHITE - *Unsteady and Transitional Flows Behind Roughness Elements*. AIAA Journal, 44(11):2504-2514 (2006).
- [33] E. GARNIER - *Stimulated Detached Eddy Simulation of a Three-Dimensional Shock/Boundary Layer Interaction*. Shock Waves, vol 19, No 6, pp 476-486 (2009).
- [34] V. GLEIZE, R. SCHIESTEL and V. COUAILLIER - *Multiple Scale Modeling of Turbulent Nonequilibrium Boundary Layer Flows*. Phys. Fluids 8(10), October 1996.
- [35] P.S. Granville - *The Calculation of the Viscous Drag of Bodies of Revolution*. David Taylor Model Basin Report 849 (1953).
- [36] W. HAASE, B. AUPOIX, U. BUNGE and D. SCHWAMBORN - *FLOMANIA European Initiative on Flow Physics Modelling*. Springer, Notes on Numerical Fluid Mechanics and Multidisciplinary Design, Vol. 94 (2006).
- [37] T. HERBERT - *Parabolized Stability Equations*. AGARD Report 793 (1993).
- [38] H. IACOVIDES and M. RAISEE - *Recent Progress in the Computation of Flow and Heat Transfer in Internal Cooling Passages of Turbine Blades*. International Journal of Heat and Fluid Flow, Vol 20, pp 320-328 (1999).
- [39] S. IMAO, M. ITOH and T. HARADA - *Turbulent Characteristics of the Flow in an Axially Rotating Pipe*. International Journal of Heat and Fluid Flows, Vol. 17, pp. 444-451.
- [40] L. JACQUIN - *Scales in Turbulent Motions*. Aerospace Lab., Vol. 1 (2010).
- [41] A. KEATING, U. PIOMELLI, E. BALARAS and H. KALTENBACH - *A Priori and a Posteriori Tests of Inflow Conditions for Large Eddy Simulation*. Physics of Fluids, vol 16, No 12, pp 4696-4712.
- [42] E. LABOURASSE and P. SAGAUT. *Reconstruction of Turbulent Fluctuations Using a Hybrid RANS/LES Approach*. J. Comp. Physics, 182: 301-336.
- [43] M.T. LANDAHL - *A Note on Algebraic Instability of Inviscid Parallel Shear Flows*. J. Fluid Mech., 98(2):243-251 (1980).
- [44] B.E. LAUNDER and B.I. SHARMA - *Application of Energy-Dissipation Model of Turbulence to the Calculation of Flow near a Spinning Disc*. Letters in Heat and Mass Transfer, Vol. 1, pp. 131-138 (1974).

- [45] P. LUCHINI - *Reynolds-Number Independent Instability of the Boundary Layer Over a Flat Surface: Optimal Perturbation*. J. Fluid Mech., 404:289-309 (2000).
- [46] I. MARY and P. SAGAUT - *Large Eddy Simulation of Flow Around an Airfoil Near Stall*. AIAA Journal, vol 40, N° 6, pp 1139-1145 (2002).
- [47] I. MARY and G. NOLIN - *Zonal Grid Refinement for Large Eddy Simulation of Turbulent Boundary Layers*. AIAA Paper 2004-0257, Reno, US.
- [48] E. MASSON, V. GLEIZE and R. SCHIESTEL - *New Multiple-Scale Approach for the Numerical Simulation of Non-Equilibrium Boundary Layer Flows*. 5<sup>th</sup> International Symposium on Turbulence, Heat and Mass Transfer, Dubrovnik, Croatia, September 25-29 (2006).
- [49] M. MATSUBARA and P.H. ALFREDSSON - *Disturbances Growth in Boundary Layers Subjected to Free-Stream Turbulence*. J. Fluid Mech., 430:149-168 (2001).
- [50] F.R. MENTER - *Two-Equation Eddy-Viscosity Turbulence Models for Engineering Applications*. AIAA Journal, Vol. 32, N° 8, pp. 1598-1605 (1994).
- [51] F. MENTER and M. KUNTZ - *A Scale-Adaptive Simulation Model Using Two-Equation Models*. AIAA paper 05-1095, Reno (2005).
- [52] F.R. MENTER, R.B. LANGTRY, S.R. LIKKI, Y.B. SUZENX, P.G. HUANG and S.VÖLKER - *A Correlation-Based Transition Model Using Local Variables Part I-Model formulation*. ASME Journal of Turbomachinery, 128:413-422 (2006).
- [53] R. MICHEL - *Détermination du point de transition et calcul de la traînée des profils d'aile en incompressible*. Onera Publication N° 58 (1952).
- [54] M.V. MORKOVIN - *The Many Faces of Transition*. In Viscous Drag Reduction, Wells, C.S. editor Plenum Press (1969).
- [55] D. NAOI, A. SHAVIT and M. WOLFSHTEIN - *Two-Point Correlation and the Redistribution of Reynolds Stresses*. The Physics of Fluids, Vol. 16, N° 6, pp 738-743 (1973).
- [56] G. NOLIN, I. MARY, L. TA-PHUOC, C. HINTERBERGER and J. FROHLICH - *Coupling from LES to RANS Using Eddy Viscosity Models*. Direct and Large Eddy Simulation 6, pp 679-686, Springer, Netherlands.
- [57] M. PAMIÈS, E. GARNIER, A. MERLEN and P. SAGAUT - *Response of Spatially Developing Turbulent Boundary Layer to Active Control Strategies In The Framework of Opposition Control*. Physics of fluids, 19, 108102 (2007).
- [58] M. PAMIÈS, P.E. WEISS, E. GARNIER, S. DECK and P. SAGAUT - *Generation of Synthetic Turbulent Inflow Data for Large Eddy Simulation of Spatially Evolving Wall-Bounded Flows*. Physics of fluids, 21, 045103 (2009).
- [59] J. PERRAUD, D. ARNAL, G. CASALIS, J.P. ARCHAMBAUD and R. DONELLI - *Automatic Transition Predictions Using Simplified Methods*. AIAA Journal, 47(11), pp 2676-2684 (2009).
- [60] P. QUÉMÉRÉ and P. SAGAUT - *Zonal Multidomain RANS/LES Simulations of Turbulent Flows*. International Journal of Numerical Methods for Fluids, 40: 903-925.
- [61] R.H. RADETSKY, M.S. REIBERT, W.S. SARIC and S. TAKAGI - *Effect of Micron-Sized Roughness on Transition in Swept Wing Flows*. AIAA Paper 93-0076, (1993).
- [62] J. RENEUX, P. BEAUMIER and P. GIREAUDOUX-LAVIGNE - *Advanced Aerodynamic Applications with the elsA Software*. Aerospace Lab., vol 2 (2010).
- [63] F. RICHEZ, I. MARY, V. GLEIZE and C. BASDEVANT - *Simulation and Modeling of a Laminar Separation Bubble on Airfoils*. IUTAM Symposium on "Unsteady Separated Flows and their Control" Corfu, Grèce 18-22 juin 2007.
- [64] F. RICHEZ, I. MARY, V. GLEIZE and C. BASDEVANT - *Zonal RANS/LES Coupling Simulation of a Transitional and Separated Flow Around an Airfoil Near Stall*. Theoretical and Computational Fluid Dynamics, Vol 22, pp 305-3155 (2008).
- [65] O. REYNOLDS - *An Experimental Investigation of the Circumstances Which Determine Whether the Motion of Water Shall be Direct or Sinuous, and the Law of Resistance in Parallel Channels*. Philosophical Transactions of the Royal Society of London. A, Vol. 174, pp. 935-983, 1883.
- [66] O. REYNOLDS - *On the Dynamical Theory of Incompressible Viscous Fluids and the Determination of the Criterion*. Philosophical Transactions of the Royal Society of London. A, Vol. 186, pp. 123-164, 1895.
- [67] R. RUBINSTEIN, C.L. RUMSEY, M.D. SALAS and J.L. THOMAS - *Turbulence Modelling*. Workshop NASA/CR-2001-210841 ICASE Interim Report N°37, 2001
- [68] P. SAGAUT, S. DECK and M. TERRACOL. *Multiscale and Multiresolution Approaches in Turbulence*. Imperial College Press, London, UK, 356 pages, 2006.
- [69] P. SAGAUT and S. DECK. *Large Eddy Simulation for Aerodynamics: Status and Perspectives*. Phil. Trans. R. Soc. A., 2009 367, 2849-2860.
- [70] B. SAINTE-ROSE, N. BERTIER, S. DECK and F. DUPOIRIEUX. *A DES Method Applied to a Backward Facing Step reactive flow*. C.R. Mécanique 337, 2009.
- [71] R. SCHIESTEL - *Multiple Time Scale Modelling of Turbulent Flows in one Point Closures*. Physics of Fluids, Vol. 30, No 3, pp 722-731 (1987).
- [72] R. SCHIESTEL and A. DEJOAN - *Towards a New Partially Integrated Transport Model for Coarse Grid and Unsteady Turbulent Flow Simulations*. Theoretical and Computational Fluid Dynamics, Vol. 18, pp. 443-468.
- [73] F. SIMON, S. DECK, P. GUILLEN and P. SAGAUT and A. MERLEN. *Numerical Simulation of the Compressible Mixing Layer past an Axisymmetric Trailing Edge*. Journal of Fluid Mechanics, vol 591, pp 215-253 (2007).
- [74] A.M.O. SMITH and N. GAMBERONI - *Transition, Pressure Gradient and Stability Theory*. Rept. ES 26388, Douglas Aircraft Co., El Segundo, California (1956).
- [75] P.R. SPALART, S.R. ALLMARAS - *A One-Equation Turbulence Model for Aerodynamic Flows*. La Recherche Aérospatiale, Vol. 1, pp. 5-21 (1994).
- [76] P. SPALART, W.H. JOU, M. STRELETS and S.R. ALLMARAS - *Comments on the Feasibility of LES Wings and on a Hybrid RANS/LES Approach*. In proceedings pp 137-147, 1<sup>st</sup> AFSOR Int. Conf. on DNS/LES, Ruston (1998).
- [77] P.R. SPALART - *Strategies for Turbulence Modelling and Simulations*. International Journal of Heat and Fluid Flow, Vol. 21, N° 3, pp. 252-263, June 2000.
- [78] P.R. SPALART, S. DECK, M.L. SHUR, K.D. SQUIRES, M. STRELETS and A. TRAVIN - *A New Version of Detached-Eddy Simulation Resistant to Ambiguous Grid Densities*. Theoretical and Computational Fluid Dynamics, Vol 20, pp 181-195, July 2006.
- [79] P.R. SPALART. *Detached Eddy Simulation*. Annual review of fluid mechanics, 41: 181-202 (2009).
- [80] M. TERRACOL, E. MANOHA, E. HERRERO, E. LABOURASSE, S. REDONNET and P. SAGAUT - *Hybrid Methods for Airframe Noise Numerical Prediction*. Theoretical and Computational Fluid Dynamics, 19(3):197-227 (2005).
- [81] M. TERRACOL - *A zonal RANS/LES Approach for Noise Sources Prediction*. Flow, Turbulence and Combustion. J. (FTAC), 77:161-184 (2006).
- [82] S. TRAPIER, S. DECK and P. DUVEAU - *Delayed Detached Eddy Simulation and Analysis of Supersonic inlet Buzz*. AIAA Journal, vol 46, pp 118-131(2008).
- [83] E. TROMEUR, E. GARNIER, P. SAGAUT and C. BASDEVANT - *LES of Aero-Optical Effects in a Turbulent Boundary Layer, Engineering Turbulence Modelling and Experiments 5*. W. Rodi and N. Fuyeo editors, pp. 327-336, Elsevier, Mallorca, September 16-18 (2002).
- [84] J.L. VAN INGEN - *A suggested Semi-Empirical Method for the Calculation of Boundary Layer Transition Region*. Rept. UTH-74, Univ. of Techn., Dept. of Aero. Eng., Delft (1956).
- [85] O. VERMEERSCH - *Etude et modélisation du phénomène de croissance transitoire pour des couches limites incompressibles et compressibles*. Thesis, ISAE, Toulouse (2009).

- [86] O. VERMEERSCH and D. ARNAL - *Bypass Transition Induced by Roughness elements, Prediction Using a Model Based on Klebanoff Modes Amplification*. ERCOFTAC Bulletin, 80:87-90 (2009).
- [87] A.E. VON DOENHOFF and A.L. BRASLOW - *Effect of Distributed Surface Roughness on Laminar Flow*. In Boundary layer control, vol. II, Pergamon, Lachmann editor (1961).
- [88] P.E. WEISS, S. DECK, J.C. ROBINET and P. SAGAUT - *On the Dynamics of Axisymmetric Turbulent Separating/Reattaching Flows*. Physics of Fluids, 21, 075103 (2009).

## Acronyms

2D (Two-Dimensional )  
 3D (Three-Dimensional)  
 CF (Cross-Flow)  
 DES (Detached Eddy Simulation)  
 DDES (Delayed Detached Eddy Simulation )  
 DNS (Direct Numerical Simulation)  
 EARSM (Explicit Algebraic Reynolds Stress Model)  
 EVM (Eddy Viscosity Model)  
 GIS (Grid Induced Separation)  
 LES (Large Eddy Simulation)  
 MSD (Model-Stress Depletion)  
 NLDE (Non-Linear Disturbance Equations)  
 NLEVM (Non-Linear Eddy Viscosity Model)  
 PITM (Partially Integrated Transport Modeling)  
 PSE (Parabolized Stability Equations)  
 QDNS (Quasi Direct Numerical Simulation)  
 RANS (Reynolds Averaged Navier-Stokes (equations))  
 SAS (Scale Adaptive Simulation)  
 TS (Tollmien-Schlichting)  
 URANS (Unsteady Reynolds Averaged Navier Stokes)  
 ZDES (Zonal Detached Eddy Simulation)

## AUTHORS



**Bertrand Aupoix** graduated from Supaero in 1976. He was awarded a Ph. D in 1979 and a "Thèse d'Etat" in 1987, both in the field of turbulence modeling in which he is still active. He is currently Research Director in the "Thermics, Aerothermodynamics, Control and Turbulence" (TACT) research unit in the Aerodynamics and Energetics Model Department (DMAE) at Onera Toulouse.



**Daniel Arnal** is a graduate of Ecole Nationale Supérieure de Mécanique et Aérotechnique (ENSMA) in Poitiers, France. He received his Ph. D thesis in 1976 at Onera Toulouse. He is working for more than thirty years on the topics related to laminar-turbulent transition. In 1998, he became head of the Research Unit "Transition and Instability" in the Aerodynamics and Energetics Models Department at Onera Toulouse. He published approximately 150 archival journals or meeting papers.



**Hervé Bézard** entered the Ecole Normale Supérieure of Cachan in 1983 and graduated the Agrégation of Mechanics in 1986. He joined the Applied Aerodynamics Department of Onera-Châtillon in 1988 as a research engineer and the Department of Models for Aerodynamics and Energetics of Onera Toulouse in 1994. He is a specialist in the field of turbulence modeling and computational fluid dynamics.



**Bruno Chaouat** senior Scientist in CFD Department of Onera. Background: Master Degree in Physics from University of Lille in 1984. Graduated in 1986 from Ecole Centrale Paris. Ph. D from University of Paris 6 in 1994. Research Habilitation Thesis in Fluid Mechanics from University of Paris 6 in 2007. Research topics include: Turbulence modeling, from RANS/RSM to LES, Aerodynamics, Numerical Schemes. Bruno Chaouat is the co-original developer of the PITM (partially Integrated Transport Modeling) method that allows to derive continuous hybrid RANS/LES non zonal models used in the framework of second-moment turbulence closures.



**François Chedevergne** graduated from a french engineer school (Supaéro), Dr. François Chedevergne is a research scientist working at Onera within the Fundamental and Applied Energetics Department. He is in charge of the aerothermodynamics studies of the department and is deeply involved in the development of the software platform CEDRE regarding turbulence modeling.



**Sébastien Deck** senior scientist in the Applied Aerodynamics Department. Background: Master Degree in Mechanical Engineering from Ecole Supérieure de l'Energie et des Matériaux (Orléans) in 1999. Ph. D from University of Orléans in 2002 Habilitation Thesis (HDR) from University Pierre and Marie Curie, Paris 6 in 2007. Joined Onera in 2002. Research topics include: CFD, advanced turbulence modeling (hybrid RANS/LES, LES), aerodynamics, flow control, compressible flow, unsteady data post processing.



**Vincent Gleize** received his doctoral degree in Fluid Mechanics from the Aix-Marseille University in 1994. During his Ph.D he worked on the development of multiscale turbulence models for compressible flows. From 1994 to 1995 he held a postdoctoral position in the same Department working on unstructured grid generation techniques. In 1996 he left Onera and was employed by PSA Peugeot-Citroen as a Research engineer. He was in charge of developing a new efficient numerical simulation environment for the Research Department of Aeroacoustics. Since 1997, he has been employed as a research scientist in the Numerical Simulation and Aeroacoustics Department at Onera. He started with the implementation of preconditioning methods for low speed compressible flows. From 2000 to 2001 he worked at Wright Patterson Air Force Base (Ohio, USA) in the framework of a collaboration between the French and American governments. Since nine years, he has mainly worked on the Reynolds averaged Navier-Stokes (RANS) modelling and the Large Eddy Simulation (LES) of complex turbulent steady and unsteady viscous flows.



**Philippe Grenard** graduated from the French engineer school École Polytechnique and Supaéro. Philippe Grenard is a research engineer working at Onera in the Fundamental and Applied Energetics Departement (DEFA). He is in charge of computational activities regarding the in-house CEDRE platform (modeling, development and computations) in the Liquid Propulsion Unit. His activities focus on combustion and thermal loads in the combustion chamber and nozzle of liquid propellant engines.



**Emmanuel Laroche**, research Engineer, graduated from Supaero in 1994. He works at Onera since 1995. From 1995 to 2004, he was mainly involved in turbulent heat transfer modelling applied to turbomachinery internal cooling and liquid propulsion. From 2004 to 2006, he had two year stay at Snecma as Deputy Director of the Tools and Methods Department. Current fields of interest are conjugate coupling models as well as unsteady heat transfer simulation.

F. Dupoirieux, N. Bertier

(Onera)

E-mail: francis.dupoirieux@onera.fr

# The Models of Turbulent Combustion in the CHARME Solver of CEDRE

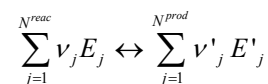
We describe the combustion models implemented in the CHARME solver of the CEDRE code dedicated to the simulation of 3D complex reactive flows. These models give the source terms linked to chemical reactions appearing in the species mass balance equations solved by CHARME. For laminar flows, Arrhenius laws are simply used but, for turbulent flows, different models have been implemented, in order to allow the user to treat diffusion flames, premixed flames or intermediate situations. All of these models are described here. The proposed models are more or less advanced according to the level of accuracy required in regard to the treatment of the turbulence-chemistry interaction. This paper does not deal with more sophisticated models, such as those based on Monte Carlo methods, which require the creation of new solvers for CEDRE.

## Introduction

The CHARME solver is dedicated to the simulation of turbulent reactive gas flows, such as those encountered in gas turbine combustors, rocket engines working with liquid or solid propellants, ramjets, scramjets, etc. The common feature of these flows is that the level of turbulence is kept as high as possible in order to prompt mass and energy transfer, but the type of flame involved in one of these combustors can be different from that in others. In the case of rocket engines using hypergolic fuels the flame can be nothing but a diffusion flame, i.e., a flame in which fuel and oxidant enter the combustion chamber separately and then meet due to transport by diffusion phenomena. On the other hand, in a gas turbine combustor, in order to prevent temperature heterogeneities which may damage turbine blades and promote pollutant emission, organizing the combustion in the shape of premixed flames is increasingly sought. In that case fuel and air are introduced into the combustion chamber by the same injection device (although not always through the same holes of this injection device) and are already mixed or quasi-mixed when they enter the combustion chamber. The combustion propagates in the mixture due to heat conduction from the burnt gases to the fresh ones. Depending on the type of flame, the situation can be very different (Box 1) and can hardly be handled by a unique physical model. Therefore the CHARME solver must contain different models that cover all the situations, from pure diffusion to pure premixed, going through partially premixed flames. Even if most of the flows with combustion are turbulent, laminar flows have to be considered as well.

## Laminar flows

For laminar reactive flows, the reaction rate is given by Arrhenius laws. The CHARME solver gives the user the possibility of introducing any type of chemical kinetics. In that case the user has to specify all the chemical reactions involved in the simulation. A reversible chemical reaction is written:



where  $N^{react}$  (resp.  $N^{prod}$ ) is the number of reactant species (resp. product species) in the reaction, the  $E_j$  (resp.  $E'_j$ ) are the reactant species (resp. product species) and the  $\nu_j$  (resp.  $\nu'_j$ ) are the stoichiometric coefficients of the reactant species (resp. product species). It is possible that species are common to both sides of the reaction when third body effects have to be taken into account.

For each reaction, the user must specify the pre-exponential factor  $A$ , the temperature exponent  $\alpha$  and the activation temperature  $T_A$  for both direct and reverse directions of the reaction. The reaction rate for a given reaction is then written:

$$\begin{aligned} \dot{\Omega}_r = & A_r^{dir} T^{\alpha_r^{dir}} \exp\left(-\frac{T_A^{dir}}{T}\right) \prod_{j=1, N_r^{react}} [c_j^r]^{\nu_j^r} \\ & - A_r^{rev} T^{\alpha_r^{rev}} \exp\left(-\frac{T_A^{rev}}{T}\right) \prod_{j=1, N_r^{react}} [c_j^r]^{\nu_j^{r'}} \end{aligned} \quad (1)$$

where the subscript  $r$  refers to the reaction, the superscript  $dir$  (resp.  $rev$ ) refers to the direct (resp. reverse) part of the reaction and  $[c]$  (resp.  $[c']$ ) is the concentration of a given reactant (resp. product) of the considered reaction.

Note that to simplify data introduction in the case of hydrogen-methane mixture combustion, the Davidenko kinetics, including 80

reactions and 21 species [1], has been directly coded in the CHARME solver. 16 of these 21 species have to be tracked by transport equations, whereas the last five are deduced from an assumption of reaction partial equilibrium.

### Box 1

In nature, combustion spontaneously appears in the shape of diffusion flame, whereas in industrial or domestic combustion devices it is sought to produce flames which are as premixed as possible.

In a diffusion flame, fuel and oxidant burn very rapidly when they meet and then disappear. Therefore, fuel and oxidant cannot be simultaneously in non-negligible concentrations at the same point of the flow, so that the flame, i. e. the reaction zone, separates the flow into two regions, one containing the fuel and the other containing the oxidant. In the flame, fuel and oxidant have zero or very low concentrations and are replaced by reaction products, i. e. burnt gases. The zero concentration in the reaction zone creates concentration gradients in both fuel and oxidant regions, which result in mass diffusion fluxes that bring fuel and oxidant to the reaction zone, i. e. to the flame. In the left part of Figure B1-1 we can see an example of such a diffusion flame. The combustion zone ends where the less abundant reactant between fuel and oxidant is totally consumed. The length of the flame is given by the proportionality relation:

$$L_f \propto \frac{VS}{D} \quad (1)$$

where  $V$  is the mean velocity of the reactants in the feeding pipes (in m/s),  $S$  is the section of the feeding pipe with the least abundant reactant (in  $m^2$ ) and  $D$  is the mass diffusion coefficient of the reactants into the burnt gases (in  $m^2/s$ ). If the flow is turbulent (as it is most of the time in industrial burners), the turbulent diffusion coefficient  $D_t$  must be considered instead of  $D$  and the flame length is considerably smaller for the same reactant flow rate. A schematic view of a usual diffusion flame is given in the left part of Figure B1-2. Typical concentration profiles obtained across this flame are shown in the upper part of Figure B1-3. Fuel and oxidant mass fraction gradients are in opposite directions and the absolute mass fluxes of fuel and oxidant which meet in the flame are in stoichiometric proportion.



Figure B1-1 - Examples of diffusion flame (left) and premixed flame (right)

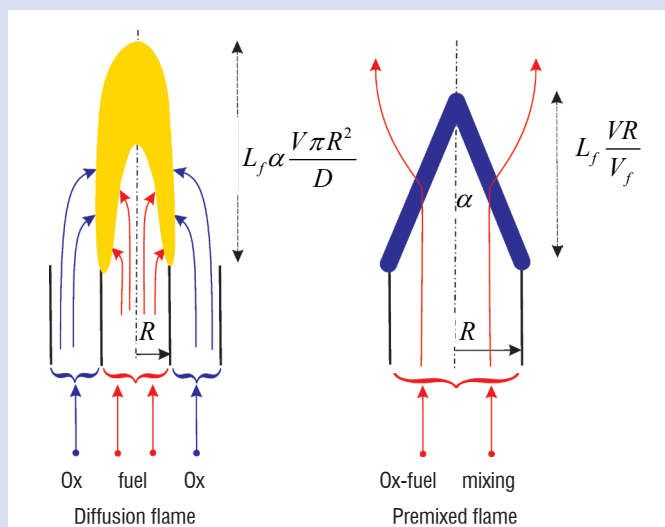


Figure B1-2 - Schematic view of diffusion and premixed flames

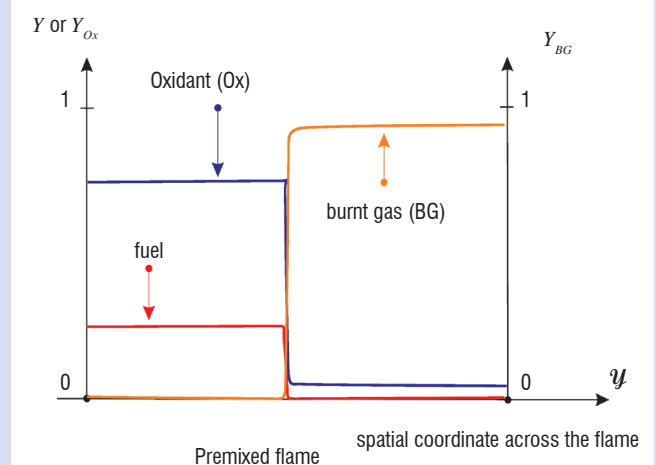
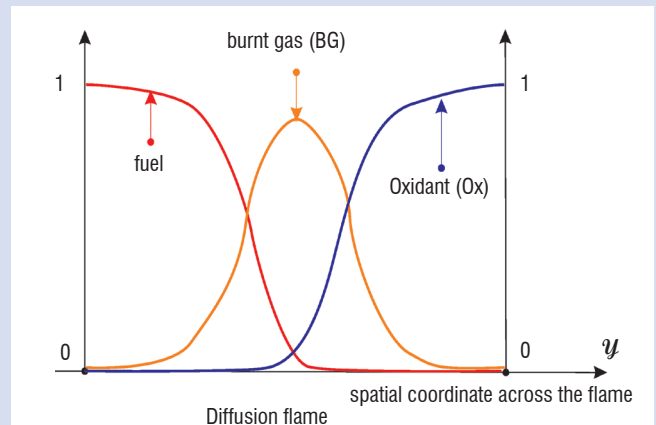


Figure B1-3 - Structure of a diffusion flame (upper part) and a premixed flame (lower part)

In premixed combustion the position of the flame, and hence its length, result from a competition between the flame velocity and the velocity of the mixture. The right part of Figure B1-2 gives the sketch of a Bunsen type premixed flame. The length of the flame is given by:

$$L_f = \frac{R}{\tan \alpha}$$

where  $R$  is the radius of the feeding pipe and  $\alpha$  is the angle defined, as indicated in Figure B1-2. By definition of  $\alpha$ , the flame velocity  $V_f$  is related to the velocity  $V$  of the gas mixture in the feeding pipe by:

$$V_f = V \sin \alpha$$

Assuming for the sake of simplicity that  $\alpha$  is small, one obtains:

$$L_f = \frac{RV}{V_f} \propto \frac{RV}{\sqrt{D_{heat} / \tau_{chem}}} \quad (2)$$

where  $D_{heat}$  is the thermal diffusivity (in  $m^2/s$ ) and  $\tau_{chem}$  is the characteristic time of the chemical kinetics (in s). If the flow is turbulent,  $D_{heat}$  must be replaced by the turbulent heat diffusivity  $D_{t,heat}$  and  $\tau_{chem}$  must be replaced by a chemical time  $\tau_{t,chem}$  obtained by averaging over the thickness of the turbulent flame. The parameter  $D_{heat}$  (resp.  $D_{t,heat}$ ) is linked to the parameter  $D$  (resp.  $D_t$ ) by the well known non-dimensional Lewis number  $D_{heat} / D$  (resp.  $D_{t,heat} / D_t$ ), which is of the order of unity. Note that, in the turbulent case, the thickness of the flame can become of the same order as its length.

The lower part of Figure B1-3 gives the typical concentration profiles in a premixed flame. These profiles are obtained when we follow streamlines crossing the flame front, represented in blue in the right part of Figure B1-2. Unlike the case of a diffusion flame, the concentration profiles of fuel and oxidant have a similar shape and the corresponding gradients are in the same direction; moreover the temperature, the evolution of which is similar to that of the burnt gas mass fraction, maintains its maximum value far from the flame, downstream of the flow.

The differences between Eqs. (1) and (2), and in the concentration profiles, point out that the physics involved for diffusion and premixed flame are different. This difference is obvious when the luminosity of the two types of flames is considered: For the diffusion flames, a yellow colour arises from the light emission by hot soot particles (in the case of CxHy fuel), while premixed flame becomes blue when CxHy decompose into C-C or C-H radicals before burning (Figure B1-1).

## Models for premixed or partially premixed turbulent flames

### Model without the influence of chemistry

When the chemistry is very fast compared to the turbulent mixing, the mean reaction rate can be expressed as a function of the turbulent quantities and mean mass fractions only because turbulent mixing is entirely piloting combustion. For perfectly premixed flows, the well known Eddy-Break-Up model of Spalding [2] leads to a very simple expression of the mean fuel consumption rate  $\tilde{\Omega}$ :

$$\tilde{\Omega} = \frac{C_{EBU}}{\tau_{turb}} \bar{\rho} \tilde{Y} \left( 1 - \frac{\tilde{Y}}{Y_{in}} \right) \quad (2)$$

where  $C_{EBU}$  is a non-dimensional constant (of the order of 5) adjusted by comparison with experiment,  $\tau_{turb}$  is the characteristic turbulent mixing time,  $\bar{\rho}$  is the mean density of the mixture,  $\tilde{Y}$  is the mean fuel mass fraction and  $Y_{in}$  is the initial fuel mass fraction, i.e., the fuel mass fraction before combustion. This formulation can be easily extended to non-premixed flames for which the mixing remains everywhere under stoichiometric conditions [3]:

$$\tilde{\Omega} = \frac{C_{EBU}}{\tau_{turb}} \bar{\rho} \tilde{Y} \left( 1 - \frac{\tilde{Y}}{\tilde{T}_r} \right) \quad (3)$$

where  $\tilde{T}_r$  is a tracking variable, which is a solution of a transport equation with the same boundary conditions as those of  $\tilde{Y}$  but without the source terms of the equations for  $\tilde{Y}$ . In other words  $\tilde{T}_r$  is

the concentration of an inert species injected under the same conditions as the fuel. If the stoichiometry is uniform,  $\tilde{T}_r$  is constant and remains equal to  $Y_{in}$ , so that Eq. (3) is reduced to Eq. (2). A symmetric formulation can be obtained for the mean oxidant consumption rate  $\tilde{\Omega}_{Ox}$  in the much less usual case of a flame that remains totally over-stoichiometric:

$$\tilde{\Omega}_{Ox} = \frac{C_{EBU}}{\tau_{turb}} \bar{\rho} \tilde{Y}_{Ox} \left( 1 - \frac{\tilde{Y}_{Ox}}{\tilde{T}_{rOx}} \right) \quad (4)$$

where the subscript  $Ox$  refers to the oxidant.

The application of Eqs. (3) and (4) only requires the solution of an additional transport equation for an inert species, but the extension of the model to mixing fluctuations across stoichiometry is less simple. In that case, the Shvab-Zeldovich variable  $\varphi$  must be introduced. By definition, this variable  $\varphi$  is equal to  $\beta Y - Y_{Ox}$ , where  $\beta$  is the ratio of oxidant mass to fuel mass under stoichiometric conditions. Source terms of the transport equations of  $\beta Y$  and  $-Y_{Ox}$  compensate each other so that  $\varphi$  is really an inert species. This makes it possible to presume its Probability Density Function (PDF)  $P(\varphi)$  from its mean value  $\tilde{\varphi}$  and its fluctuation  $\tilde{\varphi}''^2$  because in that case the transport equation of  $\tilde{\varphi}''^2$  does not include source terms resulting from coupling with chemistry. The location of the gaseous particles in the phase plane  $(Y, \varphi)$  is indicated in Figure 1. In this section we assume that combustion leads to the total consumption of the less abundant reactant, i.e. the product gases are located on the red line of Figure 1. Using this assumption, the extended expression of  $\tilde{\Omega}$  can be easily obtained (see [3]):

$$\tilde{\Omega} = \frac{C_{EBU}}{\tau_{turb}} \bar{\rho} \times \left[ \tilde{Y} \int_{\min(0, \varphi_{\min})}^0 \alpha P(\varphi) d\varphi + \frac{\tilde{Y}_{Ox}}{\beta} \int_0^{\max(0, \varphi_{\max})} \alpha P(\varphi) d\varphi \right] \quad (5)$$

where  $\alpha$  is given by

$$\alpha = \frac{Y_{\min} + (\tilde{\varphi} - \varphi_{\min}) \frac{Y_{\max} - Y_{\min}}{\varphi_{\max} - \varphi_{\min}} - \tilde{Y}}{Y_{\min} + (\tilde{\varphi} - \varphi_{\min}) \frac{Y_{\max} - Y_{\min}}{\varphi_{\max} - \varphi_{\min}} - \int_0^{\max(0, \varphi_{\max})} \frac{\varphi}{\beta} P(\varphi) d\varphi} \quad (6)$$

In these equations the subscript min (resp. max) refers to the minimum (resp. maximum) value taken by  $Y$  or  $\varphi$  in the flow inlets. This means that the corresponding quantities are perfectly known as a part of the boundary conditions.

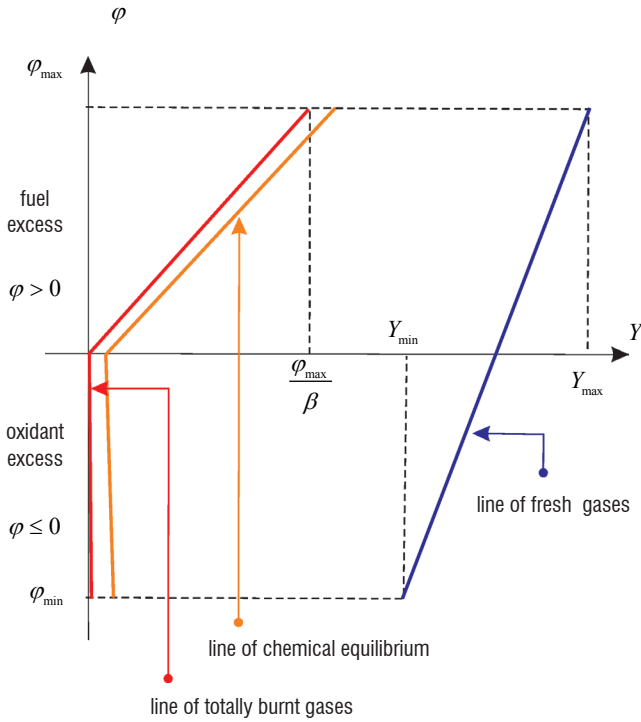


Figure 1 - Location of the gaseous particles in the  $(Y, \varphi)$  plane

Note that Eqs. (5) and (6) reduce to Eq. (3) when the mixing remains under stoichiometric conditions everywhere: Thus, the second integral of Eq. (5) vanishes since  $\varphi_{\max}$  is less than zero; in the same way the integral in Eq. (6) also vanishes and it is not difficult to establish that the quantity:

$$Y_{\min} + (\tilde{\varphi} - \varphi_{\min}) \frac{Y_{\max} - Y_{\min}}{\varphi_{\max} - \varphi_{\min}}$$

is identical to the quantity  $\tilde{T}_r$  of Eq. (3); in addition, if we take into

account that  $\int_{\min(0, \varphi_{\min})}^0 P(\varphi) d\varphi$  is equal to 1 by definition of a PDF,

the proof is complete.

Eqs. (5) and (6) make the basis of the so called CRAMER combustion model for premixed and partially premixed flames, which was implemented in the CHARME solver. This model assumes that the turbulent mixing of fresh and hot gases is slower than the chemical kinetics and thus entirely drives the mean reaction rate. In the case

of a variable fuel-air mixture ratio, it requires the resolution of two additional transport equations for  $\tilde{\varphi}$  and  $\tilde{\varphi}^2$  and the evaluation of the PDF of the inert variable  $\varphi$ . In the case of a constant mixture ratio, no additional transport equations are needed and the model reduces to the introduction of a source term in the fuel mass transport equation, calculated according to Eq. (4).

### Model taking into account chemical equilibrium data

The CRAMER model does not take into account the chemical equilibrium data in the sense that combustion leads to complete consumption of the fuel (resp. oxidant) in under-stoichiometric (resp. over-stoichiometric) conditions. In reality, at the end of the reaction the obtained temperature is lower than the temperature corresponding to a complete conversion of the fresh gases into CO<sub>2</sub> and H<sub>2</sub>O. The energy really obtained corresponds to a non complete conversion of the fuel (or oxidant in the case of fuel excess), i.e. a conversion which would stop at a non zero limiting value of the mass fraction of the fuel (or oxidant in the case of fuel excess). The corresponding location of the gaseous particles is the beige line in Figure 1. If we perfectly know the shape of this line, it is possible to extend Eqs. (5) and (6) as follows:

$$\tilde{\Omega} = \frac{C_{EBU}}{\tau_{turb}} \bar{\rho} \times \left[ \int_{\min(0, \varphi_{\min})}^0 (\tilde{Y} - Y_{eq}(\varphi)) \alpha P(\varphi) d\varphi + \frac{1}{\beta} \int_0^{\max(0, \varphi_{\max})} (\tilde{Y}_{Ox} - Y_{eqOx}(\varphi)) \alpha P(\varphi) d\varphi \right] \quad (7)$$

with  $\alpha$  given by

$$\alpha = \frac{A - \tilde{Y}}{A - B} \quad (8)$$

$$A = Y_{\min} + (\tilde{\varphi} - \varphi_{\min}) \frac{Y_{\max} - Y_{\min}}{\varphi_{\max} - \varphi_{\min}}$$

$$B = \int_0^{\max(0, \varphi_{\max})} \frac{\varphi + Y_{eqOx}(\varphi)}{\beta} P(\varphi) d\varphi - \int_{\min(0, \varphi_{\min})}^0 Y_{eq}(\varphi) P(\varphi) d\varphi$$

where the subscript eq refers to the limiting value imposed by chemical equilibrium. The calculation of  $\alpha$  and then  $\tilde{\Omega}$  must be achieved in each cell at each time step. It is not CPU time consuming, because the PDF  $P(\varphi)$  is modelled in the shape of a sum of delta and constant value functions, which leads to a very simple calculation of the integrals involving the variable  $\varphi$ . Eqs. (7) and (8) are the basis of the so called CLE ("Combustion Limitée par l'Equilibre") model [4], which was implemented in the CHARME solver. The preliminary calculation of the functions  $Y_{lim}(\varphi)$  and  $Y_{limOx}(\varphi)$  corresponding to the chemical equilibrium at the pressure of the reactive flow is required to use this model.

### Model taking into account chemical kinetics

The combustion regime of a reactive flow can be defined by use of the Borghi-Peters Diagram [5,6]. The combustion regime obtained in many industrial applications corresponds to chemical reactions taking place in wrinkled thickened flames. A straightforward idea to take into account the interaction between turbulence and combustion is

therefore to associate presumed PDF models for relevant combustion parameters with tabulated results of one dimensional premixed flame calculations. The relevant parameters are the progress variable  $c$ , which is monotonously varying from 0 in the fresh gases, to 1 in the burnt gases and, if the fuel-air mixture ratio is not uniform, the mixing variable  $z$ , which is monotonously varying from 0 on the oxidant side to 1 on the fuel side. There is obviously a linear relation between  $z$  and the previously introduced variables  $\varphi$  and  $T_r$ .

Some preliminary calculations of 1D premixed flames with detailed chemical kinetics give the gaseous mixing composition for any value of the progress variable  $c$ . If the fuel-air mixture ratio is uniform, only one 1D premixed flame calculation has to be achieved. If not, 1D premixed flame calculations have to be done for a set of  $z$  values covering the whole range of mixture ratio variation. The results are gathered in a table from which information on the mixing composition is extracted during the calculation of the reactive flow. If the fuel air mixture ratio is uniform, the variable  $c$  is the only entry of the table. If not, the table has the two entries  $c$  and  $z$ , the latter being used to select the premixed flame with the same fuel-air mixture ratio as that at the point where the composition is sought. In the calculation of the reactive flow, transport equations are solved only for the main species such as fuel, O<sub>2</sub>, CO, CO<sub>2</sub>, H<sub>2</sub>O. The mean source term for these species is obtained by convolution of the source term given by the table with the PDF of  $c$  and  $z$ . Thus:

$$\tilde{\Omega} = \iint_{c,z} \dot{\Omega}_{tab}(c,z) P(c,z) dc dz \quad (9)$$

The detailed composition of the flow is obtained from the table as well; the mass fraction  $Y^{minor}$  of the minor species is given by:

$$\tilde{Y}^{minor} = \iint_{c,z} Y_{tab}^{minor}(c,z) P(c,z) dc dz \quad (10)$$

This kind of model was introduced a long time ago (see for example [7]) and has been widely used since [8].

The determination of the PDF  $P(c,z)$  is not simple. It relies on the assumption that the correlation between  $c$  and  $z$  can be neglected and that their PDFs can be modelled from their first ( $\tilde{c}$  and  $\tilde{z}$ ) and second ( $\tilde{c}^2$  and  $\tilde{z}^2$ ) moments only. Additional transport equations are solved for these quantities. The closure of the first moment equations is simple, since  $c$  and  $z$  can be expressed as a function of the major species mass fractions. Thus,  $c$  can be defined as:

$$c = \frac{Y_{CO} + Y_{CO_2}}{Y_{CO}^{eq} + Y_{CO_2}^{eq}} \quad (11)$$

where the superscript eq refers to chemical equilibrium. The closure of the second moment equations is more complicated, especially for  $\tilde{c}^2$ , because its equation contains some correlations between source terms and concentrations. The details on the solution of these equations, which have been introduced in the CHARME solver of CEDRE, can be found in [9, 10].

### Model for Large Eddy Simulation (LES)

To save computation time, the reaction rate in LES type simulations is generally given by a global chemical kinetics adjusted to give the appropriate flame speed in one dimensional calculations. In the 3D

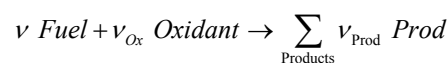
LES calculations, the flame propagation must be correctly reproduced, though the calculation grid is not refined enough to give a good description of the flame front most of the time. To comply with this constraint, the mass diffusion coefficient and the chemical kinetics parameters are modified in the LES to artificially thicken the flame front, keeping the flame speed unchanged. On the other hand, thick flames are less stretched and folded by turbulent structures than ordinary flames, so that the consumption rate of reactants is lowered. To offset this non physical effect, the reaction rate initially given by the global kinetics is multiplied by a so called Efficiency Function accounting for the real stretch and folding of the flame. All these ingredients make up the TFLES (Thickened Flame for LES) model [11], which has been introduced in the CHARME solver.

### Models for diffusion flames

As explained in box 1, the rate of reactant consumption in diffusion flames depends much more on the intensity of the mass diffusion fluxes than on the chemical kinetics<sup>1</sup>. Therefore, models of turbulent combustion for diffusion flames are mainly based on turbulence parameters and often do not involve chemical data. The simplest model for diffusion flames introduced in the CHARME solver is the popular Magnussen model [12]. According to this model, the mean reaction rate was initially given by:

$$\tilde{\Omega} = \frac{C_{Mag}}{\tau_{turb}} \min\left(\frac{Y}{\nu M}, \frac{Y_{Ox}}{\nu_{Ox} M_{Ox}}\right) \quad (12)$$

where  $C_{Mag}$  is a non-dimensional constant to be adjusted by comparison with reference experiments,  $\nu$  is the stoichiometric coefficient in the global reaction:



$M$  is the molar mass and the index refers to the oxidant. Quantities without index relate to the fuel. This model has been introduced into the CHARME solver in a slightly modified form, to take into account the influence of an ignition temperature. Thus, the mean reaction rate is written

$$\tilde{\Omega} = \frac{C_{Mag}}{\tau_{turb}} H(T - T_{ig}) \min\left(\frac{Y}{\nu M}, \frac{Y_{Ox}}{\nu_{Ox} M_{Ox}}\right) \quad (13)$$

where  $H$  is the Heaviside function ( $H(x) = 1$  if  $x \geq 0$ ,  $H(x) = 0$  otherwise),  $T$  is the gas temperature and the index  $ig$  refers to a threshold temperature. The reaction cannot start as long as the fuel and oxidant have not met and the gas temperature remains lower than  $T_{ig}$ .

Similarly to premixed flames, the notion of laminar flames can be used to build models for turbulent diffusion flame. Indeed, a turbulent diffusion flame can be considered as a laminar diffusion flame which is folded, stretched and sometimes extinguished by the turbulence. This idea gave birth to the coherent flame model [13], which states that the mean reaction rate of a reactant (fuel or oxidant) is the product of its consumption rate per flame surface unit multiplied by the flame surface per volume unit. Thus, the reaction rate of the reactant with index  $i$  is written:

$$\tilde{\Omega}_i = V_f \Sigma \quad (14)$$

<sup>1</sup> Chemical kinetics becomes important in diffusion flames if we want to calculate the flame stabilization process which takes place in small recirculation zones or in points where the flow velocity is low. Triple flames are often the key to this stabilization process.

where  $V_i$  is the consumption rate of the species  $i$  per flame surface unit and  $\Sigma$  is the flame surface per volume unit.

In its first version, the sub-model giving  $V_i$  accounts for the effects of mass diffusion and flame stretch but not for those of chemical kinetics. In the CHARME solver, the fuel consumption rate per flame surface  $V$  is therefore calculated as follows:

$$V = Y(\infty) \sqrt{\frac{D \varepsilon_{sr}}{2\pi}} \frac{\Phi + 1}{\Phi} e^{-W^2} \quad \text{with } W = \text{erf}^{-1} \left( \frac{\Phi - 1}{\Phi + 1} \right) \quad (15)$$

where  $Y(\infty)$  is the fuel mass fraction far from the flame, i. e. the fuel mass fraction in the fuel inlet section,  $D$  is the mass diffusion coefficient of the fuel in the gas mixing,  $\varepsilon_{sr}$  is the stretch rate of the flame, and  $\Phi$  is the stoichiometric ratio calculated from the fuel and oxidant mass fraction in the inlet sections ( $\Phi=1$  at stoichiometry).

The quantity  $\Sigma$  is obtained by solving the following transport equation:

$$\frac{\partial \Sigma}{\partial t} + \nabla \cdot (\tilde{v} \Sigma) = \nabla \cdot \left( \frac{v_t}{Sc_\Sigma} \nabla \Sigma \right) + \varepsilon_{sr} \Sigma - \left( \frac{V}{y} + \frac{V_{ox}}{y_{ox}} \right) \Sigma^2 \quad (16)$$

where  $\tilde{v}$  is the mean velocity of the flow,  $v_t$  is the kinematic turbulent viscosity,  $Sc_\Sigma$  is the non-dimensional Schmidt number for the quantity  $\Sigma$  (of the order of unity) and  $y$  (resp.  $y_{ox}$ ) is the mass fraction of the fuel (resp. oxidant). The two terms on the left hand side and the first term on the right hand side are the usual unsteady, convection and diffusion terms of a transport equation. The second and third terms on the right hand side stand for the creation of  $\Sigma$  by flame stretch and its consumption by the vanishing of one reactant (fuel or oxidant), respectively.

Compared to the Magnussen model, this model requires the solution of one additional transport equation for  $\Sigma$ , but describes the physics involved in a turbulent diffusion flame more accurately. Moreover, the sub-model for  $V_i$  can be easily adapted to take into account the effect of the chemical kinetics. A table containing the value of  $V_i$  for each value of  $\varepsilon_{sr}$  could be created from preliminary calculations of stretched laminar diffusion flames, performed with detailed chemical kinetics ■

## References

- [1] D. DAVIDENKO - *Contribution au développement des outils de simulation numérique de la combustion supersonique*. Ph. D. thesis, Orleans University, France (2005).
- [2] D. B. SPALDING - *Mixing and Chemical Reaction in Steady Confined Turbulent Flames*. 13th Symposium (Int.) on Combustion. The Combustion Institute, p. 649 (1971).
- [3] F. DUPOIRIEUX - *Calcul numérique d'écoulements turbulents réactifs et comparaison avec des résultats expérimentaux*. La Recherche Aérospatiale, n° 6, pp. 443-453 (1986).
- [4] F. RAVET, C. BAUDOIN and J.-L. SCHULTZ - *Modélisation numérique des écoulements réactifs dans les foyers de turboréacteurs*. Revue générale de thermique, Vol. 36, Issue 1, pp. 5-16 (1997).
- [5] R. BORGHI - *On the Structure and Morphology of Premixed Flames*. *Recent Advances in the Aerospace Sciences*, Plenum Press, New York, 117-138 (1985).
- [6] N. PETERS - *Laminar Flamelet Concepts in Turbulent Combustion*, 21st Symposium (International) on Combustion. The Combustion Institute, Pittsburgh, pp. 1231-1256 (1986).
- [7] D. BRADLEY, L.K. KWA, A.K.C LAU, M. MISSAGHI and S.B. CHIN - *Laminar Flamelet Modelling of Recirculating Premixed Methane and Propane Air Combustion*. *Combustion and Flame*, 71 :109-122, (1988).
- [8] O. GICQUEL - *Développement d'une nouvelle méthode de réduction des schémas cinétiques : application au méthane*. Ph. D. thesis, Ecole Centrale Paris (1999).
- [9] J. SAVRE - *Simulation numérique instationnaire de la combustion turbulente au sein de foyers aéronautiques et prédiction des émissions polluantes*. Ph. D. thesis of Université de Rouen France (énergétique) (2010).
- [10] J. SAVRE, N. BERTIER, Y. D'ANGELO and D. GAFFIE - *A Chemical Time Scale Approach for FPI Modeling*. *Comptes Rendus de l'Académie des Sciences (Mécanique)*, 336 : pp. 807-812 (2008).
- [11] O. COLIN, F. DUCROS, D. VEYNANTE, and T. POINSOT. *A Thickened Flame Model for Large Eddy Simulations of Turbulent Premixed Turbulent Combustion*. *Physics of Fluids*, 12 :pp. 1843-1863, (2000).
- [12] B. F. MAGNUSSEN and B. H. HJERTAGER - *On Mathematical Modelling of Turbulent Combustion with Special Emphasis on Soot Formation and Combustion*. 16th Symposium (Int.) on Combustion, The combustion Institute, p. 719 (1976)
- [13] F. E. MARBLE and J. E. BROADWELL - *The Coherent Flame Model for Turbulent Chemical Reactions*, PROJECT SQUID, Technical Report TRW-9-PU (January 1977).

## Acronyms:

CEDRE (Calcul d'Écoulements Diphasiques Réactifs pour l'Énergétique)  
 CLE (Combustion Limitée par l'Équilibre)  
 CRAMER (Combustion RAPide pour Mélanges Évolutifs en Richesse)  
 DEFA (Département d'Énergétique Fondamentale et Appliquée)  
 LES (Large Eddy Simulation)  
 PDF (Probability Density Function)  
 TFLES (Thickened Flame model for LES)



**Francis Dupoirieux** is deputy head of the Energetics department of Onera, in charge of the scientific management of the activity. He created 3D CFD tools for the numerical simulation of turbulent reactive flows that have been widely used by research laboratories and industrial partners of Onera. He also developed physical models of pollutant formation in flames. He is now involved in the development of the CEDRE code, dedicated to multiphysics problems in reactive flows. This task includes the definition of experiments for validating the models implemented in CEDRE and the global validation of this code. He is teaching thermodynamics and thermal transfer at the École Centrale Paris.



**Nicolas Bertier**, graduated from ENS Cachan and PhD from Paris VI University (2006), is senior researcher in the Energetics department of ONERA. He is in charge of the numerical simulation of reactive flows in aeronautic combustors. He has developed and validated the numerical methods and combustion models that were required to carry out LES with the CEDRE code of Onera. He is also teaching “energetics of aeronautic combustors” at Paris VI University.

D. Dutoya, L. Matuszewski  
(Onera)

E-mail: denis.dutoya@onera.fr

The CEDRE thermophysics model combines all the data and procedures that allow the calculation of the thermodynamic properties and transport coefficients of the material media that make up the multi-physics system to be analyzed. This document is more specifically concerned with the thermodynamics of compressible fluids and is limited to the study of homogenous mixtures of chemical species. Starting from the different forms of the fundamental equation of thermodynamics, it involves some useful concepts: state variables and functions, extensive and intensive properties, specific (or molar) properties of the mixture, partial properties of species in the mixture and properties of pure substances. It is shown that, in the pressure-temperature-composition variable system, the free enthalpy is a potential that all the other properties are derived from (volume, entropy, enthalpy, etc.), from which arises a set of general relations between calorific and thermoelastic coefficients. Then, different models for the calculation of the properties of pure substances are presented, from the “perfect gas” limit through real gases, to compressible liquids. These are then reused in the section that covers the way in which the properties of the mixture are calculated from those of its components. Finally, the document briefly describes how the computer data management and the thermophysics computing service are organized in an independent library called *ThermoLib*.

## Introduction

As its name indicates, numerical fluid mechanics is nothing but numerical calculation applied to solving fluid flow equations and so much the better for the reader, who will see this definition as merely obvious. Historically, this discipline was first limited to the study of potential flows. Then, it undertook the solution of the Euler equations, thus confronting the characteristics of compressible media, and, in parallel, the solution of the Navier-Stokes equations, which at first only concerned the motion of fluids with constant density. Today, the description “Navier-Stokes Code” has a nebulous coverage that includes the solution of the aerothermochemical transport equations. We recall that this hyperbolic (in time) system expresses the conservation of the extensive quantities that characterize the state of a flow: the linear momentum vector, the total energy and as many masses as the number of independent chemical species of the phase being considered (homogeneous mixture).

It was when NFM entered the world of compressible flows that thermodynamics invited itself in, through the state equations chosen to model the fluid properties. For obvious reasons, the first model used was that of the perfect gases, and it is within this restricted context that most numerical models have been developed today. In this regard we note that, based on the formalism presented in [3], the numerical flow models used by the CEDRE CODE [12, 2] were programmed

from the start with a view to using any thermodynamics whatsoever: this investment has allowed the fluid models presented here to be integrated very rapidly, and to develop them without risk of overlapping other developments.

If the only purpose of the CEDRE code was to simulate the flight of aircraft in cloud free skies, its fluid model could be described in few words: a mixture of chemical species with a fixed composition, whose behavior is similar to that of a perfect gas with constant specific heat. If it was a matter of explaining the concepts and models used in chemical engineering [19] in detail, not even several pages would suffice. The field of application of CEDRE [14] being situated well beyond the first example cited, it is the same for its modeling domain, and in particular for its fluid models: compressible, single or multiple species, possibly reactive, even multiple phase.

The CEDRE thermophysics model brings together all the data and procedures that allow the calculation of the thermodynamic properties and transport coefficients for any material medium likely to be involved in a multi-physics system, as it has been defined by the user: compressible, for which the CHARME solver calculates the flow, dispersed phases handled by the SPARTE (Lagrangian) and SPIREE (Euler) solvers, and solid materials on which the Acacia solver works. This document is more specifically concerned with the thermodynamics of the main fluid (that of Charme), and it is limited to the study

of homogenous mixtures of chemical species. For greater detail, the reader could refer to the references [1, 19], in the first chapter of the thesis report [8] and to the CEDRE theoretical manual [4].

§ “Theoretical framework” sets the theoretical framework for the modeling and states its notations. Starting from the different forms of the fundamental equation of thermodynamics, it summarizes some useful concepts: state functions and independent variables, extensive properties and intensive properties, thermodynamic potentials, specific (or molar) properties of the mixture, partial properties of species in the mixture and properties of pure substances (not mixed). § “Fluids properties” recalls that, in the so called system of natural variables (pressure, temperature and composition), the free enthalpy of the mixture is a potential from which all other first order quantities (volume, entropy, internal energy, enthalpy, etc.) are derived, and deduces all the relations between second order calorific and thermo-elastic properties. Also indicated there is how it is possible to calculate, without limitation to the special case of perfect gases, data that is indispensable to any code handling fluid mechanics, such as the specific heat ratio, the speed of sound or the partial derivatives of pressure with respect to the conservative volume quantities (mass and energy). § “Properties of species” presents different models for calculating the properties of species (not mixed), from the “perfect gas” limit, through the various models for real gases (the Viriel law and cubic state equations), to compressible liquids. These models are reused in § “Mixture models”, which shows how the properties of the mixture are calculated from its components. Finally, § “The CEDRE ThermoLib library” briefly describes how the computer management of the thermophysics calculation service is organized in an independent library called *ThermoLib*.

## Theoretical framework

The flow of a compressible fluid comprising  $n_e$  chemical species is considered, and it is assumed that this system changes sufficiently slowly for thermodynamic equilibrium to be preserved at any point in space and time (local equilibrium). In these conditions, the state of each fluid particle is defined uniquely by  $n_e + 2$  extensive quantities (i.e. proportional to the size): the volume occupied by the component considered, its internal energy  $E$  and the masses  $M_j$  of the species that it contains.

Although this set of independent variables, which will be called basic variables (or primitives) here, is sufficient to describe the state of any continuous medium in equilibrium, even if it is composed of different phases, and thus offers access to all of its properties, we will limit this dissertation to the special case of single phase fluids.

## Fundamental equation

Applied to systems of this type, thermodynamics postulates the existence of an extensive quantity called entropy, a homogenous first degree function of the basic variables, or:

$$S = S(E, V, M_j) = \frac{1}{\lambda} S(\lambda E, \lambda V, \lambda M_j), \forall \lambda > 0 \quad (1)$$

This state function only defines a stable physical system if it satisfies certain conditions of monotonicity and convexity. In particular, it must increase strictly with energy and volume, which implies that

the corresponding partial derivatives are positive. Applying the Euler theorem to the first degree homogeneous functions, postulate (1) can be written:

$$S = \frac{1}{T} E + \frac{p}{T} V - \sum_{j=1}^{n_e} \frac{g_j}{T} M_j \quad (2)$$

$$\Leftrightarrow dS = \frac{1}{T} dE + \frac{p}{T} dV - \sum_{j=1}^{n_e} \frac{g_j}{T} dM_j$$

or in the following (more classical) form:

$$E = TS - pV + \sum_{j=1}^{n_e} g_j M_j \Leftrightarrow dE = TdS - pdV + \sum_{j=1}^{n_e} g_j dM_j \quad (3)$$

Thus, the pressure  $p$ , temperature  $T$  and thermodynamic potentials per unit mass  $g_j$  for the species in the mixture are defined by:

$$\frac{1}{T} = \left. \frac{\partial S}{\partial E} \right|_{V, M_j}, \quad \frac{p}{T} = \left. \frac{\partial S}{\partial V} \right|_{E, M_j}, \quad \frac{g_i}{T} = - \left. \frac{\partial S}{\partial M_i} \right|_{E, V, M_{j \neq i}}$$

These new quantities, which only have meaning with the assumption of local equilibrium and are described as intensive because they do not depend on the size of the system, are homogenous zero degree functions of the primitive variables.

## Free energy and volume-temperature variables

If the free energy  $F = E - TS$ , also called the Helmholtz function, is used, equation (3) becomes:

$$F = -pV + \sum_{j=1}^{n_e} g_j M_j \Leftrightarrow dF = -pdV - SdT + \sum_{j=1}^{n_e} g_j dM_j \quad (4)$$

From this the partial derivatives of the free energy in the system of variables are deduced:

$$p = - \left. \frac{\partial F}{\partial V} \right|_{T, M_j}, \quad S = - \left. \frac{\partial F}{\partial T} \right|_{V, M_j}, \quad g_i = \left. \frac{\partial F}{\partial M_i} \right|_{V, T, M_{j \neq i}}$$

## Free enthalpy and pressure-temperature variables.

By replacing the internal energy by the enthalpy  $H = E + pV$  in equation (3), we immediately obtain:

$$H = TS + \sum_{j=1}^{n_e} g_j M_j \Leftrightarrow dH = TdS + Vdp + \sum_{j=1}^{n_e} g_j dM_j \quad (5)$$

From which, by introducing the free enthalpy  $G = H - TS$ , also called the Gibbs function:

$$G = \sum_{j=1}^{n_e} g_j M_j \Leftrightarrow dG = Vdp - SdT + \sum_{j=1}^{n_e} g_j dM_j \quad (6)$$

This new form of the thermodynamic postulate (Gibbs) means that, in

the  $[p, T, M_j]$  system of variables, we have:

$$V = \left. \frac{\partial G}{\partial p} \right|_{T, M_j}, \quad S = - \left. \frac{\partial G}{\partial T} \right|_{p, M_j}, \quad g_i = \left. \frac{\partial G}{\partial M_i} \right|_{p, T, M_{j \neq i}}$$

In this regard, we note that the change of variables  $[V, E, M_j] \rightarrow [p, T, M_j]$  leads to a loss of information on the zones where different phases coexist. This is the case, for example, on the phase change curves for pure substances ( $n_e = 1$ ): the pressure and temperature being related there, these two variables do not permit a complete description of the state of the system in equilibrium.

### Molar approach

Chemists prefer to measure the quantities of matter in numbers of moles. Let  $N_j$  be the number of moles of the species  $j$ ,  $N$  the total number,  $m_j$  the molar masses of the species and  $m$  that of the mixture. The change from  $M_j$  to  $N_j$  is immediate:

$$M_j = N_j m_j \Rightarrow M = \sum N_j m_j = Nm$$

In the new variables  $[p, T, N_j]$ , the equations (6) are written

$$G = \sum_{j=1}^{n_e} \mu_j N_j \Leftrightarrow dG = Vdp - SdT + \sum_{j=1}^{n_e} \mu_j dN_j$$

Here, the partial derivatives  $\mu_j$  (also denoted by  $g_{m,j}$ ) are the molar thermodynamic potentials of the species in the mixture:

$$\mu_i = m_i g_i = \left. \frac{\partial F}{\partial N_i} \right|_{V, T, N_{j \neq i}} = \left. \frac{\partial G}{\partial N_i} \right|_{p, T, N_{j \neq i}}$$

### Partial quantities

In the  $[p, T, N_j]$  system of variables, the free enthalpy is a homogeneous first degree function of the masses. It is the same for any extensive quantity  $\Psi$ , which can be translated into the following form:

$$\Psi = \sum_{j=1}^{n_e} \psi_j M_j \Leftrightarrow d\Psi = \frac{\partial \Psi}{\partial p} dp + \frac{\partial \Psi}{\partial T} dT + \sum_{j=1}^{n_e} \psi_j dM_j \quad (7)$$

The quantities  $\psi_j$  thus defined are called specific (per unit mass) partial quantities of the species in the mixture. In general, they are a function of all of the variables chosen to define the state of the system, which distinguishes them from the intrinsic properties of the same species (measured when not mixed), which only depend on the pressure and temperature, and that will be denoted here by  $\psi_j^*$ . We will return to these two important concepts later.

In terms of molar variables  $[p, T, N_j]$ , the equations (7) are written:

$$\Psi = \sum \psi_{m,j} N_j \Leftrightarrow d\Psi = \frac{\partial \Psi}{\partial p} dp + \frac{\partial \Psi}{\partial T} dT + \sum \psi_{m,j} dN_j \quad (8)$$

Here,  $\psi_{m,j} = m_j \psi_j$  is the partial molar quantity of the species  $j$  in the mixture, to be distinguished from the molar property  $\psi_{m,j}^*$  of the pure substance.

### Mass specific (or molar) quantities

The homogeneity of the state functions, such as free enthalpy relative to the masses of the species allows the study of the relations

between thermodynamic quantities to be reduced to that of a system whose total mass  $M$  remains equal to unity. The composition of such a mixture is defined by the  $n_e$  mass specific fractions  $y_j = M_j / M$ , it being understood that these new state variables are not independent because their sum is equal to unity. In the rest of this presentation, we will call any extensive quantity referred to the unit mass of the system being studied a mass specific property (or property per unit mass), that is:

$$v = \frac{V}{M}, \quad s = \frac{S}{M}, \quad e = \frac{E}{M}, \quad h = \frac{H}{M} = e + pv, \quad g = \frac{G}{M} = h - Ts, \text{ etc...}$$

We note that neither the density of the mixture ( $\rho = v^{-1}$ ) nor that of the species ( $\rho_j = \rho y_j$ ) are specific properties in the sense that is understood here. For any extensive quantity  $\Psi = M\psi$ , the equations (7) are written:

$$\psi = \sum \psi_j y_j \Leftrightarrow d\psi = \frac{\partial \psi}{\partial p} dp + \frac{\partial \psi}{\partial T} dT + \sum \psi_j dy_j \quad (9)$$

If the composition is measured in moles (8), the following molar fractions are introduced:

$$x_j = \frac{N_j}{N} = \frac{m}{m_j} y_j \quad \text{where} \quad m = \sum x_j m_j = \left( \sum \frac{y_j}{m_j} \right)^{-1}$$

and the fluid is characterized by its molar properties:

$$\psi_m = m\psi = \sum \psi_{m,j} x_j \Leftrightarrow d\psi_m = \frac{\partial \psi_m}{\partial p} dp + \frac{\partial \psi_m}{\partial T} dT + \sum \psi_{m,j} dx_j$$

To go from the specific approach (which is preferred in this presentation) to the molar approach, it is sufficient to replace the mass fractions by the molar fractions ( $y_j \rightarrow x_j$ ) in all the mathematical expressions below, and the specific quantities by the corresponding molar quantities ( $\psi \rightarrow \psi_m$ ).

## Fluid properties

### Free enthalpy and derived properties

On condition of the assumptions stated at the start of the previous section, and subject to the constraint  $\sum y_j = 1$ , the fundamental equation (6) becomes:

$$g = \sum_{j=1}^{n_e} y_j g_j \Leftrightarrow dg = vdp - sdT + \sum_{j=1}^{n_e} g_j dy_j \quad (10)$$

Of course, these relations are only valid if the function  $g$  is continuously differentiable, in other words, free of singularities related to phase changes (figure 1). As has already been remarked above, they throw light on the special status of the pressure-temperature-composition variables relative to the free enthalpy  $g$ . In this space with  $n_e + 1$  independent coordinates, the function:

$$g = g(p, T, y_j) \parallel p, T > 0, \sum y_j = 1$$

is a thermodynamic potential, which, among other things, implies that any specific property of the fluid (in the sense stated in § “Mass specific (or molar) quantities” is a linear form of  $g$  and its partial derivatives, or, with the first order of differentiation:

$$v = \frac{\partial g}{\partial p}, \quad s = -\frac{\partial g}{\partial T}, \quad g_j = \frac{\partial g}{\partial y_j} \Rightarrow h = g - T \frac{\partial g}{\partial T} = -T^2 \frac{\partial}{\partial T} \left( \frac{g}{T} \right)$$

$$\text{and } e = g - p \frac{\partial g}{\partial p} - T \frac{\partial g}{\partial T}$$

It is the same for the specific heat at constant pressure, or

$$c_p = \frac{\partial h}{\partial T} = T \frac{\partial s}{\partial T} = -T \frac{\partial^2 g}{\partial T^2}$$

and for any first order partial derivative of the properties. Because of the commutativity of the differentiation operators, these second order quantities (relative to the potential  $g$ ) are related to each other (Maxwell). Thus, in the pressure-temperature plane, we have:

$$\frac{\partial s}{\partial p} = -\frac{\partial v}{\partial T}, \quad \frac{\partial h}{\partial p} = v - T \frac{\partial v}{\partial T}, \quad \frac{\partial e}{\partial p} = v - p \frac{\partial v}{\partial p} - T \frac{\partial v}{\partial T}$$

As regards the derivatives of the first order quantities in the composition space, these are related to those of the thermodynamic potentials  $g_j$  with respect to pressure or temperature, for example:

$$v_j = \frac{\partial v}{\partial y_j} = \frac{\partial g_j}{\partial p}, \quad s_j = \frac{\partial s}{\partial y_j} = -\frac{\partial g_j}{\partial T}, \quad h_j = \frac{\partial h}{\partial y_j} = g_j - T \frac{\partial g_j}{\partial T} \text{ etc...}$$

It is easily shown that these quantities  $\psi_j$  are identical to the partial properties whose definition was given in § “Partial quantities”. Subsequently, we will show how these are calculated from the properties of pure substances  $\psi_j^*$  via a mixture model. First, we present a series of relations between thermodynamic functions that any mechanical fluid code is able to use.

### Thermodynamic relations

To simplify the expressions that follow, let:

$$r = \frac{pv}{T} = r(p, T, y_j)$$

and let the thermoelastic coefficients  $\alpha_p$  (isobaric expansion) and  $\chi_T$  (isothermal compressibility) be made dimensionless in the following way:

$$\omega_p = \chi_T p = -\frac{p}{v} \frac{\partial v}{\partial p} \Big|_{T, y_j} \quad \text{and} \quad \omega_T = \alpha_p T = \frac{T}{v} \frac{\partial v}{\partial T} \Big|_{p, y_j}$$

We note that the factor  $r$  thus defined is a specific property in the same way as the volume, that it is measured in the same units as entropy or specific heat, and that the equation that defines it as a function of the variables  $(p, T, y)$  plays the role of the equation of state for the mixture. To return to more classical notations, it is sufficient to note that:

$$r = \frac{RZ}{m} \quad (\text{J/K/kg}) \quad \text{then} \quad r_m = RZ \quad (\text{J/K/mol})$$

where  $R$  is the universal gas constant,  $m$  is the molar mass of the mixture and  $Z$  is the compressibility factor from the theory of real gases.

From the relations stated in § “Free enthalpy and derived properties”, it is easily deduced that any specific quantity derived from a first order property is expressed as a function of volume (or, what amounts to the same thing, from the factor  $r$ ), the specific heat at constant pressure and the two dimensionless thermoelastic coefficients. Here, presented in differential form and still in the system of natural variables  $(p, T, y)$ , is the table of these partial derivatives:

$$dr = (1-\omega_p)r \frac{dp}{p} + (\omega_T-1)r \frac{dT}{T} + \sum_{j=1}^{n_c} r_j dy_j$$

$$dv = -\omega_p v \frac{dp}{p} + \omega_T v \frac{dT}{T} + \sum_{j=1}^{n_c} v_j dy_j$$

$$ds = -\omega_T r \frac{dp}{p} + c_p \frac{dT}{T} + \sum_{j=1}^{n_c} s_j dy_j$$

$$dh = (1-\omega_T)v dp + c_p dT + \sum_{j=1}^{n_c} h_j dy_j$$

$$de = (\omega_p - \omega_T)v dp + (c_p - \omega_T r) dT + \sum_{j=1}^{n_c} e_j dy_j$$

We recall that these partial derivatives  $r_j, v_j, s_j, h_j$  et  $e_j$  are partial mass specific quantities (9), and that they are related by the same type of relations as the properties from which they are derived, for example:

$$r_j = \frac{pv_j}{T}, \quad h_j = e_j + r_j T, \quad \frac{\partial h_j}{\partial p} = v_j - T \frac{\partial v_j}{\partial T} \quad \text{etc...}$$

It may be necessary to use the volume rather than the pressure as the independent variable, with a state equation of the form:

$$r = \frac{pv}{T} = r(v, T, y_j)$$

In this case, let:

$$\pi_v = \omega_p^{-1} = -\frac{v}{p} \frac{\partial p}{\partial v} \Big|_{T, y_j} \quad \text{and} \quad \pi_T = \omega_T^{-1} \omega_p = \frac{T}{p} \frac{\partial p}{\partial T} \Big|_{v, y_j}$$

By combining the previously obtained results, it is found that in the new system of variables :

$$dr = (1-\pi_v)r \frac{dv}{v} + (\pi_T-1)r \frac{dT}{T} + \sum_{j=1}^{n_c} \pi_v r_j dy_j$$

$$dp = -\pi_v p \frac{dv}{v} + \pi_T p \frac{dT}{T} + \sum_{j=1}^{n_c} \pi_v p \frac{v_j}{v} dy_j$$

$$ds = \pi_T r \frac{dv}{v} + c_v \frac{dT}{T} + \sum_{j=1}^{n_c} (s_j - \pi_T r_j) dy_j$$

$$dh = (\pi_T - \pi_v) pdv + (c_v + \pi_T r) dT + \sum_{j=1}^{n_e} [h_j + (\pi_v - \pi_T) r_j T] dy_j$$

$$de = (\pi_T - 1) pdv + c_v dT + \sum_{j=1}^{n_e} [e_j + (1 - \pi_T) r_j T] dy_j$$

$$\text{where } c_v = c_p - \omega_r \pi_T r = c_p - \frac{\omega_r^2 r}{\omega_p}$$

In particular, Mayer's relation is deduced, which expresses the difference between the specific heat at constant pressure and the specific heat at constant volume:

$$c_p - c_v = \frac{\omega_r^2 r}{\omega_p} \quad (11)$$

and the specific heat ratio:

$$\gamma \equiv \frac{c_p}{c_v} = 1 + \frac{\omega_r^2 r}{\omega_p c_v} = \frac{\omega_p c_p}{\omega_p c_p - \omega_r^2 r} \quad (12)$$

As for the speed of sound in the mixture, it is easily obtained by changing to the  $(p, s, y)$  system of variables. It is found that:

$$c^2 \equiv \left. \frac{\partial p}{\partial \rho} \right|_{s, y_j} = \frac{\gamma r T}{\omega_p} \quad (13)$$

The last two equations show that a fluid model defined by an equation of the form  $g = g(p, T, y_j)$  is only stable if the following two conditions are satisfied:

$$\omega_p > 0 \text{ and } \omega_p c_p > \omega_r^2 r$$

Finally, we note that in the  $(v, T, y)$  system of variables, the free energy  $f = e - Ts$  is a more suitable state function for the calculation of its derivative properties:

$$f = f(v, T, y) \Rightarrow df = -pdv - sdT + \sum_{j=1}^{n_e} g_j dy_j$$

### Volume specific variables

The  $[\rho_j, \rho e]$  system of variables is important for the Euler approach to fluid mechanics: the masses of species and the internal energy per unit volume are the thermostatic part (i.e. without motion) of the so-called conservative quantities. In the transport equations, the fluid properties intervene via the pressure (Euler flux) and the temperature (heat flux). The result of this is that the functions:

$$p = p(\rho_j, \rho e) \Rightarrow dp = \pi_e d\rho e + \sum \pi_j d\rho_j$$

$$T = T(\rho_j, \rho e) \Rightarrow dT = \vartheta_e d\rho e + \sum \vartheta_j d\rho_j$$

and their partial derivatives, here denoted by  $\pi$  and  $\vartheta$ , play an important role. The simplest way to express these as a function of the mass specific quantities and coefficients defined in the  $[p, T, y_j]$  system of variables, is to go through the variables  $[\rho_j, T]$ . After some elementary analytic developments, we find:

$$\pi_e = \frac{\pi_T r}{c_v} = \frac{\omega_r c^2}{c_p T}, \quad \pi_j = c^2 \frac{r_j}{r} - \pi_e h_j \text{ and}$$

$$\vartheta_e = \frac{1}{\rho c_v}, \quad \vartheta_j = \vartheta_e \left( \frac{\omega_r}{\omega_p} r_j T - h_j \right)$$

It is easily verified that the speed of sound  $c$  and the partial derivative of the pressure are linked by the following relation (which can moreover be proven):

$$c^2 = h \pi_e + \sum y_j \pi_j$$

### Properties of species

As has already been noted in § "Partial quantities " and "Mass specific (or molar) quantities", any extensive quantity referred to the unit of mass of the mixture can be written

$$\psi = \sum_{j=1}^{n_e} y_j \psi_j \text{ where } \psi_j = \psi_j(p, T, y_k) = \left. \frac{\partial \psi}{\partial y_j} \right|_{p, T, y_{k \neq j}}$$

the  $\psi_j$  being, by definition, the partial mass specific properties of the species in the mixture. As for the properties of pure substances (i.e. measured outside a mixture), which, let us recall, generally differ from those above, these will be denoted by  $\psi_j^*$ :

$$\psi_j^* = \psi_j^*(p, T) = \psi_j(p, T, y_k = \delta_{jk})$$

The second equality means that the intrinsic properties and partial quantities are only equal if the mixture is composed only of the species being considered.

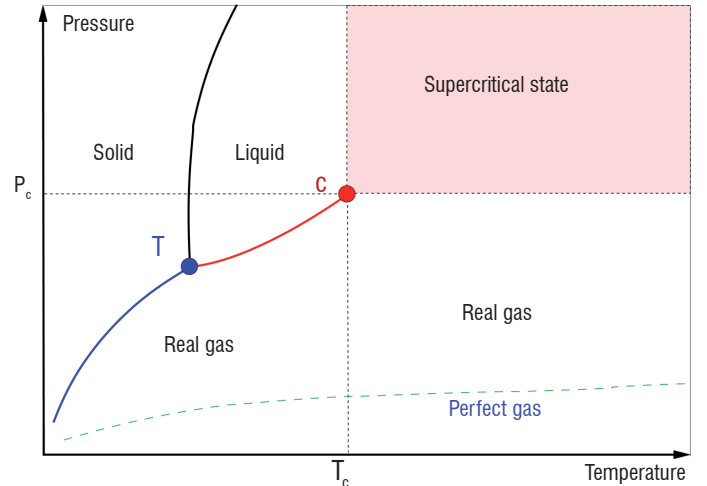


Figure 1 - Phase diagram for a pure substance

To calculate the properties of pure substances, it is normal to refer to those that are measured along a particular isobar, that is  $p = p_o = 10^5 Pa$ , and for which the variations as a function of temperature are listed in thermodynamic tables. These quantities are generally described as properties in the standard state:

$$\psi_j^o = \psi_j^o(T) = \psi_j^*(p_o, T)$$

Applied to the free enthalpy, this concept allows the following equation to be written for each substance  $j$ :

$$g_j^*(p, T) = g_j^o(T) + \int_{p_o}^p v_j^*(p, T) dp = g_j^o(T) + T \int_{p_o}^p r_j^* \frac{dp}{p} \quad (14)$$

Thus, the properties of the species  $j$  are entirely defined by its state equation, that is,

$$v_j^* = v_j^*(p, T) \text{ or } r_j^* = \frac{pv_j^*}{T} = r_j^*(p, T)$$

and its free enthalpy  $g_j^o$  in the standard state. To calculate these explicitly, it is sufficient to apply the results of Section 3 to this single species system. In the paragraphs below, we will temporarily drop the index  $j$  and the exponent "\*", it being understood that the results presented here concern either the intrinsic properties of any constituent of the mixture, or what amounts to the same thing, the properties of any single species fluid.

### Perfect gases

This is the case of any gas subject to a sufficiently low pressure for the molecules to be considered as material points (zero covolume) whose interactions are negligible, except for impacts. This purely fictitious state, or ideal state according to Anglo-Saxon terminology, can be defined without prejudging the stability of the real physical system. For example: Water vapor at atmospheric pressure and at 0° C ...

The universal molar gas constant is denoted by  $R$ ,  $m$  is the molar mass of the species considered and  $r_o$  is its specific constant per unit mass. The state equation is written

$$r^{(id)} = r_o = \frac{R}{m} \Leftrightarrow v^{(id)} = \frac{r_o T}{p} \quad \omega_p^{(id)} = \omega_T^{(id)} = 1$$

and the free enthalpy (14) becomes

$$g^{(id)}(p, T) = g^o(T) + r_o T \ln \frac{p}{p_o} \text{ where } g^o = h^o(T) - Ts^o(T)$$

Thermophysical databases such as the NIST-JANAF tables supply the information needed for the calculation of the properties in the standard state ( $p = p_o$ ) for a large number of ordinary gases. In addition to the molar masses, the following can be found:

- the enthalpies and entropies of formation measured at a reference state ( $p_o, T_o$ ),
- and a tabulation of the specific heats at constant pressure ( $p_o$ ), from which it is possible, by using the least squares method, to draw a polynomial representation over a range of temperatures suited to the calculations, that is, a limited set of species parameters and physical constants that can be combined in a reasonably sized database. This is the case for the thermog.xml file of the CEDRE calculation chain. From this, it is possible to calculate explicitly the intrinsic properties of any "perfect gas" type component, first in the standard state (isobar ( $p_o$ )):

$$h^o(T) = h_f^o + \int_{T_o}^T c_p^o dT, \quad s^o(T) = s_f^o + \int_{T_o}^T c_p^o \frac{dT}{T}, \text{ etc...}$$

And then in the entire plane ( $p, T$ ):

$$c_p^{(id)} = c_p^o(T), \quad h^{(id)} = h^o(T), \quad s^{(id)} = s^o(T) - r_o \ln \frac{p}{p_o}, \text{ etc...}$$

### Compressible liquids

Here is an example of a simplified state equation for a compressible liquid, valid in the vicinity of a reference state ( $p_o, T_o$ ):

$$v = v_o \frac{1 + \alpha(T - T_o)}{1 + \beta(p - p_o)} \text{ where } \alpha T_o \ll 1 \text{ et } \beta p_o \ll 1$$

In these conditions, the dimensionless thermoelastic coefficients are:

$$\omega_p \sim \beta p \quad \text{and} \quad \omega_T \sim \alpha T$$

Equation (14) become:

$$g \sim g^o(T) + v_o(p - p_o) \text{ hence } h \sim h^o(T) + v_o(p - p_o), \quad c_p = c_p^o(T)$$

It is easily shown that if the fluid cannot be expanded ( $\alpha = 0$ ), the ratio  $\gamma$  is strictly equal to unity. In CEDRE, this model for a fluid with little compressibility is used to evaluate the robustness and stability of numerical models initially developed for gas flows.

### Real gases

When a gas is subject to high pressures, the molecules can no longer be considered as material points and their interactions can no longer be neglected. As a result, the compressibility factor:

$$Z = \frac{v}{v^{(id)}} = \frac{r}{r_o} = \frac{pv}{r_o T}, \quad r_o = \frac{R}{m} \quad (15)$$

differs from unity, as does the fugacity coefficient ( $\varphi$ ), a dimensionless parameter whose logarithm measures the difference between the free enthalpy of a mole of real gas and the value that a perfect gas would have at the same temperature, that is, in terms of mass specific properties:

$$g(p, T) = g^{(id)}(p, T) + r_o T \ln \varphi = g^o(T) + r_o T \ln \frac{p}{p_o} + r_o T \ln \varphi \quad (16)$$

By combining equation (14) and the definition of the fugacity coefficient (16), we obtain:

$$\ln \varphi = \frac{g - g^{(id)}}{r_o T} = \frac{1}{r_o T} \int_{p_o}^p (v - v^{(id)}) dp \quad (17)$$

In this paragraph, we will assume on the one hand that the pressure  $p_o$  is sufficiently low for the standard state to coincide with that of the perfect gas (or  $Z^o \sim 1$ ) and, on the other hand, that the state equation can be written in one of the two forms below:

$$Z = \mathcal{Z}(p, T) \quad \text{or} \quad Z = \mathcal{Z}(v, T) \quad (18)$$

In these conditions and depending on the case, the logarithm of the fugacity coefficient is written:

$$\ln \varphi = \int_{p_o}^p (\mathcal{Z} - 1) \frac{dp}{p} \quad (19)$$

$$\text{or } \ln \varphi = Z - 1 - \ln Z - \int_{\infty}^v (\mathcal{Z} - 1) \frac{dv}{v} \quad (20)$$

We note in passing that the two forms (18) are only equivalent if, at a given temperature, pressure and volume vary in opposite directions,

which must be the case for the speed of sound in the substance to be calculable (see § “Thermodynamic relations”).

### Principle of corresponding states

In what follows, the critical pressure of the gas that is being considered will be denoted by  $p_c$ , its critical temperature will be denoted by  $T_c$ , and this data will be used to make the state variables dimensionless:

$$P_r = \frac{p}{p_c}, \quad T_r = \frac{T}{T_c} \quad \text{and} \quad V_r = \frac{p_c v}{r_o T_c} = Z_c \frac{v}{v_c} \quad (21)$$

According to the “principle” of corresponding states, the volume factor must be a universal function of the reduced variables. Experience shows that this is only the case for rigorously symmetrical molecules, in other words, for monatomic substances. This is why Pitzer and other authors have introduced the concept of the acentric factor  $\omega$ , this dimensionless number being assumed to represent the molecular characteristics of the gas being considered. They let:

$$Z = \frac{P_r V_r}{T_r} = \mathcal{Z}(P_r, T_r, \omega)$$

the function  $\mathcal{Z}$  being common to all species. This approximation, which is found to be fairly close to reality for most ordinary gases, allows considerable simplification of the relation between the calculation library and the thermophysical database: so that a chemical species for which “perfect gas” data is available, via the thermog.xml file for example (see § “Perfect gases”), can be treated as a real gas, it is sufficient to add the three additional constants  $p_c, T_c$  and  $\omega$  to the data for the standard state.

### Viriel expression

At moderate pressure, we can be content to express the volume factor by means of a limited expression around the perfect gas state, or

$$Z = 1 + \sum_{k>0} \frac{A_k}{V_r^k} = 1 + \sum_{k>0} B_k \left( \frac{P_r}{T_r} \right)^k$$

the coefficients  $A_k$  and  $B_k$  (related to each other) only depend on the reduced temperature and the Pitzer acentric factor.

$$A_k = A_k(T_r, \omega), \quad B_1 = A_1, \quad B_2 = A_2 - A_1^2,$$

As for the free enthalpy and the other calorific properties, they can be deduced from the fugacity coefficient (19), which here has the value:

$$\ln \varphi = \sum_{k>0} \frac{B_k}{k} \left( \frac{P_r}{T_r} \right)^k$$

### Cubic state equations

At higher pressure, it is preferable to use one of the state equations derived from the Van der Waals equation. This is the general form, with the two numbers  $\sigma_1$  and  $\sigma_2$ , as parameters and expressed as a function of the molar volume:

$$p = \frac{RT}{v_m - b} - \frac{a\alpha(T)}{(v_m + \sigma_1 b)(v_m + \sigma_2 b)} \quad \text{where} \quad \alpha(T_c) = 1 \quad (22)$$

After changing to reduced variables (21), and once we let:

$$b_r = \frac{p_c b}{RT_c} \quad \text{and} \quad a_r = \frac{p_c a}{(RT_c)^2}$$

Equation (22) becomes:

$$P_r = \frac{T_r}{V_r - b_r} - \frac{a_r \alpha(T_r, \omega)}{(V_r + \sigma_1 b_r)(V_r + \sigma_2 b_r)}$$

Both dimensional constants  $b_r$  (reduced covolume) and  $a_r$  (internal pressure coefficient) are such that the first and second derivatives of the function (23) with respect to the volume are zero at the critical point, or  $P_r = T_r = 1$ . Table 1 shows the constants for four of the best known models: Van der Waals (VdW, [18]), Redlich-Kwong (RK, [11]), Soave-Redlich-Kwong (SRK, [16]) and Peng-Robinson (PR, [9]). The first is mainly of historical interest. The correction to the Redlich-Kwong equation by Soave permits a better representation of the behavior of hydrocarbon gases close to the saturation curve.

EOS	$\sigma_1$	$\sigma_2$	$b_r$	$a_r$	$Z_c$	$\alpha(T_r, \omega)$
VdW	0	0	0.125	0.421875	0.375	1
RK	0	1	0.08664	0.42748	0.333	$T_r^{-0.5}$
SRK	0	1	0.08664	0.42748	0.333	$[1 + m(1 - T_r^{0.5})]^2$
PR	$1 - \sqrt{2}$	$1 + \sqrt{2}$	0.07780	0.45724	0.305	$[1 + m(1 - T_r^{0.5})]^c$
SRK	$m = 0.48508 + 1.54171\omega - 0.17613\omega^2$					
PR	$m = 0.37464 + 1.54226\omega - 0.26992\omega^2$					

Table - 1 Cubic state equations

As for the performance of the Peng and Robinson model, it is better on the liquid side and in the vicinity of the critical point [17]. Here we let:

$$\xi = \frac{b_r P_r}{T_r}, \quad \eta = \frac{b_r}{V_r} \quad \text{and} \quad \Theta = \frac{a_r \alpha}{b_r T_r} = \Theta(T_r)$$

The covolume  $b_r$ , being the threshold value for the reduced volume, the variable  $\eta$  defined above varies between 0 (perfect) and 1 (infinite pressure). With this notation, the state equation (23) becomes:

$$\xi = \frac{\eta}{1-\eta} - \frac{\Theta \eta^2}{(1+\sigma_1 \eta)(1+\sigma_2 \eta)} \quad (24)$$

hence, the compressibility factor is:

$$Z = \frac{\xi}{\eta} = \frac{1}{1-\eta} - \frac{\Theta \eta}{(1+\sigma_1 \eta)(1+\sigma_2 \eta)} \quad (25)$$

The fugacity coefficient (20) is deduced from the state equation (25). After integration of the function  $Z$  along each isotherm, we find:

$$\ln \phi = Z - 1 - \ln Z - \ln(1-\eta) - \Theta U(\eta) \quad (26)$$

the function being defined by

$$U = \int_0^\eta \frac{d\eta}{(1+\sigma_1 \eta)(1+\sigma_2 \eta)} \quad \text{or} \quad U = \frac{1}{\sigma_2 - \sigma_1} \ln \left( \frac{1+\sigma_2 \eta}{1+\sigma_1 \eta} \right) \quad \text{if } \sigma_1 \neq \sigma_2$$

$$U = \frac{\eta}{1+\sigma \eta} \quad \text{if } \sigma_1 = \sigma_2 = \sigma$$

From equation 26, we deduce the free energy of the real gas

$$f = g - p v = f^{(id)} - r_o T [\ln(1-\eta) + \Theta U(\eta)]$$

then, by differentiation with respect to temperature, all the calorific properties, for example:

$$e = e^{(id)} - r_o T \left[ T \frac{d\Theta}{dT} U(\eta) \right]$$

$$h = h^{(id)} + r_o T \left[ Z - 1 + T \frac{d\Theta}{dT} U(\eta) \right]$$

$$s = s^{(id)} + r_o \left[ \ln Z + \ln(1-\eta) + \left( \Theta + T \frac{d\Theta}{dT} \right) U(\eta) \right]$$

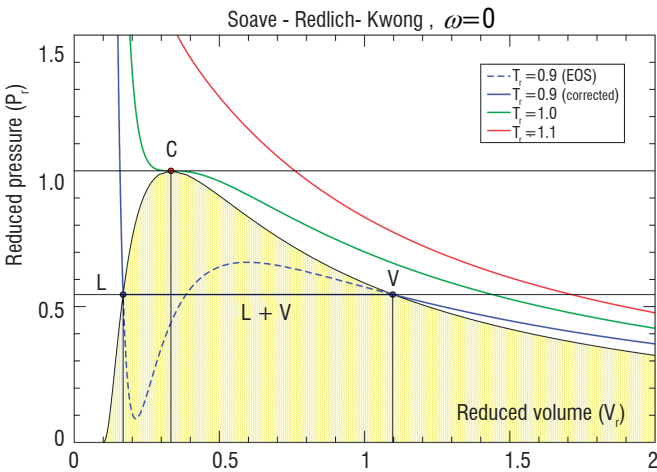


Figure 2 - Cubic state equation, Clapeyron diagram.

The state equations (22-25) are described as cubic because the calculation of the volume (or factor) from the intensive parameters (pressure and temperature) involves the solution of a third degree equation. This does not present any difficulty in the supercritical domain ( $T_r > 1$ ): the solution there is necessarily unique. Otherwise, the problem can have three solutions, as shown in figure 2. The one located in the increasing part of the curve can be eliminated automatically because it is not physical, which does not necessarily mean that the other two will be. In fact, over the entire domain above the saturation curve, each isotherm from the cubic equation must be replaced by a horizontal plateau (isobar) whose level is the saturated vapor pressure, and whose two ends are the values of the volume on the saturated liquid side (to the left) and that on the just dry vapor side (to the right), or:

$$\forall T_r < 1, \quad P_r = P_r^{(sat)}(T_r) \quad \text{if} \quad V_r^{(sat,l)} \leq V_r \leq V_r^{(sat,v)}$$

Thus, for any state equation of the form (23) and for any fixed temperature above the critical point, the saturated vapor pressure is determined by the fact that, on the one hand, the reduced volumes  $V_r^{(sat,l)}$  and  $V_r^{(sat,v)}$  are respectively the smallest and the greatest of the three real solutions of the equation

$$P_r^{(sat)} = \frac{T_r}{V_r} \mathcal{Z}(V_r, T_r)$$

And, on the other hand, the free enthalpy is continuous across the saturation curve. This equilibrium condition between coexisting phases comes down to writing the equality of the fugacity coefficients (26), or:

$$\phi(V_r^{(sat,l)}, T_r) = \phi(V_r^{(sat,v)}, T_r)$$

This type of problem can only be solved iteratively: starting from a pressure level between the two extremes of the isotherm under consideration, the volumes corresponding to the two intersection points  $L$  and  $V$  are calculated (see figure 2), then the two related fugacity coefficients are calculated by applying the formula (26), and the pressure is iterated using the following recurrence:

$$P_r = P_r \times \frac{\phi^{(L)}}{\phi^{(V)}}$$

until the fugacities are equal. Figure 3 shows the result obtained with the Soave-Redlich-Kwong equation in the case where the acentric factor is zero. We note that the leaps in the derived properties are linked to the slope of the saturation curve via the Clapeyron relation:

$$L_v = \Delta h^{(sat)} = T \Delta s^{(sat)} = r_o T_c \left[ \frac{T_r^2}{P_r} \frac{dP_r}{dT_r} \right]^{(sat)} \Delta Z^{(sat)}$$

If we assume that the specific heat of vaporization  $L_v$  is proportional to the variation of the compressibility ratio, or

$$\frac{L_v}{r_o T_c} \approx A \times \Delta Z^{(sat)} \quad \text{where} \quad A = \frac{7}{3} \ln 10 \times (1 + \omega)$$

an expression analogous to Antoine's law is deduced from the Clapeyron equation,

$$\ln P_r^{(sat)} = A \times \left( 1 - \frac{1}{T_r} \right)$$

which, as can be seen in figure 3, is close to that obtained from the state equation.

Figure 4 shows, as a function of the ratio  $P_r/T_r$  and of the values of  $T_r$ , from 0.5 to 2, the compressibility factor resulting from the Soave equation and with a correction for the Maxwell plateaux procedure. It shows, if this was needed, that in the zone of coexistence between liquid and vapor (colored yellow), where pressure and temperature are related, the fluid properties can only be calculated if additional information is available, such as the liquid mass (or volume) fraction. Furthermore, it is noted that, even at moderate pressure, the perfect gas assumption ( $Z=1$ ) is only really justified (as close as five per cent, for example) if the temperature is greater than one and a half times the critical temperature.

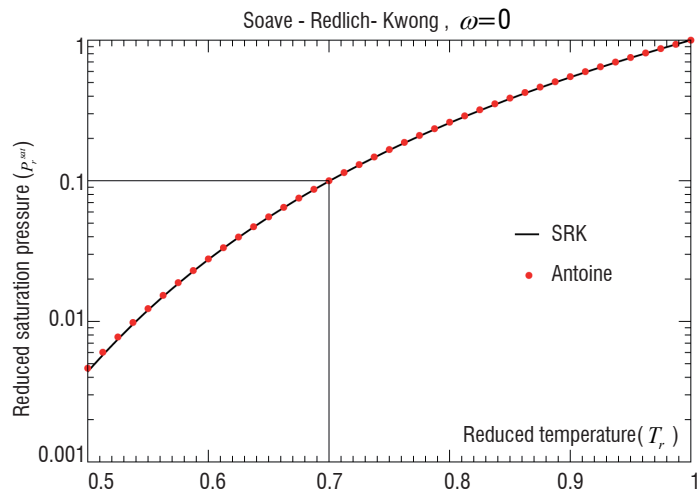


Figure - 3 - Cubic state equation, saturation curve.

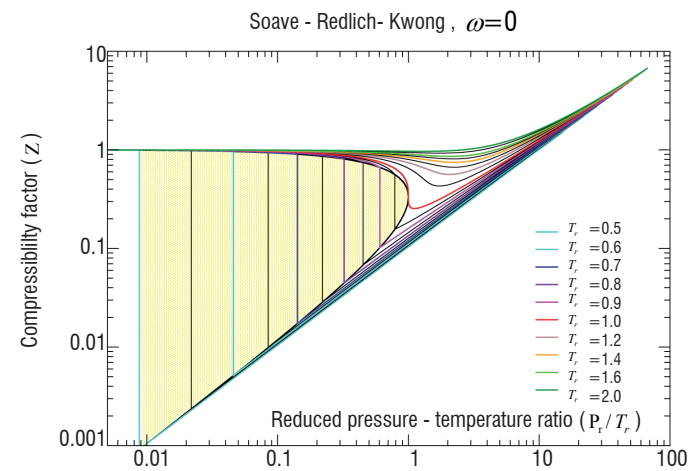


Figure 4 - Cubic state equation, compressibility factor.

## Mixture models

### Ideal mixture

We will consider the special case of an ideal mixture of perfect gases. Let  $x_j$  denote the molar fraction of the species and let  $j$  and  $p_j = px_j$  be its partial pressure. Once this constituent is placed in the mixture (and after homogenization), its thermodynamic potential becomes:

$$g_j(p, T, y_j) = g_j^*(p, T) + r_j^o T \ln x_j = g_j^o(T) + r_j^o T \ln \frac{p_j}{p_o}$$

We recall that  $r_j^o = R/m_j$  is the mass specific gas constant and that the molar fractions only depend on the composition. As a result, for an ideal mixture, and only in this case, the partial volume and enthalpy of each species in the mixture are respectively identical to the volume and enthalpy of the pure substance:

$$v_j = \frac{\partial v}{\partial y_j} = \frac{\partial g_j}{\partial p} = \frac{r_j^o T}{p}, \quad h_j = \frac{\partial h}{\partial y_j} = g_j - T \frac{\partial g_j}{\partial T} = h_j^o(T)$$

More generally, in any ideal mixture, we have:

$$v = \sum y_j v_j^*(p, T), \quad h = \sum y_j h_j^*(p, T), \quad e = \sum y_j e_j^*(p, T)$$

but

$$s = \sum y_j s_j^*(p, T) - \frac{R}{m} \sum x_j \ln x_j \quad \text{where} \quad m = \sum x_j m_j$$

### Other models

In general, the chemical activity of a component  $j$  in the mixture is defined as follows:

$$g_j(p, T, y_j) = g_j^o(T) + r_j^o T \ln a_j$$

It has been seen that, for ideal mixtures of perfect gases, this intensive quantity only depends on the partial pressure of the constituent in the mixture, that is:

$$a_j^{(id)} = \frac{px_j}{p_o}$$

This assumption implies that the fugacity coefficient of each pure

constituent ( $\alpha_j = 1$ ) is equal to unity. It is thus absolutely unsuitable for mixtures of real gases. In this case, more or less complex mixture rules are used.

The simplest rule (Kay, [5]) is only valid for mixtures of substances with similar properties. It consists of applying the principle of corresponding states on the basis of a pseudo critical point with coordinates depending on the mixture composition and the critical data of the constituents  $j$  :

$$p_c = \sum_j x_j p_{c_j}, \quad T_c = \sum_j x_j T_{c_j} \quad (27)$$

Then, it is sufficient to choose a real gas law, such as one of those presented in see § "Real gases", to write it in reduced coordinates and to apply it to the mixture:

$$Z = Z\left(\frac{p}{p_c}, \frac{T}{T_c}, \omega\right) \quad \text{where} \quad \omega = \sum_j x_j \omega_j \quad (28)$$

A less elementary model consists of writing that the molar volume of the mixture obeys a cubic state law of type (22) where the constant

(covolume) and product  $a\alpha$  (function of temperature) are calculated from the data for pure constituents, or:

$$b_j = b_r \frac{RT_{c_j}}{P_{c_j}}, \quad a_j = a_r \frac{(RT_{c_j})^2}{P_{c_j}} \quad \text{and} \quad \alpha_j = \alpha \left( \frac{T}{T_{c_j}}, \omega_j \right)$$

Applied to the Van der Waals equation ( $\alpha_j = 1$ ), the rule of the same name states that:

$$b = \sum_i x_i b_i \quad \text{and} \quad a = \sum_{i,j} x_i x_j a_{ij} \quad \text{where} \quad a_{ij} = \sqrt{a_i a_j}$$

To extend this to all the equations 22, it is sufficient to substitute the products  $a\alpha$  and  $a_{ij}\alpha_{ij}$  for the above constants  $a$  and  $a_{ij}$ .

This is the model used by the CEDRE code to calculate the properties of mixtures of real gases with cubic state equations ("GCUB1" type species, see following section). In [8] the reader can find a more complete presentation of this fluid model.

Finally, we note that, although the models presented here only need a minimum of information in the species databases, they are far too elementary to be reasonably applicable to complex systems like hydrocarbon mixtures (see [19]) or liquid solutions.

## The CEDRE ThermoLib library

The *ThermoLib* library combines all the thermo-physical model related procedures in the CEDRE chain, from loading data into an internal model to calculating the properties of any phase (homogeneous mixture of chemical species) defined during loading. This independent set of FORTRAN 90 procedures can be used by all the components in the calculation chain, including those whose source is written in C++.

Uploading data, the first operation that the user code must start with, consists of reading the fluid model data and storing it in an internal static structure (F90 derived type). It continues by reading two XML files:

- *thermog.xml* is a portable database (i.e. available on the delivery CD), which contains the pure substance data (see § "Properties species") for about sixty chemical species;
- *epicea.xml*, produced by collecting the CEDRE calculation data via the EPICEA graphic interface, brings together all the physical-chemical model parameters set by the operator, including the fluid definition data.

From the THERMOLIB service viewpoint, any "fluid" defined by the user is any set of chemical species chosen from among the items available in the database and able to form a homogeneous mixture whose properties can be calculated as a function of pressure, temperature and composition. Since this concept can be extended to solid material, we prefer to speak of a mixture (current terminology) or phase.

As for the species themselves, they are identified by their name (examples:  $N_2$ ,  $O_2$ ,  $CH_4$ ,  $CO_2$ ,  $H_2O$ , etc...), which allows the up-

loading procedure to read their data from the file *thermog.xml*. At the same time, each species is characterized by the type that the operator has assigned to it from the graphic interface: perfect gas with single polynomial representation (GP1), compressible liquid (LC1), real gas whose state equation takes on the form of a Viriel expression (GR1), real gas with cubic state equation (GCUB1), etc. Of course, the choice of type depends on the type of data in the database. Thus, a gas for which only the standard state is known can only be of the "perfect gas" type, whereas if the coordinates of the critical point and the acentric factor appear in its data, it can be allocated either to the "perfect gas" type, or to one of the "real gas" types.

We note that it is possible to allocate different types of species to the same mixture, with the exception of the GCUB1 type, which has its own mixture model. Thus, some users combine a gaseous mixture of air and water vapor (type GP1) with liquid water (type LC1), in the same "fluid" treated by the CHARME solver, by considering that the two phases would be able to maintain themselves in mechanical and thermal equilibrium (same pressure and temperature), without the equality of the chemical potentials, etc., being ensured.

The data collected during the uploading phase is classified and stored in an internal ThermoLib model. This provides management of all its internal data, so that the user does not need to be concerned with this, and can just recover the content through the extraction procedures. Examples: number of mixture of a given name, number of species defined in this mixture, names of these species, molar masses, etc.

The procedures for calculating the properties operate on a mixture with number set by the calling program. For example: calculate, for the mixture  $i_{me} = 1$ , the enthalpy ( $H$ ) and its partial derivatives with respect to pressure ( $H_p$ ), temperature ( $H_T$ ) and the mass fractions ( $H_y$ ), from the state data ( $P, T, Y$ ). To simplify vectorization and optimize the calculation time, each operation is performed on a set of  $n_s$  independent states (treatment by packets). Thus, the arguments that appear in the calling interface are real tables whose first dimension has a size equal to the size of the packet to be processed, for example:

```
INTEGER, Intent(in) : i_me
INTEGER, Intent(in) : n_s, n_esp
REAL, Intent(out) : P(n_s), T(n_s), Y(n_s, n_esp)
REAL, Intent(out) : H(n_s), H_p(n_s), H_T(n_s), H_y(n_s, n_esp)
INTEGER, Intent(out) : error
OPTIONAL, : H, H_p, H_T, H_y
```

Of course, the size  $n_{esp}$  of the second dimension of the table of compositions ( $Y$ ) must be equal to the number of species in the mixture considered: any ThermoLib calculation function verifies this first.

## Conclusion

The CEDRE thermo-physical model has allowed the field of application of the code to be extended beyond the perfect gas domain. For the moment, the modeling remains fairly elementary, in particular at the level of mixture rules, but the fact that they are encapsulated in an independent library will allow progressive enrichment and without the risk of overlapping other developments ■

## References

- [1] M.M. ABBOTT, H.C. VAN NESS - *Theory and Applications of Thermodynamics*. Schaum series, 225 solved exercises, McGraw-Hill, 1987, 342 pages. (ISBN 2 7042 1001 2).
- [2] B. COURBET, C. BENOIT, V. COUAILLIER, F. HAIDER, M.-C. LE PAPE and S. PÉRON - *Space Discretization Methods*. Aerospace Lab Issue 2 March 2011.
- [3] D. DUTOYA, M.P. ERRERA - *A formal Decomposition of the Jacobian of the Euler Equations*. Rech.Aérosp.1992-1.
- [4] D. DUTOYA - *Manuel théorique de la chaîne de calculs CEDRE*. CEDRE-MT-001-I-420x.
- [5] W.B. KAY - *Density of Hydrocarbon Gases and Vapours at High Temperatures and Pressures*. Ind. Eng. Chem., 28, 1014-1019, 1964.
- [6] B.I. LEE, M.G. KESLER - *A Generalized Thermodynamic Correlation Based on Three-Parameter Corresponding State*. AIChE J., 21, 510-527, 1975.
- [7] G.N. LEWIS, M. RANDALL - *Thermodynamics and the Free Energy of Chemical Substances*, McGraw-Hill, New York, 1923.
- [8] L. MATUSZEWSKI - *Modélisation et simulation numérique des phénomènes de combustion en régime supercritique, thèse pour l'obtention du titre de docteur de l'Université Pierre et Marie Curie (to be published) 2011*.
- [9] D.Y. PENG, D.B. ROBINSON - *A New Two-Constant Equation of State*. Ind. Eng. Chem., Fundam., 15, 59-64, 1976.
- [10] P. PERROT - *A to Z of Thermodynamics*. Oxford University Press. ISBN 0-19-856552-6, 1998.
- [11] O. REDLICH, J.N.S. KWONG - *On the Thermodynamics of Solutions*. V. an Equation of State Fugacities of Gaseous Solutions. Chem. Rev., 44, 233-244, 1949.
- [12] A. REFLOCH, B. COURBET, A. MURRONE, P. VILLEDIEU, C. LAURENT, P. GILBANK, J. TROYES, L. TESSÉ, G. CHAINERAY, J.B. DARGAUD, E. QUÉMERAIS and F. VUILLOT - *CEDRE Software*. Aerospace Lab Issue 2 March 2011.
- [13] R.C. REID, J.M. PRAUSNITZ and B.E. POLING. *The properties of Gases and Liquids*. 4<sup>th</sup> édition, McGraw-Hill , 1986.
- [14] D. SCHERRER, F. CHEDEVERGNE, P. GRENARD, J. TROYES, A. MURRONE, E. MONTREUIL, F. VUILLOT, N. LUPOGLAZOFF, M. HUET, B. SAINTE-ROSE, P. THORIGNY, N. BERTIER, J.M. LAMET, T. LE PICHON, E. RADENAC, A. NICOLE, L. MATUSZEWSKI and M. ERRERA - *Recent CEDRE Applications*. Aerospace Lab Issue 2 March 2011.
- [15] G. SCHMIDT and H. WENZEL - *A Modified Van der Waals Type Equation of State*. Chemical Engineering Science, Volume 35, Issue 7, 1980, pl503-1512.
- [16] G.S. SOAVE - *Equilibrium Constants from Modified Redlich-Kwong Equation of State*. Chem. Eng. Sci, 27, 6, 1197, 1972.
- [17] C.H. TWU, J.E. COON and D. BLUCK - *Comparison of the Peng-Robinson and Soave-Redlich-Kwong Equations of State Using a New Zero-Pressure-Based Mixing Rule for the Prediction of High-Pressure and High-Temperature Phase Equilibria*. Industrial & engineering chemistry research, ISSN 0888-5885.
- [18] J.D. VAN DER WAALS - *The Equation of State for Gases and Liquids*. Nobel lectures in Physics, 1.254-265, Elsevier, Amsterdam (1967).
- [19] J. VIDAL - *Thermodynamique, application au génie chimique et à l'industrie pétrolière*. éditions Technip. 21.

## AUTHORS



**Denis Dutoya** Ecole des Mines de Paris, Research engineer, department of numerical simulation and aeroacoustics, unit CIME. Architect and developer for the CEDRE software, numerical methods and physical models (turbulence, thermodynamics and thermochemistry, aerothermics).



**Lionel Matuszewski** is a research engineer at the Onera working in the Liquid Propulsion Unit of the Fundamental and Applied Energetics Department (DEFA). He graduated from the Ecole Polytechnique and ISAE engineer schools in 2007. His research field is mainly focused on dense fluid modeling with application to supercritical combustion.

A. Murrone, P. Villedieu

(Onera)

E-mail: angelo.murrone@onera.fr

# Numerical Modeling of Dispersed Two-Phase Flows

This paper presents some fundamental aspects of the mathematical and numerical modeling of dispersed two phase flows. The special case of gas-particle flows which is of major importance in the aerospace context is examined. The “kinetic” equation corresponding to the mesoscopic level of description is recalled and the derivation of the different models is explained. Microscale physical phenomena occurring in gas-particle flows are also described. Then an overview of the different numerical methods is given. The SPARTE and SPIREE solvers of the CEDRE code illustrate Lagrangian and Eulerian techniques respectively, implemented in a 3D complex CFD platform. Some numerical simulations are presented, showing the capacity of the solvers to deal with turbojet engines, liquid rocket engines, solid propellant rockets, icing problems, etc. The advantages and drawbacks of Lagrangian and Eulerian techniques are briefly discussed, from the theoretical and practical points of view. We also present the future developments expected in the code, taking into account the crucial challenges in numerical simulation such as Large Eddy Simulation, primary atomization, coupling “separated” and “dispersed” two-phase flow solvers, spray-film interactions.

## Introduction

The topic of two-phase flows has, in a wide variety of engineering systems, become increasingly important for optimal design and safe operations. A non-exhaustive list of examples including power systems, heat transfer systems, chemical engineering and transport systems shows that a classification is needed in order to derive the various models.

### Classification of two-phase flows

For modeling purposes we need to introduce a classification for the large variety of two-phase flows. This classification depends mainly on both the physical state of the two phases and on the flow structure. First, as regards the physical state, four combinations can be considered: gas-solid, gas-liquid, liquid-solid and liquid-liquid mixtures. Then, for the structure, and especially the interface topology, it is more difficult to establish a set of combinations because changes in the flow may be occurring continually. Nevertheless, following the work of Ishii [18], two-phase flows are generally classified into three categories according to the shape of the interface: separated flows, mixed flows and dispersed flows, as explained in Box 1.

In this paper, we shall focus on the class of dispersed two-phase flows (and more precisely on the special case of gas – particle flows) which is of major importance for many applications in the aerospace context. A set of examples is given in the next section.

### Dispersed two-phase flows in aerospace systems

Dispersed two-phase flows are involved in most aerospace propulsion systems. In turbojet engines, for example, kerosene is stored in a condensed form and injected as a spray of small droplets in the combustion chamber. Flame ignition and stability depend to a large extent on the droplet dynamics and evaporation (Figure 1 page 3). For modeling purposes, two different zones may be considered: the primary break-up zone located in the vicinity of the nozzle exit where the liquid jet is atomized into small droplets, and the spray zone where droplets are already formed and are carried by the gas flow. In the first zone, the liquid phase is continuous and a separated two-phase flow model needs to be used while in the spray zone a dispersed flow description is more appropriate.

## Box 1 - Classification of Two-phase flows

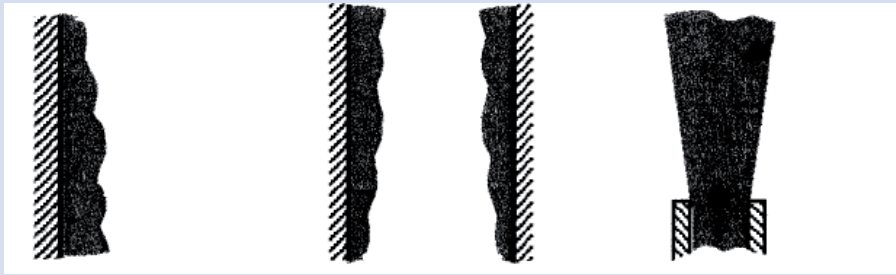


Figure B1 - 01 - Separated two-phase flows: film flow, annular flow and jet flow

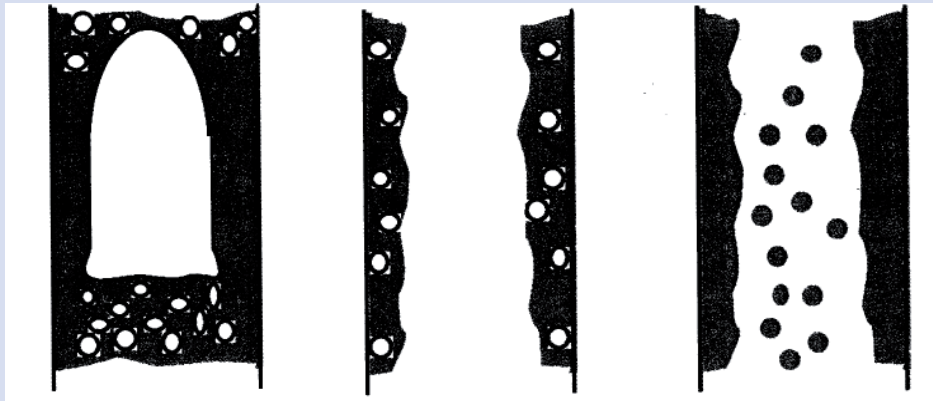


Figure B1 - 02 - Mixed two-phase flows: slog or plug flow, bubbly annular flow and droplet annular flow

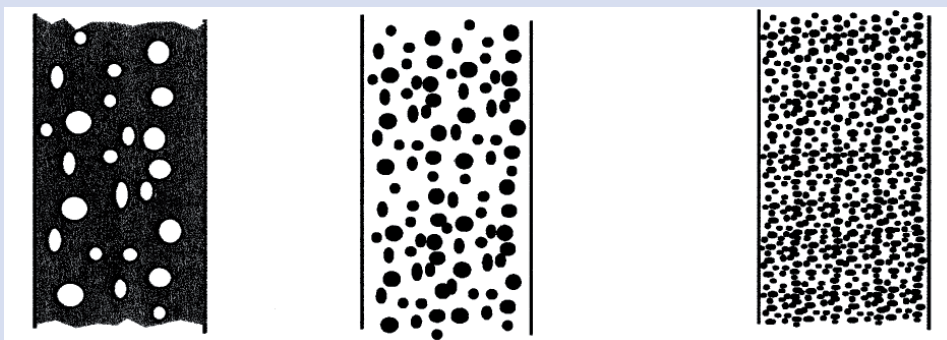


Figure B1 - 03 - Dispersed two-phase flows: bubbly flow, droplet flow and particulate flow

In separated two-phase flows, each phase plays a symmetrical role and the topology of the interface is not assumed. No hypothesis can be proposed for the shape of each phase and we cannot neglect the volume of one of the phases. There are two approaches for the mathematical description of such flows: either by tracking the interface between both fluids and solving Navier-Stokes equations in each one (Volume Of Fluid [16], Level-Set Methods [37]), or by using an averaging procedure to derive a set of conservation equations describing the two-phase flow as a whole and assuming that each phase may be simultaneously present at any point; in this second approach the smallest scales of the interface are not resolved but modelled, using the averaging procedure. The most well-known of these models is the Baer-Nunziato system of 7 equations [2], [34], but reduced models can also be used, as in [19], [24].

In the case of dispersed flows, one phase is assumed to be dilute (typical values of the volume fraction lie between  $10^{-5}$  and  $10^{-2}$ ) and composed of spherical inclusions (droplets, particles or bubbles) dispersed inside the other phase (called the “carrier phase”). All inclusions are assumed to be very small compared to the macroscopic scale of the system and therefore can be considered as pointwise. Given this assumption the flow around and inside the particles does not have to be computed. The influence of the inclusions on the carrier phase is taken into account with the introduction of source terms in the right hand side of the Navier-Stokes equations.

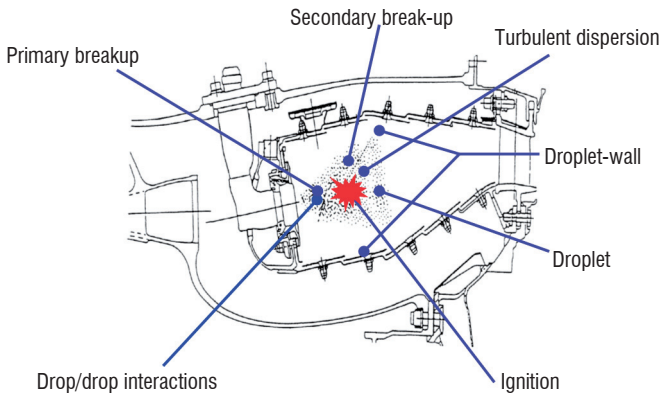


Figure 1 - Main physical phenomena occurring in the combustion chamber of a turbojet engine

In liquid fuel rocket engines, the simulation of the LOX/H<sub>2</sub> cryogenic flame process needs both separated two-phase flow and dispersed two-phase flow descriptions (Figure 2).

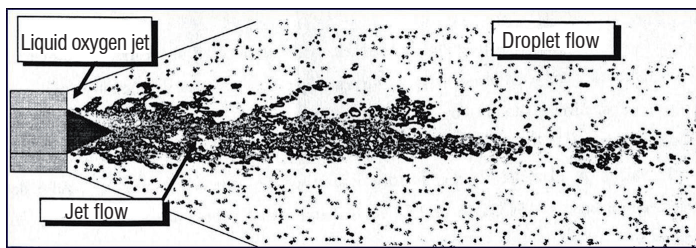


Figure 2 - Schematic representation of the turbulent reactive two-phase flow occurring in liquid fuel rocket engines. Atomization of the liquid oxygen jet, secondary breakup, evaporation and combustion

In solid propellant rockets, aluminum particles are used in order to increase the temperature of the burnt gases in the combustion chamber. When these particles burn, small alumina droplets are produced (from 1  $\mu\text{m}$  to 100  $\mu\text{m}$ ) and convected out of the nozzle in the exhaust gases. Figure 3 represents the 2D-simulation of a small-scale rocket booster (LP6) fired at the Onera-Fauga center.

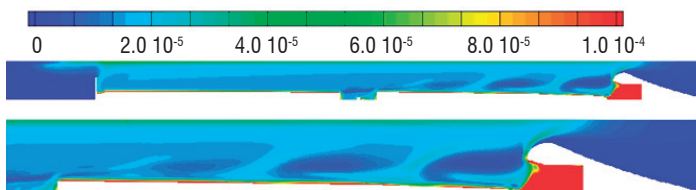


Figure 3 - LP6 solid propellant booster. Alumina droplet volume fraction field. Computation has been performed with CEDRE, using the SPIREE Eulerian solver

Gas-particle flows also play an important role in icing (Figure 4) and water ingestion phenomena (ingestion of hail, ice-crystals and rain drops in turbojet engines). For example ice accretion on aircraft is due to the presence of supercooled water droplets in the air, which may deposit or not on the aircraft surfaces depending on their size and relative velocity. SLD ice is ice formed in Supercooled Large Droplet (SLD) conditions. It is similar to clear ice, but because the droplet size is large it often extends to unprotected parts of the aircraft and forms larger ice shapes, and faster than normal icing.

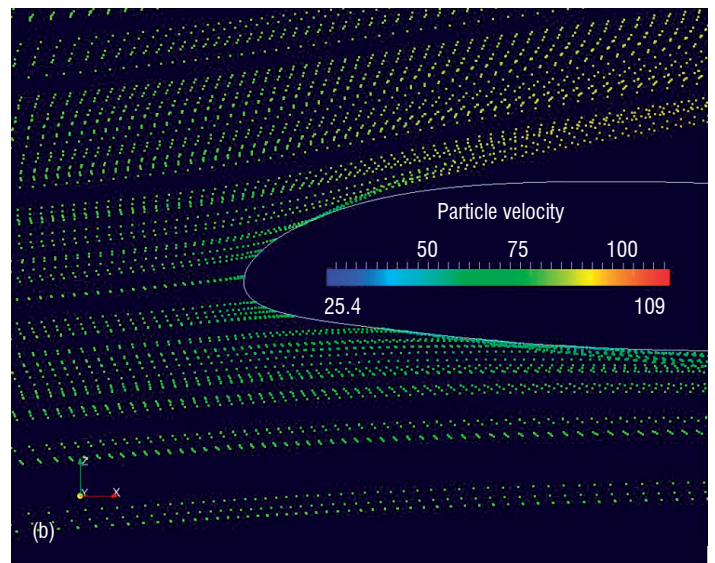
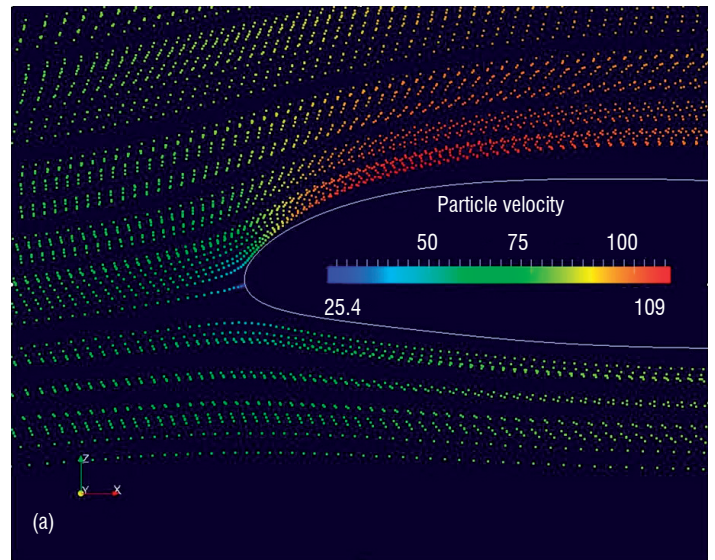


Figure 4 - Super-cooled water droplet trajectories around a NACA23012 airfoil. (a): Droplet diameter = 10.9  $\mu\text{m}$  - (b): Droplet diameter = 70.7  $\mu\text{m}$ . Both computations have been performed with CEDRE, using the SPARTE Lagrangian solver

These examples show the large variety of possible applications even if the paper is limited to dispersed two-phase flows in the aerospace context. In order to perform all these applications, ranging from Icing to Propulsion, detailed physical models as well as efficient and robust numerical methods are required. In the recent past a lot of work has been done, including the development of the CEDRE Multi-Physics Code. So this paper reviews, for dispersed two-phase flows, the physical and numerical methods to be found in the literature, and also those which are implemented in the Onera code. The paper also highlights the new objectives and future challenges we are expecting to tackle.

As regards the description of dispersed two-phase flows, two solvers have been implemented; the first, SPARTE, is based on a Lagrangian formulation while the second, SPIREE, is based on an Eulerian formulation. The drawbacks and advantages of each are discussed briefly in § Numerical methods (Box 2) but the best formulation often depends on the characteristics of the simulation. Our strategy is to use two solvers for the description of the dispersed phase. Our constant objective is to improve all the models and the numerical methods of

both the solvers in order to be able to run more and more complex industrial applications including Large Eddy Simulations (LES), Multi-Velocity Eulerian formulation, moving meshes, etc.

In the future, the major new challenge will be to develop the Multi-phase solver and to realize a coupling with the “dispersed” two-phase flow solvers. The development of a Multiphase solver has been started recently, to describe “separated” and “mixed” two-phase flow, as shown in Box 1. With the strategy of coupling solvers we intend to realize complete simulation of, for example, liquid fuel rocket engines (Figure 2). The Multiphase solver will be used to describe the atomization of the liquid oxygen jet while the secondary break-up, evaporation and combustion will be simulated with SPIREE or SPARTE. The coupling strategy will have to be done very carefully as regards the physical modeling for transition as well as the numerical methods. Note that the main difficulty for spray computation is precisely the numerical simulation of the primary atomization process.

Other challenges are expected to be the coupling of the SPIREE and SPARTE solvers to take the major advantages of each formulation, coupling the same solver used with different physical or numerical methods (as in the RANS-LES computation), coupling SPIREE or SPARTE with the recently developed FILM solver [30] for film-particle interactions etc.

## Gas-particle flow modeling

### Williams “kinetic” equation

The modeling of dispersed two-phase flows is based on a mesoscopic description of the dispersed phase. Particles are assumed to be spherical and fully characterized by a small set of variables: position  $\mathbf{x}$ , radius  $r$  (or more generally a size variable denoted by  $\varphi$ ), velocity  $\mathbf{v}$  and temperature  $\theta$ . In most applications, the particle number density function contains all the necessary information on the dispersed phase. By definition,  $f(t, \mathbf{x}, r, \mathbf{v}, \theta) d\mathbf{x} dr d\mathbf{v} d\theta$  denotes the averaged number of droplets with a size in  $[r, r + dr]$ , a velocity in  $[\mathbf{v}, \mathbf{v} + d\mathbf{v}]$ , a temperature in  $[\theta, \theta + d\theta]$  and located in the volume  $[\mathbf{x}, \mathbf{x} + d\mathbf{x}]$  at time  $t$ .

The following Boltzmann-like equation (introduced by Williams in [40] and [41]) expresses the conservation of the number density function (n.d.f)  $f$  in the phase space:

$$\frac{\partial f}{\partial t} + \nabla_{\mathbf{x}} \cdot (\mathbf{v}f) + \nabla_{\mathbf{v}} \cdot (\mathbf{F}f) + \frac{\partial}{\partial r} (Rf) + \frac{\partial}{\partial \theta} (Hf) = \Gamma + Q \quad (1)$$

In this balance equation (1), the left-hand-side stands for the “transport” of the particles in the phase space ( $\mathbf{F}$ ,  $R$  and  $H$  correspond respectively to the force acting on a particle, the evaporation rate and the heat exchange rate) while  $\Gamma$  and  $Q$  on the right-hand-side stand for the effect of fragmentation and collision phenomena respectively. Note that  $\mathbf{F}$ ,  $R$  and  $H$  depend on the local gas composition, velocity and temperature.

### Modeling of microscale physical phenomena in gas-particle flows

#### Force acting on a particle

In the most general case the total force includes contributions from drag, gravity, lift, added mass effect, pressure gradient and viscous stresses (Basset). In the following equation,  $m = (4/3)\pi r^3 \rho_p$  de-

notes the particle mass,  $\rho$  stands for the fluid density while  $\rho_p$  stands for the particle density. Vector  $\mathbf{u}$  represents the fluid velocity and  $D\mathbf{u}/Dt$  its material derivative along the trajectory.

$$m \frac{d\mathbf{v}}{dt} = \mathbf{F}_D + m\mathbf{g} + \mathbf{F}_L + \rho C_m \frac{\pi d^3}{6} \left( \frac{D\mathbf{u}}{Dt} - \frac{d\mathbf{v}}{dt} \right) - \rho \frac{\pi d^3}{6} \nabla p + \mathbf{F}_B \quad (2)$$

The first term on the right hand side of the equation (2) is the drag force  $\mathbf{F}_D$ . The second term on the right hand side is the gravitational force. The remaining terms in equation (2) correspond to the lift force, added mass effect, pressure gradient term and Basset force. The added mass coefficient  $C_m$  is in general constant, equal to the inviscid approximation:  $C_m = 0.5$  (see for instance [6]). The lift mechanism  $\mathbf{F}_L$  considers the velocity gradient around a particle moving in a non-uniform rotational flow [33]. The pressure gradient term is responsible for the buoyancy force and the Basset term, also called the history term, is due to the combination of viscous forces and particle acceleration with respect to the carrier flow.

Fortunately, including all these forces in the particle motion equation is not really necessary for aerospace applications. Because of the very high density of the particulate phase compared to the fluid phase ( $\rho / \rho_p \approx 10^{-3}$ ), the only external forces to be accounted for are the drag force and the force of gravity. The general expression of the drag force reads:

$$\mathbf{F}_D = \frac{1}{2} \rho C_D \pi r^2 (\mathbf{u} - \mathbf{v}) \|\mathbf{u} - \mathbf{v}\| \quad (3)$$

where  $C_D$  is the drag coefficient depending on the particle radius as well as on the characteristic of the fluid flow around the particle. The dynamic relaxation time is written  $\tau_v = (8\rho_p r) / (3C_D \rho \|\mathbf{u} - \mathbf{v}\|)$ . This velocity response time represents the time required for a particle to respond to a change in the fluid velocity.

#### Evaporation phenomena and heat transfer

A large variety of models are available for the description of mass and heat transfer between the particles and the gas. The simplest one is based on the  $d^2$  law [36]. In this model the droplet temperature is assumed to be constant and droplet heating is neglected. A linear regression in time for the droplet surface is then obtained. At the other extreme, much more complex models, taking into account the change in temperature profile inside the droplet, give a very accurate description of the evolution of the droplet surface temperature.

A classic intermediate model, resolving droplet heating but still not resolving internal conduction, is the infinite conductivity model. The droplet temperature is assumed to be uniform but varies with time. Such a model can be found in [1]. This evaporation model is used in the SPIREE and SPARTE solvers. The variation of the droplet surface  $\varphi = S$  obeys:

$$\dot{S} = \frac{dS}{dt} = -4\pi \frac{Sh^* \langle \rho D \rangle}{\rho_p} \ln[1 + B_M] \quad B_M = \frac{Y_s - Y_\infty}{1 - Y_s} \quad (4)$$

This expression of  $dS/dt$  is derived from the mass conservation equations for the vapor and the gas mixture under the assumption that the gas-flow around the droplet is stationary. The parameter  $B_M$  stands for the Spalding dimensionless mass transfer number. To take into account the effect of the convective transport on vaporization due to the droplet motion relative to the gas it is the so-called “film theory” that is used and the convective Sherwood number  $Sh$  is introduced. This number has to be modified ( $Sh^* = 2 + (Sh - 2) / F_M(B_M)$ ) to take

the presence of the Stefan flow into account. Note that the subscripts  $_{s,\infty}$  refer to the conditions at the droplet surface and at infinity from the droplet surface, e.g. in the external gas flow, and  $\langle \cdot \rangle$  represents an averaged value between conditions  $_{s,\infty}$ .  $D, Y$  stand, respectively, for the binary diffusion coefficient and the vapor mass fraction in the gas.

Then, if we examine the energy conservation equation, we can deduce the evolution for  $H$  which corresponds to the heat flux entering the droplet. The equation is written:

$$mc_p H = mc_p \frac{d\theta}{dt} = \lambda \pi 2r Nu^* (T - \theta) + L_v(T_s) \dot{m} \quad (5)$$

In this last equation (5), a part of the flux  $L_v(T_s) \dot{m}$  serves for vaporization. Note that  $L_v(T_s)$  represents the latent heat of vaporization at temperature  $T_s$  and  $\dot{m} = -(\rho_p \sqrt{S}) / (4\sqrt{\pi}) \dot{S}$  is the instantaneous vaporization rate. The other part  $\lambda \pi 2r Nu^* (T - \theta)$  in equation (5) serves for heating-up the droplet. Note that only the convective heat transfer (or thermal conduction) is considered around the particle. As a consequence, the expression for heat exchange between particle and fluid is given by a conductive flux possibly modified by convective effects where we have introduced  $Nu^*$  for the convective Nusselt number.

### Droplet secondary break-up

Secondary break-up is the name given to the fragmentation of a droplet under the action of the pressure and shear forces exerted by the gas on the droplet surface. This phenomenon can only occur if the relative velocity between the gas and the droplet is greater than a critical value. In dimensionless form, this threshold condition can be written:  $We > We_c$ , where  $We$  denotes the Weber number (defined below) and  $We_c$  its critical value ( $We_c \approx 12$ ). As shown in Figure 5, secondary break-up is a very complex multi-scale phenomenon which cannot be modeled in detail but rather from a statistical point of view and using experimental results.

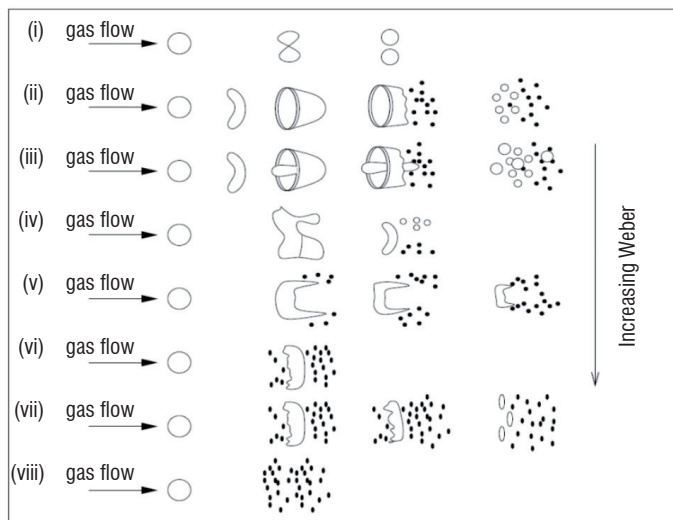


Figure 5 - Secondary break-up regimes depending on the value of the Weber number

The general form of the fragmentation (or secondary break-up) term of (1) reads as follows:

$$\Gamma(f)(\mathbf{v}, r) = -\nu_{bup}(\mathbf{v}, r) f(\mathbf{v}, r) + \int_{\mathbf{R}^+} \int_{\mathbf{R}^3} \nu_{bup}(\mathbf{v}^*, r^*) h_{bup}(\mathbf{v}, r, \mathbf{v}^*, r^*) f(\mathbf{v}^*, r^*) d\mathbf{v}^* dr^* \quad (6)$$

where  $\nu_{bup}(\mathbf{v}, r)$  denotes the breakup frequency. In SPARTE (see § Numerical Methods and Applications of the present paper) it is given by the following model, with  $\sigma$  denoting the surface tension coefficient and  $\tau_{bup}$  corresponding to the average break-up time:

$$\nu_{bup}(\mathbf{v}, r) = \begin{cases} 0 & \text{if } We \leq We_c \\ \frac{1}{\tau_{bup}(\mathbf{v}, r)} \approx \frac{1}{5} \sqrt{\frac{\rho_g}{\rho_p}} \frac{\|\mathbf{v} - \mathbf{U}_g\|}{2r} & \text{if } We > We_c \end{cases} \quad (7)$$

$$\text{where: } We = \frac{2r \rho_g \|\mathbf{v} - \mathbf{U}_g\|}{\sigma}$$

We refer to [17] for the expression of the function  $h_{bup}$  which represents the p.d.f. (probability density function) of the droplets produced by the fragmentation of a given droplet of radius  $r^*$  and velocity  $\mathbf{v}^*$ .

### Collision

Collisions occur if the dispersed phase is dense enough and if the relative velocity between particles is not too small. In the case of solid particles, collisions can only modify particle velocities but in the case of droplets both size and velocity may change and the outcome of a collision is much more complex: several regimes can be observed as depicted in Figure 6.

Collision modeling is very complex for both solid and liquid particles. A large number of studies have been devoted to this topic during the three last decades and it is not possible to summarize them all in this introductory paper. We refer for example to the work of Rabe [29] for droplet collision and Février [12] for the case of solid particles.

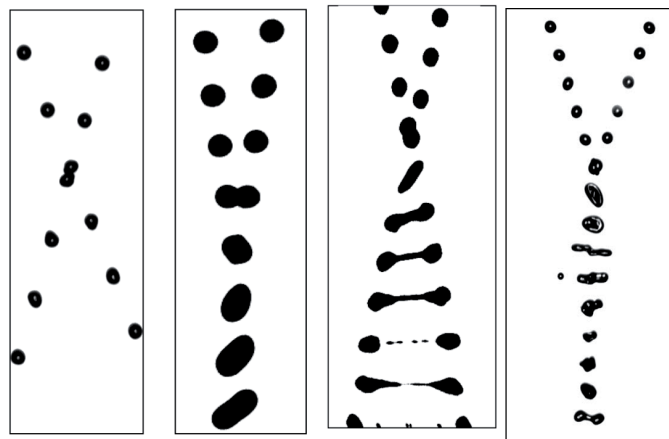


Figure 6 - Droplet collision regimes. From left to right: bouncing, coalescence, stretching separation, reflexive separation

Here, for the sake of completeness, we only give the general form of the collision term which can be used to take droplet coalescence into account:

$$Q(f)(\mathbf{v}, r) = - \int_{\mathbf{R}^+} \int_{\mathbf{R}^3} \pi(r+r^*)^2 \|\mathbf{v} - \mathbf{v}^*\| E_{coll}(r, r^*, \mathbf{v}, \mathbf{v}^*) E_{coal}(r, r^*, \mathbf{v}, \mathbf{v}^*) f(\mathbf{v}, r) f(\mathbf{v}^*, r^*) d\mathbf{v}^* dr^* + \frac{1}{2} \int_{\mathbf{R}^+} \int_{\mathbf{R}^3} \pi(r^{\%} + r^*)^2 \left[ \frac{r}{r^{\%}} \right]^{11} \|\mathbf{v}^{\%} - \mathbf{v}^*\| E_{coll}(r^{\%}, r^*, \mathbf{v}^{\%}, \mathbf{v}^*) E_{coal}(r^{\%}, r^*, \mathbf{v}^{\%}, \mathbf{v}^*) f(\mathbf{v}^{\%}, r^{\%}) f(\mathbf{v}^*, r^*) d\mathbf{v}^* dr^* \quad (8)$$

with  $E_{coll}$  being the collision efficiency and  $E_{coal}$  the coalescence efficiency [39] and

$$\begin{cases} \bar{r}^3 = (r^{\%})^3 + (r^*)^3 \\ \bar{r}^3 \bar{\mathbf{v}} = (r^{\%})^3 \bar{\mathbf{v}}^{\%} + (r^*)^3 \bar{\mathbf{v}}^* \end{cases} \quad (9)$$

This last equation simply corresponds to the conservation of mass and momentum during the coalescence process.

### Particle – wall interactions

Particle-wall interactions are of major importance for many physical or industrial processes involving gas-particle flows (spray cooling, rain and hail ingestion in turbojet engines, icing, erosion, etc.). The outcome of a particle impact on a solid wall depends on a number of parameters: particle-wall relative velocity, particle diameter, particle temperature, wall temperature, wall roughness, etc., and several interaction regimes can be experimentally observed: bouncing, splashing (or fragmentation) with partial depositing and secondary particle emission, full depositing. The description and the modeling of these complex phenomena is beyond the scope of this article and we refer to [14], amongst others, for more details.

### Fluid models

All fluid models for gas-particle flows are based on conservation equations for some particular moments of the number density function. These models can be formally derived from the kinetic equation (1) by assuming particular closure assumptions.

Let us first introduce the following notations:

$$\begin{aligned} \bar{n}(t, \mathbf{x}, r) &= \iint_{\mathbf{v}, \theta} f(t, \mathbf{x}, r, \mathbf{v}, \theta) d\mathbf{v} d\theta \\ \bar{n} \bar{\rho}(t, \mathbf{x}, r) &= \iint_{\mathbf{v}, \theta} f(t, \mathbf{x}, r, \mathbf{v}, \theta) \rho(\theta) d\mathbf{v} d\theta \\ \bar{n} \bar{\rho}(t, \mathbf{x}, r) \bar{\mathbf{v}}(t, \mathbf{x}, r) &= \iint_{\mathbf{v}, \theta} f(t, \mathbf{x}, r, \mathbf{v}, \theta) \rho(\theta) \mathbf{v} d\mathbf{v} d\theta \\ \bar{n} \bar{\rho}(t, \mathbf{x}, r) \bar{h}(t, \mathbf{x}, r) &= \iint_{\mathbf{v}, \theta} f(t, \mathbf{x}, r, \mathbf{v}, \theta) \rho(\theta) h(\theta) d\mathbf{v} d\theta \end{aligned}$$

where  $h$  stands for the particle enthalpy. Integrating the “kinetic” equation (1) with respect to  $\theta$  and  $\mathbf{v}$ , and using conventional notations, we formally get a system of balance equations of the following form:

$$\begin{cases} \frac{\partial}{\partial t} \bar{n} + \nabla_{\mathbf{x}} \cdot (\bar{n} \bar{\mathbf{v}}) + \frac{\partial}{\partial r} (\bar{n} \bar{R}) = \Gamma^1 + Q^1 \\ \frac{\partial}{\partial t} (\bar{n} \bar{\rho}) + \nabla_{\mathbf{x}} \cdot (\bar{n} \bar{\rho} \bar{\mathbf{v}}) + \frac{\partial}{\partial r} (\bar{n} \bar{\rho} \bar{R}) = \Gamma^2 + Q^2 \\ \frac{\partial}{\partial t} (\bar{n} \bar{\rho} \bar{\mathbf{v}}) + \nabla_{\mathbf{x}} \cdot (\bar{n} \bar{\rho} \bar{\mathbf{v}} \otimes \bar{\mathbf{v}} + P) + \frac{\partial}{\partial r} (\bar{n} \bar{\rho} \bar{R} \bar{\mathbf{v}}) - \bar{n} \bar{\rho} \bar{\mathbf{F}} = \Gamma^3 + Q^3 \\ \frac{\partial}{\partial t} (\bar{n} \bar{\rho} \bar{h}) + \nabla_{\mathbf{x}} \cdot (\bar{n} \bar{\rho} \bar{h} \bar{\mathbf{v}}) + \frac{\partial}{\partial r} (\bar{n} \bar{\rho} \bar{R} \bar{h}) - \bar{n} \bar{\rho} c_p \bar{H} = \Gamma^4 + Q^4 \end{cases} \quad (10)$$

The term  $P$  stands for the second order kinetic stress tensor (equivalent to a generalized pressure tensor). It is due to the dispersion of the droplet velocity distribution function. It reads:

$$P(t, \mathbf{x}, r) = \iint_{\mathbf{v}, \theta} \rho(\theta) (\mathbf{v} - \bar{\mathbf{v}}) \otimes (\mathbf{v} - \bar{\mathbf{v}}) f(t, \mathbf{x}, r, \mathbf{v}, \theta) d\mathbf{v} d\theta \quad (11)$$

In the simplest (and widely used) class of models, this last term is simply neglected which may lead to some anomalous behavior. More complex fluid models can also be used in which  $P$  is not eliminated but deduced from the resolution of additional transport equations for higher order moments of  $f$ . The description of these models is beyond the scope of this paper and we refer the reader to [35], [13], [8], [21] amongst others.

The last step to get a fluid model for the particulate phase consists in eliminating the size variable  $r$  and several options are possible. The first option leads to a two-fluid model which can be derived from the kinetic equation (1) if we proceed to an integration over the whole phase space. The information on size dispersion is lost in this derivation. The two-fluid model consists in solving an averaged description of the spray. As a consequence, the polydispersed characteristic of the spray cannot be taken into account and this limitation is a real drawback.

A second option is the sampling method in which the presumed n.d.f (number density function) is written under a sum of Dirac mass with respect to the size variable as depicted on the left hand side of Figure 7. The system for each sample is derived from the kinetic equation with the same assumptions as for the two-fluid model. The sampling method thus leads to  $N$  systems similar to system (10). As a consequence there is no interaction terms between particles of different sizes and complex phenomena such as coalescence or secondary break-up are difficult to handle in this framework. On the other hand, sampling models are very easy to implement.

Finally, the last option, often called the “multi-fluid” model or sectional model (see for instance [20], [10]), is illustrated on the right hand side of Figure 7. It has been introduced in [15]. Information on the droplet size distribution is kept at the macroscopic level thanks to a finite volume discretization with respect to the size variable. A set of equations is derived for each section and, in this type of model, sections are coupled thanks to mass, momentum and heat fluxes due to the finite volume approximation. More complex phenomena such as coalescence and fragmentation can also be easily included. The choice between first or second order is a compromise between precision of the phenomena description and the cost of the algorithms. The work presented in [9] provides some conclusions for the optimization in solid propellant combustion.

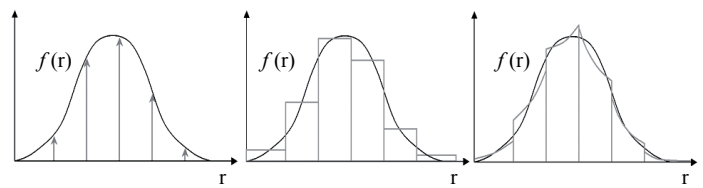


Figure 7 - Discretization of the droplet size distribution function in the sampling method (left), in the first order sectional approach (middle) and the second order sectional approach (right)

## Numerical Methods

### Introduction

The most direct numerical approach would consist in tracking all the particles present in the flow and to compute their changes individually. In such a method, each numerical particle would represent a given physical particle (or droplet). In the following, we shall refer to this method as the Discrete Particle Simulation method (DPS). For industrial applications,

this method cannot be applied because of the excessively large number of particles per unit volume and other approaches have to be used, which are based either on the discretization of the kinetic equation (1) or on the discretization of conservation equations derived from the kinetic equation. Three classes of methods may be used.

The first is the class of the so called “full spray equation methods”. These methods solve equation (1) directly by applying a finite volume or a finite difference method. But for realistic configurations, these methods are prohibited because of the high dimension number of the phase space (at least 8 in 3D).

The second is the class of Particle Methods or more generally Stochastic Particle Methods, which are also often called Lagrangian methods or Stochastic parcel methods [32]. From a physical point of view, they can be seen as a coarser version of the Discrete Particle Simulation method in which each “numerical particle” represents more than one physical particle. From a mathematical point of view, this class of methods can be interpreted as numerical methods for the direct resolution of the kinetic equation. These methods are described in section “Lagrangian methods”.

The last class of method represents all numerical methods based on “fluid models” (set of conservation equations) derived from the kinetic equation. These methods generally based on a finite volume framework are often called Eulerian methods and are described in section “Eulerian methods”.

### Lagrangian methods

Particle methods (or stochastic particle methods) are commonly used for the calculation of polydisperse sprays in various application fields (see for example [28], [11], [32] and the references therein). A complete exposition of the derivation and the implementation of such a method is beyond of the scope of this paper. We refer, for example, to [17] or for details. Here, for the sake of completeness, we present the only main features of such a numerical method.

A particle method can be interpreted as a discretization method for the kinetic equation (1). The distribution function  $f$  at time  $t$  is approximated by a weighted sum of Dirac masses,  $f_N(t)$ , which reads:

$$f_N(t) = \sum_{i=1 \dots N} w_i(t) \delta_{\mathbf{x}-\mathbf{x}_i(t)} \otimes \delta_{\mathbf{v}-\mathbf{v}_i(t)} \otimes \delta_{r-r_i(t)} \otimes \delta_{\theta-\theta_i(t)} \quad (12)$$

Each weighted Dirac mass is generally called a “parcel” or “numerical particle” and can be physically interpreted as an aggregated number of real particles (or droplets, according to the context) located around the same point  $\mathbf{x}_i$ , with the same velocity  $\mathbf{v}_i$ , the same radius  $r_i$  and the same temperature  $\theta_i$ . The weight  $w_i$  can be interpreted as the number of real particles associated with parcel  $i$  and  $N$  denotes the total number of parcels used in the computation.

Each time step of the numerical procedure is divided into 3 stages. The first one is devoted to the discretization of the l.h.s. of the kinetic Equation (1), modeling motion, heating and evaporation of the particles. The last two stages of a time step are devoted to the discretization of the collision and fragmentation operators.

### Transport step

Several numerical schemes can be used according to the desired accuracy and numerical stability constraint. In SPARTE, the new position, velocity, temperature and radius of each numerical particle are calculated according to the following scheme:

$$\left\{ \begin{array}{l} \mathbf{x}_i^{n+1} = \mathbf{x}_i^n + \mathbf{U}_g(t^n, \mathbf{x}_i^n) \Delta t \\ \quad + \left[ \mathbf{v}_i^n - \mathbf{U}_g(t^n, \mathbf{x}_i^n) \right] (1 - \alpha_i^n) \tau_p^n \\ \quad + \left[ \Delta t - (1 - \alpha_i^n) \tau_p^n \right] \tau_p^n \mathbf{g} \\ \mathbf{v}_i^{n+1} = \mathbf{U}_g(t^n, \mathbf{x}_i^n) + \alpha_i^n \left[ \mathbf{v}_i^n - \mathbf{U}_g(t^n, \mathbf{x}_i^n) \right] \\ \quad + (1 - \alpha_i^n) \tau_p^n \mathbf{g} \\ \theta_i^{n+1} = (T^*)_i^n + \beta_i^n \left[ \theta_i^n - (T^*)_i^n \right] \\ r_i^{n+1} = \left[ \frac{\rho_p(\theta_i^n)}{\rho_p(\theta_i^{n+1})} \right]^{1/3} \\ \quad \times \sqrt{\max \left[ (r_i^n)^2 - \Delta t K_{ev}(r_i^n, \theta_i^n, \mathbf{x}_i^n, \mathbf{v}_i^n), 0 \right]} \end{array} \right. \quad (13)$$

where  $\tau_p$  denotes the particle dynamical response time,  $\tau_c$  the heat exchange response time (derived from equation (5)),  $T^*$  stands for the equilibrium temperature (depending on the gas temperature and the saturation temperature according to equation (5)) and  $\mathbf{U}_g(t^n, \mathbf{x}_i^n)$  stands for the gas velocity at the particle location and:

$$\alpha_i^n = \exp\left(-\frac{\Delta t}{\tau_p}\right) \quad \beta_i^n = \exp\left(-\frac{\Delta t}{\tau_c}\right) \quad (14)$$

This is an unconditionally stable first order scheme. Higher order explicit schemes (like Runge-Kutta schemes) can also be used but they are only conditionally stable and their stability condition is very constraining for small particles (because  $\tau_p$  and  $\tau_c \rightarrow 0$ ).

It is worth mentioning that particle-wall interactions are also taken into account during the transport step. Monte-Carlo algorithms are generally used to treat complex phenomena like splashing or bouncing on a rough wall to avoid the creation of a lot of new numerical particles.

### Collision step

Several Monte-Carlo algorithms have been proposed in the literature for the treatment of droplet (or solid particle) collisions. They are inspired by methods used in molecular gas dynamics. They suppose that the computational domain is divided into cells, or control volumes, which are small enough to assume that the droplet distribution function is almost uniform over them. The algorithm used in SPARTE [17],[20] is close to the one proposed by O'Rourke [28]. In the case of droplets, it consists of the following three steps:

- i) For each computational cell  $C_j$ , containing  $N_j$  parcels randomly choose  $N_j/2$  pairs of parcels ( $(N_j-1)/2$  if  $N_j$  is odd);
- ii) For each pair  $p$ , let  $p_1$  and  $p_2$  denote the two corresponding parcels with the convention  $w_1 \geq w_2$ , where  $w_1$  and  $w_2$  denote the parcel weights; then for each pair  $p$ , randomly choose an integer  $\nu_p$  according to the Poisson distribution law:

$$P(v) = \frac{\lambda_{12}^v}{v!} \exp(-\lambda_{12}) \text{ with:}$$

$$\lambda_{12} = \pi E_{coll} E_{coal} \frac{w_1(N_j - 1)\Delta t}{vol(C_j)} (r_1 + r_2)^2 \|\mathbf{v}_1 - \mathbf{v}_2\|$$

with  $vol(C_j)$  being the volume of cell  $C_j$ ,  $E_{coll}$  the collision efficiency,  $E_{coal}$  the probability of coalescence given that the collision has occurred and  $r_1, r_2$  being the radii of parcels  $p_1, p_2$ .  $\lambda_{12}$  represents the average number of coalescences during  $(N_j - 1)$  time steps between a given droplet of parcel  $p_2$  and any droplet of parcel  $p_1$ ; this is in accordance with the fact that a given pair of parcels is chosen on average every  $(N_j - 1)$  time steps.

iii) If  $v_p = 0$ , no coalescence occurs during this time step between the parcels  $p_1$  and  $p_2$ . Otherwise, if  $v_p > 0$ , parcel  $p^1$  undergoes  $v_p$  coalescences with parcel  $p^2$  and the outcome of the collision is treated as follows: first the weight  $w_1$  of parcel  $p_1$  is replaced by  $w_1' = w_1 - v_p w_2$  and its other characteristics are left unchanged. If  $w_1' < 0$  then parcel  $p_1$  is removed from the calculation; secondly, the velocity  $v_2$  and radius  $r_2$  of parcel  $p_2$  are updated according to:

$$r_2' = (r_2^3 + v_p r_1^3)^{1/3} \quad \mathbf{v}_2' = \frac{r_2^3 \mathbf{v}_2 + v_p r_1^3 \mathbf{v}_1}{r_2^3 + v_p r_1^3}$$

and its weight  $w_2'$  is left unchanged.

### Remarks

- This algorithm allows us to take into account several collisions between two given parcels during the same time step; this is an important feature to avoid a very restrictive condition on the time step. Nevertheless, to maintain good accuracy the time step  $\Delta t$  must be chosen small enough to ensure that the average number of collisions between two given parcels,  $p_1$  and  $p_2$ , is such that:  $v_p w_2 < w_1$ .
- Other collision regimes (stretching or reflexive separation, bouncing, etc.) can also be taken into account by slightly modifying this algorithm.

### Fragmentation step (only for droplets)

Monte-Carlo algorithms must also be used during this stage to avoid the creation of too many new numerical particles. The algorithm used in SPARTE reads as follows:

i) For each numerical particle in the computational domain, compute the Weber number defined as:

$$We_i^n = \frac{2\rho_g(t^n, \mathbf{x}_i^n) \|\mathbf{v}_i^n - \mathbf{U}_g(t^n, \mathbf{x}_i^n)\|^2 r_i^n}{\sigma}$$

ii) If  $We_i^n > We^*$  (critical Weber number), then compute the particle fragmentation probability during the current time step:

$$\pi_i = 1 - \exp\left(-\frac{\Delta t}{\tau_i^{bup}}\right)$$

where  $\tau_i^{bup}$  denotes the average break-up time of the particle.

iii) Choose a random number  $\alpha$  between 0 and 1; if  $\alpha < \pi_i$  then fragmentation of the  $i$ th particle is considered to occur during the current time step and new numerical particles are created. The radius

of each new particle is randomly chosen according to the model used for the p.d.f.  $h_{bup}$  of the resulting droplets. The number of "child" numerical particles is usually chosen between 1 and 5 to ensure a good compromise between accuracy and computational cost.

### Additional remarks

- For dilute stationary two-phase flows, a variant of the particle method described above can be used. It is based on the following approximation of the stationary droplet density function:

$$f_N(\mathbf{x}, \mathbf{v}, r, \theta) = \sum_{i=1 \dots N} \int_0^T [\dot{w}_i(t) \delta_{\mathbf{x}-\mathbf{x}_i(t)} \otimes \delta_{\mathbf{v}-\mathbf{v}_i(t)} \otimes \delta_{r-r_i(t)} \otimes \delta_{\theta-\theta_i(t)}] dt \quad (15)$$

where T stands for the maximum residence time of a particle in the system and where  $\dot{w}_i$  stands for the number of particles carried along the  $i$ th numerical trajectory per unit time (particle number flow rate). From a practical point of view, calculating a macroscopic property of the dispersed phase in a given cell  $C$  of the mesh consists in computing an average over all the numerical particles pondered by their residence time in the cell  $C$ . Particle collisions cannot be taken into account but transport and fragmentation steps are treated in exactly the same way as for the unsteady particle method.

- For dense two-phase flows or combustion phenomena, influence of the dispersed phase on the gas flow has to be accounted for. Within the framework of the Lagrangian approach, source terms are easily calculated by summing the contribution of each numerical particle. An under-relaxation procedure can be applied (as in SPARTE for example) to avoid numerical instabilities when the coupling between both phases is strong and the time step between two successive exchanges is too large.

### Eulerian methods

Given the conservation form of the equations, the finite volume method is the most natural candidate for discretization of fluid models but finite difference or finite element methods could also be used. In this article we focus on the finite volume scheme implemented into the SPIREE solver, included in CEDRE. Let  $\mathbf{q}$  be the set of conservative variables. It can be a set of only 4 variables in the case of the 1D two-fluid model or a set of 6N variables in the case of the 3D polydisperse spray model with a sampling method or a sectional method (with N being the number of classes or sections). In terms of conservative variables  $\mathbf{q} = (n, \rho, \rho\mathbf{v}, \rho e)$  for each class (sampling method) or section (sectional approach), and the system of equations can be formally written:

$$\begin{cases} \frac{\partial n}{\partial t} + \text{div}(n\mathbf{v}) = S^1 \\ \frac{\partial \rho}{\partial t} + \text{div}(\rho\mathbf{v}) = S^2 \\ \frac{\partial \rho\mathbf{v}}{\partial t} + \text{div}(\rho\mathbf{v} \otimes \mathbf{v}) = S^3 \\ \frac{\partial \rho e}{\partial t} + \text{div}(\rho e\mathbf{v}) = S^4 \end{cases} \quad (16)$$

A class or a section of droplets is defined by its density  $\rho_0$  which depends on the temperature, by its diameter  $d = 2r$ , by a unique velocity  $\mathbf{v}$  and by the specific total energy  $e = \varepsilon + \|\mathbf{u}\|^2 / 2$  where the internal energy is given by  $\varepsilon = \varepsilon_{ref} + c_p(T)[T - T_{ref}]$ . An important parameter of the flow is the volume fraction  $\alpha$  which can be linked to the other variables by  $\alpha = n\pi d^3 / 6$  or  $\rho = \alpha\rho_0$ . Denoting by  $\mathbf{q}_i^n, \mathbf{q}_j^n$

the vector of the conservative variables in cells  $i, j$  of the mesh and using conventional notations, the general form of a linearized implicit finite volume scheme reads:

$$\left\{ \begin{array}{l} V_i \frac{\mathbf{q}_i^{n+1} - \mathbf{q}_i^n}{\Delta t} = \\ - \sum_{j \in v(i)} A_{ij} \left[ \begin{array}{l} \psi(\mathbf{q}_i^n, \mathbf{q}_j^n) + \frac{\partial \psi(\mathbf{q}_i, \mathbf{q}_j)}{\partial \mathbf{q}_i} (\mathbf{q}_i^n, \mathbf{q}_j^n) (\mathbf{q}_i^{n+1} - \mathbf{q}_i^n) \\ + \frac{\partial \psi(\mathbf{q}_i, \mathbf{q}_j)}{\partial \mathbf{q}_j} (\mathbf{q}_i^n, \mathbf{q}_j^n) (\mathbf{q}_j^{n+1} - \mathbf{q}_j^n) \end{array} \right] \\ + V_i \left[ \mathbf{S}(\mathbf{q}_i^n) + \frac{\partial \mathbf{S}(\mathbf{q}_i)}{\partial \mathbf{q}_i} (\mathbf{q}_i^n) (\mathbf{q}_i^{n+1} - \mathbf{q}_i^n) \right] \end{array} \right. \quad (17)$$

In this formula,  $\psi(\mathbf{q}_i^n, \mathbf{q}_j^n)$  stands for the numerical flux at the interface between left and right states  $\mathbf{q}_i^n, \mathbf{q}_j^n$  while  $\mathbf{S}(\mathbf{q}_i^n)$  stands for the source terms due to the effect of drag force, mass and heat exchanges as well as particle interaction terms in the control volume  $V_i$ .

An inherent difficulty of Eulerian methods is the construction of the numerical flux  $\psi(\mathbf{q}_i^n, \mathbf{q}_j^n)$ . In the context of the generalized unstructured meshes used in CEDRE we have selected upwind schemes for numerical stability reasons. However, the convective part of the system is only weakly hyperbolic and we need special schemes rather than the conventional schemes used for Navier-Stokes equations. The numerical flux used in SPIREE reads:

$$\psi(\mathbf{q}_i, \mathbf{q}_j) = \frac{1}{2}(\mathbf{F}_i + \mathbf{F}_j) + \frac{1}{2} \left| \langle \mathbf{u} \cdot \mathbf{n} \rangle_{ij} \right| (\mathbf{q}_i - \mathbf{q}_j) \quad (18)$$

The corresponding expressions for the Jacobian matrices used in the above implicit scheme read:

$$\left\{ \begin{array}{l} \frac{\partial \psi(\mathbf{q}_i, \mathbf{q}_j)}{\partial \mathbf{q}_i} = \frac{1}{2} \left( \langle \mathbf{u} \cdot \mathbf{n} \rangle_i + \left| \langle \mathbf{u} \cdot \mathbf{n} \rangle_{ij} \right| \right) \mathbf{I} \\ \frac{\partial \psi(\mathbf{q}_i, \mathbf{q}_j)}{\partial \mathbf{q}_j} = \frac{1}{2} \left( \langle \mathbf{u} \cdot \mathbf{n} \rangle_j - \left| \langle \mathbf{u} \cdot \mathbf{n} \rangle_{ij} \right| \right) \mathbf{I} \end{array} \right. \quad (19)$$

where  $\mathbf{I}$  stands for the identity matrix,  $\langle \mathbf{u} \cdot \mathbf{n} \rangle_i, \langle \mathbf{u} \cdot \mathbf{n} \rangle_j$  are respectively the left and right normal velocities and denotes  $\langle \mathbf{u} \cdot \mathbf{n} \rangle_{ij}$  the arithmetic averaged normal velocity at the interface. Another scheme implemented into the SPIREE solver is a Godunov type scheme which is written:

$$\psi(\mathbf{q}_i, \mathbf{q}_j) = \frac{1}{2}(\mathbf{F}_i + \mathbf{F}_j) + \frac{1}{2} \left( \left| \langle \mathbf{u} \cdot \mathbf{n} \rangle_i \right| \mathbf{q}_i - \left| \langle \mathbf{u} \cdot \mathbf{n} \rangle_j \right| \mathbf{q}_j \right) \quad (20)$$

This last scheme is based on the resolution of the Riemann problem (see [7] for example) for the convective part of the particles system. To bypass the difficulty of delta-shocks, which can occur in such a system, other very efficient schemes can be used such as kinetic schemes [3] derived from the pressureless system of gas dynamics. Note that if we consider the special case of the delta-shocks in the Riemann problem (see for example [22]), the Godunov and kinetic type schemes are very similar.

To increase the order of accuracy of the scheme, we can change, in the definition of the numerical flux, the interface values  $\mathbf{q}_i, \mathbf{q}_j$  by linearly reconstructed states according to a MUSCL (Monotonic Upwind Scheme for Conservation Laws) [38] procedure. Note that in SPIREE we choose to directly reconstruct the conservative variables

$$\mathbf{q}_{ij} = \mathbf{q}_i + \frac{1}{2}(\nabla q)_{ij} \cdot \mathbf{i} \mathbf{j} \quad \text{and} \quad \mathbf{q}_{ji} = \mathbf{q}_j - \frac{1}{2}(\nabla q)_{ji} \cdot \mathbf{i} \mathbf{j}$$

The approximate gradients  $(\nabla q)_{ij}, (\nabla q)_{ji}$  are obtained using a combination of centered and fully upwind gradients. The scheme described above is not monotone. It can create extrema and unphysical solutions. To reduce oscillations in the solution, a slope limiting procedure is used. Time integration is based on both implicit and explicit Runge-Kutta type schemes.

## Applications

In this part, we present a few numerical examples involving dispersed two-phase flows in the aerospace context. All simulations have been performed with CEDRE code using either its Lagrangian or Eulerian solver (SPARTE or SPIREE respectively). SPARTE and SPIREE are based on the models and numerical methods described above in sections 2 and 3. The detailed content of each solver in terms of available models and boundary conditions can be found in the specific paper devoted to CEDRE [30].

For icing applications, a Eulerian computation is presented in this section but it should be noted that a Lagrangian has also been suggested in the introduction for icing applications. In fact, if the droplets are large or if we need to compute very complex physical phenomena

### Box 2 - Comparison of Eulerian and Lagrangian methods

This work has looked at a large variety of models as well as numerical methods. The choice for a model associated with a numerical method is a very difficult task which depends on the application.

As far as models are concerned, the sampling method is very closely associated with the complex description of heat and mass transfer but does not allow the computation of interaction terms. The sectional approach is more complex than the sampling method but gives a better description of the size dispersion of the spray. Moreover, the sectional approach allows the computation of thick spray with the possibility of dealing with interactions (coalescence - fragmentation). A common difficulty for both sampling and sectional methods is the "mono-kinetic" hypothesis which makes the treatment of cross trajectories impossible. Some solutions exist and need to be implemented in the code.

As regards numerical methods, Lagrangian methods seem very efficient and suitable for a good level of modelling. But Lagrangian methods can induce a very high cost of computation, e.g. unsteady cases. Eulerian methods seem more suitable for parallel computations and implicit algorithms but raise the problem of numerical diffusion, while the Lagrangian method means we have the difficulty of the coupling with a Eulerian resolution of the gas dynamics.

as wall-particles interactions, then the Lagrangian approach is very useful. But, if we want to try a 3D computation on an aircraft, the Eulerian approach is better. Note that a coupling of the two methods could be of great interest.

Concerning liquid propulsion and the MASCOTTE facility, the Lagrangian method has been used because we don't compute the primary atomization and the particles are directly injected into the volume according to experimental data. The life time of the particles is very short because of evaporation and the 3D computation is less costly. The Eulerian method could also have been used by changing the domain and having a new limit for fluxes particles injection. On the other hand, with the introduction of the multiphase solver in the code, we expect to be able to realize a fully 3D Eulerian of the MASCOTTE facility by coupling SPIREE with the new solver in order to obtain the size distribution of the spray by computing primary atomization.

Concerning solid propulsion, mentioned in the introduction, the surface injection of propegrgol is very large and the number of particles due to the combustion is very high. A Lagrangian computation would have been much more expensive than the Eulerian one so SPIREE has been chosen. Nevertheless, due to the high number of particles, interaction phenomena have to be taken into account, so the sophisticated sectional approach has to be used in this case if we want a precise simulation.

### Icing applications

The experimental facility used is the PAG (Petit Anneau Givrant) located at CEPr (Centre d'Essais des Propulseurs). The model represents a three-dimensional helicopter air inlet and for this the entire wind tunnel section was modified as illustrated in Figure 8. The arrow symbolizes the air flow path, the up-stream section is a 20 cm square and the height of the removable wall is 10 cm in order to reach the maximum air velocity of 75 m.s<sup>-1</sup> in this configuration. Two main impact zones have been characterized: the front quarter of the cylinder, instrumented with heater mats and temperature sensors, and the removable wall on the left hand side (Figure 8).

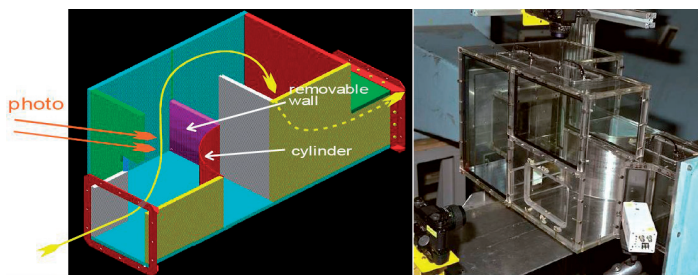


Figure 8 - Schematic representation view of the 3D duct

The Eulerian solver SPIREE is used as transport droplet module in the ONICE3D [23] Icing code developed at Onera. The problematic of degradation of performance in icing prediction is important and here we present one of the applications used to validate the Eulerian solver in the droplet capture process. Figure 9 (a) shows the numerical distribution of the water collection coefficient in the duct while in Figure 9 (b) we see the ice accreted on the cylinder in low temperature conditions (i.e. 243 K). Indeed, in low temperature cases, the droplets impinge and freeze immediately. So, the ice deposit is directly related to the water collection coefficient. The comparison shows a good agreement between experimental results and numerical simulations.

These types of Icing problem simulations using SPIREE use the same strategy as in [5], [4], [42].

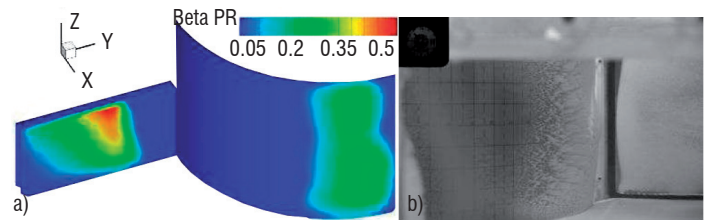


Figure 9 - Comparison between the Eulerian simulation of accretion and experiment

### Liquid propulsion

The problem of high frequency combustion instabilities is a recurrent issue for liquid rocket engine propulsion. The origin of these instabilities is the coupling between acoustic and combustion processes such as atomization, vaporization and mixing. At Onera we are concentrating our efforts on the coupling between acoustics and vaporization. In order to study this difficult problem we have proceeded step by step, performing more and more complex simulations. For each step, the numerical results were compared to theoretical data or analytical solution. The first step was to study acoustic damping in a closed 1D cavity or equipped with a nozzle. We used the Eulerian solver for the second step simulation. This second step deals with the interaction between an acoustic wave and a suspension of inert particles in a closed 1D cavity. An exact solution of the problem can be computed in such a configuration and we have successfully compared simulation results and the theory on both the shift of the frequency and the damping of the oscillations. Figure 10 gives the change in frequency shift (or the damping) against  $\omega_1 \tau_u$  where  $\omega_1$  is the wave number without particles ( $\omega_1 = \pi / L_{cavity}$ ) and  $\tau_u$  is the Stokes time which is proportional to the square of the particle diameter ( $\tau_u = \rho_l d^2 / 18\mu$ ).

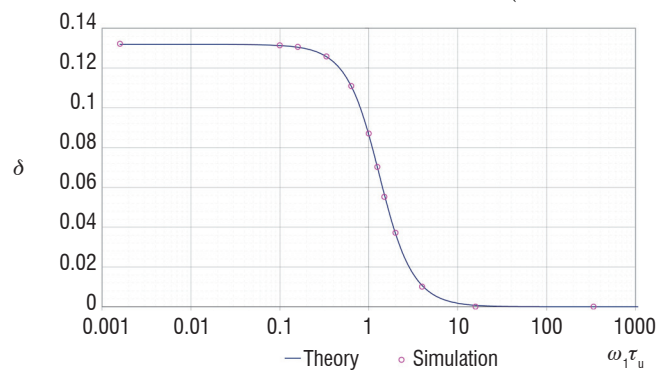


Figure 10 - Frequency shift

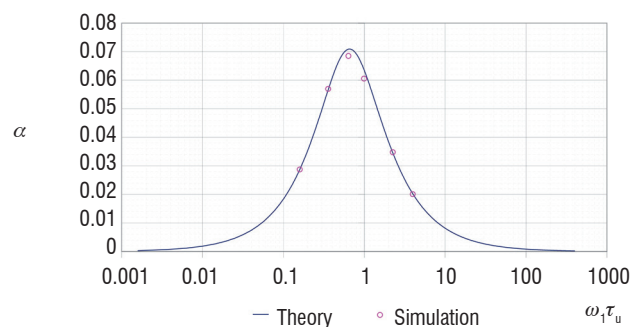


Figure 11 - Damping

Figures 12 and 13 below show another application of CEDRE related to the simulation of cryogenic propulsion. It corresponds to the simulation of an H<sub>2</sub>-O<sub>2</sub> flame in the MASCOTTE facility at Onera Palaiseau. In this case the SPARTE Lagrangian solver has been used for the simulation of the liquid phase. In both calculations, the atomization process has not been simulated and oxygen droplets have been directly injected from a fictitious surface corresponding to the limit of the primary atomization zone. We refer to [25], [26] and [27] for all the details of these computations.

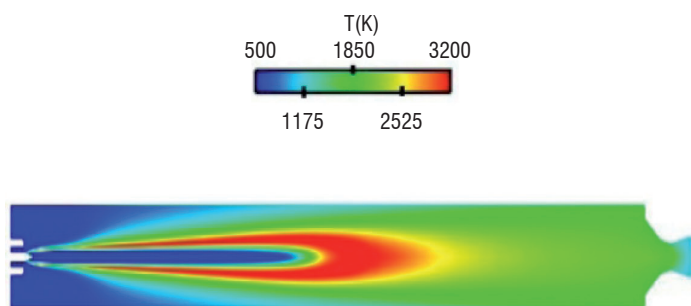


Figure 12 - 2D-RANS simulation of a GH<sub>2</sub>-LO<sub>x</sub> flame in the MASCOTTE Facility at P = 10 Bar – View of the temperature field inside the combustion chamber

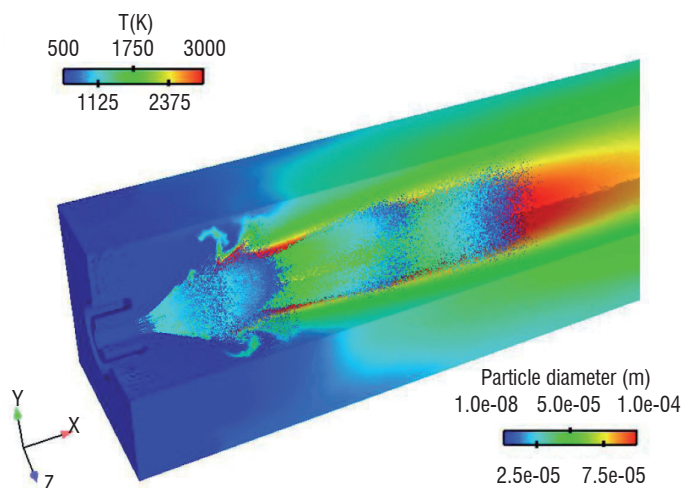


Figure 13 - 3D LES simulation of a GH<sub>2</sub>-LO<sub>x</sub> flame in the MASCOTTE Facility at P = 10 Bar – View of the temperature field and droplet position colored by their diameter

## Conclusion

In this paper, we have given an overview of the models and numerical methods used for the simulation of dispersed two-phase flows. We have emphasized that both Eulerian and Lagrangian approaches can be related to a common underlying kinetic equation corresponding to a mesoscopic level of description.

The Lagrangian procedure treats the kinetic spray equation by solving the motion of a large number of numerical particles (parcels) in space, associated with variables of time, position and droplet velocity, size and temperature or other relevant quantities. The mean spray properties are obtained by averaging over a representative sample of parcels that cross a defined volume in a certain time interval. The main advantage of the Lagrangian procedure lies in its ability to reproduce spray physical behavior with a high degree of precision: a Lagrange computation with small sample volumes, short time intervals and a large number of parcels theoretically allows a detailed prediction of almost all physical phenomena occurring in an unsteady polydisperse spray flow.

However, the computational costs increase with the number of parcels and the problematic issue in the simulation of unsteady spray flows with Euler–Lagrange methods is the optimal choice for the injection frequency of new numerical particles (or the total number of simulated trajectories in the simulation of steady flows). We have to make sure that the numerical results do not depend on this parameter. It was also observed by Riber et al. [31] that the speedup of the Euler–Lagrange method by increasing the number of processors is not ideal because of the parallel load imbalance generated by the partitioning algorithm.

The Eulerian method consists in solving balance equations for various density fields of physical droplet quantities at each position and time. A finite volume discretization is generally applied. This formulation has the advantage of simplicity (the same kind of discrete equations for both phases) and the fact that, irrespective of the amount of droplets in a region, the same number of equations have always to be solved. Hence in Euler–Euler computations a cost is added for the dispersed phase which is independent of the mass loading. In consideration of these issues, we believe that the Eulerian procedure could be a good alternative for spray LES computations, in particular for computations of dense and unsteady particle flows using massively parallelized computers.

For the two last decades, thanks to the improvement of numerical models and the increase in computational power, the numerical simulation of dispersed two-phase flows has reached an advanced level of maturity. Using its two particulate phase solvers, CEDRE offers the possibility of performing such simulations for complex 3D industrial applications. However, several challenges are still to be met. For combustion applications, the main difficulty for spray computation is the numerical simulation of the primary atomization process and its coupling with dispersed flow solvers. Until now, droplets are directly injected at some given points in the computational domain and the droplet size and velocity distributions are chosen according to some experimental data. This procedure requires empirical data which is not always available and it is not appropriate for unsteady simulations (LES or URANS). Another very important problem for industrial applications concerns the modeling of spray – wall or spray – film interactions (icing problems, spray cooling, etc.). Some models are already implemented in SPARTE and SPIREE but they have still to be improved and coupled with the film solver of CEDRE. This work is currently in progress ■

## References

- [1] B. ABRAMZON and W.A. SIRIGNANO - *Droplet Vaporization Model for Spray Combustion Calculations*. International Journal of Heat and Mass Transfer, Vol. 32, n°9, pp. 160-1618 (1989).
- [2] M.R. BAER, J.W. NUNZIATO - *A Two-phase Mixture Theory for the Deflagration-to-Detonation Transition (DDT) in Reactive Granular Materials*. Journal of Multiphase flows, 12, pp. 861-889 (1986).
- [3] F. BOUCHUT, S. JIN and X. LI - *Numerical Approximation of Pressureless and Isothermal Gas Dynamics*. SIAM J. Num. Anal, 41, pp. 135-158 (2003).
- [4] Y. BOURGAULT, Z. BOUTANIOS and W. HABASHI - *Three-Dimensional Eulerian Approach to Droplet Impingement Simulation Using FENSAP-ICE, Part 1 : Model, Algorithm, and Validation*. Journal of Aircraft, Vol. 37, n°1 (2000).
- [5] Y. BOURGAULT, W. HABASHI, J. DOMPIERRE and G. BARUZZI - *A Finite Element Method Study of Eulerian Droplets Impingement Models*. International Journal for Numerical methods in fluids. 29, pp. 4289-449 (1999).
- [6] C.T. CROWE, T.R. TROUTT and J.N. CHUNG - *Multiphase Flows with Droplets and Particles*. CRC Press (1998).
- [7] E. DANIEL, R. SAUREL, M. LARINI and J.C. LORAUD - *A Comparison Between Centered and Upwind Schemes for Two-Phase Compressible Flows*. AIAA n°2346 (1993).
- [8] O. DESJARDINS, R.O. FOX and P. VILLEDIEU - *A Quadrature-Based Moment Method for Dilute Fluid-Particle Flows*. Journal of Computational Physics 227, pp. 2514-2539 (2008).
- [9] F. DOISNEAU, F. LAURENT-NEGRE, A. MURRONE, J. DUPAYS and M. MASSOT - *Optimal Eulerian Model for the Simulation of Dynamics and Coalescence of Alumina Particles in Solid Propellant Combustion*. 7th International Conference on Multiphase Flow (2010).
- [10] G. DUFOUR and P. VILLEDIEU - *A Second Order Multi-Fluid Model for Evaporating Sprays*. M2AN, Vol. 39-5, pp. 931-963 (2005).
- [11] J.K. DUKOWICZ - *A Particle-Fluid Numerical Model for Liquid Sprays*. Journal of Computational Physics, 35, pp. 229-253 (1980).
- [12] P. FEVRIER - *Etude numérique des effets de concentration préférentielle et de corrélation spatiale entre vitesses de particules solides en turbulence homogène isotrope stationnaire*. Ph.D. Thesis, INP-Toulouse (2000).
- [13] P. FEVRIER, O. SIMONIN and K.D. SQUIRES - *Partitioning of Particle Velocities in Gas-Solid Turbulent Flows into a Continuous Field and a Spatially Uncorrelated Random Distribution: Theoretical Formalism and Numerical Study*. J. Fluid Mech. 533, 146 (2005).
- [14] N. GARCIA-ROSA, P. VILLEDIEU, J. DEWITTE and G. LAVERGNE - *A New Droplet-Wall Interaction Model*. 10th International Congress on Liquid Atomization and Spray Systems, ICLASS 2006, KYOTO, 27 August-1 September (2006).
- [15] J.B. GREENBERG, I. SILVERMAN and Y. TAMBOUR - *On the Origins of Spray Sectional Conservation Equations*. Combustion and flame 93, pp. 90-96, (1993).
- [16] C.W. HIRT and B.D. NICHOLS - *Volume of Fluid (VOF) Method for the Dynamics of Free Boundaries*. Journal of Computational Physics, 39 : pp. 201-225 (1981).
- [17] J. HYLKEMA - *Modélisation cinétique et simulation numérique d'un brouillard dense de gouttelettes. Application aux propulseurs à poudre*. Ph.D. Thesis ENSAE (1999).
- [18] M. ISHII - *Thermo-Fluid Dynamic Theory of Two-phase flow*. Volume 22 of Direction des études et recherches d'électricité de France. Eyrolles, Paris, (1975).
- [19] A.K. KAPILA, R. MENIKOFF, J.B. BDZIL, S.F. SON and D.S. STEWART - *Two-Phase Flow Modelling of DDT in Granular Materials : Reduced Equations*. Phys. Fluid, Vol. 13, pp. 3002-3024 (2001).
- [20] F. LAURENT, M. MASSOT and P. VILLEDIEU - *Eulerian Multi-Fluid Modelling for the Numerical Simulation of Coalescence in Polydisperse Dense Liquid Sprays*. Journal of Computational Physics, 194 (2), pp. 504-543 (2004).
- [21] N. LE LOSTEC, R.O. FOX, O. SIMONIN and P. VILLEDIEU - *Numerical Description of Dilute Particle Laden Flows by a Quadrature-Based Moment Method*. Annual Briefs 2008 of Center for Turbulence Research, Stanford, USA (2008).
- [22] R.J. LEVEQUE - *The Dynamics of Pressureless Dust Clouds and Delta Waves*. J. Hyperbolic Differential Equations, Vol. 1, pp. 315-327 (2004).
- [23] E. MONTREUIL, A. CHAZOTTES, D. GUFFOND, A. MURRONE, F. CAMINADE and S. CATRIS - *Enhancement of Prediction Capability in Icing Accretion and related Performance Penalties. Part I: Three-dimensional CFD Prediction of the Ice Accretion*. AIAA n°3969 (2009).
- [24] A. MURRONE and H. GUILLARD - *A Five Equation Reduced Model for Compressible Two Phase Flow Problems*. Journal of Computational Physics, 202, pp. 664-698 (2005).
- [25] A. NICOLE - *Simulation du cas Mascotte subcritique LOX/GH2 (10 bar)*. Onera RT n°1/11889 DEFA, September (2007).
- [26] A. NICOLE - *Simulation du cas Mascotte subcritique LOX/GH2 (10 bar) en 3D*. Onera RT n°4/13989 DEFA, December (2008).
- [27] A. NICOLE - *Simulation aux grandes échelles du cas Mascotte subcritique LOX/GH2 (10 bar) en 3D*. Onera RT n° 14450/06F, December (2009).
- [28] P.J. O'ROURKE - *Collective Drop Effects on Vaporizing Liquid Sprays*. Ph.D. Thesis, Los Alamos National Laboratory, New Mexico (1981).
- [29] C. RABE - *Etude de la coalescence dans les rampes de spray : application au système d'aspersion des Réacteurs a Eau Pressurisée*. Ph.D. Thesis, University of Paris 6 (2009).
- [30] A. REFLOCH, G. CHAINERAY, B.COURBET, J.B. DARGAUD, P. GILBANK, C. LAURENT, A. MURRONE, E. QUEMERAIS, P. VILLEDIEU, L. TESSÉ, J. TROYES and F.VUILLOT - *CEDRE Software*. Aerospace Lab Journal Issue 2 (2011).
- [31] E. RIBER, M. GARCIA, V. MOUREAU, H. PITTSCH, O. SIMONIN and T. POINSOT - *Evaluation of Numerical Strategies for LES of Two-Phase Reacting Flows*. Proc of the Summer Program (2006), Center for Turbulence Research, NASA Ames/Stanford Univ., pp. 197-213. 67 (2006).
- [32] M. RUGER, S. HOHMANN, M. SOMMERFELD and G. KOHNEN - *Euler/Lagrange Calculations of Turbulent Sprays : the Effect of Droplet Collisions and Coalescence*. Atomization Sprays 10 (1) (2000).
- [33] P.G. SAFFMAN - *The Lift on a Small Sphere in a Shear Flow*. Journal of fluid Mechanics. 22, pp. 385-400 (1965).
- [34] R. SAUREL and R. ABGRALL - *A Multiphase Godunov Method for Compressible Multifluid and Multiphase Flows*. Journal of Computational Physics, 150, pp. 425-467 (1999).

- [35] O. SIMONIN - *Continuum Modelling of Dispersed Turbulent Two Phase Flows*. *Combustion and Turbulence in Two Phase Flows*, VKI lecture series, (1996).
- [36] D.B. SPALDING - *The Combustion of Liquid Fuels*. In *Proceedings of the 4th Symp International on Combustion*, the Comb Institute, pp. 847-864, Baltimore (1953).
- [37] M. SUSSMAN, M. SMEREKA and S. OSHER - *A Level-Set Approach for Computing Solutions to Incompressible Two-Phase Flows*. *Journal of Computational Physics*, 114, pp. 146–159 (1994).
- [38] B. VAN LEER - *Towards the Ultimate Conservative Difference Schemes V. A Second Order Sequel to Godunov's Method*. *Journal of Computational Physics*, 32, pp. 101-136 (1979).
- [39] P. VILLEDIEU and O. SIMONIN - *Modelling of Coalescence in Turbulent Gas-Droplet Flows*, *Communication in Mathematical Science*, Supplemental Issue, No. 1, pp 13-33 (2004).
- [40] F.A. WILLIAMS - *Spray Combustion and Atomization*. *Physic of Fluid*, 1, pp. 541-545 (1958).
- [41] F.A. WILLIAMS - *Combustion Theory (Combustion Science and Engineering Series)*. Ed F A Williams, Reading, MA, Addison-Wesley (1985).
- [42] S. WIROGO and S. SRIRAMBHATLA - *An Eulerian Method to Calculate the Collection Efficiency on Two and Three Dimensional Bodies*. AIAA n°1073, (2003).

### Acronyms

- n.d.f (number density function)  
 p.d.f (probability density function)  
 DPS (Discrete Particle Simulation method)  
 SLD (Supercooled Large Droplet)

### AUTHORS



**Angelo Murrone** is a senior scientist in the Fundamental and Applied Energetics Department at Onera. His research concerns the numerical modeling of “dispersed” and “separated” two-phase flows. He is currently in charge of the development of the Eulerian solver SPIREE in the CEDRE multi-physics Code.



**Philippe Villedieu** is a senior scientist in the Multiphase Flow Research Unit at Onera and associate professor at the National Institute of Applied Science (INSA) of Toulouse. He is in charge of the development of the SPARTE solver, which is the Lagrangian spray module in CEDRE

L. Tessé, J.-M. Lamet  
(Onera)

E-mail: lionel.tesse@onera.fr

# Radiative Transfer Modeling Developed at Onera for Numerical Simulations of Reactive Flows

Radiative flux and power have to be calculated in many applications simulated using CFD, such as the prediction of pollutant emissions and the service life of aero-engine combustors, the design of thermal protection systems and ignition of solid propellant rocket motors, the design of spacecraft heat shields for atmospheric (re-) entries, and so on. In such configurations, the media are composed of gases (combustion products or plasma) and particles (soot, alumina, water droplets). Since the use of a line-by-line approach is not possible in industrial configurations, radiative properties are computed with an approximate band model. For gas radiative properties, this model is formulated either in terms of the absorption coefficient or in terms of transmissivity. To deal with any kind of problems, the Monte Carlo method has been chosen to solve the integral form of the Radiative Transfer Equation (RTE) allowing the use of the two formulations of the gas radiative property model. For media that can be dealt with using a model formulated in terms of the absorption coefficient, the Discrete Ordinates Method (DOM), that solves only the differential form of the RTE, has also been developed since it is reputed to consume less computation time than the Monte Carlo method. In this paper the fundamental relations of thermal radiation are first summarized. Then, both of the numerical methods and all the gas and particle radiative property models used at Onera to solve the RTE are described. Finally, some examples of typical applications studied at Onera with ASTRE (Monte Carlo) and REA (DOM) solvers are presented briefly.

## Introduction

In CFD simulations, it is often necessary to compute the radiative fluxes at the calculation domain boundaries and/or the radiative powers in the volume of the domain. Radiative power is equal to the opposite of the radiative flux divergence that appears in the total energy conservation equation of the Navier-Stokes system.

In most flames, radiative transfer significantly influences the temperature field and hence the concentration of reactive species. On the other hand, the radiative power field depends to a great extent on the temperature and the composition of the medium. There is a strong coupling between combustion and radiative transfer, particularly in the presence of soot particles. Therefore it is important to take radiation into account to predict, for instance, the pollutant emissions of an aero-engine combustor. In particular, NO<sub>x</sub> formation is very sensitive to the temperature level. Moreover, convective heat fluxes on the combustor walls are considerably reduced with a film cooling technique. This makes radiative heat flux calculation indispensable for a satisfactory prediction of the thermal gradients inside the walls which govern combustor service life.

A second kind of application in which radiation plays a significant role is aluminized solid propellant rocket engines. In order to protect the structural parts of the motor several types of thermal protecting materials are used. The prediction of convective and radiative fluxes on these materials is important since the flux levels directly affect performance (ablation in the nozzle throat, impulse to weight ratio) and the safety of the motor. The flux levels may be of the order of several MWm<sup>-2</sup> and radiative contributions, from combustion gases and alumina particles, range from practically 100% (internal parts) to about 10% (divergent part of the nozzle). Moreover, it has been shown that radiative fluxes have a strong effect on the ignition of a solid rocket motor, due to the radiative heat feedback on the propellant surface, which is a significant fraction of the total heat feedback.

A last example of possible applications is atmospheric (re-)entries. High velocities encountered in these kinds of flows (up to 12 km/s for Earth re-entry) lead to the formation of a shock in front of the heat shield of the spacecraft. Gases behind the shock can be ionized, dissociated and under chemical and thermal nonequilibrium conditions. High rotational, vibrational and electronic temperatures give rise to a strong radiative emission in the shock layer, which increases

the heat flux on the surface of the spacecraft. Kinetics and radiative transfer are strongly coupled because both depend on energy state populations. Therefore, the radiative transfer needs to be computed to be able to predict the shock layer position and design the heat shield. Moreover, in the Mars Premier project, preliminary computations tended to prove that the effects of radiation heating could be crucial during the aerocapture phase in the Martian atmosphere. As a matter of fact, radiation emitted in the wake region of the orbiter could overheat the payload and put a question mark over the technology of the thermal protection system.

For a given configuration, the most suitable gas radiative property model depends on the thermophysical conditions. If a gas radiative property model formulated in terms of transmissivity is needed, it is the integral form of the RTE (Radiative Transfer Equation) that has to be solved. If a model formulated in terms of the absorption coefficient can be used then the integral and the differential forms of the RTE can be solved since transmissivities can be obtained from the absorption coefficients. Therefore, two numerical methods have been developed at Onera: the Discrete Ordinates Method (DOM) and the Monte Carlo method. The first offers a good compromise between accuracy and CPU time, but it solves only the differential form of the RTE with a gas radiative property model formulated in terms of the absorption coefficient. Moreover, its use requires some assumptions about physical phenomena modeling (impossible to take into account spectral correlations and turbulence-radiation interaction for example). The Monte Carlo method is a powerful tool that can be used to solve any kind of problem since it solves the integral form of the RTE, but this statistical method has a reputation for its heavy consumption of CPU time.

The paper is divided into five parts. The first part goes over the fundamental relations of thermal radiation and the second describes two numerical methods used at Onera to solve the RTE. The third and fourth parts focus on gas and particle radiative property models. The last part then briefly presents the available models and typical applications studied at Onera with ASTRE (Monte Carlo) and REA (DOM) solvers.

## Fundamental relations of thermal radiation

Consider a participating medium enclosed by opaque walls and characterized by a refractive index equal to unity (this assumption is valid in most of the gas flows studied at Onera). At any point  $M$  of this three-dimensional system (volume and boundaries), the radiative flux vector can be defined as:

$$\vec{q}^R(M) = \int_0^{+\infty} \int_{4\pi} I_\nu(M, \vec{u}) \vec{u} d\Omega d\nu \quad (1)$$

where  $\nu$  is the wavenumber ( $m^{-1}$ ),  $\vec{u}$  a unit direction vector,  $d\Omega$  an infinitesimal solid angle (Sr) around the direction  $\vec{u}$  and  $I_\nu(M, \vec{u})$  the directional monochromatic radiative intensity ( $Wm^{-2}Sr^{-1}(m^{-1})^{-1}$ ). This intensity represents the radiative energy flow per unit time, unit solid angle, unit wavenumber and unit area normal to the considered direction.

From the definition of the radiative flux vector, expressions of wall radiative flux  $\phi^R$  ( $Wm^{-2}$ ) and of radiative power  $P^R$  ( $Wm^{-3}$ ) can be derived:

$$\phi^R(B) = -\vec{q}^R(B) \cdot \vec{n}_B = - \int_0^{+\infty} \int_{4\pi} I_\nu(B, \vec{u}) \vec{u} \cdot \vec{n}_B d\Omega d\nu \quad (2)$$

$$P^R(M) = -[\vec{\nabla} \cdot \vec{q}^R]_M = - \int_0^{+\infty} \int_{4\pi} \left[ \frac{\partial I_\nu(s, \vec{u})}{\partial s} \right]_{s=s_M} d\Omega d\nu \quad (3)$$

where  $B$  is a point on boundaries,  $\vec{n}_B$  the unit surface normal at the point  $B$  (pointing away from the surface into the medium) and  $M$  a point in the medium. The radiative power is equal to the opposite of the radiative flux divergence that appears in the total energy conservation equation of the Navier-Stokes system. The wall radiative flux is needed to solve heat conduction problems inside the walls.

The integral over the solid angle in equation (2) can be split into two parts: directions pointing towards the surface (incident radiation impinging onto the surface and absorbed by the wall) and directions pointing outwards from the surface into the medium (radiation emitted by the wall). This gives:

$$\phi^R(B) = \underbrace{\int_0^{+\infty} \int_{2\pi(\vec{u} \cdot \vec{n}_B < 0)} \alpha_\nu(B, \vec{u}) I_\nu^{inci}(B, \vec{u}) |\vec{u} \cdot \vec{n}_B| d\Omega d\nu}_{\text{absorption}} - \underbrace{\int_0^{+\infty} \int_{2\pi(\vec{u} \cdot \vec{n}_B > 0)} I_\nu^{emi}(B, \vec{u}) |\vec{u} \cdot \vec{n}_B| d\Omega d\nu}_{\text{emission}} \quad (4)$$

where  $I_\nu^{inci}(B, \vec{u})$  and  $I_\nu^{emi}(B, \vec{u})$  are, respectively, the incident directional monochromatic radiative intensity ( $Wm^{-2}Sr^{-1}(m^{-1})^{-1}$ ) impinging onto the surface at the point  $B$  and the directional monochromatic intensity emitted by the wall at the point  $B$ . Under the assumption of Local Thermodynamic Equilibrium (LTE means that relaxation processes occur rapidly in such a way that the energy states are populated according to Boltzmann's distribution)  $I_\nu^{emi}(B, \vec{u})$  can be expressed as the product  $\epsilon_\nu(B, \vec{u}) I_\nu^o(T_B)$  and the directional monochromatic absorptivity  $\alpha_\nu(B, \vec{u})$  is taken to be equal to the directional monochromatic emissivity  $\epsilon_\nu(B, \vec{u})$ .  $I_\nu^o(T_B)$  is the monochromatic equilibrium (or blackbody) intensity ( $Wm^{-2}Sr^{-1}(m^{-1})^{-1}$ ) and  $T_B$  is the wall temperature at point  $B$  (K).  $I_\nu^o(T)$  is also called the Planck function and is written:

$$I_\nu^o(T) = \frac{2hc_0^2 \nu^3}{e^{hc_0\nu/kT} - 1} \quad (5)$$

where  $h = 6.6261 \times 10^{-34}$  Js is Planck's constant,  $c_0 = 2.998 \times 10^8$  ms<sup>-1</sup> is the speed of light in the vacuum and  $k = 1.3807 \times 10^{-23}$  JK<sup>-1</sup> is Boltzmann's constant. Emission by solid walls is characterized by equilibrium intensity because, in all the CFD simulations performed at Onera, solids can be considered to be at LTE.

Equations (3) and (4) show that it is necessary to know the field of directional monochromatic intensity  $I_\nu(s, \vec{u})$  to be able to compute radiative power and flux. This field can be obtained by solving the Radiative Transfer Equation (RTE) which describes the change of the radiative intensity along a ray. The differential form of the RTE is obtained by making an energy balance on the radiative energy traveling in the direction  $\vec{u}$  between the locations  $s$  and  $s + ds$ . This leads to:

$$\frac{\partial I_\nu(s, \vec{u})}{\partial s} = \underbrace{\eta_\nu(s) + \frac{\sigma_\nu(s)}{4\pi} \int_{4\pi} I_\nu(s, \vec{u}') \Phi_\nu(s, \vec{u}' \rightarrow \vec{u}) d\Omega'}_{\text{gain by emission and incoming scattering}} - \underbrace{(\kappa_\nu(s) + \sigma_\nu(s)) I_\nu(s, \vec{u})}_{\text{loss by absorption and scattering}} \quad (6)$$

where  $\eta_\nu$  is the monochromatic emission coefficient ( $\text{Wm}^{-2}\text{Sr}^{-1}$ ),  $\kappa_\nu$  the monochromatic absorption coefficient ( $\text{m}^{-1}$ ) and  $\sigma_\nu$  the monochromatic scattering coefficient ( $\text{m}^{-1}$ ). These three coefficients are considered to be isotropic. The quantity  $\Phi_\nu(s, \vec{u}' \rightarrow \vec{u})$  is called the scattering phase function and describes the angular distribution of the scattered intensity.  $\Phi_\nu(s, \vec{u}' \rightarrow \vec{u}) d\Omega' / 4\pi$  can be interpreted as the probability of a ray, propagating in direction  $\vec{u}'$ , to be scattered in the direction  $\vec{u}$  at location  $s$ .

The transient form of the RTE is not presented here. The transient term on the left-hand side of equation (6) has been neglected because, for the vast majority of flows studied at Onera, the characteristic time of radiation propagation is very small compared to the characteristic times of the other physical phenomena involved.

Equation (6) can be rewritten in order to be integrated over an optical thickness from a point  $s' = s_{B_0}$  at the wall to a point  $s' = s$  inside the medium, giving:

$$I_\nu(s, \vec{u}) = \underbrace{I_\nu^{leav}(s_{B_0}, \vec{u}) \tau_\nu(s_{B_0}, s)}_{\text{part due to wall}} + \underbrace{\int_{s_{B_0}}^s S_\nu(s', \vec{u}) \tau_\nu(s', s) ds'}_{\text{part due to source function along the optical path}} \quad (7)$$

where  $S_\nu(s', \vec{u})$  is the source function (emission and incoming scattering) defined as:

$$S_\nu(s', \vec{u}) = \eta_\nu(s') + \frac{\sigma_\nu(s')}{4\pi} \int_{4\pi} I_\nu(s', \vec{u}') \Phi_\nu(s', \vec{u}' \rightarrow \vec{u}) d\Omega' \quad (8)$$

and  $\tau_\nu(s', s)$  is the monochromatic transmissivity given by:

$$\tau_\nu(s', s) = \exp\left[-\int_{s'}^s (\kappa_\nu(s'') + \sigma_\nu(s'')) ds''\right] \quad (9)$$

Equation (7) is known as the integral form of the RTE. This equation is interpreted physically as the monochromatic intensity, at location  $s$  in direction  $\vec{u}$ , being composed of two terms. The first is the contribution of intensity leaving the wall (or entering the enclosure if it is an open boundary), which decays exponentially due to extinction (absorption and scattering) over the optical distance  $\|s - s_{B_0}\|$ . The second term results from emission and incoming scattering in the direction  $\vec{u}$  by all the elements  $ds'$  along the path from  $s_{B_0}$  to  $s$ , reduced by exponential attenuation between each location of emission and incoming scattering  $s'$  and the location  $s$ .

The monochromatic intensity leaving the wall at point  $B_0$  in direction  $\vec{u}$  can be expressed as the sum of emitted and reflected intensities, given by:

$$I_\nu^{leav}(B_0, \vec{u}) = \varepsilon_\nu(B_0, \vec{u}) I_\nu^o(T_{B_0}) + (1 - \varepsilon_\nu(B_0, \vec{u})) I_\nu^{inci}(B_0, \vec{u}^*) \quad (10)$$

if the wall is a specularly reflecting surface;  $-\vec{u}^*$  is the symmetrical direction of  $\vec{u}$  about  $\vec{n}_{B_0}$ . If the wall is a diffusively reflecting surface, equation (10) becomes:

$$I_\nu^{leav}(B_0, \vec{u}) = \varepsilon_\nu(B_0) I_\nu^o(T_{B_0}) + \frac{1 - \varepsilon_\nu(B_0)}{\pi} \int_{2\pi(\vec{u} \cdot \vec{n}_{B_0} < 0)} I_\nu^{inci}(B_0, \vec{u}') |\vec{u}' \cdot \vec{n}_{B_0}| d\Omega' \quad (11)$$

Finally, the expressions for the radiative flux and power are obtained respectively by substituting equation (7) into equation (4) and equation (6) into equation (3). This leads to:

$$\varphi^R(B) = \underbrace{\int_0^{+\infty} \int_{2\pi(\vec{u} \cdot \vec{n}_B < 0)} \alpha_\nu(B, \vec{u}) \left[ I_\nu^{leav}(B_0, \vec{u}) \tau_\nu(s_{B_0}, s_B) + \int_{s_{B_0}}^{s_B} S_\nu(s', \vec{u}) \tau_\nu(s', s_B) ds' \right] |\vec{u} \cdot \vec{n}_B| d\Omega d\nu}_{\text{absorption}} - \underbrace{\int_0^{+\infty} I_\nu^o(T_B) \int_{2\pi(\vec{u} \cdot \vec{n}_B > 0)} \varepsilon_\nu(B, \vec{u}) |\vec{u} \cdot \vec{n}_B| d\Omega d\nu}_{\text{emission}} \quad (12)$$

$$P^R(M) = \underbrace{\int_0^{+\infty} \kappa_\nu(M) \int_{4\pi} I_\nu(M, \vec{u}) d\Omega d\nu}_{\text{absorption}} - \underbrace{4\pi \int_0^{+\infty} \eta_\nu(M) d\nu}_{\text{emission}} \quad (13)$$

When the medium is a mixture of gases and particles, the monochromatic absorption coefficient of the medium is given by:

$$\kappa_\nu(M) = \kappa_\nu^{gas}(M) + \kappa_\nu^{part}(M) \quad (14)$$

The monochromatic scattering coefficient and the monochromatic scattering phase function are only due to particles in the medium. Scattering by gas molecules is never taken into account in CFD simulations since its effect on heat radiative transfer is always negligible in the considered applications.

Combination of equations (9) and (14) leads to:

$$\tau_\nu(s', s) = \exp\left[-\int_{s'}^s \kappa_\nu^{gas}(s'') ds''\right] \times \exp\left[-\int_{s'}^s (\kappa_\nu^{part}(s'') + \sigma_\nu(s'')) ds''\right] = \tau_\nu^{gas}(s', s) \times \tau_\nu^{part}(s', s) \quad (15)$$

When a gas radiative property model formulated in terms of transmissivity is used, equation (13) cannot be used directly. Another expression for the radiative power can be obtained by substituting equation (7) into equation (13), giving:

$$P^R(M) = \underbrace{\int_0^{+\infty} \kappa_\nu(M) \int_{4\pi} \left[ I_\nu^{leav}(B_0, \vec{u}) \tau_\nu(s_{B_0}, s_M) + \int_{s_{B_0}}^{s_M} S_\nu(s', \vec{u}) \tau_\nu(s', s_M) ds' \right] d\Omega d\nu}_{\text{absorption}} - \underbrace{4\pi \int_0^{+\infty} \eta_\nu(M) d\nu}_{\text{emission}} \quad (16)$$

It is worth noticing that the multiplication of equation (14) by equation (15) results in:

$$\begin{aligned} \kappa_\nu(s)\tau_\nu(s',s) &= \kappa_\nu^{gas}(s)\tau_\nu^{gas}(s',s)\tau_\nu^{part}(s',s) + \kappa_\nu^{part}(s)\tau_\nu(s',s) \\ &= -\frac{\partial \tau_\nu^{gas}(s',s)}{\partial s}\tau_\nu^{part}(s',s) + \kappa_\nu^{part}(s)\tau_\nu(s',s) \end{aligned} \quad (17)$$

Using relation (17) in equation (16) we obtain:

$$\begin{aligned} P^R(M) &= \int_0^{+\infty} \int_{4\pi} \left[ \begin{array}{l} \left. \begin{array}{l} -\frac{\partial \tau_\nu^{gas}(s_{B_0},s)}{\partial s} \Big|_{s=s_M} \tau_\nu^{part}(s_{B_0},s_M) \\ + \kappa_\nu^{part}(s_M)\tau_\nu(s_{B_0},s_M) \end{array} \right| I_\nu^{leav}(B_0,\bar{u}) \\ \left. \begin{array}{l} -\frac{\partial \tau_\nu^{gas}(s',s)}{\partial s} \Big|_{s=s_M} \tau_\nu^{part}(s',s_M) \\ + \kappa_\nu^{part}(s_M)\tau_\nu(s',s_M) \end{array} \right| S_\nu(s',\bar{u})ds' \end{array} \right] d\Omega d\nu \\ &= \underbrace{-4\pi \int_0^{+\infty} \eta_\nu(M)d\nu}_{emission} \quad (18) \end{aligned}$$

Equation (18) is useful when a gas radiative property model formulated in terms of transmissivity is used because the gas absorption coefficient does not appear.

Assuming LTE (it is usually the case for combustion applications but not always for atmospheric entry flows), the monochromatic emission coefficient of the medium can be written:

$$\eta_\nu(M) = \kappa_\nu^{gas}(M)I_\nu^o(T_M^{gas}) + \sum_{k=1}^{N_{part}} \kappa_\nu^{p,k}(M)I_\nu^o(T_M^{p,k}) \quad (19)$$

where  $N_{part}$  is the number of particle sizes considered in the simulation. These particles can be in thermal nonequilibrium with the gases.

When the medium does not contain particles or particles are not taken into account in radiative transfer calculation, relation (18) can be expressed more simply as:

$$\begin{aligned} P^R(M) &= \int_0^{+\infty} \int_{4\pi} \left[ \begin{array}{l} \left. \begin{array}{l} -\frac{\partial \tau_\nu^{gas}(s_{B_0},s)}{\partial s} \Big|_{s=s_M} I_\nu^{leav}(B_0,\bar{u}) \\ + \int_{s_{B_0}}^{s_M} \frac{\eta_\nu(s')}{\kappa_\nu(s')} \frac{\partial^2 \tau_\nu^{gas}(s',s)}{\partial s \partial s'} \Big|_{s=s_M} ds' \end{array} \right| d\Omega d\nu \\ \underbrace{\hspace{10em}}_{absorption} \end{array} \right] \\ &= \underbrace{-4\pi \int_0^{+\infty} \eta_\nu(M)d\nu}_{emission} \quad (20) \end{aligned}$$

where the ratio  $\eta_\nu / \kappa_\nu$  can be replaced by the Planck function, given by equation (5), at LTE conditions.

All the previous equations involve monochromatic quantities, but in practical cases such as industrial configurations, it is not possible to perform line by line calculations since this approach requires more than  $10^6$  spectral points. Therefore it is necessary to average these equations over a spectral interval and to use a radiative property model providing quantities averaged over a spectral band. However, it is not always easy to write the averaged equations in a form that is suitable for the quantities given by the radiative property model. Sometimes it is not possible to take into account spectral correlations between radiative quantities.

When radiative transfer occurs in turbulent flows then turbulence-radiation interaction (TRI) has to be taken into account (see Box 1).

## Numerical methods developed at Onera

Several numerical methods can be used to compute radiative transfer [23], [32]. Two of them have been developed at Onera: the Monte Carlo method in the ASTRE solver and the discrete ordinates method in the REA solver. These two solvers are included in the CEDRE code [6].

The following two sections describe the two numerical methods. The reader should bear in mind that, to facilitate comprehension, the expressions in this part involve monochromatic radiative properties. However, in the ASTRE and REA solvers, these methods have been used in association with spectral band models, which are explained in the following parts.

### Monte Carlo method

Monte Carlo is a generic name for a large class of statistical numerical methods based on a sampling technique. Applied to thermal radiation problems, this kind of method consists in following a finite large number of "energy bundles" through their transport histories, from their points of emission to their points of absorption. An energy bundle is a discrete amount of power (W), which can be thought of as a group of photons bound together. Bundle characteristics (wavenumber, initial direction, point of emission) and physical events along bundle trajectories (absorption, scattering, reflection off walls) are chosen according to probability distributions by drawing random numbers. This is why Monte Carlo simulations are often referred as direct simulations of radiative transfer by statistical distributions of energy over space, direction and wavelength, and results obtained with Monte Carlo methods are often considered as reference solutions. As Monte Carlo methods are statistical, exact results can be approached if enough bundles are followed. Another advantage of Monte Carlo methods is that even the most complicated problem can be solved with relative ease.

As the Monte Carlo method applied to thermal radiation problems consists in emitting, following and absorbing energy bundles (in a similar way to what happens to a photon), the equations solved are not exactly those presented in the previous part. In particular, the source function along the bundle trajectories is taken to be equal to zero: only absorption and direction changes by scattering are considered.

## Box 1 - Turbulence-Radiation Interaction (TRI)

In the first section of this article, the transient term of the Radiative Transfer Equation (RTE, see equation (6)) has been neglected because, for the vast majority of flows, the characteristic time of radiation propagation is very small compared to the characteristic times of the other physical phenomena involved. This means that radiation is instantaneous compared to the other physical phenomena, like turbulence, combustion, convection or conduction. Therefore it appears that a model of the Turbulence-Radiation Interaction (TRI) is needed when a radiative transfer calculation is coupled with a turbulent combustion computation, based on a Reynolds-Averaged Navier-Stokes (RANS) approach, which provides only time-averaged quantities. In Large Eddy Simulation (LES), taking into account TRI, is a less crucial problem because only the effects of the subgrid scale fluctuations on radiation have to be modeled.

To simplify the equations, let us take a turbulent flow which can be considered as a non scattering medium at Local Thermodynamic Equilibrium (LTE), like a turbulent sooty flame. Under these assumptions and without taking into account TRI, the RTE is written:

$$\frac{\partial I_\nu(s, \bar{u})}{\partial s} = \kappa_\nu (\langle T(s) \rangle, \langle P(s) \rangle, \langle f_\nu(s) \rangle, \langle x_i(s) \rangle) [I_\nu^o (\langle T(s) \rangle) - I_\nu(s, \bar{u})] \quad (I-1)$$

where  $\langle T(s) \rangle$ ,  $\langle P(s) \rangle$ ,  $\langle f_\nu(s) \rangle$  and  $\langle x_i(s) \rangle$  are, respectively, the time-averaged temperature, pressure, soot volume fraction and molar fractions of species contributing to radiation. The calculations for the radiative properties and intensities are based on time-averaged quantities. When TRI is taken into account, the RTE that has to be considered becomes:

$$\frac{\partial \langle I_\nu(s, \bar{u}) \rangle}{\partial s} = \langle \kappa_\nu(s) I_\nu^o(s) \rangle - \langle \kappa_\nu(s) I_\nu(s, \bar{u}) \rangle \quad (I-2)$$

This equation shows that two correlations are required: the correlations between absorption coefficient fluctuations and those of equilibrium intensity (given by equation (5) and very sensitive to temperature fluctuations) and between absorption coefficient fluctuations and those of incident radiative intensity. If the fluctuations of  $T, P, f_\nu$  and  $x_i$  are known then it is not difficult to model the first correlation because it involves two terms which depend only on local quantity fluctuations (single-point statistics). Modeling the second correlation is more complex because the incident radiative intensity, given by equation (7), depends on quantity fluctuations in all the cells crossed by the optical path. That is why TRI is very often partially taken into account by assuming:

$$\langle \kappa_\nu(s) I_\nu(s, \bar{u}) \rangle \approx \langle \kappa_\nu(s) \rangle \langle I_\nu(s, \bar{u}) \rangle \quad (I-3)$$

This assumption, commonly called the Optically Thin Fluctuation Approximation (OTFA) in the literature, is valid when, for all wavenumbers  $\nu$ :

$$\langle \kappa_\nu(s) \rangle \Lambda \ll 1, \quad (I-4)$$

where  $\Lambda$  is the characteristic dimension of large turbulent eddies (or turbulence length scale). Due to the significant dynamics of gas spectra (see for example Figure 1 or 4) it is difficult to evaluate the error generated by the use of the OTFA.

It is worth noticing that some authors [21][22][37] have developed methodologies to take into account full TRI; i.e., with the two fluctuation correlation terms in equation (I-2). For more information about studies dealing with TRI, the reader should consult this review article [4].

TRI is still a current topic of research. Recent studies [8] [30] use Direct Numerical Simulations (DNS) in order to model the effects of the subgrid scale fluctuations on radiation in LES.

To emphasize the principle of the Monte Carlo method, assumptions that simplify the equations are considered in the paragraphs that follow. First, a gas radiative property model formulated in terms of the absorption coefficient is used. To see an example of the implementation in a Monte Carlo method of a gas radiative property model formulated in terms of transmissivity, the reader may refer to the work of Rouzaud et al. [31] or the thesis of Lamet [17]. Secondly, turbulence-radiation interaction (TRI) is not taken into account here, but the thesis of Tessé [35] [37] deals with this subject. Finally, only the conventional Forward Method (FM) is presented here. For informa-

tion about reverse, backward or reciprocal methods the reader should consult references [12], [23], [36] respectively.

Moreover, in order to reduce the variance, the pathlength method [12], also called "energy partitioning" [23], is used. The random number generation, to determine the pathlength traveled before total absorption of an energy bundle, is replaced by the calculation of exponential absorption along the path. Therefore, a bundle contributes to every cell it traverses. A bundle is traced until it either leaves the enclosure or until its energy is depleted below a given cutoff level.

Consider an enclosure filled by a nonisothermal, heterogeneous, absorbing, emitting and scattering media and discretized into  $N_V$  volume and  $N_S$  surface elements. Each element is supposed to be isothermal and homogeneous and radiative properties, except the phase function, are assumed to be isotropic.

The Monte Carlo statistical estimation of the radiative power in an arbitrary volume element  $q$  is written:

$$\tilde{P}_q^{FM} = \frac{1}{V_q} \left[ \sum_{i=1}^{N_V+N_S} \tilde{P}_{iq}^{ea} - P_q^e \right] \quad (21)$$

where  $V_q$  is the volume of element  $q$  and  $\tilde{P}_{iq}^{ea}$  the statistical estimation of the power emitted by the element  $i$  and absorbed by the volume element  $q$ .  $P_q^e$  is the power emitted by the volume  $q$  defined by:

$$P_q^e = \int_{V_q} \int_{4\pi} \int_0^{+\infty} \eta_{qv} dv d\Omega dV = 4\pi V_q \int_0^{+\infty} \eta_{qv} dv \quad (22)$$

since an element is considered to be isothermal and homogeneous and the spectral emission coefficient  $\eta_v$  is assumed to be isotropic.

The statistical estimation of the power emitted by the cell  $i$  and absorbed by the volume element  $q$  is written:

$$\tilde{P}_{iq}^{ea} = \frac{P_i^e}{N_i} \sum_{n=1}^{N_{iq}} \sum_{c=1}^{N_{pqn}} \tau_{v_n}(E_{in}, F_{qcn}) \alpha_{qcv_n} \quad (23)$$

where  $P_i^e$  is the power emitted by the element  $i$ ,  $N_i$  the total number of bundles leaving the cell  $i$  and  $P_i^e/N_i$  the initial power of a bundle leaving the cell  $i$ .  $N_{iq}$  represents the number of bundles leaving the cell  $i$  and reaching the volume element  $q$  and  $N_{pqn}$  the total number of crossings of the volume  $q$  by the  $n^{th}$  bundle path issued from the element  $i$ .  $\tau_{v_n}(E_{in}, F_{qcn})$  is the spectral transmissivity between the emission point  $E_{in}$  and  $F_{qcn}$  the  $c^{th}$  inlet point in the volume  $q$  of the  $n^{th}$  bundle path. The spectral transmissivity is given by:

$$\tau_{v_n}(E_{in}, F_{qcn}) = \exp\left(-\sum_{m=1}^{M_{qcn}-1} \kappa_{mv_n} \ell_m\right) \prod_{h=1}^{N_{rc}} (1 - \varepsilon_{hv_n}) \quad (24)$$

where  $\ell_m$  is the distance traveled through the volume element  $m$  and  $\kappa_{mv_n}$  the spectral absorption coefficient in the volume element  $m$ .  $m=1$  and  $m=M_{qcn}$  correspond respectively to the first volume element crossed by the bundle path and the last one for the  $c^{th}$  crossing (the volume element  $q$ ).  $N_{rc}$  is the number of wall reflections along the bundle path between the points  $E_{in}$  and  $F_{qcn}$ ,  $h$  the index of wall reflections along this bundle path and  $\varepsilon_{hv_n}$  the local wall spectral emissivity.

The spectral absorptivity  $\alpha_{qcv_n}$  is given by:

$$\alpha_{qcv_n} = 1 - \exp(-\kappa_{qv_n} \ell_{qc}) \quad (25)$$

where  $\ell_{qc}$  represents the length of the  $c^{th}$  crossing of the volume element  $q$  by the bundle path.

If the cell  $q$  is a surface element, the volume  $V_q$  is replaced by the area  $A_q$  in equation (22) and the spectral absorptivity  $\alpha_{qcv_n}$  is replaced by the diffuse spectral emissivity  $\varepsilon_{qv_n}$  in equation (23). Moreover, the power emitted by the cell  $q$  becomes:

$$P_q^e = \pi A_q \int_0^{+\infty} \varepsilon_{qv} I_v^o(T_q) dv \quad (26)$$

The number of bundles leaving the cell  $i$  is determined according to either:

$$N_i = \frac{N}{N_V + N_S} \quad (27)$$

or:

$$N_i = \frac{P_i^e}{\sum_{k=1}^{N_V+N_S} P_k^e} N \quad (28)$$

where  $N$  is the total number of bundles involved in the simulation. Equation (27) ensures a spatial uniform distribution of the bundles, while the initial power of a bundle is almost the same for all the bundles with equation (28).

Bundle characteristics (the emission point  $E$  inside cell, the polar and azimuthal angles  $\theta$  and  $\varphi$  characterizing the initial direction and the wavenumber  $\nu$ ) and scattering events along bundle trajectories are considered to be random variables. Therefore, they are chosen according to probability distributions by drawing random numbers in the range 0 to 1 and by assuming these random numbers to be equal to a suitable cumulative distribution functions, i.e.:

$$R_{X_n} = \int_{X_{\min}}^{X_n} f(X) dX \quad (29)$$

where  $X_n$  represents the randomly chosen value of the random variable  $X$ ,  $R_{X_n}$  a random number uniformly drawn in the interval [0;1] and  $f(X)$  the Probability Density Function (PDF) of the random variable  $X$ .

For a volume element  $i$ , the joint PDF  $f_i(E, \theta, \varphi, \nu)$ , based on emission, is obtained from the following relations:

$$f_i(E, \theta, \varphi, \nu) dV_i d\theta d\varphi d\nu = \frac{\eta_{iv} dV_i d\Omega d\nu}{\int_{V_i} \int_{4\pi} \int_0^{+\infty} \eta_{iv} dv d\Omega dV} = \frac{1}{\int_{V_i} dV} dV_i \frac{\sin\theta}{\int_0^\pi \sin\theta' d\theta'} d\theta \frac{1}{\int_0^{2\pi} d\varphi'} d\varphi \frac{\eta_{iv}}{\int_0^{+\infty} \eta_{iv} dv'} dv \quad (30)$$

$$f_i(E, \theta, \varphi, \nu) dV_i d\theta d\varphi d\nu = \frac{1}{V_i} dV_i \frac{\sin\theta}{2} d\theta \frac{1}{2\pi} d\varphi \frac{\eta_{iv}}{\int_0^{+\infty} \eta_{iv} dv'} dv \quad (31)$$

where  $d\Omega = \sin\theta d\theta d\varphi$  is an infinitesimal solid angle. Equation (31) shows that the joint PDF  $f_i(E, \theta, \varphi, \nu)$  can be factored into a product of the four marginal PDF, i.e.:

$$f_i(E, \theta, \varphi, \nu) dV_i d\theta d\varphi d\nu = f_{i1}(E) dV_i \times f_{i2}(\theta) d\theta \times f_{i3}(\varphi) d\varphi \times f_{i4}(\nu) dv \quad (32)$$

since the emission point  $E$ , the two angles  $\theta$  and  $\varphi$  and the wavenumber  $\nu$  are statistically independent due to some assumptions (an element is considered as isothermal and homogeneous and the spectral emission coefficient  $\eta_v$  is assumed to be isotropic).

For a diffuse surface element  $i$ , equation (31) becomes:

$$f_i(E, \theta, \varphi, \nu) dA_i d\theta d\varphi d\nu = \frac{1}{A_i} dA_i 2 \cos \theta \sin \theta d\theta \frac{1}{2\pi} d\varphi \frac{\varepsilon_{iv} I_v^o(T_i)}{\int_0^{+\infty} \varepsilon_{iv'} I_{v'}^o(T_i) dv'} dv' \quad (33)$$

where  $\cos \theta$  stands for  $|\vec{u} \cdot \vec{n}_B|$  in the emission term of equation (4). Moreover, the polar angle  $\theta$  varies from 0 to  $\pi/2$ .

Identifications of equations (31) and (33) with equation (32) provide all the PDF that can be substituted in equation (29) in order to determine all the random variables (emission point, angles and wavenumber). For example, the wavenumber  $\nu_n$  of the  $n^{\text{th}}$  bundle leaving the volume element  $i$  is chosen according to:

$$\int_0^{\nu_n} \eta_{iv} d\nu = R_{\nu_n} \int_0^{+\infty} \eta_{iv'} d\nu' \quad (34)$$

where  $R_{\nu_n}$  is a random number uniformly drawn in the interval [0;1]. For simple PDF, such as those of the angles, analytical integration can be performed leading to inverse relations  $X_n = g(R_{X_n})$ . For a volume element, the two angles of the  $n^{\text{th}}$  bundle leaving the volume element are given by:

$$\cos \theta_n = 1 - 2R_{\theta_n} \quad (35)$$

$$\varphi_n = 2\pi R_{\varphi_n} \quad (36)$$

For a diffuse surface element, equation (36) remains suitable while equation (35) becomes:

$$\cos \theta_n = \sqrt{R_{\theta_n}} \quad (37)$$

It is worth noticing that, for a surface element, the angles are defined in the local coordinate system of the surface element, with the unit surface normal pointing in its  $z$ -direction (i.e., the polar angle is measured from the unit surface normal).

In a scattering medium, we also have to randomly determine the distance traveled by a bundle before a change of direction due to scattering occurs. As exponential attenuation due to absorption is computed all along a bundle path, the probability for a bundle to be scattered between the distances  $s$  and  $s + ds$  is:

$$f_{scat}(s) ds = \exp\left[-\int_0^s \sigma_v(s') ds'\right] \sigma_v(s) ds \quad (38)$$

where  $f_{scat}(s)$  represents the scattering PDF at location  $s$  ( $s = 0$  at the emission point and at each scattering location). Substitution of the expression for the scattering PDF into equation (29) gives:

$$\int_0^{\ell_{scat}^{nk}} \sigma_{\nu_n}(s) ds = -\ln(R_{scat}^{nk}) \quad (39)$$

where  $\ell_{scat}^{nk}$  is the distance traveled by the  $n^{\text{th}}$  bundle between the  $(k-1)^{\text{th}}$  and  $k^{\text{th}}$  scattering events and  $R_{scat}^{nk}$  a random number uniformly drawn in the interval [0;1].

In the case of isotropic scattering, equations (35) and (36) can be applied to determine the angles of scattering direction, while in an anisotropic scattering medium, these angles are obtained from the following relations:

$$\int_0^{\varphi_s^{nk}} \int_0^{\pi} \Phi_{j\nu_n}(\theta, \varphi, \theta', \varphi') \sin \theta' d\theta' d\varphi' = R_{\varphi_s^{nk}} \int_0^{2\pi} \int_0^{\pi} \Phi_{j\nu_n}(\theta, \varphi, \theta', \varphi') \sin \theta' d\theta' d\varphi' = 4\pi R_{\varphi_s^{nk}} \quad (40)$$

$$\int_0^{\varphi_s^{nk}} \int_0^{\theta_s^{nk}} \Phi_{j\nu_n}(\theta, \varphi, \theta', \varphi') \sin \theta' d\theta' d\varphi' = 4\pi R_{\theta_s^{nk}} \quad (41)$$

$\Phi_{j\nu_n}(\theta, \varphi, \theta', \varphi')$  is the spectral scattering phase function in the volume element  $j$  containing the  $k^{\text{th}}$  scattering point of the  $n^{\text{th}}$  bundle.  $\theta$  and  $\varphi$  are the angles characterizing the propagation direction before scattering occurs. It is worth noticing that the angles of scattering direction  $\theta_s^{nk}$  and  $\varphi_s^{nk}$  given by equations (40) and (41) are defined in a local coordinate system having its origin at the scattering point and its  $z$ -direction unit vector equal to the unit direction vector of the bundle before scattering occurs (i.e.,  $\theta_s^{nk}$  is measured from the unit direction vector of the bundle before scattering occurs).

In order to control computation convergence, it is possible to subdivide a calculation into  $Q$  sub-calculations. For example, if  $10^8$  bundles are followed, a mean radiative power  $\bar{P}^R$  is calculated with all these bundles, and  $Q = 100$  sub-means  $P_1, P_2, \dots, P_Q$  are calculated with  $10^6$  bundles each. Then, the variance  $\gamma^2$  of the mean radiative power  $\bar{P}^R$  is:

$$\gamma^2 = \frac{1}{Q-1} \left[ \sum_{k=1}^Q (P_k - \bar{P}^R)^2 \right] = \frac{1}{Q-1} \left[ \sum_{k=1}^Q P_k^2 - \frac{1}{Q} \left( \sum_{k=1}^Q P_k \right)^2 \right] \quad (42)$$

Using the central limit theorem it can be shown that to reduce the standard deviation by half the total number of bundles has to be quadrupled, leading to quadrupled computation time.

This technique of subdivision into sub-calculations is very convenient for parallelization. Indeed, as the sub-calculations are all independent, they can be easily distributed on computer cores. Moreover, this leads to a parallelization efficiency close to 100% because there is no communication needed between parallel cores during bundle history generation. However, memory storage problems may be encountered when the mesh is composed of a very large number of cells because each computer core has to deal with the whole computation domain.

## Discrete ordinates method

The Discrete Ordinates Method (DOM) is based on a discrete representation of the directional variation of the radiative intensity. Thus, the differential form of the Radiative Transfer Equation (RTE, see equation (6)) is replaced by a system of partial differential equations (one equation for each ordinate direction) and integrals over a range of solid angles are approximated by weighted sums over the ordinate directions within that range. Gaussian quadratures called level symmetric or  $S_N$  quadratures are often used. That is why DOM is also called the  $S_N$  method.  $N$  is an even number that indicates the order

of the solution. In a three-dimensional problem,  $N_d = N(N + 2)$  discrete ordinates directions are considered.

So the RTE is replaced by a set of  $N_d$  equations. The equation corresponding to the  $m$ -direction is written as:

$$\begin{aligned} \vec{u}_m \cdot \vec{\nabla} I(s, m) = \eta_v(s) - (\kappa_v(s) + \sigma_v(s)) I_v(s, m) \\ + \frac{\sigma_v(s)}{4\pi} \sum_{j=1}^{N_d} w_j I_v(s, j) \Phi_v(s, j, m) \end{aligned} \quad (43)$$

where the  $w_j$  are the quadrature weights associated with the directions  $\vec{u}_j$  or  $j$ . Equations (43) need boundary conditions, giving the intensities leaving the wall in each direction  $m$ , to be solved. For a diffuse surface, the monochromatic intensity  $I_v(B_0, m)$  leaving the wall at point  $B_0$  in direction  $m$  (such as  $\vec{u}_m \cdot \vec{n}_{B_0} > 0$ , where  $\vec{n}_{B_0}$  is the unit surface normal at the point  $B_0$ , pointing away from surface into the medium) can be expressed as:

$$\begin{aligned} I_v(B_0, m) = \varepsilon_v(B_0) I_v^o(T_{B_0}) \\ + \frac{1 - \varepsilon_v(B_0)}{\pi} \sum_{j \substack{(N_d/2 \text{ values}) \\ \vec{u}_j \cdot \vec{n}_{B_0} < 0}} w_j I_v(B_0, j) |\vec{u}_j \cdot \vec{n}_{B_0}| \end{aligned} \quad (44)$$

Equations (43) and their corresponding boundary conditions (44) show that the intensity in direction  $m$  depends on the intensities in all the directions  $j$  when wall reflection or scattering is present. Therefore, in these cases, an iterative procedure is needed to compute all the intensities.

Since the unit direction vector  $\vec{u}_m$  is independent of the space coordinates, the left-hand side term of equation (43) can be written as:

$$\vec{u}_m \cdot \vec{\nabla} I_v(s, m) = \text{div}(I_v(s, m) \vec{u}_m) \quad (45)$$

Consider an enclosure filled by a non-isothermal, heterogeneous, absorbing, emitting and scattering medium and discretized into volume and surface elements. Each element is assumed to be isothermal and homogeneous and the radiative properties, except the phase function, are assumed to be isotropic.

To set up the numerical solution, a control volume technique, such as the one used in fluid mechanics problems, is applied to equations (43). By substituting equation (45) into equation (43), integrating it over a volume element  $V_i$  and using the divergence theorem, equation (43) becomes:

$$\begin{aligned} \sum_{f=1}^{N_i^{\text{faces}}} -\vec{u}_m \cdot \vec{n}_f A_f I_v(f, m) = \\ \left[ \eta_{iv} - (\kappa_{iv} + \sigma_{iv}) I_v(C_i, m) + \frac{\sigma_{iv}}{4\pi} \sum_{j=1}^{N_d} w_j I_v(C_i, j) \Phi_{iv}(j, m) \right] V_i \end{aligned} \quad (46)$$

where  $N_i^{\text{faces}}$  is the number of faces constituting the envelope of the volume  $V_i$ ,  $\vec{n}_f$  the inward surface normal of the face  $f$  (pointing

away from the face  $f$  into the volume  $V_i$ ),  $A_f$  the area of the face  $f$ ,  $I_v(f, m)$  the monochromatic intensity on the face  $f$  in direction  $m$ ,  $C_i$  the center of the volume  $V_i$  and  $I_v(C_i, m)$  the monochromatic intensity at point  $C_i$  in direction  $m$ . To obtain equation (46) the assumption has to be made that the intensities  $I_v(f, m)$  and  $I_v(C_i, m)$  are constant over the area  $A_f$  and the volume  $V_i$  respectively.

In order to reduce the number of unknowns in equation (46) a spatial differencing scheme is used to express the face intensities as a function of the volume intensities. The step scheme is chosen for its simplicity and robustness. With this spatial differencing scheme, the face intensities are given by the following relations:

- if  $\vec{u}_m \cdot \vec{n}_f < 0$ ,  $I_v(f, m) = I_v(C_i, m)$
- if  $\vec{u}_m \cdot \vec{n}_f > 0$ , either  $I_v(f, m) = I_v(C_{if}, m)$  or  $I_v(f, m)$  is given by relation (44) if the face  $f$  is a boundary.

$C_{if}$  is the center of the volume element that has the face  $f$  in common with the volume element  $V_i$ . Use of the step scheme in equation (46) leads to:

$$\begin{aligned} I_v(C_i, m) = \\ \frac{\sum_{\substack{f \\ \vec{u}_m \cdot \vec{n}_f > 0}} |\vec{u}_m \cdot \vec{n}_f| A_f I_v(C_{if}, m) + \left[ \eta_{iv} + \frac{\sigma_{iv}}{4\pi} \sum_{j=1}^{N_d} w_j I_v(C_i, j) \Phi_{iv}(j, m) \right] V_i}{(\kappa_{iv} + \sigma_{iv}) V_i + \sum_{\substack{f \\ \vec{u}_m \cdot \vec{n}_f < 0}} |\vec{u}_m \cdot \vec{n}_f| A_f} \end{aligned} \quad (47)$$

An iterative procedure, based on a Gauss-Seidel algorithm, is used to compute, for each wavenumber, all the directional intensities defined at all the element centers (volumes and surfaces). Once these intensities have been determined, it is possible to calculate the radiative flux and power with the following relations:

$$\begin{aligned} \phi^R(B_0) = \int_0^{+\infty} \varepsilon_v(B_0) \sum_{\substack{j \substack{(N_d/2 \text{ values}) \\ \vec{u}_j \cdot \vec{n}_{B_0} < 0}}} w_j I_v(B_0, j) |\vec{u}_j \cdot \vec{n}_{B_0}| dv \\ - \pi \int_0^{+\infty} \varepsilon_v(B_0) I_v^o(T_{B_0}) dv \end{aligned} \quad (48)$$

$$P^R(C_i) = \int_0^{+\infty} \kappa_{iv} \sum_{j=1}^{N_d} w_j I_v(C_i, j) dv - 4\pi \int_0^{+\infty} \eta_{iv} dv \quad (49)$$

## Gas radiative property models

Absorption/emission spectra of gases have significant spectral dynamics, changing to a considerable degree with thermophysical conditions. For example, figure 1 shows absorption spectra at high resolutions of  $CO_2$  species (on the left,  $x_{CO_2} = 0.02$  and  $x_{N_2} = 0.98$ ) and air plasma (on the right) for different temperatures at atmospheric pressure.

If radiative properties can be calculated beforehand at high resolution and for each set of thermochemical conditions encountered, radiative transfer can be accurately computed by using the line-by-line (LBL) approach. With this approach, radiative transfer problems could be solved directly considering the relations given in the two previous parts. However, the LBL approach, which consists in solving the RTE for each wavenumber (several millions of spectral points in general), requires too much CPU time and memory storage for industrial applications. To simplify the RTE resolution and radiative property calculation approximate models at low resolution are generally used. Nevertheless, these models have to take spectral correlation effects into account due to the gas spectra line structure (see Box 2).

In the literature two kinds of approximate models are usually used: global models and band models. Global models, such as the Weighted Sum of Gray Gases (WSGG) [14], the Spectral Line-based Weighted sum of gray gases (SLW) [7] or the Absorption Distribution Function (ADF) [26], allow the direct solution of the RTE with radiative properties relative to the whole spectrum. These models are accurate and convenient for uniform media but it becomes difficult to define the parameters of these models for non-uniform gaseous mixtures. In addition, global models are incompatible with the treatment of particles or non-gray walls. Band models are generally more accurate but more costly in terms of computational resources. In this modeling the spectrum is subdivided into bands and radiative properties are averaged over each spectral band. Under LTE conditions, to minimize spectral correlation problems, the bands have to be sufficiently narrow to consider the Planck function constant over each band for all considered temperatures (this can be explained by the fact that, when equation (6) or (7) is averaged over a spectral band, the average of the product of a radiative quantity with the Planck function can be considered equal to the product of the averages if the Planck function is almost constant over each spectral band). Several band models for gas radiative properties exist in the literature, but only band models, used in the radiation solvers developed at Onera (REA and ASTRE), are presented in the following sections.

The first two sections are dedicated to two well-known band models which are used to take into account spectral dynamics in radiative transfer problems: the Correlated-K (CK) model and one type of Statistical Narrow Band (SNB) model. The former, which is formulated in terms of the absorption coefficient, is appropriate for solving the two RTE formulations described in the first part, while the latter, formulated in terms of mean transmissivity, is only suitable for RTE formulation in terms of transmissivity. In the last section, the basic box model is presented. This simplified model can be used when spectral correlation effects can be neglected. For each model, cases of uniform and non-uniform media are discussed, as well as the case of media composed of several radiating species.

## Correlated-k (CK) model

### Uniform media

To compute average radiative properties, as, for example, transmissivities, knowledge of spectral band line positions is not necessary. Knowledge of the distribution function of the absorption coefficient is sufficient. This is the idea on which the CK model, initially used for atmospheric applications [13], is based. The cumulative distribution function used is defined by:

$$g(k) = \frac{1}{\Delta \nu} \int_{\nu \in \Delta \nu / k_\nu \leq k} d\nu \quad (50)$$

for  $k \in [k_{\min}; k_{\max}]$ , where  $k_{\min}$  and  $k_{\max}$  are the extreme values, reached in the spectral band  $\Delta \nu$ , of the reduced monochromatic absorption coefficient  $k_\nu$ , defined as the ratio  $\kappa_\nu / xp$ . Mean transmissivity of a uniform column of length  $l$  can be expressed with the function  $g$ :

$$\bar{\tau}^{\Delta \nu}(l) = \frac{1}{\Delta \nu} \int_{\Delta \nu} \exp(-xplk_\nu) d\nu = \int_{k_{\min}}^{k_{\max}} \exp(-xplk) \frac{\partial g}{\partial k} dk \quad (51)$$

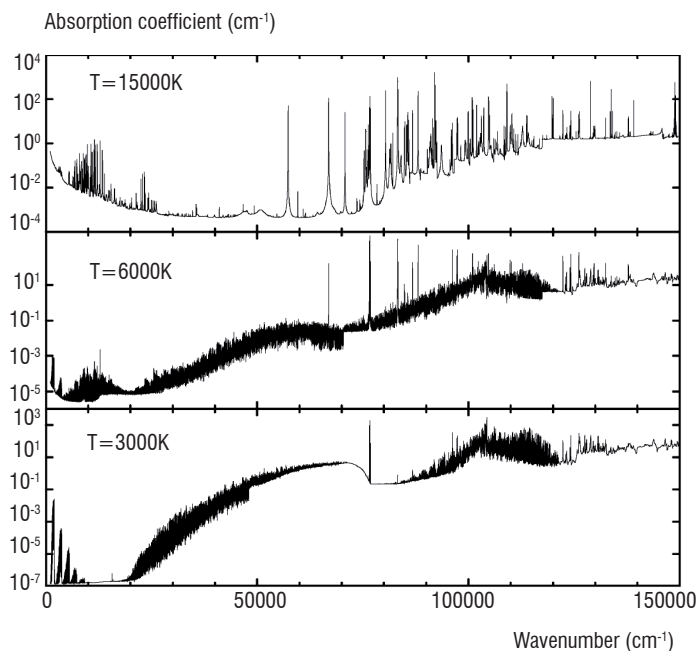
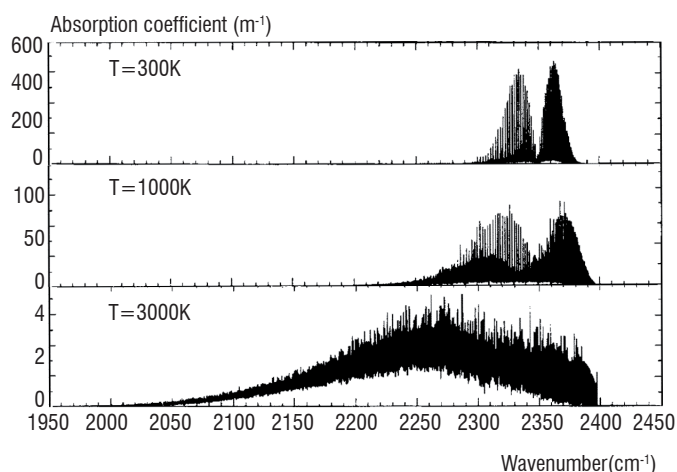


Figure 1 - Absorption spectra of  $CO_2$  species (on the left – extracted from Ref. [34]) and air plasma (on the right – extracted from Ref. [3]) at atmospheric pressure for different temperatures.

## Box 2 - Spectral correlation phenomenon

The phenomenon of spectral correlation is due to the spectral dynamics of emission and absorption spectra and the fact that emission is spectrally located at the same position as absorption. The following simple example demonstrates the importance of this phenomenon in radiative transfer problems where integrated values are usually wanted.

Consider two columns 1 and 2, characterized respectively by an emissivity  $\varepsilon_\nu$  and a transmissivity  $\tau_\nu$  (see figure B2-01) of two spectral lines (crudely represented by two crenels) located in a spectral interval  $\Delta\nu$ . The monochromatic intensity emitted by column 1 and transmitted by column 2 can be expressed as  $I_\nu = I_\nu^\circ(T_1)\varepsilon_\nu\tau_\nu$ , where  $T_1$  is the temperature of column 1. To simplify,  $I_\nu^\circ(T_1)$  is assumed to be constant over the spectral band  $\Delta\nu$  and equal to  $I_{\nu_c}^\circ(T_1)$  where  $\nu_c$  is the center of the band  $\Delta\nu$ . The intensity averaged over the band  $\Delta\nu$  is then written:

$$\bar{I}^{\Delta\nu} = I_{\nu_c}^\circ(T_1) \frac{1}{\Delta\nu} \int_{\nu_c - \Delta\nu/2}^{\nu_c + \Delta\nu/2} \varepsilon_\nu \tau_\nu d\nu = 0 \quad (II-1)$$

This intensity is equal to zero because the product  $\varepsilon_\nu \tau_\nu$  is equal to zero for any wavenumber included in the spectral band  $\Delta\nu$ . Indeed, emission by column 1 is located exactly at the same spectral positions where absorption in column 2 occurs. This result takes spectral correlations entirely into account. As real spectra do not have a structure as simple as those described in figure B2-01 another approach to calculate this mean intensity would be to not consider spectral correlations but to use the mean values of emissivity and transmissivity of the two columns. The result is:

$$\bar{I}^{\Delta\nu} = I_{\nu_c}^\circ(T_1) \bar{\varepsilon}^{\Delta\nu} \bar{\tau}^{\Delta\nu} = I_{\nu_c}^\circ(T_1) \frac{1}{\Delta\nu} \int_{\nu_c - \Delta\nu/2}^{\nu_c + \Delta\nu/2} \varepsilon_\nu d\nu \times \frac{1}{\Delta\nu} \int_{\nu_c - \Delta\nu/2}^{\nu_c + \Delta\nu/2} \tau_\nu d\nu = \frac{2}{9} I_{\nu_c}^\circ(T_1) \quad (II-2)$$

which gives a result totally different from relation (II-1), both quantitatively and qualitatively.

This is a simple example but it is a good illustration of how not accounting for spectral correlations between emission and absorption terms can lead to absurd results. As explained in the section "Gas radiative property models", spectral correlation effects can be more or less significant depending on the type of application.

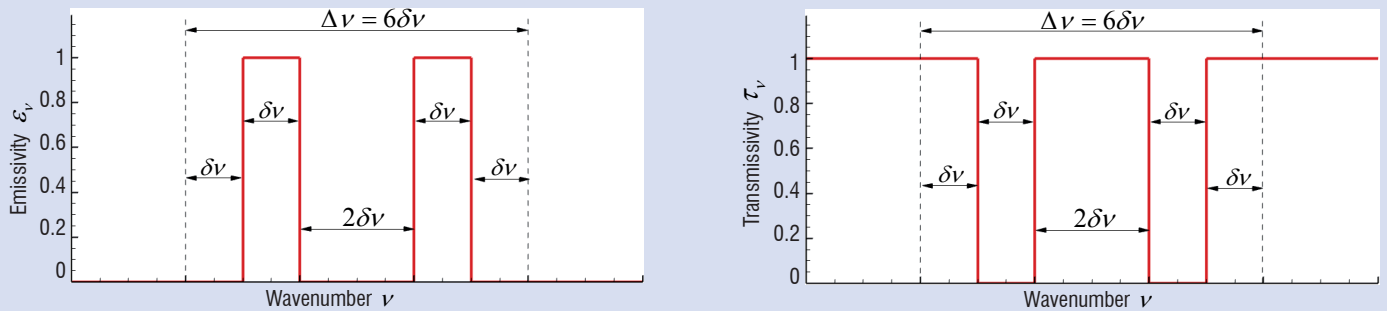


Figure B2-01- Emissivity of column 1 (on the left) and transmissivity of column 2 (on the right).

where  $x$  is the molar fraction of the absorbing species and  $p$  the pressure in the column. The function  $\partial g / \partial k$  represents the inverse Laplace transform of  $\bar{\tau}^{\Delta\nu}(l)$ . By introducing the inverse function of  $g, G \rightarrow k(G)$ , relation (51) can be written:

$$\bar{\tau}^{\Delta\nu}(l) = \int_0^1 \exp(-xplk(G)) dG \quad (52)$$

In fact,  $k(G)$  is the absorption coefficient reordered vs the wavenumber scaled by  $dG = d\nu / \Delta\nu$ , as shown in figure 2. It is convenient to use this function because  $k(G)$  is monotonous and increasing, inversely as the function  $\nu \rightarrow k_\nu$  which has significant spectral dynamics. Therefore, integration in relation (52) can be achieved using quadrature with a small number of points (about ten usually):

$$\bar{\tau}^{\Delta\nu}(l) = \sum_{i=1}^n w_i \exp(-xplk(G_i)) \quad (53)$$

where  $n, G_i$  and  $w_i$  are the quadrature order, points and weights respectively.

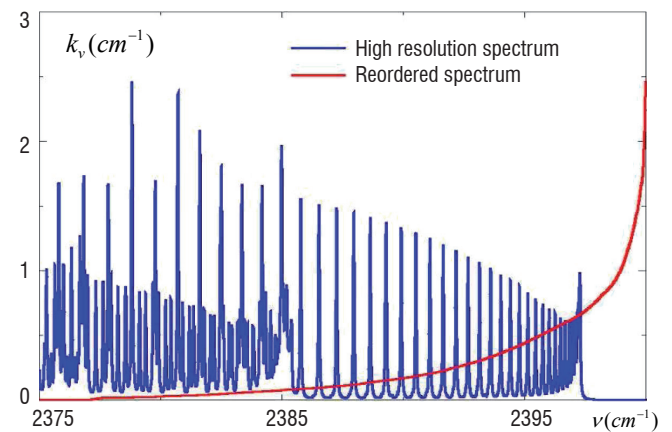


Figure 2 - Example of a reordered spectrum on a spectral band [29].

## Non-uniform media

This model is extended to non-uniform media by assuming that the rearrangement function  $\nu \rightarrow G$  is spatially independent. This assumption on spectral correlations allows association of the reordered absorption coefficients for different thermophysical conditions. Therefore, the mean transmissivity of an inhomogeneous column is approximated by:

$$\bar{\tau}^{\Delta\nu}(l) = \sum_{i=1}^n w_i \exp\left[-\int_0^l x(s)p(s)k(G_i, s)ds\right] \quad (54)$$

The weights  $w_i$  and the values  $k(G_i, s)$  for each narrow band are the CK model parameters. In practical cases, the values  $k(G_i, s)$  depend on temperature, pressure and the gas mixture composition. This method, based on the reordering of the absorption coefficient to express the mean transmissivity, can be also used for any radiative quantities that depend on  $\kappa_\nu$ , such as the mean radiative intensity at any point  $M$  of abscissa  $s$ :

$$\bar{I}^{\Delta\nu}(s) = \sum_{i=1}^n w_i I_{G_i}(s) \quad (55)$$

where  $I_{G_i}(s)$  is the pseudo-monochromatic intensity at the point  $M$  at the pseudo wavenumber  $G_i$ . This intensity satisfies, for each quadrature point, the following RTE formulation (given here at LTE conditions without scattering):

$$\frac{\partial I_{G_i}(s)}{\partial s} = x(s)p(s)k(G_i, s)\left[\bar{I}^{\Delta\nu}(s) - I_{G_i}(s)\right] \quad (56)$$

When two species  $A$  and  $B$  may absorb in the same spectral band, the following approximation:

$$\bar{\tau}^{\Delta\nu}(l) = \bar{\tau}_A^{\Delta\nu}(l) \times \bar{\tau}_B^{\Delta\nu}(l) \quad (57)$$

can be used with a good degree of accuracy since there is no physical reason to have significant correlations between the spectra of different species. Thereby, the mean transmissivities  $\bar{\tau}_A^{\Delta\nu}$  and  $\bar{\tau}_B^{\Delta\nu}$  are calculated with relation (54), leading to:

$$\begin{aligned} \bar{\tau}^{\Delta\nu}(l) &= \sum_{i=1}^n w_i \exp\left[-\int_0^l x_A(s)p(s)k_A(G_i, s)ds\right] \\ &\quad \times \sum_{i=1}^n w_i \exp\left[-\int_0^l x_B(s)p(s)k_B(G_i, s)ds\right] \\ &= \sum_{i=1}^n \sum_{j=1}^n w_i w_j \exp\left[-\int_0^l \left(x_A(s)p(s)k_A(G_i, s) + x_B(s)p(s)k_B(G_j, s)\right)ds\right] \end{aligned} \quad (58)$$

The latter expression can be interpreted as the use of an  $N^2$ -point quadrature with the weights  $w_i w_j$ . The average intensity is given by the following relation:

$$\bar{I}^{\Delta\nu}(s) = \sum_{i=1}^n \sum_{j=1}^n w_i w_j I_{G_i G_j}(s) \quad (59)$$

where each intensity  $I_{G_i G_j}(s)$  satisfies the following RTE formulation (given here at LTE conditions without scattering):

$$\begin{aligned} \frac{\partial I_{G_i G_j}(s)}{\partial s} &= \left(x_A(s)p(s)k_A(G_i, s) + x_B(s)p(s)k_B(G_j, s)\right) \\ &\quad \times \left[\bar{I}^{\Delta\nu}(s) - I_{G_i G_j}(s)\right] \end{aligned} \quad (60)$$

These relations can easily be extended to  $m$  absorbing species considering an  $N^m$ -point quadrature.

## Statistical Narrow Band (SNB) model

### Uniform media

Another band model group is the family of Statistical Narrow Band (SNB) models. The random SNB model of Mayer and Goody [13] has been chosen for the applications studied at Onera. This model is based on statistical assumptions for line positions and intensities within a narrow band of width  $\Delta\nu$ , allowing the transmissivity of a uniform column of length  $l$ , averaged over  $\Delta\nu$ , to be expressed as:

$$\bar{\tau}^{\Delta\nu}(l) = \frac{1}{\Delta\nu} \int_{\Delta\nu} \exp(-xpl\kappa_\nu) d\nu = \exp\left(-\frac{\bar{W}}{\delta}\right) \quad (61)$$

where  $\delta = \Delta\nu / N$  is the mean spacing between the  $N$  line positions within  $\Delta\nu$ , and  $\bar{W}$  is the mean black equivalent line width of these lines, defined as:

$$\bar{W} = \frac{1}{N} \sum_{r=1}^N \int_{-\infty}^{+\infty} [1 - \exp(-\kappa_\nu^r l)] d\nu \quad (62)$$

where  $\kappa_\nu^r$  is the contribution of the  $r^{\text{th}}$  line to the absorption coefficient. Many analytical expressions for  $\bar{W} / \delta$  have been proposed in the literature by assuming: (i) a suitable probability distribution function (PDF)  $P(S)$  of line intensities (of the PDF usually used, the uniform distribution, the Goody exponential distribution and the Malkmus tailed inverse-exponential distribution can be mentioned), (ii) a unique spectral line shape for all lines, Gaussian (to characterize the Doppler broadening effect) or Lorentzian (to characterize the collisional broadening effect), with a constant half-width at half-maximum (HWHM)  $\gamma_0^D$  or  $\gamma_0^L$ . All analytical expressions of  $\bar{W} / \delta$ , summarized in Ref. [34], actually depend on only two parameters,  $\bar{k}$  and  $\bar{\beta}$ . The first of these,  $\bar{k}$ , can be identified with a reduced mean absorption coefficient and is always related to the mean line intensity  $\bar{S} = \int SP(S)dS$  by the relation  $\bar{k} = \bar{S} / \delta$ . The second,  $\bar{\beta}$ , characterizes the degree of line overlapping and is always proportional to the ratio  $\gamma_0^{L/D} / \delta$  (L/D stands for 'Lorentz' or 'Doppler'). The parameter  $\bar{\beta}$  can be generated from a spectroscopic database or from curve fitting. In the latter method the analytical expression  $\bar{W}_{L/D} / \delta$  is fitted to the curve of growth (defined as the opposite of the logarithm of the mean transmissivity versus the column length  $l$ ), obtained with line by line calculation.

Under some thermophysical conditions the lines have a Voigt profile, for which there is no analytical expression of the mean black equivalent line width  $\bar{W}_V$ . Several approximations of  $\bar{W}_V$ , based on expressions of  $\bar{W}_L$  and  $\bar{W}_D$ , for Lorentz and Doppler regimes respectively, can be used. The expression of Ludwig [20] is generally an accurate approximation:

$$\frac{\bar{W}_V}{\delta} = xpl\bar{k} \sqrt{1 - \Omega^{-1/2}} \quad (63)$$

with:

$$\Omega = \left[1 - \left(\frac{1}{xpl\bar{k}} \frac{\bar{W}_D}{\delta}\right)^2\right]^{-2} + \left[1 - \left(\frac{1}{xpl\bar{k}} \frac{\bar{W}_L}{\delta}\right)^2\right]^{-2} - 1 \quad (64)$$

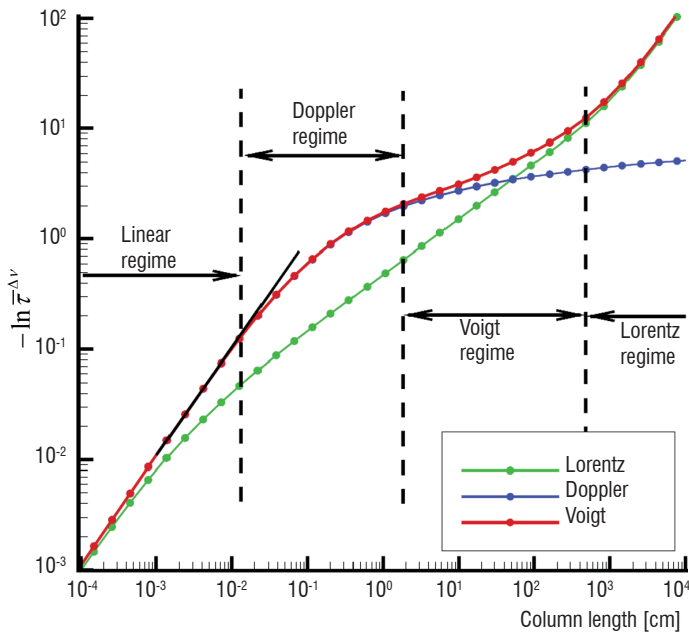


Figure 3 - Typical curve of growth depending on the broadening regime [17].

Figure 3 shows an example of the typical curve of growth for a spectral band of  $1000 \text{ cm}^{-1}$  ( $112000\text{--}113000 \text{ cm}^{-1}$ ) for the  $\text{N}_2$  Birge-Hopfield system at atmospheric pressure and  $8000 \text{ K}$ . The different broadening regimes, like Doppler and Lorentzian regimes, are indicated in figure 3. The parameters  $\beta_D$  and  $\beta_L$  are adjusted to fit expression (63) to the curve of growth.

### Non-uniform media

Different approximations exist in the literature allowing the extension of SNB models to the case of non-uniform gaseous columns. An extensive review of these approximations is given by Young [39]. The classic Curtis-Godson (CG) approximation used in practical cases is briefly presented here.

The main assumption of CG approximations is that the curves of growth of a non-uniform column versus the optical path  $u = \int_0^l x(s)p(s)ds$  have the same behavior as those obtained for uniform columns. Therefore, mean transmissivity is written:

$$\bar{\tau}^{\Delta\nu}(l) = \exp\left(-\frac{\overline{W_V^*}}{\delta}\right) \quad (65)$$

where  $\overline{W_V^*}/\delta$  is given by equations (63) and (64), in which the product  $xpk_l$  is replaced by:

$$\overline{k^* u} = \int_0^l x(s)p(s)\overline{k(s)} ds \quad (66)$$

Moreover, the terms  $\overline{W_L}/\delta$  and  $\overline{W_D}/\delta$  in equation (64) are replaced, respectively, by  $\overline{W_L^*}/\delta$  and  $\overline{W_D^*}/\delta$ , which are calculated with the same analytical formulations as those used for a uniform column, but with  $k^*$  and  $\beta_{L/D}^*$  instead of  $\overline{k}$  and  $\overline{\beta_{L/D}}$ . With the classic CG approximation,  $\beta_{L/D}^*$  is expressed as:

$$\beta_{L/D}^* = \frac{1}{\overline{k^* u}} \int_0^l x(s)p(s)\overline{k(s)}\overline{\beta_{L/D}^*}(s) ds \quad (67)$$

The “\*” parameters are consequently obtained from parameters calculated for uniform media.

If two species  $A$  and  $B$  absorb in the same spectral band, the approximation given by equation (57) can be used.

### Box model

In some applications, the spectral correlation effect on radiative transfer can be weak. This is the case, for example, when the medium is optically thin or when the absorption spectrum has weak spectral dynamics. The latter case is illustrated in figure 4 which shows spectral emissivities of two  $\text{H}_2\text{O}-\text{N}_2$  mixture columns at two different pressures but with the same optical path ( $xpl$  product). The collision broadening effect leads to smooth radiative properties at high pressure in such a way that the spectral dynamics become weaker.

In these situations, information on the spectral distribution (distribution function for the CK model, overlapping parameter  $\beta$  for the SNB model) can be ignored and the model parameter is only the reduced absorption coefficient  $\overline{k}$  (box model parameter).

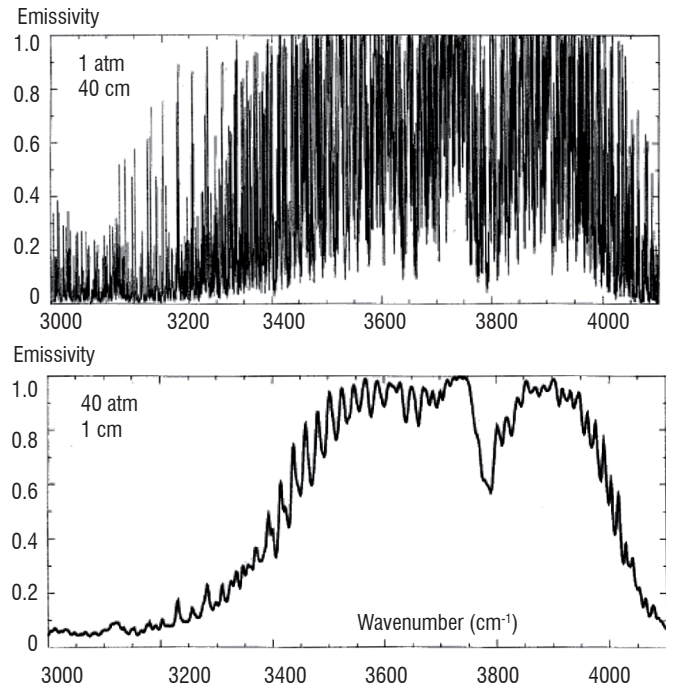


Figure 4 - Emissivity spectra of two  $\text{H}_2\text{O}-\text{N}_2$  mixture ( $x_{\text{H}_2\text{O}} = 0.5$ ) columns at  $800 \text{ K}$  as a function of pressure condition at a constant product  $xpl$  [34].

If the integral form of the RTE (see equation (7)) is used then the transmissivity, averaged over  $\Delta\nu$ , of a uniform column of length  $l$  can be expressed to a good approximation as:

$$\bar{\tau}^{\Delta\nu}(l) = \exp(-xpk_l) \quad (68)$$

For non-uniform media the following relation is simply used:

$$\bar{\tau}^{\Delta\nu}(l) = \exp\left(-\int_0^l x(s)p(s)\overline{k(s)} ds\right) \quad (69)$$

and for mixture media, a relation quite similar to equation (57) can be used.

## Radiative property models of particles

When a photon interacts with a medium containing small particles, the radiative intensity may be changed by absorption and/or scattering. This situation is mostly encountered in a combustion engine where soot or alumina particles are present.

This part of the paper only deals with radiative properties of spherical particles, since particles are assumed to be spherical in the applications studied at Onera. Moreover, scattering is considered as independent. In this situation, the radiative properties of a cloud of spherical particles of radius  $r$ , interacting with an incident radiation of wavenumber  $\nu$ , are governed by only two independent non-dimensional parameters [23]:

- complex index of refraction of the particles:  

$$m(s, \nu) = n(s, \nu) - ik(s, \nu),$$
- size parameter (also called the Mie parameter):  $x = 2\pi r\nu$ .

Note that the complex index  $m$  is a function of wavenumber and local thermophysical conditions at the point of abscissa  $s$ .

When the size parameter is not very small or very large compared to unity, the radiative properties are usually determined from the Mie theory, a general theory describing interaction between an electromagnetic wave and a spherical particle. In other cases, this theory can be simplified: the Rayleigh theory (for  $x \ll 1$ ) and geometric optics (for  $x \gg 1$ ) are recovered. The case  $x \ll 1$  is, in particular, discussed in the third section.

## Radiative property expressions

From a general point of view, the absorption (or scattering) phenomenon is quantified by an efficiency factor  $Q_{\text{abs}}$  (or  $Q_{\text{sca}}$ ) which is defined as the ratio between the absorption (or scattering) cross section and the actual surface particle  $\pi r^2$ . The Mie theory gives analytical expressions [1] to calculate these efficiencies for an isolated particle, assumed to be spherical, homogeneous and isothermal. The expressions depend on the local complex index of refraction of the particle and the Mie parameter. Figure 5 shows typical changes in the efficiency coefficients as a function of the Mie parameter for alumina particles.

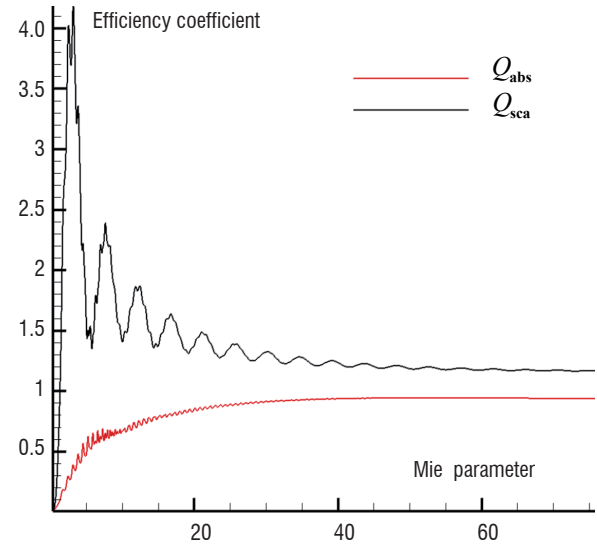


Figure 5 - Absorption and scattering efficiency coefficients for alumina particles ( $m = 1.7 - 2.10^{-3}i$ ).

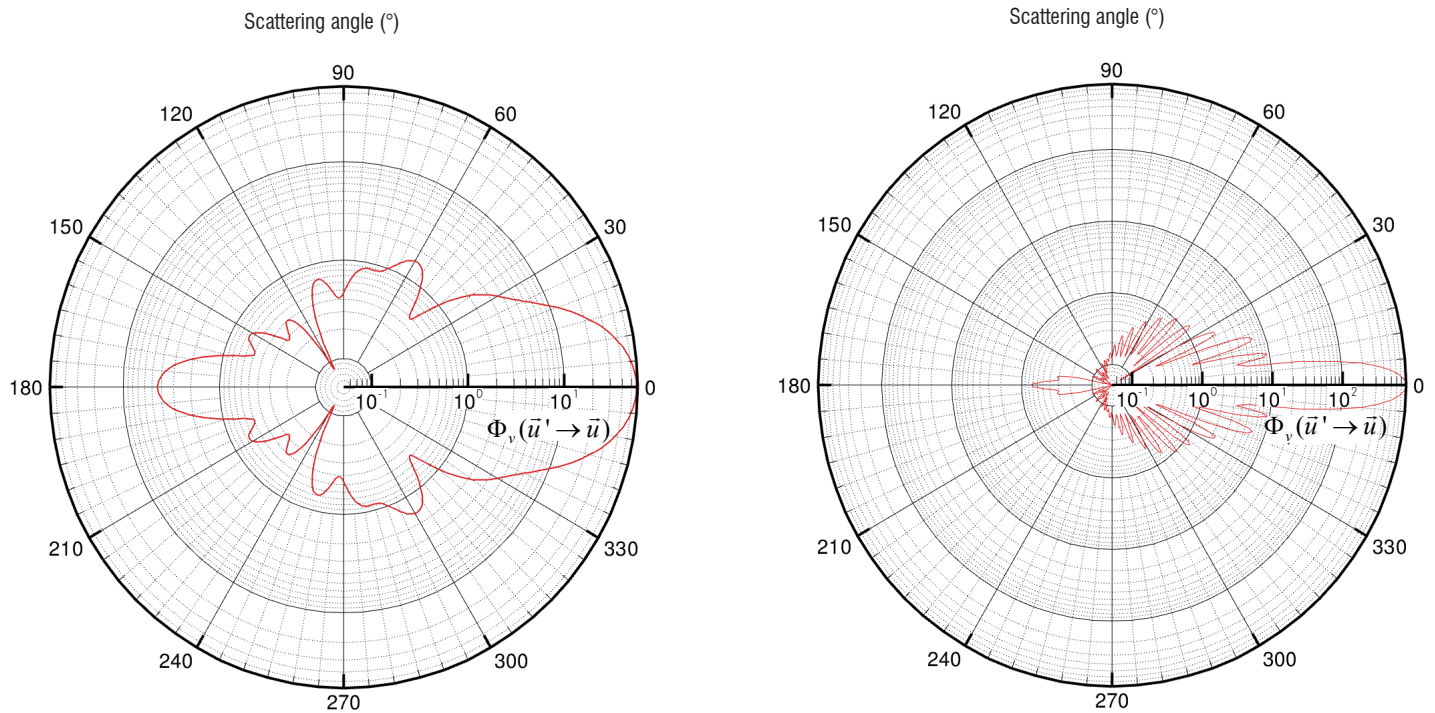


Figure 6 - Polar plots of the scattering phase function for a single alumina particle ( $m = 1.7 - 2.10^{-3}i$ ) with  $\nu = 10000 \text{ cm}^{-1}$  and  $r = 1 \text{ }\mu\text{m}$  (on the left),  $r = 4 \text{ }\mu\text{m}$  (on the right).

From the efficiencies  $Q_{abs}$  and  $Q_{sca}$  the absorption and scattering coefficients at the point of abscissa  $s$  can be obtained for a cloud of particles of non-uniform size:

$$\kappa_v(s) = \int_0^\infty \frac{3}{4} \frac{Q_{abs}(m(s), r, \nu)}{r} f_V(r, s) dr \quad (70)$$

$$\sigma_v(s) = \int_0^\infty \frac{3}{4} \frac{Q_{sca}(m(s), r, \nu)}{r} f_V(r, s) dr \quad (71)$$

where  $f_V(r, s) dr$  is the volume fraction, at the abscissa  $s$ , of the particles having a radius between  $r$  and  $r + dr$ .

To characterize anisotropic scattering due to particles, the scattering phase function is required. Its expression is:

$$\Phi_v(s, \vec{u}' \rightarrow \vec{u}) = \frac{1}{\sigma_v(s)} \int_0^\infty \frac{3}{4} \frac{Q_{sca}(m(s), r, \nu)}{r} \Phi_v(s, \vec{u}' \rightarrow \vec{u}, r) f_V(r, s) dr \quad (72)$$

where  $\Phi_v(s, \vec{u}' \rightarrow \vec{u}, r)$  is the scattering phase function given by analytical expressions from Mie theory for one size of particle. Figure 6 gives, for example, polar plots of the scattering phase function for two radii of alumina particle at  $10000 \text{ cm}^{-1}$ .

### Radiative property modeling

Since particles are often present simultaneously with gases it is more convenient to consider the same spectral discretization for both. Therefore, particle radiative properties have to be averaged over spectral bands  $\Delta\nu$ . However, contrary to the case of gas radiation, the spectral dynamics of particle absorption spectra is, in general, sufficiently weak to make the spectral correlations insignificant. In this situation the box model can be used and the model parameters are only the absorption and scattering coefficients and the phase function averaged over each spectral band.

Considering a radius discretization  $\Delta r_i$ , expression (70), for example, becomes:

$$\bar{\kappa}^{\Delta\nu}(s) = \sum_i \frac{1}{\Delta\nu} \int_{\Delta\nu} \int_{\Delta r_i} \frac{3}{4} \frac{Q_{abs}(m(s), r, \nu)}{r} f_V(r, s) dr d\nu \quad (73)$$

If the spectral bands are sufficiently narrow to consider the complex index  $m$  to be constant over each spectral band then the double integration can be reduced to only one, over the Mie parameter  $x$  [15]:

$$\bar{\kappa}^{\Delta\nu}(s) = \sum_i \frac{3}{4} f_{V,i}(s) \int_{\Delta x_i} \frac{Q_{abs}(m(s), x)}{x} g(x - x_i) dx \quad (74)$$

In this expression,  $f_{V,i}(s) \Delta r_i$  is the volume fraction of particles having a radius contained in the interval  $\Delta r_i$  and the Mie parameter  $x_i$  is equal to  $2\pi r_i \nu_c$  where  $\nu_c$  is the centre of the band  $\Delta\nu$  and  $r_i$  the centre of the interval  $\Delta r_i$ .  $g(x - x_i)$  is a distribution function describing the variation of  $x$  due to a particle size distribution in  $\Delta r_i$  and variation of  $\nu$  in  $\Delta\nu$ . Several forms of the  $g$  function have been used by various researchers. A modified gamma distribution is generally used. The choice of the parameters characterizing this distribution depends on the type of application.

Similarly, expressions (71) and (72) can be expressed as:

$$\bar{\sigma}^{\Delta\nu}(s) = \sum_i \frac{3}{4} f_{V,i}(s) \int_{\Delta x_i} \frac{Q_{sca}(m(s), x)}{x} g(x - x_i) dx \quad (75)$$

$$\bar{\Phi}^{\Delta\nu}(s, \vec{u}' \rightarrow \vec{u}) = \sum_i \frac{3}{4} \frac{f_{V,i}(s)}{\bar{\sigma}^{\Delta\nu}(s)} \times \int_{\Delta x_i} \frac{Q_{sca}(m(s), x)}{x} \Phi_x(s, \vec{u}' \rightarrow \vec{u}) g(x - x_i) dx \quad (76)$$

If the medium contains several types of particles (each type of particle being characterized by a different complex index of refraction) then the mixture radiative property calculation presents no difficulty because the radiative properties of the particles (absorption and scattering coefficients and phase function) are additive.

### Rayleigh scattering regime

If the particles are sufficiently small to assume the Mie parameter  $x$  to be very small compared to unity (for instance, primary soot particles or gas molecules satisfy the condition  $x \ll 1$ ), the radiative properties can be easily obtained by considering the appropriate limit of the general Mie equation solution: the Rayleigh scattering regime. In this case the Mie parameter dependences of the efficiencies are:  $Q_{abs} \propto x$  and  $Q_{sca} \propto x^4$ . As  $x \ll 1$ , scattering can be neglected in comparison to absorption.

In the Rayleigh regime the absorption efficiency is given by a simple analytical formula giving a simple expression for the absorption coefficient [23]:

$$\kappa_v(s) = \frac{36\pi n(s, \nu) k(s, \nu)}{(n^2(s, \nu) - k^2(s, \nu) + 2)^2 + (2n(s, \nu)k(s, \nu))^2} \nu f_V(s) \quad (77)$$

$$= A(s, \nu) \nu f_V(s)$$

where  $f_V(s)$  is the local volume fraction of particles and  $A(s, \nu)$  a function depending on the real and imaginary parts of the local complex index of the particles. Thus, for sufficiently narrow spectral bands, as previously discussed, the average absorption coefficient is expressed as:

$$\bar{\kappa}^{\Delta\nu}(s) = A(s, \nu_c) \nu_c f_V(s) \quad (78)$$

### Available models and typical applications

The development of radiative property models, presented in the two previous parts, requires data such as spectroscopic databases for gases or complex indices of refraction for particles. The following sections give a description of the gas and particle radiative property models, implemented in the radiation solvers (ASTRE and REA) developed at Onera. In particular, the available models for two main applications, radiation in flames (combustion) and radiation in plasmas (atmospheric entry problems), are presented. The majority of gas radiative property models have been developed by the EM2C laboratory or in collaboration with them. In this case, the model development is based on HTGR spectroscopic databases [24].

## Radiation in combustion applications

Flames emit, scatter and absorb radiation mainly in the infrared spectral range. The participating medium is in general constituted of combustion gases and particles such as: (i)  $CO_2$ ,  $H_2O$ ,  $CO$  molecules, and soot particles, for air breathing combustion (laboratory flames or combustion chamber), (ii)  $CO_2$ ,  $H_2O$ ,  $CO$ ,  $HCl$  molecules, and alumina particles, for aluminized solid propellant combustion.

### Air breathing combustion at atmospheric pressure

For atmospheric pressure applications, the spectral dynamics of the gas absorption coefficient is so significant that accurate radiative transfer prediction needs a spectrally correlated model.

For the treatment of  $CO_2$  and  $H_2O$  radiation in the infrared spectral range, a CK model is used. Model parameters have been generated by Soufiani and Taine [33] for applications in the 300-2500 K temperature range. A seven-point quadrature has been used (the same for the two species and for all the spectral bands). The pseudo-monochromatic absorption coefficient  $k_A(G_i, s)$  is given by the following expression (subscript A represents  $CO_2$  or  $H_2O$  species):

$$k_A(G_i, s) = x_A(s) p_{atm} [T(s) Q_A(T(s))]^{-1} k_A^*(G_i, s) \quad (79)$$

where  $Q_A(T(s))$  is the partition function of the absorbing molecule at the temperature  $T(s)$  at the abscissa  $s$ . The parameters  $k_A^*(G_i, s)$  are tabulated as a function of  $T$  (a set of 16 temperature values). In the case of  $H_2O$  they are also tabulated versus  $x_{H_2O}$  (a set of 5 values) to take into account the strong dependence of line broadening on the molar fraction  $x_{H_2O}$ . The useful wavenumber range (150-9300  $cm^{-1}$ ) has been divided into 44 spectral bands with a variable width for  $H_2O$ .  $CO_2$  absorbs radiation in only 17 of these bands. For an RTE formulation in terms of transmissivity, the model is constituted of 308 spectral points ( $44 \times 7$ ) whereas 1022 ( $17 \times 7 \times 7 + (44-17) \times 7$ ) spectral points are necessary for an RTE formulation in terms of the absorption coefficient due to the double quadrature required in the overlapping bands.

In addition, it may be necessary to take soot particle radiation into account but soot particle aggregation is not considered. As primary soot particles are very small spherical particles, expressions valid for the Rayleigh regime can be used and scattering can be neglected. To compute the average absorption coefficient expression (78) has been simplified to the following [35], [37]:

$$\bar{\kappa}^{\Delta\nu}(s) = 5.5\nu_c f_\nu(s) \quad (80)$$

due to lack of information on values, of real and imaginary parts of the soot refraction index, over the whole spectrum and as a function of soot composition and temperature.

For example, the sooty turbulent ethylene jet flame experimentally studied by Coppalle and Joyeux [5] has been simulated [37], [38]. The CK model, for the gas mixture, associated with equation (80), for soot particles, has been used to compute radiative transfer in the flame. Figure 7 shows the TRI effect (see Box 1) on the radiative power field.

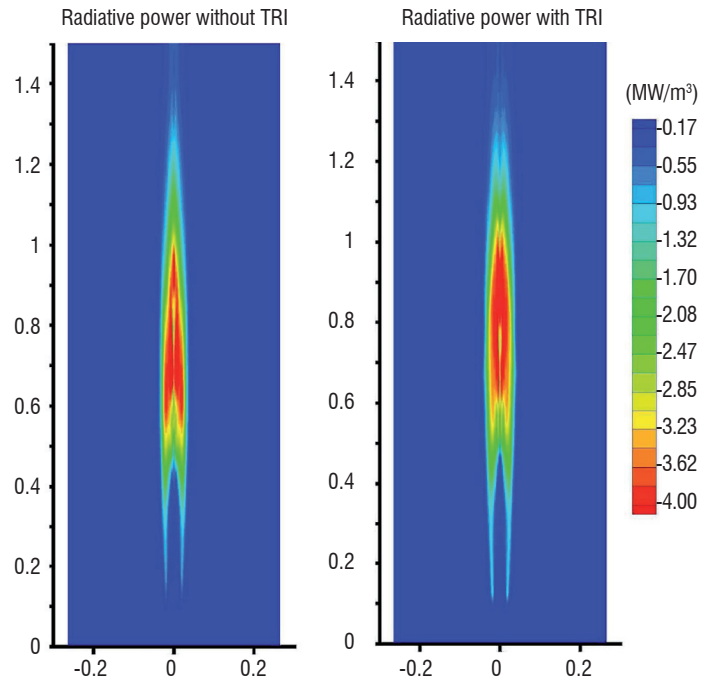


Figure 7 - Radiative power without (on the left) and with (on the right) turbulence-radiation interaction in a sooty turbulent ethylene jet flame [37], [38].

### Air breathing combustion at high pressure

At high pressure, due to the collision broadening effect, the absorption spectra display smoother spectral dynamics than those at atmospheric pressure. In this case, the spectral correlation effect is weak and the box model can be used to model the gas radiative properties. Such an approach has been used by Pierrot [25] to deal with  $CO_2$ ,  $H_2O$  and  $CO$  radiation at high pressure in an aeronautical combustion chamber. This model is called the High Pressure Box Model (HPBM). The model parameters are the reduced absorption coefficients  $\bar{\kappa}$  which are extracted from the SNB model parameters developed by Soufiani and Taine [33]. The temperature and spectral ranges considered are 700-2500 K and 150-9300  $cm^{-1}$ . The temperature grid is composed of 10 values with a constant step equal to 200 K. The spectral range is divided into 367 bands of constant width equal to 25  $cm^{-1}$ . This model version is called HPBM 367.

To reduce CPU times, Pierrot has enlarged the band width, grouping bands with similar radiative properties. The new model is then constituted of 26 bands (HPBM 26) and gives similar results in terms of accuracy at high pressure.

If the configuration studied produces a significant quantity of soot particles, their radiation can be taken into account in the same way as for combustion at atmospheric pressure (see previous subsection).

Figure 8 shows a typical application result. Radiative transfer has been calculated in a combustion chamber using the HPBM 26 model for  $CO_2$ ,  $H_2O$ ,  $CO$  radiation and equation (80) for soot particle radiation. Negative values indicate that local emission is greater than local absorption and vice versa.

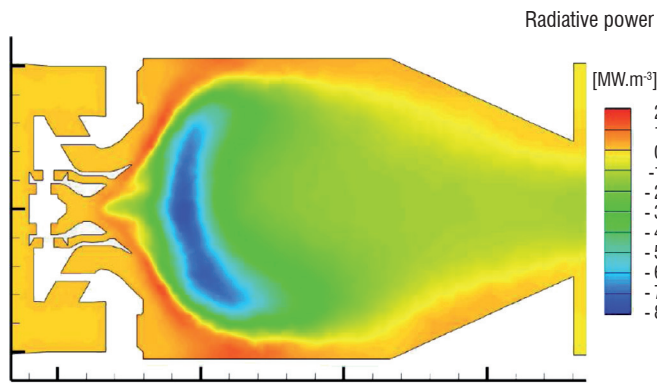


Figure 8 - Radiative power field in a combustion chamber at 10 bar, fitted with a multipoint injector.

### Combustion in an aluminized solid propellant rocket engine

In a solid propellant motor, temperatures up to 3600 K, and pressure between 50 to 150 bar, are reached in the combustion chamber. In this situation, radiative transfer in the chamber can be calculated without taking into account spectral correlation, for the same reasons as those given in the previous subsection.

For the gas radiative property model, the box model, developed by Duval [11], with consideration of the  $CO_2$ ,  $H_2O$ ,  $CO$  and  $HCl$  species, is used. The  $\bar{k}$  parameters are tabulated for a 300-3500 K temperature range, and for 43 spectral bands of variable width between 150 and 9300  $cm^{-1}$ .

The radiative properties of alumina particles are calculated using Mie theory. Absorption and scattering coefficients and phase function are computed on the assumption that the distribution function  $g$  in equations (74), (75) and (76) is a Gaussian function. In general, several classes of particle sizes are used (typically between one and five samples) to describe particle size distribution. The complex refraction index of alumina is modeled as a function of wavenumber and temperature in accordance with the expressions given by Dombrovsky [9] or Joumani [15].

### Radiation in atmospheric (re-)entry applications

Two SNB models for atmospheric (re-)entry applications have been implemented: one for the Martian atmosphere at Local Thermodynamic Equilibrium (LTE) [28], [31] and the other for the Earth's atmosphere at non-LTE conditions [17].

#### Martian atmosphere entry

Rivière et al. [28] have modeled, with an SNB approach, the infrared radiative properties of  $CO/CO_2$  mixtures between 500 and 5000  $cm^{-1}$  for temperature and pressure ranges limited to 4000 K and 100 Pa respectively. For these thermophysical conditions, line broadening is mainly due to the Doppler effect. Consequently the model parameters are  $\bar{k}$  and  $\beta_D$ . Of the different line intensity distributions which have been tested, the exponential distribution was used, giving:

$$\frac{\overline{W_D}}{\delta} = \overline{\beta_D} E \left( \frac{\overline{k u}}{\overline{\beta_D}} \right) \quad (81)$$

where  $E(y)$  is defined as:

$$E(y) = \frac{1}{\sqrt{\pi}} \int_{-\infty}^{+\infty} \frac{y \exp(-x^2)}{1 + y \exp(-x^2)} dx \quad (82)$$

Parameters have been generated from LBL calculations using a Voigt profile: the  $\bar{k}$  parameters have been obtained from spectra averaged over spectral bands and the  $\overline{\beta_D}$  parameters have been adjusted on the theoretical curve of growth with a least-squares fit.  $CO$  and  $CO_2$  parameters have been generated for a temperature grid between 1000 and 4000 K with a 200 K step. For the spectral grid, spectral bands of 25  $cm^{-1}$  were considered.

Figure 9 shows an example of the application of the SNB model for a  $CO_2/CO$  mixture. Radiative flux has been calculated on the surface of a Martian entry vehicle (AEROFAST demonstrator [19]) for a trajectory point.

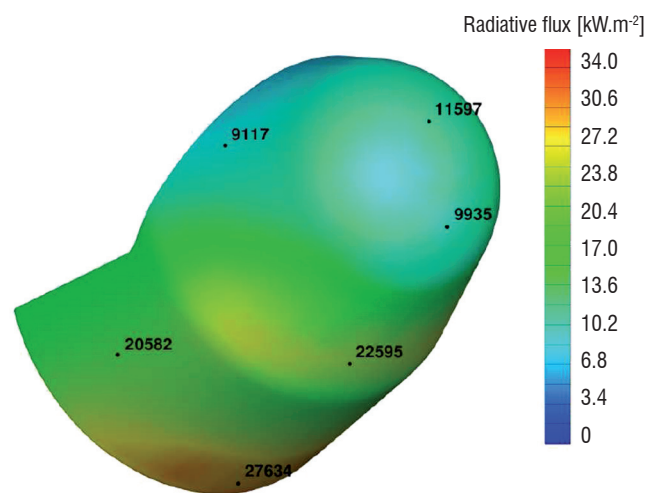


Figure 9 - Radiative flux on the surface of a Martian entry vehicle with a biconic shape.

### Earth's atmosphere re-entry

Lamet et al. [18] have developed a hybrid model (SNB-box-LBL) of the radiative properties in non-LTE  $N_2 - O_2$  plasmas such as those encountered on Earth re-entry. For this kind of non-LTE application, a multi-temperature approach is generally used. Transrotational ( $T$ ) and electrovibrational/free electron ( $T_{ve}/T_e$ ) temperatures can reach 50000 K and 25000 K respectively, and pressure conditions are about a few bar in the shock layer. Given these temperatures, the spectral interval considered is 1000  $cm^{-1}$  to 200000  $cm^{-1}$ .

An SNB model was formulated for optically thick (in re-entry applications) electronic systems of diatomic molecules involved in air plasmas ( $N_2$  VUV systems,  $NO$  UV systems, and  $O_2$  Schumann-Runge system). Considering the thermophysical conditions, the lines have a Voigt profile. The model parameters are  $\bar{k}$ ,  $\overline{\beta_D}$  and  $\overline{\beta_L}$ . Of the different line intensity distributions which have been tested, the exponential distribution and the tailed-inverse exponential distribution have been selected for the Doppler and Lorentz contributions respectively, giving:

$$\frac{\overline{W_D}}{\delta} = \overline{\beta_D} E\left(\frac{\overline{ku}}{\overline{\beta_D}}\right) \quad (83)$$

$$\frac{\overline{W_L}}{\delta} = 2\overline{\beta_L} \left( \sqrt{1 + \frac{\overline{ku}}{\overline{\beta_L}}} - 1 \right) \quad (84)$$

where  $E(y)$  is given by relation (82).

The parameters have been generated from line by line calculations in the Voigt regime: the parameters  $\overline{k}$  have been obtained by averaging absorption spectra over each spectral band and the parameters  $\overline{\beta_D}$  and  $\overline{\beta_L}$  have been adjusted to fit expression (63) to the theoretical curves of growth. Moreover, the parameters  $\overline{\eta} / \overline{\kappa}$ , present in relation (20), have been calculated to take into account non-equilibrium conditions. In fact, in non-LTE conditions, this ratio, which can have significant spectral dynamics, is not equal to the Planck function. Moreover, it has been checked that there is no spectral correlation

problem between  $\overline{\eta} / \overline{\kappa}$  and  $\overline{\tau}$ . Parameters have been tabulated for a band width equal to  $1000 \text{ cm}^{-1}$  and a two temperature grid  $(T, T_{ve})$ .

For continua and optically thin molecular systems, a box model has been used. For the latter's contribution, mean emission and absorption coefficients have been tabulated on the same two-temperature grid. For continua, mean emission and absorption coefficients have been tabulated as functions of  $T_e$  in the range 500-25000 K [16]. Finally, for atomic lines, the line by line approach has been retained due to the unsatisfactory results obtained with an SNB model. For this contribution, Stark broadening is also taken into account since this kind of broadening is generally significant in Earth re-entry conditions (ionized plasma above 10000 K). Half-widths at half-maximum are calculated as explained in Ref. [27].

This hybrid modeling has been used to calculate, for a trajectory point, the radiative flux at the surface of an Earth re-entry probe (FIRE II [2], see Figure 10) due to radiative transfer in the shock layer. The Monte Carlo methodology has been used with 20 and 200 millions rays [17] ■

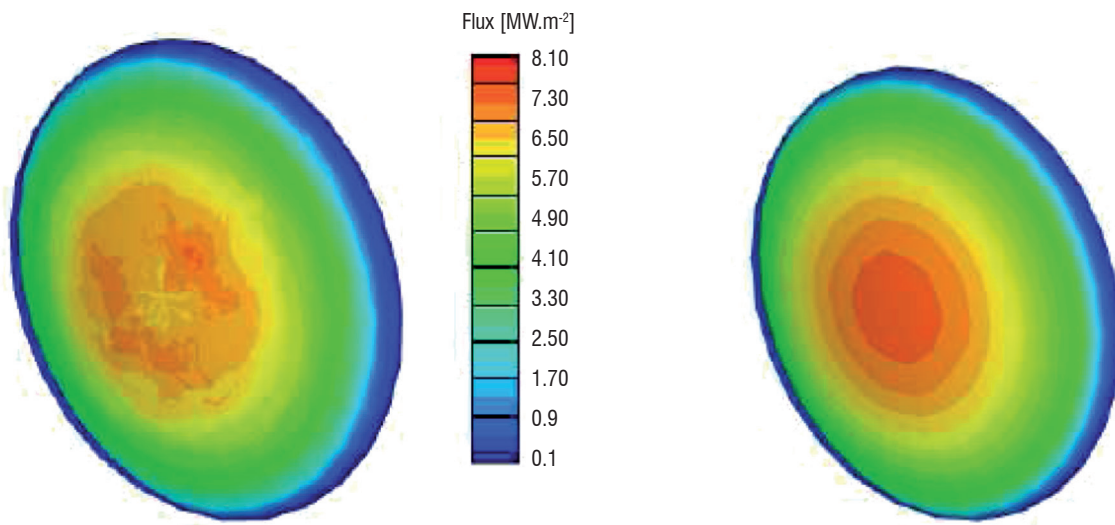


Figure 10 - Radiative flux on the front shield of an Apollo type vehicle (FIRE II [2]). Results obtained for a trajectory point with a Monte Carlo method with 20 millions rays (on the left) and 200 millions rays (on the right) [17].

### Acknowledgements

The authors would like to thank Francis Dupoirieux and Luc-Henry Dorey for their contributions to the development of the radiative transfer solvers. The authors also thank the EM2C laboratory of Ecole Centrale Paris for providing gas radiative property models.

### References

- [1] C. F. BOHREN and D. R. HUFFMAN - *Absorption and Scattering of Light by Small Particles*. John Wiley, New York, 1983.
- [2] D. L. CAUCHON - *Radiative Heating Results from the Fire II Flight Experiment at a Reentry Velocity of 11.4 Kilometers per Second*. Technical Report NASA TM X-1402, 1972.
- [3] S. CHAUVEAU - *Constitution de bases de données spectroscopiques relatives à un plasma d'air. Application au calcul de transfert radiatif*. Thèse de doctorat, École Centrale Paris, 2001.
- [4] P. J. COELHO - *Numerical Simulation of the Interaction Between Turbulence and Radiation in Reactive Flows*. Progress in Energy and Combustion Science, Vol. 33, pp. 311-383, 2007.
- [5] A. COPPALLE and D. JOYEUX - *Temperature and Soot Volume Fraction in Turbulent Diffusion Flames: Measurements of Mean and Fluctuating Values*. Combustion and Flame, Vol. 96, pp. 275-285, 1994.
- [6] A. REFLOCH, B. COURBET, A. MURRONE, P. VILLEDIEU, C. LAURENT, P. GILBANK, J. TROYES, L. TESSÉ, G. CHAINERAY, J.B. DARGAUD, E. QUÉMERIS and F. VUILLOT, - CEDRE Software. Aerospace Lab Issue 2 March 2011.
- [7] M.K. DENISON and B.W. WEBB - *The Spectral Line-Based Weighted-Sum-of-Gray-Gases Model in Nonisothermal Nonhomogeneous Media*. Journal of Heat Transfer, Vol. 117, pp. 359-365, 1995.

- [8] K. V. DESHMUKH, M. F. MODEST and D. C. HAWORTH – *Direct Numerical Simulation of Turbulence-Radiation Interactions in a Statistically One-Dimensional Nonpremixed System*. Journal of Quantitative Spectroscopy and Radiative Transfer, Vol. 109, pp. 2391-2400, 2008.
- [9] L. A. DOMBROVSKY - *On Possibility of Determination of Disperse Composition of Two-Phase Flow Using Light Scattering under Small Angles*. Teplof. Vys. Temp, 1982.
- [10] F. DUPOIRIEUX, L. TESSÉ, A. AVILA and J. TAINE - *An Optimized Reciprocity Monte Carlo Method for the Calculation of Radiative Transfer in Media of Various Optical Thicknesses*. International Journal of Heat and Mass Transfer, Vol. 49, pp. 1310-1319, 2006.
- [11] R. DUVAL - *Transferts radiatifs dans les moteurs à propergol solide*. Thèse de doctorat, École Centrale Paris, 2002.
- [12] J. T. FARMER, J. R. HOWELL - *Monte Carlo Strategies for Radiative Transfer in Participating Media*. Advances in Heat Transfer, Vol. 31, pp. 1-97, 1998.
- [13] R.M. GOODY and Y.L. YUNG - *Atmospheric Radiation*. Oxford Univ. Press, New York, 1989.
- [14] H.C. HOTTEL and A.F. SAROFIM - *Radiative Transfer*. McGraw-Hill, New York, 1967.
- [15] Y. JOUMANI - *Transferts radiatifs dans les moteurs à propergol solide*. Thèse de doctorat, Université de Valenciennes et du Hainaut Cambresis, 2001.
- [16] J.-M. LAMET, Y. BABOU, PH. RIVIÈRE, M.-Y. PERRIN and A. SOUFIANI - *Radiative Transfer in Gases Under Thermal and Chemical Nonequilibrium Conditions: Application to Earth Atmospheric Re-entry*. Journal of Quantitative Spectroscopy and Radiative Transfer, Vol. 109, Issue 2, pp. 235-244, January 2008.
- [17] J.-M. LAMET - *Transferts radiatifs dans les écoulements hypersoniques de rentrée atmosphérique terrestre*. Thèse de doctorat, École Centrale Paris, 2009.
- [18] J.-M. LAMET, PH. RIVIÈRE, M.-Y. PERRIN and A. SOUFIANI - *Narrow-Band Model for Nonequilibrium Air Plasma Radiation*. Journal of Quantitative Spectroscopy and Radiative Transfer, Vol. 111, Issue 1, pp. 87-104, January 2010.
- [19] G. LEPLAT, J.-L. VÉRANT and J.-M. LAMET - *AEROFast European Collaborative Project: Computational Aerothermodynamic Analysis of a Biconic Vehicle Design for Mars Aerocapture*. Technical Report Onera n° RT 3/14925, 2010
- [20] C.B. LUDWIG, W. MALKMUS, J.E. REARDON and J.A.L. THOMSON - *Handbook of Infrared Radiation from Combustion Gases*. Technical Report NASA SP-3080, Washington DC, 1973.
- [21] R. S. MEHTA, D. C. HAWORTH and M. F. MODEST - *Composition PDF/Photon Monte Carlo Modeling of Moderately Sooting Turbulent Jet Flames*. Combustion and Flame, Vol. 157, pp. 982-994, 2010.
- [22] R. S. MEHTA, M. F. MODEST and D. C. HAWORTH - *Radiation Characteristics and Turbulence-Radiation Interactions in Sooting Turbulent Jet Flames*. Combustion Theory and Modelling, Vol. 14, N° 1, pp. 105-124, 2010.
- [23] M. F. MODEST - *Radiative Heat Transfer*. Academic Press, 2nd edition, 2003.
- [24] M.-Y. PERRIN, PH. RIVIÈRE and A. SOUFIANI - *Radiation Database for Earth and Mars Entries*. Lecture Series on Non-equilibrium Gas Dynamics, from Physical Models to Hypersonic Flights. (RTO-AVT-VKI), 2008.
- [25] L. PIERROT - *Développement, étude critique et validation de modèles de propriétés radiatives infrarouges de CO<sub>2</sub> et H<sub>2</sub>O à haute température. Application au calcul des transferts dans des chambres aéronautiques et à la télédétection*. Thèse de doctorat, École Centrale Paris, 1997.
- [26] PH. RIVIÈRE, A. SOUFIANI, M. Y. PERRIN, H. RIAD and A. GLEIZES - *Air Mixture Radiative Property Modeling in the Temperature Range 10,000-40,000 K*. Journal of Quantitative Spectroscopy and Radiative Transfer, Vol. 56, pp. 29-45, 1996.
- [27] PH. RIVIÈRE - *Systematic Semi-Classical Calculations of Stark Broadening Parameters of NI, OI, NII, OII Multiplets for Modelling the Radiative Transfer in Atmospheric Air Mixture Plasmas*. Journal of Quantitative Spectroscopy and Radiative Transfer, Vol. 73, pp. 91-110, 2002.
- [28] PH. RIVIÈRE, M.-Y. PERRIN and A. SOUFIANI - *Line-by-Line and Statistical Narrow-Band Calculations of Radiative Transfer in Some Atmospheric Entry Problems*. In Proceedings of the First International Workshop on Radiation of High Temperature Gases in Atmospheric Entry, Lisbon, pp. 189-196. ESA SP-533, 2003.
- [29] PH. RIVIÈRE. Private Communication, 2010.
- [30] M. ROGER, P. J. COELHO and C. B. DA SILVA – *The Influence of the non-Resolved Scales of Thermal Radiation in Large Eddy Simulation of Turbulent Flows: a Fundamental Study*. International Journal of Heat and Mass Transfer, Vol. 53, pp. 2897-2907, 2010.
- [31] O. ROUZAUD, L. TESSÉ, T. SOUBRIÉ, A. SOUFIANI, PH. RIVIÈRE and D. ZEITOUN - *Influence of Radiative Heating on a Martian Orbiter*. Journal of Thermophysics and Heat Transfer, Vol. 22, N° 1, pp. 10-19, January-March 2008.
- [32] R. SIEGEL and J. R. HOWELL – *Thermal Radiation Heat Transfer*. 4<sup>th</sup> edition, Taylor and Francis, New York, 2002.
- [33] A. SOUFIANI and J. TAINE - *High Temperature Gas Radiative Property Parameters of Statistical Narrow-Band Model for H<sub>2</sub>O, CO<sub>2</sub> and CO, and Correlated-K Model for H<sub>2</sub>O and CO<sub>2</sub>*. International Journal of Heat and Mass Transfer, Vol. 40, pp. 987-991, 1997.
- [34] J. TAINE and A. SOUFIANI - *Gas IR Radiative Properties: From Spectroscopic Data to Approximate Models*. Advances in Heat Transfer, Vol. 33, pp.295-414, 1999.
- [35] L. TESSÉ - *Modélisation des transferts radiatifs dans les flammes turbulentes par une méthode de Monte Carlo*. Thèse de doctorat n°2001-34, École Centrale de Paris, 2001.
- [36] L. TESSÉ, F. DUPOIRIEUX, B. ZAMUNER and J. TAINE - *Radiative Transfer in Real Gases Using Reciprocal and Forward Monte Carlo Methods and a Correlated-k Approach*. International Journal of Heat and Mass Transfer, Vol. 45, pp. 2797-2814, 2002.
- [37] L. TESSÉ, F. DUPOIRIEUX and J. TAINE - *Monte Carlo Modeling of Radiative Transfer in a Turbulent Sooty Flame*. International Journal of Heat and Mass Transfer, Vol. 47, pp. 555-572, 2004.
- [38] L. TESSÉ, S. AVILA, F. DUPOIRIEUX and J. TAINE - *Coupled Modeling of Aerothermochemistry, Soot Formation and Radiation in a Turbulent Diffusion Flame*. In Proceedings of the 13<sup>th</sup> International Heat Transfer Conference (IHTC-13), Sydney, Australia, August 13-18, 2006.
- [39] S. J. YOUNG - *Nonisothermal Band Model Theory*. Journal of Quantitative Spectroscopy and Radiative Transfer, Vol. 18, pp.1-28, 1977.

## Acronyms

CFD (Computational Fluid Dynamics)  
 CG (Curtis-Godson)  
 CK (Correlated-K)  
 CPU (Central Processing Unit)

DNS (Direct Numerical Simulation)  
 DOM (Discrete Ordinates Method)  
 HWHM (Half-Width at Half-Maximum)  
 HPBM (High Pressure Box Model)

LBL (Line-By-Line)  
LES (Large Eddy Simulation)  
LTE (Local Thermodynamic Equilibrium)  
OTFA (Optically Thin Fluctuation Approximation)  
PDF (Probability Density Function)

RANS (Reynolds-Averaged Navier-Stokes)  
RTE (Radiative Transfer Equation)  
SNB (Statistical Narrow-Band)  
TRI (Turbulence-Radiation Interaction)

## AUTHORS

---



**Lionel Tessé** received his Ph.D. degree, in energetics and the physics of transfer, from the École Centrale Paris in 2001. For his Ph.D. he worked on the modeling, using the Monte Carlo method, of radiative transfer in a turbulent sooty flame, focusing on the interaction between turbulence and radiation. He has been a research scientist at Onera, in the Applied and Fundamental Energetics Department, since 2001. His research topics include the modeling and simulation of radiative transfer in aeroengine combustors, solid propellant rocket motors and hypersonic flows occurring during atmospheric (re-)entries. He is in charge of the development of the ASTRE code (Monte Carlo) and is involved in the development of the REA code (DOM), both codes dedicated to radiative transfer computations.



**Jean-Michel Lamet** graduated from the École Supérieure d'Ingénieurs de Poitiers in 2005 and received his Ph.D. degree from École Centrale Paris in 2009. For his Ph.D. he worked on the radiative transfer in atmospheric re-entry hypersonic flows. He now holds a position of research scientist in the Onera Applied and Fundamental Energetics Department. His activity includes the modeling and simulation of radiative transfer in combustion chambers and hypersonic flows. He is involved in the development of the ASTRE and REA codes dedicated to radiative transfer.

# Space Discretization Methods

B. Courbet, C. Benoit, V. Couaillier,  
F. Haider, M.C. Le Pape, S. Péron

(Onera)

E-mail: : bernard.courbet@onera.fr

Onera codes for CFD and Energetics are mostly based on a finite volume methodology. Within this common framework, a wide variety of space discretization techniques are available depending on the required degree of precision, on the kind of mesh and on the application domain. This paper describes three particular topics which are central to the codes developed at Onera. The first section discusses cell-centered and cell-vertex techniques in the context of structured meshes and their extension to unstructured zones. The second part shows how efficient third order schemes can be implemented on Cartesian and curvilinear overlapping grids. Finally, the third section presents a Muscl-type discretization methodology currently used on general polyhedral meshes, with indications on its generalization to high-order precision.

## Introduction

This paper presents some of the space discretization methods used in the codes developed at Onera for Fluid Dynamics and Energetics ( see [6] [33] for overall descriptions of ElsA and CEDRE and [34] [37] for examples of applications). All the other numerical and modelization issues will be presented in separate papers; for instance time integration will be found in [28].

Many other projects on innovative methods are underway at Onera and may be a future source of progress for industrial and research codes [3] [25].

Both codes are based on a finite volume methodology [19], with concerns focused on common topics, such as:

- Precision is an essential quality of numerical results. Standard second order interpolation procedures may not be sufficient for applications such as acoustics or Large Eddy Simulations, and several higher order techniques under development or already in application will be described;
- Stability and robustness is an essential requirement for an intensive use on a large number of physical configurations;
- Computational efficiency (memory requirements and execution time) is important as complex simulations are very demanding in terms of computer resources;
- Geometric complexity is increasing in everyday research and industrial applications. Depending on the type of application, structured or non-structured meshes can be used to deal with this issue. Even within the restrictive framework of space discretization, methods cannot be described in detail and only a few important themes have been selected for this presentation.

The remainder of this paper consists in three sections:

- The first one, Finite volume cell centered discretization for MB-structured and hybrid meshes (V. Couaillier, M.C. Le Pape) discusses basic choices for finite volume space discretization on hexahedral meshes including non-structured zones;
- The second section, Third-order scheme in an overset grids framework (C. Benoit, S.Péron) shows how geometric complexity can be taken into account through overlapping structured or Cartesian meshes while maintaining third order precision;
- The last section, Finite volume techniques on polyhedral meshes (B. Courbet, F.Haider) describes the Muscl-type space discretization on general non-structured meshes implemented in CEDRE. These methods can be applied to any kind of polyhedral cells and are thus very well suited to complex geometries. The paper also shows how third-or fourth order interpolation is possible in this framework.

The methods described in the two first sections have been implemented in ElsA, whereas the third part is related to CEDRE.

## Finite volume cell centered discretization for mb-structured and hybrid meshes

### Introduction

This part summarizes some aspects of finite volume space discretization in multi-block structured and hybrid solvers developed at Onera, especially for curvilinear meshes adapted to industrial type applications, that is to say complex mesh topologies. As this presentation is far from exhaustive in terms of the possibilities of a finite volume discretization scheme, we refer the reader to Fletcher [14], Hirsch [20],

Peyret and Taylor [32], for instance, for more detailed presentations of the computational methods for Fluid Dynamics in curvilinear meshes.

Generally speaking, the extension to a multidimensional scheme of 1D numerical schemes is not straightforward. In fact, for a given method defined in 1D, several parameters can vary in 2D and 3D, for example:

- The mesh topology, which is a main point for the numerical method implementation, can be based on different approaches: Mono-domain or multi-domain structured, unstructured, structured/unstructured hybrid. Moreover, adaption techniques may be considered: mesh deformation, mesh motion, local refinement, Automatic Mesh Refinement (AMR).
- The discretisation approach : Finite Differences, Finite Volumes, Finite Elements.

If we restrict the method to finite volume schemes considered in this paper, we still have to specify the unknown localization (numerical field): Cell vertex (control volume = mesh cell + node redistribution), Node centered (control volume = dual mesh cell centered on a mesh node), Cell centered (control volume = mesh cell). The following paragraph is devoted to highlighting some of the choices which were made in elsA. software [7].

### Cell centered FV in Multi-block structured meshes

#### Lax-Wendroff Scheme

Several extensions of the Lax-Wendroff scheme have been proposed in multi-space-dimensions, for the Euler and the Navier-Stokes equations, differing by their non-linear properties and their molecular dependence. For more details concerning these properties, see the complete study done by Lerat [26].

One original formulation of the Lax-Wendroff scheme associated with an efficient multi-grid method has been proposed by Ni for Euler and Navier-Stokes turbomachinery simulation [31], and then used by several authors (see for instance [10] or [15]). This formulation, which is a cell-vertex approach, is very easy to implement but does not preserve the good numerical properties of the original Lax-Wendroff scheme extended on a curvilinear mesh by Lerat [26] (the Ni's scheme is not dissipative in the sense of Kreiss).

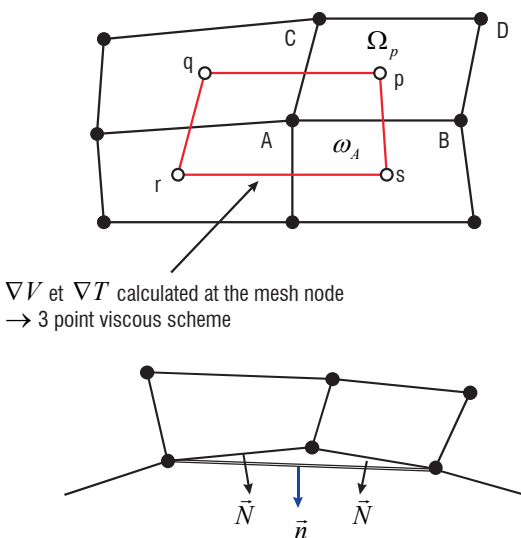


Figure 1 - Lax-Wendroff-Ni scheme

Figure 1 presents the two types of control volumes used in the Lax-Wendroff-Ni scheme for the space-discretization, the mesh cell control volume and the dual cell control volume, as well as the two types of surface normals used for the treatment of the boundary conditions. The time derivatives are replaced by space derivatives by using the following relation:

$$w_A^{n+1} = w_A^n - \Delta t \bar{\nabla} \cdot (F_C - F_V)_A^n + \frac{\Delta t^2}{2} \bar{\nabla} \cdot (A \bar{\nabla} \cdot (F_C - F_V))_A^n \quad (1)$$

The gradients appearing in the viscous terms are evaluated at the nodes by using an integral formula based on a dual control volume:

$$\bar{\nabla} \bar{V}_A = \frac{1}{V(\omega_a)} \int_{\partial \omega_a} \bar{V} \otimes \bar{n} ds \quad (2)$$

Then the first order term is evaluated at the centers of the mesh cells:

$$\bar{\nabla} \cdot (F_C - F_V)_p = \frac{1}{V(\Omega_p)} \int_{\partial \Omega_p} (F_C - F_V) ds \quad (3)$$

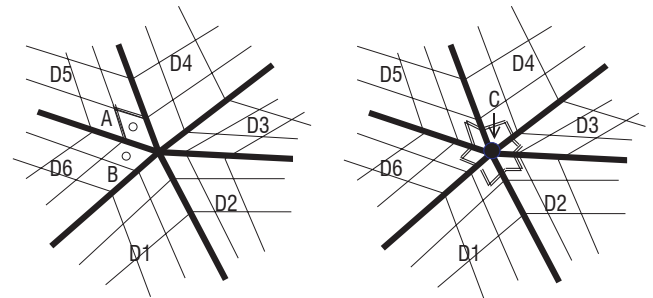
and then distributed at the nodes by using an arithmetic averaging

$$\bar{\nabla} \cdot \varphi_A = \frac{1}{4} \sum_{j=p,q,r,s} \bar{\nabla} \cdot \varphi_j \quad \text{or a volume averaging (Hall approach).}$$

From the first order terms approximated at the cell centers, the second order term can be evaluated directly at the nodes by using a relation analogous to (2), or by using the distribution formulae introduced by Ni for his multi-grid scheme. The artificial dissipation terms are calculated following each mesh direction.

#### Jameson scheme

This scheme is in fact the most popular scheme used in the CFD community and many 3D research or industrial structured codes developed for complex configurations are based on this approach [21]. Nevertheless, among these codes, two main approaches exist: the node centered approach (for instance [8] [22]) and the cell centered approach (see for instance [5], [40]), with various implementations of the original numerical dissipation adapted to the type of the mesh. The cell vertex approach seems to be more accurate near bodies for the Euler simulations, but this advantage disappears for Navier-Stokes simulations due to the mesh refinement. The main advantage of the cell centered approach is that, in a multi-domain structured approach, there is no problem of multiple point matching (Figure 2-a) or multiple boundary conditions at a given point, and this leads to a robust method for solving complex geometrical configurations. However, in the cell vertex approach, a correct treatment for a point located at a several domain intersection is possible (Figure 2-b), but more difficult to implement in a general approach for structured codes because it depends on the number of domains, as presented in figure 3.



a) Cell centered approach      b) Cell vertex approach  
Figure 2 - multi-domain interface treatment

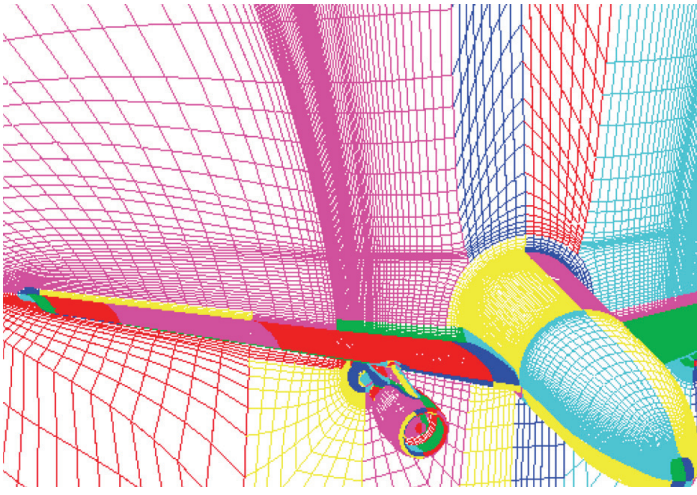


Figure 3 - Wing/Fuselage/Pylon/engine configuration – Multi-block structured mesh

The Jameson scheme is presented below in its cell centered version:

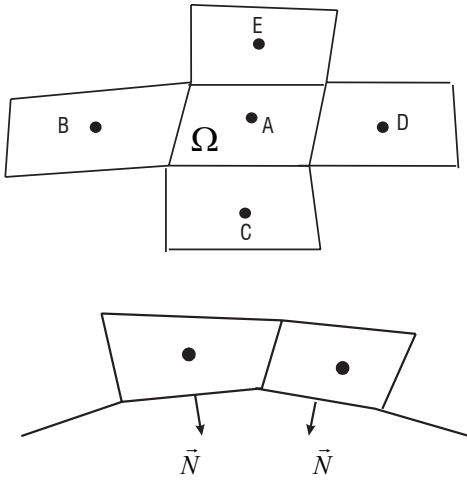


Figure 4 - Cell centered discretization for the Jameson scheme

Figure 4 presents an inner cell control volume used for the space-discretization of the cell centered Jameson scheme, and a boundary cell control volume.

At each step of the Runge-Kutta time-stepping, the solution is updated as follows:

$$w_A^{(p+1)} = w_A^{(0)} - \Delta t \bar{\nabla} \cdot (F_C^{(p)} - F_V^{(0)})_A \quad (4)$$

The gradient of the velocity is discretized using a mean formula :

$$\bar{\nabla} \bar{V}_A = \frac{1}{V(\Omega_A)} \int_{\bar{\Omega}_A} \bar{V} \otimes \bar{n} ds : \text{viscous term calculation} \quad (5)$$

Then the divergence term can be estimated by using the same type of mean formula:

$$\bar{\nabla} \cdot (F_C - F_V)_A = \frac{1}{V(\Omega_A)} \int_{\bar{\Omega}_A} (F_C - F_V) \bar{n} ds$$

where a space centered discretization is performed:

$$\int_{\bar{\Omega}_{AD}} (F_C - F_V) \bar{n} ds = \frac{1}{2} [(F_C - F_V)_A + (F_C - F_V)_D] \int_{\bar{\Omega}_{AD}} \bar{n} ds \quad (6)$$

As for the Lax-Wendroff scheme, the artificial dissipation terms are calculated following each mesh direction.

In the space discretization presented before, the way used for discretizing the viscous term, which is very easy to implement because only one type of control volume is used, corresponds to a five-point scheme. This leads to decoupling odd and even points, this being a drawback from a numerical point of view, because additional artificial dissipation is required even in the viscous region as boundary layers. This can play a significant role when looking at very accurate solutions for basic configurations.

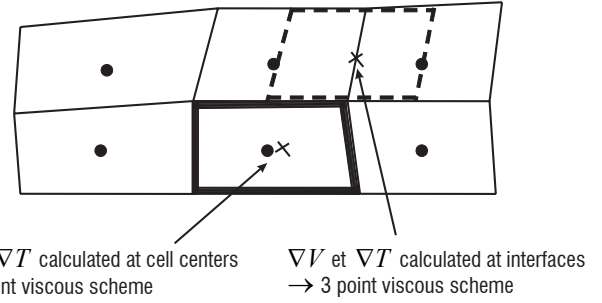


Figure 5 - Viscous term discretization

Then, a three-point scheme (per mesh direction) can be obtained by using staggered cells in each space direction as presented in figure 5, for which the gradients are evaluated at the face centers. In that case, odd and even points are coupled and no artificial dissipation is required in the viscous region, but this approach is more expensive and more difficult to implement in a multi-domain code. Nevertheless, from a practical point of view and for complex configurations in which meshes are not regular, the five-point scheme is widely used.

### FV Hybrid solvers on composite meshes

Numerical methods used for the simulation of three-dimensional compressible viscous flows have reached a high level of validity and efficiency and are used as a basic tool for designing turbomachinery and aircraft components. However, most of these methods are based on multi-domain structured grid solvers, which imply a time-consuming mesh generation phase, especially when complex industrial geometries are concerned, and also restrains the application of automatic grid adaptation technologies. On the other hand, the unstructured mesh approach enables the use of automatic mesh generators even on complex geometries, and increases the flexibility for mesh adaptation strategies. A new numerical procedure is developed for the resolution of the three-dimensional Euler and Reynolds-Averaged Navier-Stokes equations. It allows for the implementation in a single global solver of unstructured and hybrid structured-unstructured grids in order to combine as much as possible the efficiency and accuracy of structured solvers and the flexibility and adaptativeness capabilities of unstructured solvers.

At Onera, the first developments on hybrid solvers (as defined above) were carried-out in the years 1994-1998 [23] [24]. The method developed in this work for the solution of the Euler and Reynolds-Averaged Navier-Stokes equations in 3D by means of adaptive unstructured and hybrid grids has clearly demonstrated its value in industrial applications, in which the flexibility of unstructured mesh generation and adaptation is a critical necessity. Satisfactory agreement between ex-

perimental data and computed results validated the numerical method implemented for the resolution of the Euler and Reynolds-Averaged Navier-Stokes equations. An original local mesh enrichment method has been developed and applied on two- and three-dimensional test cases. Convergence acceleration techniques based on agglomeration multi-grid methods was also built up.

Since 2007 this work has been implemented in elsA, and the project elsA-hybrid is now includes new inline development with the end users' requirements for external flow and internal flow simulations (industrial partners, in-house Onera users). In the present part we will briefly describe some aspects of the numerical method implemented for the unstructured meshes as well as the matching techniques between structured and unstructured blocks.

## 2nd order FV scheme in unstructured meshes

### Unstructured solver

The space discretization used at the present time is based on a finite volume decomposition of the computational domain in polygonal control volumes corresponding to the cells of the mesh, leading then to the so-called cell-centered approach. Two different spatial schemes have been implemented:

- A space-centered scheme combined with non linear 2nd order and linear 4th order artificial dissipation terms (Jameson type);
- An upwind method based on the Roe's Flux Difference Splitting scheme and a MUSCL extrapolation of Van Leer, with various limiters. Both approaches are second order accurate in space on regular meshes, (except near flow discontinuities where a first order accuracy is recovered as for the structured schemes). The treatment of the boundary conditions is based on characteristic relations.

The time integration process uses a multi-step method, either the classical 4-step Runge-Kutta method or the backward Euler method, and is performed in a single time loop including structured and unstructured blocks. Implicit methods are developed, first a LU-SSOR method [28] adapted to unstructured meshes.

### Structured / Unstructured block matching technique

The mesh generation flexibility associated with unstructured methods makes it possible in principle to easily ensure point coincidence at the structured block / unstructured block boundaries. In this case the use of a cell-centred scheme in both types of meshes allows for conservative treatment on these block boundaries thanks to the exchange of numerical fluxes through the same interfaces (see Figure 6a). In this case, we use 2nd order FV schemes and the numerical fluxes are computed by means of the values evaluated respectively on the left side and on the right side of the interface and then corresponding either to a structured or to an unstructured reconstruction scheme. This means that the common flux defined at the interface corresponds to a hybrid methodology, the local consistency and the stability of the time-loop process deriving, from a heuristical point of view, from the properties of the separate structured and unstructured schemes.

For various reasons, the use of a node-centered unstructured solver could be of value: number of unknowns, accuracy, etc.; leading to non-conformal matching boundaries (Figure 6b). In that case we must use either interpolation techniques to compute the fluxes on both sides separately [23], or local mesh reconstruction to get com-

mon space discretization on the common boundaries [4]. The first solution is not conservative in the principle, but if the cell sizes are close together, the corresponding error is small, whereas the second treatment provides the conservativity property but is more difficult to implement for general curvilinear boundaries in 3D meshes.

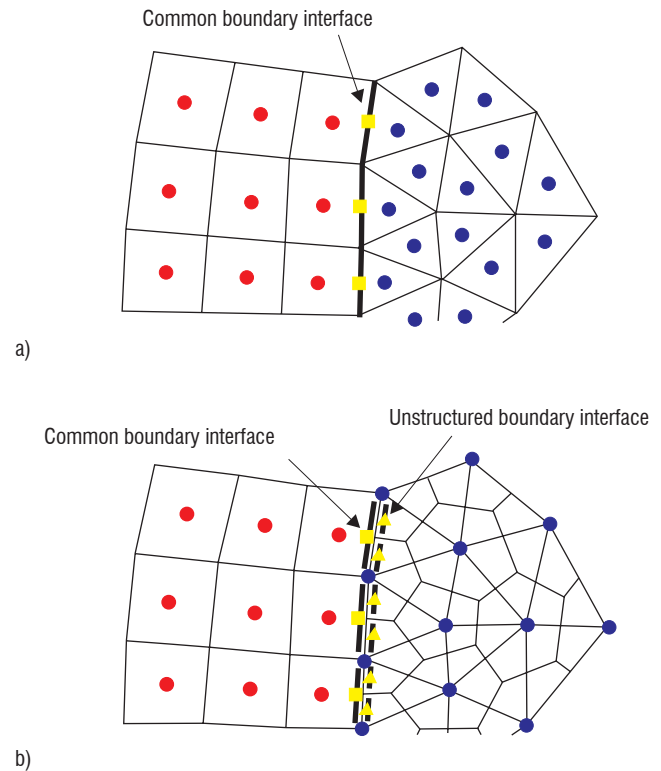


Figure 6 - Structured / unstructured block matching – Cell vertex versus cell centered

### Mesh adaptation

Automatic mesh adaptation tends to correct the numerical error inherent to an initial improper grid node distribution. Isotropic as well as anisotropic mesh refinements have been studied and implemented at Onera.

A method for the automatic adaptation of unstructured grids has been proposed in [24]. The basis of this method comes from a local anisotropic mesh enrichment idea. Most of the refinement procedures applied on unstructured grids are based on an isotropic division of cells. On the contrary, the present method relies on an anisotropic division of cells over the edges. An original error estimator, which is obtained from an evaluation of the interpolation error on the edges of the mesh, takes into account the mixed discretization of the solution in a first order accurate part near discontinuities, and a second order accurate part elsewhere. This error estimator is applied to determine which cells of the mesh have to be divided. After each step of enrichment, the distorted mesh is optimized by Laplacian-like smoothing and edge swapping. Applications of the adaptation procedure coupled with the numerical method have been used on several test cases (airfoil, wing, isolated rotor). There are plans to couple with the elsA software in the near future.

The first computations with unstructured isotropic mesh refinements were recently performed with elsA. Mach number gradient computation across interfaces determines which cells must be divided. Applications of the adaptation procedure coupled with the numerical method are fulfilled on the NACA0012 airfoil and on the ONERA M6

wing. The value of this adaptation procedure is clearly seen in the presented result (Figure 7) with the excellent capture of the flow features after four cycles of adaptations/CFD computations.

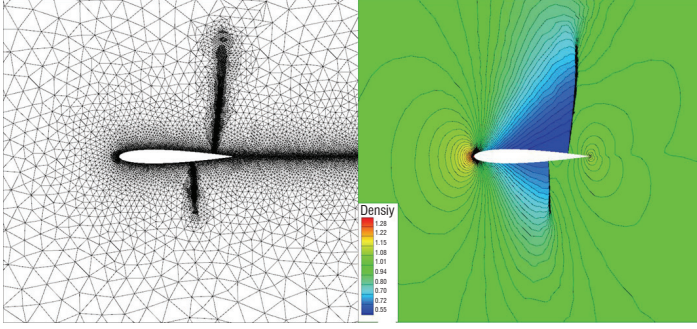


Figure 7 - NACA0012 airfoil – Euler transonic computation – unstructured mesh refinement

## Third-order scheme in an overset grids framework

### Introduction

In this part, the computational domain is discretized by a set of curvilinear structured grids around bodies completed by a set of regular Cartesian grids.

There are various reasons to justifying the choice of this grid topology. First, on structured grids (that is i,j,k-ordered grids), the numerical scheme is generally more computationally efficient than on unstructured grids (that is grids made of tetrahedrons, hexahedrons, etc. with no particular order). Besides, various studies have proven that a numerical scheme on Cartesian grids is even more efficient and accurate. As a matter of fact, on regular Cartesian grids, numerical scheme formulae are simplified and no metrics storage is required. Another advantage of Cartesian grids is the simplicity of the formulation of high-order schemes.

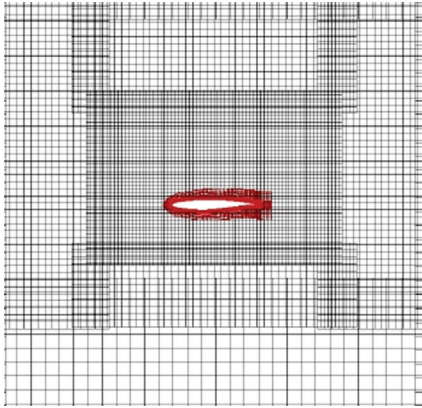


Figure 8 - Example of curvilinear-Cartesian topology around a 2D airfoil

An example of the kind of mesh topology studied here is given in figure 8. The shortly extended meshes around the airfoil are structured and the remaining part of the domain is meshed with regular structured Cartesian grids. All of the grids are overset, which means that an overlap between all grids exists. Fluid variables are transferred between all grids using interpolations in those overlap regions. The transfer technique used here is called Chimera and was first introduced by Steger et al. [38]. The set of Cartesian grids is automatically generated, given the set of curvilinear grids around the bodies and it can be also adapted to the solution during

the computation. The method can be also applied with unstructured grids around the bodies (see [41]).

This kind of mesh topology has been first introduced by Meakin [29] and also developed by Benoit and Jeanfaivre [2] with applications to helicopter rotor flows in hover.

This part of the paper presents the adaptation of a third-order numerical scheme to this kind of mesh topology. More details can be found in [19]. We first present the third-order scheme on curvilinear grids, then its formulation on Cartesian grids. Finally, we present the adaptation of this scheme to overlap boundaries together with third-order interpolations.

### Third-order finite volume scheme on curvilinear meshes

On curvilinear grids, a third-order space accurate scheme is used. This scheme is based on the work of Cinnella, Lerat and Rezgui [35, 9] in a finite-volume formulation. For the sake of simplicity, this scheme is presented in 2D and for the Euler equations. Let  $p, \eta, u, v, E$  and  $H$  denote the pressure, density, Cartesian velocity components, total energy and total enthalpy. For a perfect gas:

$$p = (\gamma - 1)\rho\left(E - \frac{u^2 + v^2}{2}\right)$$

where  $\gamma$  is the ratio of specific heats. The Euler equations for two dimensional inviscid flow can be written in integral form:

$$\frac{d}{dt} \int_{\Omega} w d\Omega + \int_{\partial\Omega} F(w) \cdot n d\Gamma = 0 \quad (7)$$

where:

$$w = \begin{pmatrix} \rho \\ \rho u \\ \rho v \\ \rho E \end{pmatrix}, \quad f(w) = \begin{pmatrix} \rho u \\ \rho u^2 + p \\ \rho uv \\ \rho uH \end{pmatrix}, \quad g(w) = \begin{pmatrix} \rho v \\ \rho uv \\ \rho v^2 + p \\ \rho vH \end{pmatrix}$$

and  $\Omega$  is a bounded domain with boundary  $\partial\Omega, n$ , is the unit outward normal to  $\partial\Omega$ , and  $F(w) = [f(w), g(w)]$  is the flux density. We define a structured mesh composed of quadrangular cells  $\Omega_{j,k}$  (Figure 9) and denote the cell centers by  $C_{j,k}$  and the cell edges by  $\Gamma_{j+\frac{1}{2},k}$ , or  $\Gamma_{j,k+\frac{1}{2}}$ :

$$\partial\Omega_{j,k} = \{\Gamma_{j+\frac{1}{2},k}, \Gamma_{j,k+\frac{1}{2}}, \Gamma_{j-\frac{1}{2},k}, \Gamma_{j,k-\frac{1}{2}}\}$$

Applied to the cell  $\Omega_{j,k}$  the conservation laws (7) become:

$$\frac{d}{dt} \int_{\Omega_{j,k}} w d\Omega + \sum_{\Gamma \in \partial\Omega_{j,k}} \int_{\Gamma} F(w) \cdot n d\Gamma = 0$$

The numerical flux density  $F_{j+\frac{1}{2},k}$  through the edge  $\Gamma_{j+\frac{1}{2},k}$  of the cell  $\Omega_{j,k}$ , is an approximation to:

$$\frac{1}{|\Gamma_{j+\frac{1}{2},k}|} \int_{\Gamma_{j+\frac{1}{2},k}} F(w) \cdot n d\Gamma$$

To define a local reference frame on the edge  $\Gamma_{j+\frac{1}{2},k}$ , let  $\xi$  be an axis

passing through the adjoining cell center, oriented from  $C_{j,k}$  to  $C_{j+1,k}$  and let  $\eta$  be an axis on  $\Gamma_{j+\frac{1}{2},k}$ . Let E be the intersection point of the  $\eta$  and  $\xi$  axis.

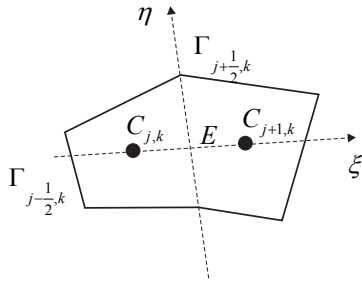


Figure 9 - Definition of the local frame of reference

Performing a Taylor expansion in the  $\eta$ -direction, a third-order approximation of the exact flux is:

$$\frac{1}{|\Gamma_{j+\frac{1}{2},k}|} \int_{\Gamma_{j+\frac{1}{2},k}} F(w) n d\Gamma = (\phi + \beta_1 \phi_\eta + \beta_2 \phi_{\eta\eta})|_E + O(h^3) \quad (8)$$

With  $F = F.n$  and:

$$\beta_1 = \frac{\int_{\Gamma_{j+\frac{1}{2},k}} (\eta - \eta_E) d\eta}{|\Gamma_{j+\frac{1}{2},k}|} = O(h)$$

$$\beta_2 = \frac{\int_{\Gamma_{j+\frac{1}{2},k}} (\eta - \eta_E)^2 d\eta}{2|\Gamma_{j+\frac{1}{2},k}|} = O(h^2)$$

where  $\eta_E$  is the coordinate of  $E$  on the  $\eta$ -axis ( $\eta_E = 0$ ) and

$$b = |C_{j,k} C_{j+1,k}|$$

To complete the discretization of (8), we must provide third, second and first-order approximations for  $\phi_E, \phi_{\eta_E}$  and  $\phi_{\eta\eta_E}$  respectively. This is done in a centered way by using weighted average and difference operators taking into account the locations of  $E$  and of the surrounding cell centers. A Third-order approximation of  $\phi_E$  is obtained by cancelling the error term introduced by the weighted average which discretizes  $\phi_E$  to second-order accuracy. Numerical flux is third-order accurate [35] on moderately deformed meshes and at least second-order accurate on highly-distorted meshes. If the grid deformations were neglected, the above weighted numerical flux would be reduced to:

$$F_{j+\frac{1}{2},k} = \left( \mu_1 \phi - \frac{1}{8} \delta_1^2 \mu_1 \phi + \frac{1}{24} \delta_2^2 \mu_1 \phi \right)_{j+\frac{1}{2},k}$$

where  $\delta_1, \delta_2, \mu_1$  and  $\mu_2$  denote the following discrete operators:

$$(\delta_1 u)_{j+\frac{1}{2},k} = u_{j+1,k} - u_{j,k}, \quad (\delta_2 u)_{j+\frac{1}{2},k} = u_{j,k+1} - u_{j,k}$$

$$(\mu_1 u)_{j+\frac{1}{2},k} = \frac{1}{2}(u_{j+1,k} + u_{j,k}), \quad (\mu_2 u)_{j+\frac{1}{2},k} = \frac{1}{2}(u_{j,k+1} + u_{j,k})$$

### Formulation of the scheme on a regular Cartesian mesh

Let us express the complete scheme on a regular Cartesian grid, since this type of grid is our main concern in our mesh topology. With  $\phi = f$  on  $\Gamma_{j+\frac{1}{2},k}$  and  $\phi = g$  on  $\Gamma_{j,k+\frac{1}{2}}$ , the scheme reads:

$$F_{j+\frac{1}{2},k} = \left[ \left( I - \frac{1}{8} \delta_1^2 + \frac{1}{24} \delta_2^2 \right) \mu_1 f \right]_{j+\frac{1}{2},k}$$

$$F_{j,k+\frac{1}{2}} = \left[ \left( I - \frac{1}{8} \delta_2^2 + \frac{1}{24} \delta_1^2 \right) \mu_2 g \right]_{j,k+\frac{1}{2}}$$

The finite volume scheme can be rewritten in the very simple form:

$$\left[ w_t + \frac{\delta_1}{\delta x} \left( I - \frac{1}{6} \delta_1^2 \right) \mu_1 f + \frac{\delta_2}{\delta y} \left( I - \frac{1}{6} \delta_2^2 \right) \mu_2 g \right]_{j,k} = 0 \quad (9)$$

This Cartesian scheme is purely directional, i.e it involves points only in the  $x$  and  $y$  directions passing through the cell center  $C_{j,k}$ . This formulation of the third-order of the numerical scheme on regular Cartesian grids, which can be seen as a finite difference formulation, is strictly equivalent to the finite volume approach. The expression (9) is much simpler than the general finite volume formula and will be implemented this way on the Cartesian grids of the mesh adaptation method for efficiency reasons.

### Numerical dissipation

Centered schemes are non dissipative and are therefore subject to numerical instabilities due to the growth of high-frequency modes. Consequently, the Jameson artificial dissipation [21] is incorporated in previous formulations.

For instance for the Cartesian scheme, this leads to modification of the numerical fluxes in the  $j$  direction (with similar modification in the  $k$  direction) as follows:

$$F_{j+\frac{1}{2},k} = (F - D)_{j+\frac{1}{2},k}$$

with the dissipation:

$$(D)_{j+\frac{1}{2},k} = \rho(\bar{A})_{j+\frac{1}{2},k} (\epsilon_2 \delta_1 w - \epsilon_4 \delta_1^3 w)_{j+\frac{1}{2},k}$$

where  $\bar{A}_{j+\frac{1}{2},k}$  is an average of the Jacobian matrix  $A = df / dw$ ,  $\rho(A)$

denotes the spectral radius of matrix  $A$  and:

$$\epsilon_{2j+\frac{1}{2},k} = k_2 \max(v_{j,k}, v_{j+1,k}), \quad \epsilon_{4j+\frac{1}{2},k} = \max(0, k_4 - \epsilon_{2j+\frac{1}{2},k})$$

$$v_{j,k} = \frac{|p_{j+1,k} - 2p_{j,k} + p_{j-1,k}|}{|p_{j+1,k} + 2p_{j,k} + p_{j-1,k}|}$$

where  $p$  is the static pressure and  $k_2, k_4$  are constant parameters. In a region where  $w$  is smooth,  $k_2 = O(h^2)$  and  $k_4 = O(1)$ , so that the dissipative terms are  $O(h^3)$  and the whole scheme remains third-order accurate.

### High-order mesh adaptation method

As previously said, the mesh adaptation method of Meakin is based on the Chimera technique. For high-order numerical schemes, it has been demonstrated that linear interpolation is not sufficient to maintain the overall global accuracy of an overset-grid technique at the same order as the interior numerical scheme. The third-order interpolation procedure used here is based on directional Lagrange polynomials. The numerical solution on Grid A at point  $x$  is interpolated from points  $x_0, x_1$  and  $x_2$  located on Grid B (Figure 9), the formulae used are:

$$w(x) = \sum_{j=0}^n w_j l_j(x), \quad l_j(x) = \frac{\prod_{k=0, k \neq j}^n (x - x_k)}{\prod_{k=0, k \neq j}^n (x_j - x_k)}$$

In order to be more accurate, the third point on Grid B  $x_0$  is chosen such as:

$$\begin{cases} x_0 = x_1 - \delta x & \text{if } |x - x_1| < \frac{\delta x}{2} \\ x_0 = x_2 + \delta x & \text{otherwise} \end{cases}$$

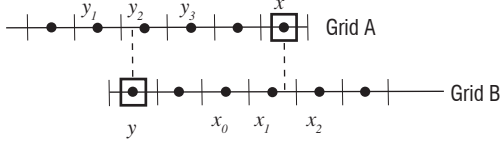


Figure 10 – Interpolated points for high-order Chimera transfers

### Modification of schemes near overlap boundaries

In the overlap region, the number of grid points has to be sufficient to ensure a proper communication between the grids. In particular, an interpolated point must be computed from interior points. If a valid interpolation cell cannot be found, the interpolated point is called an orphan point. In our technique, in order to diminish the occurrence of orphan points, only one layer of interpolated cells is used. Nevertheless, the third-order scheme is a five-point stencil scheme and it must therefore be reformulated near interpolated points in order to preserve the global order of accuracy.

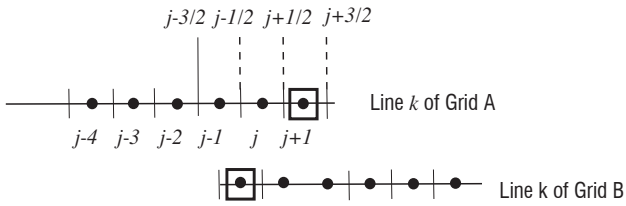


Figure 11 – Minimum overlap with one layer of interpolated cells

In figure 11, the values on the last cell face  $(j+3, k)$  of Grid A are always interpolable 2 by Lagrange interpolation, otherwise Grid B would be too small and thus useless. A specific treatment based on upwind formulae is performed for the calculation of physical flux and the artificial viscosity flux at the face  $(j+1/2, k)$ . It uses the interpolated value  $2 f_{j+\frac{3}{2}, k}$ :

$$F_{j+\frac{1}{2}, k} = -\frac{1}{84} f_{j-2, k} - \frac{1}{60} f_{j-1, k} + \frac{5}{12} f_{j, k} + \frac{11}{12} f_{j+1, k} - \frac{32}{105} f_{j+\frac{3}{2}, k}$$

$$D_{j+\frac{1}{2}, k} = \rho(\bar{A})_{j+\frac{1}{2}, k} \left( \varepsilon_2 (w_{j+1, k} - w_{j, k}) - \varepsilon_4 \left( \frac{1}{7} w_{j-2, k} - \frac{9}{5} w_{j-1, k} + 5 w_{j, k} - 7 w_{j+1, k} + \frac{128}{35} w_{j+\frac{3}{2}, k} \right) \right)$$

with:

$$v_{j+1, k} = \frac{\begin{vmatrix} 2p_{j, k} + \frac{16}{5} p_{j+\frac{3}{2}, k} - \frac{1}{5} p_{j-1, k} - 5p_{j+1, k} \\ 2p_{j, k} + \frac{16}{5} p_{j+\frac{3}{2}, k} + \frac{1}{5} p_{j-1, k} + 5p_{j+1, k} \end{vmatrix}}{\begin{vmatrix} 2p_{j, k} + \frac{16}{5} p_{j+\frac{3}{2}, k} + \frac{1}{5} p_{j-1, k} + 5p_{j+1, k} \\ 2p_{j, k} + \frac{16}{5} p_{j+\frac{3}{2}, k} - \frac{1}{5} p_{j-1, k} - 5p_{j+1, k} \end{vmatrix}}$$

These formulae allow to preserve the global third-order of accuracy of the overset grids method.

### Application

This methodology was validated in [36] and the practical third-order demonstrated. We present here a simulation of a helicopter isolated blade in forward flight. The tip Mach number is  $M_{tip} = 0.646$ , the blade advance ratio is  $\mu = 0.4$ . In figure 12, the blade mesh together with the set of adapted Cartesian grids is presented for an azimuth of 440 degrees. The total number of points in the mesh is 19 million points. The Q-criterion exhibiting the vortical wake of the blade shows that this wake is well-captured by the adapted mesh.

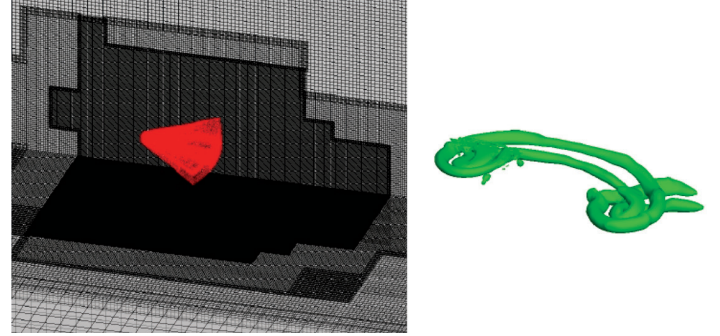


Figure 12 - Mesh and Q-criterion for an isolated blade in forward flight

### Finite volumes on polyhedral meshes

#### Context and motivation

The methods described in this section were originally developed within the CEDRE software [33] for application domains focused on energetics and propulsion, which are often characterized by very complex geometries [37]. With the need to take more and more technological details into account, it quickly became obvious that the setting up of structured hexahedral mesh calculations was often too much time consuming.

On the other hand, many types of automatic mesh generation software were gradually becoming available. Tetrahedral meshers were the first to appear, but current software often mixes several types of elements, for instance tetrahedra, prisms, pyramids and hexahedra. Other kinds of elements are also becoming available in some meshers : hexahedra trimmed by boundaries, hexahedra with refinement, polyhedral mesh obtained as the dual of a tetrahedral original mesh etc.

Furthermore, the mesh can be subjected to a topological alteration in the course of calculation. Adaptive mesh refinement is a well-known example, but another interesting situation is shown on figure 13. In this example, the moving mesh fitted to a rotating solid (green) partly overlaps the Cartesian grid of a the fluid container (blue). The effective mesh used for this ALE calculation is made of the overlapping mesh and the visible part of the Cartesian grid, which is trimmed in a very general way into various polygonal (polyhedral in 3D) shapes. The methods used in this calculation were originally developed in the FLUSEPA software of ASTRUM and have been subsequently applied to CEDRE.

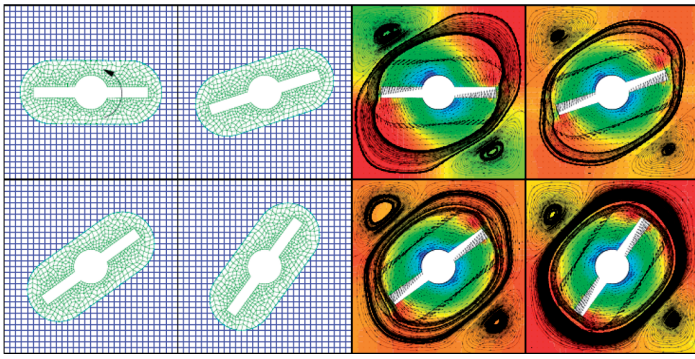


Figure 13 - Conservative overlapping : example of mesh, pressure field and streamlines

These examples show that a general polyhedral mesh of the physical domain is very desirable in dealing with complex flow situations.

### The geometric and kinematic model

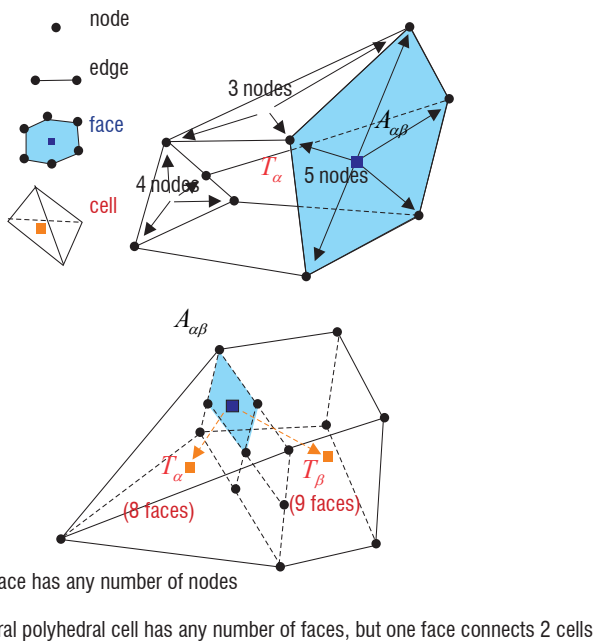


Figure 14 - Polyhedral finite volume cells and faces

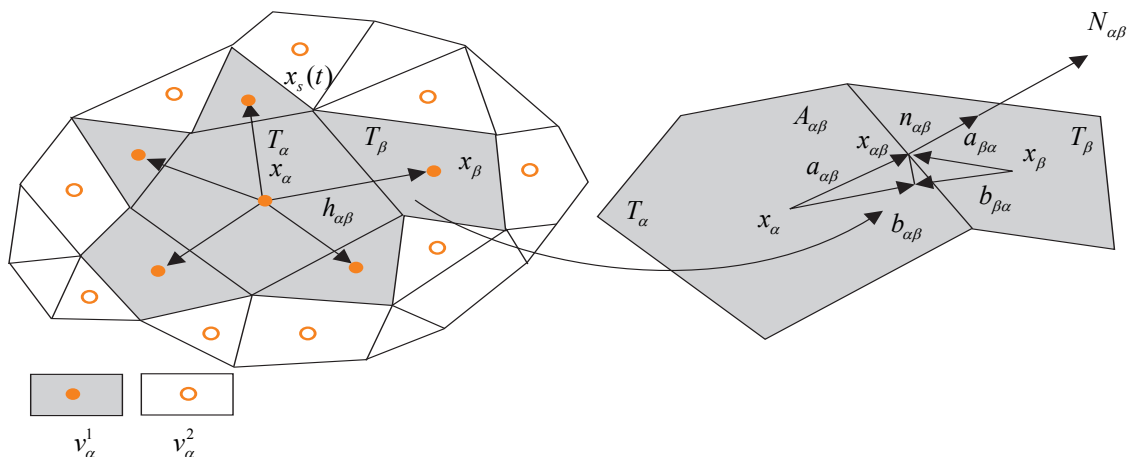


Figure 15 - Geometry of cells and faces and neighborhoods (two-dimensional sketch)

The following conditions define a general polyhedral mesh (figure 13):

- Every cell face  $A_{\alpha\beta}$  is a triangulation lying on a generally non-planar polygonal contour with any number of vertices. The common point  $K_{\alpha\beta}$  of the triangulation can be defined in several ways; one natural choice is to identify  $K_{\alpha\beta}$  with the gravity center of the triangulated face.
- Every cell  $T_\alpha$  is bounded by any number of faces  $A_{\alpha\beta}$ . Conversely, an internal face  $A_{\alpha\beta}$  always connects two cells  $T_\alpha$  and  $T_\beta$  exactly.

If the positions  $x_s(t)$  of vertices are known, every cell  $T_\alpha$  is completely defined. One can then calculate for instance the surface vector  $N_{\alpha\beta}$ , area  $S_{\alpha\beta}$  and gravity center  $x_{\alpha\beta}$  of  $A_{\alpha\beta}$ ,

$$N_{\alpha\beta} \square \int_{A_{\alpha\beta}} \mathbf{n} dA, \mathbf{n}_{\alpha\beta} \square \frac{N_{\alpha\beta}}{|N_{\alpha\beta}|}, S_{\alpha\beta} \square \int_{A_{\alpha\beta}} dA, x_{\alpha\beta} \square \frac{1}{S_{\alpha\beta}} \int_{A_{\alpha\beta}} \mathbf{x} dA \quad (10)$$

and the volume  $V_\alpha$  and gravity center  $x_\alpha$  of  $T_\alpha$ :

$$V_\alpha \square \int_{T_\alpha} dV, x_\alpha \square \frac{1}{V_\alpha} \int_{T_\alpha} \mathbf{x} dV \quad (11)$$

The gravity centers of faces and cells are convenient Gauss points allowing exact quadrature for linear functions:

$$\begin{aligned} \text{If } w(x) \text{ is linear, } \int_{T_\alpha} w(x) dV &= V_\alpha w(x_\alpha) \\ \text{and } \int_{A_{\alpha\beta}} w(x) dA &= S_{\alpha\beta} w(x_{\alpha\beta}) \end{aligned} \quad (12)$$

Figure 15 defines additional notations for the interface  $A_{\alpha\beta}$  between two cells  $T_\alpha$  and  $T_\beta$ :

$$\mathbf{h}_{\alpha\beta} \square \mathbf{x}_\beta - \mathbf{x}_\alpha, \mathbf{a}_{\alpha\beta} \square \mathbf{x}_{\alpha\beta} - \mathbf{x}_\alpha, \mathbf{b}_{\alpha\beta} \square \left( \mathbf{a}_{\alpha\beta} \cdot \frac{\mathbf{h}_{\alpha\beta}}{|\mathbf{h}_{\alpha\beta}|} \right) \frac{\mathbf{h}_{\alpha\beta}}{|\mathbf{h}_{\alpha\beta}|} \quad (13)$$

The first neighborhood  $v_\alpha^1$  of  $T_\alpha$  is defined as the set of all cells  $T_\beta$  sharing a face  $A_{\alpha\beta}$  with  $T_\alpha$ , plus  $T_\alpha$  itself (figure 15). More generally, the second neighborhood  $v_\alpha^2$  is made of  $v_\alpha^1$  plus all the first neighbors of cells inside  $v_\alpha^1$  etc. The first neighborhood  $v_\alpha^1$  is convenient for algorithm description, but the reciprocal neighborhood  $W_{\alpha\beta}^1$  of face  $A_{\alpha\beta}$ , which is made of  $T_\alpha$  and  $T_\beta$  is equivalent and often more adapted to implementation. Other kinds of neighborhoods (for instance through vertices or edges) could be used, but it was de-

cided for simplicity to base all algorithms only on  $v_\alpha^1$  and its iterates  $v_\alpha^2 \dots v_\alpha^l \dots$ .

This definition of geometry is generally time-dependant. If the movement of every vertex is known, all the above properties of cells and faces are known functions of time.

### Governing equations and state variables

In this paper, we consider a continuum characterized by a set of  $n_q$  conserved quantities per unit volume depending on space and time  $q = q(x, t)$ . Alternatively, the local state can also be represented by a system of intensive variables  $u = u(x, t)$  which is more convenient in some contexts. Both descriptions are equivalent, i.e. we can define a one-to-one mapping between  $u$  and  $q$ ,

$$q = Q(u) \quad \text{or} \quad u = U(q) \quad (14)$$

In the special case of a compressible fluid flow with fixed composition,  $q$  includes mass, momentum and total energy per unit volume ( $n_q = 5$  scalar variables). In the absence of phase transition, a convenient set of intensive variables is made up of pressure, temperature and macroscopic velocity:

$$q = \begin{bmatrix} \rho \\ \rho \mathbf{v} \\ \rho e_t \end{bmatrix}, \quad u = \begin{bmatrix} p \\ T \\ v \end{bmatrix} \quad (15)$$

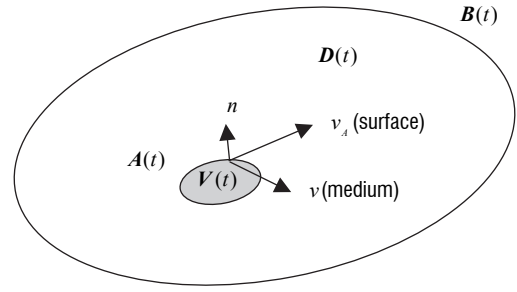
This particular set of  $q$  and  $u$  variables is only given as an elementary example, since fluid dynamics and energetics include many other models [13]. For instance, the above definition of  $u$  does not hold for flows with phase transition. In Reynolds Averaged turbulent flows, additional quantities describe turbulence [1], whereas the mixture composition introduces further degrees of freedom in aerothermochemistry [13] [12] etc. Completely different systems are also needed, for instance for conduction in solids, particles in the Eulerian approach or fully multiphase flow [33] [30]. Wherever possible, this paper avoids modelization details and concentrates on generic equations and methods for Eulerian solvers, with Lagrangian methods for particles being described in [30].

The keystone of the Eulerian physical models considered in the sequel is a set of balance equations for  $q(x, t)$ . The most general form of these equations expresses conservation on any moving and possibly deformable control volume  $V(t)$  bounded by a surface  $A(t)$  with velocity  $v_A(x, t)$  (figure 16 a):

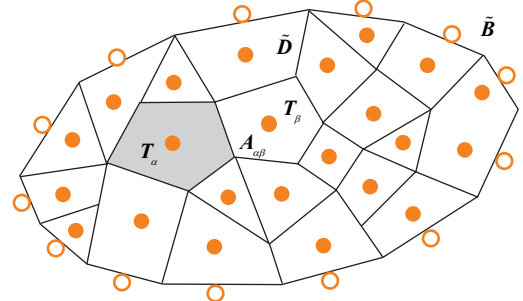
$$\forall V(t), \quad \frac{d}{dt} \int_V q dV = - \int_A (q(\mathbf{v} - \mathbf{v}_A) + \mathbf{f} + \varphi) \cdot \mathbf{n} dA + \int_V s dV \quad (16)$$

Equation (16) states that the quantity of  $q$  inside  $V(t)$ , which is a function of time only, varies under the influence of non dissipative fluxes (flux density  $q(\mathbf{v} - \mathbf{v}_A) + \mathbf{f}$ , where the first term represents advection), dissipative fluxes (flux density  $\varphi$ ) and sources per unit volume. This system of conservation laws must be completed by a thermodynamic model for the continuum [13], phenomenological relationships to express the dissipative fluxes  $\varphi$  and models for sources  $s$ , which will be supposed to be of the form

$$\mathbf{f} = \mathbf{f}(u), \quad \varphi = \varphi(u, \nabla u) \quad \text{with} \quad \varphi(u, 0) = 0, \quad s = s(u, \nabla u, \dots) \quad (17)$$



a) Physical domain and boundary control volume  $V(t)$



b) Discrete approximation of domain and boundary cells and locations for discrete variables

Figure 16 - Notations for space discretization

Where the field of state variables is sufficiently regular, the integral form (16) is equivalent to a system of partial differential equations

$$\partial_t q = -\nabla \cdot (q\mathbf{v} + \mathbf{f} + \varphi) + s \quad (18)$$

Conservation equations (16) or (18), (17) must be completed by a proper set of boundary conditions along the limits  $x_B(t)$  of the region  $D(t)$  of interest and by an initial condition.

If  $s = 0$ ,  $q(x, t) = \text{constant}$  is a solution of (18). It is of course also a solution of the integral form (16) because

$$\forall V(t), \quad \frac{d}{dt} \int_V dV = \int_A \mathbf{v}_A \cdot \mathbf{n} dA \quad (19)$$

is a kinematic identity which states that the rate of variation of the volume of  $V(t)$  is exactly equal to the volume swept by the surface  $A(t)$  per unit time.

### A family of Finite Volume methods on general polyhedra

To derive space discretization, one common approach in CFD and connected domains is the finite volume method. In fact, this term does not really describe a method but rather a point of view on space discretization which can lead to a large number of distinct algorithms. The starting point is the balance equation (16) written on a control volume (or cell) defined by  $T_\alpha$ . Let us define the volume  $V_\alpha(t)$  of  $T_\alpha$

$$V_\alpha(t) \square \int_{T_\alpha} dV \quad (20)$$

and the mean values  $q_\alpha(t)$  of conserved quantities on  $T_\alpha$

$$q_\alpha(t) \square \frac{1}{V_\alpha} \int_{T_\alpha} q(x, t) dV \quad (21)$$

With these notations, the balance equation (16) reads

$$\frac{d}{dt} (V_\alpha q_\alpha) = - \sum_{\beta \in \mathcal{I}_\alpha} \int_{A_{\alpha\beta}} (q(\mathbf{v} - \mathbf{v}_A) + \mathbf{f} + \varphi) \cdot \mathbf{n} dA + \int_{T_\alpha} s dV \quad (22)$$

where normal flux densities are integrated on all the faces  $A_{\alpha\beta}$  of the cell. The mean value  $q_\alpha(t)$  is an obvious candidate as the space-discrete degree of freedom associated with  $T_\alpha$ , but it is of course equivalent to the use of the set of natural variables  $u_\alpha(t) \square U(q_\alpha(t))$  for this purpose.

An important property of the finite volume approach is that it automatically leads to exactly conservative space discretizations: if we sum equations (22) for any cluster  $\{T_\alpha\}$  of neighboring cells, the fluxes along internal interfaces cancel and the variation rate of conserved quantities inside the cluster is only due to the integral of fluxes along the limits of  $\{T_\alpha\}$  and the volume integral of sources inside  $\{T_\alpha\}$ . Conservativity is a very desirable property in engineering analysis as it allows a non-ambiguous evaluation of mass, momentum and energy transfers independently of the mesh size.

Up to this point, no approximation has been made and (22) can be considered as exact. The next step will be to derive approximations for fluxes and sources at the right-hand side of (22) as functions of the space-discrete degrees of freedom in a certain neighborhood of face  $A_{\alpha\beta}$ . The family of finite volume methods implemented in CEDRE can be viewed as an extension of MUSCL schemes to general polyhedral meshes, which were initially defined for structured grids [40]:

- For each cell  $T_\alpha$  and fixed  $t$ , we define a polynomial reconstruction  $w_{q,\alpha}(x)$  (or  $w_{u,\alpha}(x)$ ) which approximates the field of the state variables on  $T_\alpha$  (for simplicity,  $t$  will be omitted in the statement of  $w_q$  and  $w_u$ ). The reconstruction is designed to be  $k$ -exact, i.e. exact if each component of the original function is locally a polynomial of degree  $k$ . The  $l$ -th order derivatives  $l=1 \dots k$  defining the polynomial are evaluated algebraically from the state variables on a neighborhood of  $T_\alpha$ , for example with the help of a least-squares technique.

- This reconstruction allows the evaluation of state variables at any point of  $A_{\alpha\beta}$  with precision  $O(h^{k+1})$  (where  $h$  is the order of magnitude of  $|h_{\alpha\beta}|$ ) and the reconstruction from cell  $T_\beta$  gives rise to a second evaluation with the same precision. A non-linear limitation formula eliminates possible local extrema in these evaluations. First order derivatives along  $A_{\alpha\beta}$  can also be evaluated with the help of both reconstructions.

- The surface and volume integrals at the right-hand side of (22) can be evaluated through Gauss quadrature, with enough quadrature points to meet the precision of the reconstruction.

- Finally, numerical flux formulas adapted to physics must be applied at every Gauss point. This stage is purely local and involves no interpolation.

The precision of the space discretization depends only on interpolation (first and second item above) and quadrature (third item) which are independent of physics, whereas stability also depends on the physics involved in fluxes and sources and their numerical approximations (fourth item).

In (22), all geometric quantities are generally time-dependent due to mesh movement and deformation: this formulation is usually known as ALE (for Arbitrary Lagrangian Eulerian). Volume conservation (19) for  $T_\alpha$  reads

$$\frac{dV_\alpha}{dt} = \sum_{\beta \in \mathcal{N}_\alpha} \int_{A_{\alpha\beta}} v_A \cdot \mathbf{n} dA \quad (23)$$

If the motion law of every vertex is known,  $v_A$  can be calculated at every point along  $A_{\alpha\beta}$ , as well as the integrals on the right-hand side of (23). If we set

$$v_{An,\alpha\beta} \square \frac{1}{|N_{\alpha\beta}|} \int_{A_{\alpha\beta}} v_A \cdot \mathbf{n} dA \quad (24)$$

volume conservation simply reads

$$\frac{dV_\alpha}{dt} = \sum_{\beta \in \mathcal{N}_\alpha} v_{An,\alpha\beta} |N_{\alpha\beta}| \quad (25)$$

We stress that (25) need not be added as a supplementary ALE equation since it is an automatic consequence of a correct evaluation of time-dependent volume and face velocity. It can be checked that under the preceding general hypotheses for interpolation, constant states  $q_\alpha(t) = q^0 = \text{constant}$  are automatically solutions of the semi-discrete conservation equations (22) for any mesh movement and deformation.

## Methods with piecewise linear reconstruction ( $k=1$ )

### Reconstruction on $T_\alpha$

The local reconstruction  $w_{q,\alpha}(x)$  for  $q(x,t)$  is chosen to be linear on  $T_\alpha$ :

$$w_{q,\alpha}(x) = q_\alpha + \sigma_{q,\alpha} \cdot (x - x_\alpha) \quad (26)$$

where  $\sigma_{q,\alpha}$  is a consistent approximation of the gradient at the center of gravity of  $T_\alpha$

$$\sigma_{q,\alpha} = (\nabla q)_\alpha + O(h). \quad (27)$$

As stated before (12), the mean value of the linear reconstruction is equal to its value at the gravity center  $x_\alpha$ :

$$\frac{1}{V_\alpha} \int_{T_\alpha} w_{q,\alpha}(x) dV = w_{q,\alpha}(x_\alpha) = q_\alpha \quad (28)$$

If the change of variable (second equation (14)) is applied to (26), we get

$$\begin{aligned} U(w_{q,\alpha}(x)) &= U(q_\alpha + \sigma_{q,\alpha} \cdot (x - x_\alpha)) \\ &= U(q_\alpha) + \frac{\partial U}{\partial q}|_{q=q_\alpha} \sigma_{q,\alpha} \cdot (x - x_\alpha) + 0(x - x_\alpha)^2 \end{aligned} \quad (29)$$

The second order term in (29) is of the same order as the approximation error in (26). We then get a linear reconstruction for  $u$

$$w_{u,\alpha}(x) = u_\alpha + \sigma_{u,\alpha} \cdot (x - x_\alpha) \quad (30)$$

where

$$\sigma_{u,\alpha} = \frac{\partial U}{\partial q}|_{q=q_\alpha} \sigma_{q,\alpha} = (\nabla u)_\alpha + O(h) \quad (31)$$

is a consistent approximation for the gradient of  $u$  at cell center. The reconstructions (26) and (30) are distinct but both are second order accurate. The latter is sometimes preferred as it gives better results in many practical cases and we will only use this form in the sequel.

One of the simplest ways to evaluate  $\sigma_{u,\alpha}$  is through a least-squares criterion, for instance a best fit between  $w_{u,\alpha}$  and the neighboring state variables :

$$\text{Find } \sigma_{u,\alpha} \text{ such as } M_{\alpha}^j = \sum_{\beta \in V_{\alpha}^1} (w_{u,\alpha}^j(x_{\beta}) - u_{\beta}^j)^2 \quad (32)$$

is minimum for every state variable  $j$ .

Solving (32) leads to a linear dependency between  $\sigma_{u,\alpha}$  and the state variables in  $V_{\alpha}^1$

$$\sigma_{u,\alpha}^j = \sum_{\beta \in V_{\alpha}^1} \mathbf{g}_{u,\alpha\beta} (u_{\beta}^j - u_{\alpha}^j) \quad (33)$$

Nonlinear limitation can be applied to (33), but direct limitation of interface state variables is generally sufficient (see next section).

### Interpolation along interfaces

The preceding reconstruction gives rise to two distinct second order evaluations of  $u$  at face center  $x_{\alpha\beta}$  :

$$\begin{aligned} u_{\alpha\beta} &= w_{u,\alpha}(x_{\alpha\beta}) = u_{\alpha} + \sigma_{u,\alpha} \cdot \mathbf{a}_{\alpha\beta} \\ u_{\beta\alpha} &= w_{u,\beta}(x_{\alpha\beta}) = u_{\beta} + \sigma_{u,\beta} \cdot \mathbf{a}_{\beta\alpha} \end{aligned} \quad (34)$$

In the case of steep variations, some of these state variables can lie far outside the bounds defined by  $u_{\alpha}$  and  $u_{\beta}$ , and several nonlinear limitation procedures have been implemented to replace  $u_{\alpha\beta}$  and  $u_{\beta\alpha}$  by

$$u_{\alpha\beta}^{lim} = L(u_{\alpha\beta}, u_{\alpha}, u_{\beta}) \quad , \quad u_{\beta\alpha}^{lim} = L(u_{\beta\alpha}, u_{\beta}, u_{\alpha}) \quad (35)$$

which lie inside the interval defined by  $u_{\alpha}$  and  $u_{\beta}$ . The limiting function  $L$  is designed to degenerate into classical limiters like Van Leer, Minmod, etc., on Cartesian grids.

The asymmetry between  $u_{\alpha\beta}$  and  $u_{\beta\alpha}$  (or  $u_{\alpha\beta}^{lim}$  and  $u_{\beta\alpha}^{lim}$ ) will be used for upwinding in characteristic fluxes, but other evaluations can be built, for instance arithmetic or Roe mean value

$$u_{\alpha\beta}^{sym} = \frac{1}{2}(u_{\alpha\beta}^{lim} + u_{\beta\alpha}^{lim}) \quad , \quad u_{\alpha\beta}^{roe} = U^{roe}(u_{\alpha\beta}^{lim}, u_{\beta\alpha}^{lim}) \quad (36)$$

An obvious first order approximation of the interface gradient of  $u$  is

$$\sigma'_{u,\alpha\beta} = \frac{|\mathbf{b}_{\beta\alpha}|}{|\mathbf{h}_{\alpha\beta}|} \sigma_{u,\alpha} + \frac{|\mathbf{b}_{\alpha\beta}|}{|\mathbf{h}_{\alpha\beta}|} \sigma_{u,\beta} \quad (37)$$

but a compact evaluation of the normal gradient is also available from  $u_{\alpha}$ ,  $u_{\beta}$ ,

$$\sigma''_{u,\alpha\beta} = \frac{u_{\beta} - u_{\alpha}}{\mathbf{n}_{\alpha\beta} \cdot \mathbf{h}_{\alpha\beta}} \quad (38)$$

It is possible to combine these two evaluations for a consistent one-parameter family of interface gradients

$$\sigma_{u,\alpha\beta} = \sigma'_{u,\alpha\beta} + \theta(\sigma''_{u,\alpha\beta} - \sigma'_{u,\alpha\beta} \cdot \mathbf{n}_{\alpha\beta}) \mathbf{n}_{\alpha\beta} \quad (39)$$

If  $\theta=1$ , (37) is used only for the non-normal contribution of the gradient, whereas the normal part stems from the compact evaluation (38). This evaluation of gradient has been studied in [27] and proved very effective for dissipative fluxes.

### Discrete conservation laws

As indicated before, each surface or volume integral at the right-hand side of (22) needs only one quadrature point:

$$\frac{d}{dt}(V_{\alpha} q_{\alpha}) = - \sum_{\beta \in V_{\alpha}^1} [ q(v - v_A) + \mathbf{f} + \varphi ]_{\alpha\beta} \cdot \mathbf{N}_{\alpha\beta} + V_{\alpha} [ s ]_{\alpha} \quad (40)$$

where the subscripts  $\alpha\beta$  and  $\alpha$  stand respectively for the center of face  $x_{\alpha\beta}$  and cell  $x_{\alpha}$ .

Setting

$$F_n \square (q(v - v_A) + \mathbf{f}) \cdot \mathbf{n}, \quad \text{and} \quad \varphi_n \square \varphi \cdot \mathbf{n} \quad (41)$$

(40) reads more simply

$$\frac{d}{dt}(V_{\alpha} q_{\alpha}) = - \sum_{\beta \in V_{\alpha}^1} [ F_n + \varphi_n ]_{\alpha\beta} | \mathbf{N}_{\alpha\beta} | + V_{\alpha} [ s ]_{\alpha} \quad (42)$$

### Numerical fluxes

The last step will be to pinpoint the numerical fluxes used on the right-hand side of (42):

- The non-dissipative flux density  $[ F_n ]_{\alpha\beta}$  from  $T_{\alpha}$  to  $T_{\beta}$  is evaluated through an approximate Riemann solver using  $u_{\alpha\beta}^{lim}$  and  $u_{\beta\alpha}^{lim}$  as arguments. Among many other possibilities, we can cite the Roe numerical flux:

$$\begin{aligned} [ F_n ]_{\alpha\beta} &= \frac{1}{2} (F_n(u_{\alpha\beta}^{lim}) + F_n(u_{\beta\alpha}^{lim})) \\ &+ \frac{1}{2} \left| \frac{\partial F_n}{\partial q} \right|_{\alpha\beta}^{roe} (Q(u_{\alpha\beta}^{lim}) - Q(u_{\beta\alpha}^{lim})) \end{aligned} \quad (43)$$

where the Jacobian matrix  $\frac{\partial F_n}{\partial q}$  is evaluated for the Roe mean value of  $u_{\alpha\beta}^{roe}$ .

- The dissipative flux is evaluated directly from the constitutive law for  $\phi$

$$[ \varphi_n ]_{\alpha\beta} | \mathbf{N}_{\alpha\beta} | = \varphi(u_{\alpha\beta}^{sym}, \sigma_{u,\alpha\beta}) \cdot \mathbf{N}_{\alpha\beta} \quad (44)$$

### Properties

These methods have been used for several years in the Eulerian solvers of CEDRE (multispecies fluid flow, Eulerian model for dispersed particles, heat conduction in solids, see examples of calculation results in [37]). Feedback from numerous calculations as well as theoretical studies [17] shows that:

- The above procedure usually gives stable calculations provided that mesh resolution is adequate and the numerical fluxes are adapted to the physics. However, instability can occur when the information from neighborhood  $V_1$  is not sufficient for gradient calculation in some directions: this occurs almost inexorably on tetrahedral meshes in three dimensions. This problem has been thoroughly studied in [16] [17], which shows that using the second neighborhood  $V_2$  is mandatory in that case ; this work provides simple ways to define second neighborhood stable interpolations based on post-processing of (31). Among many other important results, this thesis also shows that the mean-square method tends to be optimal for stability.

- For unsteady simulations, the predominant error in the sense of the modified (equivalent) equation is second order dispersive, which may be insufficient for Large Eddy Simulation or acoustics.

## Methods for higher order reconstruction ( $k > 1$ )

In theory,  $k$ -exact polynomial reconstructions lead to finite volume discretizations of order  $k+1$ . The case  $k=3$  is of particular importance because 4-th order discretizations dramatically reduce the numerical dissipation, which makes them very valuable for applications in Large Eddy Simulation (LES) and acoustics. In the practice of computations on unstructured grids, however, there are several obstacles to this approach.

- First, the stencil size for  $k$ -exact reconstruction of polynomials

in  $d$  dimensions must be at least equal to  $\binom{d+k}{k}$ . Recent work

[16] [18] has shown that the stability of the MUSCL scheme requires stencil sizes that are several times larger than this minimal size. On unstructured grids, the connectivity data, i.e. which cells contribute to the reconstruction in a specific cell, must be computed, sorted and accessed during runtime.

- Second, a modern unstructured CFD code like CEDRE runs on parallel architectures with a large number of processors, each of which handles a small domain of the partitioned grid. Cells near a domain border may have a reconstruction stencil that overlaps the other domain. For those cells, the connectivity data must be handled and transferred from domain to domain. Furthermore, the size of the overlapping parts of the stencils may vary from cell to cell, creating the need to send data packets of varying length from processor to processor. This can seriously impair the scalability of the code, i.e. the capability to run  $n$  times faster on a system with  $n$  times the number of processors.

These problems suggest the need for  $k$ -exact reconstruction algorithms that require only data exchange between adjacent cells. This can be done in the following way: A polynomial  $p$  of degree  $k$  is

completely determined by its cell average over  $T_\alpha$  and its  $k$  derivatives at the barycenter of the cell. A  $k$ -exact reconstruction is therefore equivalent to the exact reconstruction of the  $m$ -th derivatives for  $1 \leq m \leq k$ . In practice, such a reconstruction of the  $m$ -th derivative will be a sum of the form

$$w_\alpha^{(m)} = \sum_{\beta \in W_\alpha} w_{\alpha\beta}^{(m)} u_\beta \quad (45)$$

where  $W_\alpha$  is a reconstruction stencil that may be very large. For  $k$ -exactness one must have

$$w_\alpha^{(m)} = \sum_{\beta \in W_\alpha} w_{\alpha\beta}^{(m)} u_\beta = D^{(m)} u \Big|_{x_\alpha} \quad (46)$$

whenever  $u$  is a polynomial of degree  $k$ . The main idea is to replace the sum over the large neighborhood  $W_\alpha$  in (45) by a successive sum over the first neighborhood  $V_1$

$$w_\alpha^{(m)} = \sum_{\beta \in V_1} \tilde{w}_{\alpha\beta}^{(m)} \cdot \sum_{\gamma \in V_1} w_{\beta\gamma}^{(m)} u_\gamma \quad (47)$$

This approximation method can be seen as analogous to exact differentiation where the  $m$ -th derivative is obtained by successive differentiation, i.e.  $D^{(m)} u = D^{(1)} \cdot D^{(m-1)} u$ . The principal challenge is of course to preserve the  $k$ -exactness of the reconstruction in (37). Such methods have recently been developed at the DSN department of Onera for  $k=2$  and  $k=3$ . They have been successfully tested for the linear advection equation. Figure 17 shows the result of the linear advection of a Gaussian hat in 2D.

Last but not least, the use of  $k$ -exact polynomial reconstruction requires the use of higher order quadratures to compute the numerical fluxes at the cell interfaces with the necessary precision, otherwise the order of the numerical scheme will be reduced. Quadratures that are exact on polynomials of degree  $k=3$  are already implemented in CEDRE ■

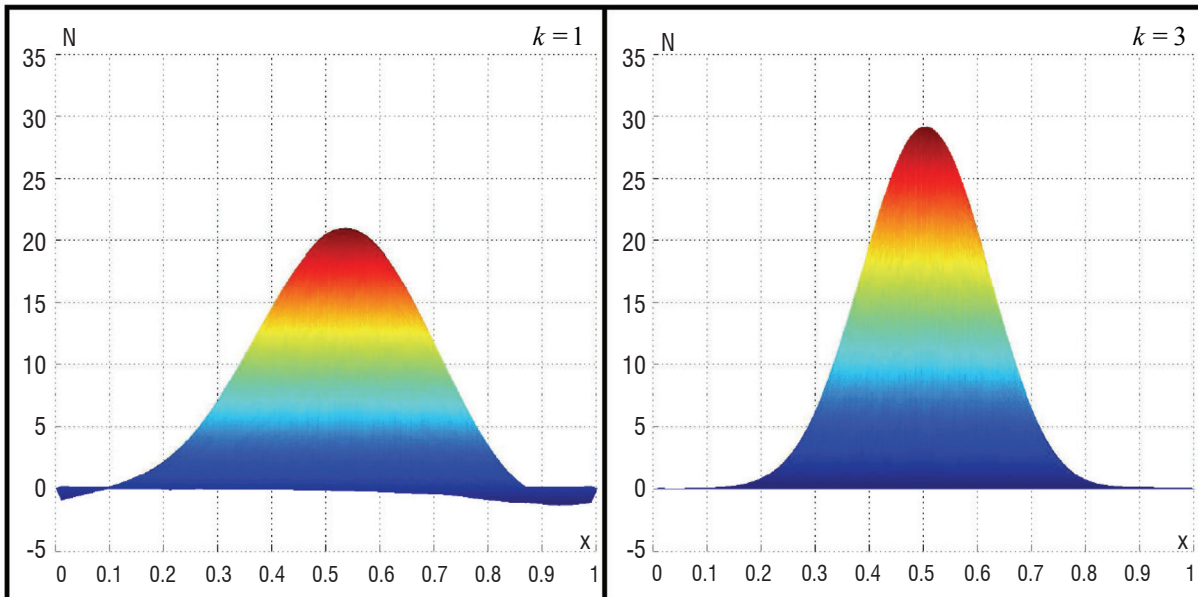


Figure 17 - Advection of a Gaussian hat with  $k=1$  and  $k=3$

## References

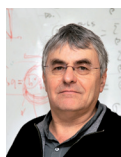
- [1] B. AUPOIX, F. CHEDEVERGNE, D. ARNAL, E. LAROCHE, S. DECK and F. GLEIZE - *Transition and Turbulence Modelling* . Aerospace Lab. Issue 2. 2011.
- [2] C. BENOIT and G. JEANFAIVRE - *Three Dimensional Inviscid Isolated Rotor Calculations Using Chimera and Automatic Cartesian Partitioning Methods*. Journal of the American Helicopter Society, (2003), pp. 128-138.
- [3] G. BILLET and J. RYAN - *A Runge Kutta Discontinuous Galerkin Approach to Solve Reactive Flows: the Hyperbolic Operator*. submitted to Journal of Computational Physics.
- [4] P. CALI, V. COUAILLIER and A. JAMESON - *Conservative Interfacing for Turbomachinery Applications*. ASME Paper 2001-GT-357, 2001.
- [5] W.J. CALVERT, A.W. STAPLETON, P.R. EMMERSON, C.R. BUCHANAM and C.M. NOTT - *Evaluation of a 3D Viscous Code for Turbomachinery*. ASME paper 97-GT-78, 1997.
- [6] L. CAMBIER - *elsA Software*. Aerospace Lab. Issue 2. 2011.
- [7] L. CAMBIER and M. GAZAIX - *elsA – An Efficient Object Oriented Solution to CFD Complexity*. AIAA Paper 2002-0108, 2002.
- [8] R.V. CHIMA - *Viscous Three-Dimensional Calculations of Transonic Fan Performance*. AGARD CP 510, Paper 21, 1991.
- [9] P. CINNELLA and A. LERAT - *A Study of Turbulent Compressible Flows Over Oscillating Airfoils Using a High-Order Numerical Scheme*. Computational Fluid Dynamics Journal special issue, 9 (2001), pp. 257-271.
- [10] V. COUAILLIER, P. VEYSSEYRE and A.M. VUILLOT - *3-D Navier-Stokes Computations in Transonic Compressor Bladings*. Proceedings of the 10th ISABE Conference, 1991.
- [11] R.L. DAVIS, R.H. NI and J.E. CARTER - *Cascade Viscous Flow Analysis Using the Navier-Stokes Equations*. Jour. Of Propulsion, Vol. 3, pp 406-414, 1987
- [12] F. DUPOIRIEUX, N. BERTIER, V. SABELNIKOV and P. GILBANK - *The Models of Turbulent Combustion in the CHARME Solver of CEDRE* . Aerospace Lab. Issue 2. 2011.
- [13] D. DUTOYA and L. MATUSZESKI - *Thermodynamics in CEDRE* . Aerospace Lab. Issue 2. 2011.
- [14] C.A.J. Fletcher - *Computational Techniques for Fluid Dynamics Specific Techniques for Different Flow Categories*, 2nd edition, Springer, 1991.
- [15] M.B. GILES - *Stator/Rotor Interaction in a Transonic Turbine*. AIAA Paper 88-3093.
- [16] F. HAIDER - *Discrétisation en maillage non structuré général et application*. Phd Thesis, Université Pierre et Marie Curie, 2009
- [17] F. HAIDER, J.P. CROISILLE and B. COURBET - *Stability of the Muscl Method on General Unstructured Grids for Applications to Compressible Flows*, Fifth International Conference on Computational Fluid Dynamics, Seoul, 2008 Springer Verlag
- [18] F. HAIDER, J.P. CROISILLE and B. COURBET - *Stability Analysis of the Cell Centered Finite-Volume Muscl Method on Unstructured Grids Numer. Math.*, vol. 113, 2009, pp. 555-600
- [19] C. HIRSCH - *Numerical Computation of Internal and External Flows*. John Wiley & Sons, 1988
- [20] C. HIRSCH - *Numerical Computation of Internal and External Flow*. Fundamentals of Computational Fluid Dynamics, Butterworth-Heinemann Elsevier, Second edition 2007
- [21] A. JAMESON, W. SCHMIDT, and E. TURKEL - *Numerical Solutions of the Euler Equations by Finite Volume Methods Using Runge-Kutta Time Stepping*, AIAA Paper, 81-1259 (1981).
- [22] N. KROLL - MEGAFLOW – *A Numerical Flow Simulation System*. Proceedings of the ICAS Conference, Melbourne, 1998.
- [23] M. LEFÈBVRE - *Développement de nouvelles techniques numériques pour la résolution des équations de Navier-Stokes tridimensionnelles stationnaires sur des maillages hybrides structurés/non structurés*. Thèse de doctorat « thermique et énergétique », Ecole Centrale de Lyon, 1998.
- [24] M. LEFÈBVRE, V. COUAILLIER and J.M. DUBOUÉ - *Numerical Methods on Adaptive Hybrid Grids for the Solution of Euler and Navier-Stokes Equations*. Proceedings of the 4th ECCOMAS Conference, J. Wiley, 1998.
- [25] J.-M. LE GOUEZ, V. COUAILLIER and F. RENAC - *High Order Interpolation Methods and Related Urans Schemes on Composite Grids*. 48th AIAA Aerospace Sciences Meeting, Orlando, Florida, 2010
- [26] A. LERAT - *Implicit Methods of Second-Order Accuracy for the Euler Equations*. AIAA Computational Fluid Dynamics Conference, Danvers, 1983.
- [27] N. LETERRIER - *Discrétisation spatiale en maillage non-structuré de type général*. Phd Thesis, Université Pierre et Marie Curie, 2003
- [28] C. MARMIGNON, V. COUAILLIER and B. COURBET - *Solution Strategies for Integration of Semi-Discretized Flow Equations in elsA and CEDRE*. Aerospace Lab. Issue 2. 2011.
- [29] R. MEAKIN - *Adaptive Spatial Partitioning and Refinement for Overset Structured Grids*. Computer Methods in Applied Mechanics and Engineering, 189 (2000), pp. 1077- 1117.
- [30] A. MURRONE and P. VILLEDIEU - *Numerical Modelling of Dispersed Two-Phase Flow* . Aerospace Lab. Issue 2. 2011
- [31] R.H. NI - *A Multiple Grid Scheme for Solving the Euler Equations*. AIAA Journal, Vol. 20, pp. 1565-1571, 1982.
- [32] R. PEYRET and T.D. TAYLOR - *Computational Methods for Fluid Flow*. Springer Verlag, 1983.
- [33] A. Refloch, et Al. - *CEDRE Software*. Aerospace Lab. Issue 2. 2011
- [34] J. RENEAUX and al - *Advanced Aerodynamic Applications with the elsA Software*. Aerospace Lab. Issue 2. 2011
- [35] A. REZGUI, P. CINNELLA, and A. LERAT - *Third-Order Accurate Finite Volume Schemes for Euler Computations on Curvilinear Meshes*. Computers and Fluids, 30 (2001), pp. 875-901.
- [36] O. SAUNIER, C. BENOIT, G. JEANFAIVRE, and A. LERAT - *Third-Order Cartesian Overset Mesh Adaptation Method for Solving Steady Compressible Flow*. International Journal for numerical methods in fluid, 57 (2008), pp. 811-838.
- [37] D. SCHERRER and al - *Recent CEDRE Applications*. Aerospace Lab. Issue 2. 2011
- [38] J. STEGER, F. DOUGHERTY, and J. BENEK - *A chimera grid scheme*. Advances in Grid Generation. K.N. Ghia and U. Chia, eds., ASME FED, 5 (1983), pp. 59-69.

[39] B. VAN LEER - *Towards the Ultimate Conservative Difference Scheme V. A Second-Order Sequel to Godunov's Method*. Journal of Computational Physics, vol. 32, no 1, pp, 101-136, 1979

[40] A.M. VUILLOT, V. COUAILLIER and N. LIAMIS - *3D Turbomachinery Euler and Navier-Stokes Calculations with a Multi-Domain Cell-Centered Approach*. AIAA paper 93-2576, 1993.

[41] A. WISSINK, M. POTSDAM, and V. SANKARAN - *A Coupled Unstructured-Adaptive Cartesian CFD Approach for Hover Prediction*. 66th AHS Forum, 2010.

## AUTHORS



**Bernard Courbet** Ecole Centrale Paris, Research engineer, department of numerical simulation and aeroacoustics, unit CIME Architect and developer for the CEDRE software, numerical methods for polyedral meshes.



**Christophe Benoit** Ecole Centrale Nantes, Doctoral Degree, Mechanics, ENSAM Research engineer, department of numerical simulation and aeroacoustics, unit CS2A Numerical geometry and mesh.



**Vincent Couaillier** Doctoral degree Master in Numerical Analysis University Pierre et Marie Curie (UPMC) Head of the unit NUMF (Numerical Methods for Fluid Mechanics), department of numerical simulation and aeroacoustics Algorithms and software developments.



**Florian Haider** Master of Physics, University of Technology, Vienna Austria Master of Mathematics (Analysis and Geometry), University Pierre et Marie Curie Paris 6 Master of Mathematics (Mathematics and Applications), University Pierre et Marie Curie Paris 6 Doctoral Degree, Mechanics, University Pierre et Marie Curie Paris 6 Research engineer, department of numerical simulation and aeroacoustics, unit CIME Research on numerical methods for unstructured grids, software development for the project CEDRE



**Marie-Claire Le Pape** Ecole Centrale Lyon, Research engineer, department of numerical simulation and aeroacoustics, unit NUMF Chimera methods, hybrid mesh development and validation in ELSA



**Stéphanie Péron** Ecole Centrale Marseille DEA ENS Cachan Research engineer, department of numerical simulation and aeroacoustics, unit CS2A Mesh generation, adaptation and assembling, Cartesian solver with third order schemes.

C. Marmignon, V. Couaillier,  
B. Courbet

(Onera)

E-mail: claude.marmignon@onera.fr

# Solution Strategies for Integration of Semi-Discretized Flow Equations in elsA and CEDRE

This paper is devoted to the presentation of a selection of time integration methods used in the Onera elsA and Cedre software dedicated to the resolution of the compressible Navier-Stokes equations. The selected methods are given in the framework of steady and unsteady flow simulations. Emphasis is put on methods for the resolution of algebraic systems associated with time integration methods for space-discretized equations.

## Introduction

Onera is developing two new-generation computational programs for the solution of the compressible Navier-Stokes equations, elsA and Cedre. elsA is more particularly dedicated to the aerodynamics of the flows and Cedre is well adapted to fluid mechanics phenomena in energetics. Both codes are based on similar time integration methods, which allows a unified presentation of the schemes used. We consider here a formulation where the time discretization is separated from the space one. The choice of a time integration algorithm is an essential criterion to ensure efficiency and robustness of numerical simulations and depends on the nature of the flow to compute. In this paper, we are going to classify the methods as steady or unsteady flow.

After space discretization, a system of ordinary differential equations is obtained and a large number of methods are available for the solution this system. Two important families of time integration are developed in our codes. The first one is the family of Runge-Kutta multistage methods and the second one is the family of multi step ones. Only these last ones are investigated in this paper. In the framework of stationary flows, we are interested in the theme of linearization and techniques of approximate factorization. The linear algebraic system is solved by iterative methods, direct methods being prohibitive in terms of memory requirements. A very large number of iterative methods are available in the literature. A presentation of the two main methods implemented in elsA (LU Relaxation) or Cedre (GMRES resolution) is done. The convergence acceleration techniques based on multigrid methods that have been used at Onera for many years for block-structured meshes are also presented.

In the framework of unsteady flow calculations, a dual time-stepping approach in which a steady state with respect to the dual time is ap-

proximately reached at each physical time-step is described. Calculation between two physical instants leads to the resolution of a system of pseudo-unsteady equations in dual time and is carried out using convergence acceleration techniques developed within the framework of the steady problems (multi-grid method, local time step, implicit phase with respect to dual time).

## ODE system

The purpose of this paper is to present the time integration of the flow equations for numerical simulations of compressible flows as used in the Cedre or Elsa software [19],[6]. We shall describe here only some of the present methods in this software. We are interested in laminar or turbulent flows as well as in reacting flows. The governing equations are solved in their integral conservation law form using a cell-centered finite volume formulation.

Let  $\Omega_h$  be a polygonal approximation of the physical domain  $\Omega \subset R^d$  ( $d=1,2,3$ ) made of non-overlapping and non-empty polyhedra. The set of the faces of a polyhedron  $K$  is denoted by  $\partial K$  and for each face on  $K$ ,  $n_{e,K} \in R^d$  represents the outward unit normal to the face  $e$ . Given a face  $e$  of  $K$ ,  $K_e$  is the unique polyhedra in  $\Omega_h$  which shares the same face  $e$  with  $K$ . Discretizing the conservation equations in  $\Omega_h$  leads to

$$\int_K \frac{\partial W}{\partial t} dV + \int_{\partial K} [F_c(W) - F_v(W, \nabla W)] \cdot n dS = \int_K T(W) dV \quad (1)$$

where  $W$  represents the state vector of conservative variables,  $F_c$  and  $F_v$  are respectively the convective and diffusive fluxes and  $T$  is the source term. The fluxes are discretized in space using some

suitable approximation. The convective flux is discretized for example with flux vector or difference splitting schemes, or space centered scheme plus artificial dissipation. A central differencing is generally used for the viscous terms. The source term is evaluated using variables at cell centres.

We obtain a system of ordinary differential equations, the so-called semi-discrete problem:

$$\frac{d}{dt}(W_K |K|) + R_K = 0 \quad (2)$$

where  $R_K$  denotes the residual vector and is defined by

$$R_K = \sum_{\partial K_e} R_{\partial K_e} - T_K |K| = \sum_{\partial K_e} (F_c - F_v)_{\partial K_e} - T_K |K| \quad (3)$$

If all the mesh point values  $W_K$  are gathered in a column vector  $U$ , the system can be rewritten

$$\frac{dMU}{dt} + R(U) = 0 \quad (4)$$

In the general ALE case,  $M$  depends on time,  $M = M(t)$ . In finite volumes on a motionless mesh,  $M$  is typically a constant diagonal or block diagonal matrix. For simplicity, most methods will be described in this particular case.

## Time discretization

### Explicit and implicit methods

Both explicit and implicit methods are available to integrate the system (4) numerically. The choice of a time integration algorithm is an essential criterion to ensure efficiency and robustness of numerical simulations and depends on the nature of the flow to be computed. For a general system of ordinary differential equations,  $R(U)$  is a non-linear function of  $U$ . To compute stationary flows, a first-order accurate implicit Euler method is often chosen since time accuracy is not required to reach steady state. On the other hand, fast unsteady flows involving high frequency phenomena require explicit time integration of Runge-Kutta type, for example [10], and do not allow the use of large time steps. For slow unsteady problems, the numerical cost of an unsteady cycle is strongly reduced by the use of implicit methods of integration in time, increasing the numerical stability domain of the schemes and thus allowing the use of large time steps. The difference between explicit and implicit time integration scheme is the time step at which the residual vector  $R$  is evaluated.

### Multistep Method

Two important families of time integration methods are developed in our codes. The first one is the family of Runge-Kutta multistage methods which allow high orders in time and are explicit. The reader is referred to [11] for details. Another important family of time integration methods is the family of multi step methods, which allow implicit time integration options. The high accuracy can then be achieved by involving multiple time steps. In this framework, we can introduce the particular two-step method (three time levels) in the following form:

$$M \frac{[(1+\xi)U^{n+1} - (1+2\xi)U^n + \xi U^{n-1}]}{\Delta t} = -[\theta R^{n+1} + (1-\theta+\varphi)R^n - \varphi R^{n-1}] \quad (5)$$

The incremental form is written:

$$M \frac{[(1+\xi)\Delta^n U - \xi \Delta^{n-1} U]}{\Delta t} = -[\theta R^{n+1} + (1-\theta+\varphi)R^n - \varphi R^{n-1}] \quad (6)$$

with  $\Delta^n U = U^{n+1} - U^n$ .  $\theta, \xi$  and  $\varphi$  are three parameters allowing control respectively of the implicitness of the method, the order of the finite difference of  $dU/dt$  and the number of time levels for  $R$ . In our context, we mainly applied the particular schemes with  $\varphi = 0$ . In this case, it can be shown that the schemes are second order accurate for  $\xi = \theta - 1/2$ . For  $\xi = 0$  and  $\theta = 1/2$ , the resulting scheme is known as the Crank-Nicholson method and is therefore second-order accurate in time.

Classic explicit time integration ( $\theta = 0$ ) may be written as

$$M \frac{(1+\xi)\Delta^n U - \xi \Delta^{n-1} U}{\Delta t} = -R^n \quad (7)$$

where  $R$  is evaluated at time step  $n$ .

## Methods for steady flows

The theme of linearization and approximate factorization for the development of implicit methods for compressible Navier-Stokes equation solution has been tackled by many authors. The reader can refer to the retrospective overview by Briley and Mac Donald [5] for more details.

### Approximate Jacobian linearizations

In this chapter, we are mainly interested in the numerical simulation of steady flow.

If  $\theta \neq 0$ ,  $R^{n+1} = R(U^{n+1})$  is evaluated using a Jacobian linearization around the state  $U^n$  thanks to a second order Taylor expansion,

$$R^{n+1} = R^n + \Delta^n R = R^n + \frac{\partial R}{\partial U} \Delta^n U + O(\Delta U^2). \quad (8)$$

Up to second order,

$$R^{n+1} = R^n + \frac{\partial R}{\partial U} (U^n) \Delta^n U \quad (9)$$

and the equation (6) becomes

$$\left[ M \frac{(1+\xi)}{\Delta t} + \theta \left( \frac{\partial R}{\partial U} \right)^n \right] \Delta^n U = - \left[ R^n + \varphi \Delta t (R^n - R^{n-1}) \right] + M \frac{\xi}{\Delta t} \Delta^{n-1} U. \quad (10)$$

With the exception of  $\Delta^n U$ , all the quantities are known at time step  $n$ .

The left-hand side of (10) is generally a large sparse and non symmetric matrix. This means that many of elegant algorithms for positive definite matrices will not work on equation (10). Also, since equation (10) will be solved many thousands of times, speed is prominent. Since a steady state solution is wanted, it may not be necessary to solve (10) very accurately, since only the converged solution is of any interest. Therefore, an approximate Jacobian is usually applied in the linearization. An approximate Jacobian associated to a first order upwind discretization is often selected. In

the framework of steady flow simulations, the loss in consistency between the space-discretized operators and the approximate Jacobian is no problem. On the other hand, it can have as consequence a reduction of stability range. By choosing a small enough time step, we can note that the matrix in (10) may always be made block diagonal dominant.

For simplicity, the present development uses first-order time differencing ( $\xi = 0$ ) and a two time level space-discretized term  $R$  ( $\varphi = 0$ )

$$\left[ M \frac{1}{\Delta t} + \theta \left( \frac{\partial R}{\partial U} \right)^n \right] \Delta^n U = -R^n \quad (11)$$

If  $\theta = 1$ , the scheme is the backward Euler method. For later discussion, we write

$$A \delta U = -R^n \quad (12)$$

with

$$A = \left[ M + \theta \Delta t \left( \frac{\partial R}{\partial U} \right)^n \right] \quad (13)$$

and

$$\delta U = \frac{\Delta^n U}{\Delta t} \quad (14)$$

$A$  is a block-diagonal matrix of 5x5 blocks for tridimensional Euler equations for instance. In practice, the most usual simplifications of the implicit operator are diagonalization of all or part of the blocks of the implicit matrix or factorization (ADI or LU methods).

Diagonalization consists in transforming, wholly or partly, the blocks of the Jacobian matrices occurring in the implicit phase into diagonal matrices. It is generally associated with a factorization.

### Approximate factorization methods

The purpose of the techniques of approximate factorization is to simplify the inversion of the matrix system. Indeed, the matrix system cannot be tridiagonal anymore when implicit schemes are applied to multidimensional problems. The factorizations include alternating (ADI) implicit, Lower-Upper (LU) and line relaxation schemes.

The ADI alternate direction technique consists in substituting for the implicit operator a factorized operator along the direction of the grid [17],[18],[2], [4]. Due to the difference between the original matrix and the resulting matrix, upon remultiplication, this procedure introduces errors that can cause a reduction in convergence speed. A modified approximate factorization (MAF) procedure, also called diagonally dominant alternate direction implicit (DDADI), that can regain a part of the convergence rate loss caused by the standard AF is sometimes proposed.

Such techniques are no longer valid for unstructured grids so that the system has to be solved by one of the two large families of methods available for the resolution of the linear algebraic system (4): the direct and the iterative methods. Direct methods are prohibitive in terms of memory requirements and in practice iterative must be considered.

### Iterative methods

A very large number of iterative methods are available in the literature. A presentation of the two main methods implemented in elsA (LU Relaxation) or Cedre (GMRES resolution) is described here.

### GMRES resolution

Iterative methods aim at building a sequence of iterates  $\delta U_0 = -R^n$ ,  $\delta U_1, \dots, \delta U_\nu$  such as  $\delta U_\nu \rightarrow A^{-1} \delta U_0$  when  $\nu \rightarrow \infty$ .

GMRES is a nonlinear Krylov method, i.e. it builds a sequence of iterates  $\delta U_\nu$  belonging to the Krylov subspace

$$K_\nu = \text{span} \{ \delta U_0, A \delta U_0, \dots, A^{\nu-1} \delta U_0 \} \quad (15)$$

More precisely, GMRES finds  $\delta U_\nu \in K_\nu$  so as to minimize the Euclidian norm of the residual  $r_\nu = A \delta U_\nu - \delta U_0$ :

- as the dimension of  $K_\nu$  cannot be larger than the order  $m$  of  $A$ ,  $|r_\nu| = 0$  when  $\nu = m$ : in exact arithmetics, the method would converge in a finite (though very large !) number of iterates ;

- as the dimension of  $K_\nu$  grows with  $\nu$ , the sequence of residuals  $r_\nu$  is necessarily decreasing, and no residuals oscillation is possible. The minimum principle underlying the method is thus a very sound basis for iterations, which distinguishes GMRES from other Krylov methods.

GMRES is very efficient in terms of CPU time in that it needs only one matrix-vector product per iterate. Of course, computational effort and storage needs increase with the dimension of the Krylov space, which means that it is generally not advisable to use this method with a large Krylov space ( $\nu \geq 100$  for instance). Nevertheless, the restarted version of GMRES puts an end to the orthogonalization process at a given number  $\nu_{res}$  of iterates and Krylov vectors, then resumes iterations with a new sequence of  $\nu_{res}$  of iterates and Krylov vectors etc. Restarted GMRES thus has a storage requirement of  $\nu_{res}$  Krylov vectors only although at the price of slower convergence.

GMRES is generally applied to a preconditioned system equivalent to the original one. For instance, left preconditioning amounts to multiplying (...) by a matrix  $B^{-1}$  such that  $B^{-1}A$  is in some sense closer to the unit matrix. In Cedre,  $B$  is chosen as the block-diagonal part of  $A$ ; although very simple, this preconditioning has the advantage of solving exactly the local part of the implicit system, for instance the contribution of the sources associated with chemical reactions or turbulence.

GMRES with block-diagonal preconditioning turns out very efficient for solving implicit systems from various solvers (multispecies reactive fluid flow, conduction in solids etc). The convergence mechanism of the nested iterative process including time marching and internal GMRES iterates was carefully studied in a PhD thesis [20] :

- at every time step, a few tens of iterations allow a moderate

reduction of  $r_\nu$  typically,  $\frac{|r_\nu|}{|r_0|} \sim 0.1$  to 0.001 for  $\nu = 20$  at very large

time step  $\Delta t$ . Of course, convergence is much faster for relatively small time steps;

- spectral analysis of convergence shows a dramatic reduction of high frequency components in the course of GMRES iterates. Even though  $|r_\nu|$  does not converge to very low values, GMRES practically

kills all high frequencies in  $r_n$ , which is sufficient to preserve the stability of implicit time iterates  $U^n$ . This distinguishes GMRES from relaxation methods like Jacobi or Gauss-Seidel, for which the reduction rate tends to be the same for all frequencies: for these methods, a huge number of iterates may be necessary to preserve stability at large time steps, specially in presence of dissipative fluxes.

On the other hand, GMRES does have limitations which must be taken into account:

- the nonlinear iterates depend on a small number of global sensors (scalar products and norms, in particular  $|r_n|$ ) for a very large number of degrees of freedom, which means that residuals in some regions and for some components of  $U$  may not be properly taken into account. For physical soundness, the Euclidian norm in the  $\delta U$  space must of course use dimensionless components; in some cases, the choice of scaling may have a significant effect on the quality of the solution. For instance in Reynolds Averaged Navier-Stokes simulations, improper scaling can lead to a poor solution;

- GMRES works well as long as numerical fluxes and sources are sensible, but convergence can be very awkward otherwise. In a low Mach number flow for instance, using a classical compressible numerical flux formula results in a very poor GMRES resolution, whereas a low-Mach number flux ensures efficient iterations;

- In case of preconditioning, time conservativity is not built-in and is only approximate.

GMRES has been used in Cedre in various contexts:

- its primary use is for finding steady asymptotic states in Reynolds Averaged Navier-Stokes or conductive heat transfer simulations...

- ... but it has also been used as the linear solver for time-dependent simulation with Runge-Kutta type implicit schemes [3].

## LU relaxation

After trying several relaxation methods in the context of the elsA solver, the LU relaxation is often used to invert the large matrices. The matrix of the implicit stage is then split into its block diagonal ( $D$ ), block lower ( $L$ ) and block upper ( $U$ ) submatrices so that  $A = L + D + U$ . Each block of  $D$  is associated with its own cell. The implicit LU relaxation approximate factorization can be implemented for 3D hybrid structured or unstructured grid.

The resolution of the implicit operator is based on an approximation of the exact matrix  $(L + D + U)$  by  $(L + D)D^{-1}(U + D)$ . The system is approximated by a method of relaxation with forward and backward sweeps through the domain. The method sweeps through the mesh from the lower left corner to the right upper corner during the forward sweep. In order to avoid a bias in the iteration scheme and some error accumulations, alternating sweeps in both direction is used. The backward sweep starts at the end-point of the first step. Each relaxation cycle writes in the form of two stages:

$$(L + D)\Delta U^{(p+1/2)} = -R^n - U\Delta U^{(p)} \quad (16)$$

$$(U + D)\Delta U^{(p+1)} = -R^n - L\Delta U^{(p+1/2)} \quad (17)$$

where  $p \in [0, p_{\max}]$  and indicates the number of the relaxation cycle.

These two sweeps are repeated several times and  $U^{n+1} = U^n + U^{(p_{\max}+1)}$ ,  $p_{\max}$ , corresponding to the maximum number of the relaxation cycle. The choice of the number of relaxation cycles

must lead to a satisfactory speed of convergence, and a weak value such as two ( $p_{\max} = 1$ ) can prove to be a good compromise. When this number tends towards  $+\infty$ , the method is convergent for an unfactored matrix with a strictly dominant diagonal and this whatever the initial vector.

In the case of an unstructured grid, a grid reordering algorithm is necessary for efficiency of the LU relaxation method. For structured grids, the LU relaxation sweeps are usually performed by using hyper planes  $i + j + k = C^{te}$ . The main interest of these sweeps by hyper planes is to order the matrix in lower and upper triangular matrices.

Forward sweep updates point  $(i, j, k)$  using already updated values at  $(i-1, j, k)$ ,  $(i, j-1, k)$ ,  $(i, j, k-1)$  while backward sweep uses  $(i+1, j, k)$ ,  $(i, j+1, k)$  and  $(i, j, k+1)$ . However, this procedure is particularly well adapted to structured grids and does not extend easily to unstructured grids. In order to get a similar LU relaxation algorithm for unstructured grids, a special grid re-ordering procedure is required. This re-ordering procedure was proposed by Soetrisno, Imlay and Roberts in [21].

For unstructured grid, the previous reordering of cells allows a clear definition of the lower and upper matrices  $\mathcal{L}$  and  $\mathcal{U}$  and the proposed algorithm can be applied.

## Multigrid method

The multigrid method using a sequence of fine to coarse grids, thus denoted H-multigrid, has been extensively used for practical 3D turbulent flow configurations for many years in block-structured finite volume codes in the CFD community.

This part presents convergence acceleration techniques based on multigrid methods, which have been used at Onera for many years for block-structured meshes. The first developments for the solution of Euler and Navier-Stokes system have been coupled with Lax-Wendroff type schemes [8],[9] based on the multigrid method proposed by Ni [16]. Then cell centered Jameson type schemes were used for complex configurations typical of industrial-type problems, and new multigrid methods proposed by Jameson [12] were implemented at Onera [7] and especially in the elsA software.

The time integration of this system of ordinary differential equations is carried out using multi-stage Runge-Kutta scheme (the Backward Euler scheme corresponds to a one-step scheme). To enhance convergence to steady state, local time stepping as well as implicit residual smoothing is used. In general classical iterative approaches are well adapted for rapidly damping high frequency error components on a given grid. The remaining errors, associated with the smoother low frequency error components, are responsible for the slow convergence. These low frequency error components on the fine grid appear as higher frequencies on the coarser grid. Thus, to enhance faster convergence of the solution to steady state on the fine grid, the multigrid idea is to use the coarser grids to smooth the fine grid low frequency errors on the coarse grids.

## Multigrid : Description of the FAS algorithm

The multigrid technique uses a sequence of successively coarser grids to efficiently damp the perturbations. Denoting the grid level by

a subscript, a sequence of grids  $h_1, \dots, h_m, \dots, h_M$  are then defined, where  $h_1$  denotes the finest grid and  $h_M$  represents the coarsest grid.

The multigrid strategy employed is the Full Approximation Storage (FAS) scheme in conjunction with Runge-Kutta time stepping proposed by Jameson. This strategy is used to improve the convergence rate of a multi-block solver for the solution of Euler and Reynolds-Averaged Navier-Stokes equations. The Jameson's FAS algorithm for a simple V-Cycle can then be summarised as follows:

- Compute the residual  $R_{h_1}$  and start with a q-stage Runge-Kutta time stepping to update the solution on the finest level  $h_1$ .

The following steps are repeated right up to the coarsest level  $m = 2, \dots, M$  which corresponds to the Restriction step :

- Recompute the residual  $R_{h_{m-1}}(u_{h_{m-1}})$  on the previous level and calculate the modified residual to be transferred from grid level  $h_{m-1}$  to the level  $h_m$  :

$$R_{h_{m-1}}^{(*)} = R_{h_{m-1}}(u_{h_{m-1}}) + P_{h_{m-1}} \quad (18)$$

where  $P_{h_{m-1}}$  is the added forcing function defined below with  $P_{h_1}$  on the finest level.

- Transfer the solution and residual vectors from the previous grid  $h_{m-1}$  to the next coarser grid  $h_m$  using respectively the fine to coarse transfer operators  $T_{h_{m-1}}^{h_m}$  and  $\hat{T}_{h_{m-1}}^{h_m}$  :

$$\bar{u}_{h_m} = T_{h_{m-1}}^{h_m} u_{h_{m-1}} \quad (19)$$

$$\bar{R}_{h_m} = \hat{T}_{h_{m-1}}^{h_m} R_{h_{m-1}}^{(*)}$$

- Compute the forcing function for the residuals on the grid level  $h_m$  which is the difference between aggregated residuals transferred from grid  $h_{m-1}$  and the residuals recalculated on  $h_m$  :

$$P_{h_m} = \bar{R}_{h_m} - R_{h_m}(\bar{u}_{h_m}) \quad (20)$$

where  $R_{h_m}(\bar{u}_{h_m})$  is the residual vector computed on the grid level  $h_m$  using the transferred solution vector  $\bar{u}_{h_m}$  from the previous grid level  $h_{m-1}$ .

- Start Runge-Kutta time stepping on the coarse level  $h_m$  using the following reformulated version, to take into account the forcing function as well as to include sub-iterations if necessary, coupled with an implicit smoothing technique (IRS or LU):

$$\left\{ \begin{array}{l} u_{h_m}^{(0)} = \bar{u}_{h_m} \text{ or } \bar{u}_{h_m}^{(q)} \\ \Delta \tilde{u}_{h_m}^{(1)} = \alpha_1 \frac{\Delta t_{h_m}}{\Omega_{h_m}} [R_{h_m}(u_{h_m}^{(0)}) + P_{h_m}] \\ \Theta_{h_m} \Delta u_{h_m}^{(1)} = \Delta \tilde{u}_{h_m}^{(1)} \\ u_{h_m}^{(1)} = u_{h_m}^{(0)} + \Delta u_{h_m}^{(1)} \\ \vdots \end{array} \right. \quad (21)$$

$$\left\{ \begin{array}{l} \vdots \\ \Delta \tilde{u}_{h_m}^{(q)} = \alpha_q \frac{\Delta t_{h_m}}{\Omega_{h_m}} [R_{h_m}(u_{h_m}^{(q-1)}) + P_{h_m}] \\ \Theta_{h_m} \Delta u_{h_m}^{(q)} = \Delta \tilde{u}_{h_m}^{(q)} \\ u_{h_m}^{(q)} = u_{h_m}^{(0)} + \Delta u_{h_m}^{(q)} \end{array} \right. \quad (21)$$

Note that upon convergence, when the residual on the finest level goes to zero, the term  $R_{h_m}(u_{h_m}^{(0)}) + P_{h_m}$  in the above equation which

can be rewritten as  $R_{h_m}(u_{h_m}^{(0)}) + [\bar{R}_{h_m} - R_{h_m}(\bar{u}_{h_m})]$  goes as well to zero. Thus, no correction is computed on the coarser levels and driven back to the finest level.

- Updated solution on coarse grid  $h_m$  :

$$u_{h_m} = u_{h_m}^{(q)} \quad (22)$$

The accumulated corrections from each coarser grid are then successively passed back to finer levels by interpolation ( $m = M, \dots, 2$ ). This represents the prolongation step: Transfer the correction from the grid level  $h_m$  to the next finer one  $h_{m-1}$ .

- Transfer the correction from the grid level  $h_m$  to the next finer one  $h_{m-1}$  :

$$u_{h_{m-1}}^{(+)} = u_{h_{m-1}} + I_{h_{m-1}}^{h_m} (u_{h_m}^{(+)} - \bar{u}_{h_m}) \quad \text{avec } u_{h_M}^{(+)} \equiv u_{h_M} \quad (23)$$

where  $I_{h_{m-1}}^{h_m}$  is the coarse to fine grid prolongation or interpolation operator from grid  $h_m$  to the next finer one  $h_{m-1}$  with  $u_{h_M}^{(new)} \equiv u_{h_M}$  on the coarsest grid.

The implemented strategies include V and W cycles as well as options for full multigrid (FMG) versions. In the present multigrid approach, only full coarsening algorithms are employed. Thus, a sequence of coarser grids is extracted from the initial given fine grid by deleting every other grid line in each coordinate direction.

Further, the boundary conditions on the coarse grids are treated in the same way as in the fine grid.

Special attention is given to the intergrid transfer operators in the cell-centered formulations in which the variables are located at cell centers. Thus, the transferred variable locations change from one grid to another, which is not the case in a cell vertex or node centered formulation. For the fine to coarse operators, the standard approach is used. The transfer of flow variables conserves mass, momentum and energy by the rule:

$$\bar{u}_{h_m} = \frac{\sum \Omega_{h_{m-1}} u_{h_{m-1}}}{\sum \Omega_{h_{m-1}}} \quad (24)$$

and the residual transferred to grid  $h_m$  is the sum of the residuals computed on the eight cells of the fine grid :

$$\bar{R}_{h_m} = \sum R_{h_{m-1}}^{(*)} \quad (25)$$

where the summations range over the cells on the fine grid composing each cell on the coarser grid.

For the coarse to fine operator, in order to damp the high frequency errors, an efficient prolongation operator possessing inherent smoothing properties and well adapted for multiblock computational mesh is introduced. The basic idea is to project the cell centered corrections ( $u_{h_m}^{(new)} - \bar{u}_{h_m}$ ), denoted here by the symbol  $\Phi$ , in a conservative manner to the nodes of the coarse grid by the relation:

$$\Phi_{h_m}^{(Node)} = \frac{\sum_{\{Cell/Node \in Cell\}} \Omega_{h_m}^{(Cell)} \Phi_{h_m}^{(Cell)}}{\sum_{\{Cell/Node \in Cell\}} \Omega_{h_m}^{(Cell)}} \quad (26)$$

where the numbering of the nodes are given as in figure 1.

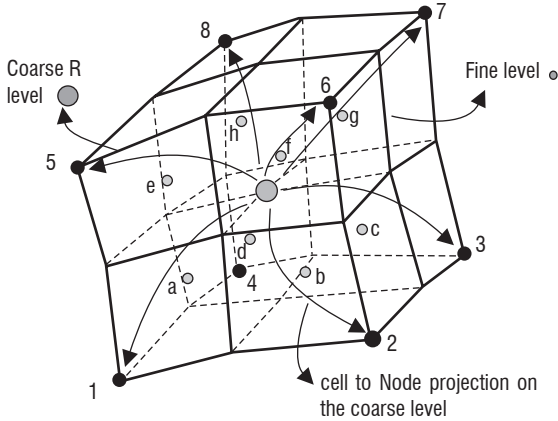


Figure 1 - Coarse to fine inter-grid operator

This conservative smoothing is found to be quite efficient in all our applications. For multi-block computational mesh, the exact interfaces are also taken into account in this cell-to-node projection process. For the four finer (in 2D) cells, which are then exactly included in the coarser grid cell, a volume weighted interpolation is used to compute the cell centered corrections:

$$\Phi_{h_{m-1}}^{(a)} = \frac{\sum_i \Omega_i \Phi_{h_m}^{(i)}}{\Omega} \quad (27)$$

where  $\Omega$ , the volume of the coarse grid cell  $h_m$ , is the summation of the included fine grid cell volumes

The interpolation coefficients could be based on linear interpolation, inverse distance interpolation or inverse volume interpolation to get better accuracy, but not necessarily better smoothing properties.

For inviscid computations, this leads to an efficient procedure and good convergence properties are obtained for a wide range of 3D applications. Further, to treat complex multi-block configurations with limited number of cells in one direction, the idea of using linear dissipation terms on the coarse grids is also implemented. This consists in using a simple constant coefficient second order dissipation term on the coarser grids instead of the nonlinear artificial dissipation model.

### Strategy for turbulent flows

In the case of the RANS equations, the approach adopted is to compute the viscous terms on the coarser grids too. Thus, their influences are also taken into account in the forcing functions on the coarser

grids. Different turbulence models are available in the solver, ranging from algebraic models to two equation models. These models are used to compute the turbulent quantities only on the finest grid level. On the coarser grids, they are obtained by interpolating the values from the finest level. This leads to a very direct approach with algebraic models, while with one or two equation models, the corresponding turbulence model equations are solved separately decoupled from the flow equations. In the solver, one Runge-Kutta iteration is carried out to update the turbulent quantities on the fine grid. Thus, different new turbulence models can easily be included in the present environment.

### Strategy for multigrid cycles

In order to ensure robustness in  $V$  cycles without multigrid on turbulent quantities, sub-iterations are performed on the corresponding equations (let say 2 subiterations on the  $k-w$  system for a  $V$  cycle with 2 or 3 grids). Concerning the present multigrid DG implementation, we have used a P1 approximation on the fine grid and a P0 approximation on the coarse grid, leading to small overcost when using multigrid (20% additional cost per iteration).

### Onera M6 wing multigrid computations

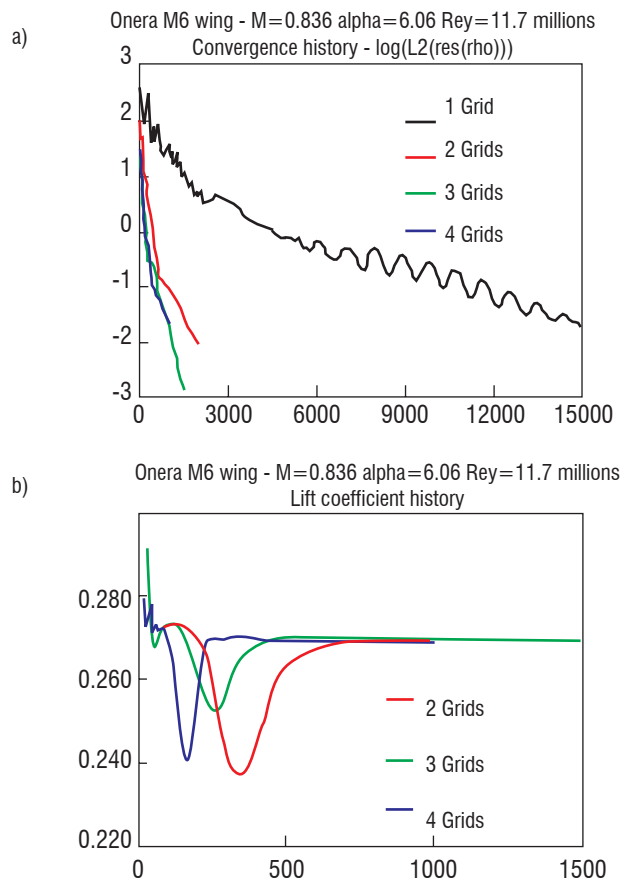


Figure 2 : Onera M6 wing transonic computation – Convergence evolution  
a) L2 norm of residual – b) lift coefficient

The Onera M6 wing is a basic 3D test case widely presented in the literature in order to validate numerical methods and turbulence models. The flow field is computed here by the solution of the RANS equation with the Wilcox  $k-\omega$  model at a free stream Mach number of 0.836, an angle of attack of 6.06° and a free stream Reynolds number of  $11.7 \cdot 10^6$ . The C-O mesh used for the computations is

composed of 193x49x65 points, corresponding to  $y^+ \approx 1$  almost everywhere on the wing.

Figure 2 illustrates convergence histories of computation performed with the implicit LU method respectively without multigrid (1 grid), and with multigrid with different number of coarse grids (2, 3 and 4 grids). For that test case we have a ratio gain of 5 for a 4-grid computation, knowing that a multigrid cycle is about 25% to 35% more expensive than a single iteration (monogrid cycle).

## Time integration for unsteady flow simulations

The majority of flow fields encountered in engineering applications are unsteady. In unsteady applications, some of the most widely used methods of the two step family (6) are the explicit method of Adams-Bashworth ( $\varphi = 1/2$ ), and the implicit Crank-Nicholson ( $\theta = 1/2$ ) and Gear methods ( $\theta = 1$ ,  $\xi = 1/2$ ). The main drawback of explicit schemes lies in the numerical stability limit on  $\Delta t$ , but the CPU cost per iteration is low, since no matrices have to be invert. For implicit methods, large time steps can be applied. Nevertheless, for unsteady flow problems, accuracy requirements tend to restrict the maximum time step.

### Dual time stepping

Unsteady flow can also be computed by a dual time-stepping approach [13], [14], [15] in which a steady state with respect to the dual time is approximately reached at each physical time-step. Calculation between two physical instants leads to the resolution of a system of pseudo-unsteady equations in dual time and is carried out using convergence acceleration techniques developed within the framework of the steady problems (multi-grid method, local time step, implicit phase with respect to dual time).

In order to use the dual-time stepping method, an additional term is introduced in the equation

$$M \left( \frac{dU}{dt} \right)^{n+1} + R(U^{n+1}) = 0 \quad (28)$$

where for simplicity of presentation we assume  $\theta = 1$

This term corresponds to derivative in dual time of the conservative variables. The form of the equation relative to dual time then becomes:

$$M \frac{dU^{n,m}}{d\tau} + \hat{R}(U^{n,m+1}) = 0 \quad (29)$$

with

$$\hat{R}(U^{n,m+1}) = M \frac{dU^{n,m+1}}{dt} + R(U^{n,m+1}) \quad (30)$$

Indices m and n are respectively attached to dual time and physical time. The sub-iterations in dual time thus relate to the index m. The term  $\hat{R}_k(U^{n,m+1})$  represents the unsteady residual. With convergence of sub-iterations ( $m \rightarrow \infty$ ), the first term of equation is null and the aerodynamic field satisfies:

$$\hat{R}(U^{n,\infty}) = \hat{R}(U^{n+1}) = 0 \quad (31)$$

Thus, the aerodynamic field indeed corresponds to the unsteady solution of the physical problem at the instant  $(n+1)\Delta t$ .

In order to speed up the convergence to the pseudo-steady state, scheme can be made implicit with respect to  $\tau$ . Generally, a simple first-order space discretization is retained to build the implicit stage. If no motion of  $K$  is considered, the scheme is written:

$$\left[ M \frac{1}{\Delta\tau} + M \frac{(1+\xi)}{\Delta t} + \theta \frac{\partial R(U^{n,m})}{\partial U} \right] \Delta^m U = - \left[ R(U^{n,m}) + \varphi \Delta t (R(U^n) - R(U^{n-1})) \right] + \frac{\xi}{\Delta t} M (U^{n,m} - U^{n-1}) - \frac{(1+2\xi)}{\Delta t} M (U^{n,m} - U^n) \quad (32)$$

with  $\Delta^m U = U^{n,m+1} - U^{n,m}$ .

The time accuracy of the method depends on the temporal discretization of the physical time derivative.

### Implication of Runge-Kutta-Heun methods

Implicit methods can also be of interest in unsteady simulations when unresolved time scales which do not participate in the solution can none the less destabilize explicit calculations. A classical example is low Mach number flows for which we may want to capture unsteady advection while acoustics is of no importance. In that case, the ratio of the convective velocity scale  $v$  to the speed of sound  $c$  is the Mach number, which tends to zero. For mesh size of order  $h$ , the time step to resolve advection is  $\sim h/v$  and is much larger than the maximum allowable time step for explicit stability  $\sim h/c$ .

Gear methods are examples of implicit schemes currently used in unsteady applications. Their main drawback is in being multi step methods that need several initial conditions  $\dots U^{-1}, U^0$ . That is why it was decided to develop implicit variants of one step Heun and Runge-Kutta methods.

A simple explicit method for the integration of (4) is

$$\begin{aligned} M \delta U^* &= -R(U^n) \\ M \delta U &= -\theta R(U^*) - (1-\theta)R(U^n) \end{aligned} \quad (33)$$

where

$$\delta U^* = \frac{U^* - U^n}{\Delta t}, \text{ and } \delta U \text{ is given by (14).}$$

If  $\theta = 1/2$ , (33) is second order accurate and is known as Heun's method.

Following the model of linearized backward Euler (12), a possible candidate for the implication of (33) is the three parameter method,

$$\begin{aligned} \left[ M + \theta_1 \left( \frac{\partial R}{\partial U} \right)^n \right] \delta U &= -R^n \\ \left[ M + \theta_2 \left( \frac{\partial R}{\partial U} \right)^* \right] \Delta^n U &= -\theta R^* - (1-\theta)R^n \end{aligned} \quad (34)$$

which needs two linear system resolutions per time step. In the same way, Runge-Kutta methods with three or four evaluations have implicit variants with additional parameters (34) and variants are investigated in detail in [3], which studies stability and precision for this large class of methods. This work also defines a method for correcting the approximation of the Jacobian matrix in the implicit system, and show applications to Large Eddy Simulation ■

## References

- [1] J. BARDINA and J. C.K. LOMBARD - *Three Dimensional Hypersonic Flow Simulations with the CSCM Implicit Upwind Navier–Stokes Method*. AIAA Paper No. 87–1114, 1987.
- [2] R. BEAM and R. WARMING - *On the Construction and Application of Implicit Factored Schemes for Conservation Laws*. SIAM-AMS Proceedings; 11:85-129, 1978.
- [3] N. BERTIER - *Simulation numérique des grandes échelles en maillage non structuré pour l'aérothermique*. Phd Thesis, Université Pierre et Marie Curie, 2006
- [4] W.R. BRILEY and H. MC DONALD - *Solution of the Multidimensional Compressible Navier–Stokes Equations by a Generalized Implicit Method*. J Computat Phys, 24:372-397, 1977)
- [5] W.R. BRILEY and H. MC DONALD - *An Overview and Generalization of Implicit Navier-Stokes Algorithms and Approximate Factorization*. Computers & Fluids 30:807-828, 2001.
- [6] L. CAMBIER, M. GAZAIX, S. HEIB, S. PLOT, M. POINOT, JP. VUILLLOT, J.-F. BOUSSUGE and M. MONTAGNAC - *elsA Software*. Aerospace Lab issue 2, 2011.
- [7] R. COLLERCANDY - *Multigrid Strategy for Euler and Navier-Stokes Computations for Flows Around Complex Aerospace Configurations*. Proceedings of the 4th ECCOMAS, 1998
- [8] V. COUAILLIER and R. PEYRET - *Theoretical and Numerical Study of Ni's Multigrid Method*. La Recherche Aéronautique, English Edition, pp. 9-24, 1985
- [9] V. COUAILLIER - *Multigrid Method for Solving Euler and Navier-Stokes Equations in Two and Three Dimensions*. Proceedings of the 8th GAMM Conference, Delft, 1989
- [10] G.W. GEAR - *Numerical Initial Value Problems in Ordinary Differential Equations*. Prentice-Hall, New Jersey 1971
- [11] C. HIRSCH - *Numerical Computation of Internal and External Flows*. Butterworth-Heinemann Elsevier, Second edition 2007
- [12] A. Jameson - *Multigrid Algorithms for Compressible Flow Calculations*. Lecture Notes in Mathematics No 1228, Multigrid II – Proc. Cologne-Springer-Verlag, 1985
- [13] A. JAMESON - *Time Dependent Calculations Using Multigrid with Applications to Unsteady Flows past Airfoils and Wings*. AIAA Paper No. 91–1259, 1991
- [14] N. MELSON, M. SANETRIK and H.L. ATKINS - *Time-Accurate Navier-Stokes Calculations With Multigrid Acceleration*. 6th Copper Mountain Conference on Multigrid Methods, 1993
- [15] N. MELSON and M. SANETRIK - *Multigrid Acceleration of Time-Accurate Navier-Stokes Calculations*. 7th Copper Mountain Conference on Multigrid Methods, 1995
- [16] R.H. NI - *Multigrid Acceleration of Time-Accurate Navier-Stokes Calculations*. 7th Copper Mountain Conference on Multigrid Methods, 1995
- [17] D.W. PEACEMAN and H.H. RACHFORD - *The Numerical Solution of Parabolic and Elliptic Differential Equations*. SIAM Journal; 3:28-41, 1955
- [18] R. PULLIAM and D. CHAUSSEE - *A Diagonal Form of an Implicit Approximate Factorization Algorithm*. Journal of Computational Physics, 39:347-363, 1981
- [19] A. REFLOCH, B. COURBET, A. MURRONE, P. VILLEDIEU, C. LAURENT, P. GILBANK, J. TROYES, L. TESSÉ, G. CHAINERAY, J.B. DARGAUD, E. QUÉMERAIS and F. VUILLLOT - *CEDRE Software*. Aerospace Lab issue 2, 2011.
- [20] G.SELVA - *Méthodes itératives pour l'intégration implicite des équations de l'aérothermochimie sur des maillages non-structurés*. Phd Thesis, Ecole Centrale Paris, 1998.
- [21] M. SOETRISNO, S.T. IMLAY and D.W. ROBERTS - *A Zonal Implicit Procedure for Hybrid Structured-Unstructured Grids*. AIAA Paper No. 94–0645, 1994.

## Acronyms

e/sA	(Ensemble Logiciel pour la Simulation en Aérodynamique)
CEDRE	(Calcul d'Écoulements Diphasiques Réactifs pour l'Énergétique)
GMRES	(Generalized Minimal RESidual)
LU	(Lower/Upper)
ADI	(Alternating Direction Implicit)

## AUTHORS

---



**Claude Marmignon**, graduated from ENSH Grenoble. He received a PhD from the Ecole des Mines de Paris in 1987. He is currently senior scientist in charge of the development of numerical methods for complex flows in the CFD and Aeroacoustics Department.



**Vincent Couaillier** received his doctoral degree Master in Numerical Analysis from the University Pierre et Marie Curie (UPMC) in 1985. He has been working in the CFD & Aeroacoustics Department of Onera for algorithms and software developments. He is presently head of the unit NUMF “Numerical Methods for Fluid Mechanics” in the CFD and Aeroacoustics Department.



**Bernard Courbet**, graduated from Ecole Centrale de Paris. He is Research engineer, Developer as part of the CEDRE software team.

J. Peter, G. Carrier, D. Bailly,  
P. Klotz, M. Marcelet, F. Renac

(Onera)

E-mail: jacques.peter@onera.fr

# Local and Global Search Methods for Design in Aeronautics

Optimization is used at all stages of aircraft design. In the early phases (also called preliminary or conceptual design) multicriteria Pareto optimization [11] based on heuristic laws is carried out. Conversely, in the late design phases, accurate structural and aerodynamics predictions are required to steer small changes of a baseline shape through mono-objective optimization. This article is devoted to the local and global optimization methods actually used during this second part of the design process.

Through discretization, parametrization, and numerical simulation, the design problem can be formulated mathematically as a finite-dimensional optimization. Hence a good knowledge of global and local optimization algorithms is important to aerodynamic design engineers. The classical algorithms which are currently used at Onera for shape design are presented. Besides, many local optimization algorithms require the gradient of the functions of interest with respect to the design parameters. The different ways to compute those derivatives - often called "sensitivities" - are also described. Numerous 2D and 3D applications were dealt with at Onera using the methods described; they are presented in a companion article [14] and also briefly described in a course [1].

## Introduction

Numerical optimization aims at locating the minima of a regular function (called objective function) on a finite-dimensional design space, while satisfying a certain number of constraints (expressed as inequality verified by the so-called constraint functions). More precisely, local optimization aims to find a local optimum in the region of an initial guess, whereas global optimization aims to find the global optimum on the whole design space. These problems are, of course, the mathematical counterparts of mechanical optimization problems - like drag minimization of an aircraft or maximization of the total pressure recovery of a supersonic aircraft air intake - as soon as (a) a mesh and a numerical simulation tool are available; (b) the shape of the object to be optimized has been parametrized/a mesh deformation technique is available to propagate its deformation to the whole mesh; (c) the objective and constraints of the mathematical optimization problem have been expressed as functions of the geometry and state variables, which are usually the results of dedicated post-processing tools.

Numerical optimization for aircraft design was introduced almost as soon as mature simulation codes appeared. The aerodynamic

optimizations carried out by G.N. Van der Plaats at Nasa in the mid 70's illustrate this early interest in optimization [18]. At that time, 2D and simple 3D configurations were considered, simplex or descent methods were used and the gradients required by descent methods were estimated by the finite-differences.

Since then, the framework of aerospace optimization has known at least three drastic extensions: (1) several global optimization methods have been defined and intensively used (evolutionary algorithm, particle swarm, ant colony, simulated annealing,...); (2) surrogate functions (neural network, Kriging, polynomial regression, support vector machine,...) have been used for a part of the evaluations of the global optimization methods leading to significant cost reductions; (3) adjoint vector and direct differentiation methods have been defined, studied and increasingly frequently used to compute the gradients necessary for descent algorithms.

The next section presents the basic definitions and theorems. The third section is dedicated to global search methods. The fourth section is devoted to descent methods. The fifth section describes the adjoint and direct methods that can efficiently compute the gradient of the functions of interest with respect to the design parameters. All

of the last three sections concentrate on the methods which were found to be among the most efficient and are actually used at Onera for aerodynamic design.

## Notations, mathematical problem and properties

### Mathematical optimization problem

In this first subsection, the classical notations of a mathematical finite-dimensional optimization problem are defined. Let  $\alpha$  be the current vector of the input space (design vector). Let us denote  $n_f$  its dimension. The vector  $\alpha$  is supposed to vary in  $D_\alpha$  (the design space), a parallelepiped of  $\square^{n_f}$ . The objective function to minimize on  $D_\alpha \subset \square^{n_f}$  is denoted  $J(\alpha)$ . The constraints of the problem are supposed to be formulated through  $n_c$  functions  $G_j(\alpha)$ , that are negative at admissible design points. Only inequality constraints are considered here, as for most practical design problems an adequate choice of the design parameters enables us to avoid equality constraints. Obviously the local and global optimization problems read

Global [resp. local] optimum search

Seek for  $\alpha^* \in D_\alpha$  such that  $J(\alpha^*) = \text{Min } J(\alpha) \text{ over } D_\alpha$  design space [resp. on  $V$ , neighborhood of  $\alpha^*$ ]  
and  $\forall j \in [1, n_c] \quad G_j(\alpha^*) \leq 0$

In most common situations, the objective and constraint functions are at least continuous. In this presentation, for the sake of simplicity, the functions and state equations are supposed to have  $C^1$  regularity and, in some sections, also  $C^2$  regularity.

### Optimization problem stemming from a numerical simulation

In the framework of aircraft or turbomachinery design, the functions of interest depend on a distributed state field and geometrical variables that are linked by a system of non-linear equations discretizing the governing equations of fluid dynamics. Let us note  $S(\alpha)$ , the coordinates of the surface mesh of a solid body. From any surface mesh,  $S(\alpha)$ , a volumic mesh  $X(\alpha)$  is built. Both  $S$  and  $X$  are also supposed to have  $C^1$  regularity. The Jacobian  $dX/d\alpha$  can always be estimated by finite differences and in some cases by the following product of Jacobians  $\frac{dX}{d\alpha} = \frac{dX}{dS} \frac{dS}{d\alpha}$ . The state variables (aerodynamic conservative variables) are noted  $W$  (vector of size  $n_w$ ). State variables and mesh satisfy the discrete equations of fluid mechanics – a discrete form of Reynolds averaged Navier-Stokes (RaNS) equations, for example. In the framework of finite-difference/finite-volume methods, these equations read:  $R(W, X) = 0$  (in general, nonlinear set of  $n_w$  equations). These equations are also supposed to have  $C^1$  regularity with respect to (w.r.t.) their two vector arguments. It is also assumed that, all over the design space the flow is perfectly converged and the hypothesis of the implicit function theorem is satisfied ( $\forall (W_i, X_i) / R(W_i, X_i) = 0 \quad \det(W_i, X_i) \neq 0$ ) which defines the flow field  $W$  as a  $C^1$  function of the mesh  $X$ , and then as a  $C^1$  regular function of  $\alpha$  over  $D_\alpha$ . The discrete state equations may be rewritten  $R(W(\alpha), X(\alpha)) = 0$ .

In case of an optimization problem associated with a framework of numerical simulation, the objective function is actually computed as  $J(\alpha) = \overline{J}(W(\alpha), X(\alpha))$ . The constraint functions  $G_j(\alpha)$  have the same dependencies  $G_j(\alpha) = \overline{G}_j(W(\alpha), X(\alpha))$ . The definitions of

global optimum search and local optimum search may be rewritten using  $J$  and  $G_j$ .

### The Karush-Kuhn-Tucker condition

For the unconstrained optimization of a  $C^2$  function of  $\square^{n_f}$ , classical conditions of existence for minima read:

- Local optimum located in  $\alpha^* - \nabla J(\alpha^*) = 0$  is a necessary condition.  $\nabla J(\alpha^*) = 0$  and  $H(\alpha^*)$  positive definite ( $H$  hessian matrix of  $J$ ) is a sufficient condition.

- Global optimum located in  $\alpha^* - \nabla J(\alpha^*) = 0$  is a necessary condition.  $\nabla J(\alpha^*) = 0$  and  $H(\alpha) = 0$  positive definite on  $D_\alpha$  is a sufficient condition.

For a constrained problem on a finite size domain, the necessary condition for optimality is more complex to express. Actually, we first have to introduce more explicit notations for the parallelepiped design space  $D_\alpha$  :

$$D_\alpha = [\alpha_{1,l}, \alpha_{1,u}] \times [\alpha_{2,l}, \alpha_{2,u}] \times [\alpha_{3,l}, \alpha_{3,u}] \dots \times [\alpha_{n_f,l}, \alpha_{n_f,u}]$$

Then the domain bounds are rewritten as  $2n_f$  additional constraints  $G_{n_c+1}(\alpha) = \alpha_{1,l} - \alpha_1, G_{n_c+2}(\alpha) = \alpha_1 - \alpha_{1,u}, \dots$

...,  $G_{n_c+2n_f}(\alpha) = \alpha_{n_f} - \alpha_{n_f,u}$ .  
For an optimization problem with inequality constraint the classical necessary conditions for optimality in  $\alpha^*$  are the so-called ‘‘Karush-Kuhn-Tucker’’ conditions:  $\alpha^*$  is an admissible state

$$\nabla J(\alpha^*) + \sum_j \lambda_j^* \nabla G_j(\alpha^*) = 0 \quad \forall j \in [1, n_c + 2n_f] \quad \lambda_j^* G_j(\alpha^*) = 0$$

(the last proposition means that only the constraints attaining the limit value zero may have their gradient included in the linear combination of gradients)

An illustration of the KKT condition for a 2D problem is presented by figure 1. The functions are:

$$J(\alpha) = \alpha_1^2 + 3\alpha_2^2, \quad G_1(\alpha) = 1 - \alpha_1 + \alpha_2^2, \quad G_2(\alpha) = 4 - \alpha_1 - 2\alpha_2.$$

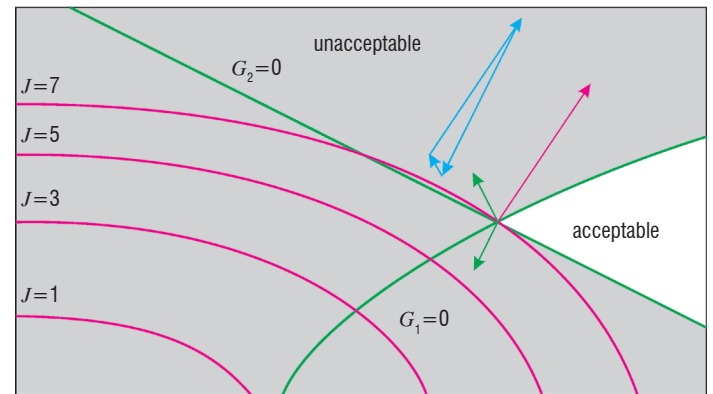


Figure 1 - KKT condition for a 2D example

## Global search methods

### Stochastic methods

Stochastic optimization methods refer to non deterministic, direct search algorithms, and belong to the family of global search methods. As a direct search method, a stochastic algorithm is suited for optimization problems presenting non-differentiable or even non-continuous functions. However, the main advantage of stochastic methods, which

have a common peculiarity of introducing some randomness in their search process, is their ability to deal with multimodal optimization problems since they (can) provide the global minimum for problems with several local minima. This interesting feature, directly inherited from the stochastic nature of their search process, is achieved at the price of a significant increase of the number of function evaluations during the optimization process, compared to local methods.

Stochastic methods cover a wide variety of algorithms. The most popular stochastic algorithms which have been concretely applied to engineering design optimization problems are (not an exhaustive list): evolutionary algorithms, a category of methods which includes Genetic Algorithms (GA) [5][6] and Differential Evolution (DE) [15][16] algorithms, the Simulated Annealing (SA) [7] method, the Particle Swarm Optimization (PSO) [8] method and the Ant Colony Optimization technique [3]. Compared to a pure randomized search (which can be considered as a stochastic method), the previously cited methods are all grounded on some simple heuristics or more complex biologically or nature inspired metaheuristics which provide them with better performances, at least for some classes of optimization problems.

Over the past ten years, several applications of stochastic optimization methods to aerodynamic and multidisciplinary design optimization problems have been performed at Onera [1][3]. Several of these applications relied on GADO [12], a GA developed at Rutgers University.

### Surrogate based methods

Stochastic methods are effective search algorithms and can reach the optimal solution without getting trapped into local minima. However a large number of evaluations are usually required to obtain this optimal point. Typically, even the “greediest” (most efficient, possibly less robust) stochastic methods will require several thousand evaluations to provide an optimum design. The aerodynamic-related experiences conducted at Onera with such optimization techniques involved analyses requiring less than 10 minutes (wall-clock) on super-computers. Such analysis time was achieved typically for 3D Euler simulation (in meshes of about 500.000 nodes) or 2D RANS simulation. This yielded a total time of one to two weeks for an optimization, while the target time for actual design applications in industry would be 1 day, or even half a day (one night). For many years now, alternative global search methods have been studied to reduce the CPU cost. One of their features is that they use surrogate model techniques in order to strongly reduce the number of CFD computations.

A first approach consists of building a sufficiently accurate model that presents the same optimal point than the objective function. Current response surfaces based methods used for global optimization can be categorized on the basis of the type of response surface and method used to determine the new design points with which to enrich the surrogate model. A first approach is based on surrogate model construction from an initial sampling. The model’s accuracy depends on the sampling size and the location of the data points. So space filling techniques are better than the classical ones, because they cover the design space in a uniform way. A second approach consists in using infill criteria. A first model is build from a small size initial sampling. The predictor and an estimate of the model’s error are used to determine new search points. Finally, a third approach consists of using a stochastic optimization algorithm and evaluating the different individuals of the population with the surrogate model.

## Surrogate model techniques

### Artificial Neural Network (ANN)

Multi-layer perceptron is the most popular neural network architecture, typically consisting in a hidden layer placed between the input and the output of the neural network. The number of neurons of the hidden layer ( $N_c$ ) is a given parameter defining the degrees of freedom of the model. The internal connections between neurons of consecutive layers are characterized by unknown weights and an activation function  $\Phi(z) = \frac{1}{1 + e^{-z}}$ .

$$\hat{J}_{ANN}(\alpha) = \sum_{j=1}^{N_c} B_j \Phi \left( \sum_{k=1}^{n_f} A_{jk} \alpha_k + A_{j0} \right) + B_0$$

where  $\alpha_k$  is the k-th component of  $\alpha$ . The weights A, B are estimated with a gradient-based optimization procedure by solving the system for a database  $(\alpha^l, J(\alpha^l)) \quad l \in [1, n_{db}]$  ( $\alpha^l \in \square^{n_f}$ ). Because the weights are not unique, more than one network must be built in order to choose the one providing the best prediction.

Model complexity increases with neuron number. Too few neurons can lead to under fitting. Too many neurons can contribute to over fitting, in which all training points are well fitted, but the fitting curve oscillates widely between these points.

### Radial Basis Functions (RBF)

This surrogate model has been developed for the interpolation of scattered multivariate data. It appears as a linear combination of N radial basis  $\psi(r)$ , of the form:

$$\hat{J}_{RBF}(\alpha) = \sum_{i=1, N} w_i \psi_i(\|\alpha - c^i\|)$$

where  $w_i$  represents the weights of the linear combination,  $c^i$  is the  $i$ th of the N basis function centers. A strong simplification consists in imposing N to be equal to  $n_{db}$ , the number of data points and the centers  $c^i = \alpha^i$ . This leads to the matrix equation  $\Psi w = y$ , which gives the weights by inversion ( $\Psi$  being the symmetric matrix defined by  $\Psi_{ij} = \psi(\|\alpha^j - \alpha^i\|)$ ). The choice of the radial basis function can have an important effect, since Gaussian and inverse multi-quadric basis functions lead to a symmetric positive definite matrix. Estimating the other parameters, like a (see table 1), is an additional task.

Thin plate spline	$\psi(r) = r^2 \ln r$
Gaussian	$\psi(r) = e^{-r^2/2\sigma^2}$
Multi-quadric	$\psi(r) = (r^2 + a^2)^{1/2}$
Inverse multiquadric	$\psi(r) = (r^2 + a^2)^{-1/2}$

Table 1 - Examples of radial basis functions

## Kriging

While building this surrogate model, one assumes that the output function is the sum of a regression and a stochastic part. The last one is supposed to have zero mean and follow second order stationary process described by a correlation model  $\mathfrak{R}(\theta, d)$  (see table 2).

Exponential	$\mathfrak{R}(\theta, d) = e^{-\theta d ^p}$
Gaussian	$\mathfrak{R}(\theta, d) = e^{-\theta d^2}$
Spline cubic $\xi = \theta d $ $0 < a < 1$	$\mathfrak{R}(\theta, d) = \begin{cases} (1-3/a)\xi^2 + (1+a)/a^2\xi^3 & 0 \leq \xi \leq a \\ (1-\xi)^3 / (1-a) & a \leq \xi \leq 1 \\ 0 & 1 \leq \xi \end{cases}$

Table 2 - Examples of correlation models

The likelihood is maximised in order to estimate the unknown parameters  $\theta$  and  $p$ . In the case of ordinary kriging, the surrogate model relations are:

$$\hat{J}_{ok}(\alpha) = \hat{\mu} + r^T \mathbf{R}^{-1} (J_s - \mathbf{1} \hat{\mu}) \quad \hat{\mu} = \frac{\mathbf{1}^T \mathbf{R}^{-1} J_s}{\mathbf{1}^T \mathbf{R}^{-1} \mathbf{1}},$$

where  $r$  is the correlation vector between the prediction point and the data points ( $r_i = \mathfrak{R}(\theta, \|\alpha^i - \alpha\|)$ ),  $J_s = (J(\alpha^1), J(\alpha^2), \dots, J(\alpha^{n_{db}}))$  is the vector of the function values of the data points,  $\mathbf{R}$  is the correlation matrix for the sample points ( $\mathbf{R}^{ij} = \mathfrak{R}(\theta, \|\alpha^i - \alpha^j\|)$ ),  $\mathbf{1}$  is a vector of ones of size  $n_{db}$ . The estimate of variance at unsampled points is given by:

$$s^2(\alpha) = \sigma^2 \left[ 1 - r^T \mathbf{R}^{-1} r + \frac{(1 - \mathbf{1}^T \mathbf{R}^{-1} r)^2}{\mathbf{1}^T \mathbf{R}^{-1} \mathbf{1}} \right]$$

### Initial sampling techniques

An initial sampling is essential to obtain an accurate surrogate model, as all the parameters of the surrogate models are estimated from data points (location and function value). Those techniques can be divided into two categories:

- Classical samplings: Full factorial and Central Composite Design (CCD) are the more basic forms of sampling. They present the drawback that the size of the sampling increases exponentially with the number of design variables. D-optimal design is suitable for higher dimensional problems. In the case of systematic error, an appropriate design must fill the design space rather concentrate on the boundaries.

- Space filling samplings: Space filling samplings spread data sampling points throughout the entire design space. The most common methods are Orthogonal arrays, Latin Hypercube, Hammersley and uniform samplings. They cover the design space in a uniform way and in general are adapted to large scale problems.

### Adaptive sampling techniques

The use of an initial sampling leads to a globally accurate model. However, it is unlikely that the model is sufficiently accurate in the region of the predicted optimum. Hence infill points have to be defined to improve the model's accuracy. The location of these new points is

based on a criterion. Several classical criteria are presented in [16]. The most important is the Expected Improvement (EI). It consists of calculating the expected accuracy improvement, given the predictor  $\hat{J}$  and the variance  $s^2$ :

$$EI = \begin{cases} (J_{\min} - \hat{J}(\alpha)) \Phi \left[ \frac{J_{\min} - \hat{J}(\alpha)}{s(\alpha)} \right] + s \varphi \left[ \frac{J_{\min} - \hat{J}(\alpha)}{s(\alpha)} \right] & \text{if } s > 0 \\ 0 & \text{if } s = 0 \end{cases}$$

where  $\Phi$  and  $\varphi$  are, respectively, the normal cumulative distribution function and probability density function.

### Acceleration of stochastic algorithms using surrogate models

The acceleration of a GA is obtained from the reduction of the number of exact function evaluations by the costly numerical simulation codes (CFD code in the case of aerodynamics). This involves a surrogate model which provides more or less accurate evaluations of  $J(\alpha)$  and  $G_i(\alpha)$ , at negligible CPU cost. The use of a surrogate model instead of the numerical simulation code usually preserves the robustness of the complete optimization process. Actually, the dynamic improvement of the surrogate model is more appropriate for converging to the optimum value.

Several approaches have been defined to partly replace the numerical simulation codes by a global surrogate model. The sampling points are generally obtained after one or several generations of a classical stochastic research. Then, the model is updated online, from the new generated points, when the optimization process is going on. Due to the curse of dimensionality, the accuracy of the global surrogate models becomes more and more difficult to insure for high number of variables (high  $n_f$ ). In order to overcome this drawback, another approach involving local surrogate models can be used during the search process. Finally, the two types of models (local and global) can be used to improve the speeding up of the optimization process

### Local Search Using Derivatives – Descent Methods

A descent method is an iterative method for the solution of a local optimization problem. Starting from an initial point, it attempts to converge to an optimum, using local information (most often function value and gradient) at the current point to compute the next iterate.

In the following pages, we do not present the popular algorithms for 1D minimization (dichotomy, golden number, polynomial interpolation...) which are well described in many classical books [19]. On the contrary, we focus on the multiple dimension case, without and with constraints. The main point for each algorithm presentation is the definition of the descent direction. Obviously for optimization based on complex flow simulation, the search of the descent step is always based on a cheap algorithm like polynomial interpolation.

### Descent methods for unconstrained optimization

In this part, we focus on the search of an optimum of the objective function on the design space  $D_\alpha = \square^{n_f}$ . The straight forward algorithm (steepest descent) that simply goes down the direction opposite the gradient of  $J$  is not described here, as it is known to often be inefficient. The conjugate gradient and BFGS methods are described.

## Conjugate gradient methods

The idea behind Conjugate gradient methods comes from the analysis of the behavior of the steepest descent for the specific case of positive definite quadratic forms ( $J(\alpha) = \frac{1}{2} \alpha^T H \alpha + b^T \alpha$ ).

In this case, the conditioning of the positive definite matrix  $H$  strongly affects the robustness and convergence speed of the steepest descent. To improve robustness, at step  $k$  Conjugate Gradient methods use a descent direction  $d^k$  orthogonal to  $d^{k-1}$  in the sense of  $H$  -  $(d^{k-1})^T H d^k = 0$

$$d^k = -\nabla J(\alpha^k) + \beta^k d^{k-1} \quad \beta^k = \frac{(\nabla J(\alpha^k))^T H d^{k-1}}{(d^{k-1})^T H d^{k-1}}$$

### Conjugate gradient algorithm

Set  $k = 0$  and  $d^{-1} = 0$ , an initial point  $\alpha^0$  and a stopping tolerance  $\varepsilon$

**While**  $\|\nabla J(\alpha^k)\| > \varepsilon$  **do**

    Compute  $d^k = -\nabla J(\alpha^k) + \beta^k d^{k-1}$

    Find  $t^*$  by line search on  $q(t) = J(\alpha^k + t d^k)$

    Update current iterate  $\alpha^{k+1} = \alpha^k + t^* d^k$  and set  $k = k + 1$

**End while**

Two formulas have been proposed for computation of  $\beta^k$  for extension to non quadratic cases. The first one is based on another formula of  $\beta^k$  in the quadratic positive definite

case  $\beta^k = \frac{\|\nabla J(\alpha^k)\|^2}{\|\nabla J(\alpha^{k-1})\|^2}$  which can be directly applied to a non-

quadratic function as it does not refer to matrix  $H$  anymore. The second extension, proposed by Polak and Ribière in 1969, also reduces to the same algorithm in the quadratic positive definite case (see below, as then  $\nabla J(\alpha^k)^T \nabla J(\alpha^{k-1}) = 0$ ). It is known to lead to a more efficient algorithm for specific applications.

$$\beta_{FR}^k = \frac{\|\nabla J(\alpha^k)\|^2}{\|\nabla J(\alpha^{k-1})\|^2} \quad \beta_{PR}^k = \frac{\|\nabla J(\alpha^k)\|^2}{\|\nabla J(\alpha^{k-1})\|^2} - \frac{\nabla J(\alpha^k)^T \nabla J(\alpha^{k-1})}{\|\nabla J(\alpha^{k-1})\|^2}$$

A more efficient algorithm requires more information, in particular information about the second derivatives of the function to minimize. Newton methods have been devised for this reason.

## Newton and quasi-Newton methods - Principle

The classical Newton method is originally a method to find the roots of the equation  $z(\alpha) = 0$  by approximating the function  $z$  by successive linear expansions. Starting from the current iterate  $\alpha^k$ , substituting  $z$  by its linear approximation leads to  $z(\alpha^k + d^k) = z(\alpha^k) + \nabla z(\alpha^k) \cdot d^k + o(\|d^k\|)$ . Neglecting the term  $o(\|d^k\|)$  yields  $d^k = -[\nabla z(\alpha^k)]^{-1} \cdot z(\alpha^k)$  and is used to calculate the next iterate  $\alpha^{k+1} = \alpha^k + d^k$ . The same method can be used as an optimization algorithm, by solving the Karush-Kuhn-Tucker optimality condition. In this case, the function  $z(\alpha)$  becomes the gradient  $\nabla J$  of the objective function  $J$  and the gradient  $\nabla z$ , its Hessian  $\nabla^2 J$ . At each iteration  $k$ , the descent direction has to be computed by the formula  $d^k = -[\nabla^2 J(\alpha^k)]^{-1} \cdot \nabla J(\alpha^k)$

## Newton algorithm

Set  $k = 0$ , an initial point  $\alpha^0$  and a stopping tolerance  $\varepsilon$

**While**  $\|\nabla J(\alpha^k)\| > \varepsilon$  **do**

    Compute  $d^k = -[\nabla^2 J(\alpha^k)]^{-1} \cdot \nabla J(\alpha^k)$

    Update current iterate  $\alpha^{k+1} = \alpha^k + t^* d^k$  and set  $k = k + 1$

**End while**

The important advantage of this method resides in its convergence in the region of the solution, which is superlinear in general and quadratic (at each iteration, the number of exact digits is doubled) if  $J$  has  $C^3$  regularity.

Besides, the drawbacks of Newton's method are also well-known: (1) the Hessian is required: in most engineering problems, an explicit form of the objective function is unavailable. The Hessian must be computed numerically which requires a large number of the objective function evaluations; (2) in high dimensional spaces, the solution of the linear system at each iteration is very CPU demanding; (3) Newton methods diverge violently far from the optimal point; (4) this algorithm converges on the closest stationary point, not necessarily the global minimum. Quasi-Newton methods were developed to circumvent these drawbacks.

Considering this list of drawbacks, the quasi-Newton realizes an improvement over the above Newton method based on two main ideas:

- First, the stability problems of the method can be avoided by adding a line-search process in the algorithm. Actually, noting that the requirement  $J(\alpha^{k+1}) < J(\alpha^k)$  enforces stability, the Newton increment  $d^k$  is considered as a direction, along which a line-search is performed to reduce the function  $q(t) = J(\alpha^k + t d^k)$ . It can be proved that the line-search is possible if and only if the Hessian of the objective function is positive definite.

- Secondly, rather than computing the Hessian matrix, its inverse is approximated by a matrix  $H$  which evolves during the iterations. This matrix can be chosen symmetric positive definite. An algorithm following this approach will be presented in the next section. Next algorithm describes the steps of a generic quasi-Newton algorithm.

### Generic quasi-Newton algorithm

Set  $k = 0$ , an initial point  $\alpha^0$ , a stopping tolerance  $\varepsilon$ , an initial matrix  $\overline{H}^0$  positive definite (generally, the identity matrix)

**While**  $\|\nabla J(\alpha^k)\| > \varepsilon$  **do**

    Compute  $d^k = -\overline{H}^k \nabla J(\alpha^k)$

    Make a line search for  $q(t) = J(\alpha^k + t d^k)$  initialized by  $t = 1$

    Update current iterate  $\alpha^{k+1} = \alpha^k + t^* d^k$

    Compute new matrix  $\overline{H}^{k+1}$

    set  $k = k + 1$

**End while**

### BFGS method

Let us now explain how the approximate invert of the Hessian, matrix  $\overline{H}^k$  evolves during the iterations. The method presented here was introduced by C. Broyden, R. Fletcher, D. Goldfarb and D. Shanno. It is certainly the most popular quasi-Newton algorithm. The matrix

$\bar{H}^{k+1}$  is computed from  $\bar{H}^k$  and some vectors attached to iteration  $k$  and  $k+1$  computations according to following formulas

$$s^k = \alpha^{k+1} - \alpha^k$$

$$y^k = \nabla J(\alpha^{k+1}) - \nabla J(\alpha^k)$$

$$\bar{H}^{k+1} = \bar{H}^k - \frac{s^k (y^k)^T \bar{H}^k + \bar{H}^k y^k (s^k)^T}{(y^k)^T s^k} + \left[ 1 + \frac{(y^k)^T \bar{H}^k y^k}{(y^k)^T s^k} \right] \frac{s^k (s^k)^T}{(y^k)^T s^k}$$

### Constrained optimization

Actually, most complex industrial problems lead to multi-dimensional constrained optimization. Two efficient algorithms for this task (feasible direction method and sequential quadratic programming) are described here. The presentation of classical methods that are seldom used for design in aeronautics (method of centers, sequential linear programming) can be found in [19]

#### Feasible direction method

The goal of feasible direction method is to build a sequence of points  $\alpha^k$  such that  $\alpha^{k+1} = \alpha^k + td^k$  where the displacement along direction  $d^k$  leads to lower values of both, the objective and the active constraints (all constraints satisfying  $G_j(\alpha^k) = 0$ ). After  $d^k$  has been defined, the factor  $t$  is determined by a mono-dimensional optimization. Let us now derive the definition of  $d^k$ . As before, the indexes are the ones of the iteration ( $k$ ) of the algorithm. The vector  $d^k$  must satisfy  $\nabla J(\alpha^k).d^k \leq 0$  and  $\forall j / G_j(\alpha^k) = 0 \quad \nabla G_j(\alpha^k).d^k \leq 0$ .

The tricky point is determining the vector  $d^k$  ensuring the best descent. For a simple two dimensional problem ( $n_f = 2$ ) with one active convex constraint  $G_1$ , it is easy to check that the minimization [ $\text{Min} \nabla J(\alpha^k).d^k \leq 0$  with  $\nabla G_1(\alpha^k).d^k \leq 0 \quad \forall j / G_j(\alpha^k) = 0$ ] will lead to a vector  $d$  that points towards inadmissible states (see figure 2). To tackle this issue, scalar factors  $\theta_j$  are included in the problem [ $\nabla G_j(\alpha^k).d^k + \theta_j \leq 0 \quad \theta_j > 0 \quad \forall j / G_j(\alpha^k) = 0$ ]

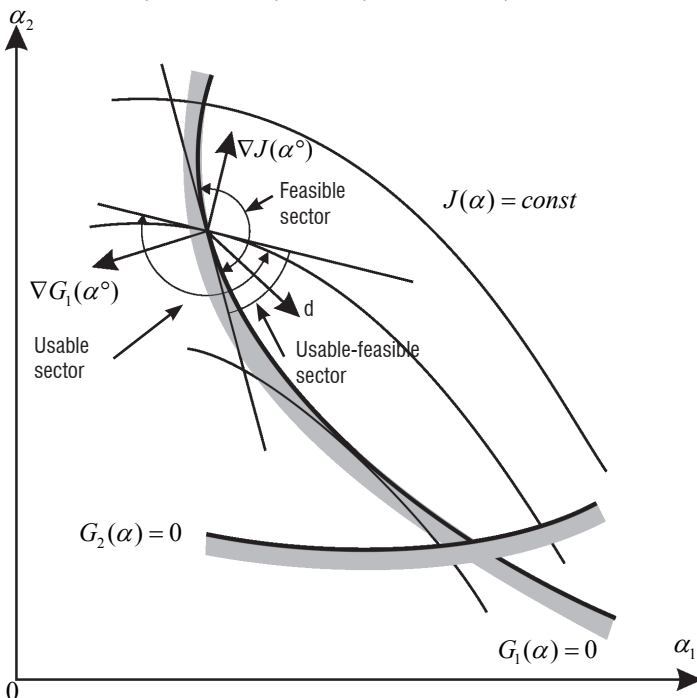


Figure 2 - Principle of feasible direction search

One wants to link the value of  $\theta_j$  with the one of  $\nabla J(\alpha^k).d$ . Eventually, the search for the best direction for descent is reformulated as follows

Maximize  $\beta$  find  $d^k$  bounded  
 $\nabla J(\alpha^k).d^k + \beta \leq 0$  and  
 $\nabla G_j(\alpha^k).d^k + \theta_j \beta \leq 0 \quad \theta_j > 0 \quad \forall j / G_j(\alpha^k) = 0$

Obviously, if  $G_j$  is a linear constraint then  $\theta_j = 0$  is suitable. For non linear constraints the simplest choice is  $\theta_j = 1$ . More complex formulas are presented in [19].

#### Feasible direction method

Set  $k = 0$ , an initial point  $\alpha^0$ , a stopping tolerance  $\varepsilon$

**While** KKT conditions not satisfied **do**

Find  $d^k$  (bounded) which maximizes  $\beta$  subject to

$$\nabla J(\alpha^k).d^k + \beta \leq 0 \text{ and}$$

$$\forall j / G_j(\alpha^k) = 0 \quad \nabla G_j(\alpha^k).d^k + \theta_j \beta \leq 0.$$

Make a line search for  $q(t) = J(\alpha^k + td^k)$

Update current iterate  $\alpha^{k+1} = \alpha^k + t^* d^k$  and set  $k = k + 1$

**End while**

#### Sequential Quadratic Programming (SQP)

In this method, an auxiliary function of the descent vector  $d$  is introduced. It is a quadratic approximation of  $J(\alpha + d)$ . The heart of the algorithm reads

$$\text{Minimize } Q(d) = J(\alpha^k) + \nabla J(\alpha^k).d + \frac{1}{2} d^T B^k d$$

$$\text{Subject to } \nabla G_j(\alpha^k).d^k + \delta_j G_j(\alpha^k) \leq 0.$$

where  $B$  is a positive definite matrix equal to the identity matrix  $I$  at the first step and to an approximation of the hessian for the next iterations. Parameter  $\delta_j$  is taken equal to 1 if the constraint is strictly respected ( $G_j(\alpha^k) \leq 0$ ) and to a value in  $[0,1]$  if the current design point  $\alpha^k$  violates constraint  $G_j(\alpha)$ . See reference [19], for more information about hessian estimation, and monodimensional search after determination of  $d$ .

#### Sequential quadratic programming

Set  $k = 0$ , an initial point  $\alpha^0$ , a stopping tolerance  $\varepsilon$ , an initial approximate Hessian matrix  $B^0$

**While** KKT conditions not satisfied **do**

Find  $d^k$  which minimizes

$$Q(d) = J(\alpha^k) + \nabla J(\alpha^k).d + 0.5 d^T B^k d$$

$$\text{Subject to } \nabla G_j(\alpha^k).d^k + \delta_j G_j(\alpha^k) \leq 0.$$

Update current iterate  $\alpha^{k+1} = \alpha^k + d^k$  and set  $k = k + 1$

Build  $B^{k+1}$ , for example from BFGS formula

**End while**

#### Sensitivity evaluations for descent methods

This section will describe in some detail the main methods of gradient evaluation, firstly finite differences, followed by discrete versions of the direct and adjoint methods. A detailed bibliography of all of the methods presented and more material (continuous adjoint, exact

duality, second-order derivatives, frozen turbulent-viscosity assumption...) can be found in [12].

### Finite differences

The application of finite differences to an entire flow solver is by far the simplest means of obtaining solution gradients, as it requires no modification of the solver itself. As a result it was one of the first sensitivity evaluation methods to be used. To start, the numerical flow solution corresponding not only to  $\alpha$  but also to perturbed states  $\alpha + \delta\alpha$  and possibly  $\alpha - \delta\alpha$  is calculated. For the typical case of  $\delta\alpha$  representing a geometry modification, this implies a mesh deformation  $X(\alpha + \delta\alpha)$  and a new flow solution on the modified mesh satisfying  $R(W(\alpha + \delta\alpha), X(\alpha + \delta\alpha)) = 0$ . An approximation of objective functions derivatives in the direction  $\delta\alpha$  can then be computed using a finite difference formula, such as the second-order accurate formula

$$\frac{dJ(\alpha)}{d\alpha} = \frac{\bar{J}(W(\alpha + \delta\alpha), X(\alpha + \delta\alpha)) - \bar{J}(W(\alpha - \delta\alpha), X(\alpha - \delta\alpha))}{2\delta\alpha}$$

The entire matrix ( $dJ(\alpha)/d\alpha$ ,  $dG_1(\alpha)/d\alpha$  ...) may be evaluated at a cost of  $2n_f$  flow solutions, or if a first-order difference is used  $n_f + 1$  flow solutions, making the method impractical for large design spaces. Another serious disadvantage is that the choice of the step size  $\delta\alpha$  is critical to the accuracy of the result. The fundamental limitations of finite differences have led to the investigation of alternative means of gradient evaluation.

### The discrete direct method

Under the assumption that the discrete residual  $R$  is once continuously differentiable with respect to the flow field and mesh in a neighborhood of  $W(\alpha)$  and  $X(\alpha)$ , the discrete form of the governing equations  $R(W, X) = 0$  may be differentiated with respect to each component of  $\alpha$  to give

$$\left(\frac{\partial R}{\partial W}\right) \frac{dW}{d\alpha_i} = -\left(\frac{\partial R}{\partial X} \frac{dX}{d\alpha_i}\right) \quad (1)$$

This may be regarded as a linear system in unknowns  $\frac{dW}{d\alpha_i}$ , where (or even) may be evaluated by finite differences  $\frac{d\alpha_i}{dX}$  as  $\left(\frac{\partial R}{\partial X} \frac{dX}{d\alpha_i}\right)$

in the previous section, and the partial derivatives could be evaluated for example by hand. The dimension of the system is the number of degrees of freedom in the non-linear equations  $n_w$ , and it can be regarded as a linearization of those equations. Given the  $n_f$  solutions  $\frac{dW}{d\alpha_i}$  the derivatives of the functions of interest are

$$\frac{dJ}{d\alpha_i} = \frac{\partial \bar{J}}{\partial X} \frac{dX}{d\alpha_i} + \frac{\partial \bar{J}}{\partial W} \frac{dW}{d\alpha_i} \quad \text{and} \quad \frac{dG_k}{d\alpha_i} = \frac{\partial \bar{G}_k}{\partial X} \frac{dX}{d\alpha_i} + \frac{\partial \bar{G}_k}{\partial W} \frac{dW}{d\alpha_i}$$

where again the partial derivatives are in principle easy to evaluate, as  $J$  is a known, explicit function of  $W$  and  $X$ . Hence the  $2n_f$  non-linear solutions required for second-order flow finite differences have been replaced by one non-linear and  $n_f$  linear solutions, all of

dimension  $n_w$ , and the dependence on finite differences has been confined to the relatively cheap mesh update procedure.

### The discrete adjoint method

There are many ways to derive the discrete adjoint equations, the one given here is chosen for its similarity to the derivation of the continuous adjoint. Let the direct linearization (1) be premultiplied by an arbitrary line vector  $\lambda$  of dimension  $n_w$ , so that

$$\forall \lambda \in \mathbb{R}^{n_w} \quad \lambda^T \left(\frac{\partial R}{\partial W}\right) \frac{dW}{d\alpha_i} + \lambda^T \left(\frac{\partial R}{\partial X} \frac{dX}{d\alpha_i}\right) = 0.$$

Adding this expression to last but one equation of previous subsection,

$$\forall \lambda \in \mathbb{R}^{n_w} \quad \frac{dJ}{d\alpha_i} = \frac{\partial \bar{J}}{\partial X} \frac{dX}{d\alpha_i} + \frac{\partial \bar{J}}{\partial W} \frac{dW}{d\alpha_i} + \lambda^T \left(\frac{\partial R}{\partial W}\right) \frac{dW}{d\alpha_i} + \lambda^T \left(\frac{\partial R}{\partial X} \frac{dX}{d\alpha_i}\right),$$

Hence the term  $\frac{dW}{d\alpha_i}$  may be eliminated by choosing the arbitrary vector  $\lambda$  to satisfy  $d\alpha_i$

$$\lambda^T \left(\frac{\partial R}{\partial W}\right) + \left(\frac{\partial \bar{J}}{\partial W}\right) = 0 \quad \text{or} \quad \left(\frac{\partial R}{\partial W}\right)^T \lambda = -\left(\frac{\partial \bar{J}}{\partial W}\right)^T \quad (2)$$

the adjoint equation, a linear system in unknowns  $\lambda$  the adjoint solution, with respect to the objective function  $J$ . Given  $\lambda$  the sensitivities may be written

$$\frac{dJ}{d\alpha_i} = \frac{\partial \bar{J}}{\partial X} \frac{dX}{d\alpha_i} + \lambda^T \left(\frac{\partial R}{\partial X} \frac{dX}{d\alpha_i}\right).$$

The critical point is that, because  $\alpha$  does not appear in (A), that linear system must only be solved once for each function to be differentiated. Hence the full matrix ( $dJ(\alpha)/d\alpha$ ,  $dG_1(\alpha)/d\alpha$  ...) may be evaluated at a cost of  $1 + n'_c$  linear system solutions of size  $n_w$ , substantially independent of  $n_f$  (where  $n'_c$  is the number of active constraints at a specific step of the optimization process; only the gradients of those constraints are then needed).

### Robustness enhancement using recursive projection method

Both linearized and adjoint equations (equations (1) and (2)) are large sparse linear systems which can not be directly inverted for large size simulations. Most often an iterative procedure involving an approximate Jacobian  $(\partial R / \partial W)^{(APP)}$  is used. The corresponding algorithm reads (for the adjoint method):

$$\left(\frac{\partial R}{\partial W}\right)^{(APP)T} (\lambda^{(l+1)} - \lambda^{(l)}) = -\left(\frac{\partial \bar{J}}{\partial W}\right)^T - \left(\frac{\partial R}{\partial W}\right)^T \lambda^{(l)}$$

Hence linear systems that appear in discrete gradient computation are very often solved by an iteration procedure of the form:

$$x^{(l+1)} = F(x^{(l)}) = \Phi x^{(l)} + M^{-1}b \quad (3)$$

Algorithm (3) aims at solving  $Ax = b$ . The matrix  $\Phi = I - M^{-1}A$  represents the iteration matrix of the numerical scheme whereas  $M$  denotes a preconditioning matrix.

Whether or not the iteration procedure converges to the solution  $x = A^{-1}b$  depends upon the eigenvalues of  $\Phi$ . Here, we follow the Recursive Projection Method (RPM) introduced by Shroff and Keller [15] for the stabilization of unstable recursive fixed point iteration procedures.

Suppose the iteration diverges thus implying that there are  $m \geq 1$  eigenvalues of  $\Phi$  with a modulus greater than unity:

$$|\lambda_1| \geq \dots \geq |\lambda_m| \geq 1.$$

Define the subspace  $\mathbf{P} = \text{span}\{e_1, \dots, e_m\}$  spanned by the eigenvectors associated to these eigenvalues and  $\mathbf{Q} = \mathbf{P}^\perp$  its orthogonal complement in  $\square^N$ . These subspaces form a direct sum in  $\square^N$ , hence every vector can be decomposed in a unique way as the sum

$$\forall x \in \square^N, \quad \exists x_p \in \mathbf{P}, x_Q \in \mathbf{Q} : x = x_p + x_Q.$$

The orthogonal projectors onto the subspaces  $\mathbf{P}$  and  $\mathbf{Q}$  are denoted  $P$  and  $Q$  respectively. Let  $V \in \square^N$  be a matrix whose columns constitute an orthonormal basis for  $P$ , then the projectors are defined by  $\mathbf{P} = VV^T, \mathbf{Q} = I - P$  where  $I$  denotes the identity matrix and exponent  $T$  is the transpose operator. Note that since  $\mathbf{P}$  is an invariant subspace of  $\Phi$  we have  $Q\Phi P = 0$ . Then, the RPM iteration reads

$$\begin{aligned} x_Q^{(l+1)} &= QF(x^{(l)}) \\ x_p^{(l+1)} &= x_p^{(l)} + (I - P\Phi P)^{-1} (PF(x^{(l)}) - x_p^{(l)}) \\ x^{(l+1)} &= x_Q^{(l+1)} + x_p^{(l+1)} \end{aligned} \quad (4)$$

According to Shroff and Keller, the RPM iteration converges even when the original iteration (3) diverges [15]. The implementation of the algorithm (4) requires the construction of the projectors  $P$  and  $Q$  and hence the evaluation of the orthonormal basis.

The method for computing  $V$  is the following: Consider the vector  $v_1 = \Delta x_Q^{(l-k+1)}$  where  $\Delta x_Q^{(j)} = x_Q^{(j+1)} - x_Q^{(j)}$  and the matrix  $\hat{A} = Q\Phi Q$ . Define the Krylov subspace of dimension  $k$  generated by  $v_1$  and  $\hat{A} : \mathbf{K}_k = \text{span}\{v_1, \hat{A}v_1, \dots, \hat{A}^{k-1}v_1\}$ . Let  $K_k = (v_1, \hat{A}v_1, \dots, \hat{A}^{k-1}v_1)$  a matrix whose columns span the subspace  $\mathbf{K}_k$ . Compute the  $QR$  factorization  $K_k = Q_k R_k$  where the columns of  $Q_k$  form an orthonormal basis of  $\mathbf{K}_k$  and where the absolute values of the diagonal elements of the upper triangular matrix  $R_k$  are sorted in a decreasing order.

If the algorithm (3) fails to converge, vectors for  $V$  are chosen on the basis of the following condition. For the largest  $1 \leq j \leq k-1$  such that

$$\left| \frac{R_{j,j}}{R_{j+1,j+1}} \right| > \kappa$$

the first  $j$  columns of  $Q_k$  are added to  $V$ . The parameter  $\kappa$  stands for the Krylov acceptance ratio and its inverse represents a bound for the residual of the computed eigenspace of  $\hat{A}$ .

### Adjoint method for aeroelasticity

When gradient computation is carried out in an aeroelastic framework, the state variables can be divided into two parts:  $W$  and  $D$ , where  $W$  stands for the aerodynamic conservative variables at the center of the cells of the volume mesh  $X(\alpha)$  and  $D$  represents the structural displacements of the nodes of the structural model associated

with the solid body considered. In addition, a new mesh  $Z(\alpha)$  must be introduced for the structural model. The structural mesh can depend a priori on the vector of shape parameters. However, if the solid body planform remains unchanged when  $\alpha$  varies within the design space, this dependency vanishes. The state variables and meshes satisfy the discrete equations of both fluid mechanics ( $R_a$ ) and structural mechanics ( $R_s$ ),

$$\begin{cases} R_a(W, D, X(\alpha), Z(\alpha)) = 0 \\ R_s(W, D, X(\alpha), Z(\alpha)) = 0 \end{cases}.$$

In general,  $R_a$  is a set of nonlinear equations (of size  $n_a$ ) but  $R_s$  is a set of linear equations (of size  $n_s$ ). These equations are coupled through the aerodynamic loads  $L_s$  which stimulate the structural model:

$$L_s = L_s(W, D, X, Z),$$

and through  $D_a$  the displacements of which are transmitted backwards to the volume mesh so as to follow the structural displacements (this can be done in a two-step manner using surface mesh transfer intermediately):

$$D_a = D_a(D, Z).$$

The current volume mesh  $X(\alpha)$  is actually a function of the initial volume mesh  $X_0(\alpha)$  on which the structural displacements are transferred, and which, incidentally, is actually directly controlled by  $\alpha$ ,

$$X = X(X_0, D_a(D, Z)).$$

These couplings introduce a number of issues regarding load transfer consistency and conservativeness first, and mesh deformation second, which have been extensively dealt with in literature. The reader can, for instance, refer to the articles of Farhat et al., Maman et al., Arian and Smith et al.<sup>1</sup>

Assuming that this coupled system has  $C^1$  regularity too with respect to its four vector arguments, that  $W(\alpha)$  has  $D(\alpha)$  regularity, and that,

$$\begin{cases} R_a(W(\alpha_i), D(\alpha_i), X(\alpha_i), Z(\alpha_i)) = 0 \\ R_s(W(\alpha_i), D(\alpha_i), X(\alpha_i), Z(\alpha_i)) = 0 \end{cases},$$

$$\det \left[ \begin{pmatrix} \partial R_a / \partial W & \partial R_a / \partial D \\ \partial R_s / \partial W & \partial R_s / \partial D \end{pmatrix} (W(\alpha_i), D(\alpha_i), X(\alpha_i), Z(\alpha_i)) \right] \neq 0$$

the implicit function theorem allows us to define  $W$  and  $D$  as  $C^1$  functions of  $X$  and  $Z$  in a neighborhood of  $X(\alpha_i)$  and  $Z(\alpha_i)$ , and therefore thanks to the assumed regularity of  $X(\alpha)$  and  $Z(\alpha)$ , as functions of  $\alpha$  in a neighborhood of  $\alpha_i$ . We suppose this property to be true on the entire design domain  $D_\alpha$ , so that we may use  $W(\alpha)$  and  $D(\alpha)$  notation, and rewrite the discrete coupled equations

$$\begin{cases} R_a(W(\alpha), D(\alpha), X(\alpha), Z(\alpha)) = 0 \\ R_s(W(\alpha), D(\alpha), X(\alpha), Z(\alpha)) = 0 \end{cases}.$$

We assume that the discrete residual ( $R_a, R_s$ ) is  $C^1$  differentiable with respect to the state variables ( $W, D$ ) and to the meshes ( $X, Z$ ) in a neighborhood of  $(W(\alpha_i), D(\alpha_i))$  and  $(X(\alpha_i), Z(\alpha_i))$ , so that the discrete form of the discrete coupled equations can be differentiated with respect to  $\alpha$ :

<sup>1</sup> A detailed bibliography including these authors can be found in [9]

$$\begin{cases} \frac{\partial R_a}{\partial W} \frac{dW}{d\alpha} = -\frac{\partial R_a}{\partial D} \frac{dD}{d\alpha} - \frac{\partial R_a}{\partial X} \frac{dX}{d\alpha} - \frac{\partial R_a}{\partial Z} \frac{dZ}{d\alpha} \\ \frac{\partial R_s}{\partial D} \frac{dD}{d\alpha} = -\frac{\partial R_s}{\partial W} \frac{dW}{d\alpha} - \frac{\partial R_s}{\partial X} \frac{dX}{d\alpha} - \frac{\partial R_s}{\partial Z} \frac{dZ}{d\alpha} \end{cases}$$

Given the  $n_f$  solutions ( $dW/d\alpha, dD/d\alpha$ ) of the linear coupled system above, the derivatives of  $J$ , are:

$$\frac{dJ}{d\alpha} = \frac{\partial J}{\partial W} \frac{dW}{d\alpha} + \frac{\partial J}{\partial X} \left( \frac{\partial X}{\partial X_0} \frac{dX_0}{d\alpha} + \frac{\partial X}{\partial D_a} \left( \frac{dD_a}{dD} \frac{dD}{d\alpha} + \frac{dD_a}{dZ} \frac{dZ}{d\alpha} \right) \right).$$

As for the aerodynamic adjoint method, the discrete coupled equations are multiplied by two arbitrary line vectors  $\Lambda_a^T$  (of size  $n_a$ ) and  $\Lambda_s^T$  (of size  $n_s$ ), so that:

$$\begin{cases} \Lambda_a^T \frac{\partial R_a}{\partial W} \frac{dW}{d\alpha} + \Lambda_a^T \frac{\partial R_a}{\partial D} \frac{dD}{d\alpha} + \Lambda_a^T \frac{\partial R_a}{\partial X} \frac{dX}{d\alpha} + \Lambda_a^T \frac{\partial R_a}{\partial Z} \frac{dZ}{d\alpha} = 0 \\ \Lambda_s^T \frac{\partial R_s}{\partial D} \frac{dD}{d\alpha} + \Lambda_s^T \frac{\partial R_s}{\partial W} \frac{dW}{d\alpha} + \Lambda_s^T \frac{\partial R_s}{\partial X} \frac{dX}{d\alpha} + \Lambda_s^T \frac{\partial R_s}{\partial Z} \frac{dZ}{d\alpha} = 0 \end{cases},$$

$$\forall (\Lambda_a, \Lambda_s) \in (\square^{n_a}, \square^{n_s}).$$

Adding both these equations to the derivatives of  $J$ ,

$$\begin{aligned} \frac{dJ}{d\alpha} &= \left( \frac{\partial J}{\partial W} + \Lambda_a^T \frac{\partial R_a}{\partial W} + \Lambda_s^T \frac{\partial R_s}{\partial W} \right) \frac{dW}{d\alpha} \\ &+ \left( A \frac{\partial X}{\partial D_a} \frac{dD_a}{dD} + \Lambda_a^T \frac{\partial R_a}{\partial D} + \Lambda_s^T \frac{\partial R_s}{\partial D} \right) \frac{dD}{d\alpha} \\ &+ A \frac{\partial X}{\partial X_0} \frac{dX_0}{d\alpha} + A \frac{\partial X}{\partial D_a} \frac{dD_a}{dZ} \frac{dZ}{d\alpha} \\ &+ \left( \Lambda_a^T \frac{\partial R_a}{\partial Z} + \Lambda_s^T \frac{\partial R_s}{\partial X} \frac{\partial X}{\partial D_a} \frac{dD_a}{dZ} + \Lambda_s^T \frac{\partial R_s}{\partial Z} \right) \frac{dZ}{d\alpha}, \\ &\forall (\Lambda_a, \Lambda_s) \in (\square^{n_a}, \square^{n_s}), \\ \text{with } A &= \left( \frac{\partial J}{\partial X} + \Lambda_a^T \frac{\partial R_a}{\partial X} + \Lambda_s^T \frac{\partial R_s}{\partial X} \right). \end{aligned}$$

The so-called adjoint vectors  $\Lambda_a$  and  $\Lambda_s$  are chosen such that each term containing  $dW/d\alpha$  or  $dD/d\alpha$  disappears from the expression of  $dJ/d\alpha$ . This leads to the adjoint coupled equations:

$$\begin{cases} \left( \frac{\partial R_a}{\partial W} \right)^T \Lambda_a = - \left( \frac{\partial J}{\partial W} \right)^T - \left( \frac{\partial R_s}{\partial W} \right)^T \Lambda_s \\ \left( \frac{\partial R_s}{\partial X} \frac{\partial X}{\partial D_a} \frac{dD_a}{dD} + \frac{\partial R_s}{\partial D} \right)^T \Lambda_s = - \left( \frac{\partial J}{\partial X} \right)^T \\ \quad - \left( \frac{\partial R_a}{\partial X} \frac{\partial X}{\partial D_a} \frac{dD_a}{dD} + \frac{\partial R_a}{\partial D} \right)^T \Lambda_a \end{cases}$$

Once the adjoint vectors  $\Lambda_a$  and  $\Lambda_s$  have been solved from the linear coupled system above, the derivatives of  $J$  are:

$$\begin{aligned} \frac{dJ}{d\alpha} &= \left( \frac{\partial J}{\partial X} + \Lambda_a^T \frac{\partial R_a}{\partial X} + \Lambda_s^T \frac{\partial R_s}{\partial X} \right) \frac{\partial X}{\partial X_0} \frac{dX_0}{d\alpha} \\ &+ \left( \frac{\partial J}{\partial X} + \Lambda_a^T \frac{\partial R_a}{\partial X} + \Lambda_s^T \frac{\partial R_s}{\partial X} \right) \frac{\partial X}{\partial D_a} \frac{dD_a}{dZ} \frac{dZ}{d\alpha} \\ &+ \left( \Lambda_a^T \frac{\partial R_a}{\partial Z} + \Lambda_s^T \frac{\partial R_s}{\partial X} \frac{\partial X}{\partial D_a} \frac{dD_a}{dZ} + \Lambda_s^T \frac{\partial R_s}{\partial Z} \right) \frac{dZ}{d\alpha}. \end{aligned}$$

Function  $J$  has been assumed to depend only on the aerodynamic variables  $W$  and  $X$ . This does not reduce the generality of the method; indeed, one can easily introduce a direct dependence of  $J$  on  $D$  and  $Z$ , as long as the partial derivatives  $\partial J / \partial D$  and  $\partial J / \partial Z$  are available.

The interested reader is invited to consult the classical literature on the subject, including in particular the articles of Sobieszcanski-Sobieski, Farhat, Maute, Martins and Haftka<sup>1</sup>.

## Conclusion

Optimization in aeronautics has been a very active topic since the 70's. Several engineering disciplines, like structure and aerodynamics, have benefited from the progress accomplished in this field, at the crossroad of mathematics, numerics and computer science. The purpose of this article was not to present all of the methods that can be used for design in aeronautics, but only those that were found efficient and actually used at Onera for design with a special focus on aerodynamic design applications [14].

Huge advances have been made during the last twenty years, in particular in the fields of global optimization (see § Global search methods) and gradient computation (see § Sensitivity evaluations for descent methods), paving the way for the first concrete and conclusive applications of these methods for solving design problems, capturing, at least partially, the complexity of real-life industrial design problems. Future advances may concern the efficient coupling of flow analysis and shape optimization, also of global and local optimization algorithms ■

<sup>1</sup> A detailed bibliography including these authors can be found in [9]

## Acknowledgements

The authors are deeply grateful to their colleagues Manuel Bompard (Onera/DSNA), S. Burguburu (Onera/DAAP) and R.P. Dwight (TU-Delft) for their contributions, encouragements and the sharing of ideas.

## References

- [1] M. BOMPARD, J. PETER - *Local Search Methods for Design in Aeronautics*. In RTO-AVT-167 Lecture Series "Strategies for optimization and automated design of gas turbine engines". 2010.
- [2] G. CARRIER - *Multi-disciplinary Optimization of a Supersonic Transport Aircraft Wing Plan-form*. ECCOMAS 2004, European Congress on Computational Methods in Applied Sciences and Engineering, Jyväskylä, 24-28 July 2004.
- [3] G. CARRIER - *Single and Multipoint Aerodynamic Optimizations of a Supersonic Transport Aircraft Wing Using Optimization Strategies Involving Adjoint Method and Genetic Algorithm*. ERCOFTAC Conference, Las Palmas, 5-7 April 2006.
- [4] J.-L. DENEUBOURG, J.-M. PASTEELS, J.-C. VERHAEGHE - *Probabilistic Behaviour in Ants: a Strategy of Errors?* Journal of Theoretical Biology, 105, 1983.
- [5] D.E. GOLDBERG - *Computeraided Gas Pipeline Operation Using Genetic Algorithms and Rule Learning*. Doctoral dissertation, University of Michigan, Ann Arbor, MI. (University Micro-films No. 8402282), 1983.
- [6] J. H. HOLLAND - *Adaptation in Natural and Artificial Systems*. Ann Arbor, MI: University of Michigan Press, 1975.
- [7] S. KIRKPATRICK, C.D. GELLAT, M.P. VECCHI - *Optimization by Simulated Annealing*. Science, 220(4598), 671-680, 1983.
- [8] J. KENNEDY, R. EBERHART - *Particle Swarm Optimization*. In Proceedings IEEE international conference on neural networks Vol. 4, p.1942-1948, 1995.
- [9] M. MARCELET J. PETER, G. CARRIER - *Sensitivity Analysis of a Strongly Coupled System Using the Discrete Direct and Adjoint Approach*. Revue Européenne de mécanique numérique. Vol. 17, 1077-1106, 2008.
- [10] J. MÖLLER - *Studies of Recursive Projection Methods for Convergence Acceleration of Steady State Calculations*. Licenciate Thesis, Royal Institute of Technology (KTH), TRITA-NA-0119, 2001.
- [11] V. PARETO - *Cours d'économie politique*. Lausanne. F. Rouge. 1896/97.
- [12] J. PETER, R.P. DWIGHT - *Numerical Sensitivity Analysis: a Survey of Approaches*. Computers and Fluids 39 (2010) 373–391.
- [13] K. RASHEED - *GADO: A Genetic Algorithm for Continuous Design Optimization*. Tech. Report DCS-TR-352, Dept. of Computer Science, Rutgers, The State University of New-Jersey, 1988, Ph D. Thesis.
- [14] J. RENAUX, Ph. BEAUMIER, Ph. GIRODROUX-LAVIGNE - *Advanced Aerodynamic Applications with the elsA Software*. Aerospace Lab. Issue 2. 2011.
- [15] G.M. SHROFF, H.B. KELLER - *Stabilisation of Unstable Procedures: The Recursive Projection Method*. SIAM Journal of Num. analysis. Vol 30, 1099-1120, 1993.
- [16] R. STORN, K. PRICE - *Differential Evolution - a Simple and Efficient Heuristic for Global Optimization Over Continuous Spaces*. Journal of Global Optimization 11: 341-359, 1997.
- [17] R. STORN - *On the Usage of Differential Evolution for Function Optimization*. Biennial Conference of the North American Fuzzy Information Processing Society (NAFIPS). pp. 519-523, 1996.
- [18] G. VANDERPLAATS, R. HICKS - *Numerical Airfoil Optimization Using a Reduced Number of Design Coordinates*. Tech. Rep. TMX 73151, NASA (1976).
- [19] G. VANDERPLAATS - *Numerical Optimization Techniques for Engineering Design: with Applications*. McGraw Hill, 1984.

## Acronyms

ANN	(Artificial Neural Network)
BFGS	(Broyden-Fletcher-Goldfarb-Shanno method)
CCD	(Central Composite Design)
CFD	(Computational Fluid Dynamics)
CPU	(Central Processing Unit)
EI	(Expected Improvement)
GA	(Genetic Algorithm)
PSO	(Particle Swarm Optimization)
RaNS	(Reynolds averaged Navier-Stokes)
RPM	(Recursive Projection Method)
SA	(Simulated Annealing)
SQP	(Sequential Quadratic Programming)



**Jacques Peter** After graduating from Ecole Polytechnique (1992), he received a PhD in mechanics from Ecole des Arts et Métiers (1996). He has been working in the CFD Department of Onera since 1998. He is presently in charge of numerical methods for optimization and control for this department.



**Gérald Carrier** is currently working as a research engineer in the Applied Aero-dynamic department of Onera. In charge of several research projects related to numerical optimisation, he has an experience of more than 10 years in applying local and global optimization methods for aerodynamics and multi-disciplinary design problems.



**Didier Bailly** graduated from Estaca in 1985, he was awarded a PhD in 1996 from the University PARIS VI in the field of near-critical point fluid hydrodynamics. His current activities are in the field of drag extraction methods from numerical or experimental data and the use of surrogate models in optimization.



**Patricia Klotz** obtained a PhD from SupAero in 1991. She joined the Onera Mathematical Modelling and Numerical Simulation group in 1995 where she focused on surrogate based optimization applied to combustion chambers design. Currently she is in charge of an internal research project on surrogate modeling.



**Meryem Marcellet** After graduating from SupAero (2005) and the Georgia Institute of Technology of Atlanta (2005), she received a PhD in mechanics from Ecole des Arts et Metiers (2008). She has been working since 2008 in the CAE Department of Onera in the domain of analytical gradient evaluation for aeroelastic problems and multidisciplinary optimization.



**Florent Renac** Florent Renac is currently research scientist at the Computational Fluid Dynamics and Aeroacoustics Department of Onera. He graduated from the École Normale Supérieure de Cachan in 1999 and received a PhD degree from Univeristy Paris VI in 2004 (in collaboration with Fundamental and Experimental Aerodynamics Department of Onera). His research activity includes aerodynamic sensitivity analysis, high-order discretization methods and robust time discretization.

M. Errera, A. Dugeai,  
Ph. Girodroux-Lavigne,  
J.-D. Garaud, M. Poinot,  
S. Cerqueira, G. Chainerau  
(Onera)

E-mail: marc.errera@onera.fr

# Multi-Physics Coupling Approaches for Aerospace Numerical Simulations

The purpose of this paper is to present coupling strategies for aerospace numerical calculations. In the first part, the basic approach used relies on the partitioned coupling of a finite-volume Navier-Stokes solver and a finite-element solid code. These two separate and independent simulation tools carry out exchanges via a coupling library. Two different applications illustrate the capabilities of this coupling method. The main advantage of this approach is to benefit, for each software application, from the experience developed by a large number of specialists over many years. In the second approach, mono-disciplinary software is extended to multi-physics modeling, by adding new simplified modules for other disciplines and by implementing specific coupling algorithms. The modeling of aeroelastic systems is presented as well as several applications to demonstrate the capabilities of this method. Finally, a software structure for code coupling is described in the third part. It consists of an Open System approach, based on a powerful open source assembly of public interfaces.

## Introduction

### Coupled problems

The adjective “coupled” appears frequently in the literature, in different contexts and sometimes with different definitions. In this paper, we have adopted the definition proposed by Zienkiewicz [1]:

“Coupled formulations are those applicable to multiple domains and dependent variables, which usually describe different physical phenomena in which:

- neither domain can be solved separately from the other
- neither set of dependent variables can be explicitly eliminated”

At this stage, it is convenient to mention that there are two distinct categories. In the first, domains may totally or partially overlap. In the second, they interact through a common interface. Both of these categories are considered in this paper.

Computational Fluid Dynamics (CFD) is the most sophisticated type of airflow model. It predicts the detailed spatial distribution of velocity, temperature and pressure, by solving the flow governing equations. CFD programs can provide detailed predictions of convective and temperature distribution, but need input information from the solid, such as deformations or temperature field. Computational Structural Dynamics (CSD) tools, on the other hand, are unable to give information on the airflow and convective characteristics (pressure, heat transfer coefficients, etc.) are usually empirical. Coupling CFD and CSD eliminates many of these assumptions, since the information provided by each model is complementary. It is therefore a very attractive solution, but robust and efficient interaction models between

the fluid and the solid media are generally required. Furthermore, it may be very computationally expensive, if specific approaches are not used.

### Partitioned strategy for fluid-structure coupling

Fluid-Solid coupling - Fluid-Structure Interaction (FSI) or/and Conjugate Heat Transfer (CHT) - can be achieved via two different methods. In the monolithic approach, the equations are solved simultaneously, i.e., they directly operate on the aggregated fluid and structure equations. On the contrary, in the partitioned solution approach, systems are spatially decomposed into partitions. This decomposition is based on physical considerations. The solution is separately advanced in time over each partition. The partitions interact with each other on a common physical interface. Partitioned techniques are widely popular, because they allow the direct use of specifically designed solvers for different fields and may offer significant benefits in terms of efficiency over the monolithic techniques. Moreover, smaller and better conditioned subsystems are solved, instead of one overall problem. All the cases presented in this paper use this partitioned technique.

In order to obtain coupled results on a level of detail generally provided by CFD, the solid and fluid must be solved in sequence (staggered strategy). Interaction effects are accounted for by transmission and synchronization of coupled state variables, the results on the coupled interface being compared and consequently corrected. Although the idea and principle of this code coupling concept is straightforward, this approach can be challenging in practice, due to three main discontinuities between fluid and solid models. First, there is a time-scale discontinuity due to the significant difference between the two media. Second, there is a space-scale discontinuity. The last

discontinuity can be referred to as a “CPU discontinuity” and is due to the discrepancy between the memory requirement and the execution time, between a fluid and a solid solver.

Specific coupling treatments need to be developed to bridge these discontinuities: numerical algorithms, a search process, appropriate numerical approximations, coupling strategies and a computing environment. As a consequence, the radically different physics, length scales, dynamics and objectives involved in multidisciplinary aerospace problems require the use of a wide range of simulation multi-physics approaches.

### Software architecture

A multi-physics problem has three layers to be overcome before an actual operating simulation is achieved on a computer. The first is the physical layer, the coupled system is decomposed into physical fields and their mathematical models are described by means of field equations. The second layer consists in the numerical treatment of this dynamical coupled system. Fields are discretized in space and time and an appropriate numerical algorithm must be determined. The third and last layer is the software, i.e., the numerical algorithm is programmed using one or more programming languages on a hardware system.

A complex simulation can involve several types of software, for example: an in-house code made by a single engineer, COTS<sup>1</sup>, or even Open Source software. The application writer picks up the codes he needs, makes an assembly of these codes using a Steering language and finally obtains a complex software system. The hardware platform for this simulation can be complex too, for instance a large cluster of Linux nodes connected to a remote workstation and these connections can be synchronous or asynchronous.

### Multi-physics approaches

Each discipline has developed specialized tools, which must be adapted to multidisciplinary applications. The purpose of each application may be: purely static (static on both sides of the coupled interface), a mixed stationary/non-stationary solution, or it can be a complete transient solution. The most efficient numerical approach for each solution must be designed carefully and the resulting coupled interface treatment must guarantee stability, consistency and accuracy properties.

Coupling CFD and CSD is a very challenging approach and the goal of this paper is to present some particular aspects and global strategies applied to various specific aerospace problems. This paper is organized as follows:

In the first part, the basic approach relies on the partitioned coupling of a finite-volume Navier-Stokes solver (CEDRE code) and a finite-element solid code (Z-set code) is presented. This coupling is based on the use of an interface library. Two different applications illustrate the capabilities of this coupling method.

In the second part, the modeling of aeroelastic systems is presented. The aim of aeroelasticity is either to compute the behavior of the coupled system at equilibrium, or to determine the potential occurrence of instability of a fluid-structure dynamic system.

In the third part, a software architecture for code coupling is described. It consists of an Open System approach, based on a powerful open source assembly of public interfaces.

## External coupling

### Numerical strategy

The basic approach used in this section is the loose coupling of a finite-volume Navier-Stokes code and a finite-element solid code, a coupling library being in charge of transferring information from one code to the other. In this approach, independent models are simulated separately and the fluid-solid interaction is achieved by partitioning the problem into fluid and solid parts, solved separately with boundary conditions calculated by the other part. This leads to a sequential treatment that can be seen as a Conventional Serial Staggered procedure. During the coupling process, these solvers are called alternately. Specific algorithms are then required, specifically in transient problems [2]. Only this approach allows a direct extension to general multidisciplinary problems.

### The flow solver

The computer code in the fluid, known as CEDRE, can compute turbulent and reactive flows of realistic aerospace configurations and is widely used for a great variety of scientific and engineering problems: turbojet, ramjet, solid propellant rocket and cooling circuits. This code is a three-dimensional finite-volume unstructured code. The governing equations are the time-dependent Navier-Stokes equations, which express the conservation laws of mass, momentum, total energy and any other scalar quantity, written in the conservation form. Details about the Navier-Stokes solver can be found in another papers [3], [4] of this issue.

### The solid solver

The computer code in the solid, known as Z-set, is a three-dimensional finite-element code. It is an advanced object-parallel code for structural mechanics, with many non-linear solution capabilities. More details about this code are given in Box 1.

### The coupling library

In order to reduce the effort involved in coupling the two codes, a loose coupling approach has been chosen and the exchange of physical data between the finite-volume fluid code and the finite-element solid code is performed through the MpCCI library [5]. It is a code coupling interface for multidisciplinary applications. Instead of just transferring data from one process to another, MpCCI takes into account the grids as well as the processes on which the data is located. Due to the different discretization techniques for the CFD and CSD simulations, the fluid-solid interface is represented by different grids. The task of MpCCI is to calculate the neighborhood relations when these grids are non-matching and to transfer the coupling values across the interface. This library has allowed us to couple pre-existing physics applications with a limited amount of modification and to continue to develop them independently.

<sup>1</sup> Commercial Off The Shelf: software made and sold by a commercial company

## Box 1 - Z-set: a Computational mechanics toolkit for material and structures

Z-set is a versatile toolkit developed by the École des Mines ParisTech, Onera and NWNumerics. Its development started in the early 80s to model the non-linear response of material specimens subjected to various loads. Initially specialised in highly non-linear material models, it has evolved over the years and is now a full-featured state-of-the-art finite element solver.

Initially written in Fortran77, it was entirely re-engineered during the 90s and is now completely developed in an object oriented framework, using C++ as the implementation language.

It addresses the entire modeling chain in the field of computational mechanics and thus contains pre and post graphical and batch processing, meshing tools, optimisation tools, sequential and parallel finite element solvers, a large material library, etc. Furthermore, its multithreaded core components take full advantage of modern SMP architectures.

The reader is invited to look at <http://www.zset-software.com> to get a complete overview of Z-set's features. It is possible to model more or less any structural mechanical problem, even using innovative modern methods such as parallel processing, extended finite elements, adaptive re-meshing and non-local models, etc.

The Z-set design is based on a dynamic object factory pattern, coupled with a plug-in technique, which allows the end-user to modify and enrich the package without any modification to the core code. For instance, the coupling methods described in this issue have been entirely developed within a plug-in, *without* any modification to the main code.

Two different space applications illustrate the capabilities of this coupling method. First, a fluid-solid coupling interaction in a solid propellant rocket motor is presented and then an aero-thermo-mechanical study in the Vulcain 2 rocket engine. The latter involves three independent solvers.

### Fluid-structure interaction for a solid propellant rocket motor

Fluid Structure Interactions (FSI) have been shown to be extremely important in the analysis of pressure oscillations in Solid Propellant Rocket Motors (SPRM) (see Box 2). To improve the physical understanding of pressure oscillations inside SPRM, a coupling methodology involving two codes, CEDRE and Z-set, has been developed for the flow and structure subsystems respectively.

#### Partitioned approach

In this coupled study, the FSI is achieved by partitioning the problem into fluid and solid parts, solved separately with interacting boundary conditions [6]. Figure 1 shows the sequence of iteration steps. It starts with the calculation of the aerodynamic field (Path 1).

The resulting pressure distribution is transferred to the finite element nodes (path 2). Using this new interface conditions the structural code computes the deformation of the structure (path 3). The resulting displacements modify the fluid surface grid and consequently change not only the boundary conditions (path 4), but also the entire grid in the fluid domain in the next step (path 5).

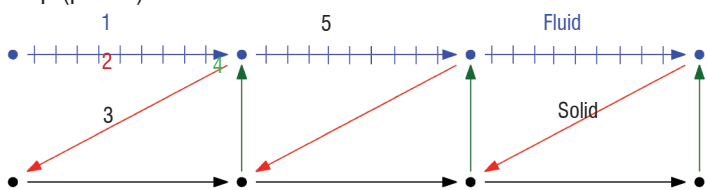


Figure 1 - Subcycled Conventional Serial Staggered procedure for FSI.

### Two-Dimensional problem in the field of solid propulsion

The potential of the coupling strategy in handling two-dimensional transient FSI problems is assessed by computing an experimental case, performed by the IUSTI laboratory [7]. Such an experimental device describes a flexible panel protruding into a shock tube and submitted to a shock wave. A close-up view of the experimental set-up is given in figure 2.

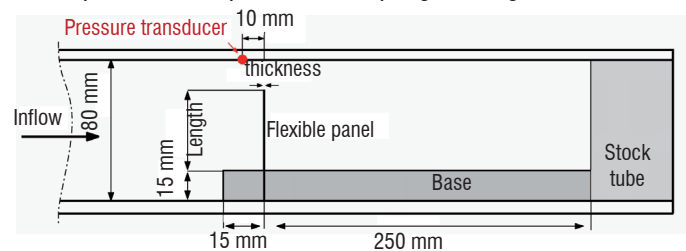


Figure 2 - IUSTI experimental setup.

The panel is fixed on a base, assumed to be infinitely rigid. As a shock travels down the tube, pressure gradients result in a panel motion. In this experiment, fluid pressure evolution is measured by a pressure transducer and top panel displacement is monitored. Furthermore, ombroscopic pictures provide visual information on the behavior of the transmitted and reflected shocks.

#### Numerical model

The coupled simulation is performed considering an isotropic steel panel (linear elastic), with a Young's Modulus  $E=220$  GPa and a density  $\rho=7600$  kg.m<sup>-3</sup>, with a length equal to 40 mm and 1 mm thickness. The shock wave moves from the inlet boundary condition, where air is injected at standard atmosphere conditions, at a Mach number of 1.2. Considering the short duration of the experimental run, turbulence is neglected. For such a compressible flow, Rankine-Hugoniot relations allow the determination of pressure and temperature values related to the shock wave. The coupling time step is taken to be equal to 10<sup>-6</sup> s, which is about 100 times smaller than the structure characteristic time. Mesh resolution and time step have been chosen in order to ensure a sufficient numerical accuracy of the coupled dynamics.

## Box 2 - Pressure oscillations in solid rocket engines

Early to be discovered in the late 1930's, unsteady motion in Solid Propellant Rockets were the first examples of combustion instabilities in propulsion systems. Since that time, extensive work has been done on pressure oscillations arising in a number of large Solid Propellant Rocket Motors (SPRM), including the Space Shuttle RSRM, Titan and Ariane 5 boosters. Reason for such intensive concern can be found in significant vibrations transmitted to the payload.

Several mechanisms had been identified as the chief origin of instabilities arising in solid-fuel motor configuration. Those mechanisms involve the sensitivity of burning surfaces to pressure and velocity fluctuations and purely fluid mechanical processes leading to the interaction of large scale vortices with acoustic waves B2-[1].

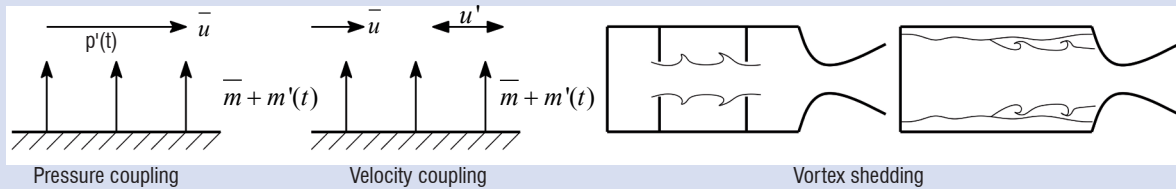


Figure B2-01 - Possible mechanisms for pressure oscillations in SRM

Among all the potential causes of flow unsteadiness, shear layers caused by protruding inhibitors (as a result of the propellant consumption) or by the geometry of the grain and the unstable behaviour of the flow induced by wall injection are of major importance B2-[2]. As a consequence, computational efforts made to better understand pressure oscillations inside SRM require, for instance, the accurate prediction and modeling of inhibitors and/or propellant mechanical response under fluid stress. Coupling physical models through independent physics solvers can be now achieved thanks to multi-physics numerical approaches.

### References

- B2-[1] G.A. FLANDRO and H.R. JACOBS – *Vortex Generated Sound in Cavities*. AIAA Paper 73-1014, 1973  
 B2-[2] F.E.C. CULICK - *Unsteady Motions in Combustion Chambers for Propulsion Systems*. NATO Research and Technology Organisation, December 2006.

## Numerical results and comparison with experimental data

The interaction between the shockwave and panel gives rise to a transmitted and a reflected shockwave. A detailed description of the physical phenomena involved is discussed in detail by Giordano [7].

As shown in figure 3, numerical schlierens present a good agreement with experimental ombroscopic pictures and thus indicate that the flow field dynamic is being quite well captured.

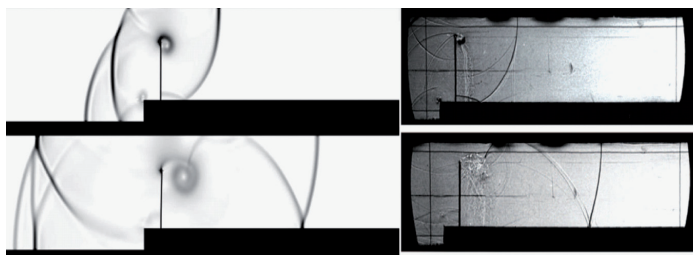


Figure 3 - Numerical schlierens (left) and experimental ombroscopic pictures (right)

A plot of the pressure at the position of the experimental transducer is reported in figure 4, paying particular attention to the

pressure time evolution. Although there is a slight difference for  $t > 0.0025s$ , probably due to some boundary condition reflection error for the reflected shockwave, the two plots show a similar transient evolution. As a result, from fluid dynamic loads, the panel movement (figure 4) is also well captured and falls within experimental uncertainties. All these comparisons between numerical and experimental data emphasize that the coupling method succeeds when computing highly transient phenomena and thus should be used to cope with more elaborate computations involving stronger coupling phenomena.

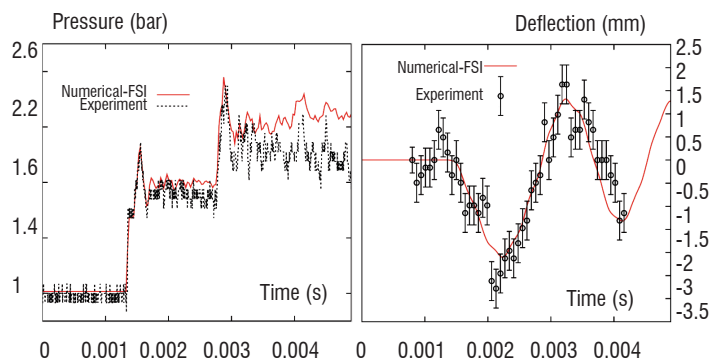


Figure 4 - Pressure evolution at probe location (left) and corresponding panel deflection (right).

# Simulation of a rocket nozzle

## Vulcain 2

The nozzle of a Vulcain 2 engine is subjected to many types of solicitations. It is assembled from *Inconel 600* tubes, a material resistant to high temperatures. Since it has to withstand the heat generated by the exhaust gases (~3000 K), it is cooled by Hydrogen circulation. The nozzle must withstand severe thermo-mechanical loads during pre-flight testing and during the actual flight. In non-reinforced nozzles, this cyclic loading causes progressive bulging of the tubes, which in turn modifies the circulation of both the exhaust and coolant fluids. The simulation of the complete system thus requires a fully coupled approach.

## Model

The complete system is extremely complex, so this study will be restricted to a single tube portion, located near the critical zone of the nozzle (Figure 5).

Decoupled studies by Roos and Chaboche [8] have shown that a nonlinear elasto-visco-plastic material behavior is needed to properly model the bulging of the tubes; the authors have identified a Norton flow law:

$$\|\dot{\epsilon}^p\| = \left\langle \frac{\|\sigma - X\| - R - k}{K} \right\rangle^n$$

where  $\|\dot{\epsilon}^p\|$  is the plastic strain rate,  $\sigma$  is the stress tensor,  $X$  is the kinematic hardening term,  $R$  is the isotropic hardening,  $k$  is the initial flow stress, and  $K$  and  $n$  are both Norton viscosity coefficients [9]. All parameters appearing in this behavior are strongly dependent on the temperature.

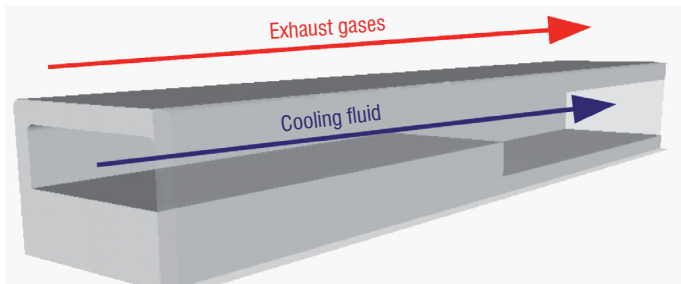


Figure 5 - Tube section model.

For this computation, the coolant fluid is considered a perfect gas; the partitioned approach will allow us to switch to more complex fluid models later on, without needing a full re-design of the coupling software. The exhaust gases are not simulated: a simple Robin thermal boundary condition is applied on the structure to represent them.

On the cold fluid side, both mechanical and thermal interactions are taken into account. Preliminary decoupled computations have shown that the deformation of the structure does not significantly influence the fluid flow, at least in this particular configuration. This part of the coupling was thus neglected and we kept only those shown in figure 6.

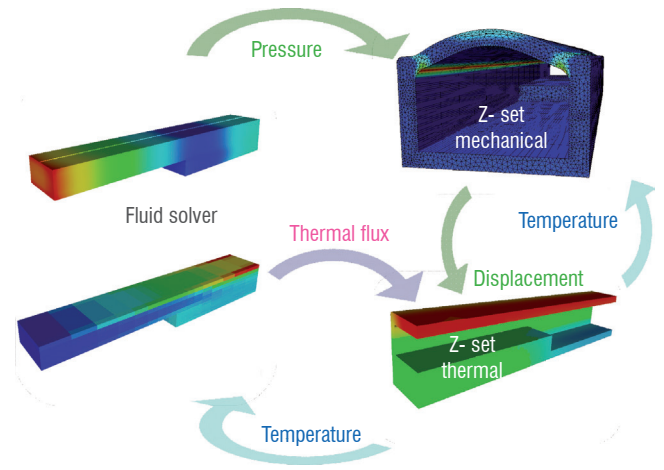


Figure 6 - Aero-thermo-mechanical coupling sequences.

Note that in this model, the mechanical and thermal responses of the structure are computed by two separate solvers, running on different meshes. It turns out that the same software (Z-set, see Box 1) is able to do both computations, but they are considered separate in the algorithm below.

## Algorithm design for an aero-thermo-mechanical problem

The standard coupling algorithms [6] are adapted to this 2½ code coupling. Our experience has indeed shown that each application requires a specific tailoring of the algorithm, in order to benefit from the specificities of the problem. In this coupled problem, the main interest is in the response of the structure to a typical load and the coolant fluid is only modeled in order to obtain reasonable boundary conditions. The algorithm is thus designed around the structure, rather than around the fluid.

For the sake of simplicity, let us first consider the thermal coupling. The characteristic time of the structure is extremely large compared to that of the fluid. The algorithm considers the fluid as stationary around each of the configurations of the structure and standard coupling algorithms, such as those presented by [10], are adapted as follows:

```

While t < t_max :
  repeat:
    predict flux (or alpha) at interface
    solve solid thermal problem
    send temperature at interface from S to F
    solve fluid
    send flux (or alpha) at interface from F to S
  until prediction is good enough
  t ← t + Δt
    
```

Figure 7 - Coupling algorithm for a thermal problem: S stands for structure solver and F for fluid solver,  $\alpha$  is the convection coefficient at the interface.

The algorithm presented in figure 7 features three specificities:

- it includes correction steps, because a fully explicit algorithm (e.g., one without correction steps) would require extremely small time steps to ensure stability;
- the coupling frequency is not fixed: each solver is allowed to adapt it during computation, depending on the evolution of the coupled variables;

• in order to further improve the convergence speed of this coupling algorithm, Robin boundary conditions are used at the interface; we refer to [10] for further details.

Let us now complete this algorithm to include mechanical coupling. There are two additional terms to take into account:

- the volumic thermo-mechanical coupling within the structure;
- the mechanical coupling at the surface between the fluid and the structure, as can be seen in figure 6.

It has been decided that the mechanical code should impose only its displacement variables on the thermal code and nothing on the fluid. The mechanical problem can thus run alongside the other two codes, without needing a full synchronization with them. The algorithm is shown in figure 8.

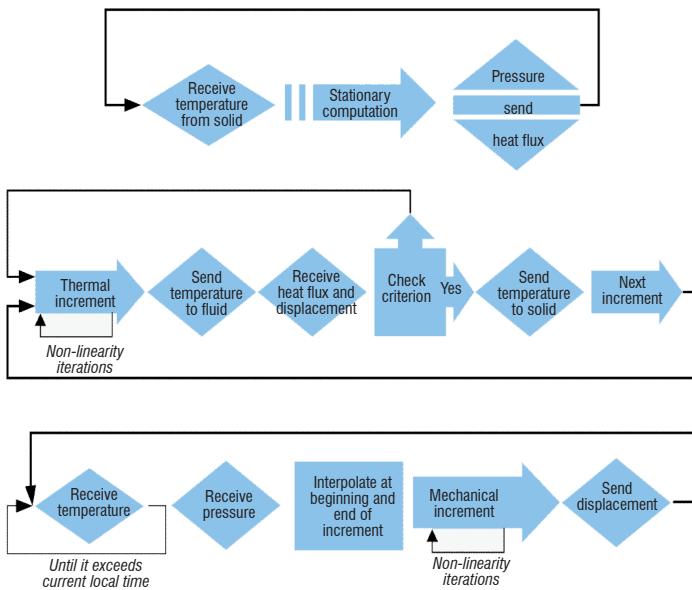


Figure 8 - Algorithm implementation in the fluid code (top), thermal code (middle) and mechanical code (bottom)

## Results and performance

Our designed algorithm is applied to a 20 second simulation, corresponding to the first part of a test sequence. At this point, the thermal problem is mostly stabilized, but the mechanical problem will still continue to evolve due to creep for the rest of the test (600 s). Figure 9 presents the solution at the end of this first sequence. The asynchronous 3-code algorithm performs well on this application. Concerning the thermal part, the adaptive coupling time steps require a minimal number of coupling time steps: they are sufficiently small at the beginning of the computation when the thermal fluxes evolve rapidly and become progressively larger when it starts to stabilize.

The use of Robin interface conditions between the structure thermal problem and the fluid also allows for larger time steps, without destabilizing the coupled process [10]. The use of asynchronism permits a reduced number of time steps for the mechanical solver: at the beginning of the computation, when the temperature is still low, it behaves elastically and accepts large time steps; however, when the thermal problem reaches higher temperatures, the mechanical problem enters a more complex, nonlinear stage, where it is principally governed by the visco-plasticity terms and requires small time steps. This type of model problem demonstrates the feasibility of a coupled resolution

within the context of nonlinear mechanics, 3-code interactions and strongly coupled physics. Future work will include the simulation of more realistic models that can be confronted with experimental results and the extension to physics with less contrasted characteristic times.

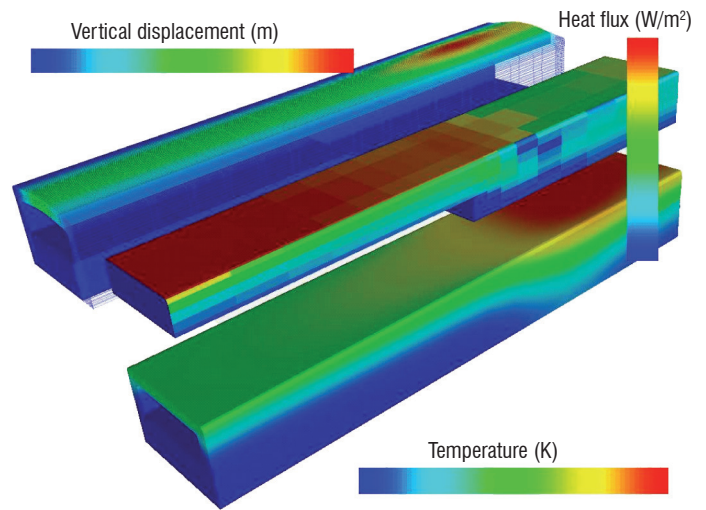


Figure 9 - Coupled aero-thermo-mechanical results: vertical displacement (top), heat flux (middle) and temperature (bottom) after 20s of simulation.

## Aeroelasticity: introduction

Aeroelasticity is the scientific discipline that studies the coupled behavior of a mechanical system basically submitted to 3 kinds of loads: elastic forces, aerodynamic forces and inertial forces.

Figure 10 depicts the well known Collar triangle that details the various scientific domains dealing with the interactions between these 3 sources:

- 1: Flight dynamics
- 2: Static aeroelasticity
- 3: Structural dynamics
- 4: Dynamic aeroelasticity

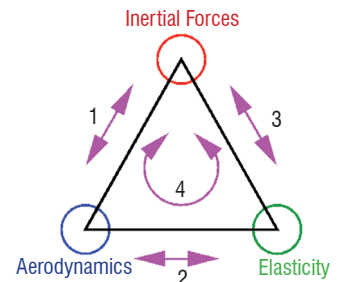


Figure 10 - Collar triangle.

The aim of aeroelasticity is, either in the static or in the dynamic case, to be able on the one hand to predict the behavior of a coupled system at equilibrium and, on the other hand, to investigate the potential occurrence of instability of the fluid-structure coupled system. At equilibrium, the objective is to predict the coupled structural deformations and stresses, and the aerodynamic loads. A proper evaluation of the structure deformations under operating conditions is necessary to precisely predict, and possibly optimize, the performance of the aeronautical system, aircraft lift and drag, for example. Aeroelastic instability may appear in the static case, leading to static divergence and in the dynamic case, with the so-called flutter phenomenon. Of course, the study of the instability conditions is of prominent importance, in order to ensure the flight-safety of aeronautical structures, due to the catastrophic explosive character of flutter. The coupled fluid-structure

mechanical system may also be non-isolated and be subjected to additional external forces, such as gravity, forced excitation, or unsteady aerodynamic excitation (wake or gust response) and may be coupled with the flight control system, thus introducing additional complexity into the study of the coupled system behavior.

## The modeling of aeroelastic systems

### Structural modeling

For many years, flutter has been considered such a dangerous and badly understood phenomenon, that designers have tried to build stiff and rather compact aeronautical structures to get rid of it. Flight deformations were supposed to remain very limited. Therefore, for aeroelastic studies, the structural behavior is classically supposed to be properly represented by a linear, small deformation model. The dynamic behavior of such an aeroelastic structure is modeled by a differential equation in time, involving mass, damping and stiffness matrices, and external aerodynamic loads:

$$M\ddot{x} + D\dot{x} + Kx - F_A(t, x, \dot{x}) = 0$$

In the static case, the equilibrium is given by the following steady equation:

$$Kx_{stat} - F_A(x_{stat}) = 0$$

Several numerical models are possible. A finite element approach is more general, but modal reduction is frequently used. In this case, the solution may be projected on the basis of the modal eigenvectors  $\Phi$  of the undamped system. The structural dynamics equation becomes reduced to:

$$\mu \ddot{q} + \beta \dot{q} + \gamma q - \Phi^T F_A(t) = 0$$

where  $q$  stands for the generalized coordinate vector,  $\mu = \Phi^T M \Phi$ ,  $\gamma = \Phi^T K \Phi$ ,  $\beta \approx \Phi^T D \Phi$  and  $\Phi^T F_A(t)$  is the unsteady generalized aerodynamic force vector (GAF).

Today, aeronautical designers strive to benefit from the flexibility of the structure, to improve aircraft and engine performances. Aircraft lifting surfaces and engine bladings become thinner, wider and more flexible. Structural deformations tend to increase and the need for better modeling arises. It may be necessary to take into account structural non-linearities, such as friction, mechanical clearances, or even geometrical non-linearities due to large displacements. The tendency is to benefit from more sophisticated fluid and structural modeling via FSI with FE non-linear solvers.

### Aerodynamic modeling

For many years, steady and unsteady linear methods have been the only tools available in the subsonic and supersonic regimes to analyze the aeroelastic behavior of aeronautical structures. Here again, improving the performance of aircraft requires a better understanding of the steady and unsteady aerodynamic operating conditions of the aeronautical structures. More sophisticated numerical aerodynamic models have been developed, especially in the transonic regime, where strong non-linear aerodynamic phenomena occur, such as shocks, boundary layers and flow separations. RANS and URANS solvers have been developed, first for steady applications, then in the

unsteady domain, and these are now of common use, even for aero-elastic applications.

In the unsteady case, specific numerical features of the aerodynamic solvers are necessary for aeroelastic applications. The main issue is to be able to take into account the structural deformations. This requires:

- the availability of mesh deformation techniques;
- the taking into account of grid velocity;
- efficient and time-consistent unsteady resolution schemes;
- convergence acceleration techniques.

The solvers must handle static and dynamic RANS and URANS equations, with a variety of turbulence models. Due to the large CPU costs of aeroelastic computations, parallelization of the solvers has become compulsory today. *elsA*, which is currently Onera's multi-block structured grid aerodynamic solver, is the development tool chosen for aeroelasticity studies. More information about *elsA* is available in this issue.

### Transfer techniques

One of the key issues for multidisciplinary simulation is to ensure the proper transfer of interacting variables between the various physical models involved. As far as aeroelasticity is concerned, the simulation must ensure:

- the proper load transfer, from the fluid domain to the structure;
- the proper displacement (and velocity) transfer, from the structure to the fluid.

Therefore, it is necessary to define a fluid-structure interface that allows data exchanges between both domains. However, it must be pointed out that, in the general case, the structural and fluid discretization grids at the interface are distinct. Specific transfer techniques must be implemented that totally depend on the physical models used for both domains.

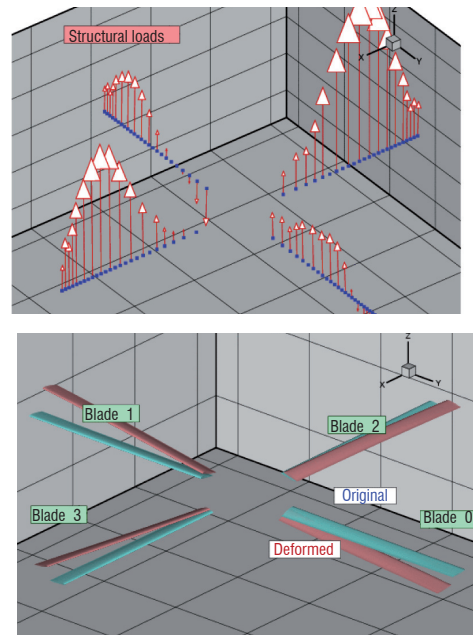
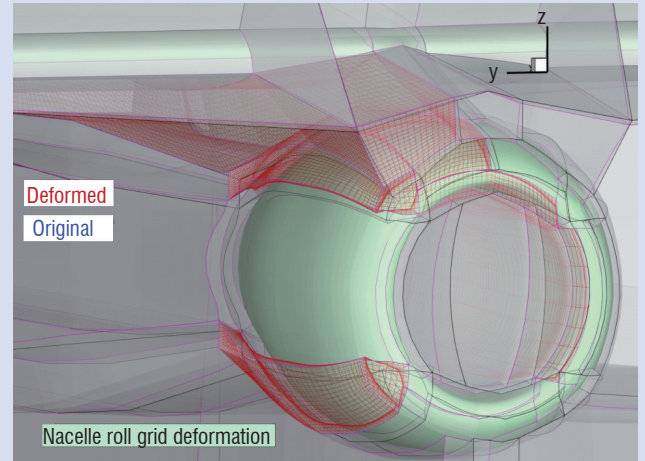


Figure 11 - Example of a beam structure model compared to aerodynamic surface grid (helicopter case).

### Box 3 - Mesh deformation

Taking into account the motion of the structure is a general issue for numerical aeroelasticity purposes. A first approach is to keep the aerodynamic grid unchanged, using a specific aeroelastic boundary condition that takes into account wall velocity. This approach may be valid for inviscid two-dimensional computations, but appears to be unsuccessful in the 3D case and for viscous flows. Therefore, developing efficient and robust aerodynamic grid deformation techniques has been a research topic since the eighties. At that time, Batina first proposed to take advantage of a structural analogy in order to deform aerodynamic grids. The idea was to build a discrete spring network, located on the edges of the 3-dimensional aerodynamic grid, and to solve the static elastic equilibrium of the system, boundary displacements being prescribed.

Other structural analogy techniques are also used. The *elsA* code has several such techniques [12]. In particular, it may solve the grid deformation problem using a linear elastic material analogy, combined with finite element modeling. Due to the basic properties of the structural stiffness matrices, efficient linear system resolution techniques may be implemented, such as the pre-conditioned conjugated gradient. The so-called volume-spline (or infinite-plate) technique is also a structural deformation inspired technique that solves the problem of an infinite two-dimensional elastic plate, loaded at discrete nodes. This model leads to the resolution of a bi-Laplacian PDE, independent from any grid topology information. Related methods are based on the resolution of similarly built linear systems, using radial basis functions (RBF).



Integral methods are also popular, some of them corresponding to a linear aerodynamic flow problem analogy. Purely analytical techniques are also available, such as the transfinite interpolation technique, or fitting techniques, however, based on expensive distance computations. In order to reduce the computational cost, multilevel techniques combining analytical and structural analogy methods may also be implemented.

When the modal approach is used for the structural modeling, generalized quantities are naturally used for the transfer of loads (generalized forces  $\Phi^T F_A(t)$ ) and displacements (generalized coordinates  $q : x = \Phi q$ ). In this case, the conservation of virtual work is strictly ensured, but equivalent mode shapes  $\Phi$  must be defined also on the aerodynamic surface grid, which implies the use, in a pre-processing step, of interpolation or fitting techniques. When using finite element structural modeling, things may be more complicated. Displacement transfers need to be performed via interpolation or fitting techniques at each coupling step. Load transfer must satisfy the conservation of mechanical work at the fluid/structure interface. Several approaches are available to do this, such as the so-called “nearest neighbor” strategy and methods based on the virtual work conservation principle.

#### Aeroelastic dynamic stability prediction

Several approaches may be used in order to analyze the dynamic stability of a fluid-structure coupled system. The first one corresponds to a weak coupling approach, in the frequency domain, where the fluid solver is implemented to compute the aerodynamic response to an unsteady structural forced motion. Classically, harmonic vibration motions following modal deformations of the structure ( $q_n(t) = q_n^* e^{pt}$ ) are prescribed and give access to the values of the generalized harmonic forces for a single value of the excitation frequency. So-called “pulse” excitation techniques may alternatively be used to obtain harmonic GAFs within a frequency range, with a single aerodynamic

simulation. In the weak coupling approach, aerodynamic forces may be considered as additional aerodynamic stiffness and additional positive or negative damping terms of the mechanical system:

$$(p^2 \mu + p(\beta - B) + (\gamma - A))q^* = 0$$

$$(A + j\omega B) = \frac{\Im(\Phi^T F_A)}{\Im(q^*)}$$

Complex eigenvalues of the coupled system expressed in the frequency domain are extracted and give access to the frequencies and dampings. A negative damping value leads to an unstable behavior of the system.

In a second approach, the resolution is carried out in the time domain, following a strong coupling method. In this case, a staggered scheme is used to solve the fluid and structure equations, in order to benefit from the large discrepancy between both domain typical time steps. An additional mechanical convergence loop is necessary to simultaneously achieve the convergence of deformation, fluid and structural coupled equations. In this process, load and displacement transfers are performed up to convergence at each coupling step. The time histories of coordinates or loads are analyzed in the frequency domain, to obtain the eigen-frequencies and damping values of the coupled fluid-structure system.

## Box 4 - Turbomachinery aeroelasticity

Turbomachinery aeroelasticity involves additional complexity at several levels [16]. First of all, rotation must be taken into account, which leads to extra centrifugal and gyroscopic force terms for the numerical formulation. The second point is the cyclic periodic design of such machines. Concerning the structural dynamics, these effects induce an increase in the eigen frequencies of the system with rotation speed (Campbell diagram) and the occurrence of complex mode shapes, combined with inter-blade dephasing. On the other hand, the aerodynamic flow exhibits complicated features, such as shocks, boundary layers and separation, as well as tip and hub corner vortices. Instability may be produced by unsteady aerodynamic features, inducing classical flutter or stall, or choke flutter. Unsteady phenomena, such as a rotating stall may propagate over the complete wheel.

Moreover, turbomachines are made of a set of several wheels, rotating at different speeds and all interacting together. Even in the rigid blade case, the global aerodynamics must be considered as unsteady, due to the periodic effect of the blade passing of adjacent wheels. As a consequence, the numerical cost of unsteady aeroelastic simulations may be even more important than for external flows around aircraft. This is the reason why reduction techniques are necessary, in order to keep the CPU cost acceptable for every-day industrial use. As an alternative to URANS modelling, linearized formulations have been proposed to reduce computational costs. Harmonic Balance formulations are also under development and already show promising results for single frequency problems, and they may be of great interest in the case of multi-stage unsteady applications. Geometric reduction is possible for the weak coupling approach, in the framework of the dynamic aeroelastic stability analyses. In this case, harmonic forced motion simulations can be conducted on a single sector of the machine, using a specific space-time periodic boundary condition at upper and lower boundaries of the channel. Due to the vicinity of the blades, the inter-blade phase angle of the modal vibration is a main parameter in the study of the dynamic aeroelastic stability of blade rows. In-phase or out-of-phase blade vibrations lead to different aerodynamic damping values. Moreover, the aeroelastic behaviour is highly dependent on the operating conditions of the machine, rotation speed and pressure ratio.

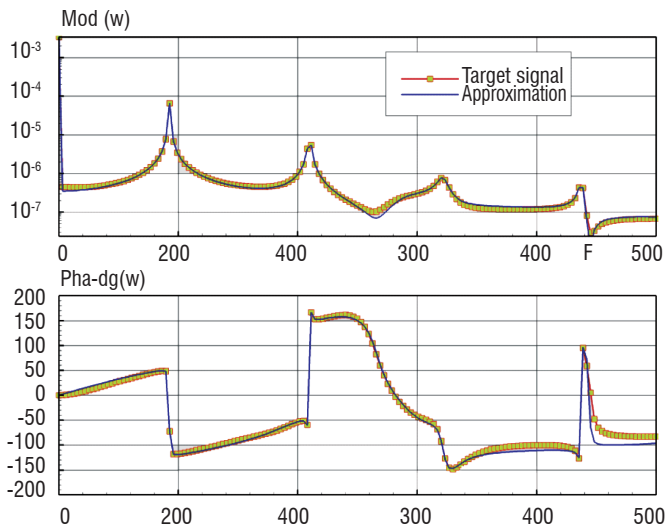


Figure 12 - Identification technique applied to extract frequencies and damping information from unsteady signals.

## e/sA/Ael simulations

### Ael subsystem overview

The fluid-structure problem can be formulated as a coupled field problem, where the solutions are coupled only at the boundary interfaces between the fluid and the structure. It is then possible to run separate solvers for the flow computation and the structure computation, and to reach a coupled solution by exchanging information at the common fluid-structure boundaries. However, in most aeroelastic problems, the structure may be assumed to be linear. In this case, it is much easier and more efficient to extract the structural information from a full finite element model in a pre-processing step and to solve the mechanical system directly in the aerodynamic code. This is the strategy that has been adopted to extend the aerodynamic e/sA solver for fluid-structure coupling.

A general framework has been developed in the optional “Ael” subsystem of e/sA over the last few years, in order to extend e/sA to different types of static or unsteady aeroelastic simulations (figure 13).

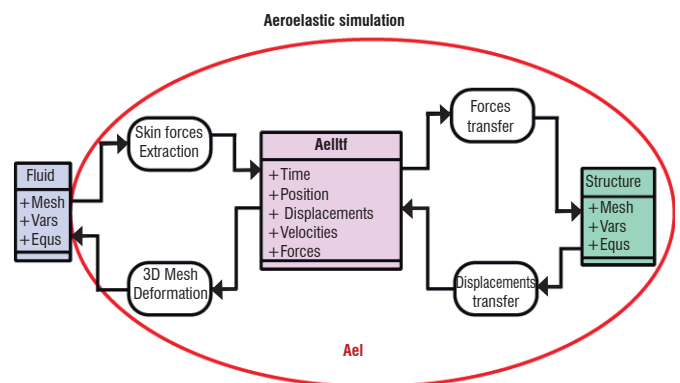


Figure 13 - e/sA/Ael aeroelastic subsystem.

The purpose of these simulations is the prediction of the in-flight static or dynamic behavior of flexible aerodynamic structures and their aeroelastic stability. This “Ael” subsystem gives access in a unified formulation to different types of aeroelastic simulations, while minimizing the modifications of the flow solver. The available simulation types range from non-linear and linearized harmonic forced motion computation, to static coupling and consistent dynamic coupling simulations in the time-domain, with different levels of structural modeling (“reduced flexibility matrix” for static coupling, modal approach, or full finite element structural model).

### Aerodynamic modeling available within Ael

Euler and RANS equations are available for static aeroelasticity, using the e/sA/Ael module. In the dynamic case, several specific formulations are available for aeroelastic modeling. The most general is the

URANS model, but alternate models may be used for periodic unsteady simulations:

$$\frac{\partial W}{\partial t} + \frac{\partial F}{\partial x} = 0$$

The first one is the linearized URANS formulation. In this case, the flow field is considered to be the sum of a steady part and a small time harmonic perturbation field:

$$W = W_s + \delta W^* e^{j\omega t}$$

These assumptions lead to a complex formulation, taking into account structural motion via mesh deformation, specific boundary conditions and ALE. A linear system is solved using the LU-SSOR classical approach, giving access to the first harmonic of the perturbation field and thus to unsteady loads due to the vibration motion of the structure.

Another alternate approach is the harmonic balance method [11]. The Time Spectral Method (TSM), available in elsA as from version 3.4, is dedicated to the simulation of time-periodic flows. Basically, the flow is assumed to be given by a Fourier series expansion of  $2N+1$  terms:

$$W = \sum_{n=-N}^{n=N} \omega_n e^{jn\omega t} F = \sum_{n=-N}^{n=N} f_n e^{jn\omega t}$$

The TSM casts a time-periodic Unsteady RANS problem to the simultaneous resolution of  $2N+1$  coupled steady RANS problems, corresponding to a uniform sampling of the time-period. This odd number stands for stability and allows the capturing, at the most, of the  $N$ th harmonic of the fundamental frequency {Shannon 1949}. The coupling is handled by a pseudo-spectral time derivative only valid for periodic flows. This operator appears as a source term of the steady Navier-Stokes equations. The convergence of steady problems is better mastered than the unsteady transient of U-RANS simulations, which enables a better efficiency for the resolution of time-periodic problems.

## Applications

### Prediction of control surface efficiency

An accurate prediction of the effectiveness of control surfaces is needed, both for aircraft manoeuvre studies and for load alleviation control. The prediction of aileron efficiency, taking into account aeroelastic effects, is investigated here for the case of the HiReTT wing model, experimentally investigated in ETW. Rigid wing and flexible wing simulations have been achieved for transonic flow conditions, in the case of a  $3^\circ$  down deflection of the aileron [13].

The rigid wing computation clearly overestimates the global coefficient variations (see Table 1), due to a deficient shock location (Figure 14c). A good prediction of the lift and drag fluctuations is provided, on the other hand, by the static coupling simulation, which takes into account the small change of wing deformation induced by the aileron deflection, see figure 14d.

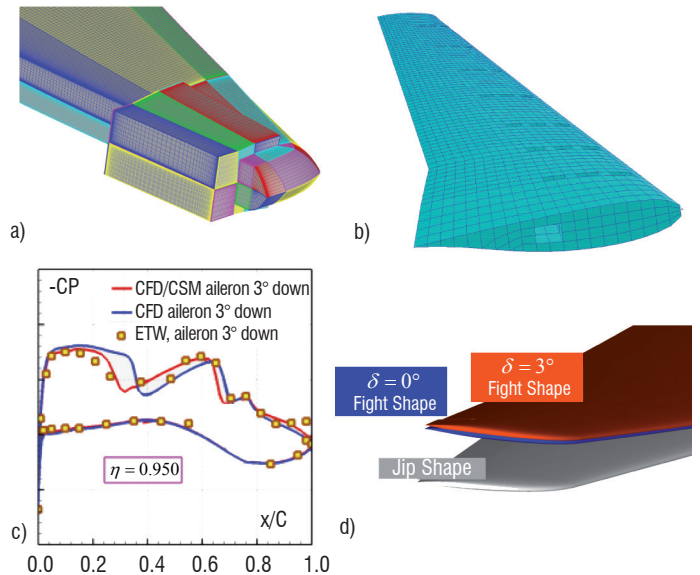


Figure 14 - a) Aerodynamic Chimera grid, b) structural finite element model, c) pressure distributions, d) wing deformations.

	$C_L \delta=0^\circ$	$C_L \delta=3^\circ$	$dC_L/d\delta$	$C_D \delta=0^\circ$	$C_D \delta=3^\circ$	$dC_D/d\delta$
Rigid wing	0.4750	0.4908	5.26 E-03	0.0235	0.0245	3.3 E-04
Flexible wing		0.4835	2.83 E-03		0.0243	2.7 E-04
Experiment	0.4869	0.4956	2.90 E-03	0.0250	0.0257	2.3 E-04

Table 1 - Lift and drag variations induced by the aileron deflection.

### Aeroelastic stability of a centrifugal compressor

The Aeroelasticity and Structural Dynamics Department of Onera (DADS) has been involved in the MACAO project of the French "pole de compétitivité" Aerospace Valley, in cooperation with Airbus, the SAF-RAN group and local aerospace companies. The aim of the actions carried out was the study of the dynamic aeroelastic stability of a Turbomeca centrifugal compressor model, using non linear aerodynamic modeling. The wheel is about 30 cm in diameter and consists of 11 sectors, each of these including a main and a secondary blade. The rotation speed of the selected operating point is roughly 50,000 rpm.

The elsA solver has been implemented in RANS and URANS mode, using a Smith kl turbulence model and an upwind Roe space discretization scheme. Weak coupling aeroelastic simulations have been performed to study the dynamic stability of blade-only vibration modes and blade-and-hub vibration modes.

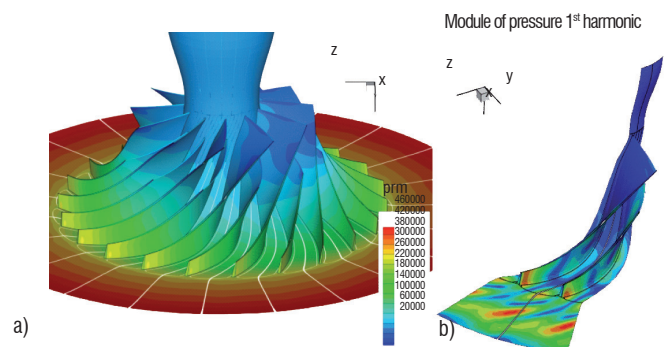


Figure 15 - (a) Centrifugal compressor mean pressure - (b) aerodynamic response to zero-dephasing vibration (pressure module 1st harmonic).

This second action leads to additional issues concerning the aerodynamic grid deformation. The structural analogy mesh deformation tool has been successfully implemented in this case and has helped to run a set of aeroelastic simulations at the targeted operating point, giving access to the aeroelastic dampings of the selected vibration modes, for various inter-blade phase angles. The intention of further study is to perform similar analyses in the case of the modeling of the blade tip clearance at the shroud. In order to reduce the CPU cost of these computations, TSM, as well as wall law approach simulations, are under investigation for this model.

### Counter-rotating open rotor (CROR) aeroelasticity

The aeroelastic stability of a CROR has been studied within the framework of the European DREAM project. The model consists of a front 12 blade propeller and a rear 10 blade propeller. Two operating conditions have been selected: a take-off case at  $M=0.25$  and a cruise case at  $M=0.78$ . These models have been scaled to a 1/5.1 ratio, for the purpose of conducting wind tunnel experiments. The analysis of the aeroelastic stability of the front wheel has been performed, using the weak coupling approach in the frequency domain. Therefore, generalized aerodynamic forces must be computed for time harmonic motions following vibration mode shapes at natural frequencies for each operating point. The effect of the second wheel has been taken into account in this study, using a mixing plane boundary condition at the interface between front and rear wheels. This is of course a strong simplification: unsteady perturbations generated by the passing of the rear blades are neglected. However, this assumption allows the reduction of the numerical model to a single passage for each propeller, combined with the use of the space-time periodic boundary condition. To do this, the space-time periodic boundary condition available in *e/sA* has been updated, in order to take into account the use of an absolute velocity formulation in a rotating frame, which is of common usage for propeller simulations.

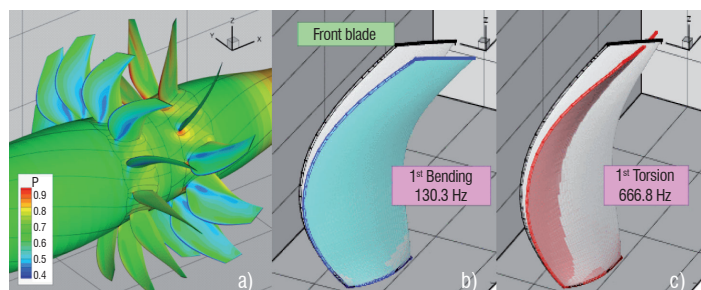


Figure 16 - (a) CROR static pressure at TO (b) 1<sup>st</sup> bending mode - (c) 1<sup>st</sup> torsion mode.

Aerodynamic damping values have been extracted for both operating points and for the three first modes of the front blade, showing a stable behavior of the propeller. Additional studies have also been conducted, to analyze the forced response of the rear propeller due to wake passing of the first propeller blades, and the static deformation of the propeller due to aerodynamic loads.

### Dynamic coupling in the time-domain

The possibility of predicting flutter at transonic speeds, through direct Navier-Stokes coupled simulations in the time domain, has been validated in the case of a wing/body model experimentally studied in the Onera Modane S2 wind tunnel [14]. Dynamic coupled simulations have been run for different stagnation pressures, using the 6

first structural modes. As shown in figure 17, a good correlation with the experimental results is observed in the frequencies and the damping coefficients, which are computed from the dynamic responses.

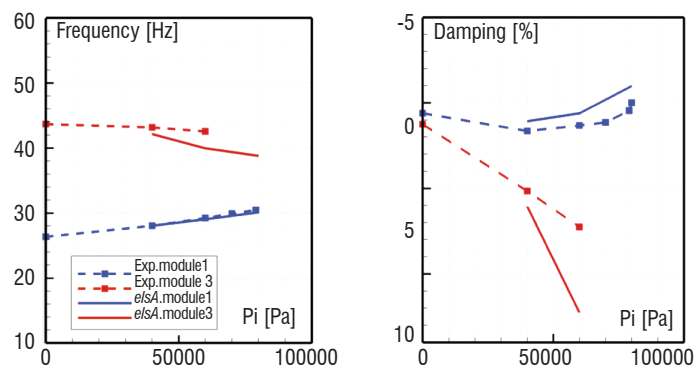


Figure 17 - Flutter diagram for  $M_\infty=0.84$ ,  $\alpha=0^\circ$ .

The appearance of limit-cycle oscillations (LCO) is another important aeroelastic phenomenon, which may only occur when non-linear effects are present in the fluid-structure system. Even if the LCO behavior does not directly lead to a catastrophic failure, such as for example the flutter phenomenon, it may considerably reduce the fatigue life of the structure.

The capability to predict the appearance of aerodynamically induced LCO has been investigated in the case of the NLR7301 airfoil equipped with a 2-dof structural system allowing heave and pitch motions [15]. The predicted time evolution of the pitch angle (figure 18) exhibits the characteristic limited amplitude phenomenon experimentally observed by DLR in the case of this airfoil.

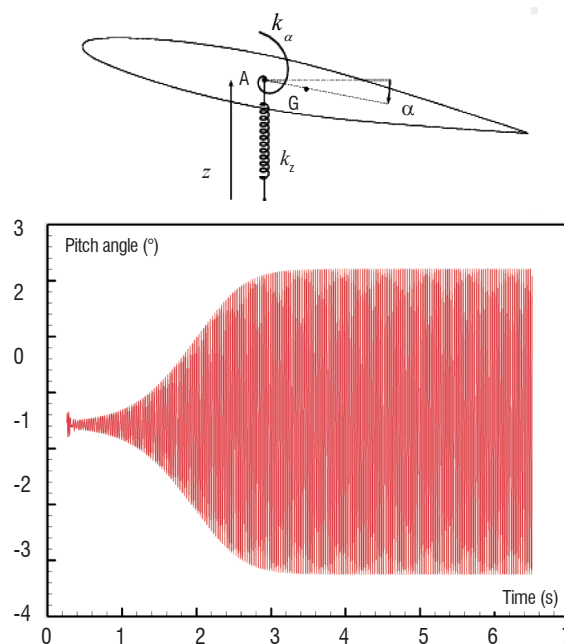


Figure 18 - Experimental set-up studied at DLR, and numerical simulation of the LCO phenomenon.

### Gust response in time-domain

The design of aircraft requires the nonlinear response to a gust field to be taken into account. The dynamic loads that are induced by a gust may moreover be significantly increased by the highly flexible

structures of modern aircraft. The prediction of the gust loads on the structure of an aircraft thus becomes increasingly important during the development and certification phases of a project. *e/sA* has been recently extended, in order to take into account an analytical perturbation velocity field, which may be used to model a gust. The developments allow direct aerodynamic and aeroelastic gust response simulations to be performed in the time-domain.

Figure 19 compares the dynamic gust response predicted at transonic flight conditions, without/with taking into account the wing flexibility. In this case, the frequency of the “1-cosine” gust is very close to the frequency of the first torsion mode of the wing. This explains the much higher unsteady loads observed in the dynamic coupled simulation.

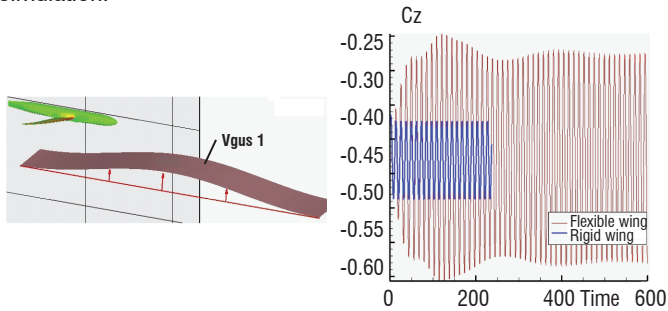


Figure 19 - Comparison between the aerodynamic and aeroelastic gust response, in the case of a wing/body configuration.

## Underlying software architecture

The multi-physics simulations presented in the previous sections are performed on complex software systems. The following section focuses on this software and specifically on the code interfaces (that is, the set of functions used to interact with other software).

Nowadays, a complex simulation is performed through the use of several codes running on distributed heterogeneous computers, rather than running a single monolithic code. This situation leads to a large set of interfaces. In this section, it is shown that a common interface definition helps to reduce the entire software life cycle (development, integration, use and maintenance effort).

### The need for a common interface

The codes involved in a multi-physics simulation can be one of four types: legacy code (i.e., code no longer developed but still used and maintained), COTS (Commercial Off the Shelf), Open Source and in-house codes. All these codes have communication capabilities to a greater or lesser extent, which is a key issue for multi-physics simulations.

Each code provides its own interface, which is a means to interact with the user or with another application and is usually based on the use of files and/or functions. An interface formally defines how to control, send and receive data.

On the one hand, some codes have their own opaque and proprietary file format. In this case, the data exchange is only possible using specific

proprietary tools. There are even monolithic codes with no interaction capabilities, which is indeed an issue for multi-physics simulation purposes. On the other hand, some codes supply a public and documented format, so that any other tool can be used to read/write the file or to connect to the network. Such programs generally provide a large set of functions, available through an Application Programming Interface (API).

Since each program defines its own interface, a straightforward approach leads to a connection graph, such as that in figure 20. Each connected code requires a dedicated interface to each other peer-code. In the worst case, such a graph is complete and should be avoided. Figure 21 shows a connection graph with a common interface, the so-called software bus, with a minimal connection graph.

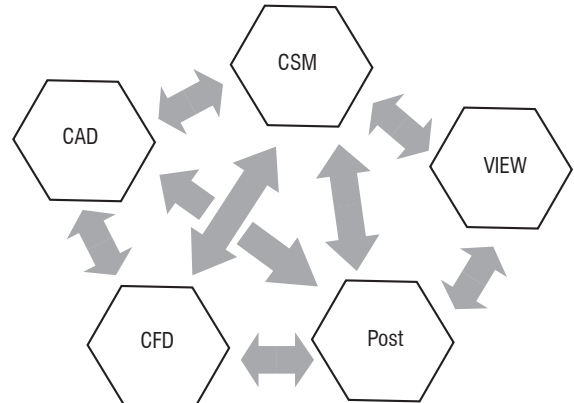


Figure 20 - One-to-one interfaces.

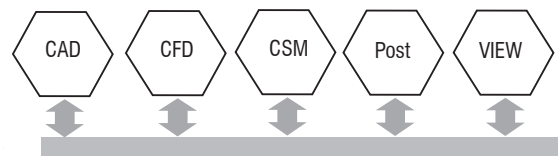


Figure 21 – Software bus.

NSCOPE (Numerical Simulation Components in an Open Python Environment), adopted by some Onera software (e.g., *e/sA*, see previous section) provides a public and non-proprietary interface. The *e/sA* solver, like most Onera tools, is not Open Source, but can easily be connected to Open Source software: an interface can be open while its implementation is not.

NSCOPE specifies the three elements of an interface: the control and communication are performed by Python, the data is handled by both CGNS [19] for the logical representation and HDF5 (see the hdf group website) for the physical representation. These CGNS/Python and CGNS/HDF5 technologies are Open Source, public and allow any application to connect to NSCOPE-compliant tools. NSCOPE is neither a library, nor a proprietary specification, it is a set of technologies recommended to increase interoperability.

### Integration strategies

The integration is the assembly of several codes in order to achieve a multi-physics simulation. This could be performed in a specific separate controller, or directly in the application. As mentioned in the Vulcan 2 case described above, each application is a specific case and requires a specific algorithm, which impacts control, data exchange and even data representation.

Three examples are now given that show how the Open Python approach helps to achieve an easy, low cost and maintainable integration of a multi-physics application. Each example focuses on a single element of the interface, namely the data model, communication and control.

**Example: data transformation**

The use of CGNS/Python as a common data model and data structure was demonstrated within the framework of the CHANCE project with Eurocopter [17]: fluid/structure code-coupling was developed for a helicopter rotor application.

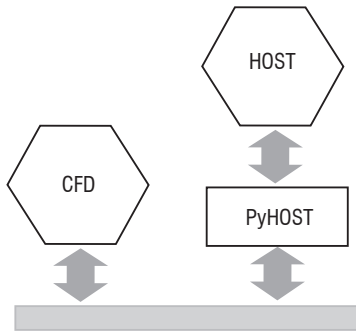


Figure 22 - The pyHOST adapter.

The coupling involved flight mechanics, with the structure via the HOST software (in-house Fortran Eurocopter code, with few interoperability features). First, data had to be transformed between HOST and *e/sA*. An adapter was developed to provide HOST with an NSCOPE interface (CGNS/Python). The main difficulty was to couple *e/sA*, which computes the full rotor in parallel whereas HOST only manages a single blade model. Moreover these two codes operate on different time scales.

The pyHOST interface (see figure 22) was restricted to the needs of the simulation, but the definition and implementation follow the NSCOPE recommendations. No change was necessary in *e/sA*, because it was already NSCOPE compliant.

**Example: communication**

The communication layer sends and receives data from/to the codes. Some simulation frameworks provide their own communication layer and the coupling application must use it.

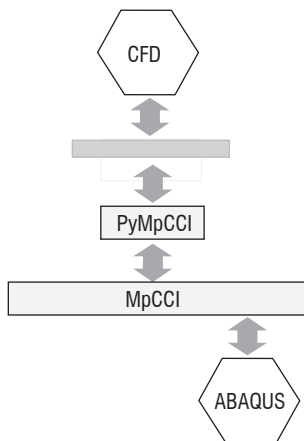


Figure 23 - Communication vs open communication layer.

In a specific project in cooperation with SNECMA, the use of the MpCCI library was mandatory. Thus, an NSCOPE compliant interface was developed on top of MpCCI API. This interface provides the user with a full CGNS/Python interface and a communication layer built using a Python network library.

**Example: process control**

The Python programming language was used to develop the steering and control application in a PhD thesis [18] conducted in connection with the Eurocopter SHANEL project. This project included a fluid/structure code-coupling application for a helicopter rotor. One of the goals was to add an external CSM/CSD commercial software (MSC.MARC) into a workflow already using *e/sA* and HOST.

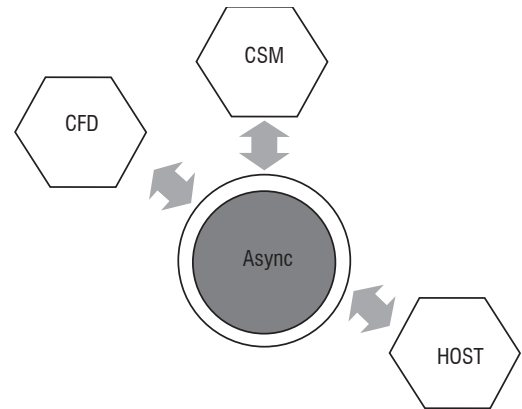


Figure 24 - Asynchronous Python server.

The simulation had to run on a heterogeneous network, due to user MSC.MARC license issues. A classical workstation was involved, as well as a supercomputer handling batch queues. The application had to synchronize all codes across the network, using an asynchronous server, which was in charge of storing data as it came from the different codes. With the use of the XMLRPC library of Python, this server had no more than 10 lines. The actual PhD could then focus on the global algorithm of the simulation, not the software middleware. SHANEL also led to the specification of a CGNS fluid/structure code-coupling interface.

## Box 6 - Python

Python is a programming language, born in the Netherlands in 1994. Its father, Guido van Rossum, has designed a nice and extensible language for network testing purposes. The language rapidly became very used in two communities having good programming skills: the Internet and numerical simulation. The language is object oriented, interpreted and can be extended by providing a Python interface to existing C or Fortran libraries. The syntax is clear and easy to learn, the language types are usual scalar types such as integers, real numbers and strings and also container types such as lists or dictionaries.

```
A=4
B=2.34*4
C=[ A, B, ['This', 'is', 'an heterogeneous list'], [0.03, 0.2e-12]]
```

Its object oriented features makes it possible (1) to create one's own application types and (2) to support good software structure for one's codes.

Python has a large number of embedded libraries, the standard installation provides the users with all of the services related to the operating system, the network, the graphical user interfaces, etc. These libraries are called modules, and the modules can be packaged, in order to be shipped to an application or another user, and then imported before use.

```
import math
def circ(R):
    C=2*math.PI*R
    return R
print R(5.28)
```

In the domain of numerical simulation, the best library comes from the so-called 'SciPy' package. This includes in particular the numpy library. This very efficient library offers many classes, functions and extensions to manipulate arrays. An array can be mapped to a C or Fortran array, so that Python/numpy can be used as a nice interface for numerical simulation functions in C, C++ or Fortran. This library is clever enough to allow almost all kinds of mapping to numerical functions and the cells in your actual Fortran array can be read/written even.

```
import numpy
a=numpy.array( [[1,2,3],[4,5,6]], dtype=numpy.float64, order='Fortran')
a[0][1]=7
```

A module creation can be a simple file in the Python language declaring and implementing constants and functions. It can be more complex, if it is extended with a Fortran function. In this case, it is necessary to draw a box around the Fortran or C code. This box is a C code and uses the Python C/API functions. It translates the Fortran data to and from Python. Extending Python in such a way is something common: there are many code generators, such as SWIG or F2PY, that take a Fortran or C code and automatically generate the Python interface.

Python is said to be a 'steering language'. It is used to encapsulate existing codes and gather them into a single large program, and it ensures network communication between existing codes, for code-coupling for example, or allows the user to quickly write a nice graphical interface for his application. Moreover, the very good portability of Python makes it run on all known platforms and, as a matter of fact, there is now almost no standard platform without Python installed as default.

Python is a very convenient interface and may be chosen as the top level language for many application programs.

## Conclusions

Many aeronautical problems are basically multiphysics problems, in which the behavior of a system depends on the interaction between several distinct disciplines. In the past, these coupling effects were often ignored, or crudely taken into account, due to lack of computational capabilities. Today, with the increase in computer power, multiphysics numerical simulations are being used increasingly more in order to obtain accurate solutions, needed for the optimization and performance improvement of aeronautical components.

This paper has presented two different approaches developed at Onera to solve such multi-physics problems via a partitioned strategy. In the first one, separate and independent simulation tools are coupled via a coupling library. The main advantage of this approach is to benefit, for each software, from the experience developed by a large number of specialists over many years. In the second approach, mono-disciplinary software is extended to multi-physics modeling by adding new simplified modules for other disciplines and by the implementation of specific coupling algorithms. The advantage of this approach is to provide a simple and efficient computational environment for the simulation of steady and unsteady coupled processes.

However, in both cases, coupling may be challenging, due to great disparities between the fluid and the solid physical models. In particular for dynamic problems, the main numerical difficulty arises from the significant discrepancy between time scales of both media. The studies presented in this paper suggest that partitioned strategies increase the accuracy and details of numerical results, due to the complementary information from the fluid and the solid domains only if specific well designed mathematical models are used.

In the last part of this paper, an Open System approach has been presented. It is based on a powerful open source assembly of public interfaces developed at Onera for software coupling strategies.

### Acknowledgements

The authors would like to thank the French governmental DPAC and DGA agencies and the European Commission for funding the research studies presented. Several researchers must be acknowledged for their work and their contributions to this paper: C. Liauzun for the Gust response simulations and F. Sicot for the Time Spectral Method topic. Finally, we wish to thank the Z-set software development community in general, and more particularly A. Roos and F. Feyel, for their help in setting up these simulations.

### References

- [1] O.C. ZIENKIEWICZ - *Coupled Problems and their Numerical Solution*. Numerical Methods in Coupled Systems. Edited by R.W. Lewis, P. Bettess, and E. Hinton, John Wiley and Sons Ltd, 1984.
- [2] M. ERRERA, B. BAQUE and M. REBAY - *A Numerical and Experimental Study of Transient Conjugate Heat Transfer in a Flat Plate*. International Symposium on Convective Heat & Mass Transfer in Sustainable Energy, April 26- May 1, 2009, Hammamet, Tunisia.
- [3] A. REFLOCH, B. COURBET, A. MURRONE, P. VILLEDIEU, C. LAURENT, P. GILBANK, J. TROYES, L. TESSÉ, G. CHAINERAY, J.B. DARGAUD, E. QUÉMERAIS and F. VUILLOT - *CEDRE Software*. Aerospace Lab Issue 2 March 2011.
- [4] D. SCHERRER, F. CHEDEVERGNE, P. GRECARD, J. TROYES, A. MURRONE, E. MONTREUIL, F. VUILLOT, N. LUPOGLAZOFF, M. HUET, B. SAINTE-ROSE, P. THORIGNY, N. BERTIER, J.M. LAMET, T. LE PICHON, E. RADENAC, A. NICOLE, L. MATUSZEWSKI and M. ERRERA - *Recent CEDRE Applications*. Aerospace Lab Issue 2 March 2011.
- [5] K. WOLF - *A General Coupling Library for Multidisciplinary Simulation*. Workshop on Scalable Software Multiscale Coupling and Computational Earth Science. SSS 2001 December 3-5, The University of Tokyo, Japan.
- [6] S. PIPERNO, C. FARHAT, and B. LARROUTUROU - *Partitioned Procedures for the Transient Solution of Coupled Aeroelastic Problems Part i: Model Problem, Theory and Two-Dimensional Application*. Computer Methods in Applied Mechanics and Engineering, 124:79-112, 1995.
- [7] J. GIORDANO & al. *Shock Wave Impacts on Deforming Panel, an Application Of Fluid-Structure Interaction*. Shock Waves, 14:103-110, 2005.
- [8] A. ROOS and J.L. CHABOCHE - *Vulcain II Cooling Tubes. Final report*. Tech. rep. RT 2/08500, Onera 2005.
- [9] J. BESSON, G. CAILLETAUD, J.L. CHABOCHE, S. FOREST and M. BLÉTRY – *Non-linear mechanics of materials*, Springer 2010.
- [10] F.X. ROUX and J.D. GARAUD – *Domain Decomposition methodology with Robin interface matching conditions for solving strongly coupled fluid-structure problems*. International Journal for Multiscale Computational Engineering, 2009.
- [11] G. DUFOR, F. SICOT, G. PUIGT, and C. LIAUZUN - *Contrasting the Harmonic Balance and Linearized Methods for Oscillating-Flap Simulations*. AIAA Journal No 4 Volume 48, April 2010.
- [12] A. DUGEAI – *Aeroelastic Developments in the elsA Code and Unsteady RANS Applications*. International Forum on Aeroelasticity and Structural Dynamics, 28 June-1 July 2005, Munich, Germany.
- [13] P. GIRODROUX-LAVIGNE – *Fluid-Structure Coupling Using Chimera Grids*. International Forum on Aeroelasticity and Structural Dynamics, 21-25 June 2009, Seattle, USA.
- [14] P. GIRODROUX-LAVIGNE - *Recent Navier-Stokes Aeroelastic Simulations Using the elsA Code for Aircraft Applications*. International Forum on Aeroelasticity and Structural Dynamics, 18-20 June 2007, Stockholm, Sweden.
- [15] P. GIRODROUX-LAVIGNE - *Prediction of Limit Cycle Oscillations Induced by Aerodynamic non-Linearities*. NATO RTO Symposium AVT-152 on Limit-Cycle Oscillations and other Amplitude-Limited. Self-Excited Vibrations, 5-8 May 2008, Loen, Norway.
- [16] A. DUGEAI - *Turbomachinery Aeroelastic Developments and Validations Using Onera elsA Solver*. International Forum on Aeroelasticity and Structural Dynamics, 18-20 June 2007, Stockholm, Sweden.
- [17] M. COSTES, M. POINOT, and B. CANTALOUPE - *CHANCE Program: Strong Coupling Between elsA and HOST*. RT 1/07782 DAAP SPAe, Onera, 2005.
- [18] B. ORTUN - *CSM/CFD Coupling for the Dynamic Analysis of Helicopter Rotors*. PhD Thesis dec.2008, Onera.
- [19] M. POINOT - *SHANEL Project Phase 1 - Synthesis Report RTS1 - Task A4b : Pre/Post Processing and Simulation Environment CSM Extensions of the CGNS Standard*. RT 8/11826 DAAP DGA/DET/CEP, Onera, 2008.

It must be noted that work is currently underway to develop new coupling libraries able to exchange the information between solvers and to automate the search, interpolation and communication processes over a large number of processors in a distributed environment. The existence of such a tool will allow us to concentrate on numerical and mathematical models in fluid-structure interactions. In particular, this approach will also allow aeroelastic modeling to be improved, by taking into account both fluid and structural non-linearities ■

## Acronyms

CFD (Computational Fluid Dynamics)  
CSD (Computational Structural Dynamics)  
RANS (Reynolds Averaged Navier-Stokes)  
URANS (Unsteady Reynolds Averaged Navier-Stokes)  
HOST (Helicopter Overall Simulation Tool)  
RBF (Radial Basis Functions)  
LUSSOR (Lower Upper Symmetric Successive Over Relation method)  
ALE (Arbitrary Lagrangian Eulerian)  
FSI (Fluid-Structure Interaction)  
CHT (Conjugate Heat Transfer)

COTS (Commercial Off The Shelf)  
MpCCI (Mesh-based parallel Code Coupling Interface)  
SPRM (Solid Propellant Rockets Motors)  
IUSTI (Institut Universitaire des Systèmes Thermiques Industriels)  
TSM (Time Spectral Method)  
ETW (European Transonic Windtunnel)  
CROR (Counter-Rotating Open Rotor)  
LCO (Limit-Cycle Oscillations)  
NSCOPE (Numerical Simulation Components in an Open Python Environment)  
CGNS (CFD General Notation System)  
CPU (Central Processing Unit)

## Web sites

<http://www.python.org>  
<http://www.hdfgroup.org>  
<http://www.cgns.org>  
<http://numpy.scipy.org>  
<http://www.zset-software.com>  
<http://elsa.Onera.fr>  
<http://cedre.Onera.fr>

## AUTHORS



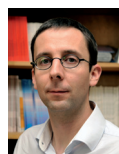
**Marc Errera**, graduated from the "Ecole Centrale de Paris" in 1980 and obtained a Research Habilitation Thesis (Thèse d'Etat) from the University Pierre & Marie Curie (Paris 6) in 1990, in the field of in-cylinder flow in reciprocating engines. He is currently in charge of multidisciplinary projects.



**Alain Dugeai**, an Engineer of "Ecole Centrale de Paris", has been working at Onera since 1988, in the "Aeroelastics and Structural Dynamics" department. He is currently in charge of numerical aerolasticity developments for turbomachines.



**Philippe Girodroux-Lavigne**, an Engineer of "Ecole Centrale de Lyon", has been working at Onera since 1979, first in the "CFD and Aeroacoustics" department, then in the "Aeroelastics and Structural Dynamics" department, where he is involved in aircraft numerical aeroelasticity studies.



**Jean-Didier Garaud** received his PhD in 2008 from the University Pierre & Marie Curie (Paris 6) and Onera, on the topic of numerical analysis and computational mechanics. He is now an engineer in the Department of Metallic Materials and Structure, in charge of Z-set's multiphysics capabilities.



**Marc Poinot** is a software engineer at Onera. He obtained a Masters Degree in Computer Science from Paris XI Orsay, France. He is working in the CFD team, where he is in charge of interoperability topics for code coupling and numerical simulation platforms. He is member of the CGNS steering committee and he initiated and actively participated in the migration of CGNS to HDF5 and Python.



**Stéphane Cerqueira** followed a double degree - French Engineer (Supmecca - Paris)/Master in Aerospace (Laval University/Ecole Polytechnique de Montréal/Mc Gill University - Canada). His PhD is focused on Fluid-Structure Interaction inside Ariane V's Solid Propellant Rocket Motors and was supported by CNES/Onera.



**Gilles Chaineray** received his PhD in energetics and heat transfer, in 1995. The PhD research activities were focused on study of rotating flow and heat transfer, and the development of Anisotropic Stress Model. He is now in charge of the development of thermal and mechanical coupling of the CEDRE code with other codes such as Z-set, ABAQUS, MARC, Code\_Saturne.

L. Cambier, M. Gazaix, S. Heib,  
S. Plot, M. Poinot, J.-P. Veillot  
(Onera)  
J.-F. Boussuge, M. Montagnac  
(Cerfacs)

E-mail: laurent.cambier@onera.fr

# An Overview of the Multi-Purpose *e/sA* Flow Solver

Development of the *e/sA* software for complex external and internal flow aerodynamics and multidisciplinary applications started in 1997 at Onera. Due to the multi-purpose nature of *e/sA*, many common basic CFD features can be shared by a wide range of aerospace applications: aircraft, helicopters, turbomachinery, missiles, launchers... The *e/sA* software is based on an Object-Oriented design method and on an Object-Oriented implementation based on three programming languages: C++, Fortran and Python. The *e/sA* strategy for interoperability is based on a component approach that relies on standard interfaces for the CFD simulation components. This paper presents an overview of the capabilities of the *e/sA* software in terms of modeling, mesh topology, numerics and boundary conditions, whereas a more detailed description of these capabilities is given in companion papers of this issue of the electronic journal. The importance of High Performance Computing activities is outlined in the present paper.

## Introduction

Unlike other industries, such as the automobile industry, the simulation software used for aerodynamic analysis and design in the aeronautic industry is not usually provided by commercial software vendors, but is generally developed either by Research Establishments or sometimes by the aeronautic industry itself. The overview of software tools used for flow simulation in the European aeronautic industry, presented in [26], shows that in Europe they are mostly managed by Research Establishments. One major reason for this is that the high levels of accuracy and reliability required today for improving aeronautic design are obtained through long term expertise and innovative research in various areas: physical modeling, numerical methods, software efficiency on rapidly evolving hardware and validation by comparison with detailed experimental data.

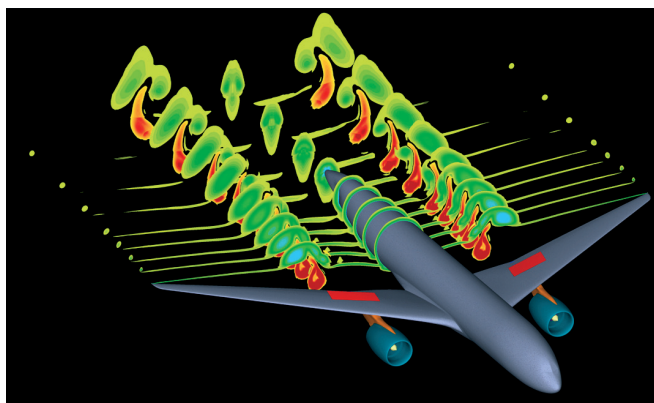
The *e/sA* software (<http://elsa.onera.fr>) for complex external and internal flow aerodynamics and multidisciplinary applications has been developed at Onera since 1997 [4], [6]. The main objective is to offer the French and European aerospace community a tool that capitalizes on the innovative results of Computational Fluid Dynamics (CFD) research over time and is able to deal with miscellaneous industrial applications. The range of aerospace applications dealt with using *e/sA* (aircraft, helicopters, tilt-rotors, turbomachinery, counter-rotating open rotors, missiles, launchers, etc.) is very wide, as shown in figure 1 presenting a few examples of *e/sA* results. A

large variety of the advanced aerodynamic applications handled by *e/sA* is presented in [25]. Note that it is quite uncommon for a CFD tool to deal both with external flows around airframes and with internal flows in turbomachinery; since it allows common basic CFD features to be shared, we clearly consider that it is an advantage. The research, development and validation activities are carried out using a project approach in cooperation with the aircraft industry and external laboratories or universities (see Box 1). This project approach has been the result, at Onera as elsewhere, of the change in CFD software development from a one-code, one-developer paradigm at the beginning of the eighties to a team-based approach necessary to cope with the complexity of today's CFD. The effort carried out in France and coordinated by Onera with *e/sA* was also initiated approximately at the same time as projects in other countries, such as the WIND-US flow solver of the NPARC Alliance [3] or the FAAST program at NASA Langley RC [19] in the United States or the TAU flow solver in Germany [14].

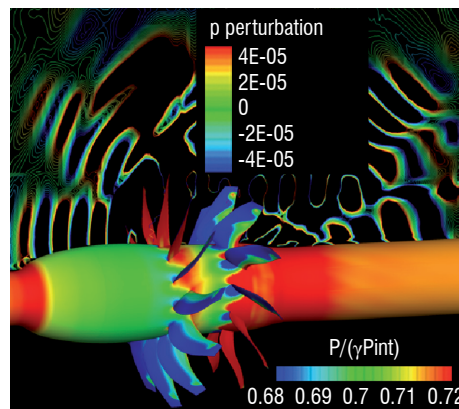
This paper gives a general presentation of the *e/sA* solver, and mainly focuses on software topics such as Object-Oriented design and implementation, software interoperability or High Performance Computing. Only a general overview of the capabilities of the *e/sA* software in terms of modeling, mesh topology, numerics, aeroelasticity and optimum design is presented here, whereas a more detailed description of these capabilities and results, showing evidence of their functionality and correctness, is given in companion papers of

this issue of the electronic journal ([1] for transition and turbulence modeling, [8] for space discretization methods on various mesh topologies, [21] for time integration methods, [10] for aeroelasticity,

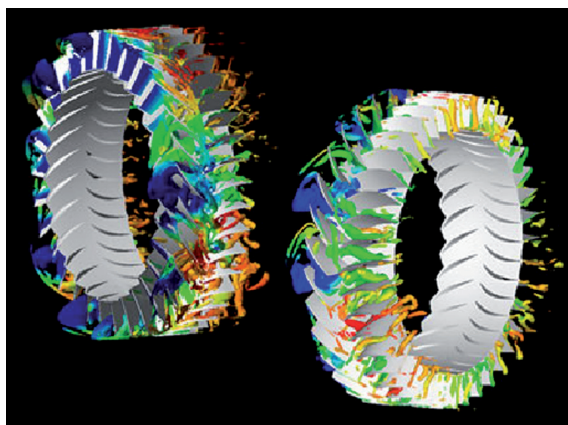
[22] for optimum design). Also, the reader should refer to another companion paper [25] for a detailed presentation of the application results of *e/sA*, which only appear in this paper as illustrations.



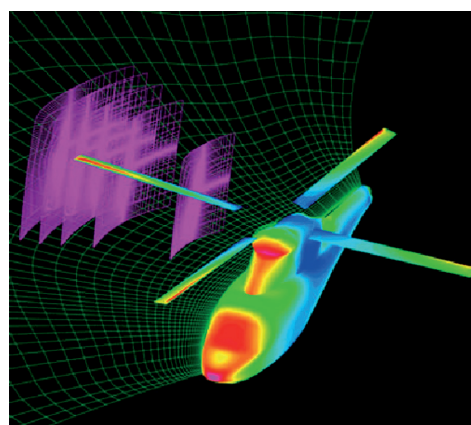
a) Transport aircraft configuration: simulation of the flow around an aircraft with deployed spoilers



c) CROR configuration: simulation of the flow around a CROR for an aeroacoustics study



b) Turbomachinery configuration: simulation of the rotating stall in an axial compressor stage



d) Helicopter configuration: simulation of the interaction between the main rotor and the fuselage

Figure 1 – Examples of applications carried out with *e/sA*

## Box 1 - Internal and external developers and users

Many partners, not only inside Onera but also in external laboratories and universities and in the aerospace industry, contribute to the development of new capabilities and to the validation of *e/sA*. Inside Onera, the CFD and Aeroacoustics Department of Onera coordinates the *e/sA* software project and contributes to the development in terms of software architecture, numerical methods or CPU efficiency. Several other Departments take part in development and validation activities related to *e/sA* software: namely the Applied Aerodynamics Department for thorough validation and some specific applied aerodynamics developments, the Aerodynamics and Energetics Modeling Department for transition and turbulence modeling and fundamental validation, and the Aeroelasticity and Structural Dynamics Department for fluid/structure capability development and validation.

Since 2001, there has been a partnership with the Cerfacs research organization for *e/sA* development, and Cerfacs has taken part in many developments, dealing, in particular, with mesh strategies, numerical methods and CPU efficiency, since that time. Other labs also take part in the development and validation of *e/sA*, such as the Fluid Mechanics and Acoustics Lab of “École Centrale de Lyon” for development of complex turbomachinery boundary conditions, the applied research center Cenaero (Belgium) for turbomachinery flow simulation and the DynFluid lab of “Arts et Métiers ParisTech” for high accuracy numerical schemes. The use of *e/sA* in French engineering schools or universities is also developing for academic teaching purposes.

*e/sA* is today intensively used as a reliable design tool in the French and European aeronautic industry. In turbomachinery industry, *e/sA* is used in the design teams of Safran group (Sneema and Turbomeca in France, Techspace Aero in Belgium). For transport aircraft configurations, *e/sA* is one of the two CFD programs used at Airbus for performance prediction and for design (the other one is the TAU software from DLR, see [5]). Among other industry partners, we should mention Eurocopter for helicopter applications and MBDA for missile configurations.

## Why a multi-purpose tool for solving the Navier-Stokes equations?

CFD methods and software have improved tremendously over the last forty years. Whereas in the 1970s, CFD software for design was mostly based on formulations assuming the flow to be inviscid, today CFD codes solving the Navier-Stokes equations (see Box 2) have become standard tools in the aeronautic industry [27]. The improvements concern various areas: mesh topology capabilities, physical modeling, numerical algorithms. However, in each of these areas, there is no universal method answering all of the problems. The best choice of methods depends on the type of application and on the levels of accuracy, robustness and efficiency that are required. In the case of mesh topology capabilities, the relative advantages and disadvantages of Cartesian structured grids, curvilinear structured grids and unstructured grids are well-known today and in recent years it has become clearer that an association of various types of grids in a single simulation is very powerful.

It is also well-known that transition and turbulence modeling which is required for the simulation of turbulent flows has to be adapted to the type of application and even to local flow phenomena. For example, a classical eddy viscosity model should give good results at low cost for the flow simulation around an airfoil at low angle of attack, whereas Large Eddy Simulation would be required for the simulation of the flow for near stall conditions. The selection of the best numerical algorithm strongly depends on the flow regime (subsonic, transonic or supersonic flow) and on the compromise which is required between accuracy, efficiency and robustness.

One solution could be to build dedicated software focusing on a narrow application domain. But this solution leads to a proliferation of specific software tools, which is very difficult to maintain, document, optimize and port to different computers. In fact, real-world applications today require a large range of capabilities. And if the best choice of methods depends on the type of application, it is also true that one specific method may be useful for various types of applications (see below in the section “Mesh topology capabilities” one example of this with the Chimera method). Also, the scientific community is looking for

larger and more complex simulations, and it has become increasingly necessary to involve and combine several models and/or several meshing strategies in the same flow simulation.

So, CFD software designers are faced with the challenge of meeting a very wide range of requirements, while keeping software complexity and development cost under control. Thus, a very broad range of CFD capabilities has to be grouped together in an interoperable and evolving software package. To cope with these broad requirements, the designers of the *e/sA* software chose to rely on an Object-Oriented design method as will be described below and *e/sA* was one of the first Object-Oriented major scientific packages written in C++ [13].

This choice was quite successful since there has been an intensive development of *e/sA* throughout the years. Today, *e/sA* is being developed towards a component architecture (see the section dealing with interoperability) to cope with ever increasing requirements: smart integration in the simulation environments of the aeronautic industry, runtime control of the simulation, coupling with external software for multi-disciplinary applications, etc. Coupling independent components through a common high-level infrastructure provides a natural way to reduce the complexity.

## Object-Oriented design and implementation

The *e/sA* software is based on an Object-Oriented (OO) design method. The central concept of OO design is the class: a class encapsulates data and methods. The class interface is a way of communicating with class users. The most important difference between procedural and OO programming is the switch from function to class as the fundamental abstraction. OO programming is interesting because it makes it easier to think about programs as collections of abstractions and to hide the details of how these abstractions work to users who do not care about these details. OO programming can be used to partition problems into well-separated parts, none of which needs to know more about the others than absolutely necessary. This ability to break a large, developing program down into parts that can be pursued independently, thus enhancing collaboration among multiple contributors, explains why integration of new developments is easier in an OO software.

### Box 2 - Mathematical model of *e/sA*: the Navier-Stokes equations

Navier-Stokes equations are the main mathematical model of aerodynamics in the continuous regime, for which the characteristic length scales are large compared with the mean free path of the molecules. These equations result from the application of the principles of mechanics and thermodynamics, and, in integral form, express an equilibrium between a volume term expressing the time variation of mass, momentum (mass times velocity) and total energy (sum of internal energy and kinetic energy) contained in a volume  $\Omega$ , and a surface flux term corresponding to the exchanges between the fluid inside  $\Omega$  and the fluid outside  $\Omega$ .

The Navier-Stokes equations are completed, on the one hand, by behavior laws representing the irreversibility effects associated with viscosity and thermal conductivity, and, on the other hand, by state laws describing the thermodynamic properties of the fluid.

As a result of the low viscosity of air, flows in aeronautics applications are turbulent. Turbulence is included in the Navier-Stokes equations which represent all the turbulence scales. However, Direct Numerical Simulation which relies on solving the instantaneous Navier-Stokes equations is still very far from being applicable to real world applications. Therefore, a statistical approach has to be added to the Navier-Stokes equation, which leads to Reynolds Averaged Navier-Stokes or to Large Eddy Simulation (see [1] for further details).

One important objective of *e/sA* is to reap the benefits of the OO approach without impairing numerical efficiency. Since nearly all CPU time of CFD calculations is spent in computing loops acting over quantities such as cells, nodes or interfaces, the OO design of *e/sA* does not deal with objects such as individual cells or fluxes, since loops operating on them would suffer a high penalty. Conversely, outside of loops, it has been shown with *e/sA* design that OO concepts may be introduced without any significant CPU penalty.

The last version of *e/sA* delivered includes about 600 classes grouped in 26 modules specialized for a given CFD task. The OO model based on CFD experience has been defined using the classical UML (“Unified Modeling Language”) method. Ideally, developers should be able to work inside a module, without having to know the implementation details of the other modules. Achieving a good breakdown is very important for achieving ease co-operative of development and maintenance. A UML modeling tool was used to define the initial design of *e/sA*, but without relying on the automatic code generation capability. The use of such a tool appeared to be too difficult for managing the cooperative development of *e/sA* and was given up.

Each module in *e/sA* is identified by a key of 3 to 5 letters. Inside each module, each class name is then prefixed by the key of the module to which it belongs. As an example, the `TurKL` class associated with the  $(k, l)$  turbulence model belongs to the `Tur` module which deals with turbulence modeling and transition prediction.

Some of turbulence models implemented in *e/sA* are built on the Boussinesq hypothesis. Their common feature is the use of the eddy viscosity which can be calculated either by an algebraic turbulence model, a subgrid-scale model or using transport equations. Each turbulence model is implemented through a specific class, which is derived from the abstract base class `TurBase`. All the classes deriving from the abstract class `TurBase` share its interface which declares the method `compMut()`. When manipulated in terms of the interface defined by `TurBase`, the concrete classes do not have to be known by the client classes. Client classes are only aware of the abstract class. In *e/sA*, the client classes of the `Tur` class hierarchy are the diffusive fluxes (see module `Fxd` below) that manipulate a pointer to an instance of a class derived from `TurBase` by means of:

```
tur -> compMut()
```

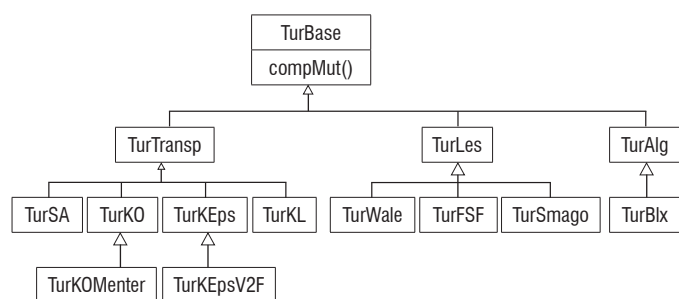


Figure 2 – UML model of the `Tur` module

The computation of the eddy viscosity depends on each particular turbulence model and cannot be performed in the `TurBase` abstract class. Polymorphism allows the correct version of `compMut()` to be called dynamically, without any explicit coding by the programmer. As a consequence, adding a new turbulence model will not modify the code of the client class. Figure 2 presents a simplified and reduced view of the UML class diagram of `Tur`.

*e/sA* design also follows the objective of organizing the modules into layers in such a way that each layer should mainly affect the layers above (see Figure 3). That means that classes in a layer are only allowed to use services of classes of lower layers (or of same layer); the goal of this organization is to achieve mono-directional relationships. The advantage is then that maintenance becomes easier since one layer’s interface only affects the next layers. We will now present the main modules of *e/sA*.

The lowest layer contains all of the low level modules, such as the `Fld` module (corresponding to the data storage classes which encapsulate the dynamic memory needed to store any computational data), the `Pcm` module (dealing with the implementation on parallel computer architectures, it encapsulates the message passing interface) or the `Sio` module dealing with IO (Input/Output).

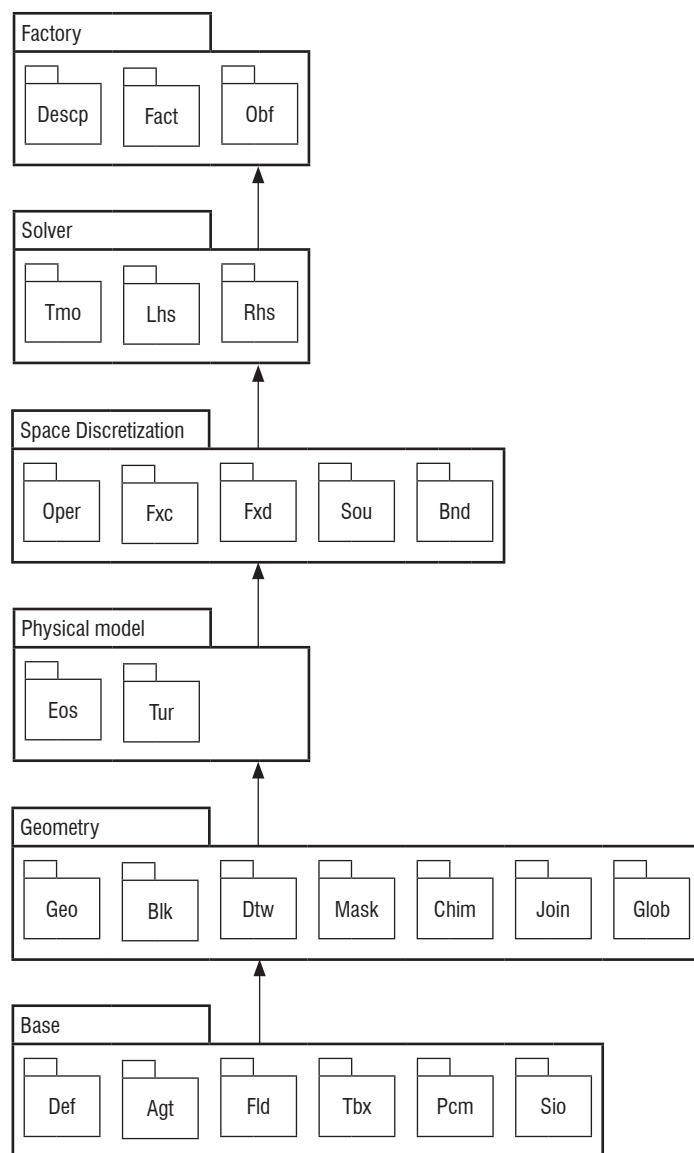


Figure 3 – *e/sA* design organization

Then, the geometry layer contains all of the modules which describe geometrical and topological elements:

- `Blk`: defines the “block” notion. A block corresponds to a region of the discretized physical space defined by a mesh. Blocks are specialized to take into account grid motion, Arbitrary Lagrangian-Eulerian (ALE) technique and Hierarchical Mesh Refinement (HMR) features;

### Box 3 - Joint development project

The *e/sA* project is a joint development project including organizations and individuals located at several geographic places. This cooperative development involving developers at different sites is greatly facilitated by the use of a simple and robust version control system: the Concurrent Version System (CVS), and soon the Subversion system (SVN). The version control system maintains a central “repository” which stores files and gathers them into coherent and named sets of revisions. The developers work in private workspaces and use the repository as a common basis for source exchange. Only one person, called the “integrator”, is allowed to “commit” the set of changes done by a developer back into the repository. Each new production of the software approximately includes 5 to 10 developments.

A delivered release of the software is a particular production, corresponding to a higher level in documentation and validation quality than a current production. Average time between two successive delivered releases of *e/sA* is 12 to 18 months, and generally about 5 intermediate productions are made.

Communication is obviously one of the key elements in a joint development project. A Web site (<http://elsa.onera.fr>) facilitates information transmission. This site, including restricted areas for external users and developers, gives, in particular, access to the documentation (User Reference Manual, User Starting Guide, Developer’s Guide, Validation report...), the validation scripts (around 170 test cases at the present time in the validation database) and the problem tracking database. A specific email address is available for software support.

- **Geo**: defines the abstraction of the computational grid and provides with all geometrical ingredients used by the finite volume formulation (metrics: volume of cells, surface of cell interfaces; topological relations between geometrical entities: cells, interfaces, nodes);
- **Dtw**: contains all of the distance and boundary-layer integral thickness computations;
- **Mask**: defines concepts, such as masks for blanking, defined in the Chimera technique;
- **Chim**: contains the grid assembly used within the Chimera technique;
- **Join**: deals with multi-block computations with various types of multi-block interface connectivity: 1-to-1 abutting, 1-to-n abutting or mismatched abutting.

The physical model layer includes the **Eos** module which computes quantities such as pressure, temperature (according to the equation of state of the gas) or laminar viscosity coefficient, and the **Tur** module already quoted above.

The space discretization layer gathers several important modules for the computation of the terms of the equations to solve and of the boundary conditions:

- **Oper**: defines the operator notion. Each operator class is responsible for the computation of a single term in CFD equations: convective flux (**Fxc**), diffusive flux (**Fxd**), source term (**Sou**);
- **Bnd**: contains the numerous classes devoted to the large variety of boundary conditions.

The solver layer contains:

- **Rhs**: builds the (explicit) right hand side of the equation system;
- **Lhs**: deals with all the implicit methods;
- **Tmo**: manages the main iterative time loop.

Finally, the top layer is the factory layer which is responsible of the dynamic creation of all objects (in OO methods, “objects” mean “instances of the class”) and in particular includes the **Fact** module which implements several object “factories” to build objects from user input data coming from the interface.

In *e/sA*, the choice of programming languages was done in order to allow both respect of the OO patterns of the design and of CPU constraints. The first objective led to the mandatory choice of a true OO programming language, and the C++ language was chosen, because it is the most widely used OO language, available on all usual platforms. Besides C++ as main language for implementing the OO design, it was decided to use Fortran for the two following reasons. First, the CPU tests we carried out at the beginning of the *e/sA* project showed better CPU performance of Fortran in comparison with C. Second, some Fortran lines of legacy code were re-implemented in the *e/sA* loops. However, due to a completely new design, it was in general not possible to keep the complete subroutines of the legacy code. These Fortran routines are very similar to private class methods: since they do not appear in the public class interface, they do not affect the OO design. A third programming language is used in *e/sA*: the Python language which is a freely available interpreted OO language and is used for programming the *e/sA* interface. Today, *e/sA* includes more than one million lines (600,000 in C++ , 420,000 in Fortran and 55,000 in Python).

### *e/sA* interoperability

The interoperability of a program or of a piece of software is its ability to interact with another program or piece of software. The *e/sA* software has evolved towards a software suite containing the *e/sA* kernel (mainly the CFD solver) and some additional tools (dealing in particular with pre-processing and post-processing). All the elements of the suite should be seen as boxes in a larger simulation process. Our target is the integration of these boxes into all the platforms of our customers. Each aerospace industrial company already has a large set of programs and most of the time they have in-house software systems to manage them in their own process. Then our goal is rather to be able to be integrated than to integrate. The strategy for the interoperability and the so-called “component approach” software architecture we have designed for it are tightly bound to this goal of all-platforms integration.

## The component approach

The *e/sA* component approach is based on the interface description. We use standard interfaces for the CFD simulation components. The CGNS standard (see box 4) is preferred for the data model and the Python programming language (see the box describing this language in [10]) defines the protocol, in other words the order you should respect to use the component functions. Each box in the simulation workflow, including the *e/sA* kernel, has to provide a Python interface supporting the CGNS data model: the CGNS/Python interface. When you integrate such a CGNS/Python component into a platform, the interface you use is not proprietary; it is based on Open System standards. A proprietary interface is a set of services which have a single implementation - the customer has no choice about the service provider - whilst an Open System interface should have more than one implementation. You can write Python scripts and just pass the CGNS data trees from one software tool to another in the memory of the process, or by means of a network if you have to, as long as they use the same public interface, no matter which implementation they use. This is the component interoperability which is the basis of Onera component approach.

### CGNS/Python and *e/sA*xdt

The CGNS/Python mapping of the CGNS/SIDS is used by an increasing number of Onera software components. Each tool has its own interface to CGNS/Python: the interface of the *e/sA* kernel is *e/sA*xdt. It parses CGNS/Python data trees and reads/writes *e/sA* data in the tree for the next step of the workflow. We call this tree a “shuttle tree”, just like a shuttle bus going from code to code and picking up or dropping data. During this process, we avoid the use of files, because a file access often leads to problems on large computation clusters, and because most intermediate trees are sometimes not archived and trashed as soon as they are used. These transient trees can be created, used and killed within the memory.

A CGNS/Python computation with *e/sA* uses quite simple commands, the read of the CGNS tree and the write of the resulting CGNS/Python tree:

```
import elsAxdtdt
parser=elsAxdtdt.XdtCGNS("001Disk.cgns")
parser.compute()
parser.save("Result.cgns")
```

In this simple example, all the required data is obviously embedded into the `001Disk.cgns` file: CGNS has been designed to be able to handle all the CFD data and even the specific solver parameters. Once the computation is performed, the output is obtained in `Result.cgns`, another CGNS tree.

Whereas in this first example we use files, the next example shows how a full memory transfer of CGNS/Python trees can be achieved:

```
import elsAxdtdt
from CGNS.MAP import *
(input_tree,links)=load("001Disk.cgns")
parser=elsAxdtdt.XdtPython(input_tree)
output_tree=parser.compute()
save("Result.cgns",output_tree,links)
```

The code lines are almost the same, but the architecture is quite different, because the *e/sA* interface only uses the CGNS/Python tree. The actual load and save on the disk is not performed by *e/sA*, it is performed by an Open Source module (`CGNS.MAP`) handling the CGNS/Python tree and HDF5 files.

We dissociate the *e/sA* computation from the means used for the actual data exchange. You can use the CGNS/Python tree in memory for exchanges with a network layer or a dedicated proprietary database. For example, if you run a large parallel computation with local generation of grids, the *e/sA* suite includes Python modules (Post, Converter, Generator) for this grid generation as CGNS/Python trees in memory. The solver runs on these grids, and produces one result per process. The merging of these trees is again performed in memory and the result is sent by means of a network to a remote post-processing workstation. Such a workflow limits the disk accesses on the high-performance computer and reduces the exchanges on the network to the data required for this particular application. This can be extended to the code coupling workflows [10].

### Concluding remarks on interoperability

The *e/sA*xdt interface is now used by some of our largest customers. These users are developing their own “integrated environment” with dedicated methods and tools. The common exchange backbone is based on CGNS. They can use the standard for file archiving as well as for component interoperability. The grid is generated as a CGNS tree by a commercial tool, then the proprietary process takes the tree and enriches it with *e/sA* specific parameters, the tree is submitted to the solver and the result is directly passed to a commercial visualization tool.

The next step is now to use the CGNS/Python interface in the solver itself. Such a re-design is not necessary or useful for every part of the solver. We have selected a limited set of interfaces where we can explode the solver into separate and re-usable components. Each component would provide the CGNS/Python interface and thus would increase the interoperability with a finer granularity. The next solver generation would extend its flexibility up to its inner software components and thus would be a future platform for better research and better integration into the customers' proprietary platforms.

## Box 4 - CGNS

The CGNS (CFD General Notation System) [24] provides a data model and a portable and extensible standard for exchanging and archiving of CFD analysis data. The main target is data associated with computed solutions of Navier-Stokes equations and their derivatives, but this can be applied to the field of computational physics in general.

CGNS started in the 1990s as a joint NASA, Boeing and McDonnell Douglas project. They developed the so-called SIDS (Standard Interface Data Structure) document that specifies the data model as a reference document. The first implementation was performed by ANSYS/ICEM teams on the top of the ADF (Advanced Data Format) proprietary low level storage system.

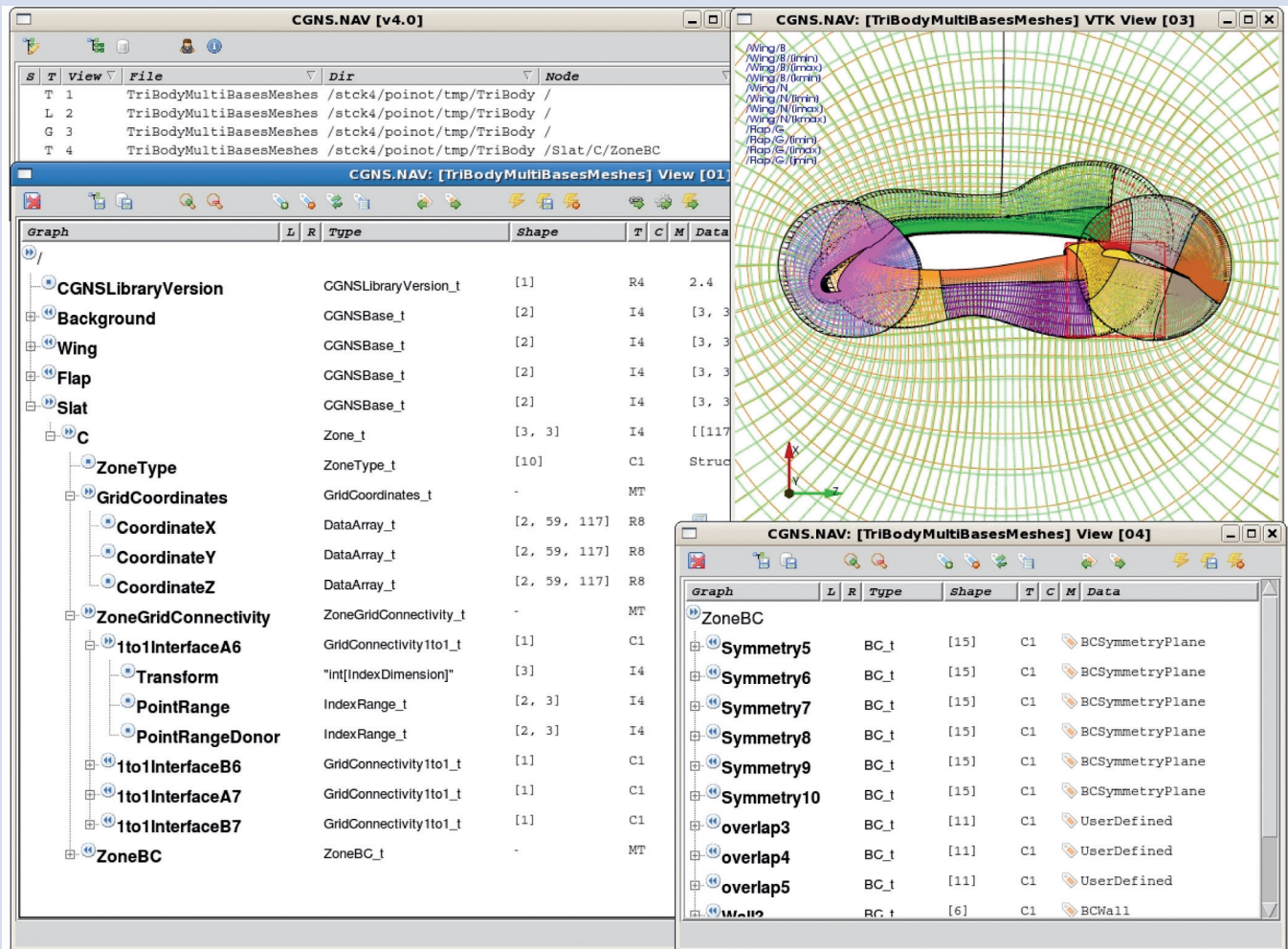


Figure B4-01 – Graphical view of a part of a CGNS tree using the Open Source CGNS.NAV tool

In 1999, the CGNS Steering Committee (CGNS/SC) was formed with academic organizations, aerospace industrial companies and software editors. Onera joined the CGNS/SC in 2001 and is an active member.

The standard is made up of a data model specification (CGNS/SIDS) which gives the name to the standard itself: Notation System. The main goal of the CGNS standard is to specify CFD data. The data can be used for exchange in a CFD workflow or as a storage conceptual model. Four CGNS implementations are available, the ADF, the HDF5 (Hierarchical Data File), the XML (eXtensible Markup Language) and finally the Python mapping. Now the main implementations are CGNS/HDF5 and CGNS/Python, the first is archiving oriented while the second is more workflow oriented. CGNS/Python is the basis of the interoperability system developed at Onera around *e/sA*.

The standard is not used for internal data representation but only for the public view of the data, in a workflow exchange, for example from the CAD to the mesh tool, or from the solver to the visualizer. More complex workflows can be defined, with unsteady computation involving both CFD and CSM or optimization algorithms.

The data model has a tree structure, starting from the root node, the base, up to the smallest nodes that can be modeled, such as a single real value or a boundary condition application range (see figure B4-01).

The standard is extensible and the CGNS/SC has a process to add new structures when some user needs are raised and agreed by members. We often define new data structures in the framework of our projects. CGNS is the good candidate for data specification when several partners have to exchange data during run-time or to exchange computing files. CGNS can hold a complete simulation context and this has an important effect: when the user defines his data model, he has to find all the required and exact data needed for the simulation, this avoids hidden behavior of codes or unwanted side-effects.

## Modeling capabilities

The *e/sA* multi-application CFD simulation platform deals with internal and external aerodynamics from the low subsonic to the high supersonic flow regime and relies on the solving of the compressible 3-D Navier-Stokes equations (see Box 2). The thermodynamic properties of the fluid may correspond either to the perfect gas assumption or to the equilibrium real gas assumption described by a Mollier diagram. *e/sA* allows the simulation of the flow around moving bodies in several formulations according to the use of absolute or relative velocities and the definition of the projection frame. This is useful when dealing with applications to turbomachinery flows, where the use of relative velocities is advantageous, and applications to flows around propellers, where the use of absolute velocities is necessary, with the same software. The bodies may be deformable, as well as the associated meshes. The gravity source term is optionally taken into account.

A large variety of turbulence models from eddy viscosity to full Differential Reynolds Stress models are implemented in *e/sA* for the Reynolds averaged Navier-Stokes (RANS) equations (see [1] for further details). The range of turbulence models includes classical one-transport and two-transport equation models, more advanced two-equation models, multi-scale four-equation models, one-layer or two-layer Algebraic Reynolds Stress models. When thermal effects are important, specific versions of models are available. Low Reynolds versions of the models are mostly used for an accurate description of the boundary layer profiles, in association with the use of a very fine mesh near the wall. However, wall laws approximating the behavior of the boundary layer near the wall are also available, which allow for the use of coarser mesh near the walls and may be used to reduce the cost of the calculations, in particular for unsteady calculations.

Special attention has been paid to laminar-turbulent transition modeling [1], which may be a key point for obtaining accurate flow predictions. A reliable design of wings or turbines often requires an accurate modeling of the transition process. Transition prediction capability in the *e/sA* RANS solver is based on application of criteria that either were previously developed at Onera for use in boundary layer codes, or result from classical criteria from literature. These criteria are used to describe Tollmen-Schlichting instabilities (including laminar separation bubble predictions), cross-flow instabilities, bypass for high external turbulence rate, attachment line contamination, wall roughness. This transition capability is available for complex geometry configurations. Nevertheless, to improve the applicability for very complex geometries, a transition model based on transport equations is now also available.

In order to deal with flows exhibiting strong unsteadiness and large separated regions, and/or to provide input data for aeroacoustic simulations, the user can perform Detached Eddy Simulations (DES) and Large Eddy Simulations (LES) [1]. The variants of DES methods available in *e/sA* (basic DES, Zonal-DES, Delayed DES) are associated with the Spalart-Allmaras model or with the Menter ( $k, \omega$ ) model. The LES approach can be used to compute the larger structures of the turbulent flows while the smaller structures are dissipated by the numerical model, either by the MILES approach, which relies on the properties of advanced upwind schemes and dissipates the unresolved turbulent structures, or by subgrid models such as the Smagorinsky, Wale and filtered structure function models available in *e/sA*.

## Mesh topology capabilities

CFD solvers may rely on several meshing paradigms such as structured body-fitted grids, unstructured grids or structured Cartesian grids. Even when considering the same configuration, there is no universally accepted definitive choice, as can be seen by looking at the contributions to the Drag Prediction Workshop ([http://aaac.larc.nasa.gov/tsab/cfdlarc/aiaa-dpw/Workshop4/presentations/DPW4\\_Presentations.htm](http://aaac.larc.nasa.gov/tsab/cfdlarc/aiaa-dpw/Workshop4/presentations/DPW4_Presentations.htm)). In that workshop, the contributions were roughly evenly divided, half of them on structured body-fitted grids and the other half on unstructured grids. Each of the mesh types has inherent advantages and disadvantages which may depend on the type of configuration and even more on the flow region of a given configuration. For example, Cartesian grids are easy to generate, to adapt, and to extend to higher-order spatial accuracy, but they are not suitable for resolving boundary layers around complex geometries. Body-fitted structured grids work well for resolving boundary layers, but the grid generation process for complex geometries remains tedious and requires considerable user expertise. General unstructured grids are well-suited to complex geometries and are relatively easy to generate, but their spatial accuracy is often limited to second order, and the associated data structures tend to be less computationally efficient than their structured-grid counterparts. Thus, today, the tendency is to couple meshing paradigms in the same software [29] or in the same coupling infrastructure [28], and this is also the way chosen for *e/sA*.

In *e/sA*, the main focus has been put firstly on structured body-fitted grids which allow for the use of very efficient numerical algorithms due to the natural (I, J, K) ordering of the hexahedral cells. Since it is generally impossible to define a unique structured body-fitted grid around complex geometries, the computational domain is divided in several adjacent or overlapping domains or blocks, in which simpler component grids can be generated more readily. Communication between component grids is achieved either by direct transfer or by interpolation across interfacing boundaries (patched grids), or by interpolation within overlapping grid regions (overset grids). In order to cope with more and more geometrically complex configurations, high flexibility advanced techniques of multi-block structured meshes are available in *e/sA*, in addition to matching techniques for 1-to-1 abutting or 1-to-n abutting patched grids. These advanced matching techniques include quasi-conservative mismatched abutting patched grids (also called totally non-coincident matchings) and Chimera technique for overlapping meshes [8].

Mismatched abutting patched grids are intensively used in industry computations with *e/sA*. The reason is that they simplify mesh generation for complex configurations, and reduce global number of mesh points for a given configuration, by preventing the propagation of mesh refinements throughout the computational domain. They are also well adapted to deal with sliding meshes.

The Chimera technique which enables a discretization of the flow equations in meshes composed of overset grids, may be applied to a wide range of configurations. The two main application domains of this method were originally dealing with the treatment of separate bodies (such as different positions of a missile below a wing) or with configurations including bodies in relative motion (for instance, helicopter rotor and fuselage or booster separation). During recent years, the Chimera method has also been increasingly used to simplify

and improve the meshing of complex configurations composed of the meshing of a basic geometry and of additional meshes adapted to joint bodies (for instance, a spoiler associated with a wing) or to geometrical details (for instance, technological effects in a turbomachinery row such as clearances, leakage slots, grooves, etc.). Finally, Chimera may also be used to achieve mesh adaptation for the simulation of phenomena involving a large range of length scales.

The development in *e/sA* of hybrid multi-block capabilities allowing for the use of unstructured meshes in some blocks of a multi-block configuration [8] presently relies on a strong cooperative effort between Onera and Cerfacs. The objective is to benefit from the high flexibility of unstructured meshes in the flow regions where it becomes too difficult to build a structured grid. Tetrahedral, hexahedral, prismatic cells are considered in this *e/sA* development, in order to be able to consider hexahedral cells near the walls, which is very important in aerodynamics for an accurate description of the boundary layers. A first set of hybrid capabilities will be available very soon in the main version of the *e/sA* software. The mismatched abutting technique is extended in *e/sA* to patch structured and unstructured grids. In the future, the plan is to also apply the Chimera technique to the matching between structured and unstructured grids.

Lastly, structured Cartesian grid capabilities are also currently being developed so that they can be part of the *e/sA* suite in the future. The Cartesian formulation enables high order spatial discretization and mesh adaptation, which in turn allows for better capturing of off-body flow phenomena such as shear layers and wakes [8]. Since some specific high order schemes have been developed in this Cartesian solver, the way forward is to couple this solver with the block-structured solver of *e/sA*. Matchings between blocks are again done using Chimera method. So, *e/sA* will soon offer a quite complete multiple-gridding paradigm providing the potential for optimizing the gridding strategy on a local

basis for the particular problem at hand, in order to cope with the increasing complexity of CFD applications (see [8] for further details on structured/unstructured and Cartesian/ curvilinear block matchings).

## Numerics and boundary conditions capabilities

The flow equations are solved by a cell centered finite-volume method [8]. Space discretization schemes include a range of second order centered or upwind schemes. Centered schemes are stabilized by scalar or matrix artificial dissipation, including damping capabilities inside viscous layers, in order to preserve accuracy. Upwind schemes are based on numerical fluxes such as van Leer, Roe, Coquel-Liou HUS, or AUSM fluxes and are associated with classical slope limiters. Second and third order Residual Based Compact schemes are also available in *e/sA*. The semi-discrete equations are integrated, either by multistage Runge-Kutta schemes with implicit residual smoothing, or by backward Euler integration with implicit schemes solved by robust LU relaxation methods [21], which in general leads to a higher efficiency with *e/sA*. An efficient multigrid technique can be selected in order to accelerate convergence. For time accurate computations, the implicit dual time stepping method or the Gear integration scheme are employed. Preconditioning is used for low speed flow simulations.

An extensive range of boundary conditions is available in *e/sA*, from standard inlet, outlet or wall conditions, to more specific conditions for helicopter configurations (such as the so-called “Froude” far field boundary conditions in hover) or turbomachinery configurations (such as the radial equilibrium condition, or – see Box 5 – the Reduced Blade Count method and the phase-lagged technique for the simulation of rotor/stator interactions). Actuator-disc models are available to economically model the effects of helicopter rotors or propellers, when complete detailed calculations are not worthwhile.

### Box 5 - Reduced Blade Count method and Phase-Lagged technique, two different approaches for simulating the time-periodic flow in a turbomachinery stage configuration

To improve turbomachinery performances, 3D Navier-Stokes flow computations in blade rows are commonly used for turbine and compressor design. Approximate steady flow calculations through multi-stage machines have become usual in design process for many years. In *e/sA*, they are performed using a specific steady condition, the mixing plane condition, to connect two consecutive rows. This condition is based on azimuthal averages which are computed at the interfaces and transferred from a row to the consecutive one. It gives a quite good prediction of the overall efficiency of a machine but of course does not give any information on the unsteady flow fluctuations. Unsteady computations are increasingly used for industrial purposes: in a complete staged machine, they are necessary when performing unsteady non periodic phenomena. They are still very expensive, as discussed in the High Performance Computing section of this paper. But under some conditions, techniques for reducing the computational domain can be used. They can be applied for time-periodic flows (in the frame of reference of each row), that is for flows where the unsteadiness is only due to the relative motion of the rows. The first technique, called “Reduced Blade Count” method [11], was introduced in *e/sA* software [23]. The computation is performed on the actual geometry with reduced blade counts. The interface between the blade rows accounts for the non equal pitches on each side of the interface by an appropriate scaling. The second technique, known as “Phase-Lagged” technique [9], or “Chorochronic” method was implemented in 2003 in *e/sA* software [2]. A single blade passage is computed for each row. The flow solution is stored on the interface boundaries and on the azimuthal periodic boundaries to deal with the phase lag which exists between rows and adjacent blade passages in a row.

Let us note  $N_1$  and  $N_2$  the actual blade numbers of two consecutive rows,  $\omega_1$  and  $\omega_2$  their rotation speeds. The flow periods are equal to  $T_1 = T_{rot} / N_2$  and  $T_2 = T_{rot} / N_1$ , respectively in the rotating frame of the first row and in the rotating frame of the second one,  $T_{rot} = 2\pi / |\omega_2 - \omega_1|$  being the time for a blade passage to make a whole revolution.

The “Reduced Blade Count” technique consists in reducing the computational domain to  $K_1$  and  $K_2$  blade passages without changing the geometry.  $K_1$  and  $K_2$  are chosen such that  $K_1/N_1$  and  $K_2/N_2$  are about the same. We assume that the flow is identical on two consecutive  $K_i$  blade passages at each instant, which is exact when the ratios  $K_i/N_i$  are equal. Between the lower and the upper boundaries, the flow continuity is enforced, which is an approximation with respect to the actual flow, since the real phase lag between these boundaries is cancelled.

We can define  $D_M$  as a mean value of the  $K_i/N_i$  ratios. This quantity represents the geometric reduction which is applied to each row to obtain the computational domain. On the interface, the two blade groups are linked by an instantaneous continuity condition through a common azimuthal extension  $e_m = 2\pi / D_M$  with a scaling given by  $\lambda_i = (N_i / K_i) (1 / D_M)$  for each row. The “Reduced Blade Count” technique induces a slight approximation since the computational periods are  $T'_1 = T_{rot} / (K_2 D_M)$  and  $T'_2 = T_{rot} / (K_1 D_M)$ , that is  $T'_i = \lambda_i T_i$ . This technique can be applied to several consecutive rows if the actual blade numbers are cooperative enough to apply a geometric reduction.

In the “Phase-Lagged” approach, the computational domain is limited to a single blade passage for each row. As the flow is time-periodic in each blade row, a phase lag exists between two adjacent blade passages. This phase lag is the time taken by a blade of the next row to cover the pitch of the row, modulo the time period of the row. The “Phase-Lagged” technique consists of storing the flow values on the azimuthal periodic boundaries and on the interface in order to use them later to build the flow.

Let us consider two space periodic points  $A$  and  $B$  of the upper and lower boundaries of the first row.  $B$  is ahead of  $A$  and what happens at time  $t$  in  $B$  will happen in  $A$  at  $t + T_2$  and more generally at  $t + T_2 + nT_1$  or has happened at  $t + T_2 - mT_1$  ( $m$  is an integer such that  $T_2 - mT_1$  is negative). The flow condition stored in  $A$  at time  $t + T_2 - mT_1$  can be used for the boundary treatment of  $B$  at time  $t$ .

The treatment of the interface relies on the same principle. At each time step, the flow continuity is enforced at the interface between one cell facet of the first row and the suitable storage of the second row, taking into account for the relative position of the rows and using the necessary spatial interpolation on the stored data.

The direct storage of flow solution may lead to very large requirements in terms of memory. The data storage is lowered to an acceptable amount by Fourier analysis.

In the framework of the TATEF2 European project [7], unsteady flow simulations of the stator-rotor interaction in a transonic turbine stage have been performed using the “Phase-lagged” approach. Figure B5-01 shows clearly shock structures obtained for high pressure ratio.

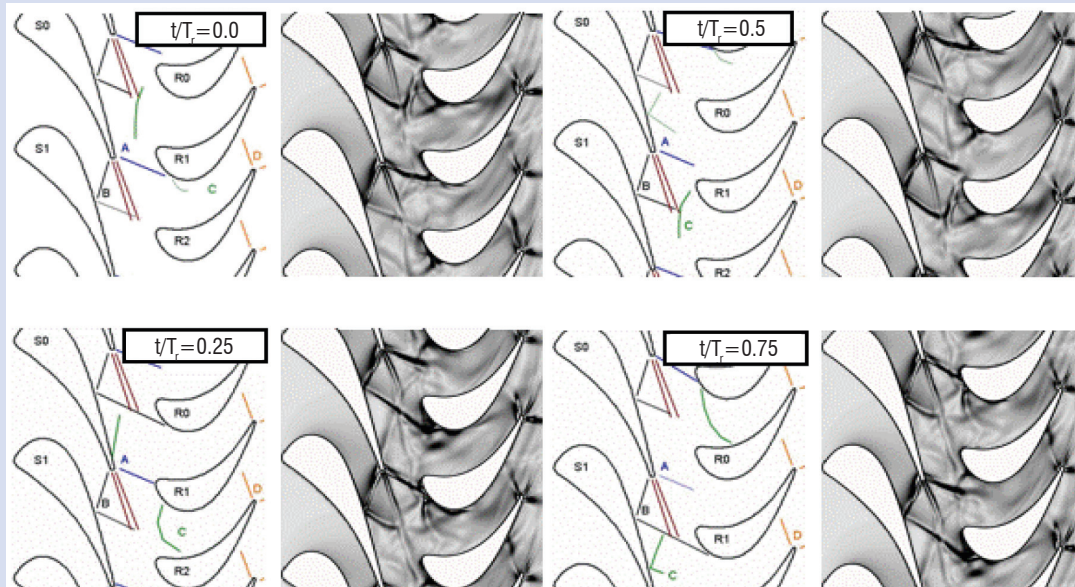


Figure B5-01 – Shock progression through the turbomachinery stage: schematic (left) and density gradient (right).  $y/H \sim 25\%$ .

The “Phase-Lagged” approach does not make any approximation on the number of actual blades and it accounts for the real time period in each reference frame. So it is more accurate than the “Reduced Blade Count” technique. Moreover, as the computational domain is limited to a single blade passage for each row, it is less expensive in terms of CPU time and computer memory. But this approach can only be applied to a single stage, whereas the “Reduced Blade Count” technique can be applied to multi-stage configurations, even when several rotors have different rotational speeds.

A generalization of the “Phase-Lagged” approach, called “multiple frequency Phase-Lagged method”, is under development in *e/sA* [18]. This method allows for unsteady computations through several rows, whilst still limiting the computational domain to one single blade-to-blade passage in each row.

## Multidisciplinary and optimization capabilities

*e/sA* also includes the *Ae1* module offering a general framework for aeroelastic applications [10]. This module provides for the following simulations:

- harmonic forced motion simulations for a given structural mode;
- linearized Euler or Navier-Stokes simulations;
- static and dynamic fluid/structure coupling simulations in time domain with different levels of structural modeling (“reduced flexibility matrix” approach for static coupling, modal approach, full finite element structural model).

The *Opt* module dealing with calculation of sensitivities by linearized equation or by adjoint solver techniques is useful for optimization and control [22]. The calculation of sensitivities consists in calculating the derivatives with respect to control parameters of objective functions such as drag or lift.

## High Performance Computing: towards massively parallel computations

As said above, typical aeronautic configurations nowadays take into account fine geometrical details, resulting in huge problem sizes, as the example of the simulation of the complete multistage compressor in Figure 4 (a simulation which does not use the approximate techniques described in Box 5 for reducing the computational domain). Moreover, although the type of physical modeling still remains mostly RANS, the major trend is to move towards URANS and even DES or LES in order to get more accurate results, leading to an estimated additional CPU cost of about two orders of magnitude.

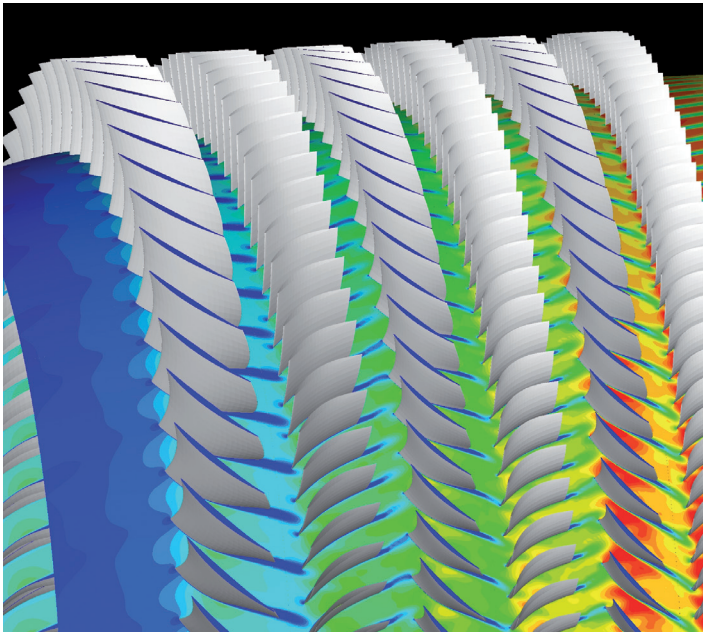


Figure 4 – Unsteady flow simulation of a multistage compressor (134 million cells) using 512 to 4096 computing cores (SNECMA configuration) [17]

To handle such demands, High Performance Computing is now unavoidable in order first to tackle simulations with very large number of points (and thus requiring a huge amount of memory), and second to reduce the CPU wall clock time as much as possible. Onera, Cerfacs and CS have made very large efforts [15, 16] to improve

the code's performance on state-of-the-art vector and x86-64 based computing platforms. In the CFD context, vector machines are now being rapidly supplanted by clusters of x86-64 based nodes due to their high operating cost and relatively poor energy efficiency (see in Figure 5 comparison between many-core and vector platforms on the simulation presented in Figure 4). *e/sA* performance improvement efforts are now entirely dedicated to massively parallel computers.

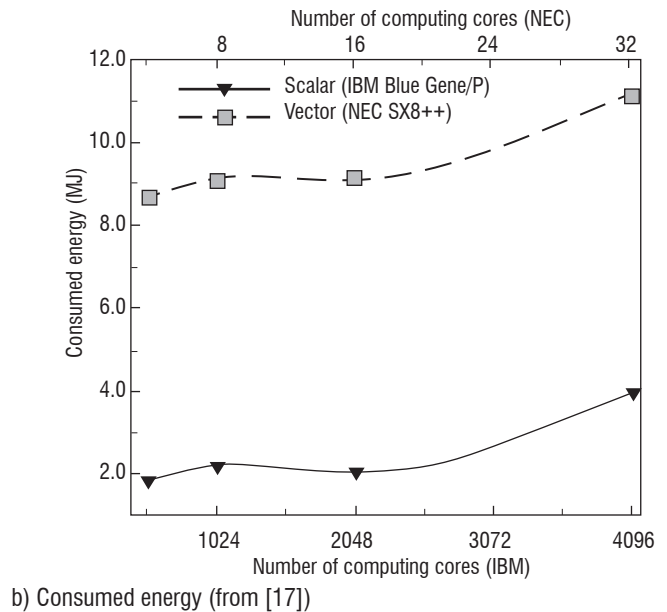
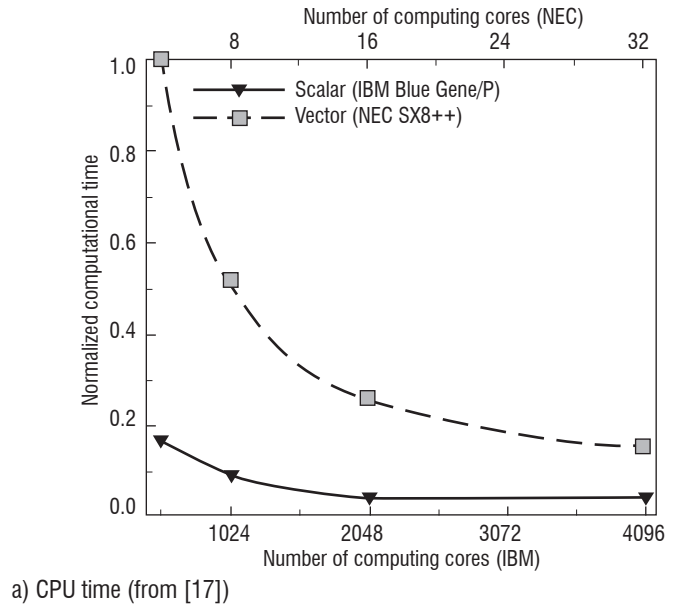


Figure 5 – Comparison between many-core and vector platforms for a single unsteady physical iteration on the multistage compressor configuration

## Parallel strategy for structured multi-block calculations with *e/sA*

The Message Passing Interface (MPI) standard library is used to implement communications between processors. *e/sA* uses a standard coarse-grained SPMD approach: each block is allocated to a processor. Several blocks can be allocated to the same processor.

As said previously, meshing a configuration with structured grids often leads to a complex multi-block topology, thus requiring specific treatments to exchange data between adjacent blocks. In the *e/sA* solver, each block is surrounded by two layers of ghost cells storing values coming from the adjacent block. If the two blocks are allocated to two different computing cores, then point-to-point message passing communication occurs. Otherwise, ghost cells are directly filled by a memory-to-memory copy.

Point-to-point communications are implemented either with blocking (`MPI_Sendrecv_replace`) or non-blocking (`MPI_Irecv/MPI_send`) point-to-point messages. Only blocking point-to-point communications require the scheduling of messages as shown by Fig. 6. The scheduling of communications comes from a heuristic coloring algorithm adapted from graph theory.

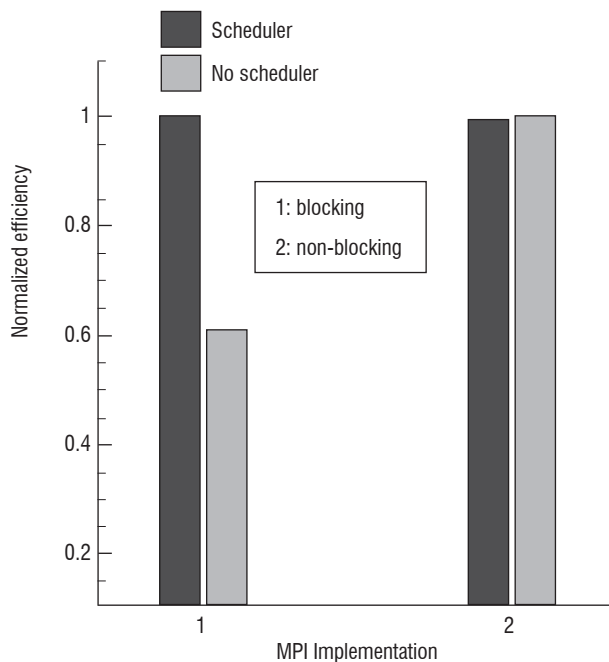


Figure 6 – Effect of the MPI blocking and non-blocking communications on *e/sA* efficiency with and without message scheduling

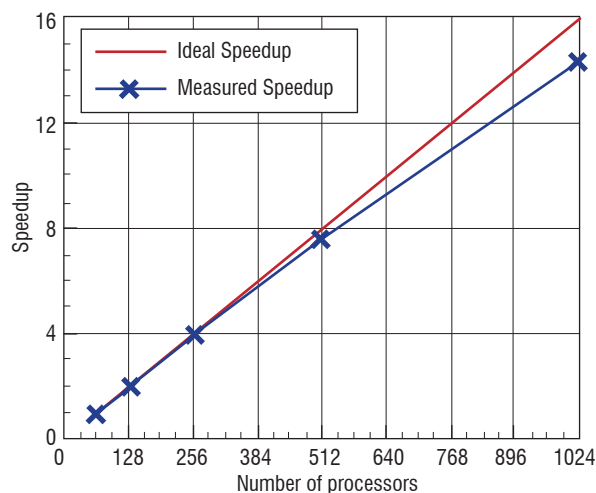
The non-coincident inter-block connectivity is implemented with blocking collective communications (`MPI_Allgatherv`). If only one computing core handles the whole inter-block connection, data exchanges come down to memory-to-memory copies without MPI messages.

### Performance discussion

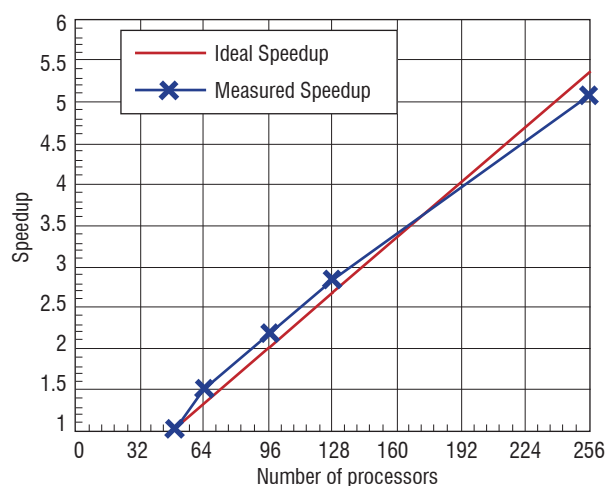
The well known Amdahl's law states that load balancing is crucial to obtain a good efficiency on parallel computers when the number of processors increases. Due to topological constraints, the number of cells in blocks can be very different, ranging from  $10^3$  to  $100^3$ . Most of the time, some blocks must be split to achieve a good load balancing. It is not clear if an optimal response can be obtained in a reasonable amount of time. Therefore, *e/sA* integrates a heuristic block splitting algorithm in the load balancing process. Based on the relative error between the number of cells allocated to the computing core and the ideal number of cells, it checks if the largest block to be allocated needs to be split. The partitioning algorithm handles many constraints such as the multigrid constraint. The so-called “greedy” load balancing

algorithm loops over all of the blocks searching for the largest one in terms of cells and allocates it to the computing core with the fewest cells until all of the blocks are allocated. Note that the number of ghost cells increases with the number of blocks split, leading to an increasing problem size. Topology modification also implies carefully handling block-based implicit algorithms since convergence may rapidly be degraded. Therefore, communications occur at each relaxation step inside the implicit LU stage.

*e/sA* has been ported to most high-performance computing platforms, achieving good CPU efficiency on both scalar multi-core computers and vector computers. As an example, Figure 7a shows typical speedup results on a civil aircraft configuration including  $27,8 \cdot 10^6$  mesh points and 1037 blocks. The numerical options include multigrid algorithm (3 levels) and the Spalart-Allmaras one-equation turbulence model. For large number of processors, the configuration has been split, ending up with 1774 blocks. The computer is the Cerfacs' BlueGene/L computer. Another concrete example (Figure 7b) is the High Lift Prediction Workshop configuration, where a good scalability is obtained up to 256 computing cores, on a SGI cluster built with Intel Nehalem processors (Onera's Stelvio computer), on a grid of  $160 \cdot 10^6$  mesh points, in 1235 blocks.



a) Generic civil aircraft configuration



b) Configuration of the High Lift Prediction Workshop 2010

Figure 7 – Normalized speedup obtained with *e/sA* on two configurations

## Future challenges in HPC

Since the performance improvement through increases in clock frequency has reached a limit, mainly due to the power dissipation problem, new parallel paradigms have emerged, namely the increase of the number of cores on a chip and the use of specialized accelerators (FPGA, GPU, Cell processor). To handle such paradigms, we have gained experience in two approaches: OpenMP thread programming and GPU using CUDA. In our previous studies on thread parallelism [20], OpenMP appeared to be less efficient compared with MPI on nodes with small numbers of cores (<16). We plan to update these studies in the context of upcoming many-core chips. In addition, we are currently building a prototype version dedicated to GPU; here the main challenge is the limited data transfer bandwidth between CPU host and GPU.

As memory bandwidth will probably remain the limiting factor on performance in the near future, major efforts are planned for both

the fine-grain parallelism (data-parallelism) and the optimized use of cache memory. This will be mandatory as the trend in increasing the number of cores implies that many cores will compete for hardware resources.

To summarize on parallel performance, *elsA* is a portable code reasonably well adapted to current generations of HPC platforms and continuous work is undertaken to strike a balance between good efficiency and maintainability. *elsA* is routinely used on hundreds of processors in industry; the biggest computation was run with 8192 cores on a  $1.7 \cdot 10^9$  point grid [12].

Note also that not only the solver, but also the pre- and post-processing steps should be fully and efficiently addressed for massively parallel configurations. Moreover, the efficiency of the whole simulation in the framework of a multiple-gridding paradigm will be a big challenge for the next few years ■

## Acknowledgements

The authors would like to thank all colleagues of several Onera Departments (CFD and Aeroacoustics, Applied Aerodynamics, Aerodynamics and Energetics Modeling, Aeroelasticity and Structural Dynamics), of Cerfacs and of development partners for their sustained effort to make the *elsA* software a powerful and reliable tool for research and for industry.

We would like in particular to acknowledge contributions of the following former and present members of the *elsA* software team in the Onera CFD and Aeroacoustics Department: A. Gazaix-Jollès, M. Lazareff, J. Mayeur, B. Michel, P. Raud, A.-M. Vuillot.

We also thank our colleagues who have provided us with the *elsA* results presented in the paper: F. Blanc (Cerfacs/Airbus) for the transport aircraft configuration, N. Gourdain (Onera Applied Aerodynamics Department, then Cerfacs) for the rotating stall turbomachinery simulation, then for the HPC turbomachinery calculation, G. Delattre (Onera Applied Aerodynamics Department) for the CROR configuration, C. Benoit, G. Jeanfaivre and X. Juvigny (Onera CFD and Aeroacoustics Department) for the helicopter configuration.

## References

- [1] B. AUPOIX, D. ARNAL, H. BÉZARD, B. CHAOUAT, F. CHEDEVERGNE, S. DECK, V. GLEIZE, P. GRECARD and E. LAROCHE - *Transition and Turbulence Modeling*. Aerospace Lab, Issue 2, 2011.
- [2] G. BILLONNET, S. PLOT and G. LEROY - *Implementation of the elsA Software for the Industrial Needs of Flow Computations in Centrifugal Compressors*. 41<sup>e</sup> colloque d'Aérodynamique Appliquée, Lyon, 2006.
- [3] R.H. BUSH, G.D. POWER and C.E. TOWNE - *WIND: The Production Flow Solver of the NPARC Alliance*. AIAA Paper 98-0935, 36<sup>th</sup> AIAA Aerospace Science Meeting and Exhibit, Reno, 1998.
- [4] L. CAMBIER, M. GAZAIX - *elsA: an Efficient Object-Oriented Solution to CFD Complexity*. AIAA Paper 2002-0108, 40<sup>th</sup> AIAA Aerospace Science Meeting and Exhibit, Reno, 2002.
- [5] L. CAMBIER and N. KROLL - *MIRACLE - A joint DLR/Onera Effort on Harmonization and Development of Industrial and Research Aerodynamic Computational Environment*. Aerospace Science and Technology, vol.12, 2008.
- [6] L. CAMBIER and J.-P. VEUILLOT - *Status of the elsA CFD Software for Flow Simulation and Multidisciplinary Applications*. AIAA Paper 2008-664, 46<sup>th</sup> AIAA Aerospace Science Meeting, Reno, 2008.
- [7] L. CASTILLON, G. PANIAGUA, T. YASA, A. DE LA LOMA and T. COTON - *Unsteady Strong Shock Interactions in a Transonic Turbine: Experimental and Numerical Analysis*. ISABE Paper 2007-1218, Beijing, China, 2007.
- [8] B. COURBET, C. BENOIT, V. COUAILLIER, F. HAIDER, M.-C. LE PAPE and S. PÉRON - *Space Discretization Methods*. Aerospace Lab, Issue 2, 2011.
- [9] J.I. ERDOS and E. ALZNER - *Computation of Unsteady Transonic Flows Through Rotating and Stationary Cascades*. NASA CR-2900, 1977.
- [10] M. ERRERA, A. DUGEAI, P. GIRODROUX-LAVIGNE, J.-D. GARAUD, M. POINOT, S. CERQUEIRA and G. CHAINERAY - *Multi-Physics Coupling Approaches for Aerospace Numerical Simulations*. Aerospace Lab, Issue 2, 2011.
- [11] A. FOURMAUX - *Assessment of a Low Storage Technique for Multi-Stage Turbomachinery Navier-Stokes Computations*. ASME Winter Annual Meeting, Chicago, 1994.
- [12] M. GAZAIX and S. CHAMPAGNEUX - *Recent Results with elsA on Multi-Cores*. Symposium on CFD on Future Architectures, DLR Braunschweig, 2009.
- [13] M. GAZAIX, A. JOLLÈS and M. LAZAREFF - *The elsA Object-Oriented Tool for Industrial Applications*. 23<sup>rd</sup> ICAS meeting, Toronto, 2002.
- [14] T. GERHOLD, V. HANNEMANN and D. SCHWAMBORN - *On the Validation of the DLR-TAU Code*. in W. NITSCHKE, H.J. HEINEMANN and R. HILBIG (Eds), *New Results in Numerical and Experimental Fluid Mechanics, NFM 72*, Vieweg, 1999.
- [15] N. GOURDAIN, L.Y.M. GICQUEL, M. MONTAGNAC, O. VERMOREL, M. GAZAIX, G. STAFFELBACH, M. GARCIA, J.-F. BOUSSUGE and T. POINSOT - *High Performance Parallel Computing of Flows in Complex Geometries - Part 1: Methods*. Computational Science and Discovery, vol. 2, 2009.

- [16] N. GOURDAIN, L.Y.M. GICQUEL, G. STAFFELBACH, O. VERMOREL, F. DUCHAINE, J.-F. BOUSSUGE and T. POINSOT - *High Performance Parallel Computing of Flows in Complex Geometries - Part 2: Applications*. Computational Science and Discovery, vol. 2, 2009.
- [17] N. GOURDAIN, M. MONTAGNAC, F. WLASSOW and M. GAZAIX - *High-performance Computing to Simulate Large-scale Industrial Flows in Multistage Compressors*. International Journal of High Performance Computing Applications, vol. 24, 2010.
- [18] L. HE and H.D. LI - *Single-Passage Analysis of Unsteady Flows Around Vibrating Blades of a Transonic Fan Under Inlet Distortion*. Journal of Turbomachinery, 2002.
- [19] W.L. KLEB, E.J. NIELSEN, P.A. GNOFFO, M.A. PARK and W.A. WOOD - *Collaborative Software Development in Support of Fast Adaptive AeroSpace Tools (FAAST)*. AIAA Paper 2003-3978, 33<sup>rd</sup> AIAA Fluid Dynamics Conference, Orlando, 2003.
- [20] F. LOERCHER - *Optimisation d'un code numérique pour des machines scalaires et parallélisation avec OpenMP et MPI*. Technical report TR/CFD/03/104, CERFACS, 2003.
- [21] C. MARMIGNON, V. COUAILLIER and B. COURBET - *Solution Strategies for Integration of Semi-Discretized Flow Equations in elsA and CEDRE*. Aerospace Lab, Issue 2, 2011.
- [22] J. PETER, G. CARRIER, D. BAILLY, P. KLOTZ, M. MARCELET and F. RENAC - *Local and Global Search Methods for Design in Aeronautics*. Aerospace Lab, Issue 2, 2011.
- [23] S. PLOT, G. BILLONNET and L. CASTILLON - *Turbomachinery Flow Simulations Using elsA Software: Steady Validations and First Abilities for Unsteady Computations*. 38<sup>th</sup> AIAA/ASME/SAE/ASEE Joint Propulsion Conference & Exhibit, Indianapolis, 2002.
- [24] D. POIRIER, S.R. ALLMARAS, D.R. MCCARTHY, M.F. SMITH and F.Y. ENOMOTO - *The CGNS system*. AIAA Paper 1998-3007, 29<sup>th</sup> AIAA Fluid Dynamics Conference, Albuquerque, 1998.
- [25] J. RENEUX, P. BEAUMIER and P. GIRODROUX-LAVIGNE - *Advanced Aerodynamic Applications with the elsA Software*. Aerospace Lab, Issue 2, 2011.
- [26] C.C. ROSSOW and L. CAMBIER - *European Numerical Aerodynamics Simulation Systems*. in E.H. HIRSCHHEL and E. KRAUSE (Eds.), *100 Volumes of 'Notes on Numerical Fluid Mechanics'*, NFM 100, Springer-Verlag, 2009.
- [27] J.B. VOS, A. RIZZI, D. DARRACQ and E.H. HIRSCHHEL - *Navier-Stokes Solvers in European Aircraft Design*. Progress in Aerospace Sciences 38, 2002.
- [28] A.M. WISSINK, J. SITARAMAN, V. SANKARAN, D.J. MAVRIPLIS and T.H. PULLIAM - *A Multi-code Python-Based Infrastructure for Overset CFD with Adaptive Cartesian Grids*. AIAA Paper 2008-927, 46<sup>th</sup> AIAA Aerospace Science Meeting, Reno, 2008.
- [29] H. YANG, D. NUERNBERGER and H.-P. KERSEN - *Towards Excellence in Turbomachinery CFD: a Hybrid Structured-Unstructured RANS Solver*. Journal of Turbomachinery, vol. 128, 2006.

#### Acronyms

ADF (Advanced Data Format)	HPC (High Performance Computing)
AUSM (Advection Upstream Splitting Method)	HUS (Hybrid Upwind Splitting)
CAD (Computer-Aided Design)	LES (Large Eddy Simulation)
CFD (Computational Fluid Dynamics)	LU (Lower Upper)
CGNS (CFD General Notation System)	MPI (Message Passing Interface)
CROR (Counter Rotating Open Rotor)	OO (Object-Oriented)
CSM (Computational Structural Mechanics)	RANS (Reynolds Averaged Navier-Stokes)
CUDA (Compute Unified Device Architecture)	SIDS (Standard Interface Data Structure)
DES (Detached Eddy Simulation)	SPMD (Single Process, Multiple Data)
elsA (ensemble logiciel pour la simulation en Aérodynamique)	TATEF2 (Turbine Aero-Thermal External Flows 2)
FPGA (Field-Programmable Gate Array)	UML (Unified Modeling Language)
GPU (Graphics Processing Unit)	URANS (Unsteady Reynolds Averaged Navier-Stokes)
HDF (Hierarchical Data File)	XML (eXtensible Markup Language)



**Laurent Cambier** graduated in 1980 from “École Centrale de Paris”, is presently Assistant Director of the CFD and Aeroacoustics department of Onera and Head of the *elsA* program coordinating research, software and validation activities.



**Michel Gazaix** graduated in 1979 from “École Normale Supérieure de Saint-Cloud” and has been a Research Scientist at Onera since 1986. In the CFD and Aeroacoustics department, his research topics include: High Performance Computing, Real Gas modeling in compressible flows, and software engineering applied to large scientific codes.



**Sébastien Heib** PhD in Numerical Analysis from Paris 6 University, joined Onera in 2001. He is presently the head of the *elsA* software project in the CFD and Aeroacoustics department.



**Sylvie Plot** graduated from “École Nationale Supérieure de l’Aéronautique et de l’Espace” in 1990. Since that time, she has been working at Onera, mainly on the development of helicopter and turbomachinery CFD capabilities. She is currently head of the “Software and Advanced Simulations for Aerodynamics” research unit of the CFD and Aeroacoustics Department.



**Marc Poinot** who received an MSc in Computer Science from Paris XI Orsay University, is a software engineer in the CFD and Aeroacoustics department of Onera. He is in charge of interoperability topics for code coupling and numerical simulation platforms. He is member of the CGNS steering committee and he initiated and actively participated to the migration of CGNS to HDF5.



**Jean-Pierre Veillot** graduated in 1969 from “École Supérieure de l’Aéronautique”, received a PhD from Paris 6 University in 1975. He was Assistant Director of the CFD and Aeroacoustics department when he retired from Onera in 2010 after a whole career at Onera devoted to numerical methods and software development in CFD.



**Jean-François Bousuge** graduated from the Von Karman Institute, was working as numerical simulation engineer in the automotive field until 2001 before becoming research engineer at CERFACS where he was in charge of code development on various CFD methods and algorithms until 2005. Today, he is the leader of the external aerodynamics group at CERFACS.



**Marc Montagnac** is a research engineer in external aerodynamics group at CERFACS. He graduated from the “Institut National des Sciences Appliquées” with an engineering diploma in 1994 and received a PhD in Computer Science from Paris 6 University in 1999. His primary research and professional interests are in the areas of software engineering, High Performance Computing and numerical methods.

A. Refloch, B. Courbet, A. Murrone,  
P. Villedieu, C. Laurent, P. Gilbank,  
J. Troyes, L. Tessé, G. Chaineray,  
J.B. Dargaud, E. Quémérais, F. Vuillot  
(Onera)

E-mail: alain.refloch@onera.fr

# CEDRE Software

This article gives a general description of the CEDRE® system. CEDRE® is a multi-physics platform working on general unstructured meshes intended to both advance research and process industrial applications in the fields of energetics and propulsion. The system includes a graphical user interface for data entry and a set of pre and post processing utilities. The code is organized as a set of solvers, each of which can be used to handle a particular physics, which are coupled together for the computations. Here, we briefly present the solvers: reactive gas CHARME, Eulerian dispersed phase SPIREE, Lagrangian SPARTE, conduction ACACIA, FILM for studying liquid films, radiation ASTRE and REA, as well as the Peul solver. Other programs can be used to handle other physics that are not part of energetics, such as mechanics, by means of external couplings, using in particular the in-house CWIPI library. We have made several general remarks on parallelism, as performance cannot be considered independently from the computing code. The organization of development and the importance of configuration management are highlighted and stress is put on the validation process, which is of the utmost importance for qualifying the quality of results.

## Introduction

CEDRE® is a multi-physics platform on general unstructured grids, for both research and industrial applications, in the fields of energetics and propulsion. The software architecture follows a multi-domain, multi-solver approach. Solvers are considered for each physical system: gas phase, dispersed phase, thermal fields in solids and radiation. These solvers share the CEDRE architecture and libraries, and can be coupled to perform a multi-physics computation or be operated alone. This calculation chain, which includes a graphical interface for data input, geometrical pre-processing, the calculation itself and post-processing, has capabilities oriented towards research, as well as industrial users (Astrium-ST, MBDA, Snecma, SPS, etc.). The software must meet the needs of industrial partners: decreased cycle design time, increased geometrical complexity, unsteady, multiphysical modeling and reduction of the costs. The application scope of the software includes jet engines, ramjets, rocket motors for missiles and launchers. Computations cover the fields of aerodynamics, aerothermal coupling (heat transfer), combustion, water ingestion, icing, propulsion, and aeroacoustics (jet noise, combustion instabilities). For application examples see [29].

## Process description

There are relatively few developers, given this ambitious objective. Every one of them has an expertise limited to just one or to a few technical domains (numerical analysis, modeling, graphical interfaces, meshing, computer science, parallel computing, etc.) with little overlap between individual skills. Moreover, contributors belong to several departments and sites, and often share this activity with other tasks. Some of them are PhD students for whom CEDRE is primarily a test facility for numerical methods and physical models.

A large fraction of developers also use the code in the frame of research projects. In all cases, it is expected that newly implemented methods and models will become quickly available for Onera and for industrial users. The development process has been designed to meet the above constraints.

All the elements of the project (source code, test cases, documentation, etc.) are stored in a single database, and are accessible to all developers, which facilitates exchanges and collaboration. The limited number of developers does not allow for lengthy specification documents. Instead, specifications are based on one or several

scenarios, including the desired functionalities, numerical methods or physical models, which are divided into simple development cases, included in the project database prior to any development. The results given by the code for these scenarios evolve along with the developments, until they meet the expected functions and results. All along the development process, frequent interactions between users and developers allow the appropriate match between needs and work to be checked. At the end of the development, scenarios can be used as a part of acceptance tests, and are later kept in the project database as non-regression tests.

Every development is split up into several tasks, each lasting only a few days: the size of a task depends on the nature of the development and developer preferences, but each must fulfill all non-regression tests. Besides new methods or implementation models, many tasks may include or even be entirely devoted to code refactoring, which generally aims at simplification, optimization, safety or better error handling.

Development and integration can thus follow a very short cycle, with one version per week approximately. This version meets all non-regression requirements on the development machine, and runs on the two main high performance computers of Onera. This continuous development and integration process prevents divergence between individual versions of the project, and hence facilitates integration of a large flow of new models and methods. Furthermore, it allows a very fast feedback from Onera developers and users, so that most bugs are generally fixed fairly quickly. In the same way, a rapid feedback from users is optimal for model and method improvement. In addition, annual releases are also delivered for users who need to run it on specific machines or stable versions according to their internal processes, and  $\beta$  versions are designed for industrial users in case of urgent need for new functionalities.

The above process shares several features with Agile software development as XP (eXtreme Programming) (test based and iterative development, collaboration with users, frequent deliveries, regular refactoring etc.) without corresponding precisely with any officially formalized method because of the specificities of the project [11].

## Configuration Management

Configuration management is the backbone of the project, because of specificities of the same: multi-departments, multi-sites, and multi-profiles developers. The software is mainly developed by several departments of the Onera, and involves three geographical sites although, from a computer network point of view, we can consider that we are in the presence of a single set, all the sites being interconnected with each other by a fast network.

The developer profile is either permanent, occasional, or PhD students. It is necessary for all developers to be in the same environment, because one main target of the project is the production of a competitive code for our industrial partners, that is, of a software that integrates the latest results of the advanced research, as quickly as possible. For this reason, it is necessary to have a friendly and successful tool, and the choice was made of a known commercial product, CM-SYNERGY® [32]. The interface allows the state and the history of an object to be displayed all the time (an object being in

practice a file). The color associated with an object defines its state of development, predefined in the process (working, integrate, release, etc.). This product was chosen because it proposes a task based approach, which represents a logical change (evolution or correction) brought to the software. All the objects modified within the framework of a task are automatically associated to it. The integration is thus made by blocks of objects consistent with a task. A set of tasks is then included in a folder, which contains a set of new features that can be delivered to the users. This tool, which uses an Informix database, is more than a configuration management, it is a change management tool that integrates the traceability of the requests of the users (playing the role of problem report, or bug tracking, according to various used terms). It is very easy to obtain all types of statistics (by date, by user, by type of requests, by severity, or by element of the chain of calculation). Some figures show the necessity of such a tool: for the 3.1 release, the base size was 53 GB, the number of tasks created since the beginning of the implementation of this approach was 7900, and the number of Change Requests was of the order of 1000. The development of the code represented 4500 Fortran procedures just for the numerical solver part.

## Mesh pre-processing

The calculation chain can use mesh data from many academic and industrial meshers. Some of these have direct output in the CEDRE format (Icem®, Centaur®, Harpoon®, Hexpress®, Star-ccm+®), whereas CEDRE provides a conversion utility from standard output for Gmsh, Gambit®, Cgns© formats, etc.

Geometrical pre-processing also includes many useful features, such as topological and metric verification, mesh connection calculation and mesh merging along a common surface. However, the key pre-processing is mesh partitioning with Metis [23] or Splitmesh (internal development), which is the basis for splitting the workload on the available calculation cores. Today, there is no sophisticated approach in the software to consider calculation/communication costs while assigning subdomains per processor. In the future, it is necessary to work to define the most optimal strategy.

## CEDRE and its solvers

### Common levels and solvers

The code itself consists of several solvers dedicated to physical subsystems: fluid calculation, Lagrangian and Eulerian solver for dispersed or diluted particles, heat conduction in solid walls, thermal radiation, stochastic reaction models, liquid films, etc. Many functionalities and models are common to several or all solvers, and are fulfilled by common libraries, for instance:

- all geometric calculations (cell volumes, surface vectors, Gauss points, wall distances, etc.) are performed at the common level for all solvers. This includes kinematics in the ALE case and mesh intersections for overlapping grids, general polyhedral mesh, etc.;
- thermophysical properties are calculated by a common library called Thermolib. The thermophysical model of CEDRE includes all the data and the procedures allowing the thermodynamic properties and transport coefficients of any material environment susceptible to participate in the multiphysical system, such as it was defined by the

user, to be calculated. This part is described in [8] and includes real gas of various state equations.

Finally, the common level of course includes interactions between solvers.

### The fluid solver Charme

The continuum is a mixture of an arbitrary number of species, each species having its equation of state. The state of the mixture is defined by the densities of the species, together with the total energy and the momentum per unit volume. Governing equations are:

- mass conservation for every species, including source terms if chemical reactions are present;
- energy balance for the mixture;
- momentum conservation equation for the mixture.

In practical applications, velocity may cover a very wide range, from low Mach numbers to hypersonic speeds. Turbulence is present in most simulations and is taken into account in the LES (Large Eddy Simulation)[2] or RANS (Reynolds Averaged Navier-Stokes equations) approach. In the latter case, additional scalar quantities and balance equations are added to the aerothermochemical system to describe the macroscopic properties of turbulence. For most models, these quantities include the mean kinetic energy of turbulence, and an additional scalar may be dissipation, length scale or frequency.

Many types of boundary conditions are available, including:

- inlet-outlet with various sets of imposed fixed variables and options for swirl, radial equilibrium, mixing plane, non-reflection etc.;
- symmetry, axis, no-slip;
- spatial periodicity;
- walls with various heat transfer boundary conditions, and variants for porous walls or solid fuel motors.

Space discretization is described in [3]:

- the general framework is the cell-centered finite volume approach, on possibly moving and deformable control volumes (ALE formulation);
- interpolation follows a MUSCL type methodology. For each degree of freedom, space derivatives are evaluated algebraically from some neighborhood of the current cell, which allows a polynomial reconstruction on each cell;
- this reconstruction gives rise to two distinct evaluations of each variable at every point along the interface between two cells. After limitations for monotony, these evaluations are used as input for approximate Riemann solvers;
- cell reconstruction is also the basis for interface gradient and Navier-Stokes flux evaluation.

Time integration is described in [3]:

- classical Runge-Kutta methods are used in many unsteady simulations. In some cases (low Mach number flows for instance), implicit generalizations of these methods can be useful;
- Euler implicit method can be used at large time intervals when a steady solution is expected.

For implicit schemes, large sparse linear systems are solved at each time interval with the help of the Generalized Minimal Residual method (Gmres).

### The conduction solver ACACIA

This solver is used for conductive heat transfer in solid walls, which are considered as an incompressible medium without deformation. The only state variable is thus temperature, which is governed by energy conservation:

- the heat flux is subject to the isotropic Fourier law, conductivity and specific heat being given functions of temperature. More general models are planned, for example, to deal with anisotropic media;
- sources can be considered to simulate the Joule effect, or other energy inputs.

Several types of boundary conditions are available, the most useful one being a quasi-linear relationship between heat flux and boundary temperature:

- this condition can simulate convective and radiative heat transfer in an environment with prescribed temperature;
- it can also be used as the basis for fluid-solid coupling when the fluid is calculated via the flow solver Charme.

Numerical methods are very similar to those defined for the fluid solver:

- finite volume space discretization is based on a linear reconstruction on each cell, temperature gradient being calculated through a least-squares formula. Interface gradients between two cells are computed through an interpolation formula, using state variables and gradients in both cells;
- various explicit and implicit time integration schemes are available, for instance the Euler implicit method with Gmres resolution.

### The Eulerian dispersed phase solver SPIREE

The Eulerian solver called SPIREE is devoted to the computation of dispersed two-phase flows which is of major importance for many applications in the aerospace context. In the case of dispersed flows, one phase is assumed to be diluted (typical values of the volume fraction lie between  $10^{-5}$  and  $10^{-2}$ ) and the influence of the inclusions on the carrier phase is taken into account through the introduction of source terms on the solver CHARME.

As we mentioned, SPIREE is based on the Eulerian resolution of conservation equations for some particular moments of the number density function. These equations can be formally derived from the kinetic equation introduced by Williams in [39] or [40] by assuming particular closure assumptions. Two general options are possible in the code. The first one is the sampling method, in which the number density function presumed can be written under a sum of Dirac in size. The second one, recently implemented into the code, is called the "multi-fluid" model or sectional method and has been introduced in [15].

A system of conservative equations is derived for each class or section, and then solved by a classical Finite Volume Formulation on unstructured meshes. Now, we describe the principal ingredients concerning physical modeling and numerical method implemented into the solver.

Concerning the numerical method, the convective part of the system is solved using upwind schemes based on Flux-Difference-Splitting, or on the resolution of the Riemann problem for particles [4]. The second order accuracy for spatial discretization is obtained thanks to MUSCL techniques [37]. Both explicit and implicit are used for time integration, based on Runge-Kutta method of order 1 or 2. Recent developments

concern kinetic schemes for the spatial discretization of the convective part of the system, as well as splitting method in the time integration, in order to have specific algorithms for stiff source terms.

Concerning the modeling of forces acting on particles, Drag force is implemented in the solver with different correlations. If we consider a Stokes regime, the expression of the drag force is very simple. However, if the Reynolds number increases, the Schiller-Naumann correlation [30] for example, has to be employed. For compressible regimes, a specific correction based on the relative Mach number is applied on the drag coefficient. Gravity and Unsteady acceleration source terms are also implemented in the code.

Evaporation phenomena and Heat transfer are of course implemented in the solver, and are a key issue for combustion problems in aerospace applications. Thermal transfer is implemented. Several evaporation models derived from the d2-law [31], such as for example the Abramzon-Sirignano model [1], are implemented. A N-layer model that allows the description of the detailed internal temperature distribution inside the particle is in preparation. Specific models for Aluminum combustion are also implemented.

In the sectional approach, interactions between particles are taken into account. Coalescence phenomena are still implemented, while secondary break-up is in the final step of implementation. In regard to boundary conditions, the solver includes: inlet-outlet with various sets of imposed variables, symmetry, axis, slip conditions and spatial periodicity.

The solver is principally used in Liquid and Solid propulsion. Some recent applications of the solver also concern the prediction of ice formation on aircraft [26] [24].

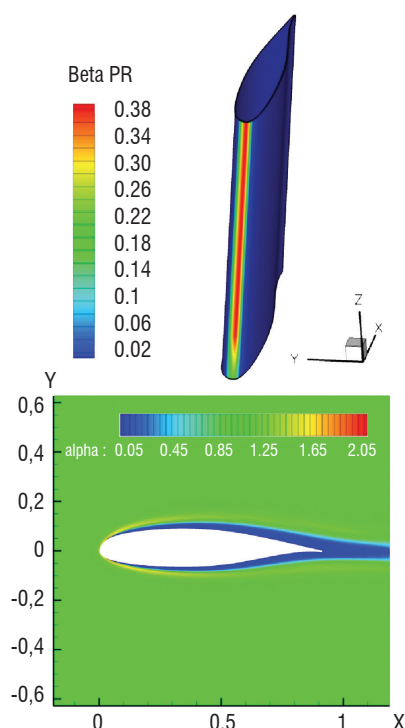


Figure 1 – Water catch collection coefficient (top) and droplet flux of mass (bottom) on the wing

## The Lagrangian dispersed phase solver SPARTE

The SPARTE solver is devoted to the simulation of a dispersed phase (composed of solid particles or droplets) suspended in a gas flow. It is based on a Lagrangian approach which means that the particulate phase is simulated by solving the motion of a large number of numerical particles (parcels) in space equipped with variables of time, position, velocity, size and temperature, or other relevant quantities. The mean dispersed phase properties are obtained by averaging over a representative sample of parcels that cross a defined volume, within a certain time interval.

The particulate phase can be composed of particles of different physical states (solid or liquid) and of different chemical composition. Specific models (for heating, phase change ...) may be chosen independently for each type of particle. In the present version, the following models are available:

- drag force, inertial forces (rotating frame);
- heat exchange;
- fusion/solidification, evaporation/condensation, multi-component evaporation/ condensation;
- collision/ coalescence;
- droplet secondary break-up;
- complex particle/wall interactions : inelastic bouncing, splashing, deposition, etc.;
- turbulent dispersion.

Most of these models are described in [25].

Two variants of the stochastic particle method can be used depending on the particle mass loading, and on whether the flow is stationary or not: the steady particle method (very efficient but with a limited range of applications) and the unsteady particle method (much more expensive but with a wide range of applications). The principles of these two methods are explained in [25].

As regards the boundary conditions, the following are currently available:

- walls with various interaction models;
- inlet with particle emission;
- outlet (free boundary);
- spatial periodicity;
- mixing plane (for a surface separating a rotating domain from a fixed one).

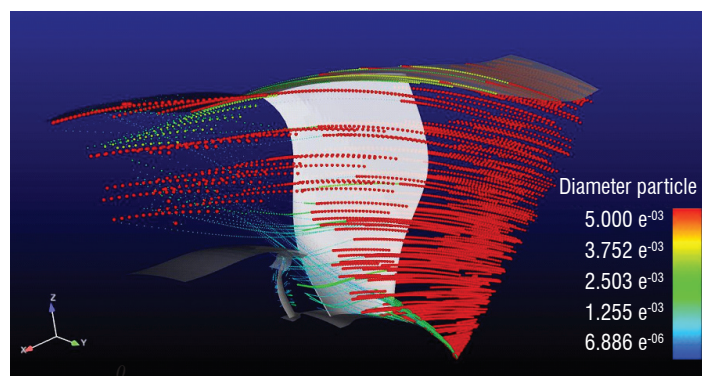


Figure 2 – Example of hail particle trajectories colored by their diameter through a turbojet engine (fan and IGV)

## The FILM solver

The so-called “FILM” solver is devoted to the computation of wall liquid films formed under multi-physics configurations (Figure 3). The solver uses an Eulerian approach to solve film equations over a three dimensional complex surface. The FILM geometry (a surface mesh) is built beforehand from the CEDRE geometry (a volume mesh).

The liquid film equations are written in an integral form (integration across the film thickness of the Navier-Stokes equations, with a no-slip condition at the bottom), and solved using a 2D finite-volume scheme [1]. The liquid Reynolds number is assumed to be small enough for the film flow to be laminar. The film thickness is obtained by solving the integral continuity equation. If the film thickness is small enough to neglect the inertial forces in comparison with the other forces (gas shear stress, film viscosity, etc.), the flow rate can be expressed as a function of the thickness. This model is called the “one-equation model” because it only requires the integral continuity equation to be solved. A second model is foreseen to treat the case where the mechanical equilibrium is not verified locally. It is called the “two-equations model” because in addition it solves the integral momentum equation (see shallow water equations).

The FILM solver is coupled with the gas phase solver CHARME for modeling the shear driven force and the pressure effects on the film motion. The disperse phase solver computes the source terms for modeling the film formation by spray impingement [27]. The FILM solver is currently coupled with the Lagrangian solver SPARTE, in which models for droplet-wall interactions have been implemented (splashing, deposition, etc.). Coupling with the Eulerian disperse phase solver SPIREE is possible as well. The FILM solver is parallelized in the same way as the other solvers. The FILM sub-domains are the surface projection of the 3D-geometry sub-domains. Therefore, there are not external exchanges between processors for data transfers between solvers.

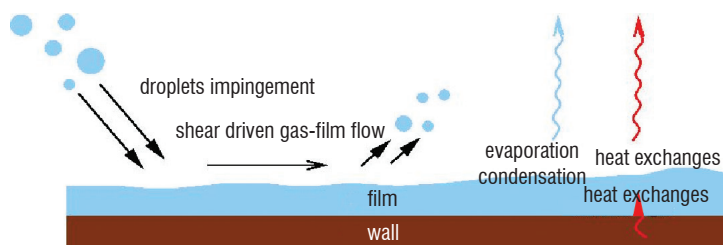


Figure 3 – Wall liquid films formed under multi-physics configurations

## Radiation solvers

In the CEDRE code, two radiation solvers have been developed: one, called REA [18], is based on a discrete ordinate method, while a Monte Carlo method is implemented in the other, named ASTRE [7][33][34]. These two methods are complementary.

The discrete ordinate method is based on a discrete representation of the directional variation of the radiative intensity. Thus, the radiative transfer equation, the integro-differential equation describing the evolution of the spectral directional radiative intensity, is replaced by a system of partial differential equations involving intensities that are angularly averaged

over each ordinate direction (one equation for each ordinate direction). Integrals over a range of solid angles are approximated by weighted sums over the ordinate directions within that range (use of a numerical quadrature).

Applied to thermal radiation problems, the Monte Carlo method consists of following a finite large number of energy bundles (an energy bundle is a discrete amount of energy, which can be thought of as a group of photons bound together) through their transport histories, from their point of emission to their point of absorption. Bundle characteristics (wavelength, initial direction, point of emission) and physical events along bundle trajectories (absorption, scattering, reflection on walls) are chosen according to probability distributions by drawing random numbers.

That is why Monte Carlo simulations are often referred to as direct simulations of radiative transfer by statistical distributions of energy over space, direction and wavelength, and results obtained with Monte Carlo methods are often considered as reference solutions. Since Monte Carlo methods are statistical, exact results can be approximated if enough bundles are followed. Another advantage of Monte Carlo methods is that even the most complicated problem can be solved with relative ease.

At the present time, REA is dedicated to radiative transfer calculation in solid propellant rocket motors. Gas radiative properties ( $H_2O$ ,  $CO_2$ ,  $CO$  and  $HCl$ ) are approximated by a box model. Two sets of parameters are available in REA for this model: the set used by Joumani [18], and the one obtained by Duval [9]. Radiative properties of alumina particles ( $Al_2O_3$ ) are calculated from the Mie theory. REA is coupled with the CHARME and SPIREE solvers. A domain decomposition technique is used to parallelize REA: each core involved in the simulation deals with only one part (which consists of one or several sub-domains) of the whole domain.

Three kinds of gas radiative property model can be used in ASTRE: Correlated-K model (CK), Statistical Narrow-Band model (SNB), and box model. Several sets of parameters for these three kinds of model are available in ASTRE. Moreover, soot, alumina and water particles, and turbulence-radiation interaction can be taken into account. All these models allow radiative transfer calculations in a wide range of applications: air breathing combustion (laboratory flames at atmospheric pressure [33][35][36] and aeroengine combustors [22]), solid propellant rocket motors, atmospheric (re-)entries [5][6][8], glass forming [5], etc. On the one hand, ASTRE is a solver of CEDRE coupled with the CHARME, PEUL and SPIREE solvers; on the other hand, ASTRE is an independent radiative transfer code able to be coupled to other codes (ZeBuLoN [5], CELHYO [17][19][28], ABAQUS [22], ANSYS [22], N3S [22], etc.) according to the considered application. Since all the bundles are statistically independent, the parallelization of ASTRE is carried out by distributing the bundles over the cores:  $N_{core}$  bundles are followed simultaneously, where  $N_{core}$  is the number of cores involved in the simulation. It is easy to implement such a parallelization, but memory storage problem may be encountered when the mesh is composed of a very large number of cells. Because there is no required communication among parallel cores during bundle history generation, the parallelization efficiency is close to 100%. Recently, this property of ASTRE was checked for various numbers of cores (from 16 to 2048 cores).

To obtain more information about these two solvers, the reader may refer to [19] dedicated to radiative transfer modeling used at Onera in CFD simulations.

## Box 1 - External coupling

For the simulation of domains not included in the CEDRE package, such as aeroelasticity or solid mechanics for instance, external coupling with other software is available. Thus, CEDRE can be coupled with various finite element analysis solvers, such as ABAQUS, MARC, and ZeBuLoN [B1-01]. Among large Fluid-Structure Interactions (FSI), the system coupling methods make it possible to solve steady or unsteady thermal problems, as well as structure deformation problems.

In the coupled approach used, the FSI is achieved by partitioning the problem into fluid and solid parts solved separately with boundary conditions calculated by the other part. In this partitioned procedure, the coupled problem is numerically solved using a Conventional Serial Staggered approach. In all these FSI computations, matching grids between fluid and solid are employed and therefore no non-matching load transfer scheme needs to be used.

The transfer of the physical data is performed by the coupling library MpCCI™, developed at the Fraunhofer Institute. Among all the benefits, we can report software interchanging, independent modelling and various integrated interpolations. MpCCI™ can also be used on heterogeneous distributed platforms. It allows the coupling of more than 2 codes through surface or volume.

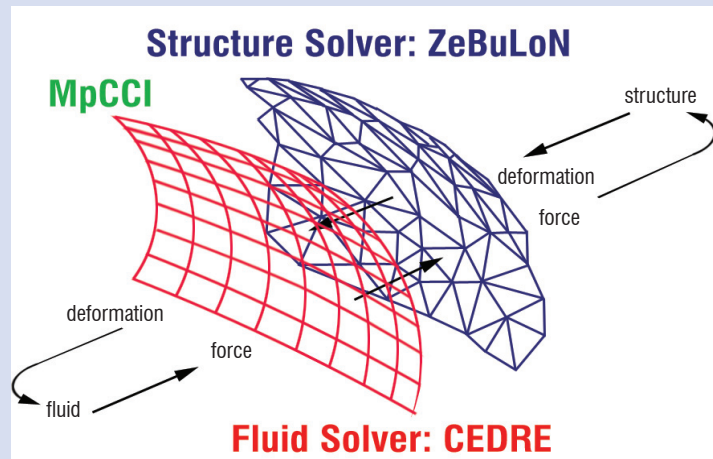


Figure B1-01 – CEDRE - ZeBuLoN coupling

Still, in a near future, the SDK version of MpCCI™, which is implemented in the CEDRE and ZeBuLoN codes, may be replaced by a less flexible version named Code Adapter. Given this uncertainty, Onera has decided to develop its own coupling library CWIPI.

### The PEUL solver

The PEUL model “Probabilistic Eulerian Lagrangian model”, consists, on the one hand, in solving the balance equations of mass, momentum, energy,  $k$  (turbulent kinetic energy) and  $\varepsilon$  (dissipation rate of  $k$ ), using a usual Eulerian discretization method and, on the other hand, in solving the thermochemical composition PDF (Probability Density Function) equation, by means of a stochastic Monte Carlo method. The characteristics of the stochastic particles are the same as those of the reactive turbulent flow. The trajectory and the composition of the gas particles are described by the equations:

$$\frac{dx_i}{dt} = \langle V_i \rangle + V_i'$$

$$\frac{dY_a}{dt} = \frac{\langle Y_a \rangle - Y_a}{\tau} + w_a$$

where  $\langle V_i \rangle$  is the average velocity given by the Eulerian resolution of the balance equation;  $V_i'$  is a velocity fluctuation calculated by a turbulent dispersion model.  $Y_a$  stands for the mass fraction of the  $a$ th chemical species ( $1 \leq a \leq n$ ), or for the enthalpy of the particle ( $a = n+1$ ).  $\langle Y_a \rangle$ , the average value of  $Y_a$ , is provided by the Eulerian calculation.  $\tau$  is a microscale mixing time evaluated

from the turbulence model.  $w_a$  is the chemical source term of a  $a^{\text{th}}$  species.

A PEUL calculation provides information about velocity, temperature, production rate and mass fraction of species of the particle, as means Lagrangian quantities. Thus, the PEUL model can treat different combustion regimes, and it is particularly adapted to calculate complex kinetics. It can be used in many applications in the domain of aircraft combustors, ramjet and scramjet and rocket engines.

The PEUL model is written as a solver of the CEDRE. This enables many physical phenomena (combustion-radiation, combustion-two phase flow, etc.) to be taken into account, thanks to solver coupling (PEUL-ASTRE-CHARME, PEUL-SPIREE-CHARME, etc.). Actually, the PEUL solver is coupled with the CHARME solver (one way coupling) and can calculate the production of pollutants in multi-domain configurations. Future work concerns the parallelization of the PEUL solver in order to simulate complex industrial configurations.

### Validation procedure

The validation database is a key component of the project: it capitalizes a large number of computations performed with CEDRE, and compares

## Box 2 - CWIPI

CWIPI (Coupling With Interpolation Parallel Interface) is a library that makes it possible to couple  $n$  parallel codes with MPI communications. Coupling is made through an exchange zone that can be discretized in a different way on any coupled code. Linear, surface or volume couplings are available. CWIPI takes into account all types of geometrical elements (polygon, polyhedral); there is no requirement about the mesh nature. CWIPI contains the following functionalities: control of coupled processes, geometrical location, interpolation, field exchange and visualization file building. The application programming interface is available in Fortran and C/C++. CWIPI can thus couple codes written in different languages. Some functionalities are called from the FVM library [13].

The coupled applications must be launched in the same MPI environment. During the initialization phase, CWIPI creates an internal communicator for each code. For every coupling defined by the user, inter communicators are created between coupled codes. From the user point of view, the inter-application communications become completely transparent even if the applications are parallel.

The user can define coupling algorithms by the use of the control parameters. These parameters are global variables that are synchronized and shared between coupled codes. By default, no variable is defined. For example, the user can define some control parameters to exchange the convergence state or the simulation time.

The field projection from a mesh A to a mesh B is carried out in three steps. The first one is the location of degrees of freedom of mesh B in mesh A. Three levels of location are defined, the first one is the partition number of the mesh, the second one is the cell number in the selected partition, and the next one is the mean values [16] computed in the selected cell. The second projection step is based on the interpolation mean values. This method is linear; the user can customize the interpolation with call-back definition. The next projection step is the interpolated field exchange.

CWIPI exports all result to Enight™ gold format files to visualize exchanged interpolated fields.

them whenever possible with the experiments carried out at Onera or other organizations, for example see [6].

The validation procedure was defined in an Onera quality report, which is partly based on the work of [14] and illustrated in [38]. A validation report is generated at each new release version of CEDRE.

CEDRE validation is based upon test case computations. A test case may feature several subcases, which consist in changing physical model parameters. In CEDRE version 3.2, the test cases fall apart in the database in 4 distinct levels according to their complexity:

- Level 1 is divided into 9 cases and 17 subcases, and refers to “academic” test cases, where simple geometry and well known physics are implied. In many cases, an analytic solution allows precise comparison with calculations;
- Level 2 features 11 cases and 13 subcases, and deals with basic functions in a simple physical context. Analytical solutions are generally not available, but comparisons between several approaches are often possible;
- Level 3 comprises 9 cases and 14 subcases, it deals with elementary well instrumented technical devices. Physical models tend to be more complex, but the quality of the measurements allows significant comparisons with experiments;
- Level 4 includes 6 cases and 7 subcases, and is concerned with complete industrial configurations. Detailed measurements are generally not available, but global results can still be compared with the actual device.

Until now, test case database organization was rather historical (aggregation of user issues), with no physical classification. Furthermore, subcases were not systematic, and some physical models were under represented. All this contributed to an opaque validation procedure.

Thus, a new structured database must be built. Other validation logics are available worldwide, such as for instance the institutional Ercoftac database [10], or Craft Tech software editors CRAVE database [21]. These databases are split into main physical problems and applicative challenges.

To apply this structure on CEDRE, we must identify the main scopes of CEDRE applications:

- aeroacoustics;
- aerodynamics;
- aerothermics;
- combustion.

Each of these disciplines relies on a main basis physics, for instance, for aerodynamics:

- free flows;
- wall flows;
- confined flows;
- flows around bodies;
- ...

All of these main basis physics may then be combined into one complete list, which will be used as a second entry on the test case matrix. On the line corresponding to a test case, ticks will mark the basis physics implied. For instance, rib test case is classified horizontally as sub-level 3, and vertically matches 3 aspects of basis physics (wall flows, imposed detachment, and heated wall).

This way, it increases the benefits of the existing database structure: each test case will be located once horizontally (according to the sublevel) and one or more times vertically (according to the basis physics). Finally, another asset of this new database is to clearly emphasize the missing cases in the actual one.

## Parallel Performance

CEDRE has proven for long to be a successful parallel code. Parallel computing uses the MPI library on the computational domains. On the former Onera cluster, usual computations would use up to 64 processors (the limitation was due to the batch class structure), while CEDRE is computed on 256 sub-domains, with 4 sub-domains on each processor. The process of distributing several sub-domains per calculation core makes it possible to take into account the memory available on various machines. An example of such a divided domain is given in Figure 4, with 256 small domains.

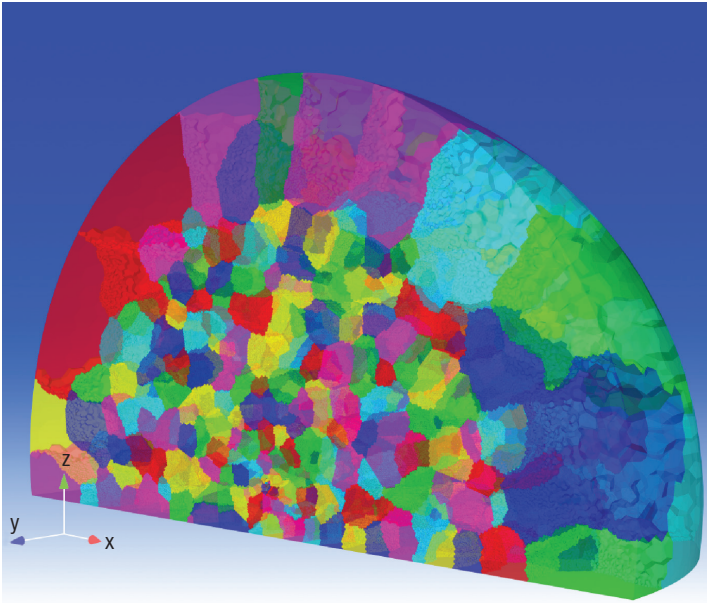


Figure 4 – An example of domain partition with CEDRE[29]

The constant increase in the need for computational power led to wonder whether CEDRE could be run on larger clusters. Recently, a computation was carried out on Onera's cluster (SGI cluster with 3000 Nehalem cores), and used 999 processors with success. The total restitution time is slightly inferior to the one obtained on previous computations (when applying scale factors corresponding to the difference in face number or the change of processors). CEDRE can be said to be supra-linear as illustrated in Figure 5 (the origin of the curve is 10 CPUs and not 1, because the case is too large to run on one processor). Two explanations are possible to explain this trend, first an effect of the processor architecture, the smaller the data to be treated are, the more they go into the cache of the processor. Second for implicit schemes, the major effect in the GMRES method is that the smaller the domains are, the less there is of calculation, because there are a fewer internal iterations, and we converge faster.

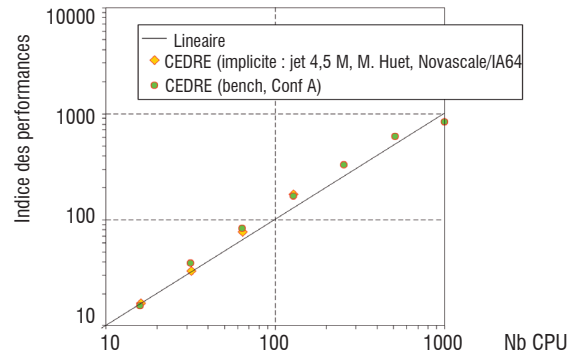


Figure 5 – Example of CEDRE performance on parallel computers

## Project features

The project gives users an external Web site [41], but also an in-house directed site project for access to management configuration plan, project management and quality plan, rules of programming, and a large number of quality procedures. The software is protected by a key mechanism and offers the possibility of private functionality. Users are invited to participate in the CEDRE users conference, which is organized annually.

The user support set up is organized on two levels; the second level corresponds to problems that need an advanced knowledge of the code, of an application point of view, while the first level concerns installation or basic problems faced by users. Even if the number of users is restricted enough, one average year of support represents 1500 exchanged e-mails, more than 100 phone conversations and direct visits, to treat on average 270 requests.

The process of code porting is organized according to 4 phases: debug, which uses the lowest level of optimization and activates the most rigorous options of the compiler (not initialized variables, programming non-in compliance with the standard, ...), optimization averages (of type -O2), which allows a reference base of non-regression to be obtained, then a final phase (type -O3) allowing to have an optimized code.

The non-regression is made on the output data; however, an additional phase defines some case tests, making it possible to ensure that there is no regression on the performance CPU of a version delivered to the other one. This operation is repeated on all of the code supporting machines (NEC SX-8, Intel Nehalem, Itanium, and IBM Power 6, x 86-64, etc.). The heart of the calculation of solvers is written in Fortran 95, a choice made because of the simplicity of the language, which contains all the features of modern languages (pointer, derived type, dynamic allocation, recursive procedure, overload of operator, module). Some Fortran 2003 features can be used if they are available on all of the available compilers (xlf95, pgi, ifort, sxf90), the portability must take into account all of the present machines, for our industrial partners.

The input/output part and certain utilities of the chain of calculation are written in C++ there. The fact of having a standard language 'far from the system', and of reducing the number of languages, allows to limit the problems of code porting. The fast evolutions of the code made complex the management of the former versions of the input files

(for example for the Graphical User Interface), to solve this problem, former ASCII files are today XML format files. This format was also retained for the thermodynamics data. The output files remain in a binary format owner, making it possible and guaranteeing a little endian/big endian portability ■

## Acknowledgements

The authors thank all of the developers, including the students for their active participations in the development of the software.

## References

- [1] B. ABRAMZON and W.A. SIRIGNANO - *Droplet Vaporization Model for Spray Combustion Calculations*. International Journal of Heat and Masse Transfer, Vol 32, N°9, 160-1618, 1989.
- [2] N. BERTIER, B. COURBET, D. DUTOYA, F. VUILLOT and P. SAGAUT - *Large-Eddy Simulation of a Subsonic Flow over a Cavity on General Unstructured Grids*. AIAA, 0679, 2004.
- [3] B. COURBET et al - *Space Discretization Methods*, Aerospace Lab n°2, <http://www.aerospacelab-journal.org>, 2011.
- [4] E. DANIEL, R. SAUREL, M. LARINI, and J.-C. LORAUD - *A Multiphase Formulation for Two-Phase Flows*. International Journal of Heat and Fluid Flow, Vol.4, 269-280, 1994.
- [5] L.-H. DOREY, L. TESSÉ, A. ROOS and F. FEYEL - *Modélisation et simulation numérique des transferts conductif et radiatif au cours des procédés de formage du verre*. Proceedings of the first Colloque International Francophone d'Energétique et Mécanique (CIFEM 2010), Saly, Senegal, 2010.
- [6] F. DUPOIRIEUX - *Optical Diagnostics Used at Onera to Characterize Turbulent Reactive Flows and to Validate Aero and Rocket Engine Combustor Modelling*, Aerospace lab n° 1, 2010.
- [7] F. DUPOIRIEUX, L. TESSÉ, S. AVILA and J. TAINE - *An Optimized Reciprocity Monte Carlo Method for the Calculation of Radiative Transfer in Media of Various Optical Thicknesses*. International Journal of Heat and Mass Transfer, Vol. 49, 1310-1319, 2006.
- [8] D. DUTOYA - Aerospace Lab n°2, <http://www.aerospacelab-journal.org/al2>, 2011.
- [9] R. DUVAL - *Transferts radiatifs dans les moteurs à propergol solide*. Thèse de doctorat, École Centrale Paris, 2002.
- [10] <http://cfd.mace.manchester.ac.uk/ercsoftac>.
- [11] <http://www.extremeprogramming.org>.
- [12] H.FOUCARD - Rouen University thesis, 1998.
- [13] Y. FOURNIER - FVM (Finit Volume Mesh), <http://www.code-saturne.org>.
- [14] J. FRENCH - *Guide for the Verification and Validation of CFD Simulations*, AIAA Technical Report G-077, 1998.
- [15] J.B. GREENBERG, I. SILVERMAN and Y. TAMBOUR - *On the Origin of Spray Sectional Conservation Equations*. Combustion and flame, 90-96, 1993.
- [16] K. HORMANN and M. S. FLOATER - *Mean Value Coordinates for Arbitrary Planar Polygons*. ACM Transactions on Graphics, 25(4):1424 -1441, 2006.
- [17] J.-M. LAMET - *Transferts radiatifs dans les écoulements hypersoniques de rentrée atmosphérique terrestre*. Thèse de doctorat, École Centrale Paris, 2009.
- [18] Y. JOUMANI - *Transferts radiatifs dans les moteurs à propergol solide*. Thèse de doctorat, Université de Valenciennes et du Hainaut Cambresis, 2001.
- [19] L. TESSÉ and J.-M. LAMET - *Radiative Transfer Modeling Developed at Onera for Numerical Simulations of Reactive Flows*, Aerospace Lab n°2, 2011.
- [20] J.-M. LAMET, PH. RIVIÈRE, L. TESSÉ, A. SOUFIANI and M.-Y. PERRIN - *Radiation Modeling for Air Plasmas in Nonequilibrium Conditions: Application to Earth Atmospheric Re-entry*. Proceedings of the 3<sup>rd</sup> International Workshop on Radiation of High Temperature Gases in Atmospheric Entry, Heraklion, Greece, 2008.
- [21] Z. LIU, K. BRINCKMAN, and S. DASH - *Automated Validation of CFD Codes for Analysis of Scramjet Propulsive Flows Using CRAVE*, Denver, USA, 2009.
- [22] E. MERCIER, L. TESSÉ and N. SAVARY - *3D Full Predictive Thermal Chain for Gas Turbine Combustor Metal Temperature*. Proceedings of the 25<sup>th</sup> International Congress of the Aeronautical Sciences (ICAS 2006), Hamburg, Germany, 2006.
- [23] <http://glaros.dtc.umn.edu/gkhome/views/metis>.
- [24] E. MONTREUIL, A. CHAZOTTES AND D. GUFFOND, A. MURRONE, F. CAMINADE and S. CATRIS - *Enhancement of Prediction Capability in Icing Accretion and related Performance Penalties. Part I: Three-Dimensional CFD Prediction of the Ice Accretion*. AIAA 3969, 2009.
- [25] A. MURRONE and P. VILLEDIEU - *Numerical Modeling of Dispersed Two-Phase Flow*. Aerospace Lab n°2, 5, 2011.
- [26] A. MURRONE - *ECLIPPS - Adaptation de la chaîne de calcul SPIREE à la problématique du givrage*. RT Onera 7/07618 DMPH/DEFA, 2006.
- [27] J. O'ROURKE and A. AMSDEN, SAE 961961, 1996.
- [28] O. ROUZAUD, L. TESSÉ, T. SOUBRIÉ, A. SOUFIANI, PH. RIVIÈRE and D. ZEITOUN - *Influence of Radiative Heating on a Martian Orbiter*. Journal of Thermophysics and Heat Transfer, Vol. 22, No. 1, 10-19, 2008.
- [29] SCHERRER D. et al - Aerospace Lab n° 2, 2011.
- [30] L. SCHILLER, A. NAUMANN - *A Drag Coefficient Correlation*. VDI Zeitung 77, vol 15, 318-320, 1935.
- [31] D.B. SPALDING - *The Combustion of Liquid Fuels*. In proceedings of the 4<sup>th</sup> Symp (International) on Combustion, the Comb Institute, Baltimore, 847-864, 1953.
- [32] Synergy CM, <http://www-01.ibm.com/software/awdtools/synergy>.
- [33] L. TESSÉ - *Modélisation des transferts radiatifs dans les flammes turbulentes par une méthode de Monte Carlo*. Thèse de doctorat, École Centrale Paris, 2001.
- [34] L. TESSÉ, F. DUPOIRIEUX, B. ZAMUNER and J. TAINE - *Radiative Transfer in Real Gases Using Reciprocal and Forward Monte Carlo Methods and a Correlated-k Approach*. International Journal of Heat and Mass Transfer, Vol. 45, 2797-2814, 2002.
- [35] L. TESSÉ, F. DUPOIRIEUX and J. TAINE - *Monte Carlo Modeling of Radiative Transfer in a Turbulent Sooty Flame*. International Journal of Heat and Mass Transfer, Vol. 47, 555-572, 2004.
- [36] L. TESSÉ, S. AVILA, F. DUPOIRIEUX and J. TAINE - *Coupled Modeling of Aerothermochemistry, Soot Formation and Radiation in a Turbulent Diffusion Flame*. Proceedings of the 13<sup>th</sup> International Heat Transfer Conference (IHTC-13), Sydney, Australia, 2006.

- [37] B. VAN LEER - *Towards the Ultimate Conservative Difference Schemes V. A Second Order Sequel to Godunov's Method*. Journal of Computational Physics, 32 : 101-136, 1979.
- [38] F. VUILLOT, D. SCHERRER, M. HABIBALLAH - *CFD Code Validation for Space Propulsion Applications*, 5<sup>th</sup> International symposium on liquid space propulsion, Chattanooga, USA, 2003.
- [39] F.A. WILLIAMS - *Spray Combustion and Atomization*. Physic of Fluid, 1:541-545, 1958.
- [40] F.A. WILLIAMS - *Combustion Theory (Combustion Science and Engineering Series)*. Ed F Williams (Reading, MA : Addison-Wesley), 1985.
- [41] WWW CEDRE : <http://www.cedre.onera.fr>.

## Acronyms

LES (Large Eddy Simulation)

RANS (Reynolds Averaged Navier-Stokes equations)

## AUTHORS



**Alain Refloch** After obtaining his PHD in astrophysics, he worked on the realization of an accretion model for neutron stars. A. Refloch is in charge of user scientific assistance at the Vector Research Computer Centre, located on the site of the X Polytechnic Centre, which makes use of the powerful CRAY 2 super computer. He joined Onera in 1990, in charge

of the scientific computation user assistance within the Scientific Computer Department. He was behind the creation of the software engineering group in 2000. He became the CEDRE software project Leader in 2003, and joined the Computational Fluid Dynamics and AeroAcoustics Department, with his group in January 2008.



**Bernard Courbet** Ecole Centrale de Paris (1976) senior scientist in Onera. Architect of the CEDRE software, in charge of the development of CHARME solver, mainly in numerical methods.



**Angelo Murrone** Senior scientist in the Fundamental and Applied Energetics Department of Onera. His research concerns numerical modeling of "dispersed" and "separated" two-phase flows. He is currently in charge of the development of the Eulerian solver SPIREE in the Multi-physics Code CEDRE.



**Philippe Villedieu** Senior scientist in the Multiphase Flow Research Unit of Onera and associate professor at the National Institute of Applied Science (INSA) of Toulouse. He is in charge of the development of the SPARTE solver, which is the Lagrangian spray module of CEDRE.



**Claire Laurent** Masters Degree in Fluid Mechanics in 2005, PhD in Energetics and Transfer in 2008. PhD research activities focused on the droplet vaporization phenomenon (thermal conduction inside droplets, multi-component vaporization, etc.), especially on experimental validation of vaporization models and the development of numerical methods for their implementation in CFD codes. Currently research engineer in the multiphase flow group of Onera, in charge of the development of the FILM solver dedicated to the wall liquid film modeling in the multiphysics CFD code CEDRE.



**Pascale Gilbank** Université Paris VI, May 1989 "Combustion to modelisation, turbulent combustion in the case of stabilization by flame-lock", in charge of the development of the PEUL solver.



**Julien Troyes** Masters Degree in "Modelisation and Simulation in Mechanics", obtained in 1999 at Joseph Fourier University in Grenoble, France. Research engineer at Onera since November 2000. His main activity is CEDRE (software package for flow computation in energetics) validation. Apart from this general topic, his research themes are focused on solid rocket motor jet applications (infrared signatures, ignition and duct overpressure waves, etc.).



**Lionel Tesse** Received his Ph.D. degree, in energetics and physics of transfer, from the École Centrale Paris in 2001. He worked on the modeling, by Monte Carlo method, of radiative transfer in a turbulent sooty flame, focusing on the interaction between turbulence and radiation. Research scientist at Onera, in the Applied and Fundamental Energetics Department, since 2001. His research topics include modeling and simulation of radiative transfer in aeroengine combustors, solid propellant rocket motors and hypersonic flows occurring during atmospheric (re-)entries. He is in charge of the development of the ASTRE code (Monte Carlo) and is involved in the development of the REA code (DOM), both codes being dedicated to radiative transfer computations.



**Gilles Chaineray** PhD in Energetics and Transfer, in 1995. The PhD research activities were focused on study of rotating flow and heat transfer, and the development of Anisotropic Stress Model able to properly describe turbulence. Currently, research engineer in charge of the development of thermal and mechanical coupling of CFD code CEDRE with external codes such as ZeBuLoN©, ABAQUS®, MARC®, Saturne©, ...



**Jean-Baptiste Dargaud** Masters Degree in Fluid and Energetics, graduate of the INSA de Rouen in propulsion and energetics. Currently carrying out PhD research at Paris VI, as a joint venture with CNES and Onera on Ignition Overpressure and jet noise induced at launcher take off.



**Eric Quemerais** Masters Degree in "Applied Mathematics", obtained in 2000, at Rennes University. Engineer at Onera since June 2008. Main activities: CWIPI (Coupling With Interpolation Parallel Interface), development and parallelization of pre-processing and post-processing.



**François Vuillot** head of the 'software design and integration for the multi-physics and energetics unit at Onera, in charge of CEDRE software.

J. Reneaux, P. Beaumier,  
P. Girodroux-Lavigne  
(Onera)

E-mail: joel.reneaux@onera.fr

# Advanced Aerodynamic Applications with the *e/sA* Software

Numerical simulation capability is one key differentiating factor in designing efficient transportation systems. With advanced numerical simulation capabilities, complex phenomena involved can be taken into account. This is illustrated in this paper through several research studies. All the simulations were carried out with the *e/sA* software developed at Onera.

In terms of performance prediction, the capabilities of the CFD software are highlighted with various applications related to aircraft drag, control surface efficiency, high-lift configuration performance and store separation. Unsteady simulations are carried out to investigate complex interactions and off-design conditions: jet simulation, buffet prediction and dynamic stall. The importance of the coupling of different disciplines is underlined through aeroelastic, aero-acoustic and aero-thermal applications related to aircraft, helicopter rotors, engine compressors and turbines.

Performance improvement for transportation vehicles can be studied with optimization and flow control techniques. The adjoint approach has been used to optimize pylons and winglets for transport aircraft and helicopter rotor blades. Flow control is regarded as a key evolution offering new solutions for performance improvement. Control of buffet onset with Vortex Generators and separation control with synthetic jets for helicopter fuselages is presented to highlight the *e/sA* software's ability to simulate actuator effects.

Various innovative concepts have been investigated using the *e/sA* software. The flying wing, the supersonic business jet, the UCAV configuration, the Counter Rotating Open Rotor and the Tilt Rotor configurations are among the most promising ones.

## Introduction

CFD capabilities are now widely used in the aerodynamic process of any transportation system. In particular, the design and the optimization of any aerodynamic shapes are based on intensive CFD applications. The CFD approach is also more and more frequently used for the determination of aerodynamic data for performance, loads and handling qualities.

The drag component can usually be determined in cruise conditions by the use of the Reynolds Averaged Navier-Stokes equations. On the other hand, off-design conditions and complex interactions sometimes require an unsteady approach such as the RANS/LES Simulation method. In order to improve the performance of the vehicle, the design problems can be tackled with Multi-Disciplinary Optimization. Flow control technologies are also promising for enhancing the aerodynamic behavior of

the configuration. Aeroelastic and aero-acoustics issues will play a greater role in modern aerospace vehicles. To address all of these issues, Onera has been developing the *e/sA* software [1], which deals with internal and external aerodynamics from the low subsonic to the high supersonic flow regime. A large variety of turbulence models from eddy viscosity to full Differential Reynolds Stress Models are implemented in *e/sA* for the Reynolds Averaged Navier-Stokes approach. High flexibility advanced techniques involving multi-block structured meshes are available in *e/sA* for handling complex configurations: these techniques include patched grid and overset capabilities (Chimera technique). The flow equations are solved by a cell-centered, finite-volume method. Space discretization schemes include second order upwind or centered schemes. The semi-discrete equations are integrated using a backward Euler approach with implicit schemes solved by robust LU relaxation methods. The convergence is improved by the use of multi-grid techniques for steady flows.

The numerical simulations must be assessed against detailed databases for all the configurations studied and for the various flow characteristics. For each specific application, Onera carries out research projects to establish broad and accurate experimental databases including advanced measurements:

- Static and unsteady pressure acquisitions through pressure taps and pressure transducers;
- Velocity measurements in the field using PIV and LDV techniques;
- Measurement of model surface deformation with strain gauges or optical methods.

For example, the availability of field measurements makes the development and the assessment of the turbulence models and the RANS/LES approach much easier.

The various applications presented in the following sections underscore the capabilities of the *e/sA* software to simulate the flow physics that is involved in non-linear effects and in complex interactions. As the *e/sA* software is currently used by many aircraft, helicopter, missile and engine makers, the examples are taken from this wide variety of applications.

## Performance prediction

### Aircraft drag prediction

In order to enhance its knowledge of the capabilities of CFD software to evaluate the drag of transport aircraft, the Onera Applied Aerodynamics Department participated in the 4<sup>th</sup> AIAA Drag Prediction Workshop held in San Antonio, Texas in June 2009 [2]. The focus of the DPW4 was on drag and moment prediction accuracy for the new wing/body/horizontal-tail NASA CRM (Common Research Model) configuration. This workshop included a grid convergence study (multi-block structured grids from  $5 \cdot 10^6$  nodes to  $50 \cdot 10^6$  nodes provided by Boeing) and a downwash study (lift polars with tail-off and tail-on at 3 deflection angles). The aerodynamic conditions were the following: Mach=0.85 (design point) and  $Re=5 \cdot 10^6$  (NASA Ames 11-ft transonic wind tunnel conditions). Experimental data for the CRM is expected to be available in 2010; it will be used for comparison and

validation purposes. The *e/sA* calculations were carried out with the Spalart-Allmaras turbulence model in fully turbulent conditions. The solutions were finally post-processed with the Onera ffd72 far-field drag extraction tool [3].

Figure 1 presents the results from *e/sA* simulations (contours of pressure) on the NASA CRM configuration including the horizontal tail plane. Figure 2 shows the viscous and wave drag integration volumes used by the ffd72 software. It is necessary to obtain a physical drag breakdown and therefore to eliminate artificial drag. This capacity is very helpful for aircraft makers. For instance, it can be seen here that no wave drag is produced on the tail.

Very good agreement has been observed between the Onera-*e/sA* results [2] and the near-field drag coefficients (pressure and friction) computed by other DPW4 participants such as Airbus, Boeing and DLR (less than 2 drag counts of difference over around 275 of total drag counts for the structured mesh approach, a drag count being  $10^{-4}$ ). Furthermore, the far-field drag extraction tool ffd72 has given Onera the singular capability of presenting the values of the different physical drag components. For example, at  $M=0.85$  and  $C_L=0.5$ , the different drag components of the configuration under consideration expressed as a percentage of the total drag are the following: viscous drag 64% (friction drag 47% plus viscous pressure drag 17%), lift-induced drag 34% and wave drag 2%.



Figure 1 – RANS computation on the NASA CRM configuration of the 4<sup>th</sup> AIAA Drag Prediction Workshop

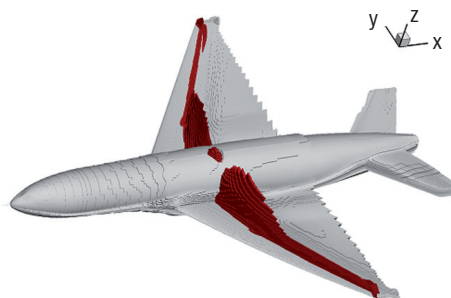


Figure 2 – Far-field drag extraction on the NASA CRM – Viscous drag (grey) and wave drag (red) productions

### Control surfaces

The determination of the efficiency of control surfaces is an important topic for the design of a modern aircraft and this must be done early in the design process. The *e/sA* software and the overset technique allow for dissociation of the structured topologies of various elements. The mesh quality of each component is increased, but complexity arises

## Box 1 - Far field drag extraction

The far-field drag extraction techniques [3] which have been developed by Onera over the past years, allow the spurious drag to be identified and removed from the drag breakdown. This spurious drag component depends on the grid refinement and quality, on the amount of artificial dissipation introduced by the numerical scheme, and on the aerodynamic conditions.

In addition, far-field drag extraction is able to produce a physical drag breakdown, which is more useful to the aerodynamicist than the pressure plus friction breakdown. This is based on the distinction between irreversible and reversible thermodynamic processes. The former imply a change in energy form and are responsible for viscous drag and wave drag. The latter involve only exchanges of mechanical energy and are responsible for induced drag. An additional advantage of the Onera drag extraction method is the possibility of obtaining a spatial distribution of the local drag.

A designer using far-field extraction besides the simpler near-field integration is then in a position to produce a more efficient shape in a smaller number of redesigns.

in the assembly phase of the various meshes. This is why Onera launched a project devoted to improving the overset technique and its assessment with a detailed experimental database [4].

The model represents a large civil transport aircraft equipped with spoilers and ailerons. The test was carried out in the Onera S2MA wind tunnel with detailed measurements such as a six-component balance, hinge moment balances for spoilers, steady and unsteady measurements, and wake surveys.

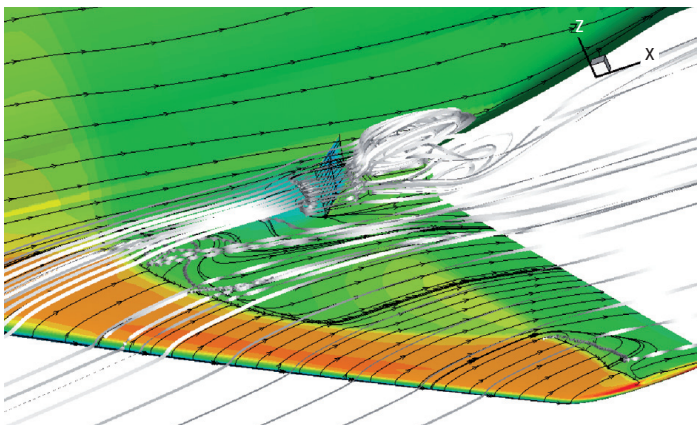


Figure 3 – RANS simulation around a spoiler in transonic flow,  $M=0.85$ ,  $\delta=45^\circ$ ,  $\alpha=3^\circ$

An example of a computation with the Spalart Allmaras turbulence model is presented in figure 3 for the configuration equipped with a  $45^\circ$  spoiler at  $M=0.85$ . The visualization underscores the complexity of the flow with strong separations upstream and downstream of the spoiler and with a deviation of the shock position compared with the span.

A comparison with the experimental results is presented in figure 4 considering pressure measurements at mid-span of the spoiler ( $y/b=0.255$ ). We can see that the CFD results agree rather well with the measurements with a good level of the computed pressure downstream of the spoiler. Many comparisons, such as the one presented above, have demonstrated the capability of the overset mesh technique to accurately predict the efficiency of the control surfaces.

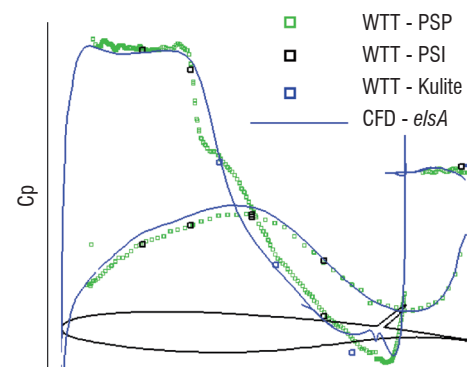


Figure 4 – Comparison between *e/sA* simulation and experiment at mid span of the spoiler,  $M=0.85$ ,  $\delta=45^\circ$ ,  $\alpha=3.95^\circ$

### High-lift configuration

Aircraft performance prediction in high-lift configurations requires good modeling of several complex phenomena such as separation and wake/boundary layer interactions, local compressible flow embedded into dominantly incompressible low Mach number regions and the transition from laminar to turbulent flows on each element. Among the various topics, an accurate estimation of the maximum lift coefficient early in the design stage is of prime importance for designers. Consequently, the following different transition mechanisms must be considered in the CFD process: Tollmien-Schlichting (TS) and cross-flow instability growths, attachment line contamination (ALT), relaminarization and separation bubble.

Transition prediction capability has been introduced into the *e/sA* code, based on the application of criteria that were developed at Onera for use in boundary layer codes. A recent implementation of a new method [5] led to the elimination of most of the topology limitations. For the streamwise instability mode, the TS criterion or the  $e^N$  method combined with Mack's relationship can be considered in combination with the Gleyzes-Habiballah criterion for 2D short bubble transition. It allows for prediction of the transition location depending on the freestream turbulence level. Crossflow instability modes have also been taken into account with a criterion based on the displacement thickness in the crossflow direction. An intermittency function  $\gamma$  is used to simulate the transition region.

In the framework of the Eurolift II project, several configurations have been considered for validation purposes [6]: a clean wing configuration at low speed, a generic high-lift rectangular wing and a more realistic three-dimensional high-lift configuration with a full span slat and flap (figure 5).

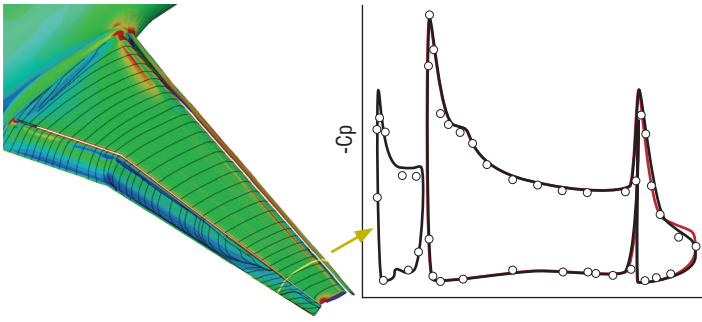


Figure 5 – Eurolift 2 configuration.  $M=0.178$ ,  $Re_c=1.38 \times 10^6$ ,  $\alpha=10^\circ$   
 Symbols: experiment, Red: fully turbulent computations, Black: transition computed internally

With a  $5.5 \cdot 10^6$  node grid provided by Airbus-Deutschland and the Spalart Allmaras turbulence model, the turbulent RANS simulation matches the experiment (Airbus-D LSWT wind tunnel test) rather well on the various elements of the wing with a slight deviation near the tip. Taking transition into account, the agreement on the flap is much better as observed on the right side of figure 5 with the disappearance of the local flow separation on the upper surface of the flap.

The use of transition prediction methods in the *e/sA* software has significantly improved the performance determination for such complex configurations. Moreover, the overset grid capability offered by the *e/sA* software is also an asset in dealing with the detailed 3D geometries of the actual high-lift configurations.

### Jet simulation

The diameter of the engines of transport aircraft has been regularly increased in recent years, requiring that they be placed nearer the wing because of ground clearance and structure constraints, thus leading to a strong interaction between the jet and the pylon. To investigate the RANS and ZDES capabilities for predicting these interaction phenomena, advanced simulations were carried out on a power-plant configuration for which a large database was assembled in the Onera S3Ch wind tunnel of the Fundamental and Experimental Aerodynamics Department (DAFE) [7].

The wall-to-wall wing model equipped with pylon and nacelle was installed in the  $0.8 \times 0.8 \text{ m}^2$  S3Ch test section of the Onera Meudon Center. The nacelle was studied and manufactured to simulate both the engine fan and core jets using an air supply system installed upstream of the nacelle. Care was taken to limit the influence of the boundary layer which develops on this system, considering boundary layer suction. The pressure ratios of the jets can be varied during the tests and the core jet temperature can be slightly increased to investigate the thermal effects. Upper and lower walls were defined to limit wall interference effects. An accurate database was established using up-to-date measurements. Probes and laser (LDV, PIV) measurements were used and analyzed considering averaged and RMS values of the flow velocity.

Simulations were carried out using the broad and accurate experimental database. These simulations were performed in order to match experiments as much as possible and for thorough assessment, including the turbulent field in the jet. Two different structured grids of respectively 20 and 40 million nodes were defined to perform the simulations: mesh adaptations were carried out to capture the mixing layers in the jets. The patched grid technique was also used to reduce the size of the meshes. In the simulations carried out with the *e/sA* software, fan and core jets were introduced thanks to injection type boundary conditions. Hybrid RANS/LES methods have attracted great interest over the past ten years as they combine the best features of the Reynolds Averaged Navier-Stokes and of Large Eddy Simulations. A Zonal DES approach [8] was chosen to avoid any difficulties when switching from the RANS to the LES mode. In this approach, the grid refinements can then be applied to the regions of interest, avoiding any detrimental influence on the boundary layer properties.

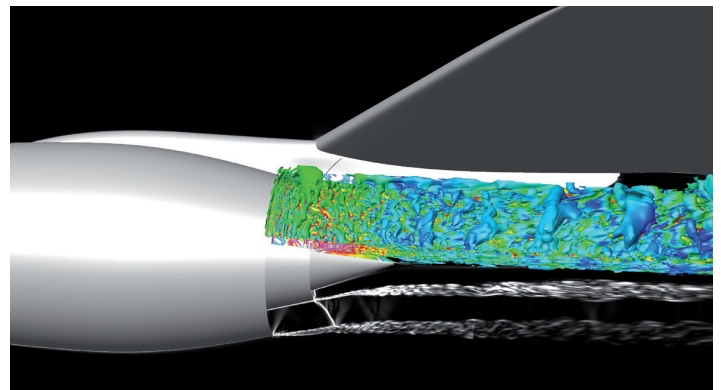


Figure 6 – Q-criterion and Schlieren type flow visualizations with Z-DES 40  $10^6$  nodes,  $M=0.84$ ,  $Re=6 \cdot 10^6$

Figure 6 presents the DES results with both the Q-criterion and Schlieren type visualization. The rolling-up of eddies in the early stage of the fan jet mixing layer can be seen. Further downstream, these eddies become streamwise due to the entrainment effects. The mixing layers between the fan and the core jets as well as between the fan jet and the flow outside of the jet are well displayed.

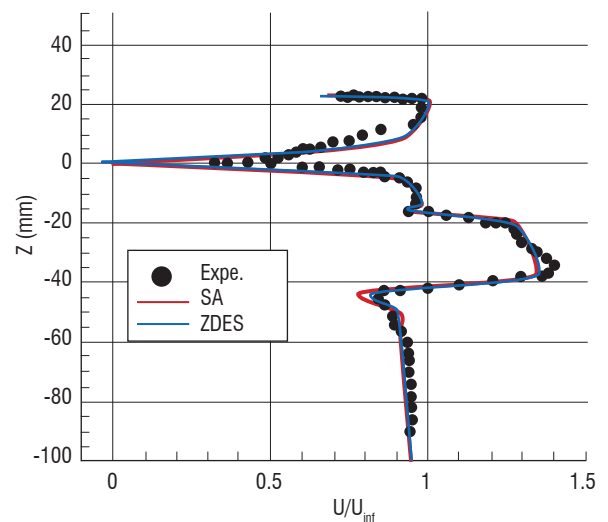


Figure 7 – Streamwise velocity profiles just downstream of the plug – Computation and S3Ch experiment

## Box 2 - DES simulation

As emphasized in the introduction, new industrial needs in aerodynamics involve for example the control of noise as well as the ability to predict dynamic loads so that the simulation of 3D unsteady turbulent flows is required. It is now commonly accepted that hybrid RANS-LES is the best strategy to drastically reduce computation costs (compared to LES) in a wide range of complex industrial applications if attached boundary layers have a significant impact on the global flow dynamics.

However, two weaknesses in the use of hybrid methods for technical flows are classically identified (see [9] for a review). The first one concerns a possible delay in the formation of instabilities in mixing layers due to the advection of the upstream RANS eddy viscosity. The second one deals with the treatment of the “grey-area”, where the model switches from RANS to LES, and where the velocity fluctuations, the “LES-content”, are expected to be not sufficiently developed to compensate for the loss of modeled turbulent stresses. This can lead to unphysical outcomes, such as an underestimation of the skin friction and at worst may it can cause premature separation or “Grid-Induced Separation” (GIS).

In order to get rid of this latter drawback, Spalart et al.[10] proposed a modification of the model length scale presented as a Delayed Detached Eddy Simulation (DDES) to delay the switch into the LES mode to prevent “model-stress depletion” (MSD). In a different spirit, Deck [8][11] proposed a Zonal Detached Eddy Simulation (ZDES) approach, in which the RANS and DES domains are selected individually. The motivation is to avoid MSD and to clarify the role of each region. In practice, ZDES switches very quickly to the LES mode, thus limiting the grey area, which is responsible for the delay in the formation of instabilities. Moreover, the valuable aspect of this approach is that the user can focus his grid refinement on regions of interest without corrupting the boundary layer properties farther upstream or downstream.

The ability to simulate three-dimensional flows in the framework of applications (attached boundary layers treated in RANS mode) has already been demonstrated thanks to thorough comparison with the available experimental data including spectral and second-order analysis (see [12] for a review).

The computed mean velocity profiles are compared with experiments (LDV profiles) in the section just downstream of the plug in figure 7. Results obtained with ZDES and RANS simulations exhibit very close characteristics when averaged fields are considered. The mixing layers are very well predicted, the wake of the upper side of the plug is slightly underestimated. Some discrepancies could come from the system for injection into the nacelle which is not taken into account and simulated with uniform injection conditions.

The  $u'w'$  unsteady component is presented in figure 8 for the RANS and ZDES simulations, and the experiment at the location just downstream of the plug. This turbulent quantity is underestimated in the mixing layer between the fan jet and the outer flow by both simulations, especially the ZDES. The mixing layers between the core and fan jets are well predicted by the ZDES simulation and underestimated by the RANS approach. In addition, the ZDES method allows all the turbulent components to be computed easily, contrary to RANS simulation.

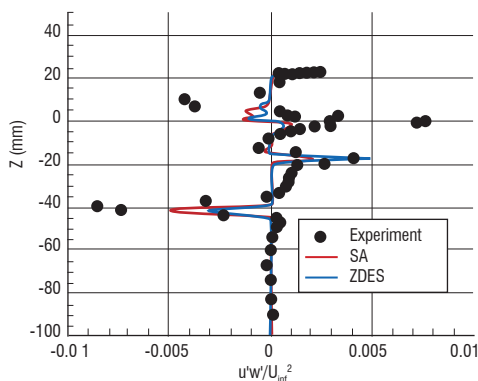


Figure 8 – The  $u'w'$  unsteady component just downstream of the plug - Computations and S3Ch experiment

The value of ZDES simulations for such configurations lies in the very large amount of information it produces together with direct access to the flow unsteadiness. This allows for a very deep analysis of turbulent structures inside mixing layers and of the interaction between the pylon wake and the jet. It is expected that the ZDES approach will open up new possibilities in the future for thermal effects and airframe noise prediction.

### Simulation of phenomena at the limits of the flight domain

#### Buffet prediction

Aircraft in flight can be subject to buffet excitation. This phenomenon is defined as the structural response to an aerodynamic excitation produced by boundary layer separations. In the case of civil transport aircraft, buffeting may cause discomfort for passengers and difficulty for the pilot to control the aircraft and can also lead to structural fatigue. Thus, buffeting limits the flight envelope in terms of lift coefficient - Mach number boundaries. The buffet onset is measured in wind tunnels using models equipped with accelerometers and unsteady pressure transducers. The prediction of buffeting in flight remains difficult however. From the aerodynamics side, the scale effects modify the extent of flow separation areas. Moreover, wind tunnel models do not have scaled inertial properties.

This is why a combined experimental and numerical approach is important to better understand and predict the physical phenomena linked to the fluctuating pressures. Hence, the Detached-Eddy-Simulation could be used to predict the main instabilities of the flow and to improve the extrapolation of wind tunnel results to flight conditions.

The assessment of the DES approach was carried out considering a wing body configuration which was tested in the S3Ch transonic research wind tunnel of the Onera Meudon center. The patched-grid method is applied in order to perform accurate simulations in the ZDES region and to limit the grid density in other RANS regions. The grid is composed of about 33 million nodes, most of them in the ZDES separated region. A simulation was performed at  $M=0.82$ ,  $Re = 3 \cdot 10^6$ , in established buffet conditions.

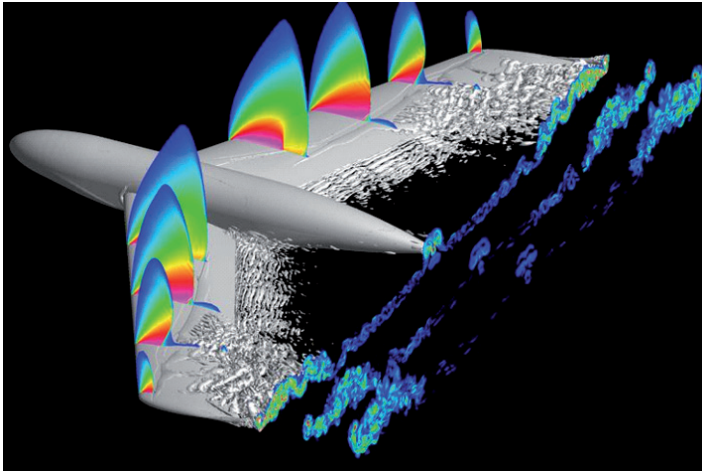


Figure 9 – ZDES computation in buffet condition.  $M=0.82$ ,  $\alpha=3.5^\circ$

In these flow conditions, a massive separation occurs and extends from the shock foot to the trailing edge in the outer part of the wing. This separated area is highly unstable and triggers the shock movement, and the buffet. The Q-criterion in figure 9 shows the roll-up of eddies in the separated area and the effect of the instabilities of the separation and the shock shape. This phenomenon, characterized by a moving separation line as well as a separation located close to the upper surface of the wing, is a very challenging and complex test case for a DES-type simulation.

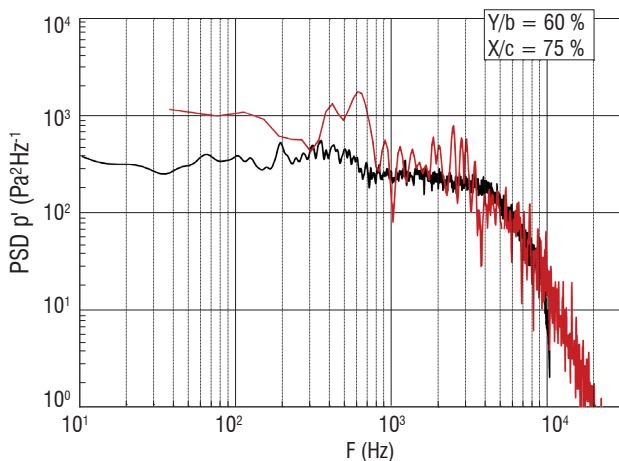


Figure 10 – Comparison of power spectral density in ZDES simulation and experiment

The power spectral density of the fluctuating part of the pressure signal at the upper side of the wing inside the separation is compared in figure 10 between an experiment and the ZDES simulation. It appears clearly that levels in the low frequency band are slightly overestimated but are properly predicted in the higher frequencies. Indeed, in these flow conditions, the buffet phenomenon is slightly over estimated which is

probably the consequence of a still too coarse grid in the separated region. Nonetheless, only ZDES type simulations allow such spectra to be obtained.

## Dynamic stall

Among aerodynamic issues encountered on helicopter rotors, dynamic stall [13] is certainly the most challenging, both in the understanding of the physical phenomena and their numerical simulation. Dynamic stall mainly occurs on the retreating blade side, where the blade operates under small velocities and large angles of attack. In these conditions, the flow over the blade section separates abruptly with the formation of a strong dynamic stall vortex that leads to a brief increase of maximum lift and very large negative pitching moments, with consequences on the aeroelastic stability of the rotor.

The numerical prediction of such unsteady, turbulent, compressible flows is very complex. Several Onera internal projects have been dedicated to this topic. In the PRF “Dynamic Stall”, large efforts were made in order to get rid of numerical errors as much as possible by trying to define well-adapted refined grids. From a modeling standpoint, the sensitivity of the numerical results to the modeling of turbulence has been assessed and one of the main conclusion is that it is essential to be able to capture the laminar to turbulent boundary layer transition as accurately as possible in order to obtain results not too far from the measurements, at least when the Mach number is low ( $M < 0.2$ ).

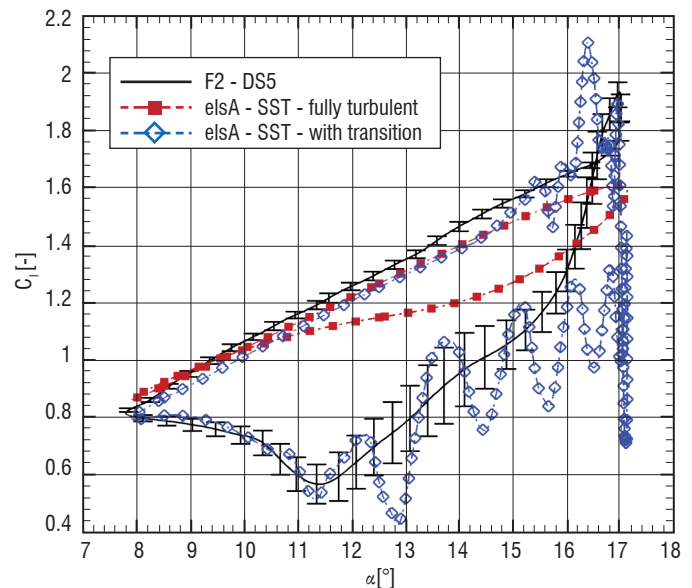


Figure 11 –  $C_l$  history of the OA209 airfoil under dynamic stall.  $\alpha=12.5^\circ \pm 4.6^\circ$ ,  $k=0.1$ ,  $Re=1.10^6$ ,  $M=0.1617$

As an example, figure 11 shows the lift history of the OA209 airfoil under dynamic stall conditions: the fully turbulent calculation in red is unable to predict the large hysteresis effects present in the measurements. When an adequate transition model is applied (blue curve), the predicted lift history becomes much better compared to the experiment, even if the airfoil tends to stall slightly too early.

However, transition is not the only concern as shown by figure 12 where the iso-contours of the velocity field are compared with the F2 experiment at the beginning of the downstroke for 2 fully turbulent computations, one with the SST and the other with the EARSM model. While the first

turbulence model does not provide any stall, but only very limited trailing edge separation, the algebraic Reynolds stress model does predict stall, although the leading edge separation is still missed.

Research efforts are now being oriented towards more advanced numerical models such as DES, LES or coupled RANS-LES methods in order to improve the fidelity of the numerical approach. The validation of these methods has been initiated for simple conditions (2D oscillating airfoil), but today would require computational efforts that are too large for realistic applications (3D rotating blade). Another important research orientation is the acquisition of experimental databases that are accurate enough not only to validate the calculations but also to improve our understanding of the physics. This is one of the objectives of the ongoing Simcos project, which aims at developing technologies to control dynamic stall. Promising wind-tunnel test results were recently obtained through the use of deployable leading-edge vortex generators.

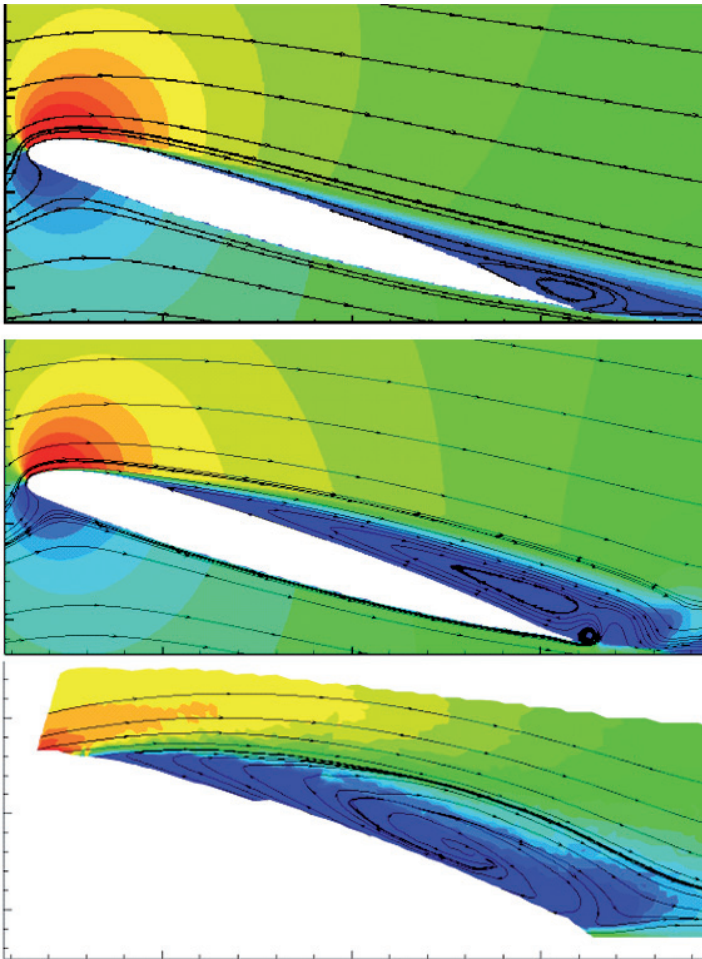


Figure 12 – Effect of turbulence model on the mean velocity around the OA209 airfoil under dynamic stall. Top: *elsA* (SST, fully turbulent). Middle: *elsA* (EARSM, fully turbulent). Bottom: LDV measurements.  $\alpha=17^\circ$ ,  $k=0.1$ ,  $Re=1.10^6$ ,  $M=0.1617$

### Store separation

With the increasing number of weapons carried under combat aircraft, the study of store separation is becoming more and more challenging. Moreover, the proximity and multiplicity of stores coupled with wider transonic firing ranges (over Mach 0.9) induce important flow interactions between the released weapon and the aircraft. To ease the meshing and flow simulation of such complex configurations, we

can use the Chimera method implemented in *elsA*, which enables a discretization of the flow equations in meshes composed of overset structured grids.

Within the framework of a national project, numerical simulations as well as experimental wind tunnel tests were carried out and helped to calibrate and validate the *elsA* Chimera method on heavy weapon separation configurations. Figure 13 illustrates the insertion of a generic cruise missile under the wing of a combat aircraft at a specific separation position. It also shows the ability of the Chimera method to capture the flow interaction between the wing and the missile, especially the transonic interaction shocks.

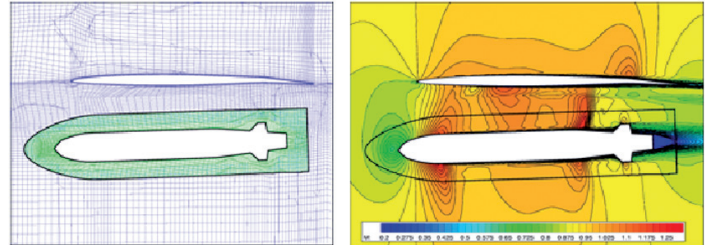


Figure 13 – Grid and Mach number in the symmetry plane of a generic cruise missile

The accurate simulation of a store separation requires the perfect restitution of the flow field under aircraft that are usually heavily loaded, which means meshing every carried store as finely as possible. Use of the Chimera method allows for separate accurate meshing of each store and its integration under the store free aircraft. This approach is used to analyze the aerodynamic characteristics of a rocket during its release from an aircraft. In this case, the tanks, the pod, the central pylon and the rocket are inserted in the grid of the plane limiting the number of nodes of the whole structured mesh to  $15 \cdot 10^6$  with a fine representation of each element.

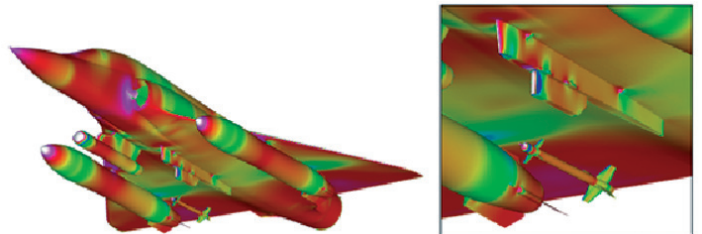


Figure 14 – Skin pressure in the case of the rocket separation

Figure 14 illustrates the skin pressure obtained in the early phase of the rocket separation. We can see the complexity of the flow field, especially around the pod and the pylon of the rocket. The Chimera technique allows for precise simulation of the complex flows under heavily loaded combat aircraft and for better prediction of the aerodynamic coefficients of the store while it is interacting with the carrier.

Within the framework of separation studies, another advantage of the Chimera method is that the released store can be repositioned anywhere under the aircraft without needing any mesh adaptation. This allows for quite simple CFD and 6 degrees of freedom flight mechanics coupling in order to compute the real trajectory of the store.

## CFD - wind tunnel synergy

The CFD approach can also be used to better understand the flow quality in the wind tunnels and to improve the wall and sting correction methods [14], [15]. Simulations of the wind tunnel with the model and supports are facilitated by some characteristics of the *elsA* software such as the patched grid and overset capabilities.

One example is given in figure 15 with a set-up in a low speed wind tunnel. The model is installed on a mast and a survey device is used to carry out wake measurements. In this research, the RANS simulations have been used to investigate the interactions between the different elements and in particular their impacts on the drag component. The flow field distortion caused by the mast and the survey device were deduced by comparing simulations with and without supports.

From a more general point of view, simulations have demonstrated the need to carefully account for Mach number and angle of attack corrections for each support in order to achieve good accuracy.

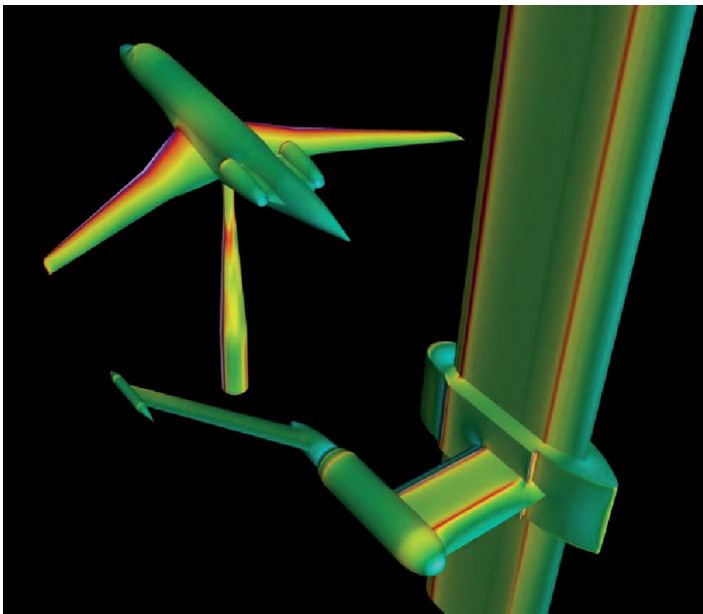


Figure 15 – Use of RANS approach to investigate the interactions between the model, the vertical strut and the probing devices in the F1 low speed wind tunnel

## Aeroelasticity

Computational Aeroelasticity (CAE) is playing an increasing role in the design and analysis of aerospace vehicles. The two examples given in this section illustrate the current state of the CAE capabilities developed in the “Aeroelasticity and Structural Dynamics” Department for the two main areas of application: airframe and turbomachinery.

### Static aeroelastic coupling on a transport aircraft

Accurate prediction of the steady state flow characteristics around a modern flexible transport aircraft requires the taking into account

of structural deformations, through a fluid-structure static coupled simulation. This section demonstrates the static aeroelastic capability of the *elsA* software in the case of a wing/body/pylons/nacelles model [16] studied in the framework of the AWIATOR European project.

The multi-block structured grid used for the aerodynamic computation includes about 7 million nodes. A subset of structural nodes, located on the wing and winglet, has been selected in the Nastran finite element structural model, in order to build the reduced flexibility matrix which is used in the fluid-structure coupling process.

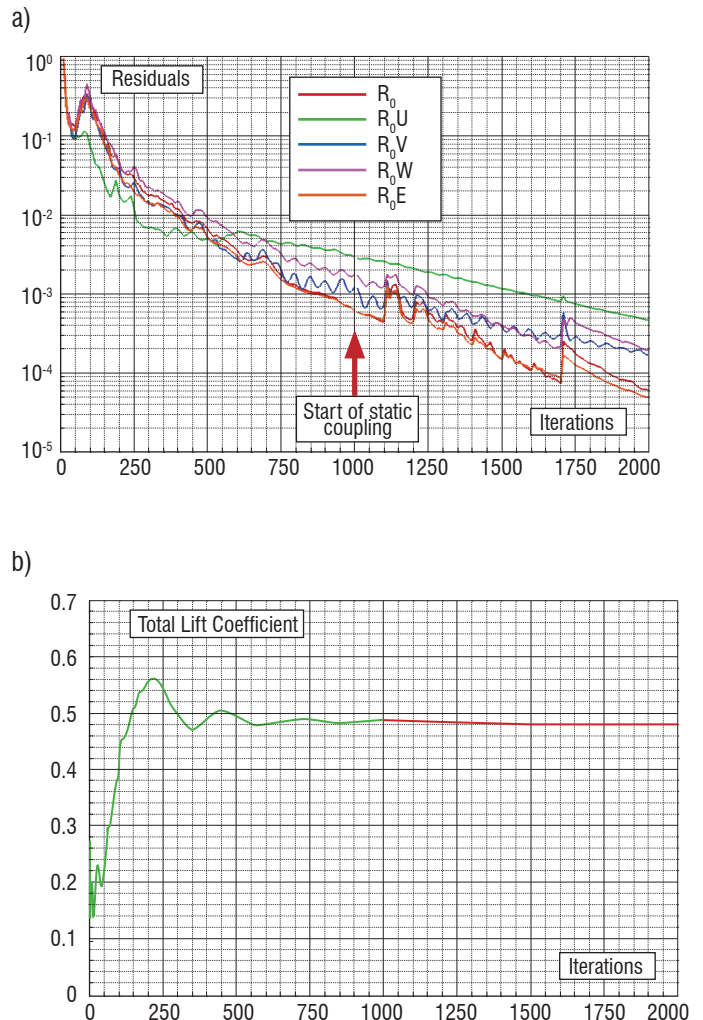


Figure 16 – Convergence of the mean flow residuals, and lift coefficient history

The flow conditions correspond to transonic speed at Mach number 0.82, for a flight altitude equal to 36,000 feet and a global lift coefficient equal to 0.49. The angle of attack has been adjusted in the numerical simulation in order to match this lift coefficient. Static coupling may be run in *elsA* starting either from the undeformed jig shape or from any deformed shape. In the latter case, it is necessary to provide the initial structural deformations. In the present case, the numerical simulation has been achieved starting from an initial “estimated flight shape” provided by Airbus.



Figure 17 – Wall pressure on the AWIATOR configuration

The 1-equation Spalart-Allmaras turbulence model has been used for the turbulence modeling. 1,000 iterations were first performed without static coupling in order to get an aerodynamic field consistent with the initial estimated flight shape, and 10 coupling cycles, with 100 flow iterations per cycle, were then computed. The structural deformations and the aerodynamic grid are updated at each coupling cycle, using the mixed analytical Transfinite Interpolation mesh deformation technique included in *e/sA*.

A 4-order magnitude decrease of the mean flow residuals was reached at the end of the simulation (figure 16). There was good agreement between the computed and measured pressure distributions in different wing sections, as shown in figure 17 and figure 18, although the computed shock locations are slightly more upstream in the middle region of the wing. As far as the wing deformations are concerned, it can be seen in figure 19 that the predicted spanwise wing vertical bending and twist deformations compare very well with the flight test measurements using the photogrammetry technique.

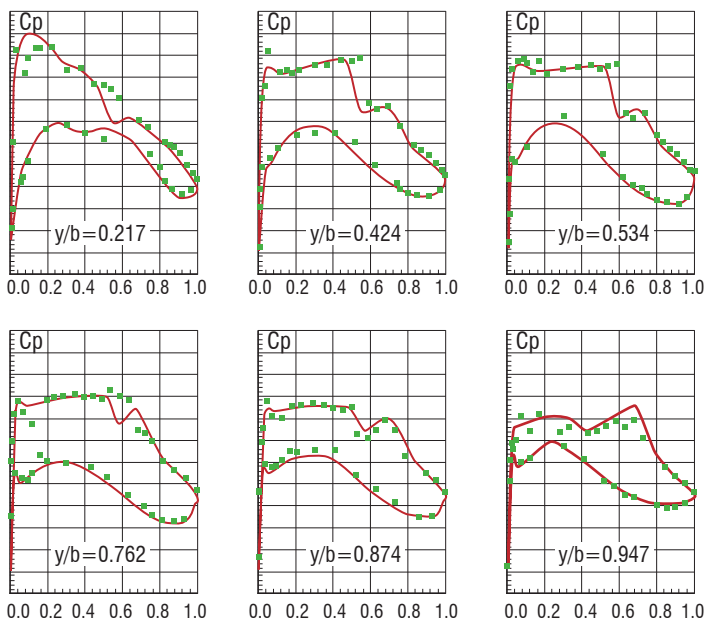


Figure 18 – Pressure coefficient distributions in several wing sections compared to flight measurements

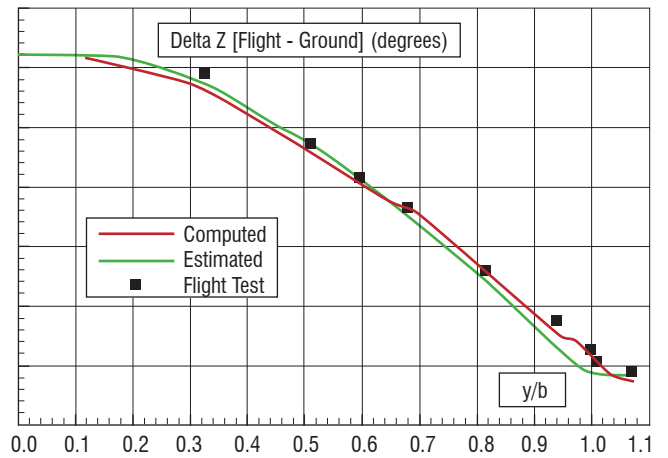
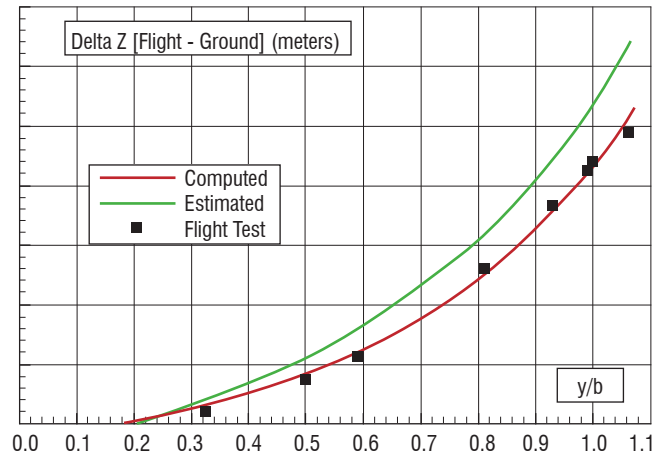


Figure 19 – Spanwise evolutions of vertical bending and twist deformations compared to flight measurements

### Axial compressor aeroelastic stability analysis

One major issue in the aeronautical turbofan design process is to ensure engine safety over its entire operating range. The design process must therefore include flutter clearance procedures. During the 80's and 90's, linear unsteady methods were widely used in the subsonic and supersonic regimes to analyze the occurrence of flutter on aeronautical structures, and they are still used as an industrial design tool. However, the design of many of today's aeronautical structures requires a better understanding of the steady and unsteady aerodynamic field, especially in the case of the transonic regime where strong non-linearities like shocks and boundary layers may occur. RANS and URANS simulations are now more and more commonly used for such purposes, at a much higher computational cost. Moreover, in the field of turbomachine aeroelasticity, additional complexities must be considered due to the effect of rotation and cyclic periodicity which leads to complex unsteady aerodynamic flows.

A numerical study was carried out at Onera (Aeroelasticity and Structural Dynamics Department) to analyze the aero-elastic stability of the compressor wide chord fan wheel model of a civil transport aircraft engine [17] with an unsteady Navier-Stokes approach. The objective of such simulations is to extract the aeroelastic damping of the structural modes of vibration for several operating points of the engine, in order to evaluate the dynamic aeroelastic stability of the fluid-structure coupled system.

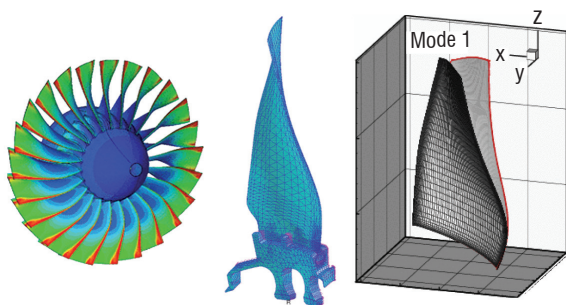


Figure 20 – Aerodynamic model - Structural fan model - First bending mode shape

The industrial fan model implemented for this study is a 24-blade wheel (figure 20). Several operating points of interest at 70 % of the nominal speed were investigated in the aeroelastic analysis, ranging from low compression up to near stall cases.

The dynamic structural behavior of the fan is represented by a finite element structural model made of roughly 50,000 grid nodes. Cyclic symmetry boundary conditions are defined at the disc sector boundaries. Complex modal bases are computed for various inter-blade phase angle values, taking into account the rotation effects of centrifugal stiffening and the gyroscopic damping.

Several aerodynamic modeling approaches have been considered. According to the cyclic periodicity of the system, single channel modeling is possible, thanks to the use of periodic boundary conditions. However, in order to take into account the incidence, distortion at inlet or geometrical or structural disturbances, it may still be necessary to model the entire 360° wheel.

In the first case, a single channel of the engine is represented using a 4 block and  $0.8 \cdot 10^6$  cell Navier-Stokes structured grid. Steady and unsteady flows are computed using the Spalart-Allmaras turbulence model and the multi-grid convergence acceleration technique. In the second approach, a complete 360°, 24-blade model was built, leading to a 60 structured block grid counting about  $20 \cdot 10^6$  cells.

Unsteady harmonic forced motion aeroelastic simulations were performed in order to get the generalized aerodynamic forces necessary to analyze the aeroelastic stability of the fan in its operating domain. These simulations were carried out using the URANS/dual time stepping classical approach (DTS), for both single sector and 360° models. Harmonic balance techniques (TSM) [18] are also now available and have been implemented and compared to the URANS results.

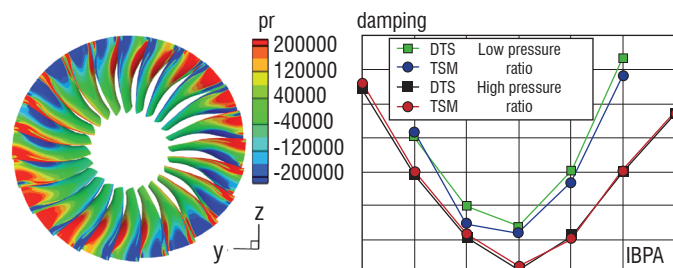


Figure 21 – Unsteady pressure harmonic analysis – Aeroelastic damping versus inter-blade phase angle

Figure 21 presents the evolution of the aeroelastic damping of the first bending mode, for both methods, and two operating points. A minimum aeroelastic damping is obtained for critical values of the inter-blade phase angle for near stall operating conditions. Such simulations are now implemented by the SAFRAN group for the evaluation of the aeroelastic stability of axial and centrifugal compressors.

### Aero-acoustics

Over the past few years, the use of CFD has been intensified for noise prediction and reduction. Among the on-going Onera areas of activity, we can cite aerodynamic noise of high-lift devices and landing gears for transport aircraft, jet noise of turbofan engines, and noise produced by propellers and helicopter rotors. Since the full aero-acoustic simulation of such configurations is out of reach, the most common strategy involves coupling of the simulation of unsteady near field aerodynamic sources and acoustic propagation in the far field, with the near field noise sources being predicted by the use of Euler, URANS or RANS/LES approaches. The Blade Vortex Interaction noise, typical of helicopter applications, has been selected in this paper to illustrate the current CFD capabilities.

Major research efforts were made for prediction of Blade Vortex Interaction noise, which remains the primary source of noise pollution in usual descent flight conditions. For many years the CFD simulation of this phenomenon, consisting of the interaction between the blades and the rotor wake, remained an important challenge as it required accurate capture and long conservation of the blade tip vortex during the rotor revolution. Within the framework of the French-German program SHANEL, the baseline HART configuration of the BO105 rotor in descent flight was used to test and validate recent developments of the *e/sA* code [19].

In a first step, an assumption of rigid blades is made and there is no coupling between the CFD and the rotor dynamics during the rotation (the kinematics of the blades are prescribed). In order to take into account the blade motion, the Chimera technique is used to overlap the different meshes. The effect of the blade grid refinement and of two different approaches for the background mesh is studied. A multi-block grid has been “manually” realized with different spatial resolutions (for a blade chord  $c$ , the coarse grid corresponds to  $\Delta h = 0.3c$ , the standard one to  $\Delta h = 0.15c$  and the fine one to  $\Delta h = 0.075c$ ). A specific solver for Cartesian grids (named Cassiopée) has been developed at Onera. It generates and automatically adapts Cartesian background grids

around a body. Several inviscid unsteady computations have been realized to study the effect of timestep, blade grid or background grid resolutions and to test high-order space schemes. On the finest mesh (figure 22), the wake structure is quite accurate with a strong vortex intensity kept during about 1.5 revolutions, which is necessary for the interaction with the following blades.

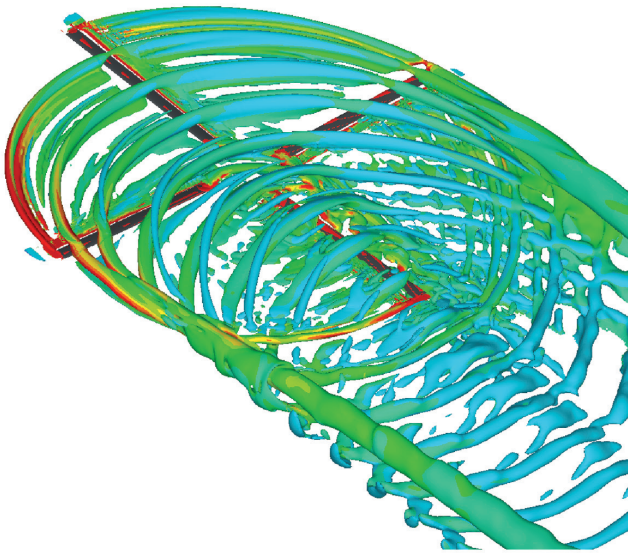


Figure 22 – Wake structure of the BO105 rotor in descent flight. Fine grid resolution

Figure 23 shows the evolution of the sectional lift coefficient  $C_z M^2$  at  $r/R=0.87$  on the advancing side. The multi-block background mesh resolutions are compared: for the coarse grid, no BVI oscillation is present. For the standard mesh ( $8 \cdot 10^6$  nodes), the most important peaks are simulated. Finally, the amplitude and the phase of all oscillations are improved with the finest mesh. Similar comparisons have been made for different numerical schemes tested on the Cartesian coarse grid. The order of both scheme and Chimera interpolations has been studied. The third order in spatial scheme noticeably improves the solution, as some BVI oscillations appear even on the standard mesh. Moreover, matrix dissipation of the Jameson scheme yields a solution comparable to the one obtained on the fine mesh ( $30 \cdot 10^6$  nodes).

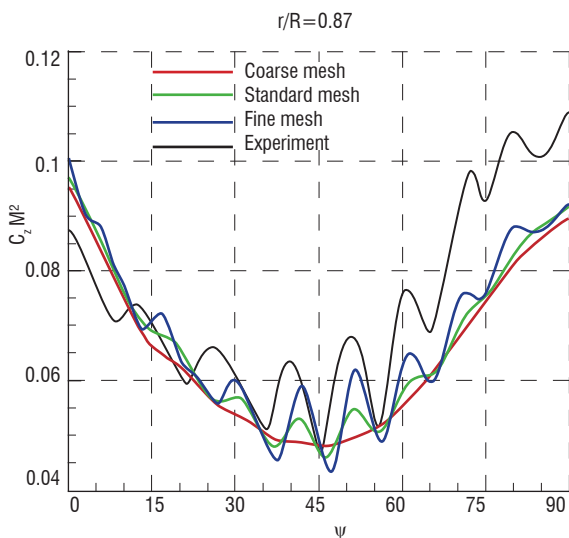


Figure 23 – Influence of mesh refinement on airload fluctuations: Advancing side Blade-Vortex-Interaction peaks

An acoustic post-processing of these CFD results has been performed by the multi-application acoustic code KIM using an integral method developed at the Onera Computational Fluid Dynamics and Aero-acoustics Department. There is a significant improvement of the noise level prediction for both the advancing and retreating blade sides, while passing from the standard to the fine mesh. The maximum noise level is increased by 7 dB and the under-estimation is reduced to 3.5 dB when comparing with the corresponding measured level. These results are very encouraging for BVI capture and understanding. Future steps in this study will consist of taking viscous effects into account and performing the coupling between aerodynamics and dynamics for a better prediction of aero-elastic effects.

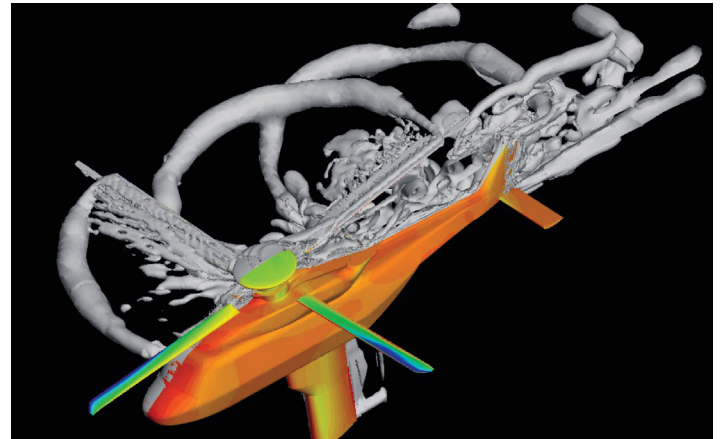


Figure 24 – Simulation of a complete helicopter configuration (including main and tail rotors) by a Chimera Cartesian technique

Another challenging application would be the prediction of the tone noise radiated by a complete configuration, such as the one studied in the GoAhead project and illustrated in figure 24.

### Thermal effects

The prediction of aero thermal effects on industrial turbines is a key aspect in the dimensioning of the mechanical parts located downstream of the combustion chamber outlet. A significant effort has been made over the past few years to validate the *elsA* code for aero-thermal applications, especially in the TATEF2 European project [20].

Time accurate simulations of the TATEF2 one stage HP turbine were carried out with *elsA* using the phase-lagged (Chorochronic) technique which allows for reduction of the computational domain to one channel of the stator and the rotor.

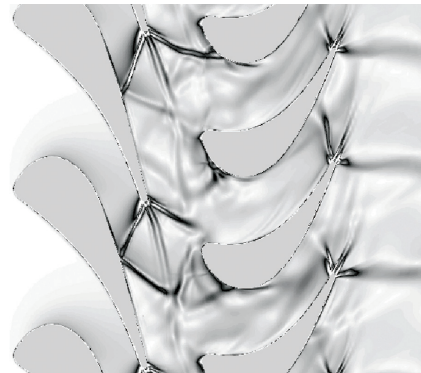


Figure 25 – Visualization of density gradients from the simulation of the TATEF2-VKI HP turbine

The configuration is characterized by the presence of strong shocks appearing on the VKI highly loaded turbine, as illustrated in figure 25 where the trailing-edge shock impact of the neighboring blades can be clearly identified.

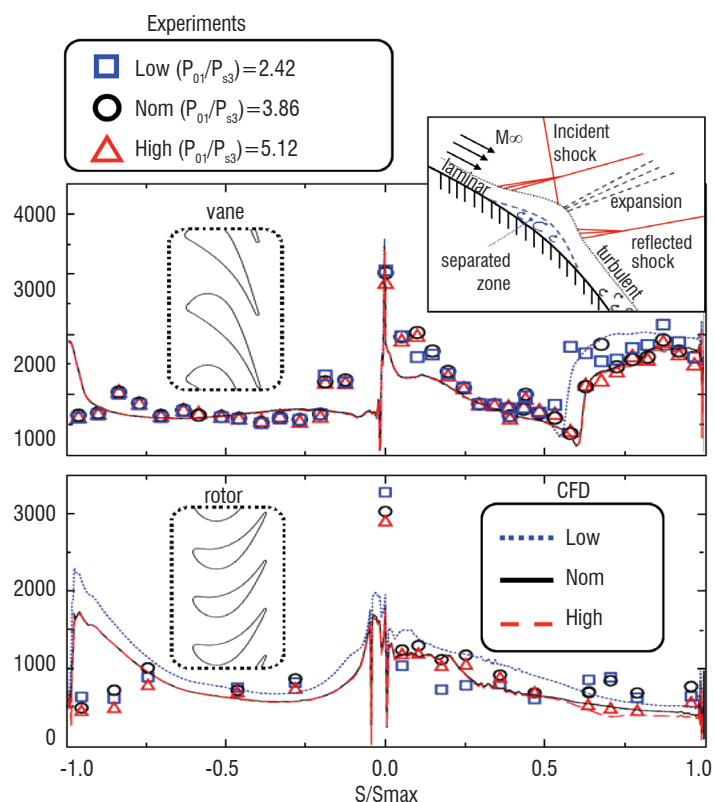


Figure 26 – Comparison between measured and calculated Nusselt number distributions (Tatef2-VKI HP turbine)

Figure 26 compares the Nusselt number distribution on the stator and the rotor for 3 different pressure ratios (Low, Nom and High). A good correlation is obtained, especially on the stator, where we can observe on the suction side the impact of the shock from the neighboring blade generating a laminar-turbulent boundary layer transition associated with an increase of heat fluxes. The improvement of such simulations would require more adapted turbulent and transition models, which is certainly a key topic of research in the near future.

## Performance improvement

Environmental factors, such as fuel consumption and air pollution, will play an important role in the future growth of the transportation system. It is imperative to improve vehicle performance. For this reason, the use of design techniques such as numerical optimization is becoming increasingly attractive. Three applications of optimization techniques are presented in this section: pylon and winglet optimization for civil transport aircraft, and helicopter blade optimization. The three applications are based on the use of gradient methods and the discrete adjoint technique which is implemented in the *e/sA* software.

## Optimization

### Pylon Optimization

The increasing size of modern aircraft engines with high by-pass ratios leads to increasing complexity of engine integration under the wing. For engine installation design, the use of the numerical optimization approach is a straightforward way to deal with the numerous aerodynamic and geometrical constraints. Furthermore, as the drag and weight penalties are of the same order of magnitude, Multi-Disciplinary Optimization could be an efficient approach to take both Aerodynamics and Structural Mechanics into account during the design [21].

As an example, the application of a hierarchical optimization for engine pylon design carried out in the VIVACE European project is presented in this section. The design of the outer board pylon of a large transport aircraft is examined in cruise conditions  $M=0.85$ ,  $Re=20 \cdot 10^6$ .

Three parameters identified as having an impact on both disciplines are considered at the higher level:

- X the variation of longitudinal position of the engine;
- Z the variation of vertical position of the engine;
- W the variation of the pylon width.

The optimization at the higher level is carried out thanks to surrogate models. This approach requires that configurations be sampled in the high level design space and optimized on the disciplinary level by varying low level parameters.

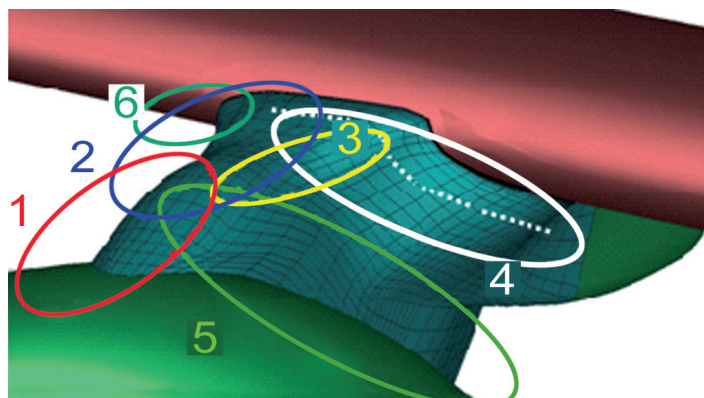


Figure 27 – Design parameters for the aerodynamic optimization of the outer pylon

The surrogate model for Aerodynamics is built with 9 samples. Each of them undergoes aerodynamic optimization carried out by a gradient method. At this lower level, parameters deal with the shape of the aerodynamic fairings as shown in figure 27. The parameterization considers 17 bumps spread on the pylon in different areas. The bumps are defined with Hicks-Henne functions in the direction of the flow whereas a cubic spline interpolation is used in the transverse direction.

In order to capture the complex transonic flow during the optimization process, the RANS approach was considered but the boundary layer was only computed accurately around the wing and the outer pylon. The corresponding mesh has  $1.5 \cdot 10^6$  nodes.

### Box 3 - Adjoint approach

Shape optimization aims at minimizing an objective function  $J$  while satisfying inequality on constraint functions  $G_k$  ( $G_k \leq 0$   $k \in [1, nc]$ ). In the framework of CFD-based optimization, all functions depend on a vector of design parameters  $\alpha = (\alpha_1, \alpha_2, \dots, \alpha_{n_p})$ , through the volume mesh,  $X$ , and the flow field,  $W$  (that is  $J(\alpha) = J(W(\alpha), X(\alpha))$ ,  $G_k(\alpha) = G_k(W(\alpha), X(\alpha))$ ) which are linked by the discrete equations for fluid dynamics:  $R(W(\alpha), X(\alpha)) = 0$ . Most often, the number of functions of interest is much smaller than the number of design parameters ( $1 + nc \ll n_p$ ).

The derivatives of the objective function and the active constraints (i.e. reaching their null bound) at the current shape represent important information for doing the optimization. These derivatives can be computed by a non-intuitive method, the adjoint vector method, whose cost is almost independent of  $n_p$ , the number of design parameters, contrary to all simpler methods.

A detailed presentation of the method, in particular a discussion about how to get not only a low CPU cost, but also low memory requirements can be found for example in [22].

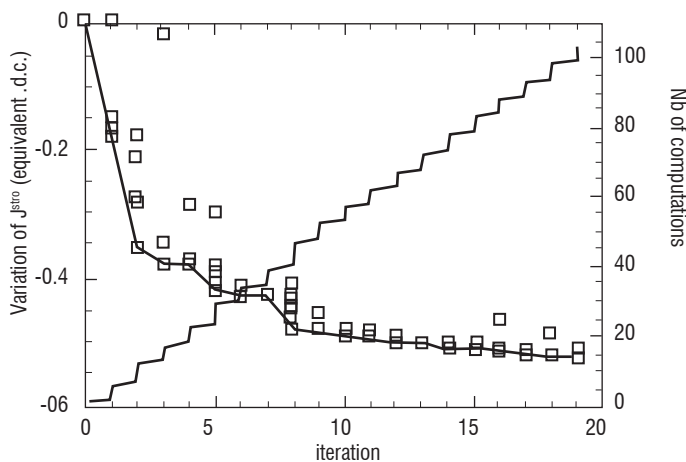


Figure 28 – Convergence of the aerodynamic optimization.

The selected optimization method requires knowledge of the gradient of the objective function which is computed by use of the RANS discrete adjoint approach implemented in the *elsA* software. To qualify the accuracy of the gradient predicted by the adjoint method, it was compared with a gradient obtained with finite differences on six design parameters controlling the height of six Hicks-Henne bumps. The agreement is moderately accurate for the dominant components, with a relative error in the 5-30% range. Keeping in mind the difficulty in deriving a finite difference gradient strictly independently of the chosen step, this was considered satisfactory enough for the purposes of the study.

Figure 28 presents the convergence of the aerodynamic optimization for one configuration. The results are satisfactory with most of the drag gain achieved with a few optimization iterations. After optimizing the configurations defined by the 9 high-level parameters, the aerodynamic response surface was established. The main trends obtained were the following:

- The drag is decreased when the engine is moved upstream;
- A wider pylon seems to decrease the drag in the investigated width range;
- The sensitivity of drag with respect to the Z variable is low.

The elaboration of this structural response surface will not be depicted in this section. Gathering information from the structure and aerodynamic surrogate models allows us to derive response surfaces for the multi-disciplinary problem.

This example has shown that an MDO approach could be used to reduce the number of design loops between disciplines. The local aerodynamic optimizations have been carried out with a gradient-based technique relying on the efficient adjoint approach implemented in *elsA* software for viscous flows.

#### Winglet optimization

The second application presented in this section focuses on the design of an integrated winglet for a civil transport aircraft. The design of such a wing-tip device is mainly driven by two disciplines, aerodynamics and structures [23]. For a fixed wing span, the use of an integrated winglet offers cruise performance improvements thanks to a lift-induced drag reduction. However, these aerodynamic characteristic improvements induce an increased structural weight of the wing due to the additional aerodynamic bending moment.

The winglet was designed by numerical optimization considering three design parameters: the winglet height, its leading edge sweep angle and its tip aerodynamic twist. All the aerodynamic analyses were carried out with the *elsA* software in the RANS mode with the Spalart Allmaras turbulence model. The different grids needed during the optimization were produced with an in-house analytical mesh deformation procedure applied to the baseline configuration grid produced with the ANSYS-ICEM-CFD mesh generator (400,000 nodes). The structural modeling used in this study, defined by the Aeroelasticity and Structural Dynamics Department, is based on the MSC-NASTRAN Finite Element software. The NASTRAN optimization capabilities were used to size the wing box structure by minimizing the structural weight of the wing. The aerodynamic loads of a 2.5 g maneuver have been used to stress the structure in this structural sizing process. The total wing weight has been estimated with the previous procedure for a set of different winglet geometries sampling the intended design space. The different results were used to build a surrogate model of the variation of the total wing weight.

The optimization problem has been formulated as a minimization problem of an aero-structure composite objective function defined as:

$$J(\alpha) = \Delta CD_{cruise}(\alpha) + \Delta weight(\alpha)/k$$

With  $\alpha$  being the design variables,  $\Delta CD_{cruise}$  the variation of the aerodynamic drag coefficient in cruise conditions,  $\Delta weight$  the variation

of the structural weight of the complete wing structure with respect to the baseline configuration and  $k$  a trade-off coefficient.

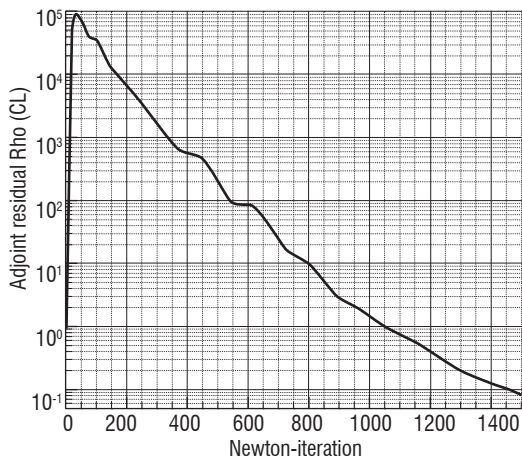


Figure 29 – Convergence of the Adjoint in transonic viscous flow

The optimization was based on the use of the DAKOTA optimization toolkit and the gradient optimizer CONMIN implementing the method of the feasible directions. The gradient of cruise lift and drag were computed by the Adjoint technique offered by the *elsA* software. As an example, figure 29 presents the good convergence of the adjoint residual versus the Newton-iterations (first component of the lift function adjoint). The aero-structural optimization was conducted at  $M=0.82$  and the optimization convergence was obtained in 14 gradient iterations. The constraints on the lift coefficients in cruise ( $CL > 0.5$  at  $M=0.82$ ) and maneuver conditions ( $CL > 0.7$  at  $M=0.60$ ) are both satisfied at convergence while the final design yields a reduction of the aero-structural objective function  $J$  of about 40 equivalent-drag counts. The overall performance increase is obtained thanks to a reduction in the wing root bending moment of more than 1%, which allows for a structural weight reduction while the cruise drag is increased by about one count. The geometry of the optimized winglet is presented and compared to the baseline configuration in figure 30.

The presented work illustrates the possibility of evolving an aerodynamic optimization into a multi-disciplinary optimization where the additional discipline (structure) is taken into account using surrogate models. It has also demonstrated, for a realistic application, the ability of the *elsA* software to supply gradients thanks to the adjoint technique, which drastically reduces the computation time of the optimization process.

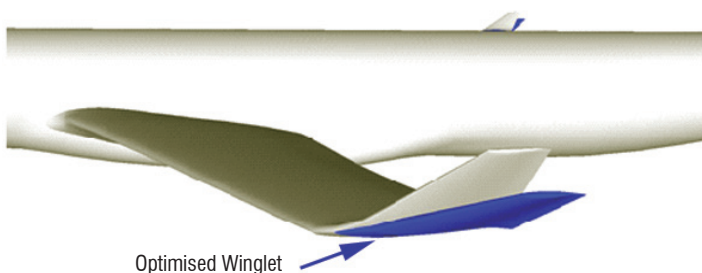


Figure 30 – Shapes of the reference and optimized winglets

### Helicopter blade optimization

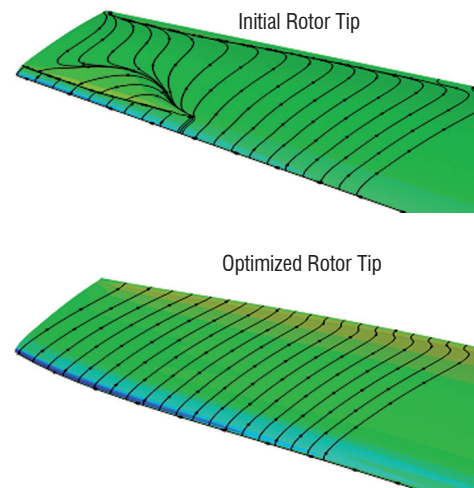
Aerodynamic shape optimization using gradient-based methods with an adjoint solver has mainly been used for fixed wing aircraft applications and very rarely for rotating wings. One reason is that

simulating the multi-disciplinary unsteady problem with CFD is already complex, even without optimization. However, because helicopter hover flight can be described as a steady flow in the relative coordinate system, optimizing a helicopter rotor blade in hover using the descent method with approximation by the adjoint formulation of the gradients can be very attractive, since the computational cost remains almost insensitive to the number of shape parameters. Specific developments to adapt the adjoint formulation in *elsA* to rotating blades have been done in the framework of a thesis [24].

In a first step, the method has been validated by solving some academic problems, such as the well-known problem of geometric twist optimization. More complex applications were treated, for example by trying to optimize the hover efficiency (figure of merit FM) of the Onera ERATO blade [25], without any constraints.

The set of shape parameters retained for this optimization allows for modifications of the blade twist, chord and sweep distributions along the blade span, with each geometrical law being described by 8 Bezier control points. The collective pitch is also added as a design variable, which brings the total number of parameters to 25. Seven iterations of the optimizer were necessary, involving 31 flow solver solutions and 7 adjoint system calls, to find a local minimum.

a)



b)

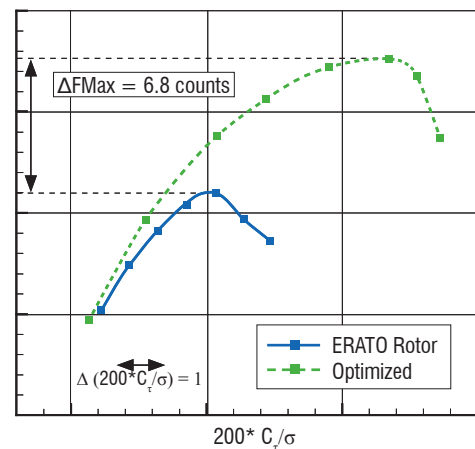


Figure 31 – Optimization of helicopter rotor blade in hover flight. On a), streamlines on the initial and optimized blades. On b), improvement on the Figure of Merit

The Figure of Merit (FM) has been improved by 6.8 counts, together with an extension of the maximum take-off weight (figure 31). The optimized shape allows for suppression of the leading-edge shock recompression and flow separation near the blade tip, for a given collective pitch angle, as shown in the left part of figure 31. For this shape optimization problem, it is worth noting that the use of the adjoint method has divided the cost of sensitivity computations by a factor of 12 in comparison with the first order finite difference method.

The adjoint formulation implemented in *elsA* allows optimizations of helicopter rotors in steady conditions with an interesting design space to be investigated. The simultaneous optimization of hover efficiency and forward flight performance is a challenging topic that will require further algorithmic developments in the future.

### Control of Flow Separation

Flow control is unanimously regarded as a key evolution, offering new solutions for performance maximization of existing designs, and, more broadly, the development of new concepts, in which separation control could be used in a multi-disciplinary approach, fully integrated with the initial screening and conception phases. Among the investigated flow control techniques, the most promising ones are the following:

- Passive, macro and sub-boundary layer vortex generators;
- Active, air-jet vortex generators;
- Active, pulsed and synthetic jets.

Three examples of applications have been selected in this section: control of the buffet phenomenon, separation control for helicopter fuselages, and suction and blowing in turbomachinery.

### Control of the buffet separation

Flow control can be applied to transonic configurations in order to reduce drag and increase separation margins. In particular, the postponement of buffet onset with flow control technologies could lead to a more efficient aircraft having a smaller wing surface. This is why Onera launched a research program aiming at achieving buffet control using either an open or a closed-loop approach. The test was carried out in the S3Ch research wind tunnel of the Meudon centre to determine the efficiency of several control devices (VGs, AJVGs, pulsed jets) that were previously defined with CFD parametric studies. RANS and URANS approaches were used to assess the 3D model and to optimize the actuator characteristics (position, geometry, flow rates). The experimental results have shown that mechanical VGs, fluidic VGs and pulsed fluidic VGs were able to suppress the massive flow separation which occurs without control between the shock foot and over the trailing edge area which is at the origin of the buffet phenomenon [26].

For passive devices, the simulation of the control effect can be done by meshing the VG's geometry. However, strong limitations can appear in terms of mesh size and computational time when complex geometries such as engine installations are being considered. That is why the Bender et al. VG model [27] has been implemented in the *elsA* software and assessed at Onera [28]. Both approaches allow the intensity of the VG vortices to be well simulated while it turns out that the VG model is the most practical method for carrying out parametric studies.

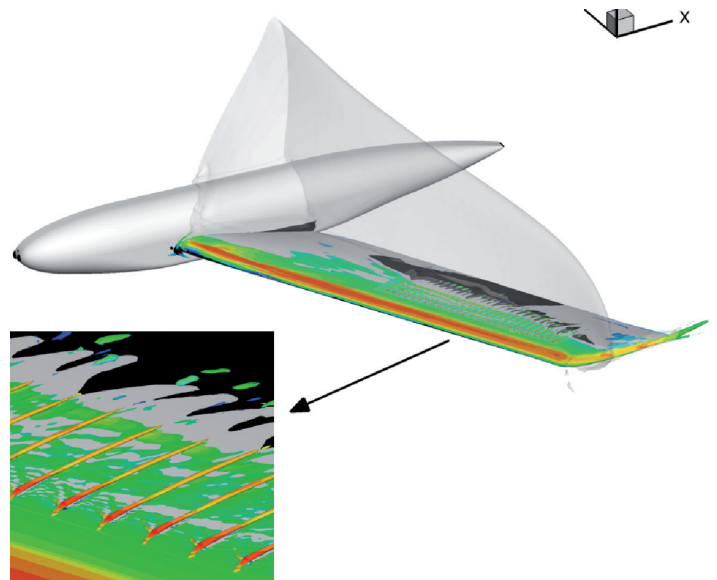


Figure 32 – Q-criterion iso-surface colored by Mach number showing the streamwise vortices created by the co-rotating mechanical VGs

Figure 32 presents the wing body configuration considered in this project and displays the results of a RANS simulation carried out with the VG devices installed on the outer part of the wing. The effects of the VGs are computed with the Bender et al. model and the computed flow is visualized by a Q-criterion iso-surface colored by the Mach number, the iso-surface  $M=1$ , and the separated zone in black. The streamwise vortices created by the co-rotating mechanical VGs are clearly visible. Small separated zones at the shock foot between the streamwise vortices are also visible, as in the experiment.

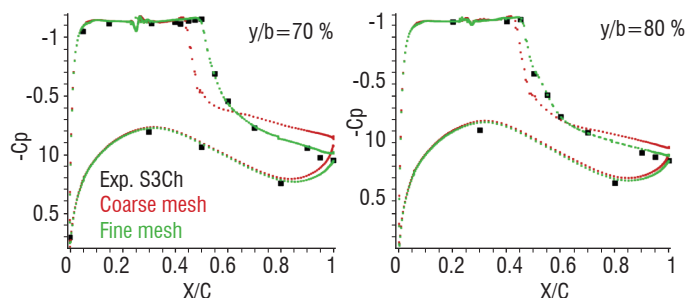


Figure 33 – Wall pressure distributions for the configuration with the co-rotating mechanical VGs

The wall pressure distributions for the controlled flow with mechanical co-rotating VGs are shown in figure 33 for two spanwise sections. The strong separation which is present on the reference configuration has been removed by the VGs. The agreement between the experimental data and the numerical simulation is very good, but with the fine mesh only ( $27 \cdot 10^6$  nodes). Good correlations have also been obtained with the fluidic VGs, taking advantage of the Chimera technique. The good quantitative agreement exhibited by the comparisons between simulations and experiment allows complex flow control applications with the *elsA* software to be investigated.

### Separation control for helicopter fuselage

It has often been noted that the cruise drag of a rotary-wing aircraft is an order of magnitude higher than the cruise drag of a fixed-wing aircraft

of the same gross weight. Function, or mission, drives the fuselage design of a rotary-wing aircraft more than aerodynamics. Accordingly, rotary-wing aircraft tend to have more bluff-body characteristics with the flow around the aft end of the fuselage typically being dominated by massive flow separation. This results not only in a large quantity of pressure drag, but also in a wake that tends to become unsteady. This, in turn, introduces undesirable, unsteady loads to the tail boom, stabilizers and tail rotor. An effort has been undertaken to study this problem on a generic fuselage with the goal of reducing the fuselage drag, while minimizing the effects of adverse lift. The drag reduction is to be achieved by the application of active flow control to the separated flow at the aft end of the fuselage.

Within the framework of the Cleansky GRC2 project, Onera has chosen to work on the ASF2 fuselage tested in the 80-90s in the F2 wind-tunnel. The first step was to perform CFD calculations of the uncontrolled flow on this geometry and to compare the results with experimental data. For steady computation, a low-Mach preconditioning method was used to enhance convergence and drag prediction accuracy, which was necessary for the low speed configurations studied here ( $M < 0.1$ ). In the case of unsteady computations, a Newton method based on the Gear algorithm was used. Finally, the  $k-\omega$  Kok turbulence model [29] was chosen among the various models implemented in *e/sA*. The initial mesh was about  $4.8 \cdot 10^6$  nodes and was refined in the separation area.

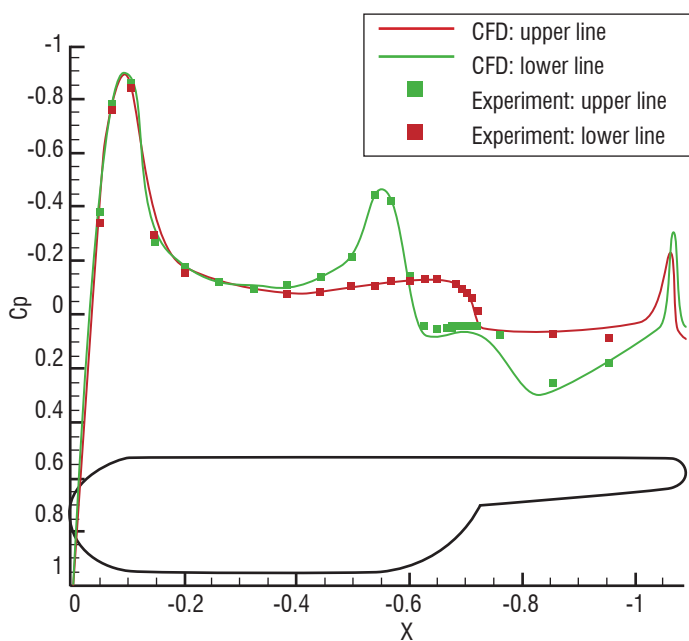


Figure 34 – Comparison of pressure distribution of the ASF2 fuselage. No incidence, no flow control

Figure 34 shows that the pressure distribution is very well predicted by the simulations, including the pressure plateau in the bottom part of the fuselage (ramp area), where massive flow separation occurs. Until now, the most promising results have been obtained by applying synthetic jets in order to control the flow separation in the ramp area. 4 slots were placed in order to “surround” the detached area (figure 35).

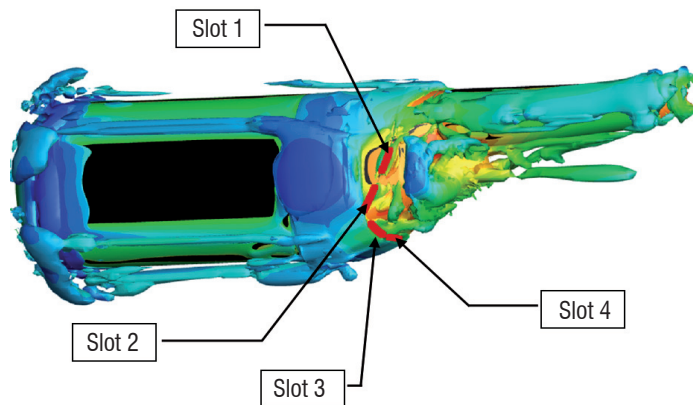


Figure 35 – Location of the 4 slots and visualization of the flow field on the ASF2 fuselage with flow control

When the 4 jets are in phase, whatever the tested condition, the drag coefficient of the fuselage increases. The interesting result is that out-of-phase jets (vertical slots out-of phase, and same for horizontal slots) allow for reduction of the unsteady load fluctuations, and also the mean drag value, as illustrated in figure 36. This reduction can reach 14% with this 4 out-of-phase jet configuration, with a  $C_{\mu}$  coefficient of 2.1% and a non-dimensional actuation frequency  $F^+ \approx 1$ , and jets oriented at  $20^\circ$  with respect to the surface normal.

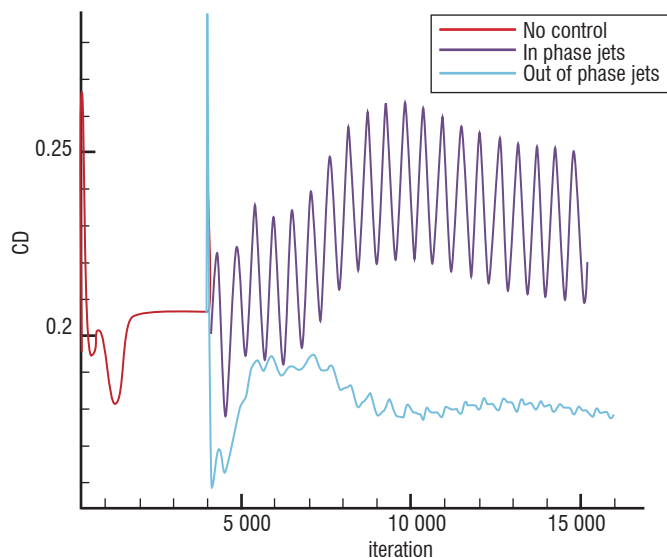


Figure 36 – Influence of synthetic jets on the helicopter ASF2 fuselage drag coefficient

A detailed analysis of the vortex structures in the uncontrolled and controlled cases is underway in order to explain the physical phenomena involved and to try to find the best control strategy for blunt fuselage drag reduction.

### Suction and blowing in turbomachinery

An efficient way to increase the pressure ratio of a compressor involves aspirating the viscous layers that can develop in the inter blade channels. This strategy has been evaluated for low pressure compressors, in the framework of a thesis [30], with the objective

of reaching a deviation as large as  $65^\circ$  for a diffusion rate of 2. The strategy is to fix the separation point on the blade by creating a sudden diffusion and curvature variation: it is then easier to appropriately locate the suction device that can be placed just after the curvature modification.

The blading was defined using *e/sA* calculations for an upstream Mach number equal to 0.7. The cascade was then defined, manufactured and tested at the LMFA for low speed conditions ( $M=0.12$ ). Non-intrusive flow measurements using PIV are compared with predictions in figure 37. The suction rate required to reach a total flow re-attachment is estimated to be 3.3%. There is a very good correlation between the calculations and the measurements, especially in the case of aspiration where the diffusion is predicted with an accuracy of 6%. Although the target deviation was almost reached in the experiment ( $62.2^\circ$  instead of  $65^\circ$ ), some lateral separations lead to a diffusion of only 30%. The next step in this study would be to define a 3D aspirated compressor stage and test it for real Mach number conditions.

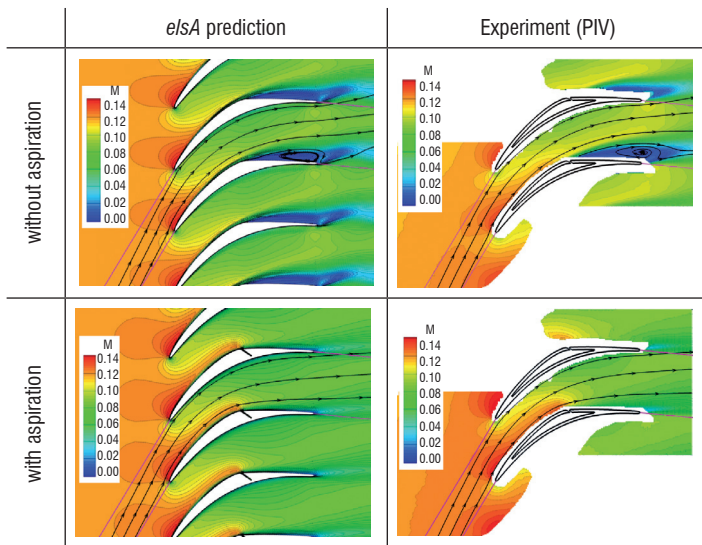


Figure 37 – Influence of surface suction on a low-pressure cascade. Comparison between calculations (left) and measurements (right)

## New concepts

### Flying wing

The aerodynamic design of modern transport aircraft is driven primarily by cruise performance and regulation considerations. Future environmental constraints will require significant reductions in emissions and noise pollution. Although the improvement in existing aircraft performance may provide a short-term answer to this problem, the development of radically novel configurations is likely to be required to meet the long-term improvement objective. The flying wing or blended wing body seems to be one of the most promising configurations for reaching efficiency higher than that of the current configurations.

For several years now, the Applied Aerodynamics Department of Onera has been working on flying wing configurations for large capacity transonic transport within the framework of national and European projects. Recently, a national research project AVECA was launched on Blended-Wing-Body configurations of

smaller capacity in close cooperation with Airbus [31]. This project aimed at designing viable flying wing geometries in terms of aerodynamic cruise performance ( $M=0.85$ ) while respecting longitudinal trimming and geometric constraints such as cabin or landing gear volumes.

In order to reach these objectives, the first step in the design consisted of redesigning the wing profiles using control points (B-splines) based on geometry deformation of several wing sections while keeping the planform of the configuration unchanged. The iterative design process was begun by modifying the inboard section, and progressively moving to the outer section of the configuration. The second step of the design involved optimizing the twist law of the outboard wing to improve the lift-to-drag ratio and the longitudinal trimming of the configuration at the design point.

To evaluate the aerodynamic performance of the various configurations during the design process, the Onera *e/sA* software was used to carry out CFD computations on a Navier-Stokes structured mesh made up of  $8.0 \cdot 10^6$  points, and the Onera far-field drag extraction code *ffd72* was used to evaluate the total drag and to determine the drag components.

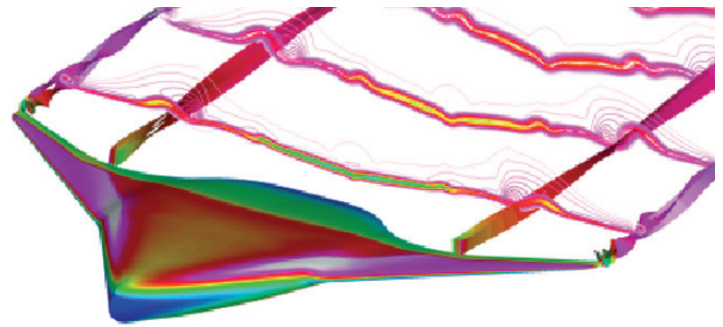


Figure 38 – Simulation on the AVECA flying wing configuration ( $M=0.87$ )

With this iterative strategy, very convincing results were obtained with an increase of the lift-to-drag ratio of 5% at the design point and of 19% at a higher Mach number ( $M=0.87$  - figure 38). These gains are mainly due to a strong decrease of the wave and viscous drag components.

In the current AVECA project, the adjoint optimization method developed in the Onera *e/sA* software will be used to automate the design process for flying wing configurations.

### Supersonic business jet

Over the past few decades, several aircraft makers have investigated various concepts for a supersonic transport aircraft (SST). More recently, a small supersonic business jet concept was proposed and studied, particularly within the European project HISAC of the 6th R&D Framework Program. The HISAC project managed by Dassault-Aviation aims at establishing the technical feasibility of an environmentally-compliant, small-size supersonic transport aircraft. Several concepts such as low noise, long range and low sonic boom were investigated through CFD simulations and wind tunnel tests.

As far as the aerodynamics are concerned, Onera's contributions have focused on the determination of the aerodynamic characteristics, the prediction of the sonic boom, the aerodynamic and MDO optimizations and high-speed wind tunnel tests. As an example of the Onera work, figure 39 presents the results of a RANS simulation carried out with the *e/sA* software for the reference configuration tested in the Onera S2MA wind tunnel. The multi-block mesh has  $11 \cdot 10^6$  nodes and the nacelle is integrated with the wing body configuration thanks to the patched-grid technique. The aerodynamic conditions are a cruise Mach number of 1.6, an angle of attack of  $5^\circ$  and a lift coefficient of 0.2 (above the cruise lift coefficient). The streamlines point to the presence of the apex and wing kink vortices induced by the fuselage and the strong sweep of the inner wing. The correlation carried out with the wind tunnel results (balance and static pressures in two lines) shows good agreement.

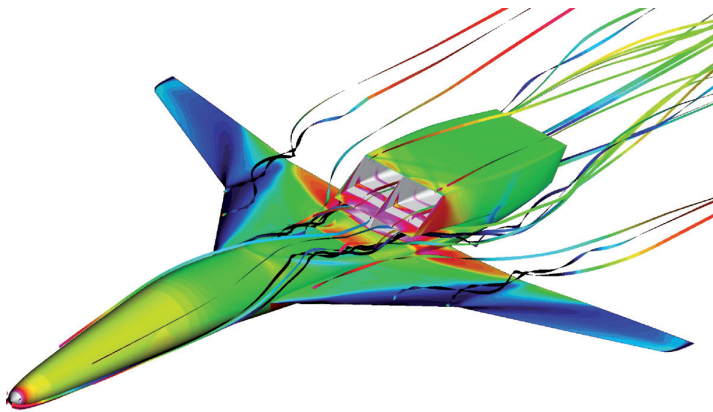


Figure 39 – Simulation of one of the HISAC business jet configurations

#### UCAV configuration

The Next generation of UCAV will be based on blended wing-body configuration with a moderate sweep angle. This kind of UCAV exhibits rather complex vortex-dominated flows when compared with highly swept delta wings. Due to the competition between the apex vortex and the wing tip vortex, these configurations exhibit strong pitch-up behavior at a relatively low angle of attack ( $\sim 17^\circ$ ) and lateral instability that can lead to serious aerodynamic stability and control issues.

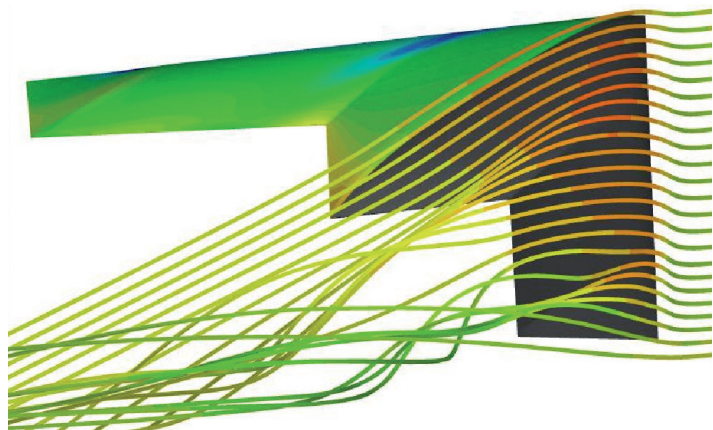


Figure 40 – Computed streamlines around the UCAV Configuration.  $M=0.14$ ,  $Re=1.6 \cdot 10^6$ ,  $\alpha=17^\circ$

For these reasons, the static and dynamic derivatives are being investigated for a representative UCAV with a CFD approach and compared to the experimental results. The configuration, named SACCON for Stability And Control CONfiguration, is a blended wing body with a moderate sweep angle ( $53^\circ$ ) defined for the purpose of an RTO project. The CFD approach is based on static computations to determine the static derivatives and on the ALE (Arbitrary Lagrangian Euler) method coupled to steady or unsteady computations to obtain the dynamic derivatives. The objectives are to compare the time-history of the pitching moment coefficient between experimental and unsteady simulation for a pitching oscillation.

Figure 40 shows the complexity of the flow obtained at high angles of attack using the Spalart Allmaras turbulence model. Two main vortices are clearly visible. When the angle of attack is increased, the tip vortex has a growing intensity and its position moves inboard. The displacement of the tip vortex along the leading edge is the origin of the pitch-up observed in the wind tunnel on this configuration. Ongoing activities are related to the use of advanced turbulence models such as EARSM and DRSM.

#### CROR

Counter-Rotating Open Rotors (CROR) represent an attractive alternative to conventional turbofan engines because of their reduced impact on the environment (fuel consumption reduction), as a consequence of their high by-pass ratio. The success of this concept will depend greatly on the noise levels radiated by the installed power plant system. The numerical simulation of a complete configuration through CFD is certainly very challenging, and can be envisaged in the near future. At present, Onera is involved together with Snecma and Airbus in many national and European projects that aim at validating the CFD methodologies that are well-suited for the prediction of accurate aerodynamic performance (take-off and cruise conditions), and for the prediction of aerodynamic noise sources.

The mixing-plane boundary condition developed in *e/sA* for turbomachinery applications has been extended to propeller applications and allows for prediction of the steady aerodynamic performance of a CROR (figure 41), under the hypothesis of azimuthally averaged interactions between propellers. Its big advantage lies in its low CPU cost.

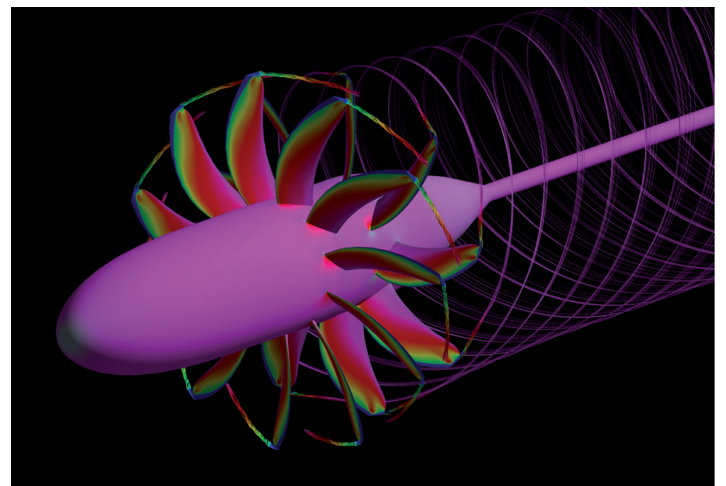


Figure 41 – Steady simulation of an Airbus CROR configuration using a mixing-plane interface between the propellers

The chorochronic conditions also developed for turbomachinery applications are an interesting and efficient way to have access to the time-accurate interactions between propellers, without needing to model all of the blades. Such simulations can predict the unsteady inputs required for an acoustic evaluation of the CROR, with moderate CPU cost; however, this method is only valid for an isolated CROR. Finally, when the objective is to study installation effects (incidence effects or interactions with the airframe), it is mandatory to model the whole configuration (360° calculation), leading to a very long CPU time (approximately ten times more than with the chorochronic method). In this case, the use of the Chimera functionalities available in the *elsA* software allows for simulations of the different rotating and fixed components of the configuration. The first applications of such a calculation have been done for an isolated CROR (figure 42), trying to better understand how well the aerodynamic interactions between the front propeller blade wakes and tip vortices and the aft propeller blades can be captured and how these interactions contribute to the radiated noise.

Further validation of the developed methodologies is necessary and is already planned for the near future, especially by comparing the numerical predictions with wind-tunnel test results.

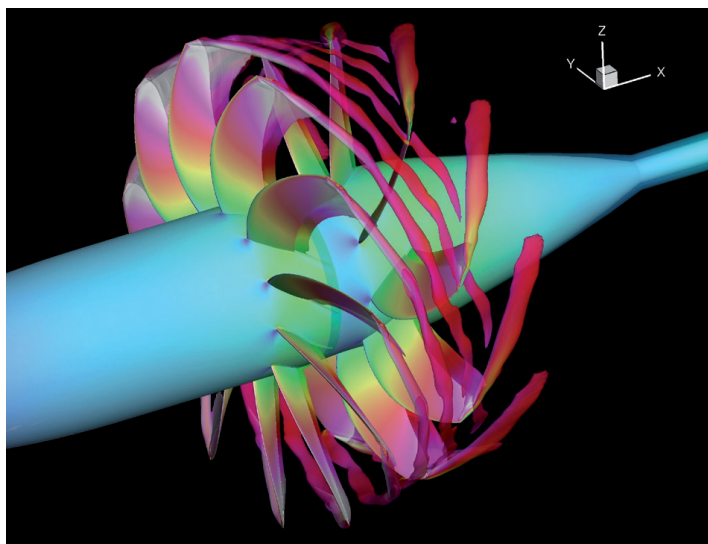


Figure 42 – Time-accurate 360° simulation of an Airbus CROR configuration using the Chimera technique

### Tilt rotor

Tilt-rotors can be defined as hybrid aircraft, combining the advantage of hover capabilities specific to helicopters, with high speed capabilities similar to propeller driven aircraft. Most of the studies initiated in Europe over the past 6 years have been based on the ERICA concept proposed by AGUSTA, which is a tilt-rotor comprising a half tilt-wing design, which aims at reducing the rotor-wing interactions through a proper choice of the outer wing incidence depending on the flight condition.

In the NICETRIP European project, the use of CFD has allowed for the investigation of complex problems, two of which are detailed below. The first one is related to cabin noise, for which the *elsA* code has been used in order to predict the aerodynamic sources of the noise radiated by aircraft in cruise conditions [33]. Steady

calculations of the isolated propeller have been compared to a time-accurate simulation of the installed configuration (figure 43): installation effects on the radiated noise have been quantified as large as 15 dBA. The origin of this large noise increase is the unsteady pressure fluctuations of the propeller blades due to the fuselage and wing tangential deviations in the propeller plane. Indeed, the peak-to-peak amplitude of the blade loading over one revolution can be as large as 3,000 N, compared with its average value of 1,825 N. The use of cyclic pitch, not actuated in the present simulations, may help in the future to reduce these fluctuations and then to decrease cabin noise.

The second activity has been to try to improve propeller cruise efficiency through optimization of the cuff shape (the cuff being the junction between the blade root and the spinner). Indeed, previous projects such as ADYN have shown that non-optimized cuff geometry can lead to a 20% reduction in cruise efficiency. Various concepts have been investigated to adapt the blade root geometry to the spinner, making intensive use of the complex Chimera functionalities available in *elsA* in order to compute geometry details including the modeling of one part of the internal spinner flow. The new proposed cuff geometry is expected to improve the cruise efficiency by more than 15% compared with the ADYN reference.

ERICA full scale - Cruise 330 kts

Q criteria iso-surface colored by vorticity magnitude

Skin pressure contour

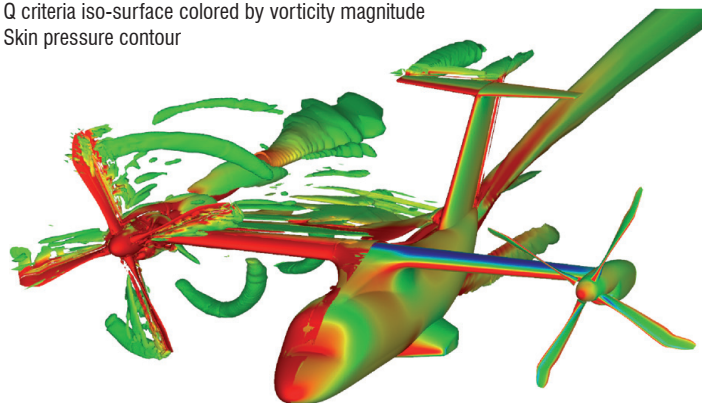


Figure 43 – Simulation of the ERICA tilt-rotor in cruise conditions

### Conclusions and future work

The wide range of applications presented in this paper shows that the *elsA* software has reached a good level of maturity. It allows for carrying out RANS simulations with high CPU performance in parallel mode, and URANS and DES simulations to accurately predict unsteady aerodynamics. The ability to take into account several turbulence models and transition criteria and to perform accurate fluid/structure coupling simulations is also a strong asset for this software. The robustness of the RANS adjoint method for the calculation of sensitivities allows for complex 3D optimization.

Most of the applications presented have been assessed with aerodynamic databases established in Onera research wind tunnels. These databases are based on the use of advanced measurement techniques to quantify the flow on model surfaces or in the flow field: Pressure and Temperature Sensitive paints, Laser Doppler Velocimetry and Particle Image Velocimetry. Multi-physics databases are also needed to assess such complex simulations.

In order to cope with complex configurations, the development of a hybrid structured/unstructured mesh strategy will be added to the available high flexibility advanced techniques of multi-block structured, patched grid and overset capabilities (Chimera technique). The applications will be then oriented towards the simulation of the complex geometries with full details.

The drag extraction and optimization techniques will be extended to URANS capabilities. The simulations of detached flows currently

carried out with the URANS and DES approaches will consider LES and DNS modes which will require new boundary conditions and refined meshes.

Multi-physics applications will also play a major role in the future with, in particular, the development of improved aero-elastic, aero-acoustic and aero-thermal simulations. These coupling applications will be eased by the adaptation of the *elsA* software to the massively parallel architectures of new computers ■

### Acknowledgements

The authors would like to thank the French government agencies DGAC and DGA and the European Commission for funding some of the previous research studies.

The results presented have also been established through very good cooperation between various Onera departments: Applied Aerodynamics, Aeroelasticity and Structural Dynamics, Fundamental and Experimental Aerodynamics, Aerodynamics and Energetics Modeling, Computational Fluid Dynamics and Aero-acoustics.

Many researchers must be acknowledged for their works and their contributions to this paper: **S. Esquieu** and **D. Hue** for the drag prediction activities, **J.L. Hantrais-Gervois** and **O. Atinault** for the control surfaces, **F. Moens** for the high-lift configuration, **V. Brunet** and **S. Deck** for the buffet prediction and jet simulations, **M. Costes** and **A. Le Pape** for the dynamic stall activities, **P. Thorigny** for the store separation, **S. Mouton** for the CFD-wind tunnel synergy, **A. Dugeai** and **F. Sicot** for the axial compressor aeroelastic stability analysis, **T. Renaud** for the blade vortex interaction noise study, **L. Castillon** for the thermal study on the TATEF turbine, **S. Mouton** for the pylon optimization, **G. Carrier** for the winglet optimization, **A. Dumont** for the helicopter blade optimization, **J. Peter** for the contribution to the adjoint technique, **J. Dandois** for the control of buffet phenomenon, **C. Liénard** for the separation control on helicopter fuselage investigation, **L. Castillon**, **A. Godard** and **S. Burguburu** for the suction and blowing effects in turbo-machinery, **M. Méheut** for the flying wing configuration, **G. Carrier** for the supersonic business jet, **J.F. Leroy** for the UCAV configuration **B. Rodriguez** and **S. Burguburu** for the CROR configuration, **J. Decours** for the tilt-rotor study.

### References

- [1] L. CAMBIER, J.P. VEUILLOT - *Status of the elsA Software for Flow Simulation and Multi-disciplinary Applications*. 46<sup>th</sup> AIAA Aerospace Sciences Meeting and Exhibit, Reno, Nevada, AIAA2008-664, 7<sup>th</sup> to 10<sup>th</sup> January 2008.
- [2] D. HUE, S. ESQUIEU and M. GAZAIX - *Computational Drag and Moment Prediction of the DPW4 Configuration Using elsA*. AIAA conference, Chicago, June 2010.
- [3] D. DESTARAC - *Far-field / Near-field Drag Balance and Applications of Drag Extraction in CFD. CFD-Based Aircraft Drag Prediction and Reduction*. Hampton, VA, 3<sup>th</sup> to 7<sup>th</sup> November 2003.
- [4] J.-L. HANTRAIS-GERVOIS, A. LEPAGE, F. TERNOY, G. CARRAZ and G. JEANFAIVRE - *Assessment of Numerical Tools to Predict Control Surface Effectiveness*. AIAA Applied Aerodynamics Conference, Chicago, 28<sup>th</sup> June to 1<sup>st</sup> July 2010.
- [5] J. CLIQUET, R. HOUEVILLE, D. ARNAL - *Application of Laminar-Turbulent Transition Criteria in Navier-Stokes Computations*. AIAA Journal, Vol. 46, N° 5, May 2008.
- [6] F. MOENS, J. PERRAUD, A. KRUMBEIN, T. TOULORGE, P. IANELLI, P. ELIASSON and A. HANIFI - *Transition Prediction and Impact on a Three Dimensional High-Lift Wing Configuration*. AIAA Journal, Vol.45, N° 5, pp 1751-1766, September-October 2008.
- [7] V. BRUNET, P. MOLTON, H. BÉZARD, S. DECK and L. Jacquin - *A Joint Numerical and Experimental Study of the Jet of an Aircraft Engine Installation with Advanced Techniques*. 3<sup>rd</sup> European Conference for Aerospace Sciences, Versailles, July 2009.
- [8] S. DECK - *Numerical Simulation of Transonic Buffet over a Supercritical Airfoil*. AIAA Journal, Vol. 43, N° 7, pp 1556-1566, 2005.
- [9] P. SAGAUT, S. DECK and M. TERRACOL - *Multi-Scale and Multi-Resolution Approaches in Turbulence*. Imperial College Press, London, UK, 2006.
- [10] P.R. SPALART, S. DECK, M.L. SHUR, K.D. SQUIRES, M. STRELETS and A. TRAVIN - *A New Version of Detached Eddy Simulation Resistant to Ambiguous Grid Densities*. Theoretical and Computational Fluid Dynamics, Vol. 20, pp 181-195, July 2006.
- [11] S. DECK - *Zonal Detached Eddy Simulation of the Flow Around a High-Lift Configuration*. AIAA Journal, Vol. 43, N° 11, pp 2372-2384, 2005.
- [12] P. SAGAUT and S. DECK - *Large Eddy Simulation for Aerodynamics: Status and Perspectives*. Phil. Trans. R. Soc. A., Vol. 367, pp 2849-2860, 2009.
- [13] K. RICHTER, A. LE PAPE, T. KNOPP, M. COSTES, V. GLEIZE and A. Gardner - *Validation of Structured and Hybrid Methods for Improved Two-Dimensional Dynamic Stall Prediction*. 10<sup>th</sup> Onera-DLR Aerospace Symposium, Berlin, 6<sup>th</sup> to 8<sup>th</sup> October 2009.
- [14] J.-J. HANTRAIS-GERVOIS, A. CARTIÉRI, S. MOUTON and J.-F. PIAT - *Empty Wind Tunnel Flow Field Computations*. International Journal of Engineering Systems Modeling and Simulation, Vol. 2, N°s 1/2, 2010.
- [15] S. MOUTON - *Numerical Investigations of Model Support Interference in a Transonic Wind Tunnel*. 44<sup>e</sup> Colloque d'Aérodynamique Appliquée, Nantes, March 2009.
- [16] P. GIRODROUX-LAVIGNE - *Progress in Steady/Unsteady Fluid-Structure Coupling with Navier-Stokes Equation*. International Forum on Aeroelasticity and Structural Dynamics, Munich, Germany, 28<sup>th</sup> June to 1<sup>st</sup> July 2005.
- [17] A. DUGEAI - *Turbomachinery Aeroelastic Developments and Validations Using Onera elsA Solver*. International Forum on Aeroelasticity and Structural Dynamics, Stockholm, Sweden, 18<sup>th</sup> to 20<sup>th</sup> June 2007.
- [18] G. DUFOUR, F. SICOT, G. PUIGT, C. LIAUZUN and A. DUGEAI - *Contrasting the Harmonic Balance and Linearized Methods for Oscillating-Flap Simulations*. AIAA Journal, Vol. 48, n°. 4, pp 788-797, April 2010.
- [19] T. RENAUD, G. PEREZ, C. BENOIT, G. JEANFAIVRE and S. PÉRON - *Blade-Vortex Interaction Capture by CFD*. 34<sup>th</sup> European Rotorcraft Forum, Liverpool, 16<sup>th</sup> to 19<sup>th</sup> September 2008.

- [20] G. PANIAGUA, T. YASA, A. DE LA LOMA, L. CASTILLON and T. COTON - *Unsteady Strong Shock Interactions in a Transonic Turbine. Experimental and Numerical Analysis*. J. of Propulsion and Power, Vol.24, N° 4, pp 722-731, 2008.
- [21] S. MOUTON, J. LAURANCEAU and G. CARRIER - *Aerodynamic and Structural Optimization of Power-Plant Integration under a Wing of a Transport Aircraft*. 42<sup>e</sup> Colloque d'Aérodynamique Appliquée AAAF, Sophia-Antipolis, 19<sup>th</sup> to 21<sup>th</sup> March 2007.
- [22] J. E.V. PETER and R. P. DWIGHT - *Numerical Sensitivity Analysis for Aerodynamic Optimization: A Survey of Approaches*. Computers & Fluids, Vol. 39, 2010.
- [23] G. CARRIER, S. MOUTON, M. MARCELET and C. BLONDEAU - *Towards Aerodynamic Design by Optimization of Transport Aircraft in a Multi-Disciplinary Context*. CEAS Conference 2007, Berlin, Germany, 10<sup>th</sup> to 13<sup>th</sup> September 2007.
- [24] A. DUMONT, A. LE PAPE - *Aerodynamic Shape Optimization of Hovering Rotors Using a Discrete Adjoint of the RANS Equations*. 65<sup>th</sup> American Helicopter Society Forum, Grapevine, 27<sup>th</sup> to 29<sup>th</sup> May 2009.
- [25] J. PRIEUR, W. SPLETTSTOESSER - *ERATO - an Onera-DLR Cooperative Program on Aeroacoustic Rotor Optimization*. 25<sup>th</sup> European Rotorcraft Forum, September 1999.
- [26] J. DANDOIS, V. BRUNET, P. MOLTON, J. ABART, A. LEPAGE and F. TERNOY - *Buffet Control by Means of Mechanical and Fluidic Vortex Generators*. AIAA Paper 2010-4975, Chicago, 28<sup>th</sup> June to 1<sup>st</sup> July 2010.
- [27] E.E. BENDER, B.H. ANDERSON and P.J. YAGLE - *Vortex Generator Modeling for Navier-Stokes Codes*, FEDSM 99-6919, July 1999.
- [28] M. MEUNIER and V. BRUNET - *High-Lift Devices Performance Enhancement Using Mechanical and Air-Jet Vortex Generators*. AIAA Journal, Vol. 45, N° 6, pp 2049-2061, 2008.
- [29] J.C. KOK - *Resolving the Dependence on Freestream Values for the k-w Turbulence Model*, AIAA Journal, Vol. 38, N° 7, pp 1292-1295, July 2000.
- [30] A. GODARD, A. FOURMAUX, S. BURGUBURU and F. LEBOEUF - *Design Method of a Subsonic Aspirated Cascade*, ASME Turbo Expo 2008, Berlin, 9<sup>th</sup> to 13<sup>th</sup> June 2008.
- [31] M. MÉHEUT, R. GRENON, G. CARRIER, M. DEFOS, M. DUFFAU - *Aerodynamic Design of Transonic Flying Wing Configurations*. CEAS/KATnet2 Conference on Key Aerodynamic Technologies, Bremen, Germany, 12<sup>th</sup> to 14<sup>th</sup> May 2009.
- [32] J.-F. LE ROY and S. MORGAND - *SACCON CFD Static and Dynamic Derivatives Using elsA*. AIAA Applied Aerodynamics Conference, Chicago, 28<sup>th</sup> June to 1<sup>st</sup> July 2010.
- [33] J. DECOURS - *Numerical Approach of Tilt-Rotors*. 10<sup>th</sup> Onera - DLR Aerospace Symposium, Berlin, 6<sup>th</sup> to 8<sup>th</sup> October 2009.

### Acronyms

CFD (Computational Fluid Dynamics)  
 RANS (Reynolds Averaged Navier-Stokes)  
 DES (Detached Eddy Simulation)  
 ZDES (Zonal Detached Eddy Simulation)  
 LES (Large Eddy Simulation)  
 DNS (Direct Numerical Simulation)  
 EARSM (Explicit Algebraic Reynolds Stress Model)  
 DRSM (Differential Reynolds Stress Model)  
 CAE (Computational AeroElasticity)  
 MDO (Multi-disciplinary Design Optimization)  
 UCAV (Unmanned Combat Air Vehicle)  
 LDV (Laser Doppler Velocimetry)  
 PIV (Particle Image Velocimetry)  
 PSP (Pressure Sensitive Paint)  
 TSP (Temperature Sensitive Paint)  
 FM (Figure of Merit)  
 VG (Vortex Generator)  
 AJVG (Air Jet Vortex Generator)

### AUTHORS



**Joël Reneaux** graduated from the "Arts et Métiers" Engineering school in 1980. At Onera, he has been involved in numerical optimization method applications, helicopter airfoil design, aircraft wing design and laminar flow technology. He is currently Head of the Civil transport Aircraft Unit of the Applied Aerodynamics Department of the Onera Meudon center.



**Philippe Girodroux-Lavigne** engineer who graduated from the "Ecole Centrale de Lyon", has been working at Onera since 1979, first in the "CFD and Aero-acoustics" department, then in the "Aeroelastics and Structural Dynamics" department, where he is involved in numerical aeroelasticity studies for static and dynamic aircraft applications.



**Philippe Beaumier** graduated from the "Ecole Centrale de Paris" engineering school in 1989. Since that time, he has been working at Onera in the field of helicopters, with the main emphasis on fluid-structure coupling on main rotor blades, aerodynamic performance prediction and aero-acoustics (BVI noise). He is currently Head of the "Helicopter, Propeller and Turbomachinery" Unit of the Applied Aerodynamics Department of the Onera Meudon center.

D. Scherrer, F. Chedevergne,  
P. Grenard, J. Troyes, A. Murrone,  
E. Montreuil, F. Vuillot,  
N. Lupoglazoff, M. Huet,  
B. Sainte-Rose, P. Thorigny,  
N. Bertier, J.M. Lamet,  
T. Le Pichon, E. Radenac, A. Nicole,  
L. Matuszewski, M. Errera

(Onera)

E-mail : dominique.scherrer@onera.fr

A selection of recent CEDRE applications in the aerospace field are presented to illustrate various functionalities of the code. These applications have been selected to cover a wide application field in aerodynamics, aerothermodynamics and combustion. Many of them are “multiphysics”, in the sense that they are based on the coupling of independent solvers for, respectively, gas flow, condensed phase transport, solid conduction, radiation, etc. Some of them include an external coupling to other codes. The presentation of each application includes the objectives of the computation, the methodology (modeling, numerics, grid, etc.) and some significant results.

## Introduction

CEDRE is the code used for nearly all energetics applications at Onera today. Its main application domain concerns internal flows in aerospace engines, but it has also been successfully used in other fields, due to its generality and its multiphysics positioning. CEDRE is based on the coupling of independent solvers for the gas flow (CHARME), a dispersed condensed phase (SPARTE in lagrangian formulation, SPIREE in eulerian formulation), solid conduction (ACACIA), stochastic gaseous particles (PEUL), radiation (REA with the DOM method, ASTRE with the Monte-Carlo method). A short description of the code and its solvers can be found in [43] and more detailed information on the methods and models can be found in other papers of the same Aerospace Lab issue [2][12][14][15][18][36][55]. In order to illustrate various functionalities of the code, some recent applications in the aerospace field are presented in this paper. The selected applications are listed hereafter with their general characteristics: RANS or LES, scientific field, specific modeling (if the case arises), solver(s).

- Aerothermodynamics of turbine blades: RANS, aerothermics, SIBLE wall function, CHARME
- Conjugate Heat Transfer applied to an effusion cooling system: RANS, fluid/structure aerothermics, MSD (CHARME's predecessor) + external coupling
- Film-cooling of a dump combustor: RANS, fluid/structure aerothermics, reactive, CHARME
- Hypersonic vehicle separation: RANS, hypersonic aerodynamics, CHARME
- Rocket engine ignition blast wave: LES, aeroacoustics, equivalent gas two-phase flow, reactive, CHARME

- Jet noise prediction: LES, aeroacoustics, CHARME + external coupling
- Flow separation in an over expanded nozzle: RANS and DDES, reactive, CHARME
- Aircraft and helicopter icing: RANS, two-phase flow, SPIREE + external coupling
- Flow instabilities in a solid propellant motor: LES, flow instability, CHARME
- Combustion in a multipoint injection burner: RANS, diphasic, reactive, radiation, CHARME + SPARTE + ASTRE + PEUL
- Reacting flow in a research ramjet combustor: RANS&LES, reactive, CHARME
- Combustion in MASCOTTE cryogenic burner: RANS, sub/supercritical fluids, reactive, CHARME + SPARTE

## Aerothermodynamics of turbine blades

### Introduction

Due to limitations of computer resources in conception processes, the development of efficient methods for internal blade cooling system simulation on coarse grids is a necessity for industrials. Onera has thus been invested in the implementation and development of such methods in its energetics code CEDRE. The main objective is to provide a set of numerical tools allowing the simulation of complex configurations with reasonable accuracy. In the aerothermodynamics context, particular attention has been paid to EARS (Explicit Algebraic Reynolds Stress Model) turbulence models [62] for their ability to simulate rotating flows. In the same time, Onera has developed an advanced wall function, SIBLE (Simple Integrated Boundary Layer

Equations) [10], able to take account for pressure gradients. The goal of the present simulations is the validation of these two models in a simplified but representative configuration.

## Configuration

The BATHIRE rig [49] is a recent facility installed at the Palaiseau Onera center, to study rotating internal blade cooling systems. The U-bend test section reproducing a part of a cooling passage is equipped with optical and thermal access so that PIV and infrared measurements can be performed. Consequently, on the same rig, we have access to the flow structure and to heat exchanges on a heated wall. This wall can be equipped with ribs but only the smooth configuration will be considered here. The geometry of the test channel consists of two parallel ducts connected with a constant height curved duct. The hydraulic diameter is kept roughly constant, equal to 50, along the rig. Based on this length, the Reynolds number is found to be equal to 25000. The Rossby number, characterizing the rotation effects, is fixed at 0.33 corresponding to a rotation rate of the rig equal to 500 rpm.

The inlet conditions are quite complex, due to the junction between the primary circuit on the rotating axis and the main channel, which induces a swirl. Reproducing this upstream condition is crucial to accurately simulate the flow and compare the results to the measurements. The retained configuration is presented in figure 1.

## Computation methodology

The computational domain has been meshed using CENTAUR, resulting in a 3D unstructured grid with 3 prism layers at the walls. Finally, only 690,000 cells are used to discretize the whole domain. This deliberate limitation was made to stay within the specification bounds, i.e. performing simulations on coarse grids.

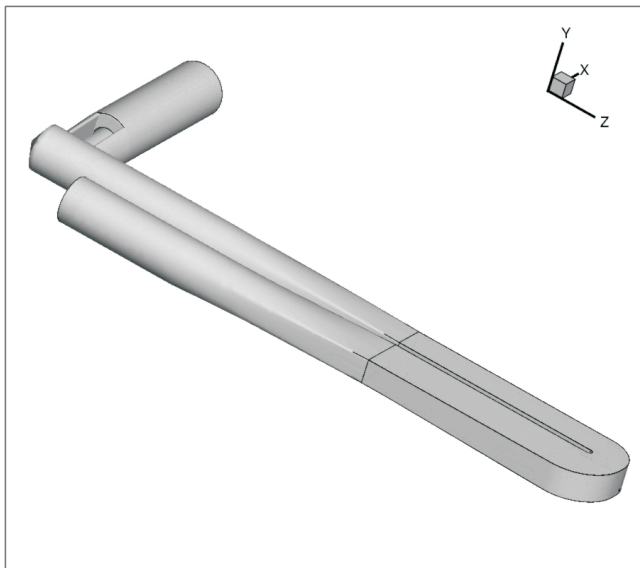


Figure 1 - Global view of the computational domain

The EARS/EAHFM models, based on the work of Wallin and Johansson [62] and Wikström [63], have been used. To complete the modeling, the SIBLE wall function [10] has been activated. This original wall model locally solves a set of boundary layer equations and thus provides a good evaluation of the friction and heat exchange coefficients, compared to a conventional wall function.

## Computation results

### PIV measurements

First, we focus on the PIV measurements and compare them to the simulation results. Globally speaking, it appears that the flow is well reproduced by the CEDRE code, using the retained models. Figure 2 illustrates this good agreement: on this plane, one can clearly identify two separation zones, placed identically in both the measurements and the simulation. Other simulations using standard turbulence models, such as the  $k-\omega$  SST of Menter, show that these models are unable to reproduce this particular phenomenon due to rotation. Good agreement must be tempered, because of a velocity deficit in the inlet plane of the U-bend. This deficit may be attributed to a bad description of the inlet swirl mentioned earlier. The grid, deliberately chosen to be coarse, may be responsible for the difference between simulation and experiments. However, the simulations clearly show the relevance of the chosen models, allowing a quite good description of the flow on a coarse mesh.

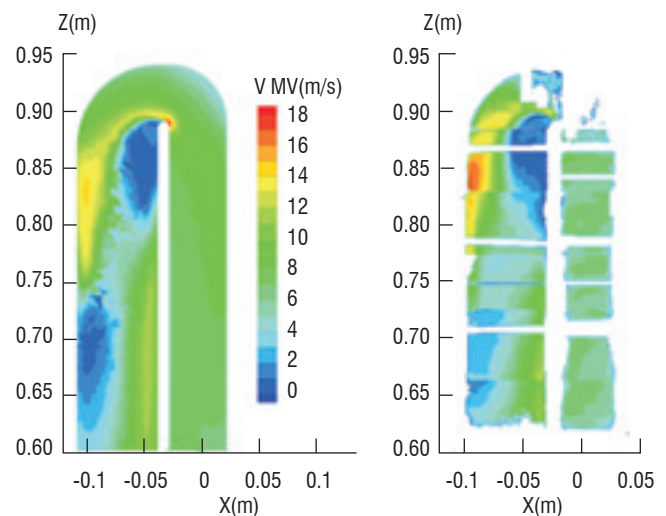


Figure 2 - Comparison between the computation (left) and the experiment (right) for the velocity magnitude

### Heat exchange measurements

Heat exchanges are deduced from the wall temperature measurements provided by the thermal camera. An estimate of the heat flux imposed at the wall is gained a posteriori from a 2D thermal conduction solver. Unfortunately, up to now, the method is such that there are many uncertainties on the deduced heat flux, in particular because of the difficulty to estimate the losses by the back side of the rig, especially during rotation tests. Finally, the heat exchange coefficient is calculated thanks to the following formula :

$$h = \frac{\varphi}{T - T_{ref}}$$

The reference temperature  $T_{ref}$  is defined as a linear interpolation between the inlet and outlet sections of the test passage following the median curvilinear path.

Numerical results are obtained with an imposed constant heat flux on the heated wall, whereas other walls are assumed adiabatic, and the same process is applied to deduce the  $h$  field. Comparison between the computation and the experiment is given in figure 3.

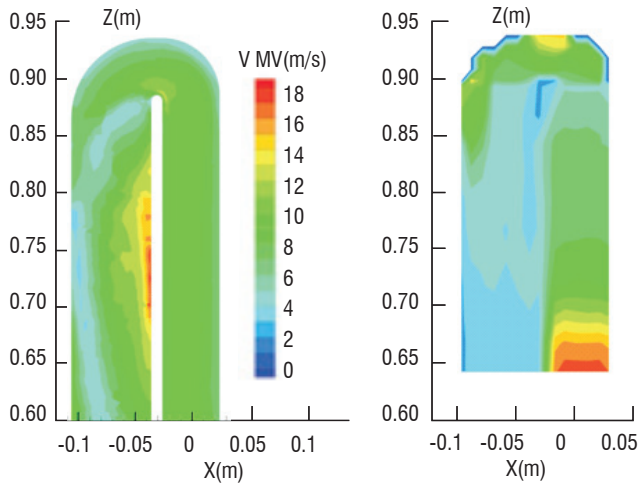


Figure 3 - Comparison between computation (left) and experiment (right) for the heat transfer coefficient  $h$

The results look different, but the average values of  $h$  are roughly the same in both the calculation and the experiment. Future tests with a reconsidered heat system should bring answers to the remaining questions, such as the one concerning the CEDRE code validation. However, a reasonable confidence can be attributed to these calculations in regard to the thermal aspects, thanks to the good agreement obtained in the aerodynamic field.

### Conclusion

Through this example, recent models implemented in the CEDRE code are shown to be able to capture the main effects encountered in the aerothermodynamics context of turbine blade cooling systems. The velocity field is quite well predicted, however some discrepancies remain concerning the thermal fields, possibly due to experimental uncertainties, for which the validation effort will be continued.

## Conjugate Heat Transfer applied to an effusion cooling system

### Introduction

The numerical test presented in this section provides a computational example of conjugate heat transfer analysis in a severe thermal case of an effusion cooling-system, in the context of a steady state problem. The basic approach used here is based on a coupled partitioned method, in which physical systems are spatially decomposed into partitions. The solution is separately advanced in time over each partition. Here it corresponds to the loose coupling of a finite-volume Navier-Stokes solver (MSD, CHARME's predecessor for structured grids), in the fluid domain and a finite-element heat conduction solver (a solver of the Zset-code) in the solid domain. The goal of this presentation is to prove that a predictive procedure may be efficient to capture the local behavior of mass and heat transfer in an effusion-cooling system.

### Geometry of the effusion system

The cooling configuration in this study has been scaled from actual combustion geometries and contains the essential physics of an effusion-cooling system, except for the curvature. It would be

unrealistic to take into account the full-coverage discrete hole film-cooling, since such a typical configuration may contain thousands of holes. As a consequence, a geometrically simple film cooling configuration has been chosen. It consists of 2 staggered rows of circular holes (elliptic in the  $xz$ -plane) with the same orientation angle  $\theta$ . Figure 4 shows a top view of the physical domain with the 12 cooling holes and also a side view of one oblique hole through the combustion skin.

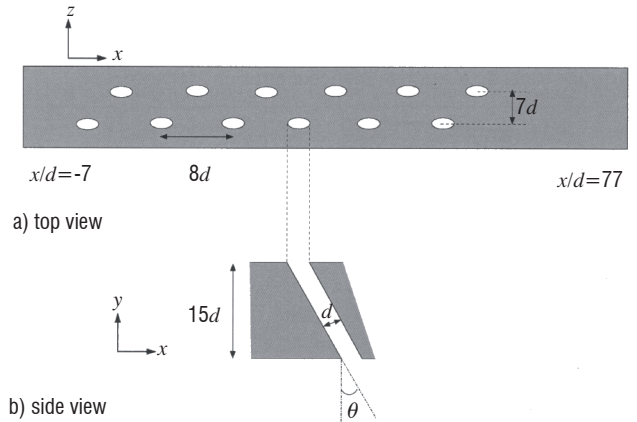


Figure 4 - Staggered arrangement of cooling holes

Geometric data relevant to the effusion cooling configuration are summarized in the following table:

hole diameter	injection angle	solid thickness	hole-to-hole spacing	solid length
0.27 mm ( $d$ )	$45^\circ$	4 mm ( $15 d$ )	2.2 mm ( $8 d$ )	22 mm ( $84 d$ )

### Computation methodology

The coupling procedure begins with an uncoupled fluid computation, assuming adiabatic surfaces. This first computation defines the initial conditions for the coupled thermal simulation. Then, the coupling algorithm consists of an unsteady time integration in the fluid, while a steady calculation is carried out in the solid [21]. Each domain is solved independently using the conditions produced by the other. At each interface separating the fluid and solid domains, we must ensure that both the temperature and the heat flux are identical in the steady state. Dirichlet conditions are imposed in the solid side, while Robin conditions are used in the fluid side. For more details, see [21] and [11]. A dynamic coupling strategy has been used here: each coupling step is automatically performed when the evolution of the fluid temperature near the coupled interface is significant. This procedure reduces the computing time significantly.

The velocity, the turbulence ratio and the total temperature of the cold mainstream are  $20 \text{ m.s}^{-1}$ , 2% and 600 K respectively. In the hot crossflow they are equal to  $370 \text{ m.s}^{-1}$ , 3% and 2200 K respectively. The Reynolds number in the hot gas flow is  $2.10^6$ . Cooling air is injected at the blowing rate of 1.2 and the momentum flux ratio is 0.5 in the hot main stream. The solid thermal conductivity is  $14 \text{ W.m}^{-1}.\text{K}^{-1}$  (steel). In this study, the flow equations are closed using the two equation  $k$ - $l$  turbulence model with wall functions [27].

## Computation results

Only the main features are presented here, more details can be found in [11] and [17]. The temperature contours are shown in figure 5. For clarification, they are plotted using two different scales, one in the solid, the other in the fluid. Several salient features may be observed. First, the formation and penetration of the effusion jets into the hot main stream is evident. It is also clear that the solid temperature pattern changes from hole to hole. Small zones of high temperature downstream in the film can also be seen. This can be partially explained by the existence of secondary flows.

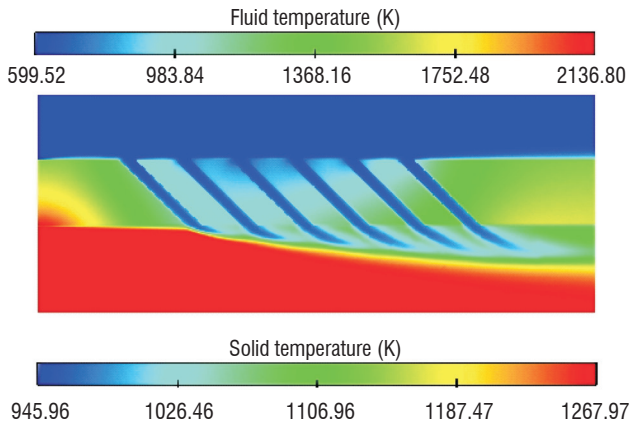


Figure 5 - Temperature field

Some streamlines are depicted in Figure 6, in an  $xy$ -plane cutting through the 1st row of holes. The incoming cooling flow separates at the sharp edge of the effusion holes and reattaches very rapidly. The main velocity in a hole is approximately  $150 \text{ m}\cdot\text{s}^{-1}$ .

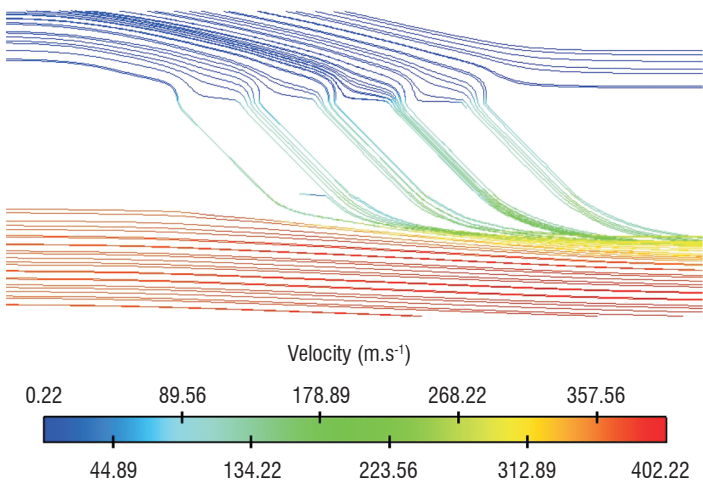


Figure 6 - Velocity streamlines

Figure 7 shows the velocity field at 4 selected  $yz$ -planes in the hot gas flow. The axial position of each plane is indicated in this series of plots. The velocity vectors are colored by the temperature magnitude. A double vortex structure has developed close to the wall, downstream of the effusion jets. The hot main stream is drawn into zones located in the middle of the two rows of holes, generating two counter-rotating vortices.

These structures allow the hot main stream to flow above the cooling jets. At increasing  $x/d$  positions, the secondary vortices become strengthened, resulting in a heat transfer enhancement, from the hot

gas to the wall. This process reduces the effectiveness of the film cooling. However, it must be remembered that film cooling flows are complex and are characterized by complicated structures (kidney vortex, shear layer vortices, wake vortices, etc.) generally not well predicted by eddy viscosity models. As a consequence, a DNS or LES approach could lead to better numerical predictions. Nevertheless, this study has shown that a coupled approach can provide detailed insights into the underlying phenomena of the effusion cooling and allows different parameters to be evaluated under realistic conditions.

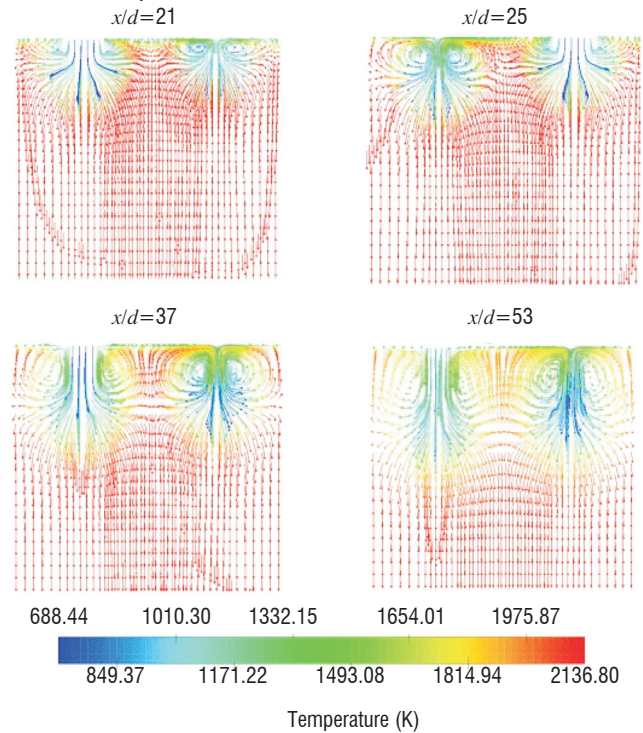


Figure 7 - Velocity vectors in  $xy$ -planes

## Conclusion

Fluid/structure coupled computations for aerothermodynamics have shown their ability to provide detailed insights into the phenomena underlying the effusion cooling. Such computations have more recently been performed with CHARME for a gas and ACACIA for a solid (two CEDRE solvers) to quantify the effect of various parameters on the heat transfers and contribute to the improvement of the CEDRE perforated wall model (see the following section, "Film-cooling of a dump combustor"). The following step for these computations is the LES approach.

## Film-cooling of a dump combustor

### Introduction

In order to cool combustion chambers, an efficient method, known as film-cooling, consists in blowing "fresh" air through multiperforated walls. In the preceding section we have seen a coupled fluid/structure computation for a small wall fraction including only a few holes. Since in actual configurations the walls can be pierced by hundreds thousands of small (diameter less than 1 mm) holes, a meshing of all these holes is unthinkable and the heat and mass transfers inside the perforated walls must be modeled. A specific model was thus developed to compute the mass flow rate through the wall and the temperature and heat flux on both wall faces locally. The model

actually provides coupled boundary conditions for the flow on each side of the wall. After a short description of the model principle, we present a simulation of an experimental dump combustor cooled by this technique. The goal of this simulation is to show the operability of the model and show its interest in the industrial design process.

### Principle of the model

The perforated wall model must not be viewed as a boundary condition for CHARME (the CEDRE Navier-Stokes solver), but as a simple analytical one-dimensional solver for the perforated wall (solid + cooling fluid) between the two faces (figure 8). Its implementation in CEDRE includes an automatic coupling with CHARME on each face of the wall.

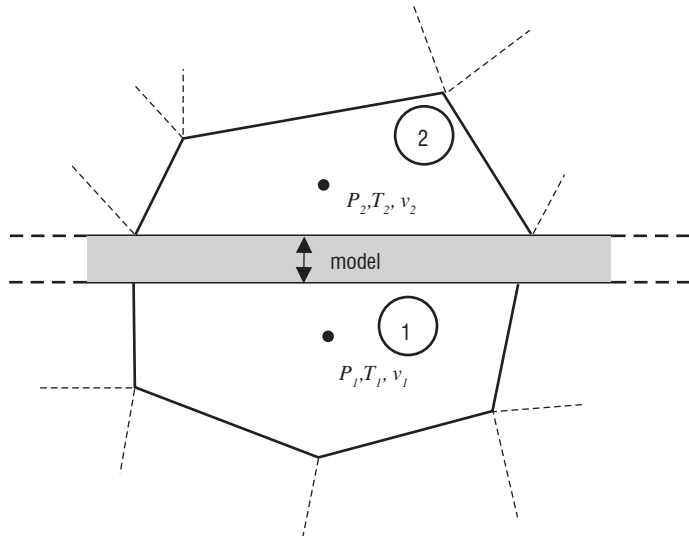


Figure 8 - Principle of the model (macroscopic point of view)

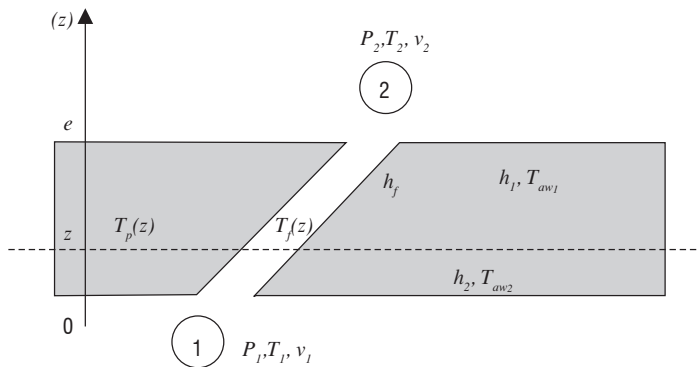


Figure 9 - Principle of the model (detailed solution)

The model is made of two independent parts, namely the aerodynamic part, which provides the mass flow rate, and the thermal part, which provides the temperatures and heat fluxes. The aerodynamic part computes the mass flow rate through the wall from a semi-empirical correlation depending on the geometry (wall thickness, hole diameter and angle, porosity) and on the pressure difference between the two faces. The thermal part is based on the analytical resolution of the coupled one-dimensional steady equation system for the cooling air temperature and the solid wall temperature, under a thermal equilibrium assumption (figure 9). Details of the equations and their solution will be the subject of another future publication.

### Dump combustor configuration

This model was applied to a DUMP combustor for two operating conditions. The combustor geometry is nearly axi-symmetric except for the fuel injection system (see figure 10).

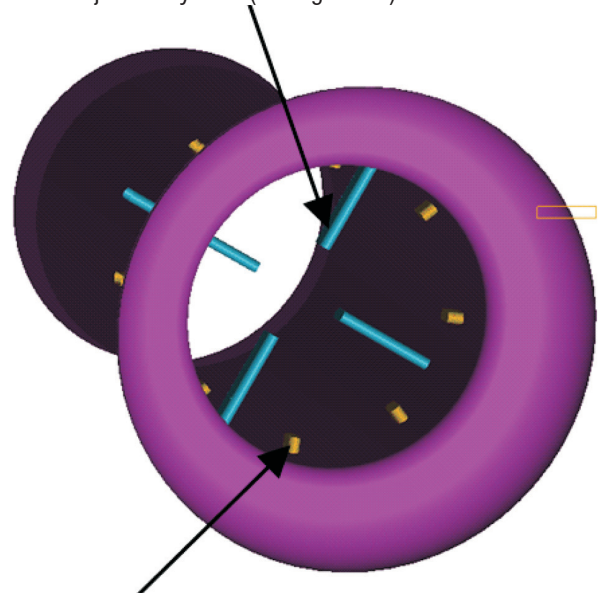


Figure 10 - Distribution of the injectors (main injectors in blue, pilot in orange)

Due to the symmetry planes, only 1/4 of the geometry is computed: the computed geometry is represented in figure 11.

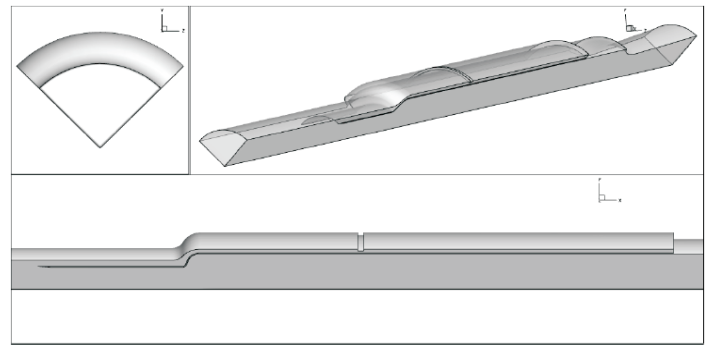


Figure 11 - Computed geometry

The multiperforated wall separating the cooling channel and the combustor is divided into three different sections with different porosity, hole orientation and hole diameter. At the interface between the first and the section, the cooling channel is partially closed over about 50% of its height, in order to increase the pressure difference in the first section, where the heat fluxes are assumed to be the highest. The main geometrical parameters are shown in figure 12.

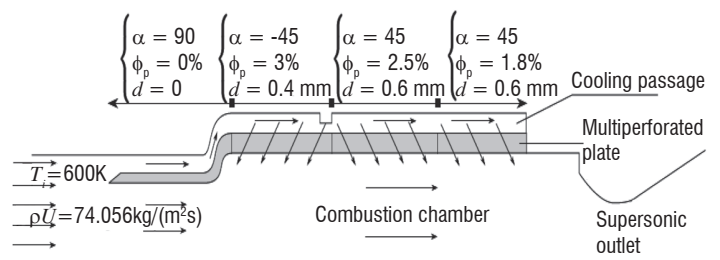


Figure 12 - Geometrical parameters of the cooling plate

Liquid kerosene is injected directly into the fluid at the position of the actual injectors (they are not meshed in our computation), as small droplets with a diameter of  $15\ \mu\text{m}$  and a temperature of 300 K.

Two operating points (presented in the table hereafter) have been computed.

Case	Air mass flow	Fluid temperature	Mixture ratio
Low Pressure	1.14 kg/s	606 K	0.6
High Pressure	7.1 kg/s	537 K	0.5

### Computation methodology

The overall system is solved using a coupled CHARME-SPARTE methodology. SPARTE is used to compute the liquid droplets, while CHARME deals with gas aerodynamics and combustion. The turbulence model is the well-known  $k-\omega$  SST and the combustion model is Eddy-Break-Up with  $C_{EBU}=4$ .

Experimental data consist in 6 temperature measurements on the cooling side of the wall. Although these points are not aligned in the experimental setup, they are all arranged behind the 4 main injectors. For symmetry reasons, we can expect them to behave almost as if they were aligned.

### Computation results

The comparison between computed and measured wall temperature is presented in figure 13 for the low pressure case and in figure 14 for the high pressure case. For each case, both measurements and computation show two peaks in the temperature curves. The first peak is due to the combustion of the “pilot” kerosene and corresponds to the reattachment of the flow downstream of the section enlargement.

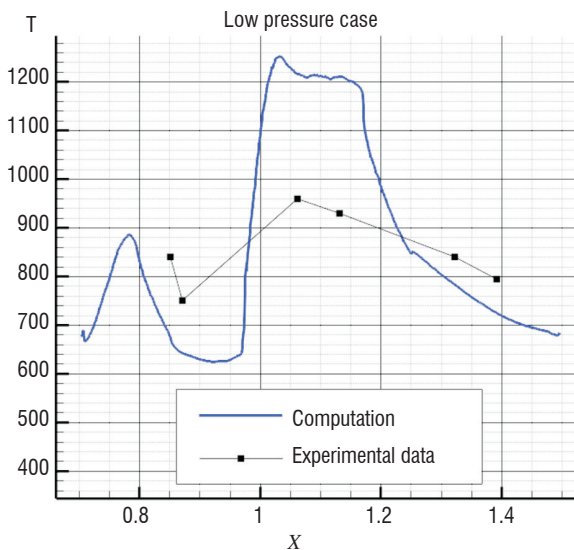


Figure 13 - Comparison between computed wall temperature and experimental data (low pressure case)

The second peak was more unexpected. In fact, as shown in figure 15, it is due to a too high pressure drop in the cooling channel at  $x=0.95$ , which corresponds to the position of the section restriction. The consequence is that the pressure difference between the cooling

channel and the combustion chamber becomes very small, and even locally negative (i.e. some combustion gases are ingested into the cooling channel) so that the cooling is no more efficient in this region, which results in a high temperature peak.

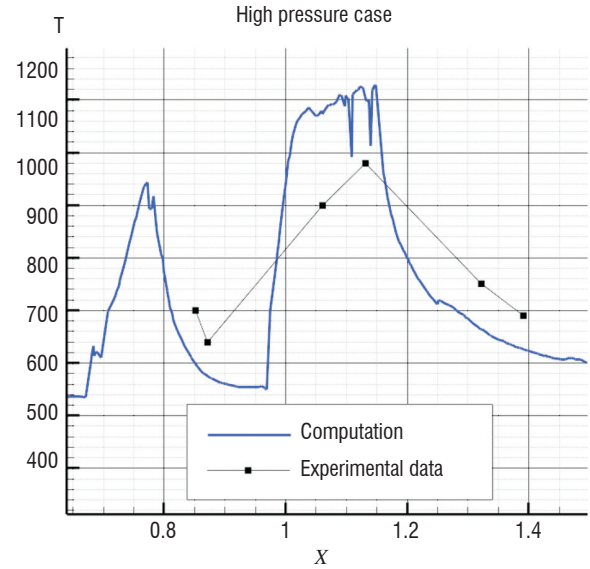


Figure 14 - Comparison between computed wall temperature and experimental data (high pressure case)

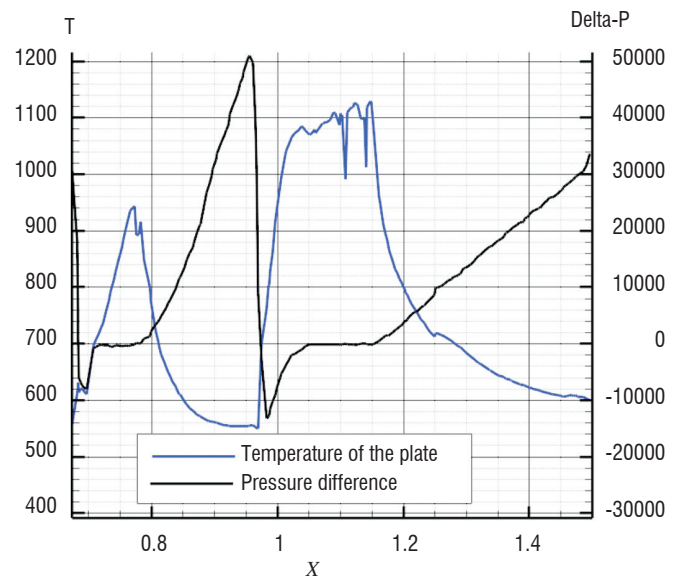


Figure 15 - Link between temperature evolution and pressure difference on the wall (high pressure case)

However, the wall temperature peak in regions where the pressure difference is vanishing seems to be overestimated by the computation. A possible explanation is the existence of small pressure fluctuations not captured by the RANS computation, which may help the fluid to move into the holes, therefore cooling the plate. The same phenomenon can be observed in the low pressure case. The combustion model, known to overestimate the gases temperature in the burner, is another possible explanation for these discrepancies.

### Conclusion

A simplified multi-perforated wall model has been developed, implemented and tested to take into account multi-perforated walls in a global CFD computation. Even though wall temperature prediction is

perfectible, the model has been proven to be capable, at a negligible computational cost, of giving qualitatively good results and makes it possible to understand the effects of the cooling channel geometry on the temperature distribution on the wall. It can also be noted that wall temperature levels depend not only on the multi-perforated wall model, but also on several other models, such as the friction computation (turbulence model and wall law), the combustion model and the radiation for example. A validation based on simpler (without combustion) dedicated experiments will make it possible to improve the accuracy of wall temperature prediction.

## Hypersonic vehicle separation

### Introduction

The interest of high-speed air breathing propulsion has been identified for many years. Capability to sustain high altitude hypersonic cruise is particularly interesting in the scope of long-range missiles. Since January 2003, MBDA and Onera have been engaged in the LEA program [51][19][20], of which the most challenging issue is to show the capability to precisely assess the thrust-minus-drag balance of an experimental scramjet vehicle. Within the framework of the LEA program, Onera conducts CEDRE numerical simulations of the separation phase between the LEA vehicle and its booster.

The test flight sequence plans are for the experimental vehicle to be boosted up to the required flight tests conditions, after an air-drop from a Russian supersonic bomber. Once they are reached, LEA separates from its booster and starts its autonomous scramjet propelled flight. The separation between LEA and its booster will most likely be one of the most critical phases of the flight experiment. Thus, RANS computations were conducted to evaluate the aerodynamic interactions between LEA and the inter-stage of the booster during separation.

Since it was impossible to comprehensively characterize all the positions of LEA during the separation phase, only the most probable relative attitudes between the vehicle and its booster have been studied. Some of them are presented in figure 16.

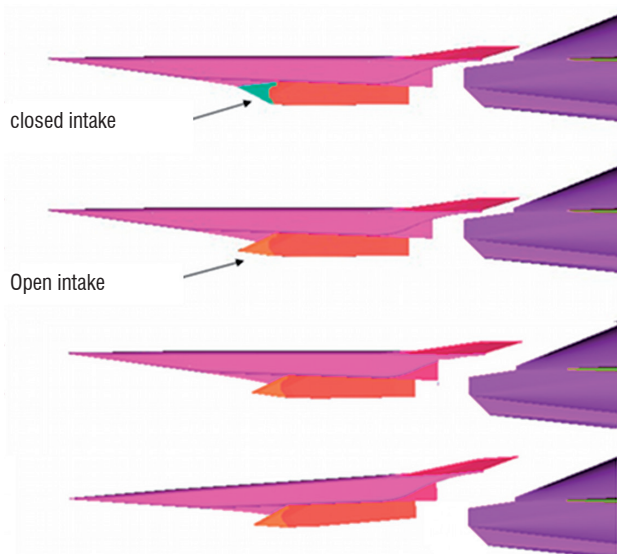


Figure 16 - Different relative separation positions studied

### Computation methodology

The simulations were conducted at Mach 7.5, with CEDRE v3.2.2 on 3D unstructured half-configuration grids (12 M elements) (figure 17). The unstructured mesh allows the modeling for both vehicles of very complex shapes and mesh refinement in the interaction region.

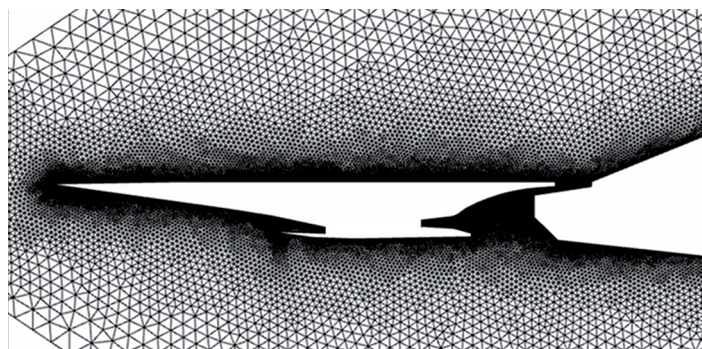


Figure 17 - Plane of symmetry of the grid used for separation computations

The RANS steady computations use the  $k-\omega$  turbulent model with a low Reynolds approach (no wall law). The spatial resolution scheme is the Advection Upstream Splitting Method (AUSM+) with additional numerical dissipation activated : this flux scheme represents a good compromise between accuracy and robustness for supersonic flows. The one step implicit formulation with a local time step based on  $dU/dt$  is used as a time integration method. The calculations were carried out on 64 processors of an Altix ICE 8200 EX SGI supercomputer and each one took 10 hours to reach convergence after 5000 cycles.

### Computation results

The computation results highlight an important flow interaction between the bow shock created by the inter-stage of the booster and the LEA nozzle boundary layer. This induces an important flow separation beginning at the maximum slope angle point of the upper part of the nozzle (figure 18). The flow separation disappears once the interaction shock is located downstream from the end of LEA's nozzle.

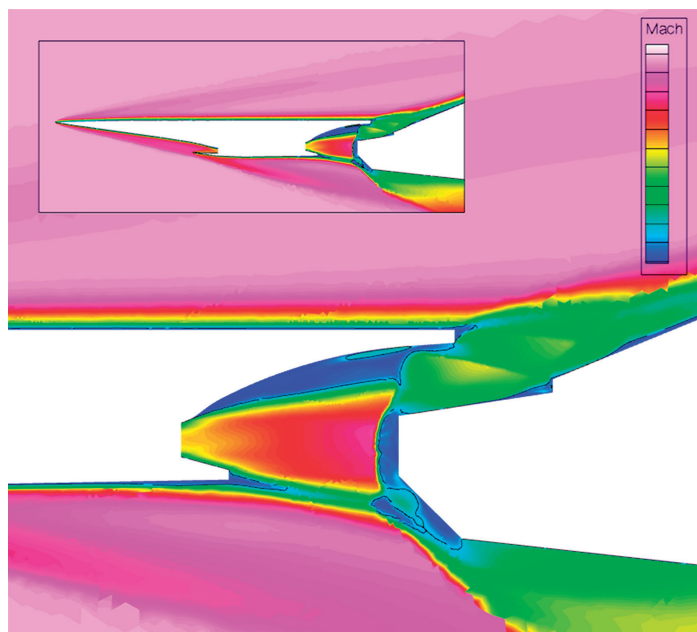


Figure 18 - Mach number in the symmetry plane (Intake opened)

When the intake is closed, figure 19 shows that the front part of the booster is in a kind of cavity flow. Then, no noticeable interaction is evidenced on the upper part of the nozzle compared to the LEA closed engine free flight computation. The free flight model could be considered unchanged in that particular case.

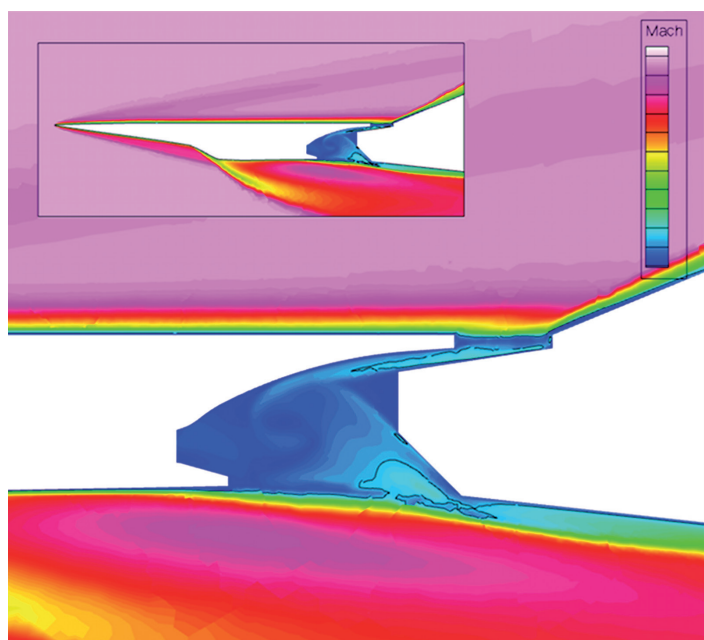


Figure 19 - Mach number in the symmetry plane (Intake closed)

## Conclusion

Aerodynamic simulations of the separation of a hypersonic vehicle were successfully performed with CEDRE. In the next phase of the study, thanks to the general thermochemical model of the code, it will be possible to evaluate the effect of a high temperature real gas flow on the interaction. The high temperature could be due to high speed flow wall friction or to an early starting of the scramjet engine. A “moving bodies” functionality, currently being developed in the code, will allow to perform unsteady computations in the future.

## Rocket engine ignition blast wave

### Introduction

During a space vehicle launch, the rapid pressure build-up in the Solid Rocket Motor (SRM) chamber generates a strong overpressure wave at the nozzle exit, known as an Ignition OverPressure (IOP). One part is transported inside the flame trench to its exit, where it generates a second acoustic wave, the Duct OverPressure (DOP). These two low frequency waves may turn out to be dangerous, since they apply strong loads to the launch pad, the launcher or its payload. One of the main concerns of the CNES/Onera AEID program is to efficiently reduce these loads. Within this framework, experimental firings of scaled down models of Ariane 5 P230 SRM (known as LP10), were carried out at the Fauga Mauzac Onera center in various configurations [58]. Two of these are selected for the current study: a free horizontal jet (case I) with slightly aluminized propellant (5% in mass) and a realistic vertical firing with a flame trench (case II) with aluminum free propellant. In both cases, the nozzle is characterized by the ratio  $A_j/A_t = 7.5625$  between its exit area and its throat area, with an exit diameter  $D_j = 70.34$  mm. Pres-

sure signals on far field and combustion chamber transducers were recorded during experiments.

The Onera CEDRE platform is used to perform numerical studies for these experiments. Various phenomena are modeled: the interaction of the acoustic waves with the environment (flame trench, ground, etc.), possible reactions between the reducing combustion products and the quenching with water of ambient air or combustion products. The inlet boundary is treated by imposing a total pressure fitting the experimental unsteady curve. The first 30 milliseconds are calculated with implicit time integration. The LES Smagorinsky sub grid model is activated.

Case I focuses exclusively on IOP: previous computations held in a 2D axisymmetric configuration yielded deceptive results regarding the amplitude and directivity [56]. Since the discrepancies were thought to be due to the 3D nature of the turbulence, 3D computations are carried out in case I. The aim of case II is to numerically characterize both IOP and DOP waves. Again, previous computations led to a quite accurate prediction of IOP and DOP, but a secondary DOP appeared, not observed during experiments [57]. The effect of the water supply in the flame trench is studied in case II. In both cases, the possible afterburning of combustion products with air is taken into account.

### Free jet configuration (case I)

In the free jet configuration, the motor is fired horizontally, 1 meter above the ground. Transducers are located along a horizontal arc centered at the nozzle throat, with a 5 m radius and extending from 20 to 60° from the jet axis.

### Computational Domain

The computational domain is a half-sphere centered on the nozzle throat, whose radius extends to 8 meters and truncated by the ground, as shown in Figure 20. It features the combustion chamber aft end, the nozzle and part of the motor structure.

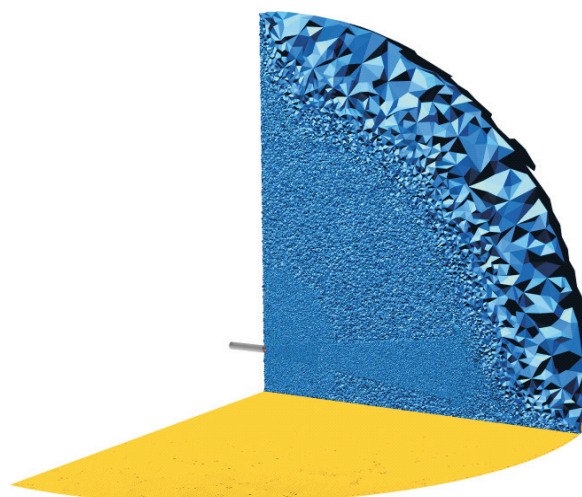


Figure 20 - Computational domain and grid

### Grid

Particular attention must be paid to the size of cells propagating acoustic waves. Bogey and Bailly [5] showed that for low order space discretization schemes (typically 2, as used in this study), a minimum of 20 points must be found in the propagative direction in the consi-

dered wavelength (PPW), in order to ensure low dispersion and dissipation. The IOP wave front characteristic period can be estimated to  $T=1$  ms, according to experimental data. The characteristic wavelength comes to  $\lambda=c \times T=0.346$  m, where  $c$  is the sound speed in the propagative area (normal conditions of pressure and temperature). Thus, the maximum cell size in the direction of propagation is  $\Delta=0.346/20=17.8$  mm. The generated cells being formed with an average number of 13 faces, they can easily be assimilated to spheres and the above criterion is to be applied to the cell diameter. In our domain, the resulting grid would yield far too many cells and a refinement procedure must be applied: cell size varies between 8 mm (at the nozzle exit) and 31 mm on computation "31", or up to 45 mm on computation "45" (at transducers). Both resultant grids contain the same finely discretized zone in the jet where most of the noise sources are located. Grid 31 features a total of 8 331 765 cells and 58 377 688 faces, and grid 45 features 4 277 630 cells and 29 917 328 faces.

## Modeling

Afterburning of propellant combustion products with air is modeled with a 17 reaction and 12 species kinetic scheme. It features the 6 major species in the combustion products, plus 5 intermediary species, plus  $N_2$ . Droplets of  $Al_2O_3$  are modeled as an equivalent gas, in order to avoid a costly two phase computation.

## Computations

Computation 31 is carried out on 1000 Intel Nehalem CPUs and requires a total of 16 h, and computation 45 requires 64 Intel Montecito CPUs during 120 h. The time step is set to  $10^{-5}$  s and is slightly reduced at start-up. Pressure traces recorded on transducer 1 ( $20^\circ$ ) for 2D axisymmetric, 3D computations and experimental data are displayed in figure 21 and directivity is plotted in figure 22. IOP amplitude is much closer to the experimental data with 3D computations. Moreover, 3D computations lead to a better-estimated directivity on high angle transducers than previous 2D ones, highlighting the preponderant effect of the 3D nature of turbulence. Finally, decreasing the propagative grid size modifies directivity in the mid-angle direction only, while slightly changing the frequency distribution.

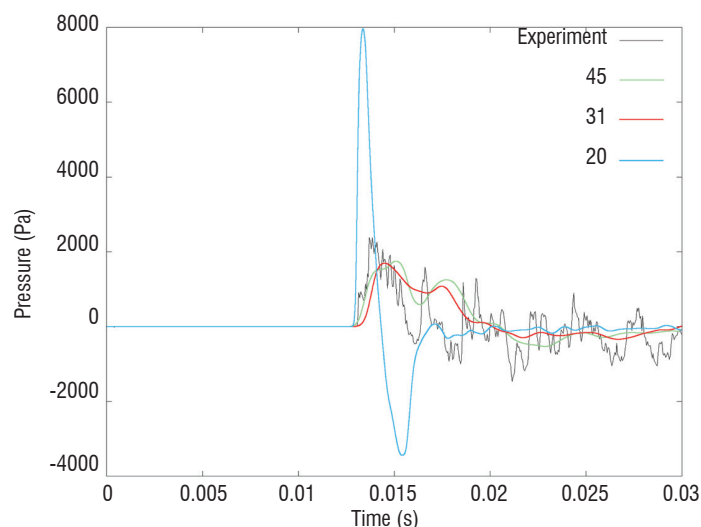


Figure 21 - Experiment/computation comparison ( $20^\circ$ , 5 m)

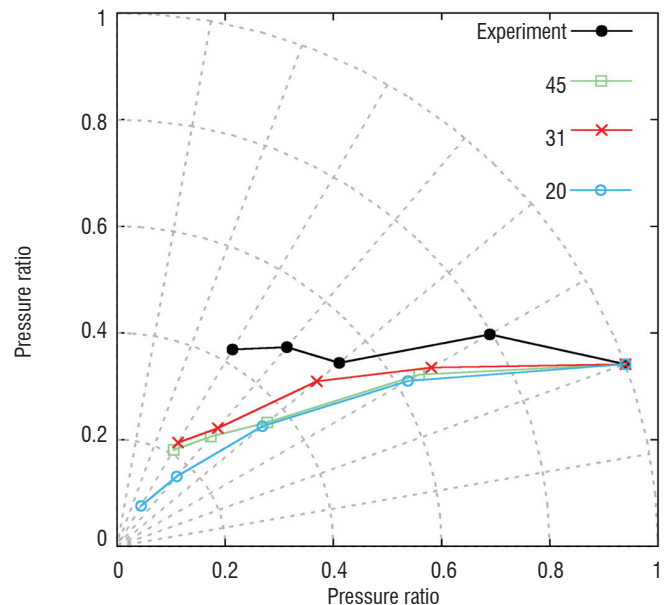


Figure 22 - Experiment/computation comparison - Directivity

## Flame trench configuration (case II)

The second experiment focuses on the IOP and DOP: the jet is fired vertically in a water supplied flame trench.

## Computational domain

The computational domain is built from a simplified geometry of the experimental set-up. It includes the combustion chamber aft end, the nozzle, the motor external structure and the flame trench (figure 23). The outside computational volume was limited to a quarter of a 3 m radius sphere, centered close to the nozzle exit.

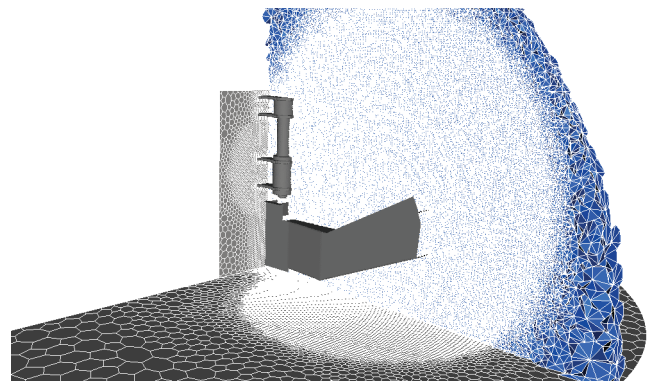


Figure 23 - Computational domain and grid

## Grid

The volumic mesh is polyedric, mainly made of 14 sided elements. The grid includes a refined zone, centered on the flame trench exit, with a cell size of 23 mm (see figure 23). This size leads to an acoustic time step equal to  $7.10^{-5}$  s (for sound speed of 340 m/s), consistent with an overall duration of 30 ms. The final grid comprises a total of 1 633 663 cells and 11 406 043 faces.

## Modeling

The combustion products are modeled by a single species, called PROP; the ambient air, called AIR, is a perfect mix of O<sub>2</sub> and N<sub>2</sub>; the species resulting from the combustion of PROP with AIR is called PROD, and is produced using an infinitely fast chemistry model (EBU/Magnussen type).

Water vaporization is taken into account by a model allowing the simulation of a two-phase flow (water plus vapor), as a mix of 2 distinct gaseous species: LIQ is an equivalent gas of the liquid state and VAP, its vapor. The inverse reaction (condensation) is not taken into account.

In addition, since the computations deal with a high density fluid, gravity is activated.

## Computations

Three calculations are performed in order to compare the 2 main phenomena that are of concern (afterburning and gas/liquid interaction): 1 inert, without water (known as ID); 1 reactive, without water (known as RD) and 1 reactive, with water (known as RW). The inert computation is run deactivating the combustion reaction and the water-free ones are run deactivating the vaporization reaction. Water is taken into account as an initial condition (a water layer of 1.5 l is added at the flame trench bottom), without additional injection during the simulation. This is not fully representative since, in the actual experiment, water is injected during all the firing. All computations are carried out on 64 Intel Montecito cores. The calculation time steps are respectively set to  $1 \cdot 10^{-5}$  s,  $1 \cdot 10^{-6}$  s and  $1 \cdot 10^{-7}$  s. Figure 24 and figure 25 compare the calculated flows (13 ms after ignition) with and without water. The effect of water on the temperature field is particularly visible.

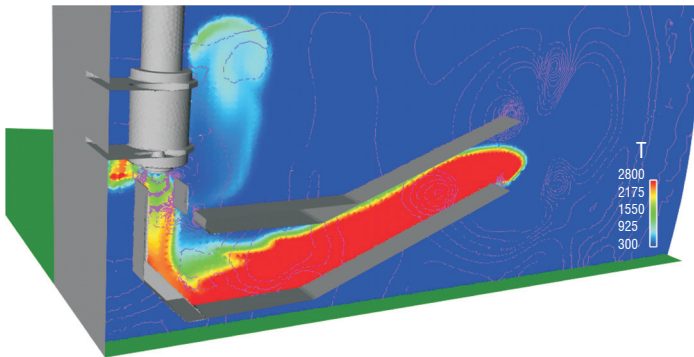


Figure 24 - Temperature field and isobar lines - Computation RD

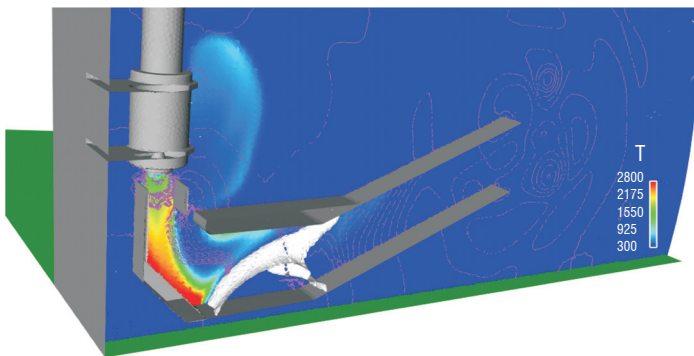


Figure 25 - Temperature field, isobar lines and iso water concentration - Computation RW

The transducer located at 5 m and 120° (figure 26) illustrates the separation of IOP (5 ms) and DOP (9 ms). The computation results are that IOP is reinforced by afterburning but that the water layer has no effect on this reinforcement. DOP is much less reinforced by afterburning and is, like IOP, nearly independent on water. Finally, a secondary DOP (14-21 ms) is observed in reactive computation without water. This secondary DOP is strongly mitigated in the reactive computation, with water in the flame trench, which reduces gas temperature near the exit.

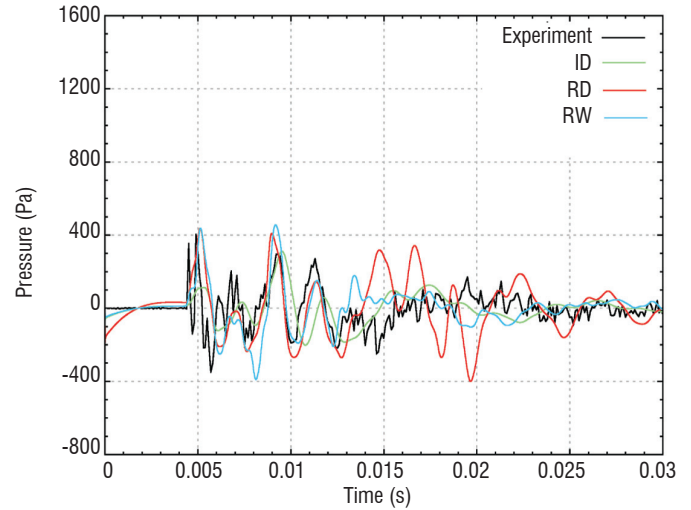


Figure 26 - Experiment/computation comparison (120°, 1.5 m)

## Conclusion

This numerical study showed the benefits that 3D unsteady computations can bring to the understanding of IOP phenomena. However, case I has revealed that propagative area discretization seems to impact the solution at a lower order than the accurate simulation of noise sources located in the jet. Thus, efforts must concentrate on this point, in order to generate the complete range of frequencies observed during experiments. The case II results complement the analysis of physical interactions affecting the generation of different overpressure waves. The computations showed the important influence of afterburning and water injection on the blast wave. Further research is needed with more realistic models for combustion and water injection.

## Jet noise prediction

### Introduction

Numerical simulations are commonly used today in aeronautics for the analysis of noise generation and radiation problems. Jet noise, which is the main source of acoustic nuisance for an aircraft at take-off conditions, is especially investigated even though high computer requirements have restricted most of the existing work to simplified and isolated configurations. One of the challenges is thus to propose and assess the quality of a suitable simulation methodology, in order to target situations of industrial interest [52][59][6][4][25][60]. Onera has been working for several years to construct a hybrid Computational-Aero-Acoustics (CAA) approach to tackle this challenge. For instance, recent studies have made it possible to evaluate the proposed approach for the case of fluidic control of single stream isothermal and hot jets [25] and for the study of installation effects in the

case of a high by-pass ratio dual stream nozzle [60]. After presenting the details of the constructed approach, the results obtained for the two above mentioned cases will be presented briefly.

## Computation methodology

The hybrid CAA approach, which is being investigated at Onera, consists in associating a Large Eddy Simulation (LES) of the jet flow to an acoustic integral formulation used to reconstruct the noise radiated to the far field. In sizing the requirements for such complex computations, the following points were considered:

- Firstly, the actual geometry must be reproduced in the computations. In particular, the exact geometry of the nozzles must be simulated in order to avoid both guessing the jet inlet conditions and forcing the jet flow to initiate the jet turbulence. Another important consideration is that most noise reduction devices involve the modification of the nozzle geometry itself (chevrons, serrations, micro-jets, etc.) which must be reproduced in the computations. In addition, it is desirable for the computations to be capable of taking into account the installation effects, which involve the nozzle surroundings (mast, pylon, wing, etc.). These geometrical requirements bear some consequences on the choice of the numerical schemes, which must be robust enough to accommodate complex, boundary fitted grids. In practice, upwind schemes of the MUSCL family were retained.

- Secondly, the computation duration, in clock time, should be short enough to allow parametric studies to select the most efficient nozzle arrangement. This implies some choices in terms of grid size and the related resolved frequency range of the LES simulations. In this regard, a deliberate choice was made to perform the LES computations with the smallest grid size compatible with the objective of capturing the main noise producing structures. A priori analysis showed that the smallest upper frequency should be of the order of  $St = 0.5$  ( $St$  being the Strouhal number, based on nozzle characteristic diameter,  $D_j$ , and exit velocity,  $U_j$ ). Moreover, an additional grid requirement came from the need to properly resolve the intense shear layer generated at the nozzle exit. These requirements, combined with the properties of numerical schemes, provided the necessary rules to design the grid in the jet noise producing regions. These rules can be applied to any configuration with the guaranty of similar flow resolution. This is an important result to ensure the meaningful comparison among different designs.

- Thirdly, the deliberate choice of tuning the computations toward actual geometries, even at reduced scale corresponding to available industrial wind tunnels (roughly 1/10), placed the computations in the high Reynolds number range (above  $10^6$ ) where the jet noise has a broadband, stochastic like, behavior. This implies that the time series produced by the computations and used to post-process the results must be long enough to avoid undesirable statistical bias. In practice, time series in excess of  $100 D_j/U_j$  must be provided by the computations.

- Finally, in regard to the above requirements, an implicit time integration scheme appears to be highly desirable. Indeed, it rapidly appeared that the smallest grid size was required at the nozzle exit to resolve the sheared flow. These small cells would drive an explicit time step to excessively small values rendering the overall computation unaffordable. Considering that the initial high shear regions should be weakly affected by acoustic wave propagation, it was assumed that these cells could be operated at a local CFL number higher than unity, provided an implicit scheme could be used. Of course, thanks to grid stretching, the regions of high acoustic activity would be operated at a local CFL number below unity for consistent acoustic wave propagation computation.

From the analysis summarized by the points above, it appears that the CEDRE solver possesses many qualities to be retained as the work horse for jet noise studies. Indeed, it offers a wide range of robust and accurate second order MUSCL schemes, combined with several efficient implicit time integration schemes (from first to third order). Moreover, its polyhedral mesh capability makes it possible to combine many types of grid elements, to design properly tailored grids. In the course of these studies, started in 2005 [28], a common grid arrangement was defined: a structured hexahedral grid was designed to accommodate early sheared regions as well as the noise producing regions of the jet flow. Thanks to the CentaurSoft grid generator, this structured patch was embedded into an unstructured grid that made it possible to precisely describe the nozzle geometries with no limitations or penalties associated with particular arrangements.

Considering the acoustic part of the aeroacoustic simulations, the choice was made to rely on a surface integral acoustic solver. The Onera KIM code [42] was retained. Early studies showed the importance [3] of properly defining the surfaces onto which the LES solution was stored and of providing the necessary cross checking capabilities to avoid spurious results. In particular, the length and position of the surfaces were found to be of crucial importance and several surfaces were systematically used to ensure that the far field results were not dependent on particular surface arrangement. In the course of these validation studies, it was shown that the Ffowcs-Williams and Hawkings integral formulation (FW-H) was better suited to the case of hot jets and that surface length should be in excess of  $20 D_j$ . The question of the closure of these surfaces was also studied and it was concluded that open surfaces could be safely used, provided that they were long enough.

This aeroacoustic methodology has been extensively tested at Onera against numerous configurations that were experimentally tested and provided a high level of confidence in the quality of the computed aerodynamic flow, as well as the near field and far field acoustic solution [33][34][40][61].

## Computation results

To illustrate the above detailed methodology, two recent computations are presented hereafter. The first one concerns installation effects and the second one concerns noise control by micro-jets.

### Case I: Installation effects (pylon) for a double stream nozzle

Following studies on several double stream nozzles, a first step was taken toward the study of installation effects by introducing the mast/pylon arrangement. The grid is presented in figure 27.

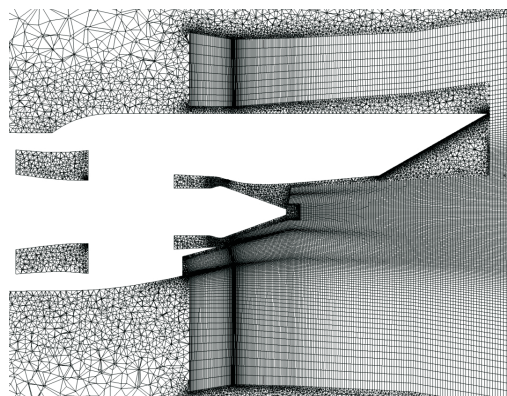


Figure 27 - Detail of the grid for the pylon configuration

The pylon region is cut into the structured hexahedra grid patch and the acoustic surfaces (figure 28) are placed in this patch, over the pylon. The grid is made of over 10 million cells and the computation is run on 64 cores of the Onera Itanium cluster. The total clock time was 360 h.

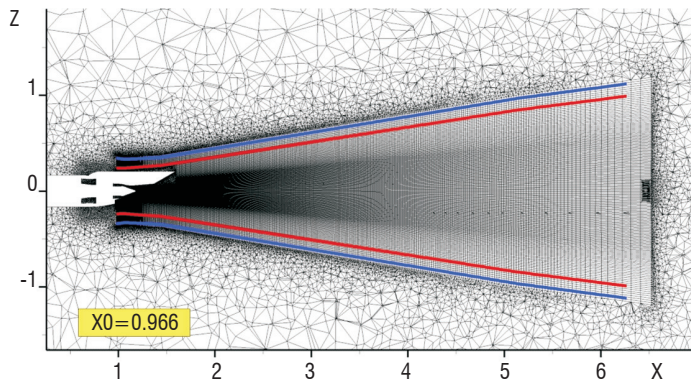


Figure 28 - Positions of the acoustic FW-H surfaces in the structured patch

The results showed good agreement with measurements performed during the course of the EU VITAL project [60]. In particular, the effects of the pylon on the jet flow (figure 29) and on the radiated noise (figure 30) were properly recovered by the simulation.

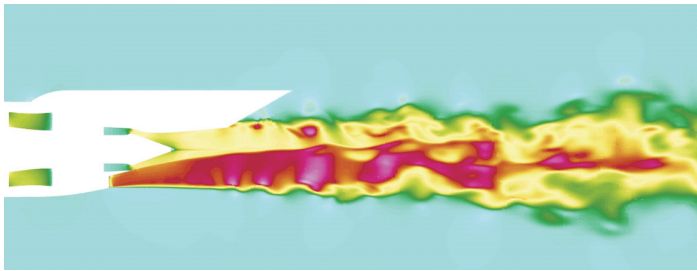


Figure 29 - Instantaneous Mach number field

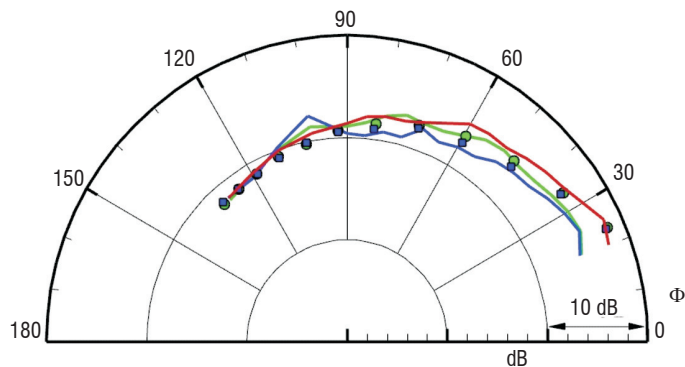


Figure 30 - Experimental (● sideline; ■ flyover) and computed (— sideline; — flyover; — without pylon) OASPL on the range [200 Hz ; 25 kHz]

### Case II: Noise control by micro-jets

Recent original works were concerned by the effects of micro-jets as a means of reducing jet noise. A single stream nozzle (from the EU JEAN project) was used and 12 micro-jets were placed in the structured grid patch around the nozzle exit. Micro-jets were not resolved in the simulation, since it would have rendered the overall computation unaffordable. Instead, source terms were added in the simulation thanks to an ad hoc model to reproduce the injected mass, momentum and energy [25]. Each micro-jet was given a source characteristic placed in one cell of the computation (cell size was chosen

to represent the actual size of each micro-jet of roughly 1 mm). Continuous or pulsed micro-jets were tested in the computations with significant results [25]. The grid arrangement is presented in figure 31.

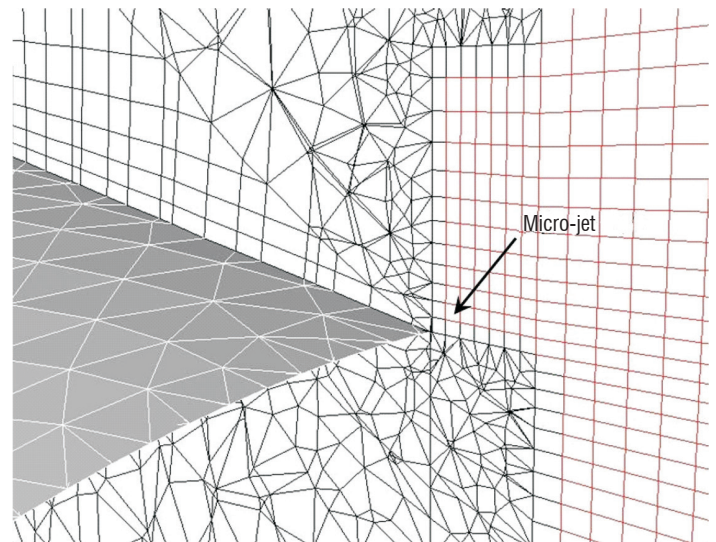


Figure 31 - Detail of the grid and micro-jet location at the nozzle lip

The effect of continuous micro-jets on the jet flow is illustrated in figure 32. The micro-jets are clearly found to modify the jet flow, in agreement with experimental observations. The effect on the radiated far field is also quite well reproduced by the simulation (figure 33).

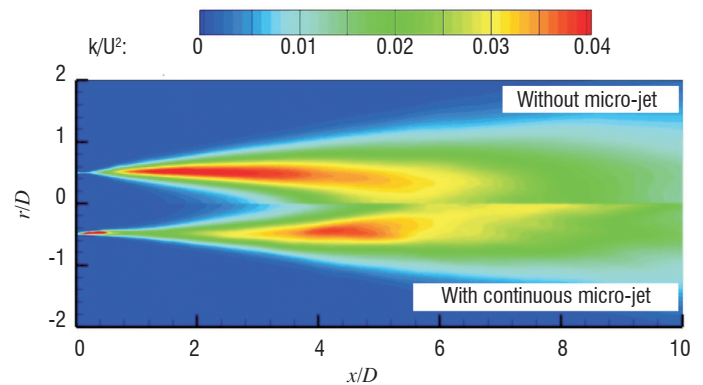


Figure 32 - Effect of continuous micro-jets on the mean turbulent kinetic energy for a hot jet case

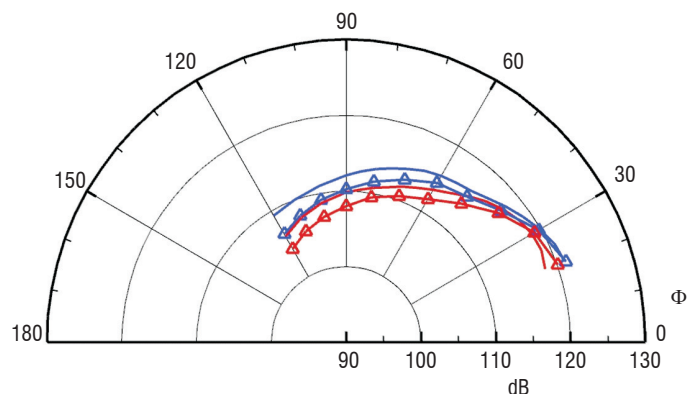


Figure 33 - Predicted directivities without and with continuous micro-jets, 30D from the nozzle exit. Isothermal jet: — baseline; —△ continuous micro-jets. Hot jet: — baseline; —△ continuous micro-jets

## Conclusion

The methodology presented proved to yield valuable results in predicting and controlling jet noise from civil aircraft. Future work will address configurations of increasing complexity, as well as the evaluation of possible control strategies. Evolutions of the CEDRE code, such as moving grids and higher order schemes, etc., will notably benefit this application field.

## Flow separation in an over expanded nozzle

### Introduction

The ATAC nozzle is a planar nozzle designed to investigate the reacting flow, when operating in over expanded conditions, i.e., with a back pressure higher than the theoretical nozzle exit pressure [38]. This experiment aims to reproduce the flow separation occurring in rocket nozzle extensions on the ground and at the beginning of the flight. A detailed review on nozzle flow separation can be found in [24]. In such conditions, outside air engulfs the extension and can burn with the remaining reducing species (unburnt  $H_2$  for instance) of the hot gases coming from the combustion chamber, creating additional thermal fluxes. The particular features of this test case are: a very high ratio between the exit and throat heights, an additional  $H_2$  injection at half of the divergent length and the existence of both experimental OH visualizations and wall measurements. In this work, numerical simulations of this test case are carried out with the CEDRE code. The purpose of this study is to evaluate two approaches, steady RANS and unsteady DDES by comparison with the experiments. First, the modeling used and the numerical methods are briefly described. Then, the computational grid and the conditions of the computations are presented. Finally, both averaged and instantaneous results are compared to the experiments and discussed.

### Physical models and numerical methods

Two approaches are used for turbulence modeling: a steady RANS approach with the  $k-\omega$  SST model and an unsteady DDES approach (see [50] for a presentation of the approach implemented in the CEDRE code), which allows the attached boundary layers to be treated in RANS while switching to LES in the separated regions. The mixture is composed of seven species ( $H_2$ ,  $O_2$ ,  $H_2O$ ,  $H$ ,  $O$ ,  $OH$ ,  $N_2$ ). The species destruction/production terms are obtained thanks to a 7 reaction kinetic scheme [16]. Apart from the general numerical methods used in the CEDRE code, Roe's flux difference splitting associated with a MUSCL interpolation is employed for the advective fluxes. This method results in a second order spatial accuracy (third order on isotropic mesh). The time integration is carried out using a first order Euler implicit scheme, with local time stepping to speed up the convergence of the RANS simulations and a global time step with a second order sub-iterated Gear scheme is employed for the DDES computation.

### Computational grid and conditions of the computations

To perform the simulations, we chose to separate the computational domain into three zones, computed independently. This separation and some views of the structured grids are illustrated in figure 34. Such a separation is made possible by the supersonic nature of the flow in the upstream nozzle (zone 1) and injector (zone 2). Thus, the

imposed conditions in the inlet sections of the over expanded region of the nozzle (zone 3) are given by the results of the steady RANS computations of zones 1 and 2. Approximately the size of the meshes of zones 1, 2 and 3, they are 1.5 million, 1 million and 6 million grid cells respectively. In zone 3, RANS and DDES computations are performed. Concerning the boundary conditions, the far field and the outlet correspond to pure air at ambient pressure and temperature. The composition of the hot gases in the upstream nozzle inlet is obtained thanks to an equilibrium computation at the given pressure, temperature and mixture ratio. In these computations, we aim at reproducing the conditions referred to as "P=25 bars, higher  $R_m$ ,  $H_2$  injection" in [38].

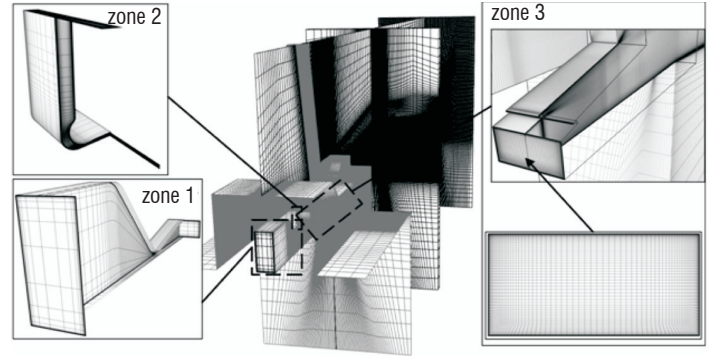


Figure 34 - Views of the meshes in the three different regions given by the separation of the computational domain

### Results and discussion

First, the time averaged OH emission throughout the span wise direction is illustrated in figure 35 and compared to the equivalent OH mass fraction visualizations for RANS and DDES. In this figure, one can notice that DDES results match the experiments better, since the reacting region is wider than that for RANS, where a clear diffusion flame is produced downstream of the separation in the mixing layer. Indeed, in reality, the reacting region oscillates in such a way that the shape evidenced in RANS cannot occur. Moreover, if we compare instantaneous OH mass fraction screenshots (DDES) to PLIF-OH measurements in the mid-span section, one can notice that the particular behavior of the flame is well reproduced by the computation.

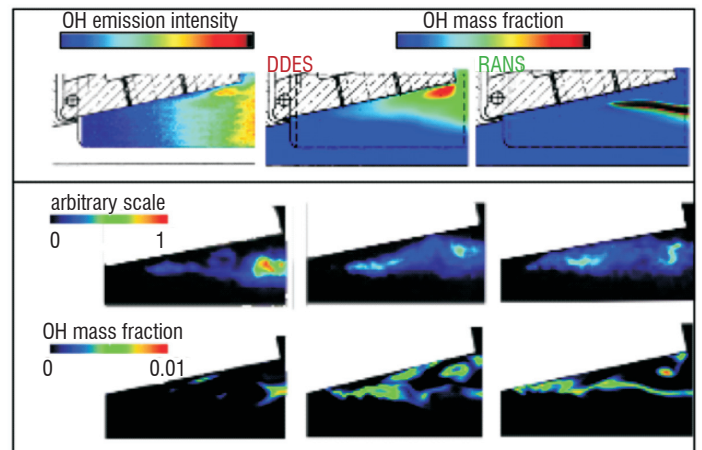


Figure 35 - (top) Averaged OH emission intensity in the spanwise direction, compared to the computations (bottom) Instantaneous PLIF-OH visualizations compared to a sequence of OH mass fraction in the mid-span section (DDES)

Concerning the wall measurements, one can compare the averaged and fluctuating pressure profiles in the second half of the extension (downstream of the injection) to the pressure measurements obtained during the campaign. These profiles are displayed in figure 36 and figure 37. It can be pointed out that the results of our simulations are in fair agreement with the measurements for the averaged pressure. Nevertheless the RMS pressure fluctuations are clearly overestimated compared to the measurements. Such a discrepancy can be explained by an insufficient spatial discretization in the separated region.

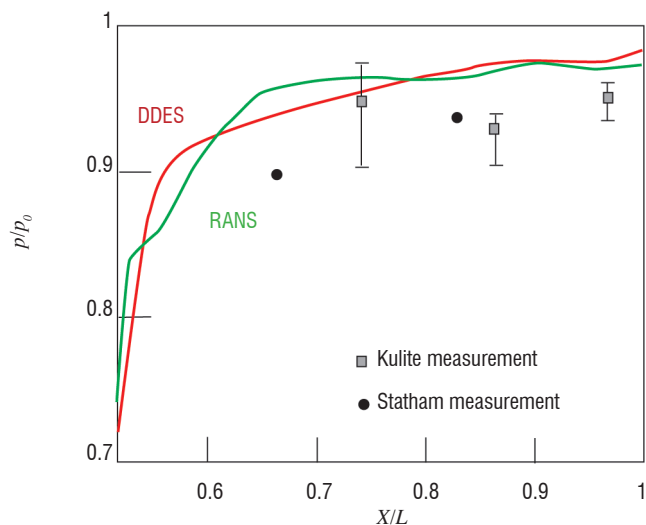


Figure 36 - Averaged wall pressure along the upper wall

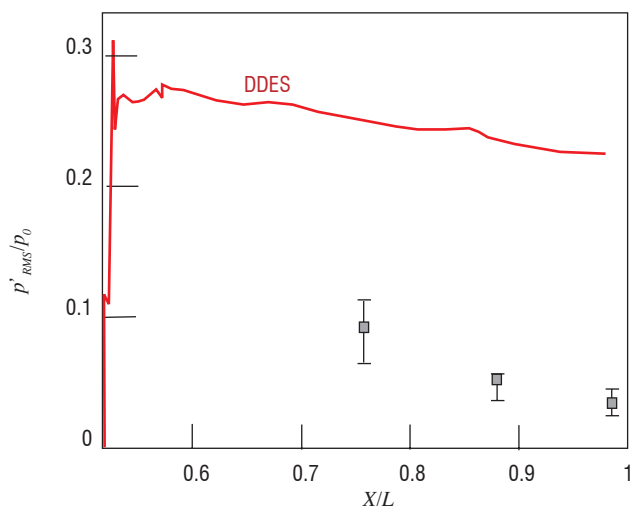


Figure 37 - RMS fluctuation of the wall pressure

## Conclusion

Both steady RANS and unsteady DDES computations of the reactive flow inside an over expanded planar nozzle were successfully carried out and compared to the available experiments. This comparison highlights that RANS is unable to take into account the strong oscillation of the flow, which results in a poor estimation of the reacting region contrary to DDES, which is in fair agreement with the measurements for both averaged and instantaneous flow fields. Moreover, wall pressure profiles are in good agreement with the experiments for both methods. For DDES, the pressure fluctuations are overestimated. Further work is required to investigate the nature of the flow oscillation and the origins of this overestimation.

## Aircraft and helicopter icing

### Introduction

Icing occurs when an aircraft flies through clouds in which super cooled droplets are suspended in the atmosphere, with an ambient air temperature below the freezing point. The droplets impinge on the aircraft surfaces and freeze, leading to ice accretion. The resulting change in the aircraft geometry can modify aerodynamic characteristics (loss of lift, rise of drag), can affect the ability of the probes to provide accurate measurements, can block helicopter moving parts, can clog air intake or even damage the engine by ice ingestion, and in the worst scenario can cause a complete loss of the control of the aircraft or rotorcraft.

Airframe icing is therefore a topic of great interest for the aerospace industry and, more particularly, for airframers, because it deals with the safety and efficient operation of aircraft under all weather conditions. Keeping in mind the expected increase of airplane traffic in the coming decades, it seems unavoidable to reduce the rate of occurrence of ice-related incidents in order to maintain public confidence in air transport. For helicopters, customer needs are increasing for flight into icing conditions with smaller aircraft, for which capability substantiation is a key challenge.

In order to comply with certification regulation rules (CS25/CS29), airframers must show that the aircraft is able to fly safely in icing conditions. However, the entire icing envelope cannot be flight-tested and icing tunnel tests are time and cost consuming. Therefore, airframers, with the support of industrial partners, research institutes or universities, have developed numerical methods and tools to cover their needs.

### Computation methodology

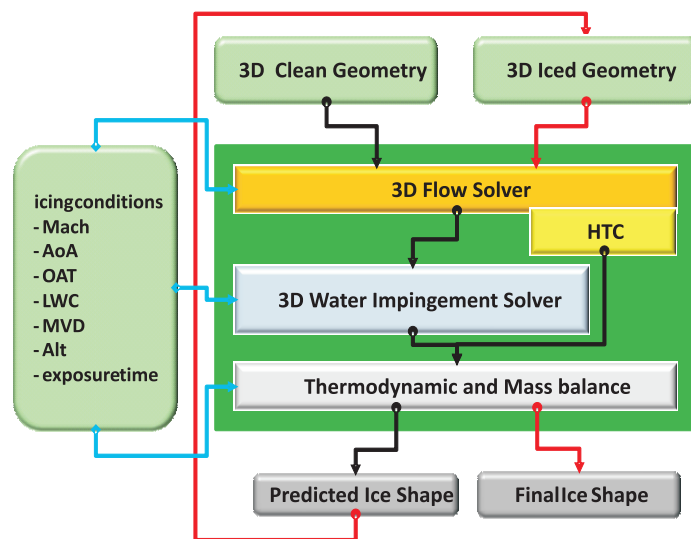


Figure 38 - Flow chart describing the predictor/corrector method to obtain a final ice shape

A recognized general methodology [32][9][31] used for the simulation of ice accretion is based on the successive computation of air flow, water droplet trajectories, collection efficiency, heat transfer balance and accreted ice. Figure 38 presents the general flow chart of the ice accretion process. The flow field and associated convective heat transfer are computed using an inviscid ap-

proach (Panel method, potential method, Euler method, etc.) coupled with boundary layer calculation or a viscid approach (RANS). The balance of forces acting on the droplets determines their trajectories and the collection efficiency coefficient  $\beta$ . Using these inputs, the resolution of the thermal and mass balance makes it possible to determine the ice thickness and then the ice shape on the considered surfaces.

All the modules that take part in the ice accretion process are usually included in a comprehensive ice accretion suite (LEWICE, ONICE2D/3D, etc.). The use of one module in a stand-alone mode or/and the replacement of one module by another is not obvious and not secured. Though such a way of working is acceptable for simple two-dimensional modules, the gradual replacement of two-dimensional methodologies by three-dimensional methodologies has led the partners of the project to ask Onera to build a modular ice accretion suite, enabling the partners to implement the modules in their own CFD environment [26][8][7] in a secured manner. Such a modular way of working offers the possibility of rationalizing the set of tools used inside an organization and then to reduce the maintenance and the associated cost.

The ONICE3D ice accretion suite satisfies these requirements. Interoperability is ensured through a CGNS [1] neutral layer. In order to ensure uniqueness and traceability, a restriction to the CGNS standard has been defined for icing purpose. Under this constraint, an in-house solver can be substituted to any of the specific components of the suite, as suggested in figure 39.

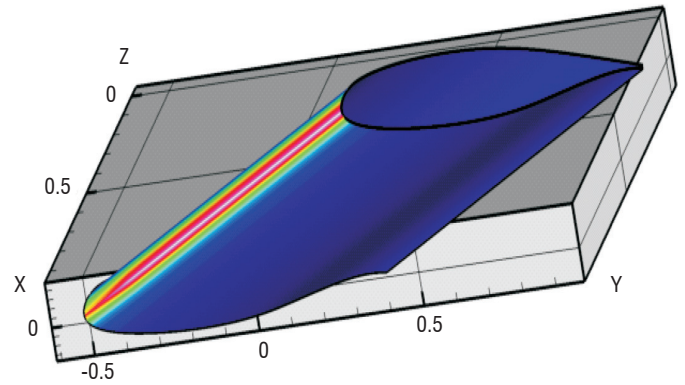


Figure 40 - Water catch collection coefficient distribution on the wing (SPIREE computation)

Figure 41 presents a comparison between SPIREE computations, Drop3D computations (Airbus code, green curves) and experiments for the classical water catch efficiency coefficient, as a function of the curvilinear abscissa. The effect of droplet diameter distribution, mono-disperse or Langmuir D, is also presented. The overall comparison shows that all computations reveal the same trend: the maximum value of the water catch collection coefficient is underestimated (value around 0.40 against 0.55 for the experimental reference). Lagrangian approach (not shown here) gives similar results. In a coherent way, the use of Langmuir D distribution improves the results near the impingement limits.

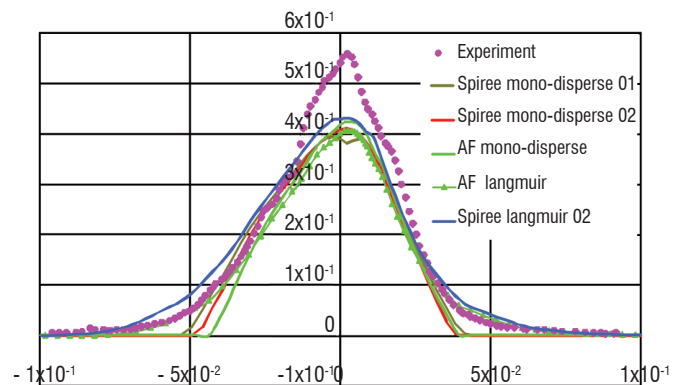


Figure 41 - Water catch collection coefficient: comparisons between reference and 3D Eulerian simulations

Figure 42 presents a close-up of the liquid water content normalized by its up-stream value. The absence of water is revealed by blue color map close to the profile. Values above unity show over-concentration that occurs when droplet trajectories are concentrated due to the profile deflection.

For the ice accretion comparison, the flight and atmospheric icing conditions slightly differ from the previous ones. The main difference is that the angle of attack is about  $2.00^\circ$  instead of  $0.00^\circ$ . Figure 43 shows the comparison between reference and numerical results. The predicted shape is in a rather good agreement though some discrepancies exist: ice thickness is 15% over estimated and the predicted limit of ice accretion is wider. However, the corrected shape should improve those results when applied.

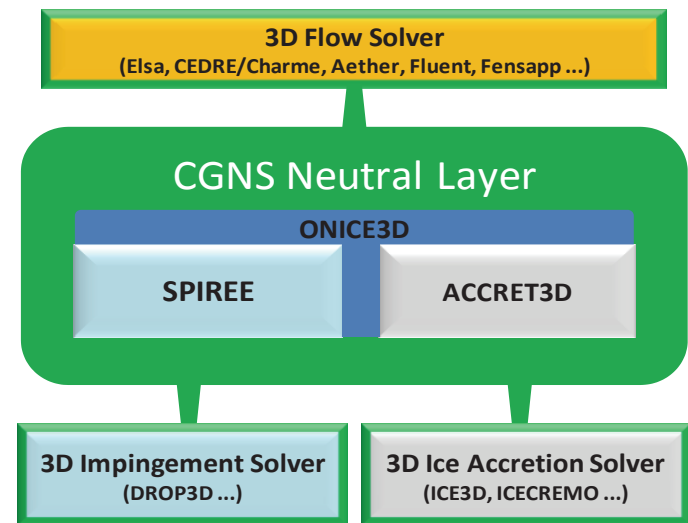


Figure 39 - ONICE3D components and the possible interoperability with other non-Onera components

### Application to ice prediction on a 3D swept wing

The first test case is representative of a  $30^\circ$  swept airfoil (figure 40) and has been selected because some experimental results on water catch collection and ice accretion are available [39][41]. Among the various atmospheric and flight conditions tested during the icing campaign, one of the cold cases is presented. The atmospheric and flight conditions used for this reference case are the following:

$$V_\infty = 67 \text{ m.s}^{-1}, T_\infty = 243 \text{ K}, P_\infty = 1013 \text{ hPa}, AoA = 0.0^\circ, LWC = 1.10 \text{ g.m}^{-3}, MVD = 20 \mu\text{m}$$

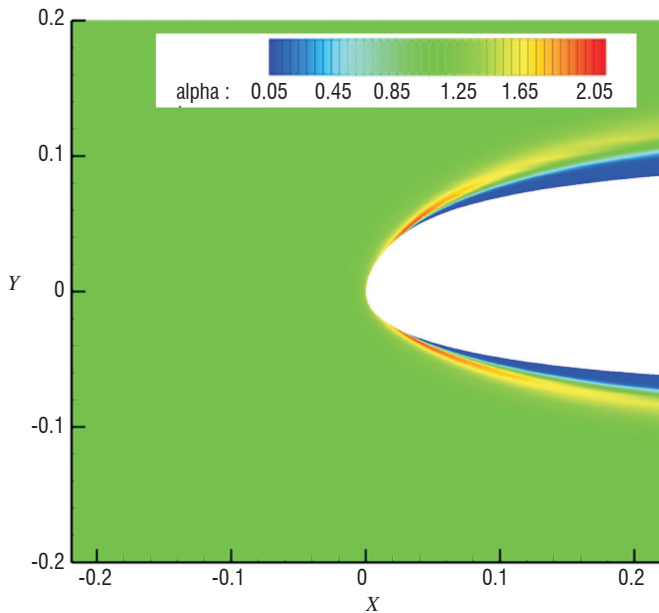


Figure 42 - Iso-contour of liquid water content distribution normalized by the up-stream value

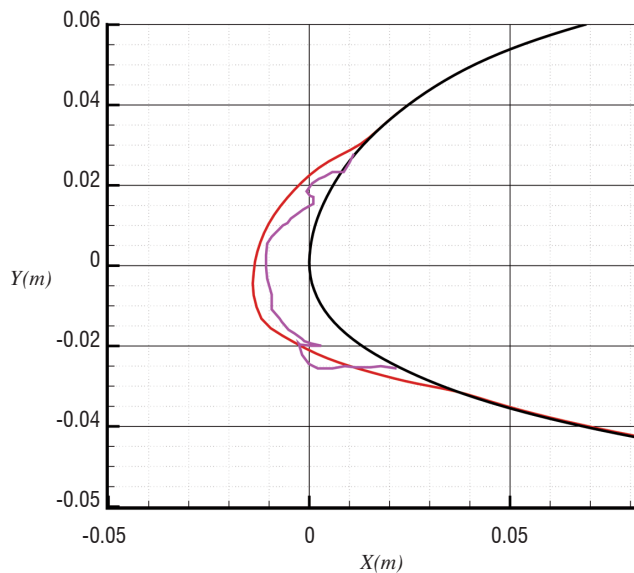


Figure 43 - iced profile normal to the leading edge

### Application to ice prediction on a 3D air intake

The second test case is representative of a helicopter air intake. Under icing conditions, ice accretion can clog the air intake or damage the engine by ice ingestion and can cause a complete loss of control of the rotorcraft. In order to avoid this kind of damage, the air intake must be protected by an anti-icer. This anti-icer is designed to fully evaporate the super-cooled liquid water droplets that impinge. Usually, it is done by electrical resistor layers.

The atmospheric and flight conditions used for this reference case are the following:

$$V_{\infty} = 75 \text{ m.s}^{-1}, T_{\infty} = 243 \text{ K}, P_{\infty} = 1013 \text{ hPa}, LWC = 0.80 \text{ g.m}^{-3}, MVD = 40 \mu\text{m}$$

Figure 44, figure 45 and figure 46 present the pressure distribution, the water catch collection coefficient distribution and the ice thickness distribution on the air intake surface respectively. These results

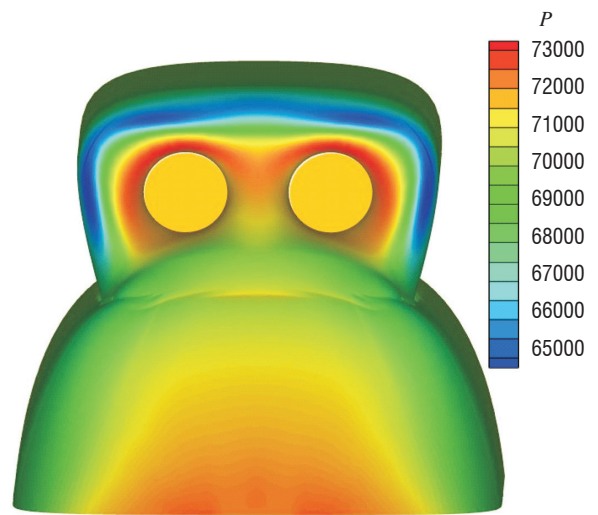


Figure 44 - pressure distribution on the air intake surface

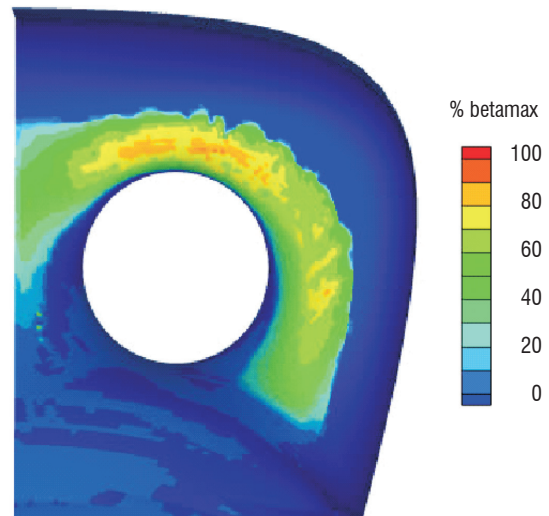


Figure 45 - water catch collection coefficient with a maximum value of 0.65

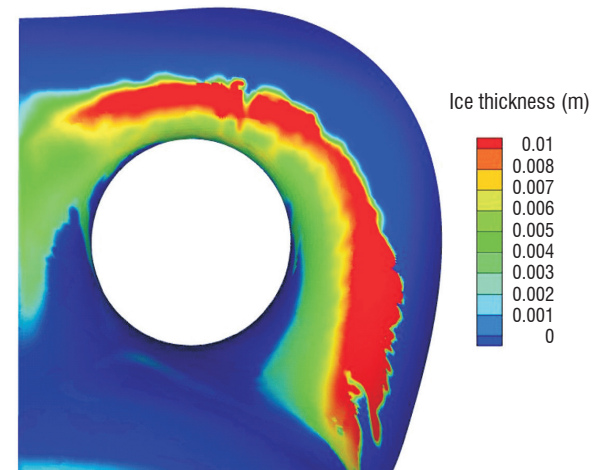


Figure 46 - ice thickness on the air intake surface

have been obtained using the CHARME solver for the aerothermics, the SPIREE solver for the eulerian transport of water droplets and the ACCRET3D solver for the ice accretion.

### Conclusion

Icing computations with a numerical suite including the eulerian solver SPIREE for water droplet transport have validated the choice of

this numerical approach. In the future, an optimization work will make it possible to reduce the computation time. Concerning modeling, the future developments will concern wall/droplet interaction (splashing, rebound, etc.), the use of a sectional approach for the droplet distribution and the extension of SPIREE to rotating configurations.

## Flow instabilities in a solid propellant motor

### Introduction

Instabilities in solid rocket motors are a critical issue. They are likely to involve thrust oscillations and consequently dynamic loads on the payload. Pressure oscillations in large segmented solid rocket motors are mainly due to the coupling of the chamber acoustics with vortex sheddings caused by hydrodynamic instabilities. These vortex sheddings can be caused either by the Taylor flow intrinsic instability (parietal vortex shedding, PVS) or by a shear layer instability in the wake of protruding inhibitors for instance (obstacle vortex sheddings, OVS).

An idea to reduce the coupling between vortex sheddings and acoustics was to give the inhibitor a 3D shape, shown in Figure 47, in order to make large vortices less coherent. It was tested twice in ARTA 03 bench firings [54] and a preliminary reduced scale experiment (1/15<sup>th</sup> LP6) has also been carried out at Onera. In the LP6 experiment, the inhibitor was made of metal, so that no deformation occurs and the shape is known precisely. The subscale LP6 experiment showed that pressure oscillations are strongly modified by the introduction of a 3D shaped inhibitor. The levels are lower than with a classical ring-shaped inhibitor. However, an instability bump remains with quite disorganized frequency changes. At the time of greatest instability (8.6 s), the oscillation level is still low but involves mainly the excitation of the second longitudinal acoustic mode.

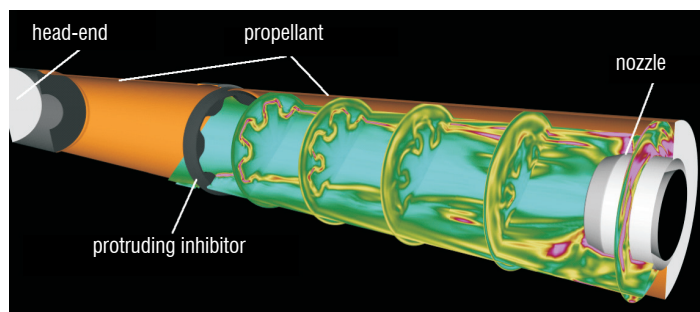


Figure 47 - Sketch of the motor and vorticity field

Numerical simulations of the experiment were performed at 8.6s, in order to provide a better understanding of the phenomena occurring in the motor (OVS and PVS interaction, enhancement of turbulence). A fixed geometry could be used, because aerodynamic and acoustic time scales are far smaller than burnback time scale.

### Computation methodology

3D computations were performed with the Finite-Volume CFD code CEDRE. A single-phase approach was used (Navier-Stokes solver, CHARME), because the propellant used in the subscale experiment does not contain aluminum particles. One must keep in mind that in actual engines, aluminum combustion plays a major role

in pressure oscillations (damping effect of the alumina particles, temperature increase, possible coupling between acoustics and aluminum combustion, etc.): for these configurations, a dedicated aluminum combustion model, available in CEDRE, must be used in association with a dispersed two-phase approach. Turbulence is treated with a MILES approach (the subgrid model is given by the numerical scheme diffusivity). The Euler fluxes are discretized with the Roe scheme. Second-order is achieved with a MUSCL scheme (with a Van Leer or a Superbee slope limiter). The temporal scheme is an explicit two-step Runge-Kutta scheme, second-order accurate.

The combustion of the propellant is simply modeled by an injection boundary condition at constant flow-rate  $q_p = 12.025 \text{ kg/s/m}^2$  and temperature  $T_p = 2688 \text{ K}$ . Inert surfaces are treated as isothermal or adiabatic walls. In the first case, the surface temperature of the protruding inhibitor is  $T_{in} = 500 \text{ K}$ , the temperature of the head-end, aft-end and cylinder walls is  $T_{he} = 2500 \text{ K}$ .

The fluid properties are: molar mass  $M = 24.394 \cdot 10^{-3} \text{ kg/mol}$ , specific heat capacity at constant pressure  $C_p = 2153.8 \text{ J/K/kg}$ , dynamic viscosity  $\mu = 8.07 \cdot 10^{-5} \text{ kg/m/s}$  and Prandtl number  $P_r = 0.45$ .

The use of unstructured grids proved to be too dissipative to reproduce the low instability levels in this configuration with a reasonable grid size. With structured grids, computations using several grids of increasing size were actually necessary to obtain significant results: computations with too coarse grids exhibit no pressure oscillation. The retained mesh is an O-grid involving 4,288,000 hexahedral cells (12,917,280 faces). It is locally refined (down to 0.5 mm) in particular close to the propellant and close to the nozzle throat.

The integration was achieved with a Courant-Friedrichs-Lewy number around  $CFL = 0.3$ . For a satisfactory frequency accuracy, a large number of iterations is often necessary for pressure oscillation characterization. The computation was run on 64 ITANIUM cores. 2.5 million cycles were made in  $180 \cdot 10^6 \text{ s CPU}$ .

### Numerical results

The computation exhibits pressure oscillations and vortex sheddings. The vorticity field downstream of the inhibitor is displayed in figure 47. A stronger interaction of both hydrodynamic instabilities, OVS and PVS, occurs where the inhibitor is shorter (at the top of figure 47). The vorticity field is perturbed by the 3D shape. Some OVS structures stemming from neighboring locations of the inhibitor interact strongly, as shown by transverse sections.

The RMS pressure oscillation level at the head-end is 318Pa if the Van Leer slope limiter is used. With a less diffusive approach (Superbee slope limiter), it increases to 425 Pa. This instability level remains low compared to the experimental measurement (2,900 Pa). However, as experimentally found, the signal is rather noisy and two dominant frequencies are identified near the first two longitudinal acoustic modes (1L and 2L, as shown in figure 48). However, the main peak in the experiment is locked on the 2L acoustic mode, whereas there is a little more energy around the 1L mode in the computation. The little discrepancies indicate that another refinement would be still necessary but the spectral behavior is globally satisfactory.

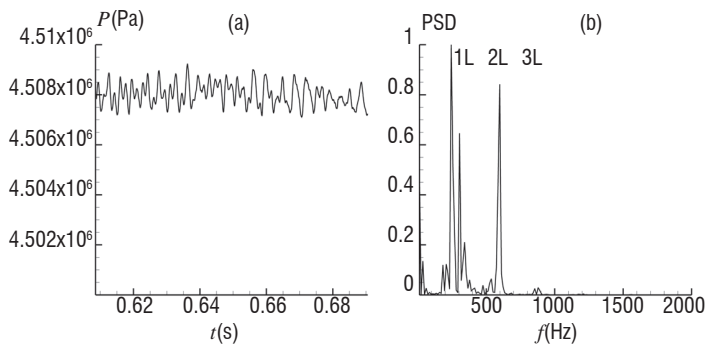


Figure 48 - Pressure at the head-end (a), power spectral density (b), computed with  $2^{13}$  points,  $\Delta f=12$  Hz,  $\Delta t=10^{-5}$  s

## Conclusion

The influence of a 3D protruding inhibitor in a reduced-scale solid rocket motor was studied by a numerical simulation with CEDRE Navier-Stokes solver CHARME. The instability level is lower than in the experiment: a more refined grid and/or a higher order spatial scheme should improve the instability level prediction. However, the spectral behavior is quite satisfactory. A strong second longitudinal acoustic mode (2L) is found, as well as some frequencies around the first longitudinal acoustic mode (1L). There are two types of vortex sheddings in the chamber : parietal (PVS) and obstacle (OVS) vortex sheddings. They interact weakly and the OVS vortices stemming from different heights of the inhibitor are in interaction, which is likely to enhance the turbulence intensity.

## Combustion in a multipoint injection burner

### Introduction

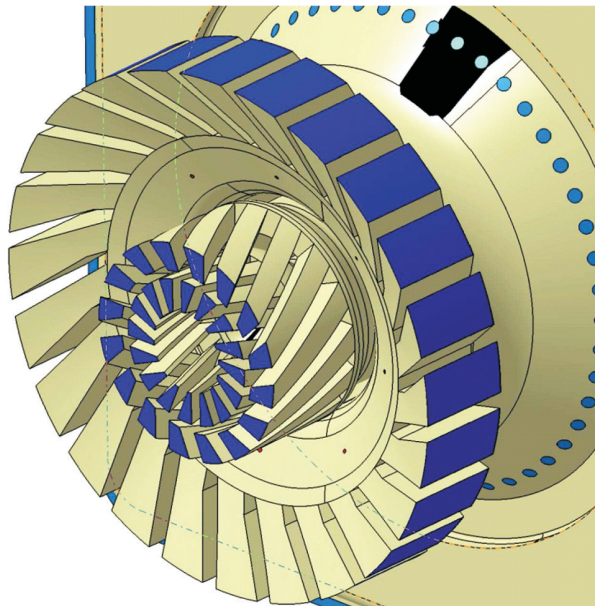


Figure 49 - Injector geometry

To comply with more and more stringent standards for pollutant emissions (NO<sub>x</sub>, CO, soot, etc.), new combustion chamber designs are required. A way to reduce pollutant emissions in the combustor consists in bringing close to each other a pilot zone and a low fuel air ratio combustion zone. This concept has taken shape through the Twin Annular Premixing Swirling (TAPS) or multipoint combustor [13]

[53], in which fuel injection occurs from multiple points around or within an air flow undergoing a strong swirl. This concept initially developed by GE is now widely studied, in particular in Europe through EEC research programs as NEWAC (New Aero Engine Core Concept), Intellect D.M. (Integrated Lean Low-Emission Combustor Design Methodology) or TLC (Towards Lean Combustion). To improve and predict performance of such concepts, different experimental and numerical studies are carried out at Onera. An example of numerical study is presented in this paper.

The objective of the study is to simulate with the CEDRE platform, the 3D reacting diphasic flow in a combustion chamber fitted out by a multipoint injector (Sneema TLC injector, figure 49). The simulated operating condition corresponds to the approach stage, where the fuel (n-decane) flow distribution is 50-50 % between the pilot and the low fuel-air ratio combustion zone.

### Computation methodology

The simulation is carried out in three steps. First of all, the 3D reacting diphasic flow is obtained with the coupled CHARME/SPARTE solvers (available in CEDRE platform) calculation. CHARME solves eulerian balance equations with a RANS  $k-l$  model. For the combustion modeling, we have used a one step infinitely fast Magnussen model [29]. The SPARTE (lagrangian) solver has been used for the tracking of the fuel droplets. The interaction between the liquid and the gas phases is taken into account through source terms in the eulerian balance equations of the gas. These source terms account for all the phenomena related to the fuel vaporization. For this kind of computation, ODFI flux difference splitting, associated with a MUS-CL approach, is employed for the advective fluxes. This method results in a second order spatial accuracy. The time integration is carried out using a first order implicit Euler scheme, along with local adaptative time step.

In a second step, the flowfields so obtained (pressure, temperature, velocity and mass fraction of majoritary species) are post-processed with the PEUL+ solver to calculate soot volumic fraction and minority species such as NO, with a partially detailed kinetic scheme (127 reactions). Concerning the interaction between turbulence and chemistry, simulations are based on a method [64] that associates the eulerian resolution of the balance equations with the lagrangian resolution of a species PDF transport equation.

Finally, in post-processing of PEUL+ results, radiative transfer in the combustion chamber is solved with the ASTRE solver which is based on a Monte Carlo approach. We have taken into account radiation from CO<sub>2</sub>, H<sub>2</sub>O and CO gas species and soot in the infrared spectral range. The radiative properties of gas species are calculated with a band model (53 bands) formulated with a mean absorption coefficient (high pressure box model) and soot radiative properties are calculated on the same spectral discretization as a gas model with an expression of absorption coefficient that is assumed to be proportional to the volumic fraction and wavenumber. We have assumed furthermore that the media is without scattering.

All calculations have been carried out on a initial mesh constituted of 600000 tetrahedrons and 1200000 faces. For each step of the computation (CHARME/SPARTE, PEUL+, or ASTRE), parallelization has or has not been carried out. The following table summarizes the main characteristics of the three computation steps.

Solver	CHARME/ SPARTE	PEUL +	ASTRE
Number of processors	64	16	4
Kind of parallelization	Geometric domain	No	Optical path
Processor type	Montecito 1.6 GHz	SX-8R 2.2 GHz	Montecito 1.6 GHz
CPU time (h/proc.)	40	40	4
Convergence characteristics	-	50000 particles	10 million rays/proc

Main characteristics of the three computation steps

**Computation results**

Figure 50 and figure 51 present the temperature and pressure obtained with CHARME/SPARTE solvers in the combustion chamber. In the pressure field, streamstraces are also represented and show clearly the two recirculation bubbles led by the swirl injection system.

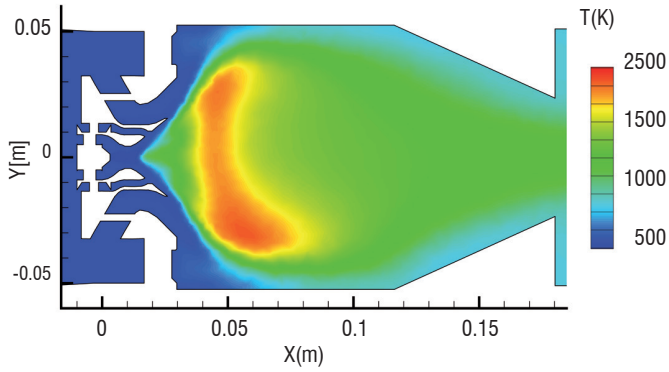


Figure 50 - Temperature field (longitudinal slice)

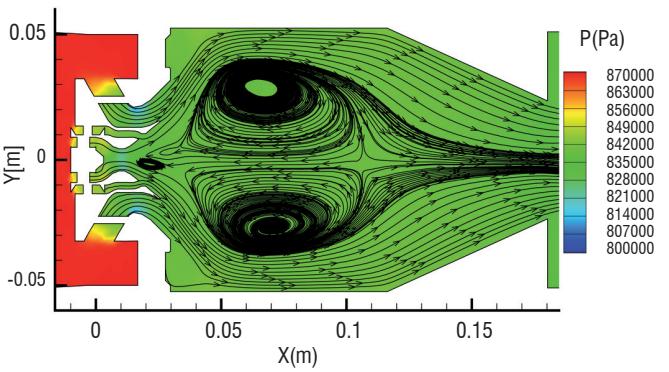


Figure 51 - Pressure field (longitudinal slice)

Figure 52 shows the NO mass fraction distribution obtained with the PEUL+ solver. The mass fraction is particularly important in the recirculation zone where temperature and residence time are high. The NO index in the outlet chamber is 4.42 g/(kg fuel), which is close to experimental data, 3.46 g/(kg fuel), measured on the M1 test bench (Onera/Palaiseau) under the same operating conditions.

Figure 53 presents the net radiative flux received by the walls of the combustion chamber. In our case, we have considered the walls as a black body emitting at 1000 K. The flux is particularly high on the system injection wall and on the side wall center.

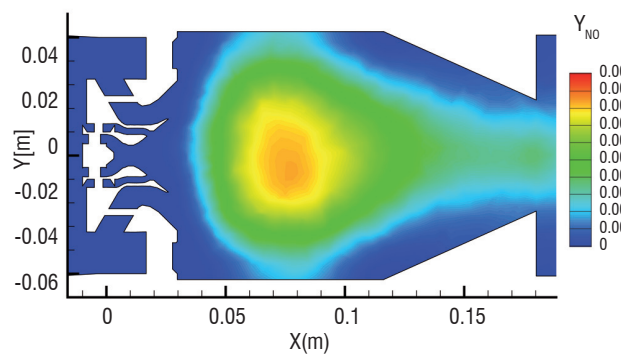


Figure 52 - NO mass fraction field (longitudinal slice)

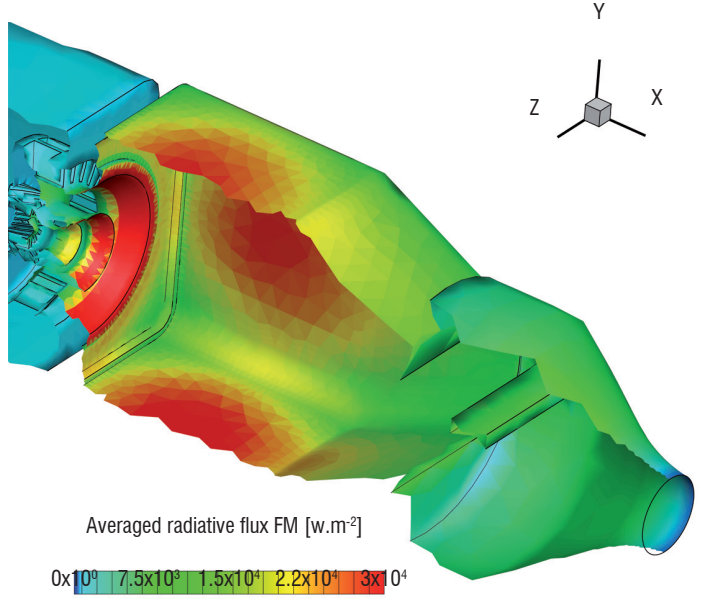


Figure 53 - Radiative flux distribution on the walls of the half combustion chamber

**Conclusion**

This study shows the ability of the CEDRE code to simulate a complex multiphysics flow in an industrial burner with realistic results. Nevertheless, this computation is only a first step since several points remain to be improved. First, even if the emission computation by PEUL+ uses a detailed chemistry, the flow calculation itself is based on a RANS approach with a basic one-step turbulent combustion model. Second, only a one way coupling is used between CHARME/SPARTE, ASTRE and PEUL+ : in particular, temperature is overestimated, since radiative heat losses have not been taken into account in CHARME.

In future work, LES (Large Eddy Simulation) will be used in conjunction with a more realistic combustion model (such as Thickened Flame for LES). Furthermore, a two way coupling methodology between flow and radiation should be used soon.

# Reacting flow in a research ramjet combustor

## Introduction

The Research Ramjet Program has been initiated some years ago at Onera with two main goals: to provide a better understanding of the non-reacting and reacting flows inside a ramjet combustor and to validate models and CFD codes in order to have numerical tools able to predict ramjet combustor performances. For the first years, a specific ramjet combustor has been designed in order to build an experimental database for non-reacting and reacting flows. The configuration is a two-inlet side-dump ramjet combustor: the main combustion chamber of rectangular cross section is fed by two lateral rectangular cross section air inlets. In fact, according to this configuration, two three-dimensional research ramjet combustors were manufactured: the first one is dedicated to hot reacting flow experiments under realistic conditions (combustion mock-up, figure 54), and the second one, at scale 1.6 with respect to the combustion mock-up, is dedicated to cold flow experiments at atmospheric pressure (transparent mock-up, figure 55).

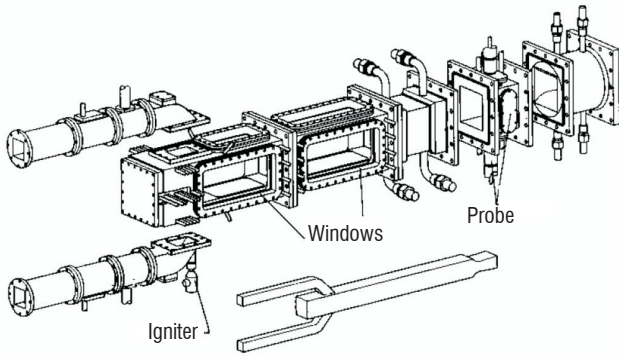


Figure 54 - View of the combustion mock-up

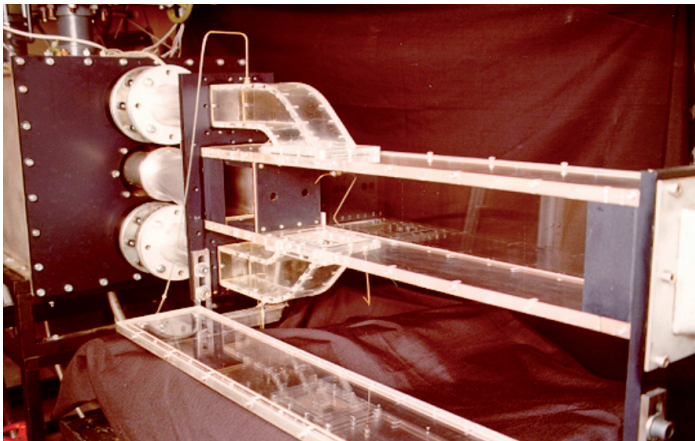


Figure 55 - View of the transparent mock-up

The combustion mock-up can be operated as a Solid Ducted Rocket (SDR) or as a Liquid Fueled Ramjet (LFRJ). In the first case, gaseous propane (representing the reducing gases coming from the gas generator) is injected into the head-end region of the combustor through two circular pipes. In the second case, liquid kerosene is injected from injectors located in the air intakes. We will focus here on the SDR operation only. Several flight conditions, with various equivalence ratios have been investigated. Experimental results using, for example, Particle Imaging Velocimetry (PIV), OH-PLIF (Planar Laser

Induced Fluorescence) imaging techniques or gas sampling analysis are available [47].

The transparent mock-up is dedicated to cold flow visualizations. In the case of a SDR simulation, two pseudo-fuel holes (propane is replaced by carbon dioxide) are located at the head-end of the combustor. Low speed pseudo-fuel-to-air mixing process has been characterized by visualizations, PIV and gas sampling analysis [48].

The complexity of the flow structure observed in such a combustor has been analyzed in many studies [44][45][47][48]. Usually, one distinguishes: i) the head-end region (also known as “dome”) of the chamber, ii) the four corner vortices which connect the dome region to the rest of the chamber and, finally, iii) the rest of the combustor. The dome region is a recirculation zone which makes easier the mixing between air and fuel before the combustion, and the four corner vortices are essential for flame stabilization. Thus, having a numerical tool able to predict the flow features in those two regions is of primary importance.

Thanks to the huge amount of experimental data obtained, essential data is available to improve and validate numerical simulations of ramjet combustors. The main – and challenging – objective is to implement a predictive numerical tool, capable of:

- characterizing the global performances of ramjet combustors (combustion efficiency and pressure recovery);
- predicting the extinction of the combustor (and especially the lean blow-out);
- predicting the combustion instabilities.

## Computation methodology

Reynolds Averaged Navier-Stokes (RANS) computations have been the first approach used to study the ramjet combustor. With this technique, only the mean flow field is resolved. Then, progress in Computational Fluid Dynamics (CFD) and increasing computer power have made possible the use of Large Eddy Simulation (LES) to study the ramjet combustor. This technique solves the filtered Navier-Stokes equations to describe the larger scales of turbulent flows, while only smaller scale effects are modeled. Although predictiveness of computations using LES approach is greater than the ones using RANS, the RANS approach is still extensively used for ramjet combustors because it is less demanding in terms of time and memory resources. Therefore, analyzing the advantages and limitations of RANS approaches and trying to improve them thanks to experiments, or LES computations, are two of the main objectives of the Research Ramjet Program. All computations have been performed with the compressible flow solver CHARME included in CEDRE.

For RANS computations, turbulence was modeled by a two-equation model, either  $k-\ell$  or  $k-\omega$  SST. No subgrid turbulence model was used in LES computations (MILES approach). For RANS and LES computations, combustion was modeled by an Arrhenius-type two-step chemical mechanism. For LES computations, two models including partial molecular mixing effects (TPaSR and EVM) were tested, without significant improvement of the results. For the RANS and LES approaches, combustion is initiated by performing a RANS calculation with an infinitely fast chemistry model. More detailed information on the modeling can be found in [44] and [45]. The computational domain – only a quarter of the mock-up due to the symmetry planes – is 3-D

and various unstructured grids, made of tetrahedra or hexahedra, and including or not the pre-injection box of carbon dioxide were used. The number of cells ranges from 200 000 to 4 000 000. A first-order Euler implicit time integration scheme, with an adaptive local time stepping for robustness, was used. Concerning the LES of the non-reacting case, the computational domain embraced the entire geometry and the grid was made up of roughly 3 000 000 hexahedra. An implicit second-order accurate Runge-Kutta method with Generalized Minimal RESidual (GMRES) resolution was used [45]. This approach is quite innovative for a LES computation and reduces the computation time significantly, compared to an explicit scheme. All those computations were performed on a 4-processor NEC SX-8R node. The CPU time ranges from 20 to 60 hours for RANS computations and reaches 960 hours for the LES computation.

### Computation results

This paper presents the results concerning two cases, both relative to the SDR operation: the low-speed non-reacting air/CO<sub>2</sub> mixing in the transparent mock-up and the reacting air/propane mixing in the combustion mock-up.

Cold flow computations were compared to velocity and CO<sub>2</sub> mass fraction fields obtained during experiments. One of the most significant results is that all the RANS simulations implemented tend to over-predict, by a factor up to two, the CO<sub>2</sub> concentration in the head-end region, while the LES approach brings a real improvement (figure 56). In fact, for this non-reacting configuration, the flow is dominated by the oscillation of the impinging jets. In contrast to the RANS approach, the use of LES allows to simulate the unsteady behavior due to the air jets, which provides a more realistic and accurate description of the mixing processes in the dome region.

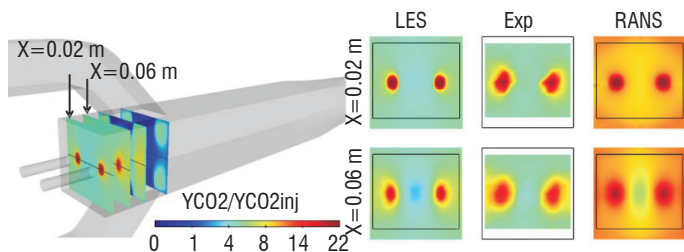


Figure 56 - Adimensionalized average CO<sub>2</sub> mass fraction fields in the dome region: comparisons between RANS (right), LES (left) and experiments (center) [44]

RANS and LES computations of air/propane combustion in the combustion mock-up have also been performed recently. The computed case corresponds to high altitude flight conditions, with an equivalence ratio  $\Phi = 0.75$ . The analysis of the LES results has allowed a better understanding of the combustion processes and has yielded information about the unsteady activity in the combustor (figure 57 and figure 58). As expected, the results of LES computations are in good agreement with experiment.

More surprisingly, some results of RANS computations are satisfying too: for example, the combustion efficiency and the mean velocity contours downstream of the air inlets (figure 59) were well predicted.

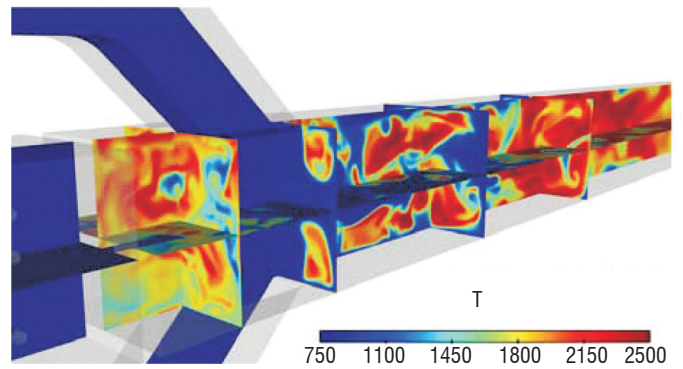


Figure 57 - Example of LES results: instantaneous temperature field

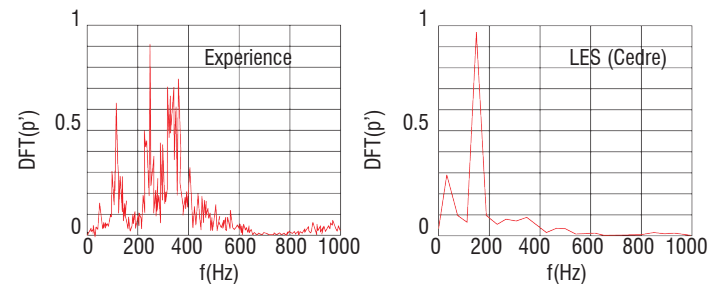


Figure 58 - Example of LES results: Fourier transformation of a pressure signal

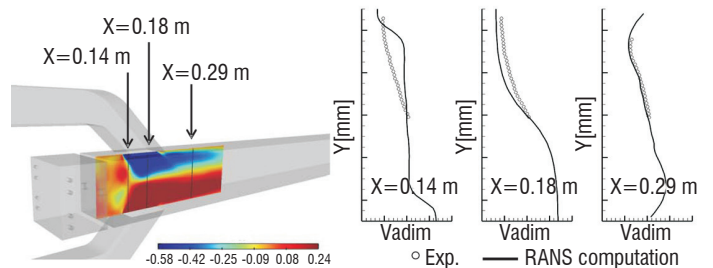


Figure 59 - Example of RANS computation result: adimensionalized transverse velocity contours – RANS vs. exp.

### Conclusion

The comparisons between RANS and LES approaches for the computation of the flow in a ramjet burner has confirmed the decisive advantage of LES when the flow is governed by large scale unsteady phenomena, as the mixing process in the dome. LES is also expected to be the most appropriate approach to predict blow-out or combustion instabilities. However, some global performances of the burner can be predicted at a much lower cost, with a reasonable accuracy, using a RANS approach for stable conditions. The two approaches should therefore be used in a complementary way.

### Combustion in the MASCOTTE cryogenic burner

#### Introduction

In the context of cost reduction and strong competition between space launchers, rocket engine design resorts more and more to simulation tools, in order to reduce design delays and development costs. These simulation tools require a detailed validation, which relies upon experimental means, such as the MASCOTTE test bench and advanced diagnostics [23]. The work described in this paper has been achieved in this context and within the fra-

network of the CNES/Onera common program on liquid propellant rocket engines.

The purpose of this work is the simulation of the LO<sub>x</sub>/H<sub>2</sub> cryogenic combustion in subcritical and supercritical regime for the MASCOTTE test configuration. The MASCOTTE test facility has been developed by Onera for fifteen years to study elementary processes, such as atomization, droplet vaporization and turbulent combustion, which are involved in the combustion of cryogenic propellants. Several versions of MASCOTTE are available. In the experiments considered, the MASCOTTE test-bench is equipped with a subscale mono-injector combustion chamber of 50 mm x 50 mm square internal section. The chamber is equipped with two side windows, which are cooled by a helium film, for visualization and optical diagnosis purposes. Temperatures in the hot gas flow are measured using CARS techniques. The MASCOTTE injector is a coaxial injector, where liquid oxygen is injected at the center and gaseous hydrogen at the periphery. In this paper, we focus on the A-10 point for subcritical regime, which corresponds to an Oxygen/Fuel ratio of 2.11 and a chamber pressure of approximately 10 bar, and on the A-60 point for the supercritical regime, where the Oxygen/Fuel ratio is around 1.54 for a chamber pressure close to 60 bar.

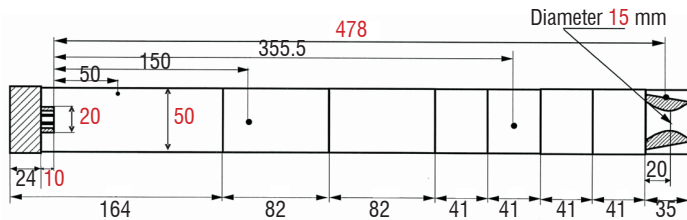


Figure 60 - Sketch of the MASCOTTE test-bench

### Subcritical regime

#### Computation methodology

The simulation of the MASCOTTE test case is difficult because various complex physical processes take place in this reactive, turbulent, two-phase flow, such as atomization, vaporization, mixing and combustion. Thus, to compute this test case, a progressive approach was adopted. First, we simulated an equivalent version of MASCOTTE in 2D-axisymmetrical gaseous configuration. Then, we investigated the influence of the various models of the CEDRE code on the flame shape in a 2D-axisymmetrical two-phase flow configuration. From this study [37], we developed and validated a turbulent combustion model, based on mixing pseudo-reactions and kinetic reactions known as TPaSR for Transported Partially Stirred Reactor [35]. Turbulence was modeled by a two-equation  $k$ - $\epsilon$  model, with a parameter set specially optimized for cryogenic combustion in a subcritical regime. The liquid phase was treated by the lagrangian solver SPARTE included in the CEDRE platform. Liquid oxygen injection is represented by a solid cone, along which droplets are injected. We showed that a non-uniform droplet distribution allowed a good coherence between the numerical results and the MASCOTTE data base. Nevertheless, some discrepancies still remain and they could come from the 2D simplification. Thus, the next step is the 3D simulation, using the optimized parameter set of the 2D simulation to complete the study.

For the 3D simulation, we meshed only 1/4<sup>th</sup> of the chamber with an unstructured grid composed of 665 600 nodes, 7.7 millions of faces and 3.8 million cells. For the first computation of this kind, the grid

was not very refined, to assess the capability of CEDRE to treat such complex configurations. We used a second order interpolation at the face center, with a Van Leer limitation. The gradient computation is provided by a Green method. The numerical Euler fluxes are based on the ODFI flux difference splitting. The time resolution is one step implicit, with local time step. The simulation is performed on the scalar parallel Bull calculator. This cluster is composed of Intel Itanium 2 processors. We used 32 processors.

#### Computation results

Figure 61 represents the computed temperature field in the steady state. A slight asymmetry can be observed between the XY plane (observation plane) and the XZ plane (transverse plane): the flame opens with a wider angle and more quickly in the observation plane than in the transverse one. This is due to the cooling helium films, present only on the walls parallel to the observation plane (figure 62).

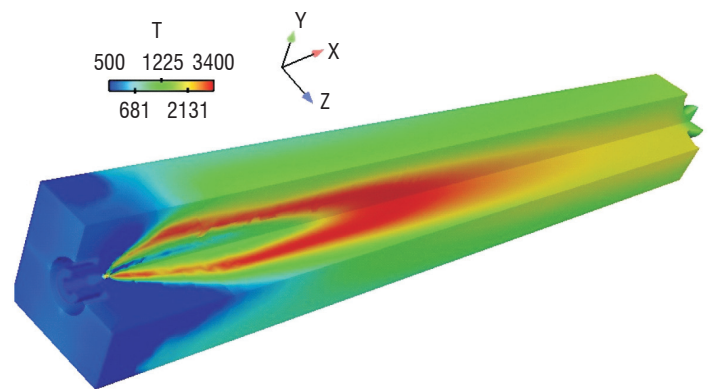


Figure 61 - Temperature field

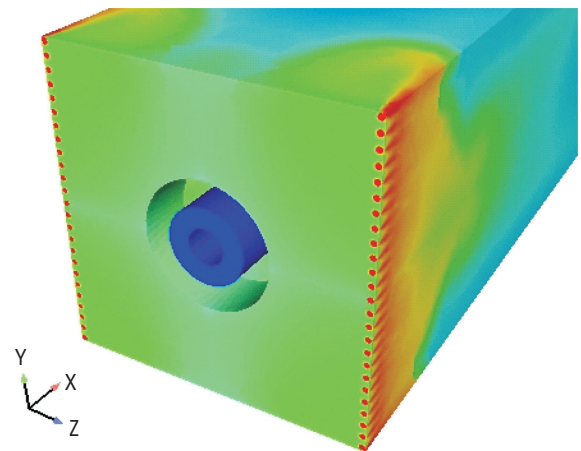


Figure 62 - Helium mass fraction

The effect of the helium films on the wall temperature is more easily visible in figure 6, where the temperature scale has been limited to 1500 K, which is the maximum value advocated by the window furnisher. One can see that the helium films are quite efficient, since the window temperature remains below this maximum value.

Figure 64 provides a comparison between simulation and experiment for the transverse evolution of temperature in the median plane, at the end of the chamber. There is a good agreement between simulation and CARS measurements. Nevertheless, some discrepancies remain in regard to the flame aperture shape, but to provide a significant comparison between simulation and experiment the computation should

supply radical OH emission like experimental images: this could be done by using ASTRE, the CEDRE radiation solver.

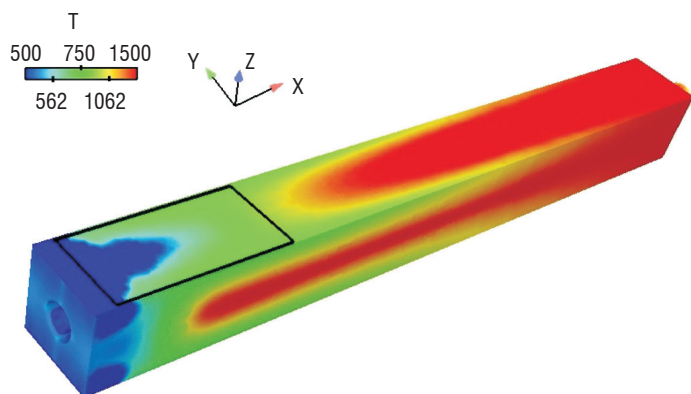


Figure 63 - Temperature field and window

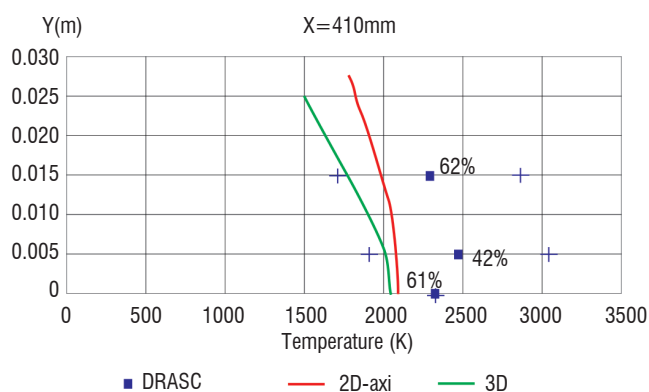


Figure 64 - Comparison CARS / simulation 2D-axi and 3D (Z=0, X = 410 mm)

## Supercritical regime

### Computation methodology

The simulation of the supercritical regime required the extension of the CEDRE code to real gas thermodynamics, in order to model the entire fluid phase (dense cryogenic injection as combustion gases) as a single monophasic medium. Following several authors [30][46], a Soave-Redlich-Kwong state equation was used for the computation of thermodynamical properties. In order to reduce the computational cost, the simulation was computed on the equivalent 2D-axisymmetrical geometry of the MASCOTTE test bench. In this case, the liquid oxygen injection tube is included in the computational domain, rather than being represented by the solid cone frontier. Aside from the thermodynamic modeling, the assumptions made concerning chemical reactions and turbulence are rather classical: for the turbulence model, we used a k-l model without any parameter optimization and the chemical model consisted in a kinetic model using an Eklund scheme [16].

The 2D-axisymmetric equivalent geometry was meshed with a light unstructured grid, composed of around 15 000 polygonal cells. This rather rough mesh is only refined near the injector, where the more representative real gas effects are expected. The choice of polygonal cells has been made to improve gradient evaluation through a least square method. Spatial interpolation, limitation, numerical fluxes and time resolution are the same as that used in the 3D subcritical computation. The simulation was performed on 8 quad core Intel Nehalem-EP processors of the scalar parallel SGI calculator.

## Computation results

Figure 65 and figure 66 present details of the density and temperature fields in the wake of the injector. Cold oxygen injection reaches liquid like densities and the flame stabilizes around the dense core. The high density gradients that may arise from turbulent mixing are smoothed, thanks to the k-l turbulent model. The lack of modeling for dense core stripping, pseudo-atomization and dense cluster micro-mixing may be a factor for the discrepancies between the simulation and observations, particularly concerning the flame aperture angle. Nevertheless, the flame length is in good agreement with OH visualization (Figure 66).

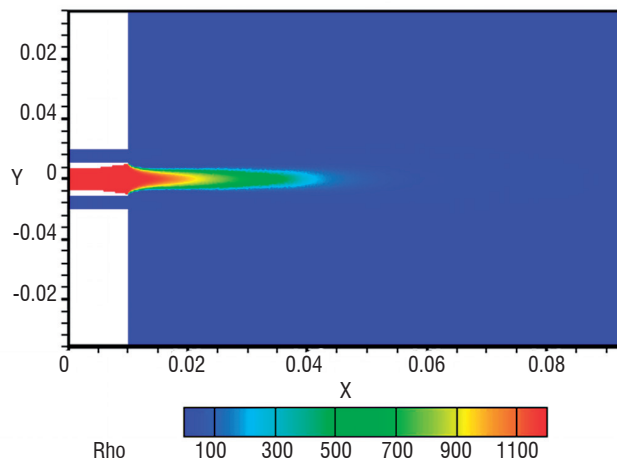


Figure 65 - Density field

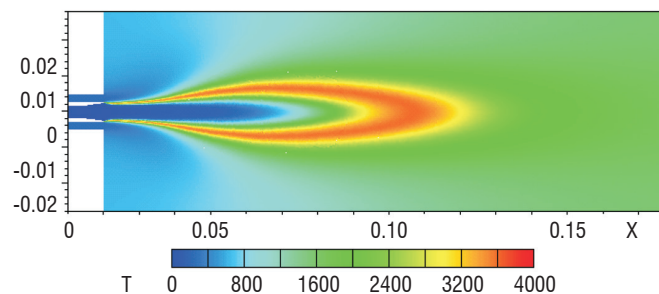


Figure 66 - Temperature field in the wake of the injector

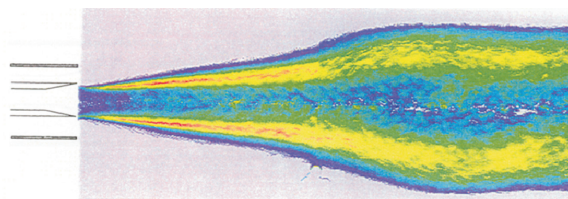


Figure 67 - OH emission visualization

## Conclusion

Computation of a liquid rocket injector is one of the most difficult CFD challenges. In the subcritical case, an important issue is the primary atomization process, which would make it necessary to call upon a real two-fluid solver, able to describe the two phases and capture the interface instabilities: the development of this solver has been undertaken in CEDRE. In the supercritical case, the problem is topologically simpler, since the fluid can be considered as monophasic, but difficulty is reported in the thermodynamic modeling. The implementation of a real gas thermodynamic mo-

del in CEDRE allows us to perform successful computations in supercritical conditions. Besides the modeling improvement, the next step will be the extension of these computations to the LES approach.

## Conclusion

The CEDRE code has been successfully used for many energetics or aerodynamics applications in the aerospace field. The main characteristics of the code (general unstructured mesh, general thermodynamics, multi-solver approach, explicit/implicit time integration, RANS/LES modeling, parallelization) are fully operational and many physical

models are available for turbulence, combustion, atomization and radiation. The prediction accuracy level is very good for some cases, but remains perfectible for others, such as flow instabilities, pollutant emissions or two-phase flows. Future progress is expected from five main development axes:

- continuous improvement of physical modeling, especially for the RANS approach, including specific validations;
- generalization of the LES approach, allowed by the continuous increase of computing power;
- high order space discretization for unstructured grids;
- new solvers for general (non-dispersed) two-phase flows, namely a film solver and a seven-equation multifluid solver;
- generalization of the external coupling ■

## References

- [1] *CFD General Notation System/Standard Interface Data Structures*. AIAA Recommended Practice, R-101-200
- [2] B. AUPOIX, D. ARNAL, H. BÉZARD, B. CHAOUAT, F. CHEDEVERGNE, S. DECK, V. GLEIZE, P. GRECARD and E. LAROCHE - *Transition and Turbulence Modeling*. Aerospace Lab, Issue 2, March 2011
- [3] A. BIANCHERIN, N. LUPOGLAZOFF, G. RAHIER and F. VUILLOT - *Comprehensive 3D Unsteady Simulations of Subsonic and Supersonic Hot Jet Flow-Fields*. Part 2: acoustic analysis, AIAA 2002-2600, 8th AIAA/CEAS Aeroacoustics Conference & Exhibit, June 17-19 2002, Breckenridge, CO
- [4] G. BODARD, C. BAILLY and F. VUILLOT - *Matched Hybrid Approaches to Predict Jet Noise by Using Large-Eddy Simulation*. AIAA 2009-3316, 15th AIAA/CEAS Aeroacoustics Conference, 11 - 13 May 2009, Miami, Florida, USA
- [5] C. BOGEY and C. BAILLY - *A family of Low Dissipative and Low Dispersive Explicit Schemes for Flow and Noise Computations*. Journal of Computational Physics, 194, 194-214, 2004
- [6] C. BOGEY, S. BARRÉ, D. JUVÉ and C. BAILLY - *Simulation of a Hot Coaxial Jet : Direct Noise Prediction and Flow-Acoustics Correlations*. Phys. Fluids, Vol. 21, No. 3, 2009
- [7] Y. BOURGAULT, W.G. HABASHI, J. DOMPIERRE and G.B. BARUZZI - *A Finite Element Method Study of Eulerian Droplets Impingement Models*. Int. Journal for Numerical Methods in Fluids, 1999
- [8] L. CAMBIER and J.P. VEUILLLOT - *Status of the elsA CFD Software for Flow Simulation and Multidisciplinary Applications*. AIAA-2008-0664, 46th AIAA Aerospace Sciences Meeting, Reno, NV, 2008
- [9] J.T. CANSDALE and I.I. MCNAUGHTAN - *Calculation of Surface Temperature and Ice Accretion Rate in a Mixed Water Droplet/Ice Crystal Cloud*. Royal Aircraft Establishment Technical Report. 77090, 1977
- [10] F. CHEDEVERGNE - *Advanced Wall Model for Aerothermodynamics*. International Journal of Heat and Fluid Flows, accepted
- [11] S. CHEMIN - *Etude des interactions fluide/structure par un couplage de codes de calcul*. Ph.D. Thesis, Université de Reims Champagne-Ardennes, 2006
- [12] B. COURBET, C. BENOIT, V. COUAILLIER, F. HAIDER, M.C. LE PAPE and S. PÉRON - *Space Discretization Methods*. Aerospace Lab, Issue 2, March 2011
- [13] W. DODDS - *Engine and Aircraft Technologies to Reduce Emissions*. UC Technology Transfer Symposium « Dreams of Flights », San Diego, March 2002
- [14] F. DUPOIRIEUX and N. BERTIER - *The models of Turbulent Combustion in the CHARME solver of CEDRE*. Aerospace Lab, Issue 2, March 2011
- [15] D. DUTOYA and L. MATUSZEWSKI - *Thermodynamics in CEDRE*. Aerospace Lab, Issue 2, March 2011
- [16] D.R. EKLUND, J.P. DRUMMOND and H.A. HASSAN - *Calculation of Supersonic Turbulent Reacting Coaxial Jets*. AIAA Journal 28 (9), pp. 1633-1641, 1990
- [17] M.P. ERRERA and S. CHEMIN - *A Fluid-Solid Thermal Coupling Applied to an Effusion Cooling System*. 34th AIAA Fluid Dynamics Conference and Exhibit, AIAA Paper 2004-2140, Portland, 28 June-1st July 2004
- [18] M.P. ERRERA, A. DUGEAI, P. GIRODROUX-LAVIGNE, J.D. GARAUD, M. POINOT, S. CERQUEIRA and G. CHAINERAY - *Multi-Physics Coupling Approaches for Aerospace Numerical Simulations*. Aerospace Lab, Issue 2, March 2011
- [19] F. FALEMPIN and L. SERRE - *LEA Flight Test Program – A First Step to an Operational Application of High-Speed Air Breathing Propulsion*. AIAA 2003-7031, Norfolk
- [20] F. FALEMPIN and L. SERRE - *French Flight Testing Program LEA – Status in 2009*, AIAA 2009-7227, Bremen
- [21] M.B. GILES - *Stability Analysis of Numerical Interface Conditions in Fluid-Structure Thermal Analysis*. International Journal for Numerical Methods in Fluids, Vol. 25, 1997, pp 421-436
- [22] F. GUILLOU - F. CHEDEVERGNE - *Internal Turbine Blade Cooling Simulation : the Smooth BATHIRE Rig Configuration*. ERCOFTAC ETMM8 2010, Marseille, France
- [23] M. HABIBALLAH, L. VINGERT, J.C. TRAINÉAU and P. VUILLERMOZ - MASCOTTE : *A Test Bench for Cryogenic Combustion Research*. 47th International Astronautical Congress, Beijing (China), October 7-11, 1996
- [24] A. HADJADJ and M. ONOFRI - *Nozzle Flow Separation*. Shock Waves, 19 :163–169, 2009

- [25] M. HUET, B. FAYARD, G. RAHIER and F. VUILLOT - *Numerical Investigation of the Micro-Jets Efficiency for Jet Noise Reduction*. AIAA-2009-3127, 15th AIAA/CEAS Aeroacoustics Conference, 11 - 13 May 2009, Miami, Florida, USA
- [26] M. HUET, F. VUILLOT and G. RAHIER - *Numerical Study of the Influence of Temperature and Micro-Jets on Subsonic Jet Noise*. 14th AIAA/CEAS, Aeroacoustics Conference, Vancouver, Canada, 2008
- [27] E. LAROCHE - *Influence of Freestream Turbulence Intensity on Cooling Effectiveness*. ASME PAPER 2001-GT-0139
- [28] N. LUPOGLAZOFF, G. RAHIER and F. VUILLOT - *Application of the Cedre Unstructured Flow Solver to Jet Noise Computations*. 1st EUCASS, 4-7 July 2005, Moscow
- [29] B. F. MAGNUSSEN and B.H. HJERTAGER - *On Mathematical Models of Turbulent Combustion With Special Emphasis on Soot Formation and Combustion*. 16th Symposium (International) on Combustion, pp. 719-729, Pittsburgh, 1977
- [30] H. MENG and V. YANG - *A unified Treatment of General Fluid Thermodynamics and its Application to a Preconditioning Scheme*. Journal of Computational Physics 189 (2003), pp. 277-304
- [31] B.L. MESSINGER - *Equilibrium Temperature of an Unheated Icing Surface as a Function of Air Speed*. Journal of the Aeronautical Sciences, Vol. 20, No. 1, pp. 29-42, 1953
- [32] E. MONTREUIL, A. CHAZOTTES, D. GUFFOND, A. MURRONE, F. CAMINADE and S. CATRIS - *Enhancement of Prediction Capability in Icing Accretion and related Performance Penalties*. Part I: Three-dimensional CFD Prediction of the Ice accretion, The 1st Atmospheric and Space Environments, San Antonio, Texas, AIAA, 2009
- [33] F. MULLER, F. VUILLOT, G. RAHIER and G. CASALIS - *Modal Analysis of a Subsonic Hot Jet LES with Comparison to the Linear Stability Analysis*. AIAA-2005-2886, 11th AIAA/CEAS Aeroacoustics Conference, 23-25 May 2005, Monterey, California, USA
- [34] F. MULLER, F. VUILLOT, G. RAHIER, G. CASALIS and E. PIOT - *Experimental and Numerical Investigation of the Near Field Pressure of a High Subsonic Hot Jet*. AIAA-2006-2535, 12th AIAA/CEAS Aeroacoustics Conference, 8-10 May, 2006, Cambridge, MA, USA
- [35] A. MURRONE and D. SCHERRER - *Large Eddy Simulation of a Turbulent Premixed Flame Stabilized by a Backward Facing Step*. 1st INCA Workshop, 2005, Villaroche (France)
- [36] A. MURRONE and P. VILLEDIEU - *Numerical Modeling of Dispersed 2-Phase Flow*. Aerospace Lab, Issue 2, March 2011
- [37] A. NICOLE, F. DUPOIRIEUX, L. VINGERT, M. HABIBALLAH and M. THERON - *Simulation of a Subcritical LOX/GH2 MASCOTTE Test Case (10 bar)*. 5th International Spacecraft Propulsion Conference, 5-8 May 2008, Heraklion (Greece)
- [38] G. ORDONNEAU, P. HERVAT, F. GRISCH, L. VINGERT and P. REIJASSE - *PLIF Investigation of Reactive Flows in the Separation Region of an Over-expanded Two-Dimensional Nozzle*. AIAA Paper, number 2006-5209, 2006
- [39] M. PAPADAKIS, R. ELANGONAN, G.A. JR. FREUND, M. BREER, G.W. ZUMWALT and L. WHITMER - *An experimental Method for Measuring Water Droplet Impingement Efficiency on Two-and Three-Dimensional Bodies*. NASA CR 4257
- [40] E. PIOT, G. CASALIS, F. MULLER and C. BAILLY - *Investigation of the PSE Approach for Subsonic and Supersonic Hot Jets. Detailed Comparisons With LES and Linearized Euler Equations Results*. Int. J. of Aeroacoustics, Vol. 5, No. 4, pp. 361 - 393, 2006
- [41] M.G. POTAPCZUK and C.S. BIDWELL - *Numerical Simulation of Ice Growth on a MS-317 Swept Wing Geometry*. AIAA-91-0263, 39th Aerospace Sciences Meeting, Reno, NV, 1991
- [42] G. RAHIER, J. PRIEUR, F. VUILLOT, N. LUPOGLAZOFF and A. BIANCHERIN - *Investigation of Integral Surface Formulations for Acoustic Post-Processing of Unsteady Aerodynamic Jet Simulations*. Aerospace Science and Technology, Vol. 8, pp. 453-467, 2004
- [43] A. REFLOCH, B. COURBET, G. CHAINERAY, J.B. DARGAUD, P. GILBANK, C. LAURENT, A. MURRONE, E. QUÉMERAIS, L. TESSÉ, J. TROYES, F. VUILLOT and P. VILLEDIEU - *CEDRE Software*. Aerospace Lab, Issue 2, March 2011
- [44] S. REICHSTADT - *Etude du mélange et de la combustion monophasique dans un statoréacteur de recherche*. Ph.D. Thesis, Université de Pau et des Pays de l'Adour, 2007
- [45] S. REICHSTADT, N. BERTIER, A. RISTORI and P. BRUEL - *Towards LES of Mixing Processes Inside a Research Ramjet Combustor*. 18th International Society of Air Breathing Engines (ISABE), Beijing, China, 2007
- [46] G. RIBERT, N. ZONG, V. YANG, L.PONS, N. DARABIHA and S. CANDEL - *Counterflow Diffusion Flames of General Fluids: Oxygen/Hydrogen Mixtures*. Combustion and Flame 154, pp. 319-330, 2008
- [47] A. RISTORI, G. HEID, C. BROSSARD and A. BRESSON - *Characterization of the Reacting Two-Phase Flow Inside a Research Ramjet Combustor*. International Conference on Liquid Atomization And Spray Systems ICLASS'03, Sorrento, Italy, 2003
- [48] A. RISTORI, S. REICHSTADT, C. BROSSARD and G. HEID - *PIV and Gas Sampling Analysis Measurements for Fuel-to-Air Mixing Study Inside a Research Ramjet Combustor*. 13th International Symposium on Flow Visualization ISFV13 / 12th French Congress on Visualization in Fluid Mechanics FLUVISU12, Nice, France (2008)
- [49] A. RISTORI, Y. SERVOUZE, M. BARAT and F. SOULIGNAC - *PIV Flow Characterization Inside a Large-Scale U-Shaped Rotating Channel*. Onera-DLR Aerospace Symposium, Göttingen, Germany
- [50] B. SAINTE-ROSE, N. BERTIER, S. DECK and F. DUPOIRIEUX - *A DES Method Applied to a Backward Facing Step Reactive Flow*. C. R. Mec., 337 (6-7): 340-351, 2009
- [51] L. SERRE and F. FALEMPIN - *PROMETHEE : the French Military Hypersonic Propulsion program*. Status in 2002, AIAA 2003-6950, Norfolk
- [52] M. SHUR, P. SPALART and M. STRELETS - *Noise Prediction for Increasingly Complex Jets*. Part I: Methods and Tests. Part II: Applications, Int. J. Aeroacoustics, Vol. 4, No. 3+4, pp. 213-266, 2005
- [53] D. L. STRAUB, K. H. CASLETON, R. E. LEWIS, T. G. SIDWELL, D. J. MALONEY and G. A. RICHARDS - *Assessment of Rich-Burn, Quick-Mix, Lean-Burn Trapped Vortex Combustor for Stationary Gas Turbine*. Journal of engineering for gas turbine and power, 27 :36-41, 2005
- [54] M. TELARA, L. JACQUES, P. LE HELLEY, T. PEVERGNE and D. RIBEREAU - *A New Concept to Reduce SRM Pressure Oscillations: the 3D Frontal Thermal Protection*. European Conference in Aerospace Sciences (EUCASS), 2005
- [55] L. TESSÉ and J.M. LAMET - *Radiative Transfer Modeling Developed at Onera for Numerical Simulation of Reactive Flows*. Aerospace Lab, Issue 2, March 2011

- [56] J. TROYES and F. VUILLOT - *Numerical Simulations of a Model solid Rocket Motor Ignition Overpressure Wave*. 44th AIAA/ASME/SAE/ASEE JPC, 2008
- [57] J. TROYES, F. VUILLOT, J. VARNIER and P. MALBÉQUI - *Numerical Simulations of Rocket Solid Motor Engine Ignition and Duct Overpressure Waves at Reduced Scale*. 45th AIAA/ASME/SAE/ASEE JPC, 2009
- [58] J. VARNIER, P. PRÉVOT, G. DUNET, M. BARAT and B. BAZIN - *Blast Wave and Afterburning at Ignition of Rocket Engines*. 13th ICSV, 2006
- [59] K. VISWANATHAN, M. SHUR, P. SPALART and M. STRELETS - *Flow and Noise Predictions for Single and Dual-Stream Beveled Nozzles*. AIAA Journal, Vol. 46, No. 3, pp. 601-626, March 2008
- [60] F. VUILLOT, N. LUPOGLAZOFF and M. HUET - *Effect of a Pylon on Double Stream Jet Noise from Hybrid CAA Computations*. AIAA-2010-2049, 16th AIAA/CEAS Aeroacoustics Conference, 7-9 June 2010, Stockholm, Sweden
- [61] F. VUILLOT, N. LUPOGLAZOFF and G. RAHIER - *Double-Stream Nozzles Flow and Noise Computations and Comparisons to Experiments*. AIAA-2008-0009, 46th AIAA Aerospace Sciences Meeting and Exhibit, 7-10 Jan. 2008, Reno, NV, USA
- [62] S. WALLIN and A.V. JOHANSSON - *An Explicit Algebraic Reynolds Stress Model for Incompressible and Compressible Turbulent Flows*. Journal of fluid mechanics, Vol. 403, pp 89-102
- [63] P.M. WIKSTRÖM, S. WALLIN and A.V. JOHANSSON - *Derivation and Investigation of a New Explicit Algebraic Model for Passive Scalar Flux*. Physics of Fluids, Vol. 12, pp 688-702.
- [64] B. ZAMUNER and F. DUPOIRIEUX - *Numerical Simulation of Soot Formation in a Turbulent Flame With a Monte-Carlo PDF Approach and Detailed Chemistry*. CST, 158 :407-438, 2000

## Acronyms:

AEID (Acoustique et Environnement Induit au Décollage)	LEA (Liotnii Experimentalnii Apparat)
AUSM (Advection Upstream Splitting Method)	LES (Large Eddy Simulation)
CAA (Computational Aero-Acoustics)	LFRJ (Liquid Fueled RamJet)
CARS (Coherent Anti-Stokes Raman Scattering)	MILES (Monotone Integrated Large-Eddy Simulation)
CFD (Computational Fluid Dynamics)	MUSCL (Monotone Upstream Schemes for Conservation Laws)
CGNS (CFD General Notation System)	OVS (Obstacle Vortex Shedding)
CPU (Central Processing Unit)	PDF (Probability Density Function)
CNES (Centre National d'Etudes Spatiales)	PIV (Particle Image Velocimetry)
DDES (Delayed Detached Eddy Simulation)	PLIF (Planar Laser Induced Fluorescence)
DNS (Direct Numerical Simulation)	PVS (Parietal Vortex Shedding)
DOM (Discrete Ordinates Method)	RANS (Reynolds Averaged Navier-Stokes)
DOP (Duct Over Pressure)	RMS (Root Mean Square)
EAHFM (Explicit Algebraic Heat Flux Model)	SDR (Solid Ducted Rocket)
EARSM (Explicit Algebraic Reynolds Stress Model)	SIBLE (Simple Integrated Boundary Layer Equations)
EBU (Eddy-Break-Up)	SRM (Solid Rocket Motor)
EVM (Extended Vullis Model)	SST (Shear Stress Transport)
GMRES (Generalized Minimal RESidual)	TAPS (Twin Annular Premixing Swirling)
IOP (Ignition Over Pressure)	TPaSR (Transported Partially Stirred Reactor)



**Dominique Scherrer** graduated from «Ecole Centrale de Paris» in 1979. He joined Onera in the Energetics Direction in 1981. His main research topics concerned droplet combustion modeling, combined cycle propulsion, scramjet design and CFD. He has been the CEDRE project manager between 1996 and 2002. He is deputy director of the Fundamental and Applied Energetics Department since 1997.



**François Chedeveigne** graduated from a french engineer school (Supaéro), Dr. François Chedeveigne is a research scientist working at Onera within the Fundamental and Applied Energetics Department. He is in charge of the aerothermodynamics studies of the department and is deeply involved in the development of the software platform CEDRE regarding turbulence modelling.



**Philippe Grenard** graduated from the french engineer school École Polytechnique and Sup'Aéro in 2004. He is a research engineer working at Onera in the Fundamental and Applied Energetics Department (DEFA). He is in charge of computational activities regarding the in-house CEDRE platform (modelling, development and computations) in the Liquid Propulsion Unit. His activities focus on combustion and thermal loads in the combustion chamber and nozzle of liquid propellant engines.



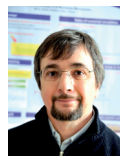
**Julien Troyes** received a Master Degree in «Modelisation and Simulation in Mechanics» in 1999 at Joseph Fourier University in Grenoble, France. He has been working at Onera as a research engineer since november 2000. His main activity is dedicated to the validation of the CEDRE software. Apart from this general topics, his research activities are focused on solid rocket motor jet applications (infrared signatures, ignition and duct overpressures waves ...).



**Angelo Murrone** graduated from "Institut Universitaire des Systèmes Thermiques Industriels " in 2000 and received his Ph. D. Degree in Mechanics and Energetics from "Université de Provence Aix-Marseille I" in 2003. He has been working as a research scientist in the Fundamental and Applied Energetics Department at Onera since 2004. His research concerns the numerical modeling of "dispersed" and "separated" two-phase flows. He is currently in charge of the development of the Eulerian solver SPIREE in the CEDRE code.



**Emmanuel Montreuil** (Associate Professor) obtained his Ph. D. Degree in Mechanics from "Université Pierre et Marie Curie – Paris 6" in 2000. He joined Onera in 2002 and has been involved in aircraft and rotorcraft icing for over 8 years, working on projects funding by the French civil aviation. He has been involved in both the development and application of several icing codes (2D and 3D), and has taken part in icing wind tunnel test campaigns in the frame work of the Onera-NASA-UIUC collaboration. He has organised and chaired sessions for the AIAA.



**François Vuillot** head of the 'software design and integration for the multi-physics and energetics unit at Onera, in charge of CEDRE software.



**Nicolas Lupoglazoff** graduated from « Ecole Nationale Supérieure de l'Aéronautique et de l'Espace» in 1987. He joined Onera in 1989 at the Energetics Direction. He is working in the CFD field and is specialized in aerodynamics and acoustics in engines, nozzles and jets.



**Maxime Huet** graduated from the "Ecole Centrale de Lyon" in 2006 and received a Master degree in Acoustics from Lyon University the same year. He joined Onera in 2007 as a research scientist. His work is mainly dedicated to jet and combustion noise simulations and their possible reduction.



**Bruno Sainte-Rose** graduated from "Ecole Centrale de Paris" in 2006 and received his Ph. D. Degree in Energetics in 2010. His Ph. D. thesis was focused on the development of turbulence and combustion models in Onera's code CEDRE. The aim of this work was to be able to run unsteady simulations of separated reactive flows. He joined the LEMMA company (Houston, Texas) in 2010, where he is working as a project engineer.



**Pascal Thorigny** joined Onera in 2001 after being graduated from ESTACA (Ecole Supérieure des Techniques Aéronautiques et de Construction Automobile). He is working in the Applied Aerodynamics Department in the "Missiles, Hypersonic and Launchers" unit as a CFD and mesh generation expert engineer. He his responsible for store separation under combat aircraft studies and in charge of the external aerodynamics and the booster separation phase characterisations of hypersonic vehicles like in the LEA project.



**Nicolas Bertier** graduated from ENS Cachan and PhD from Paris VI University (2006), is senior researcher in the Energetics department of Onera. He is in charge of the numerical simulation of reactive flows in aeronautic combustors. He has developed and validated the numerical methods and combustion models that were required to carry out LES with the CEDRE code of Onera. He is also teaching "energetics of aeronautic combustors" at Paris VI University.



**Jean-Michel Lamet** graduated from the « École Supérieure d'Ingénieurs de Poitiers » in 2005 and received his Ph.D. degree from « École Centrale de Paris » in 2009. During his Ph.D., he worked on the radiative transfer in atmospheric re-entry hypersonic flows. He now holds a position of research scientist in the Applied and Fundamental Energetic Department of Onera. His activity includes modelling and simulation of radiative transfer in combustion chambers and hypersonic flows. He is involved in the development of the ASTRE and REA code dedicated to radiative transfer.



**Thomas Le Pichon** graduated from ENSMA in 2008. He has been responsible for the Research Ramjet Program since 2009. This activity includes experimental and numerical study of the reacting flow in the Research Ramjet combustion chamber. His recent activities focused on combustion efficiency prediction, combustion instabilities and lean blow-out phenomenon.



**Emmanuel Radenac** is a research scientist at Onera. He graduated in 2003 from « Ecole Nationale Supérieure de l'Aéronautique et de l'Espace » and received his Ph.D. degree in 2006. During his Ph.D., he worked on numerical methods for thermal coupling of fluid and solid solvers (CHARME and ACCIA for CEDRE). Since 2007, he has been working in the field of solid propulsion.



**Aurélie Nicole** graduated in 1997 from ENSEEIHT in Toulouse. Then she completed her Fluid Mechanics Engineering Degree by 18 months of research at the University of Kyoto (Japan) in the nuclear engineering department. After having worked one year in the department of future project at CNES, she joined Onera in 2000 and started working on liquid rocket combustion instability. Since her arrival, she is in charge of the researches on high frequency instabilities and of the numerical simulation of reacting flow in liquid propulsion.



**Lionel Matuszewski** is a research engineer at the Onera working in the Liquid Propulsion Unit of the Fundamental and Applied Energetics Department (DEFA). He graduated from the Ecole Polytechnique and ISAE engineer schools in 2007. His research field is mainly focused on dense fluid modeling with application to supercritical combustion.



**Marc Errera** graduated from the "Ecole Centrale de Paris" in 1980 and obtained a Research Habilitation Thesis (Thèse d'Etat) from the University Pierre & Marie Curie (Paris 6) in 1990, in the field of in-cylinder flow in reciprocating engines. He is currently in charge of multidisciplinary projects.